

1 T -TiSe₂ investigated by 2PPE and TR-2PPE—a Correlated Electronic System

Dissertation
zur Erlangung des Doktorgrades
der Mathematisch-Naturwissenschaftlichen Fakultät
der Christian-Albrechts-Universität zu Kiel

vorgelegt von

Martin Wiesenmayer

Kiel, 2012

Referent:
Korreferent:
Tag der mündlichen Prüfung:
Zum Druck genehmigt:

Prof. Dr. Michael Bauer
PD Dr. Kai Roßnagel
15.06.2012
15.06.2012

gez. Prof. Dr. Lutz Kipp, Dekan

Contents

1	Introduction	1
1.1	Outline	4
2	Basics	7
2.1	Crystal and Electronic Structure of the TMDC 1 <i>T</i> -TiSe ₂	7
2.2	The Charge Density Wave Instability	11
2.2.1	Different Mechanisms of a CDW Phase Transition	14
2.3	Mathematical Description of Ultrashort Laser Pulses and Temporal Broadening	17
2.4	Photoemission of Surfaces	20
2.5	Time-Resolved Photoemission	22
2.5.1	Time-Resolved Two-Photon Photoemission (TR-2PPE)	23
2.5.2	A Short Outline of the Extraction of the Lifetime From the Autocorrelation Experiments	30
2.5.3	Two-Color Pump-Probe Experiments	32
2.5.4	The Typical Stages of the Laser Induced Excitation of the Electronic System	34
3	Experimental Setup	37
3.1	UHV Systems for Angle-integrated and Angle-resolved Photoemission Experiments	37
3.1.1	Cooling With the Liquid Nitrogen Heat Exchanger	39
3.2	Laser Systems and Optical Setups	40
3.2.1	Details of the Time-resolved IR-pump SH-probe Photoemission Experiment and Evaluation of the Data	50
3.2.2	Evaluation of the TAR-2PPE data	64
3.3	Crystal Growth and Preparation of TiSe ₂	67
4	Spectroscopy and Population Decay of a van der Waals Gap State in Layered 1<i>T</i>-TiSe₂	73
4.1	Spectroscopy of the Unoccupied States	76
4.1.1	Analysis of the Band Dispersion	76
4.1.2	SH-2PPE Spectroscopy—Analysis of the Unoccupied Bands	79
4.1.3	Spectroscopy at Varying Photon Energy	89

4.1.4	Discussion of the Surface Projected Band Structure	95
4.1.5	The Origin of the Ti Excess Atoms	97
4.2	Decay Dynamics of the Unoccupied States of 1 <i>T</i> -TiSe ₂	99
4.2.1	The Influence of Alkali Adatoms	104
4.2.2	Discussion of the Observed Time Resolved Data	106
4.3	Summary and Conclusion	109
5	Static Response of 1<i>T</i>-TiSe₂ to Thermal and Laser Excitation	111
5.1	Spectroscopy Within the Normal Phase	113
5.1.1	Detailed Overview of the Thermal Modifications	117
5.1.2	The Mean Plateau Intensity—Thermal Behavior and Applicability for Normalization	124
5.1.3	The Work Function Increase	145
5.1.4	The Thermal Modifications of the Chalcogen <i>p</i> Bands	154
5.2	Spectroscopy at Varying Incident Laser Fluence	182
5.2.1	Overview of the Laser Induced Modifications	184
5.2.2	Laser Induced Modifications of the Spectral Shape	187
5.2.3	Summary	198
5.2.4	The Momentum Range of the Laser Induced Modification of Spectral Weight	200
5.3	Spectroscopy in the CDW Phase	205
5.3.1	Thermal Dependence	205
5.3.2	Laser Fluence Dependence	211
5.4	Summary and Conclusion	217
6	Ultrafast Dynamics of the Laser Induced Modifications of the Se 4<i>p</i> Bands of 1<i>T</i>-TiSe₂	221
6.1	One-color TR-2PPE experiments in autocorrelation mode	222
6.1.1	Ultrafast Laser Induced Effects in the Room Temperature Phase	224
6.1.2	The Low Temperature charge density wave (CDW) Phase	233
6.2	Two-color pump-probe experiments on TiSe ₂	242
6.2.1	Overview of the Ultrafast Dynamics to be Expected in the Two- Color Experiment	246
6.2.2	Considerations Concerning the Two-Color Experiment	247
6.2.3	The Laser Induced Dynamics and Fluence Dependence	254
6.2.4	Oscillatory Behavior of the Intensity and Energy in the Vicinity of the Fermi Energy	267
6.3	Summary and Conclusion	276
7	Investigation of the Ultrafast Dynamics of the Backfolded Se 4<i>p</i> Bands at the \bar{M}-point	279

8 Summary	285
A Supplementary Information	291
A.1 Prerequisites for the Analysis of Spectral Modifications	291
A.1.1 Methods of Data Analysis	291
A.1.2 Homogeneity of the TiSe ₂ Surface	301
A.2 Definition of Quantities Used for Data Evaluation	306
A.2.1 The Temperature Coefficient	306
A.2.2 Evaluation of Spectral Peaks—Characteristics of a Gaussian Shape	308
A.3 Count Rate Drifts of the Experimental Setup—Stable Photoemission Using the CSA	309
A.3.1 Overview of the Unstable Photoemission Signal	310
A.3.2 Analysis of the Unstable Photoemission	313
A.3.3 Influence of the CSA on the Spectral Shape at Low Fluence	321
A.3.4 Acquisition of Stable Spectra	324
A.3.5 Some Final Remarks on the Acquisition of Stable Photoemission Spectra	326
B List of Abbreviations	329
Bibliography	354
List of Publications	355

Zusammenfassung

Im Rahmen dieser Arbeit untersuchen wir mittels spektroskopischer Methoden die elektronischen Zustände sowie deren Ultrakurzzeitdynamik zweier spezifischer Übergangsmetall-dichalcogenide - $1T$ -TiSe₂ und $1T$ -TiTe₂. Die Wahl dieser Schichtkristalle ist darin begründet, dass TiSe₂ einen Phasenübergang in einen Ladungsdichtewellenzustand bei niedrigen Temperaturen aufweist. Der Phasenübergang von $1T$ -TiSe₂ ist - obschon seit vielen Jahren intensiv untersucht - immer noch rege diskutiert. Es ist daher unser Bestreben, mit dieser Arbeit einen Beitrag zu diesem Diskurs zu leisten. TiTe₂ hingegen verbleibt metallisch leitend im gesamten Temperaturbereich und dient somit als Referenz.

Die angewandte experimentelle Methode ist die Zwei-Photonen Photoemission (2PPE), welche es erlaubt besetzte und unbesetzte Zustände zu untersuchen. Da wir - nach unserem Wissen - hier die erste 2PPE Untersuchung an TiSe₂ durchführen, untersuchen wir zunächst ausführlich die Struktur dieser Spektren. Die Kombination zeit- und winkelaufgelöster 2PPE Verfahren erlaubt es, ein unbesetztes Band zu identifizieren, welches von Pehlke et al. (Z. Phys. B **66**, 31-37, 1987) im Rahmen von Bandstrukturrechnungen für überschüssige Titanatome in der van der Waals Lücke des Kristalls vorhergesagt wurde. Dies ist - nach unserem Wissen - die erste experimentelle Beobachtung dieses spezifischen, von Titanorbitalen erzeugten Defektzustandes.

Den Kern dieser Arbeit bildet eine detaillierte Untersuchung laserinduzierter Modifikationen des 2PPE Spektrums. Der sorgsame Vergleich mit thermischen Experimenten erlaubt es, solche Effekte zu identifizieren. Eine detaillierte Analyse thermischer und laserinduzierter spektraler Modifikationen bildet die Basis für weiterführende zeitaufgelöste Experimente.

Konventionelle zeitaufgelöste 2PPE erlaubt die Identifikation ultraschneller, laserinduzierter Dynamik des elektronischen Systems. Zeitaufgelöste Pump-Probe Experimente ergänzen dies durch eine detaillierte Analyse dieser Dynamik. Hier regt ein intensiver Pump-laserpuls das elektronische System an - bei Proben in der Ladungsdichtewellephase wird diese gestört - und ein zeitversetzter Probepuls erzeugt 2PPE Spektren. Dies gestattet die Beobachtung der zeitlichen Entwicklung des elektronischen Systems nach der Anregung.

Die detaillierte Kenntnis des Zeitverhaltens nach der Anregung durch den Laser liefert wertvolle Hinweise auf vom elektronischen System oder vom Gitter getragene Prozesse. Dies ist umso mehr von Interesse, da die Diskussion um den Ursprung der Tieftemperatur-Ladungsdichtewelleinstabilität in TiSe₂ im Grunde eine Frage nach einem Gitter oder einem elektronisch vermittelten Prozess ist.

Wir schließen unsere Betrachtungen mit einem Ausblick auf ein neues zeit- und winkelaufgelöstes Photoemissionsverfahren. Durch die Kombination eines intensiven, ultrakurzen Infrarotpumpimpulses mit einem ultrakurzen höherem Harmonischen Puls von mehreren zehn Elektronenvolt Energie erhalten wir mit hoher Zeitauflösung simultan Zugang zur gesamten ersten Brillouin Zone unserer Probe. Damit können wir nicht nur am $\bar{\Gamma}$ -, sondern auch am \bar{M} -Punkt die laserinduzierte Störung der Ladungsdichtewellephase beobachten.

Abstract

In the framework of this dissertation we investigate the electronic states and their ultrafast dynamics of two specific transition metal dichalcogenide— $1T$ -TiSe₂ and $1T$ -TiTe₂—using spectroscopic methods. These layered crystals are selected, because TiSe₂ features a phase transition into a charge density wave state at low temperatures. The phase transition of $1T$ -TiSe₂ is—although studied intensively for many years—still lively discussed. Our object in view is therefore to contribute with this work to the discussion. TiTe₂, on the other hand, remains metallic conducting within the whole temperature range and thus serves as a reference.

The experimental approach used is two-photon photoemission (2PPE) which enables the investigation of occupied and unoccupied states. Because we—to our knowledge—perform the first 2PPE investigation of TiSe₂, we thoroughly analyze the structure of these spectra at first. The combination of time and angle resolved 2PPE methods enables the identification of an unoccupied band which was predicted by band structure calculations by Pehlke et al. (Z. Phys. B **66**, 31–37, 1987) for excess titanium atoms within the van der Waals gap of the crystal. This is—to our knowledge—the first experimental observation of this specific defect state derived from titanium orbitals.

The detailed investigation of the laser induced modifications of the 2PPE spectrum is the focus of this work. Careful comparison to thermal experiments enables the identification of such effects. A detailed analysis of thermal and laser induced spectral modifications builds the foundation of further time resolved experiments.

Conventional time resolved 2PPE enables the identification of the ultrafast, laser induced dynamics of the electronic system. Time resolved pump–probe experiments complement this by a detailed analysis of the dynamics. In this case, the intensive pump laser pulse excites the electronic system—for samples within the charge density wave, the CDW will be perturbed—and a temporally delayed probe pulse generates the 2PPE spectra. This allows for the observation of the temporal evolution of the electronic system after excitation.

Detailed knowledge about the temporal response after the laser excitation yields valuable information about processes driven by the electronic system or the lattice. This is very instructive, because the discussion about the origin of the low-temperature charge density wave instability of TiSe₂ is basically a question of an electronic or lattice mediated process.

We conclude our investigations with an outlook on a novel time and angle resolved photoemission method. The combination of an intensive, ultrashort infrared pump pulse and an ultrashort high harmonic pulse of several tens of electron volts energy allows for a simultaneous access to the whole first Brillouin zone of our sample with high temporal resolution. This enables the observation of laser induced perturbations of the charge density wave not only at $\bar{\Gamma}$, but also at the \bar{M} -point.

1 Introduction

The compound class of the layered transition metal dichalcogenides (TMDCs) has been intensively studied over the past decades. Some are considered model systems for a wide range of phenomena associated with a reduced dimensionality, like, enhanced correlation effects. Examples for these are charge density wave (CDW) instabilities [1–3], Mott insulator transitions [4], and superconductivity [5, 6]. $1T$ -TiSe₂, a group IV TMDC, is of particular interest. It is the only compound of this group exhibiting a charge density wave (CDW) transition which is accompanied by a structural transition associated with the formation of a $(2 \times 2 \times 2)$ super-lattice [7, 8].

The system has been the subject of a number of studies in the past, yet, there is still an ongoing and lively discussion about the origin of this phase transition [3, 7–11], as well as the conducting character—metallic or semi-metallic—of $1T$ -TiSe₂ [12–15]. Concerning the phase transition, several potential mechanisms have been proposed. Amongst others, these are:

- (i) Fermi-surface nesting [8, 9],
- (ii) a band-type Jahn-Teller mechanism [3, 7], and
- (iii) an excitonic insulator mechanism [11],

as well as combinations thereof [10]. Recently, even a competing CDW and superconducting phase was reported for copper intercalated TiSe₂ [5, 6].

A distinction between the proposed models requires a detailed investigation of the electronic structure, especially in the vicinity of the Fermi energy—it is there, where the most peculiar modifications are observed upon the phase transition. A (band-type) Jahn-Teller mechanism, for instance, is expected to be accompanied by an energy lowering of the Se $4p$ bands, which is associated with a Ti–Se bond shortening upon the transition into the CDW phase [16]. Characteristics at the Γ - and the L-point of the Brillouin zone, on the other hand, are indicative of a phase transition driven by Fermi-surface nesting [9]. A common and very efficient approach used to address such a problem is the detailed study of the system in the room temperature normal and the low temperature CDW phase by means of angle-resolved photoemission spectroscopy (ARPES), cf., e. g., references [7, 10, 14].

However, ARPES maps primarily the occupied electronic band structure. The study of the properties of the electronic excitation spectrum can also contribute to the comprehensive understanding, for instance, of the complex behavior of the TMDC compounds

discussed here. Until now, only the inverse photoemission (IPE) technique has been employed for the study of the unoccupied electronic bands of $1T$ -TiSe₂ [17–19]. The Ti $3d^*$ band {conduction band 2 (CB2) in reference [9]} was identified this way in the Γ M-direction in qualitative agreement with band structure calculations [9].

In the first experimental part of this work we apply—to our knowledge for the first time—the angle-resolved two-photon photoemission (AR-2PPE) method to map the momentum resolved, unoccupied band structure of $1T$ -TiSe₂. The two-photon photoemission (2PPE) technique allows for a significantly higher energy resolution than IPE [20]. The method can be extended to a time resolved (stroboscopic) scheme: time-resolved two-photon photoemission (TR-2PPE) or time- and angle-resolved two-photon photoemission (TAR-2PPE), which enables the monitoring of the ultrafast population decay of bulk and surface electronic excitations at a temporal resolution of a few femtoseconds ($1 \text{ fs} = 1 \times 10^{-15} \text{ s}$) [21]. Such measurements can provide insight into the decay mechanism of bulk decoupled electronic excitations. This has been shown, e. g., in the context of image potential states [21–25] and adsorbate excitations at noble metal surfaces [26–30].

Indeed, our 2PPE spectra provide evidence for the existence of a non-dispersive excitation band at $E - E_F \approx 2.3 \text{ eV}$. On the basis of previous band structure calculations we assign this band to electronic excitations of excess titanium atoms embedded in the interlayer van der Waals gap of TiSe₂. The accompanying time resolved experiments reveal a lifetime of this excess titanium atom excitation of about 7 fs, which is significantly longer than the lifetime of a Ti $3d^*$ band excitation within the TiSe₂ layers—this difference points to a considerable decoupling of the excess state excitation from the bulk electronic states and further supports our assignment to a state localized within the van der Waals gap. This result shows that an efficient decoupling of electronic excitations in resonance with bulk electronic states can emerge not only in front of a surface, but also at specific sites located within the bulk.

In the second and third part we focus on the temporal evolution of the laser induced perturbation of the CDW/PLD, using a one-color TR-2PPE and a two-color time-resolved IR-pump SH-probe photoemission scheme. Time resolved photoemission allows for the investigation of the non-equilibrium dynamics of a strongly correlated electronic system [4, 31].

For such experiments, however, we need to understand, how the static 2PPE spectra are modified for varying absorbed laser fluences, especially considering potential thermal effects. Generally, the photoemission spectrum changes in characteristic ways with the sample temperature—spectral features broaden and also binding energies, as well as the work function change [32–37]. Comparison to the laser induced modifications allows for a quantification of the corresponding thermal effects. A detailed knowledge of the laser induced increase of the sample temperature is important especially for experiments

within the CDW/PLD phase, because the absorbed pulses can already increase the sample temperature such, that the phase transition can be fully reversed. For time resolved experiments within the CDW phase the laser fluence must not be too high.

Our time resolved investigation focuses on the ongoing discussion on the mechanism of the CDW transition in $1T$ -TiSe₂ which is basically a question about the degree, to which the transition is driven by the electronic or the lattice system [3, 7–11]. In this context, the understanding of the fundamental timescales is crucial [4].

Indeed, we find agreement of our time resolved data with a combination of an electronic and lattice contribution. The screening by the laser generated free carriers destabilize the CDW [11, 14, 38], while the time scale of the spectral modifications, as well as the observation of typical thermal changes, also show a lattice contribution—the excitation of the CDW amplitude mode [39]. The latter also leads to a distinct oscillatory signal in the temporal evolution of the photoemission data—such a contribution by the amplitude mode of a CDW was also reported for other systems for photoelectron [4, 31] and reflectivity data [40–42].

An outlook on a new method capable of mapping the ultrafast dynamics within the whole first Brillouin zone concludes the experiments discussed here. This approach combines an infrared (IR) pump pulse ($h\nu = 1.57$ eV) with an extreme ultraviolet (EUV) probe pulse ($h\nu = 43$ eV) generated by high harmonic generation (HHG) [43, 44]. The generation of high harmonics is a powerful tool to provide coherent and ultrashort EUV light pulses using a tabletop system, i. e. without the need for an accelerator facility [43, 45]. It is employed, for instance, for the study of laser-assisted photoemission (LAPE) [46] which enables access to adsorbate dynamics and attosecond electron dynamics [47]—the generation of attosecond pulses was reported [48–50]. Furthermore, high harmonic (HH) were reported to be an element-selective probe for the investigation of demagnetization dynamics [51, 52].

In comparison to our earlier time resolved experiments, using EUV pulses is very advantageous for the investigation of the CDW phase transition of $1T$ -TiSe₂, because the high photon energy enables access to the full first Brillouin zone. In a single spectrum we therefore observe the laser induced temporal evolution of the spectral features at the $\bar{\Gamma}$ - and \bar{M} -point simultaneously [53, 54] with ultrashort time resolution—the pulses show durations of 32 fs for the IR and less than about 10 fs for the HHs.

Why is such data very instructive? We want to understand the (pump) laser induced temporal evolution of the perturbed CDW/PLD. Our earlier experiments are restricted to the $\bar{\Gamma}$ -point only, yet, the most prominent spectral modifications are indeed observed at the \bar{M} -point where the CDW state yields a strong contribution of the backfolded Se $4p$ bands (see section 2.2 and, e. g., references [7, 10, 14, 54, 55]). Access to the full first Brillouin zone enables a more complete picture of the dynamics involved.

1.1 Outline

This thesis is structured as follows:

- Chapter 2 presents a short overview of the theoretical base of this work. First, in 2.1 and 2.2 we discuss the peculiar characteristics of the TMDCs investigated in this work, focusing on the low temperature CDW phase and the formation of intercalate compounds for these layered systems—this will be relevant for the interpretation of our data in section 4.1. Our experiments employ ultrashort laser pulses which are necessary for 2PPE, as well as for time resolved experiments. Section 2.3 formulates the relevant mathematical description of such pulses. Section 2.4 discusses how the photoemission of a surface of a solid is to be interpreted. Finally, in section 2.5 we present time resolved photoemission experiments. We focus on the methodology and, especially considering the two color pump–probe scheme which is employed in section 6.2, generally expected dynamics induced by the absorption of an intense, ultrashort laser pulse.
- Chapter 3 shows how these methods are realized in an experimental setup. Photoemission spectroscopy relies on a complex ultrahigh vacuum (UHV) system, discussed in section 3.1, as well as a laser system capable of producing sufficiently short pulses, presented in section 3.2. We introduce the different laser systems and photoelectron analyzers used in this work. Furthermore, we show the complex laser setups necessary for the time resolved experiments performed in this work. Additionally, section 3.3 gives a short report on the growth of layered TMDCs, focusing on potential contaminations and deviations resulting from the growth process, as well as their identification.
- The experimental part of this thesis consists of chapters 4–6 which feature different experimental focuses:
 - We begin in chapter 4 with very basic questions with respect to our photoemission spectroscopic method: How does a 2PPE spectrum of $1T$ -TiSe₂ and TiTe₂ “look”? Which electronic states are mapped by such spectra? This chapter thus focuses on the basic understanding of spectroscopic data acquired using the very low photon energies characteristic for the 2PPE method. To our knowledge, no 2PPE data yet exists for these systems.
 - Our spectroscopic experiments have revealed a strong influence of the laser fluence on the spectral shape. In chapter 5 we investigate this effect further, beginning with temperature dependent data in section 5.1 which introduce a reference for the identification and quantification of thermal modifications of the spectrum. The corresponding fluence dependent experiment in section 5.2 enable us to identify peculiar laser induced effects—the temporal evolution

of these is investigated in chapter 6. The chapter concludes with section 5.3 which complements the data of section 5.1 with data for temperatures below the room temperature—well into the CDW phase. This section will especially focus on the question, whether the CDW to normal conducting phase transition can be induced solely by the absorption of the laser.

- Chapter 6 investigates the temporal evolution of the laser induced spectral modifications observed statically in section 5.2. Section 6.1 shows a fast and simple experimental approach—a one-color autocorrelation method—which enables us to identify interesting ultrafast dynamics, as well as the parameters to tune. Furthermore, we compare our two TMDCs using this method. Section 6.2 finally employs a more complex and time consuming approach—a two-color pump–probe scheme. In contrast to the autocorrelation method here the pump and probe events are distinguishable, i. e. the probe pulse does not act as a second pump, which enables a more detailed look into the temporal evolution of the laser induced perturbations.
- This thesis concludes with an outlook on a new, state-of-the-art experiment in chapter 7. Using a two-color pump–probe scheme with IR pump pulses and HH probe pulses the whole first Brillouin zone becomes accessible in a time resolved experiment with femtosecond resolution. The simultaneous access not only to the $\bar{\Gamma}$ -point, but also to the \bar{M} -point proves to be very instructive for the investigation of the laser induced perturbation of the CDW phase, because the latter region of reciprocal space is even more influenced by the phase transition.

2 Basics

This chapter provides the necessary theoretical foundation for this work. We discuss the specifics of the sample systems employed—the compound class of the transition metal dichalcogenides (TMDCs)—especially considering peculiarities arising from the layered structure of these compounds. We use ultrashort laser pulses for the two-photon photoemission (2PPE) and the time resolved experiments throughout this work. The specific challenges of generating pulses as short as possible will be tackled. Finally, we provide theoretical background to the time resolved experiments, focusing on the analysis of such data, as well as a short discussion of the general electronic dynamics associated with the excitation by an intense and ultrashort pump pulse.

2.1 Crystal and Electronic Structure of the TMDC 1*T*-TiSe₂

In general, TMDCs are compounds with the structural formula TX_2 —with T being a transition metal (group IV–VIII) and X representing two chalcogen atoms of either sulfur, selenium, or tellurium (see, e. g., references [1, 56, 57]). The TMDCs divide into layered and non-layered compounds, the latter being observed for transition metals of group VII and above [56]. In this work we investigate two titanium based TMDCs, TiSe₂ and TiTe₂, which both exhibit a qualitatively very similar crystal structure. We restrict our discussion to TiSe₂ and focus on TiTe₂ whenever considerable deviations occur.

The TX_2 crystals are built by planes of X–T–X tri-layers, i. e. a center layer of the transition metal is sandwiched in between two adjacent chalcogen layers which are hexagonally packed [56, 63]. Consequently, the TMDCs discussed here feature the typical first Brillouin zone of a hexagonal lattice (see figure 2.1). We employ photoemission from the surface of the crystals (see section 2.4), i. e. we investigate the surface projected band structure of our samples, which is described by a surface Brillouin zone with symmetry points $\bar{\Gamma}$, \bar{K} , and \bar{M} (see figure 2.1).

Figure 2.2(a) shows a three-dimensional (3D) model of such a crystal. The white spheres represent the chalcogen and the black spheres correspond to the transition metal atoms. Figure 2.2(b) presents a schematic representation of the structure of the TMDCs investigated here which is called “1*T*” in the typical nomenclature. The number denotes how many crystal planes need to be considered to define the stacking periodicity of the structure and *T* declares the trigonal symmetry of the crystal [63]—the coordination of

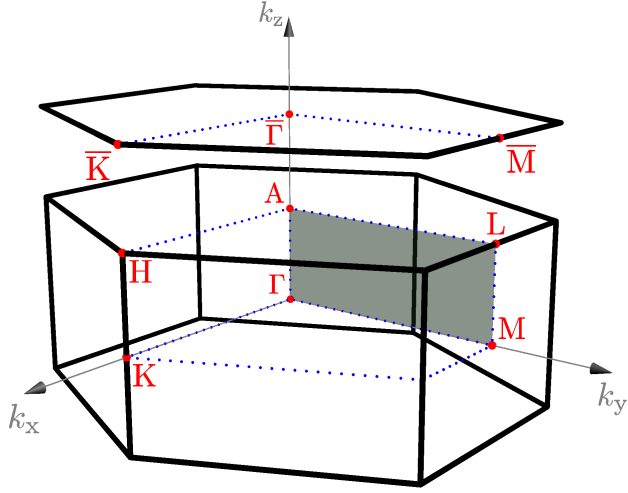
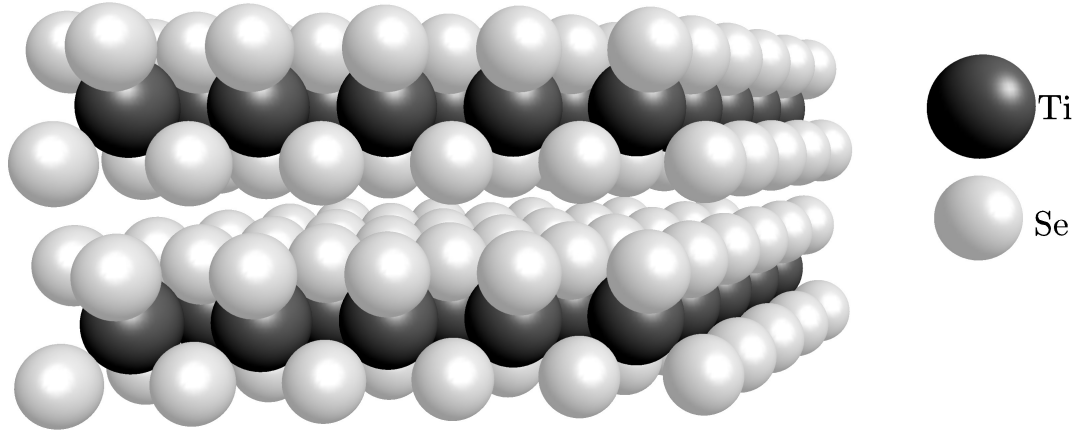


Figure 2.1: Brillouin zone of TiSe_2 . The high symmetry points are labeled. Our experiments focus on the ΓM -direction (ΓALM -plane).

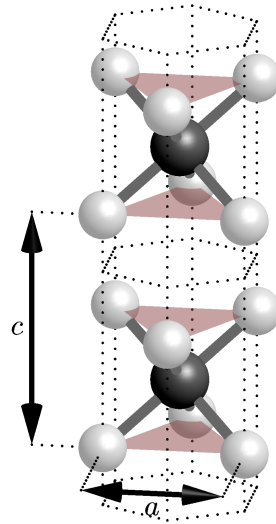
the chalcogen atoms around the transition metal is, however, octahedral [1]. For TiSe_2 the lattice parameters are $a = (3.540 \pm 0.001) \text{ \AA}$ and $c = (6.008 \pm 0.003) \text{ \AA}$ as derived from neutron scattering experiments [64, 65].

The layered structure of these TMDCs is basically a consequence of differences in the interatomic bonding. Within the crystal planes strong, for instance covalent, bonds dominate, while the planes are bound to each other only by weak, van der Waals interaction [58, 60, 63, 66]. In consequence, such crystals can be easily cleaved, i. e. the different planes can be separated by applying a small pulling force (see section 3.3), rendering the preparation of a clean surface very simple. Beside these mechanical peculiarities of the sample, the weak interaction perpendicular to the crystal planes leads to anisotropies of the sample properties, like for the conductivity [8, 56], the frequency of phonon modes [63, 67], the optical properties [68], and the electronic band structure [13].

The layered structure leads to a quasi-2D behavior of such crystals. A closer look at the band structure of $1T\text{-TiSe}_2$ and $1T\text{-TiTe}_2$ demonstrates the localization of certain electronic bands within the crystal planes. Figure 2.3 shows the band structure of $1T\text{-TiSe}_2$ schematically. Please note, that the figure does not provide calculated band structure data, but a rather crude rendition of the relevant electronic bands. The black, red, and green color corresponds to potential initial, intermediate, and final states, respectively, of the 2PPE experiments presented in this work (see chapter 4) and the bands observed in such spectra are shown by full, thick lines. The low dimensionality is directly observed, for instance, for the Se $4p_x$, $4p_y$ bands, which feature a strong dispersion parallel to the sample surface (ΓM). They show, however, only little dispersion perpendicular (ΓA , see section 4.1 and, e. g., references [9, 60, 69]), i. e. the electrons



(a) The layered crystal structure of 1T-TiSe₂.



(b) Coordination of the 1T structure.

Figure 2.2: The structure of 1T-TiSe₂. (a) Layers of titanium atoms (black spheres) are sandwiched between two layers of selenium (white spheres). The crystal sheets are composed by such tri-layers and are separated by a van der Waals gap. (b) Octahedral coordination in the 1T structure of TiSe₂. The lattice constant, a , and the distance of the crystal planes, c , are shown.

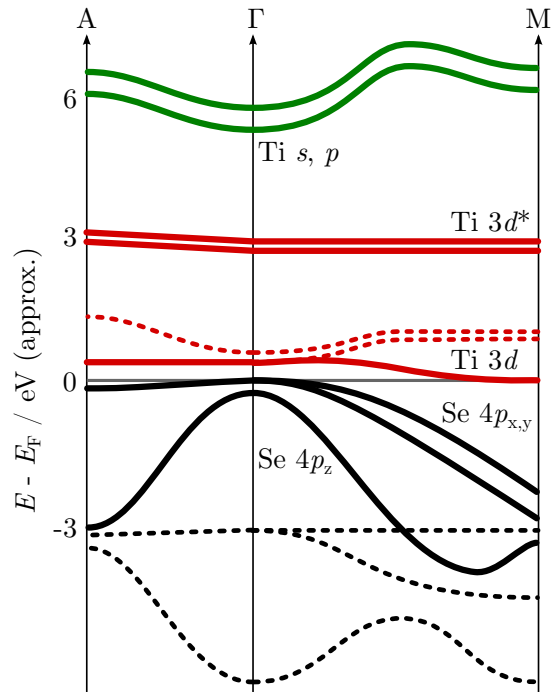


Figure 2.3: Schematic band structure of 1T-TiSe₂ based on band structure calculations [9, 58–62]. The colors represent potential initial, intermediate, and final states of the 2PPE process (see section 4). Dashed lines show bands, which are not relevant for our 2PPE spectroscopy. For details see text.

within these bands are delocalized only within the crystal planes, while they almost do not exceed the perpendicular confines of those planes by passing into an adjacent plane. In this sense, the electronic system is thus quasi-two-dimensional. This localization is also observed, for example, for the Ti $3d$ derived bands.

However, some bands, especially the Se $4p_z$ band in case of TiSe_2 , still feature considerable perpendicular dispersion, leading to a certain degree of three-dimensionality—the crystal layers are not completely decoupled. Although only van der Waals interaction contributes to the bond between the crystal planes, the Se $4p_z$ orbitals indeed hybridize. However, both the resulting bonding and anti-bonding bands are filled, thus yielding no contribution to the effective inter-plane bond [60]. The strength of this coupling can be tuned by intercalation, i. e. the introduction of atoms or molecules into the van der Waals gap of the crystals. This increases the separation of the planes, reducing the coupling and consequently reducing the perpendicular electronic dispersion [13, 70–73].

Table 2.1 summarizes and compares the essential properties of the two TMDCs, $1T$ - TiSe_2 and $1T$ - TiTe_2 , investigated in this work. Especially one distinctive characteristic is most striking: only TiSe_2 features a low temperature phase transition featuring the occurrence of a charge density wave (CDW). We therefore discuss this interesting property in detail in the following section 2.2.

2.2 The Charge Density Wave Instability

The reduced dimensionality and the corresponding anisotropy of the layered TMDCs give rise to peculiar electronic ground states which deviate from the simple Fermi gas model expected for 3D metals [84]. Low dimensional systems are prone to electronic correlations which lead to new ground states, like, charge density waves [31, 40, 76, 85, 86] or super conductivity [87–90].

Indeed, $1T$ - TiSe_2 features a phase transition into a commensurate $2 \times 2 \times 2$ charge density wave (CDW) associated with a corresponding periodic lattice distortion (PLD) upon lowering of the temperature. The critical temperature is approximately $T_0 = 202 \text{ K}$ [8]. In contrast, $1T$ - TiTe_2 is a good reference system for the investigation of CDW associated effects, as it features a very similar electronic structure [79, 91], yet, it exhibits no phase transitions at all [74, 91]. We employ this difference of TiSe_2 and TiTe_2 especially in chapters 5 and 6.

In this section we briefly address the question: *What is a charge density wave?* It is very instructive in this context to first refer to the most simple occurrence of this phenomenon in a one dimensional metal. This is shown schematically in figure 2.4. Here we focus on the general features of a CDW/PLD. Our discussion in this section, although referring to TiSe_2 , is of a general nature as the actual mechanism of the phase transition in case of $1T$ - TiSe_2 is still in dispute. Section 2.2.1 presents potential mechanisms relevant for this case.

Table 2.1: A comparison of the specific characteristics of $1T$ -TiSe₂ and $1T$ -TiTe₂. The symbols are as follows: the lattice parameters, a and c , as per figure 2.2(b), the carrier density, n , the ratio of the resistivity perpendicular and parallel to the lattice planes, $\varrho_{\perp}/\varrho_{\parallel}$, the electron–phonon coupling parameter, λ , the Debye temperature, Θ_D , and the critical temperature of the CDW phase transition, T_0 .

	$1T$ -TiSe ₂	$1T$ -TiTe ₂
a^a	$(3.540 \pm 0.001) \text{ \AA}$	$(3.778 \pm 0.001) \text{ \AA}$
c^a	$(6.008 \pm 0.003) \text{ \AA}$	$(6.493 \pm 0.001) \text{ \AA}$
crystal structure ^{b,c}	$1T$ -CdI ₂	
space group ^{b,c}	D_{3d}^3	
type	semimetal/semiconductor ^d	metal ^{e,f}
n^g	$2.8 \times 10^{20} \text{ cm}^{-3}$ to $7.1 \times 10^{20} \text{ cm}^{-3}$	$1.3 \times 10^{21} \text{ cm}^{-3}$
$\varrho_{\perp}/\varrho_{\parallel}$	2.5^h	$35\text{--}40^c$
λ	$(i) 0.37, (ii) 0.8^i$	$(i) 0.22, 0.67, (ii) 0.83^j$
Θ_D	221 K^k	225 K^j
CDW	commensurate ^l	none ^{e,f}
superlattice	$2 \times 2 \times 2^l$	
T_0	202 K^l	

^a estimated by neutron scattering, see reference [65]

^b reference [56]

^c reference [74]

^d references [12, 14], semiconducting character proposed for ideal crystals [15]

^e reference [75]

^f references [57, 76]

^g references [5, 63, 77, 78] for $1T$ -TiSe₂, references [79, 80] for $1T$ -TiTe₂

^h approximate value at 300 K, see reference [8]

ⁱ (i) derived from a reflectivity measurement [81], while (ii) is calculated using an approach for superconductive materials, see f; while the first value corresponds to a specific phonon wavevector, the latter integrates over all wavevectors.

^j estimated using a Debye model (see also section 5.1.4–d) from (i) ARPES data [74, 82] and (ii) a resistivity measurement [82]

^k reference [83]

^l reference [8]

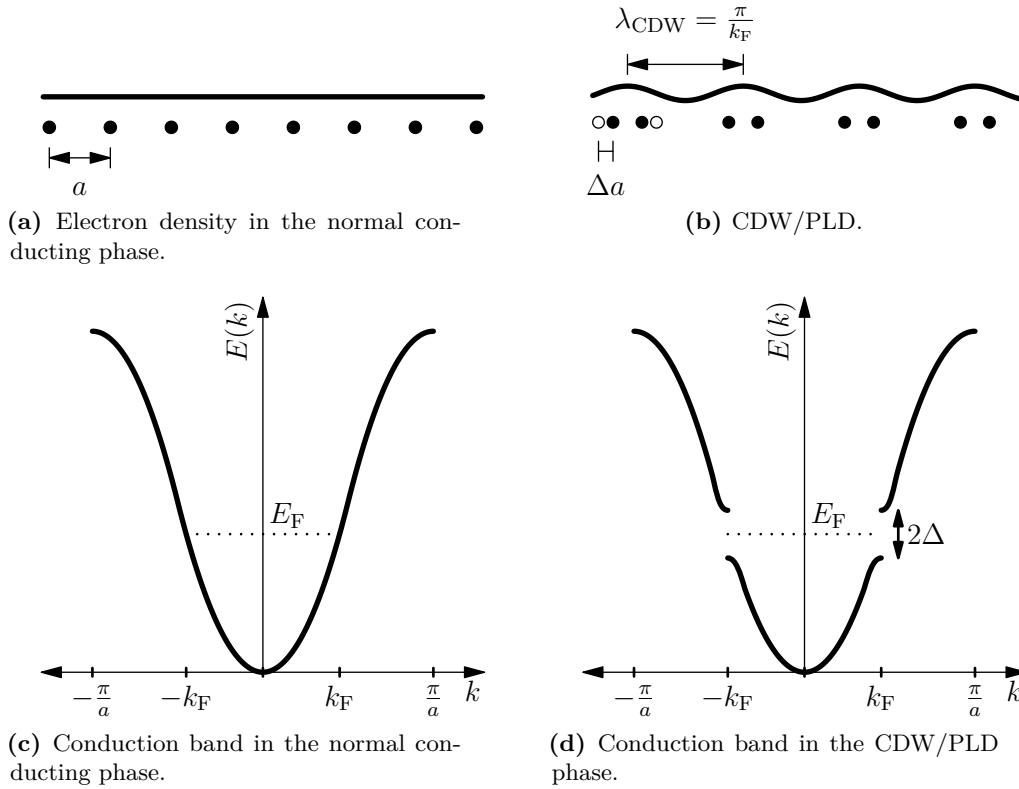


Figure 2.4: (a) In the normal conducting phase the atoms (circles) occupy their usual position (the atomic distance a is exemplary) and the electron density is distributed uniformly (line). (c) In the case of a metal the conduction band is filled to the Fermi energy E_{F} at the corresponding wavevector k_{F} . (b) Upon the CDW transition the electron density is modulated with a wavelength of $\lambda_{\text{CDW}} = \frac{\pi}{k_{\text{F}}}$. This leads to a modulation of the lattice (PLD, indicated by a shift of the atomic positions Δa which does not need to be equal for all atoms), too. (d) The CDW produces a band gap 2Δ at the Fermi surface at k_{F} . See, e. g., reference [62].

Figures 2.4(a) and (c) show the normal conducting phase of a one-dimensional (1D) metal following references [62, 76] and references therein. The charge density is constant [line in (a)], i. e. the electrons are uniformly distributed. The metal is characterized in the normal conducting phase by a partially filled electronic band [see figure 2.4(c)] cut by the Fermi energy E_F at k_F .

In one dimension, the system may lower its energy by undergoing a Peierls transition [62]. This is shown in figures 2.4(b) and (d). The CDW is a standing modulation of the charge density [line in (b)] with a wavelength $\lambda_{\text{CDW}} = \frac{\pi}{k_F}$. The CDW is accompanied by a PLD, because a lattice distortion is necessary to guarantee charge neutrality [92, 93]. The consequent increase of the periodicity of the lattice leads to a backfolding of the electronic bands (see section 3.3). In case of TiSe_2 the periodicity is doubled, leading to a commensurate $2 \times 2 \times 2$ superstructure in the CDW phase [94]. However, in general, the superstructure is often incommensurate and transitions between different CDW phases are known [62].

The formation of a CDW and PLD induces a lowering of the energy of the occupied states and an increase of the energy of the unoccupied states at E_F , i. e. an opening of an energy gap 2Δ , which reduces the one-electron band energy [76]. If this energy gap overcompensates the elastic energy necessary for the lattice distortion [62], the CDW and PLD become energetically favorable and the distortion forms the system's new ground state. Electron-phonon coupling is necessary for the described Peierls instability (see section 2.2.1 for details).

In summary, a CDW is an electronic ground state for a system governed by strong correlation effects. In this case the formation of a collective redistribution of the electron density can be energetically favorable. Charge neutrality requires a corresponding PLD, i. e. a redistribution of the ionic cores of the lattice. A CDW is characterized by a peculiar modification of the conductivity [63] which allows for its experimental identification [7, 95]. Although the described Peierls mechanism is less likely to exist for a system $>1\text{D}$, the basic effects of the CDW transition are demonstrated.

2.2.1 Different Mechanisms of a CDW Phase Transition

So far we introduced the Peierls mechanism for a CDW phase transition. However, different mechanisms may result in the formation of a CDW. In case of $1T\text{-TiSe}_2$ the occurrence of a CDW and an accompanying PLD is well known from experimental data, however, the origin thereof remains the focus of continuing discussion [3, 7–11]. A multitude of different mechanisms have been proposed, mainly differing in the degree to which the transition is driven by the electronic system or the lattice (see, e. g., reference [76])—the typical time scales of such processes [96] may provide to a better understanding in case of TiSe_2 (see chapter 6). In this section we shall therefore discuss the potential transition mechanisms briefly, focusing on their different specifics.

- If the CDW and PLD are generated by *electron-phonon* coupling, there are two distinct cases for weak and strong coupling:

The Fermi surface nesting mechanism. Weak electron-phonon coupling is a prerequisite of the Peierls mechanism presented in section 2.2. This mechanism is at its core an instability of the Fermi surface, which reflects in the wavelength of the CDW being defined by k_F ($\lambda_{\text{CDW}} = \frac{\pi}{k_F}$), i. e. the CDW is generally incommensurate [76].

However, the Peierls transition is less likely to occur for systems of higher dimensionality than 1D because of the necessary Fermi surface nesting. A reduced dimensionality is indeed crucial in real 3D systems [76, 97]. This is because of the specifics of the Fermi surfaces of such systems: ideally, for a 3D crystal the Fermi surface is a sphere. A vector \mathbf{q} coupling two electronic states at the Fermi surface can only be found for two states, or points on the sphere. For a quasi-1D system, however, the Fermi surface consists of two parallel planes, i. e. a \mathbf{q} spanning those planes can be found which connects all states on the Fermi surface simultaneously. For quasi-2D systems the Fermi surface is ideally cylindrical and the connectible states reside within lines along this cylinder [97].

In consequence, for a reduced dimensionality the presence of large parallel parts of the Fermi surface becomes more likely and thus the density of states coupled by one vector \mathbf{q} , the wave vector of the CDW, can be large. For the formation of a CDW and corresponding PLD these states need to be coupled to establish the new Brillouin zone of the superstructure as well as the energy gap necessary for the gain in electronic energy. This mechanism is thus much less likely to occur for systems of higher dimension than quasi-1D.

The band-type Jahn-Teller transition. For strong electron-phonon coupling the Fermi surface becomes less important considering the phase transition [76]. In contrast, the coherence length is short in this case which results in the importance of the local chemical bondings. The CDW tends to be commensurate with the underlying lattice. The CDW state does, furthermore, prevail above the transition temperature, T_0 , as fluctuations, i. e. only the long range coherence is lost. This corresponds to the observation of electron-hole pairs above T_0 .

While the weak coupling case is comparable to the Peierls mechanism, the strong coupling corresponds to the Jahn-Teller effect for low dimension [76]. In the picture of the band-type Jahn-Teller effect the CDW is formed as follows: The distortion of the crystal lattice by a PLD leads to an energetic lowering of the electronic bands [7] associated with the shortening of the Ti-Se bond in case of $1T$ -TiSe₂. Charge neutrality then demands the formation of a

corresponding CDW.

- A mechanism derived primarily from *electron–electron* coupling is:

The excitonic insulator transition. In case of an electronic system providing two bands close to E_F , which feature a small indirect gap or overlap, an excitonic insulator instability may occur which establishes a CDW solely by electron–electron coupling [11, 54, 55]. A prerequisite for such a mechanism is a sufficiently small number of electrons and holes as fulfilled by a semimetal. The screening is then reduced such, that the Coulomb interaction of the charge carriers allows for the formation of bound states of the electrons and holes, which are called *excitons* [84, 92, 98]. Upon the change of a sample parameter, like, e. g., the temperature, the band gap (or overlap) can be reduced below the binding energy of the excitonic ground state. The system then becomes unstable with respect to the spontaneous formation of excitons [55, 92, 98].

But how may these excitonic excitations lead to the formation of a CDW? Kohn [98] describes the occurrence of a CDW phase transition in terms of the formation of a new type of ground state. Initially, the ground state is dominated by fluctuations of the CDW in the presence of the excitons [84]. Following the argument of Halperin and Rice [92] these excitons may be modeled like a weakly repulsive Bose gas. The transition into the low temperature CDW phase is then understood in terms of a Bose condensation into the excitonic state of the lowest binding energy.

At its core the CDW transition is a purely electronic process driven by the interaction of electrons and holes. In contrast to the mechanisms originating from strong electron–phonon coupling, the PLD is a mere byproduct induced by a still present electron–phonon interaction.

- The CDW can also be the result of a primarily *phononic* process:

The antiferroelectric transition. The CDW transition of TiSe_2 shows a temperature dependence similar to the behavior observed in antiferroelectric systems, as observed by Busmann-Holder and Büttner [99]. Consequently, these authors modeled the phase transition in terms of a non-linear electron–phonon interaction based on the a ferroelectric phase transition. At the core of this mechanism lies the back-folding of a soft zone-boundary phonon mode to the center of the Brillouin zone [99]. Generally, an antiferroelectric crystal features an increase of the dielectric constant with decreasing temperature (for $T > T_0$, with the transition temperature, T_0), no spontaneous net polarization, and a small dielectric constant below T_0 [100]. The transition leads to the formation of a superstructure consisting of two lattices with anti-parallel polarization. The antiferroelectric transition is discussed by Cochran [101] in terms of an

instability of a certain phonon mode, i. e. it is understood considering the lattice dynamics. The vibration of the lattice leads to displacements of the atomic cores which may induce a polarization and an antiferroelectric superstructure may become the new ground state of the system [101]. For a detailed discussion of this mechanism refer, e. g., to references [100–102].

Please note, that simple Fermi surface nesting is very unlikely in case of 1T-TiSe₂, because of the unfavorable shape of the Fermi surface [103]; we thus do not consider this mechanism. The most lively discussed candidates to model the CDW transition in TiSe₂ are the band-type Jahn-Teller transition and the excitonic insulator transition [7, 10, 11, 76, 104, 105]. These mechanisms are not necessarily exclusive and a combination thereof was proposed, for instance, by van Wezel et al. [105] and Rossnagel [76]. Considering, that both a mechanism based on electron–phonon and electron–electron interaction is to be considered, the typical timescales of the dynamics of the electronic system and the lattice are very instructive for discerning contributions of these two systems (see chapter 6).

2.3 Mathematical Description of Ultrashort Laser Pulses and Temporal Broadening

In this section we give a very short overview of the mathematical description of laser pulses. We will briefly discuss group velocity dispersion (GVD) and third order dispersion (TOD) and the influences on the pulses thereof. Our discussion is based on references [106, 107].

The electric field $E(t)$ of a linearly polarized laser pulse is described by equation (2.1) with an envelope function $A(t)$ (temporal amplitude), the angular light frequency $\omega_0 = 2\pi\nu_0$ and the absolute phase Φ_0 , which determines the phase of the envelope and the oscillation of the electric field of the light [see e. g. 106, 107].

$$\begin{aligned} E(t) &= A(t) \cos[\Phi_0 + \omega_0 t + \phi(t)] \\ &= A(t) \cos[\Phi(t)] \end{aligned} \tag{2.1}$$

The additional time dependent phase $\phi(t)$ leads to a variation of the frequency of the pulse with time. The instantaneous light frequency $\omega(t)$ is described by:

$$\begin{aligned} \omega(t) &= \frac{d}{dt} \Phi(t) \\ &= \omega_0 + \frac{d}{dt} \phi(t) . \end{aligned} \tag{2.2}$$

Such a change of frequency within the pulse is called *chirp*.

The electric field of the pulse can be composed from monochromatic waves due to the superposition principle. $E(t)$ is then connected to a complex valued spectrum $E(\omega)$ via the Fourier transformation:

$$\begin{aligned} E(t) &= \mathcal{F}_\omega[E(\omega)](t) = \frac{1}{2\pi} \int_{-\infty}^{\infty} E(\omega) e^{i\omega t} d\omega \\ E(\omega) &= \mathcal{F}_t[E(t)](\omega) = \int_{-\infty}^{\infty} E(t) e^{-i\omega t} dt, \end{aligned} \quad (2.3)$$

following the definition of reference [106].

The spectrum derived in this way is symmetrical, i. e. it is mirrored at zero, and it is defined for positive and negative frequencies. In the following we will use the positive part of the spectrum which is sufficient to describe our pulses. Therefore, we divide the spectrum in two parts:

$$\begin{aligned} \forall \omega \geq 0, \quad E^+(\omega) &:= E(\omega) \\ \forall \omega < 0, \quad E^-(\omega) &:= E(\omega). \end{aligned}$$

Using the Fourier transform in equation (2.3) we derive $E^\pm(t)$, the electric field corresponding to positive or negative frequencies, respectively. While $E(t)$ is a real valued function, $E^\pm(t)$ are complex valued and complex conjugated functions. $E(t)$ is derived from these functions by $E(t) = E^+(t) + E^-(t) = 2\text{Re}[E^\pm(t)]$. The Fourier transform of equation (2.3) yields:

$$\begin{aligned} E^\pm(t) &= |E^\pm(t)| e^{i\Phi(t)} \\ &= \frac{1}{2} A(t) e^{i\Phi(t)}. \end{aligned}$$

Analogously the complex spectrum for positive frequencies $E^+(\omega)$ can be derived:

$$E^+(\omega) = |E^+(\omega)| e^{-i\Phi(\omega)},$$

which defines the spectral phase $\Phi(\omega)$. While the temporal phase $\Phi(t)$ defines the instantaneous light frequency $\omega(t)$ [see equation (2.2)], the spectral phase defines the group delay $T_g(\omega)$:

$$T_g(\omega) = \frac{d}{d\omega} \Phi(\omega), \quad (2.4)$$

which contains information about the relative temporal delay of the different superposed frequencies. Equation (2.5) shows the expansion of the spectral phase $\Phi(\omega)$ into a Taylor series around the central frequency ω_0 . The different order of the terms are due to different contributions to the spectral phase: (*i*) The zero order term corresponds to the

absolute phase in the time domain Φ_0 , i. e. $\Phi_0 = -\Phi(\omega_0)$. (ii) The first order term of the Taylor series leads to a temporal shift of the envelope function $A(t)$ relative to the carrier wave. (iii) The higher order terms modify the temporal structure of $E(t)$.

$$\begin{aligned}\Phi(\omega) &= \sum_{j=0}^{\infty} \frac{1}{j!} \cdot (\omega - \omega_0)^j \cdot \underbrace{\frac{d^j}{d\omega^j} \Phi(\omega)}_{\Phi^{(j)}(\omega_0)} \Big|_{\omega=\omega_0} \\ &= \Phi(\omega_0) + \Phi'(\omega_0) \cdot (\omega - \omega_0) + \frac{1}{2} \Phi''(\omega_0) \cdot (\omega - \omega_0)^2 \\ &\quad + \frac{1}{6} \Phi'''(\omega_0) \cdot (\omega - \omega_0)^3 + \dots\end{aligned}\tag{2.5}$$

Gaussian shaped pulses can be described by:

$$E_G^+(t) = a \cdot e^{-b \frac{t^2}{\Delta\tau^2}} e^{i\omega_0 t},\tag{2.6}$$

with the absolute phase and time dependent phase set to zero. The constants a and b are left arbitrary here, while the second order term of the spectral phase $[\frac{1}{2}\Phi''(\omega_0) \cdot (\omega - \omega_0)^2]$ adds a quadratic term to the temporal phase. The pulse will be chirped because of this second order term—this leads to temporal broadening. $E(t)$ is calculated by Fourier transformation of the corresponding $E(\omega)$, for details see for instance references [106, 107]. In this work we will focus on the effect on the temporal width of the pulses. Be $\Delta\tau$ the temporal full width at half maximum (FWHM) of the transform-limited pulse in equation (2.6) and $\Delta\tau'$ the corresponding temporal width of the chirped pulse, then:

$$\Delta\tau' = \sqrt{\Delta\tau^2 + \left[4 \ln(2) \frac{\Phi''}{\Delta\tau}\right]^2},\tag{2.7}$$

i. e. in presence of GVD described by the second order phase coefficient Φ'' the pulse duration increases.

The third order term $[\frac{1}{6}\Phi'''(\omega_0) \cdot (\omega - \omega_0)^3]$ of the phase leads to TOD. Due to the TOD the temporal pulse shape becomes asymmetric and side-pulses may be introduced. Although the appearance of additional side-pulses renders the FWHM useless as a measure for the pulse duration, it is still possible to derive the standard deviation σ of the pulse:

$$\sigma = \frac{1}{2} \sqrt{c_1 \Delta\tau^2 + c_2 \left(\frac{\Phi'''}{\Delta\tau^2}\right)^2},$$

with the constants $c_i, i \in \{1, 2\}$. We see, that a third order phase coefficient Φ''' always broadens the pulses. However, in the presence of additional side-pulses, the main contribution residing within the center pulse is narrower than in the TOD-free case. This leads to a peculiar problem: if the comparably weak side-pulses are not well resolved and

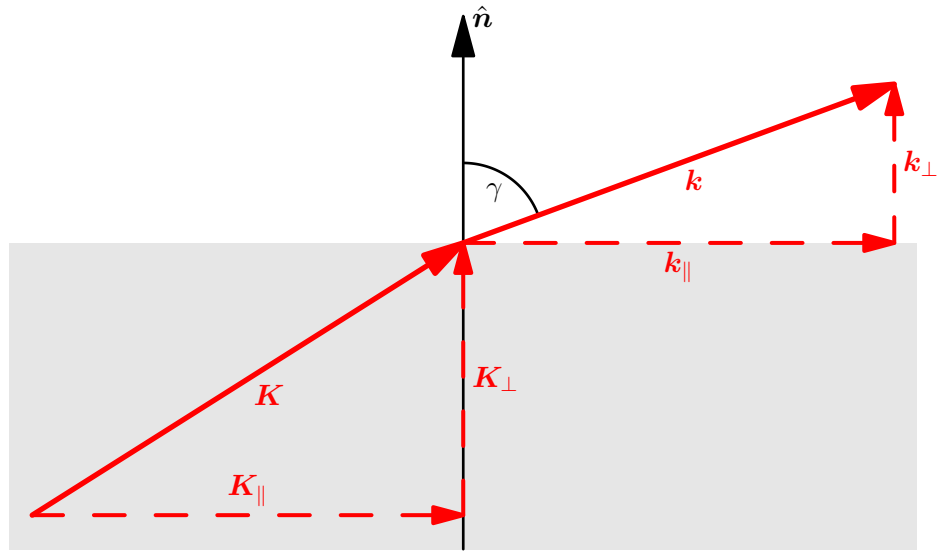


Figure 2.5: A photoelectron is transmitted through the surface of a crystal (shaded in gray, surface normal \hat{n}) into the vacuum. Its wave vector \mathbf{K} within the crystal becomes the wave vector \mathbf{k} in the vacuum, because of the loss of symmetry in the direction of \hat{n} . Only the fraction parallel to surface of the wave vector is conserved, i. e. $k_{\parallel} = K_{\parallel}$, but $k_{\perp} \neq K_{\perp}$.

consequently overlooked within the data, the pulse duration may deceptively be evaluated too small. A careful check for side-pulses generated by TOD is thus crucial. Exemplary autocorrelation shapes are presented and discussed, for instance, in the “*Handbook of Lasers and Optics*” [106].

2.4 Photoemission of Surfaces

Angle resolved photoemission enables us to simultaneously map the energy and the momentum of the photoelectrons emitted from the sample by measuring their kinetic energy and emission angle. However, the crystal symmetry perpendicular to the surface, and consequently the translational invariance, is lost [108]. Consequently, by emission of the photoelectron through the crystal’s surface into the vacuum only the wave vector component parallel to the surface is conserved, $k_{\parallel} = K_{\parallel}$, while the fraction perpendicular to surface changes, $k_{\perp} \neq K_{\perp}$.

In general, we cannot determine K_{\perp} from \mathbf{k} , but we can calculate k_{\parallel} and thus K_{\parallel} . In the following we will use k_{\parallel} exclusively, because the parallel component of the wave vector is the same within and outside of the crystal. This information is sufficient to acquire the surface projected band structure, which includes all bands projected along the perpendicular axis. For bands of only small dispersion for k_{\perp} such a band structure

reveals the parallel dispersion¹. Using the kinetic energy E_{kin} of the photoelectron:

$$\begin{aligned} E_{\text{kin}} &= \frac{\hbar^2}{2m_e} |\mathbf{k}|^2 \\ &= \frac{\hbar^2}{2m_e} (|\mathbf{k}_{\parallel}|^2 + |\mathbf{k}_{\perp}|^2) , \end{aligned} \quad (2.8)$$

we can express the parallel component of the photoelectron's wave vector as:

$$|\mathbf{k}_{\parallel}| \equiv |\mathbf{K}_{\parallel}| = \sqrt{\frac{2m_e}{\hbar^2} E_{\text{kin}}} \sin \gamma , \quad (2.9)$$

with the electron mass m_e , the reduced Planck constant \hbar , and the angle γ of the wave vector relative to the surface normal. In conclusion, we can calculate the parallel component of the photoelectron's wave vector from its experimentally measured kinetic energy and emission angle.

We will now discuss an interesting consequence of equation (2.8). The energy $E - E_{\text{F}}$ of the low energy cut-off of the spectrum increases—the spectrum becomes therefore narrower—for off-normal photoemission, i. e. for $|\mathbf{k}_{\parallel}| > 0 \text{ \AA}^{-1}$. This is because of the fact, that only photoelectrons with a positive perpendicular component of the wave vector outside the crystal ($|\mathbf{k}_{\perp}| > 0 \text{ \AA}^{-1}$) are able to reach the vacuum. For $\mathbf{k}_{\perp} < 0 \text{ \AA}^{-1}$ the electrons are reflected back into the crystal; the kinetic energy is not sufficient to pass the surface potential in this case [108, 109]. By solving equation (2.8) for $|\mathbf{k}_{\perp}|$ we derive:

$$|\mathbf{k}_{\perp}| = \sqrt{\frac{2m_e}{\hbar^2} E_{\text{kin}} - |\mathbf{k}_{\parallel}|^2} .$$

A photoelectron can only be transmitted to the vacuum for $|\mathbf{k}_{\perp}| > 0 \text{ \AA}^{-1}$, which defines a minimum value of the kinetic energy:

$$\begin{aligned} \sqrt{\frac{2m_e}{\hbar^2} E_{\text{kin}} - |\mathbf{k}_{\parallel}|^2} &> 0 \\ E_{\text{kin}} &> \frac{\hbar^2}{2m_e} |\mathbf{k}_{\parallel}|^2 . \end{aligned} \quad (2.10)$$

A consequence of equation (2.10) is an increase of the minimum kinetic energy of the photoelectron for $\mathbf{k}_{\parallel} \neq 0 \text{ \AA}^{-1}$ needed for detection outside of the crystal. From equations (2.9) and (2.10) follows a parabolic shape of the low energy cutoff of the photoemission spectra as a function of the parallel momentum [109] and a \sin^2 -shape as a function of the emission angle γ .

The work function, Φ , which is the minimum energy necessary to excite an electron from E_{F} into the vacuum [110], can only be extracted from photoemission spectra

¹If there is a considerable perpendicular dispersion, the parallel dispersion for all \mathbf{k}_{\perp} is superimposed, i. e. the band becomes a broad area in the spectrum.

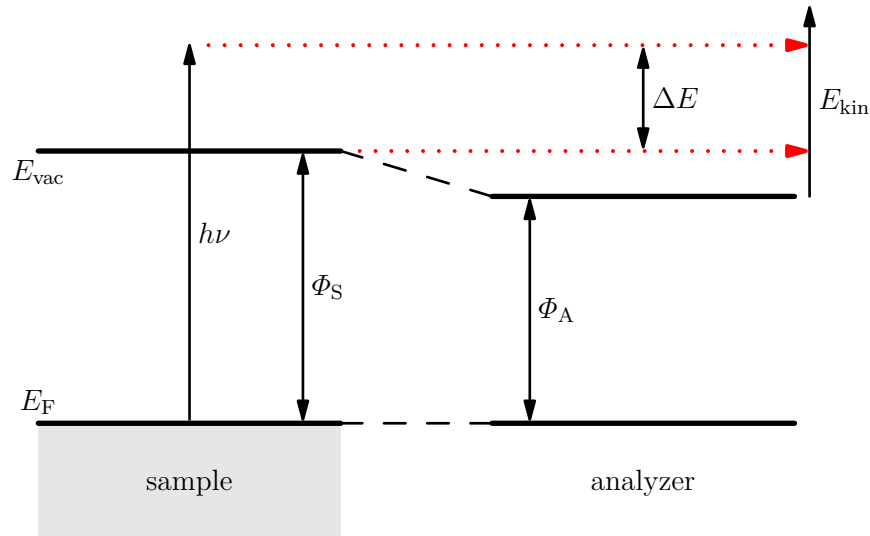


Figure 2.6: Energetic scheme for the estimation of the work function from photoemission spectra. Fermi energy, E_F , and vacuum energy, E_{vac} , of sample and analyzer in electrical contact are shown, as well as the work function of the sample, Φ_S , and the analyzer, Φ_A . Photons of energy $h\nu$ excite photoelectrons above E_{vac} of the sample. The width of the photoemission spectrum, ΔE , is defined by photoelectrons originating from E_F and those which just leave the sample, i. e. which just transcend Φ_S (red arrows).

for normal emission ($\mathbf{k}_{\parallel} = 0 \text{ \AA}^{-1}$). Figure 2.6 presents a schematic representation of the extraction of Φ from photoemission data. The high energy cutoff of the spectrum corresponds to photoelectrons originating from E_F , while the low energy cutoff corresponds to photoelectrons which are just emitted into vacuum, i. e. which have zero kinetic energy in front of the sample². We need the energetic difference of high and low cutoff of the spectrum (see the red arrows in the figure), ΔE , as well as the exciting photon energy, $h\nu$, to calculate the work function as $\Phi = h\nu - \Delta E$. For simplification we denote, from now on, the work function of the sample as Φ . Please note, that $h\nu$ corresponds to the energy of the photoelectrons at the high energy cutoff of the spectrum. A consequence of equation (2.10) is that photoelectrons with zero kinetic energy cannot be emitted for non-zero parallel momentum.

2.5 Time-Resolved Photoemission

In the following we discuss two experimental approaches which enable the study of the temporal evolution of perturbations—or non-equilibrium conditions—of the electronic

²Of course, the photoelectrons at the low energy cutoff have non-zero kinetic energy within the energy analyzer.

system on an ultrafast (femtosecond) timescale. A prerequisite for such experiments is the availability of ultrashort pulses (see section 2.3) with a temporal duration of the order of magnitude of the processes to be investigated [96], i. e. in our case of only a few ten femtoseconds. The laser capable of producing such pulses are discussed in section 3.2.

2.5.1 Time-Resolved Two-Photon Photoemission (TR-2PPE)

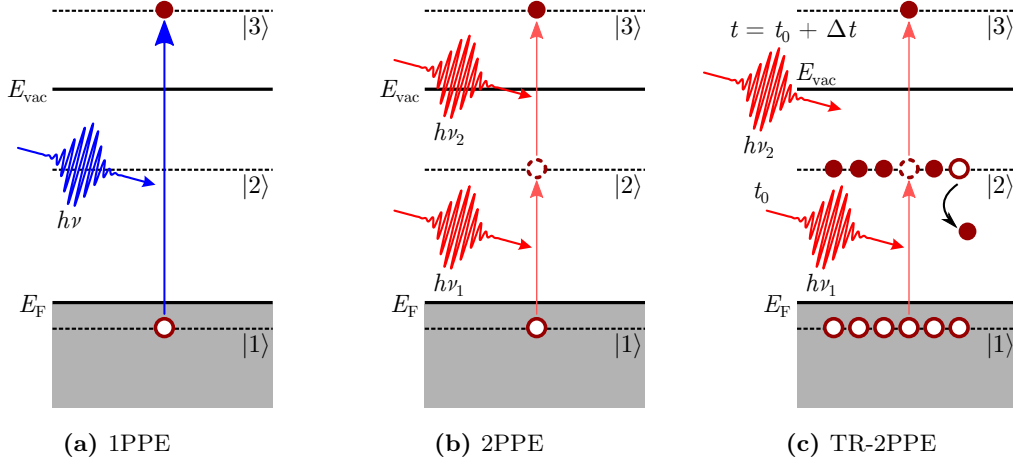


Figure 2.7: Schematic representation of the photoemission processes employed in this work. (a) The photon energy $h\nu$ is sufficient to excite an electron from the occupied initial state $|1\rangle$ into a final state $|3\rangle$ above the vacuum energy, E_{vac} , in a 1PPE excitation. (b) For 2PPE the generation of the photoelectron proceeds either resonantly or off-resonantly via an intermediate state $|2\rangle$ by the absorption of two photons with $h\nu_i < \Phi$, $i \in \{1, 2\}$, with the work function, Φ . (c) By separating two exciting laser pulses by a defined temporal delay, Δt , the evolution of the population of $|2\rangle$ generated by the first pulse is monitored by the second pulse.

To investigate the properties of the TMDCs discussed in this work, we employ the method of photoemission spectroscopy. The probably most straightforward approach is 1PPE as shown schematically in figure 2.7(a). Here one photon of sufficient energy ($h\nu > \Phi$, with work function, Φ) excites an electron from an initial state, $|1\rangle$, into a final state, $|3\rangle$, above the vacuum energy, E_{vac} , which can then be detected with respect to its kinetic energy and momentum (see section 3.1). This technique can thus only access occupied ($E - E_F \leq 0$ eV) and final states ($E - E_F \geq \Phi$) [35], depending on the photon energy.

The investigation of the unoccupied electronic states in between E_F and E_{vac} is possible by, for example, inverse photoemission (IPE) [111]. A better approach with respect

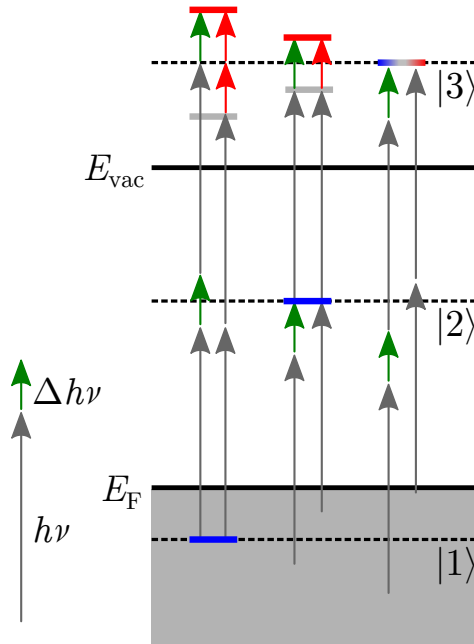


Figure 2.8: The photoelectron spectrum of initial, intermediate, and final states ($|1\rangle$, $|2\rangle$, and $|3\rangle$, respectively) is influenced differently upon changing the photon energy, $h\nu$ (gray arrow), by $\Delta h\nu$ (green arrow). The optical transitions are shown by three pairs of arrows, each showing left the transition for the changed photon energy (gray/green) and right the initial transition (gray) with the relevant difference in the energy of the photoelectron emphasized by red arrows. The electronic state mapped in the spectrum is marked by a blue bar. Initially, the photoelectrons originating from these states are excited to the energies shown by a gray bar above E_{vac} . This energy is shifted to the red bars for photons of $h\nu + \Delta h\nu$. The red arrows show the differences: $2\Delta h\nu$ for initial, $\Delta h\nu$ for intermediate, and no change at all for final states.

to the energetic resolution is 2PPE [112], which we employ throughout this work [see figure 2.7(b)]. Here, two photons are necessary to generate a photoelectron, because the photon energy is chosen such, that $h\nu_i < \Phi$ ($i \in \{1, 2\}$), while $h\nu_1 + h\nu_2 > \Phi$. If the excitation proceeds resonantly via an (initially) unoccupied intermediate state, $|2\rangle$, this state is mapped in the photoelectron spectrum, additionally to the initial and final state contributions. Of course, in case of $h\nu_i > \Phi$ a 2PPE process is still possible, but the 1PPE transition is significantly more likely, so that the signal of the 1PPE spectrum covers the less intense 2PPE contributions—we return to this phenomenon shortly when discussing the nonlinearity of the 2PPE process. Therefore, the photon energy is kept well below the work function for 2PPE experiments. Please note, that we employ one color, i. e. $h\nu := h\nu_1 = h\nu_2$, photoemission processes throughout this work; only for alignment purposes we resort to two color experiments (see section 3.2.1–d).

Therefore, 2PPE spectroscopy maps contributions of the occupied initial and the unoccupied intermediate and final states simultaneously within one photoelectron spectrum—see sections 3.2 and figure 4.7 in section 4.1 for examples. Figure 2.8 visualizes the differences in the excitation paths for the three stages of the photoemission process. A variation of the photon energy allows for a separation of these contributions [113]:

- Occupied, initial states lead to peaks in the photoelectron spectrum which shift in energy by $2\Delta h\nu$ with a photon energy change of $\Delta h\nu$. Because two photons are needed to excite an electron from an initial state, the energetic change of both photons needs to be considered.
- For intermediate states, the first photon populates this state, i. e. for a different value of the photon energy, the intermediate state is populated from a different initial state. Therefore, only the energetic change of the second photon, which generates the photoelectron, is relevant. Thus, a shift of only $\Delta h\nu$ is expected for the peaks associated with intermediate states in the spectrum.
- Spectral signatures of final states do not shift at all.

See also figure 4.7 in section 4.1.

The 2PPE process enables the investigation of the population decay of the intermediate state. This is achieved by introducing a carefully controlled temporal delay between a first absorbed laser pulse—the pump pulse—which excites electrons from the initial to the intermediate state and a second pulse—the probe pulse—which excites electrons from the intermediate to a final state above E_{vac} (see section 3.2). Figure 2.7(c) illustrates the time-resolved two-photon photoemission (TR-2PPE) process schematically. The arrival time of the pump pulse at the sample surface defines the time zero, $t_0 = 0$ fs, of the time resolved experiment, while the probe pulse is separated by a tunable temporal delay, Δt . This enables monitoring of the temporal evolution of the electronic system by the probe pulse after excitation by the pump pulse.

For the investigation of the decay of the population of an initially unoccupied intermediate state, it is sufficient to acquire a cross-correlation trace³. This is the temporal evolution of the spectral intensity integrated for a certain energy and momentum range (see section 3.2.2). In case of equal pump and probe pulses an autocorrelation trace is taken. Our objective in this section is to understand the structure of such an autocorrelation trace.

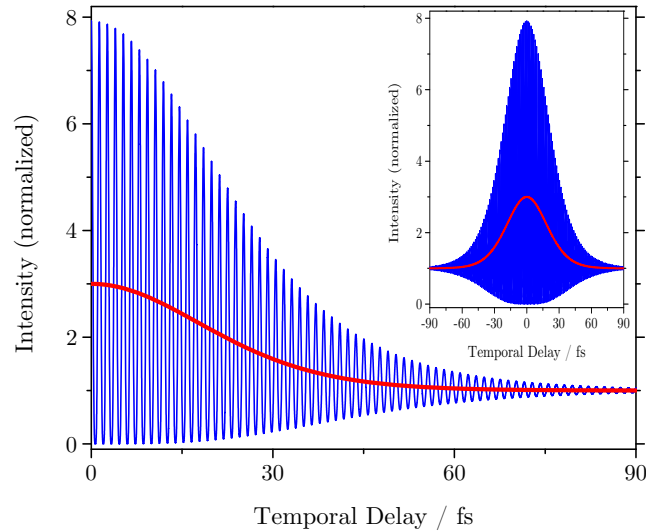


Figure 2.9: Autocorrelation trace (blue) simulated for sech^2 -shaped laser pulses of about 28 fs temporal FWHM. The ratio of peak signal at zero temporal delay Δt to the signal at $\Delta t \rightarrow \infty$, i. e. the signal for temporally separated single pulses, is 8 : 1. The phase-averaged autocorrelation trace (red) is derived by FFT filtering and shows a corresponding ratio of 3 : 1. It corresponds to the experimentally acquired autocorrelation traces (see section 3.2). The inset shows an overview of the symmetrical shape of the traces.

We first resort to the most straightforward case: the laser autocorrelation. In our experiment, such a curve can be acquired, if the lifetime of the intermediate state is negligible, which is the case for strongly off-resonant excitation—see section 3.2 for details—, i. e. the temporal evolution of the photoemission signal is solely depending on the pump and probe pulses.

We employ the quadratic intensity autocorrelation technique [106] within this work. A nonlinearity in the detection of the signal is necessary to gain insight into the temporal duration of a laser pulse. If the intensity of the pulses is linearly combined, the detected signal is basically a sum of the autocorrelation of the electric field of the

³We will see in section 6.2.4 that the analysis of more complex spectral changes, like a modification of the binding energy, require the acquisition of full spectra at different temporal delays.

pulses and an offset, i. e. it contains only information about the spectrum and intensity of the pulses [106]. By introducing a nonlinearity, for instance, by using a quadratic second harmonic generation (SHG) process for the detection, a quadratic autocorrelation, $I_{AC}(\tau)$, is acquired:

$$I_{AC}(\tau) = \int_{-\infty}^{\infty} \{ [E(t) + E(t + \tau)]^2 \}^2 dt. \quad (2.11)$$

In our photoemission experiments we use the 2PPE process, which is intrinsically a nonlinear process. The photoemission signal depends quadratically on the intensity of the incident laser pulses, i. e. 2PPE provides the necessary nonlinearity in the detection process.

An *interferometric* autocorrelation as described by equation (2.11) is presented in figure 2.9 (blue). This curve is calculated by summing the electrical fields of the laser pulses for different time delays between them. The interference of the electric fields, $E(t)$, of both pulses leads to the observed pattern of constructive and destructive interference. The maximum of this trace at $\tau = 0$, i. e. for perfect overlap of the pulses, is significantly enhanced with respect to the signal for temporally non-overlapping pulses. From equation (2.11) follows [106]:

$$\begin{aligned} I_{AC}(\tau = 0) &= \int_{-\infty}^{\infty} [2E(t)]^4 dt &= 16 \int_{-\infty}^{\infty} [E(t)]^4 dt \\ I_{AC}(\tau \rightarrow \infty) &= \int_{-\infty}^{\infty} [E(t)]^4 dt + \int_{-\infty}^{\infty} [E(t)]^4 dt &= 2 \int_{-\infty}^{\infty} [E(t)]^4 dt. \end{aligned} \quad (2.12)$$

Equations (2.12) reveal the observed intensity ratio of the autocorrelation in time zero, $I_{AC}(\tau = 0)$, and for temporally well separated pulses, $I_{AC}(\tau \rightarrow \infty)$, of 8 : 1.

Experimentally we do, however, not acquire such an interferometric autocorrelation. First, this is because of restrictions of our experimental setup. The delay stage is not stable enough to provide the necessary temporal resolution⁴. Second, the pulse duration and the population lifetime of an intermediate state of the 2PPE process can already be extracted from phase-averaged autocorrelation traces [96]. Figure 2.9 includes such an intensity autocorrelation (red), \bar{I}_{AC} , as calculated by Fourier filtering—experimentally the data is averaged by destroying the interference (see section 3.2) already during the measurement. Obviously, the ratio $\bar{I}_{AC}(\tau = 0) : \bar{I}_{AC}(\tau \rightarrow \infty)$ is reduced. Using equations (2.1) and (2.2) the electric field of our pulses is defined by $E(t) = A(t) \cos(\omega t)$, with the envelope function, $A(t)$, and the instantaneous light frequency, ω . Using this field

⁴The temporal resolution is limited by the employed translation stage. As discussed in section 3.2 the minimum step size is just sufficient to resolve the fringes of the autocorrelation trace. However, the stability of the interferometer in its entirety does not allow for the acquisition of such data. Because of vibrations an active stabilization would be needed to do so.

and equation (2.11) a rather complex dependence of $I_{AC}(\tau)$ on $A(t)$ and ω is found (for details refer to reference [106]). If only terms depending solely on $A(t)$ [or $A(t + \tau)$] are considered, i. e. if all terms depending on ω are neglected, a ratio of 3 : 1 of $\bar{I}_{AC}(\tau = 0)$ and $\bar{I}_{AC}(\tau \rightarrow \infty)$ is derived. This corresponds to the proposed phase-averaging.

The intensity autocorrelation, \bar{I}_{AC} , is represented by [106]:

$$\begin{aligned}\bar{I}_{AC}(\tau) &= \int_{-\infty}^{\infty} |E(t)E(t + \tau)|^2 dt \\ &= \int_{-\infty}^{\infty} I(t)I(t + \tau) dt ,\end{aligned}\tag{2.13}$$

with the pulse intensity, $I(t)$. In this case, \bar{I}_{AC} is a convolution of the temporal intensity profile of the laser pulse. By assuming a pulse-shape—sech² or Gaussian shapes are a good choice for our laser systems—the autocorrelation can be deconvoluted, yielding the temporal pulse shape and thus the pulse duration can be extracted [114]. In the following section 2.5.2 we will show, how the laser autocorrelation can be used to extract information on the population lifetime of the intermediate state of the 2PPE process. Before we do so, we shall shortly discuss, what to expect in a TR-2PPE experiment for non-vanishing intermediate state lifetime.

For an intermediate state with a finite lifetime, the acquired autocorrelation is modified with respect to the laser autocorrelation—a broadening of the FWHM of the trace is observed. In section 2.5.2 we discuss, how this broadening can be utilized to extract the population lifetime of the intermediate state, if the pulse duration is already known. Here, we like to establish, in general terms, how the correlation trace is influenced by the presence of an intermediate state with a finite lifetime.

In contrast to the case of a vanishing population lifetime, the observed photoemission signal is enhanced outside the temporal range of the overlap of pump and probe pulse. Even after the pump pulse ceased, the remaining population of the intermediate state can still be probed by the second pulse, i. e. the photoemission signal is modified even for temporal delays outside the pump–probe overlap. To understand the exact shape of the resulting autocorrelation, especially with respect to the broadening, the whole system of electronic states involved in the photoemission process needs to be considered. A common approach models the system within the density matrix formalism, considering the population lifetimes of initial, intermediate, and final state, as well as the dephasing times (elastic and inelastic), i. e. the loss of the optically induced coherence [96, 115], between these states.

In section 2.5.2 we discuss different approaches for the evaluation of such autocorrelation traces. As the simulation employing the density matrix formalism is rather complex and

the details of the electronic system are not fully known, for practical reasons we resort to extracting an effective population lifetime. In this work we use a rate equation approach [30], i. e. the population lifetime of the intermediate state is modeled by an exponential function $n(t) = n_0 e^{-\frac{t}{\tau}}$, with the initial population, n_0 , the population at t , $n(t)$, and a time constant, τ ; the autocorrelation is derived by a convolution of the autocorrelation of the pump and probe pulse and this exponential. This approach corresponds to the limit of rapid dephasing [115] in case of the density matrix formalism, i. e. the coherence of the electronic states and the light field is lost fastly and no coherence effects are observed within the TR-2PPE signal.

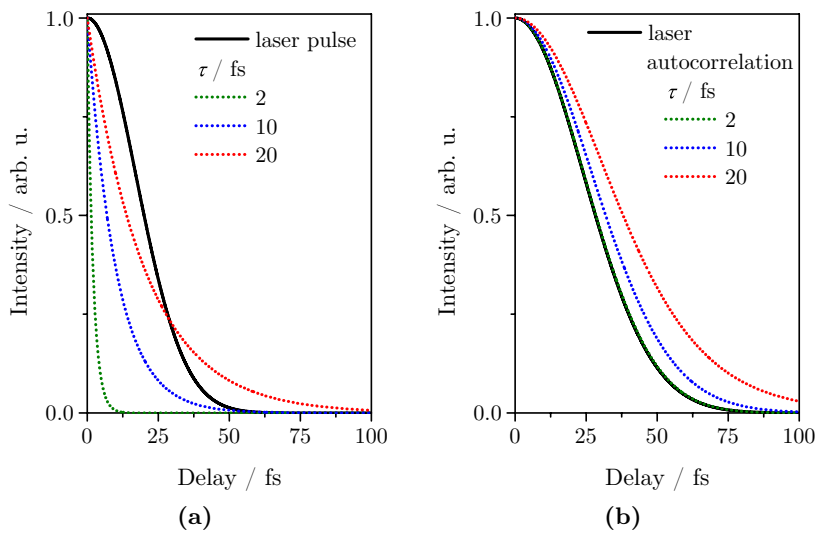


Figure 2.10: Simulation of the broadening of the autocorrelation traces in the presence of non-vanishing intermediate state lifetime. (a) We use Gaussian pulses (black) and an exponential decay of the population of the intermediate state. (b) By calculation of the convolution of the two pulse shapes we derive the laser autocorrelation (black). This trace is convolved with the exponential functions to derive the presented broadened autocorrelations.

Generally, a stroboscopic TR-2PPE experiment works the best, if the pump and probe pulses feature a significantly shorter temporal duration than the lifetime to be investigated. The population of an unoccupied electronic state relaxes on a femtosecond timescale (refer to, for instance, references [21, 26, 96]), while the typical temporal duration of the laser pulses employed here is a few tens of femtoseconds (see section 3.2). Nevertheless, if the pulse duration is at least close to the temporal range to be investigated, the lifetime can still be accessed by acquisition of a correlation trace. Additionally, a sufficiently stable laser system is crucial for the evaluation of very small lifetimes using this method. Instabilities of the laser intensity, pointing, and pulse duration basically

all modify the shape of the correlation trace. The shape of the correlation traces of subsequent measurements therefore vary slightly. For a very small lifetime the broadening of the curves is rather subtle (see figure 2.10) and it is thus masked completely by such variations.

Figure 2.10 shows calculated autocorrelations. We assume Gaussian-shaped pump and probe pulses with a FWHM of 40 fs and an exponential decay of the intermediate state lifetime with time constants of 2 fs, 10 fs and 20 fs. Figure 2.10(a) compares the laser pulse shape (black) with the exponential decay functions of the intermediate state. Figure 2.10(b) shows the laser autocorrelation (black) as calculated by convolving pump and probe pulse and the autocorrelations for the different intermediate state lifetimes, calculated by convolving the laser autocorrelation and the exponential functions (see section 2.5.2).

In conclusion, figure 2.10 demonstrates the necessity to perform a TR-2PPE experiment using at least pulse durations comparable to the time constant of the processes to be investigated. A lifetime of the intermediate state of 10 fs and 20 fs is well resolved by the corresponding broadening of the autocorrelation trace. For a very fast relaxation—2 fs in our example—the broadening is very subtle and hardly resolved. In section 4.2 we present experimental data on such a lifetime broadening. We find, that time- and angle-resolved two-photon photoemission (TAR-2PPE) allows for the identification even of very small lifetimes by employing statistical means. Although the broadening of a single autocorrelation still cannot be unambiguously evaluated, the occurrence of a small broadening can be identified, if it is observed within a certain range of the energy–momentum maps, i. e. if several autocorrelations show a consistent broadening.

2.5.2 A Short Outline of the Extraction of the Lifetime From the Autocorrelation Experiments

Our primary task concerning the acquisition of phase averaged autocorrelation traces (see figure 2.9) is the extraction of the population lifetime of the intermediate state of the 2PPE process. The laser autocorrelation is defined by the laser pulse duration alone, because it is simply the convolution of the temporal shape of a laser pulse with itself, i. e. for a given pulse shape deconvolution yields the pulse duration [106, 116]. In case of TR-2PPE the autocorrelation may be broadened, if an intermediate state of finite lifetime is involved in the process [refer to figure 4.11(b) in section 4.2], i. e. a careful analysis of the autocorrelation shape enables the extraction of the lifetime of the intermediate state involved in the photoemission process [27, 117–119].

Extraction of this lifetime can be a very complicated and delicate task. A common approach employs a density matrix formalism based on the optical Bloch equations to describe the interaction and temporal evolution of the electronic system and the optical electromagnetic field [28, 96, 120]. Adding the coupling to an external heat bath for modeling dissipative processes, like, for instance, relaxation or scattering, the Liouville–

von Neumann equation is derived from the optical Bloch equation [30, 115, 121, 122] yielding a set of coupled differential equations which are numerically solved to derive the lifetime of the intermediate state [115]. This is a rather sophisticated approach, which requires not only knowledge of the laser pulse duration—known from the laser autocorrelation—, but also assumptions on the nature of initial and final state and the dephasing times between the initial, intermediate, and final states need to be made. This method therefore requires a rather detailed understanding about the investigated system. Furthermore, several simplifications need to be made to reduce computation time, like the limit of rapid dephasing, which justification needs to be considered (we do not discuss these assumptions in detail here, refer to references [30, 121, 123]). This method yields a set of simulated data which is compared to the experimental autocorrelations. The best fitting simulation defines the lifetime [30, 53]. Considering, that the choice of parameters of this numerical method can influence the extracted intermediate state lifetime considerably, we circumvent the need for such assumptions for our TMDCs by using a much simpler approach. Please note, that we apply this formalism to the simulation of the photoemission spectrum in section 4.2, however, only in a qualitative manner.

Basically a non-zero lifetime of the intermediate state of the TR-2PPE process leads to a broadening of the autocorrelation with respect to the laser autocorrelation. This broadening can be simulated by convolving the laser autocorrelation with a exponential decay function, simulating the population decay of the intermediate state [114, 124]. The extraction of the intermediate state lifetime is thus simplified to calculation of such convolutions of laser autocorrelation and exponential functions of different time constants and a quantitative comparison of experimental data and simulation. The time constant of the exponential of the best fitting convolution yields the effective lifetime, T_1 , of the intermediate state. This simple approach is successfully applied to the extraction of the lifetime of an adsorbate excitation in our earlier publication [124], where good agreement of experimental and theoretical data is achieved using such effective lifetimes. This method does not rely on a delicate choice of suitable parameters needed, like in case of the calculation using the Liouville–von Neumann equations.

The method is based on the following procedures:

- (i) The laser autocorrelation, $I_{\text{laser}}(t)$, can be calculated for an assumed temporal pulse shape by convolution. Usually our laser pulses are Gaussian- or sech²-shaped and thus the laser autocorrelation is well fitted by such a function, i. e. the fit of the laser autocorrelation can be used directly.
- (ii) A set of exponential decay functions $I_{\text{exp}}(t) = e^{-|t|/\tau}$ for different time constants τ is calculated.
- (iii) This enables the calculation of a simulated, broadened autocorrelation, $I_{\text{AC}}(t)$, by convolution $I_{\text{AC}}(t) = (I_{\text{laser}} * I_{\text{exp}})(t)$ which yields a set autocorrelations for

different time constants τ of the exponential function. We use a numerical FFT-based algorithm.

A quantitative comparison to the experimental data (for details see section 3.2.2) yields the time constant of the exponential part of the best fitting autocorrelation which is the effective lifetime of the intermediate state, T_1 .

Throughout this work we use these effective lifetimes, T_1 , whenever we quantitatively evaluate autocorrelation data, as suggested by the work of Gauyacq and Kazansky [114]. The effective lifetime value basically corresponds to all processes influencing the autocorrelation intensity, like, e. g., a change of spectral intensity in the energetic range monitored induced by a change of binding energy of the corresponding state [119]. By assuming that the population lifetime of the intermediate state is well described by T_1 alone we implicitly assume rapid dephasing for both excitation steps of the 2PPE process [125, 126], i. e. in the absence of dephasing (i. e. the coherence of the states involved [30]) no broadening of the autocorrelation is attributed thereto and the extracted broadening is thus induced solely by the non-zero lifetime of the intermediate state. Nevertheless, our use of such effective lifetimes in section 4.2 is focused on identifying relative changes. In this case a stable extraction of lifetime values is important and the absolute value of the population lifetime of the states investigated is only of minor importance. One should, however, remember that the effective lifetimes are not necessarily identical to the population lifetimes.

2.5.3 Two-Color Pump-Probe Experiments

The time resolved TR-2PPE method presented in section 2.5.1, which is based in our case on the acquisition of one color auto- or cross-correlations, poses a conceptual drawback: in the vicinity of time zero the correlation is generally dominated by information on the temporal shape of the pulses, i. e. the laser correlation is convolved into the data. We see in section 6.1 that the interpretation of a one color experiment becomes rather difficult, if the response of the electronic system becomes more complex than the simple decay of the population of an intermediate state.

However, a two color experiment does not per se solve the presented problem. Figure 2.11(a) shows the excitation scheme using two photon energies, $h\nu_1$ and $h\nu_2$, which allow to excite two intermediate states, $|2\rangle$ and $|2'\rangle$. While the experiment opens up new excitation paths and access to new intermediate states, the convolution with the cross-correlation of the laser pulses in the vicinity of $\tau = 0$ remains. An experiment using different photon energies within a 2PPE excitation scheme to gain access to a certain intermediate state is presented, for example, by Fauster and Weinelt [127].

By carefully choosing a favorable ratio of photon energies and work function it is, however, possible to suppress photoemission paths involving only photons of the smaller energy. Our time-resolved IR-pump SH-probe photoemission setup uses photons of the

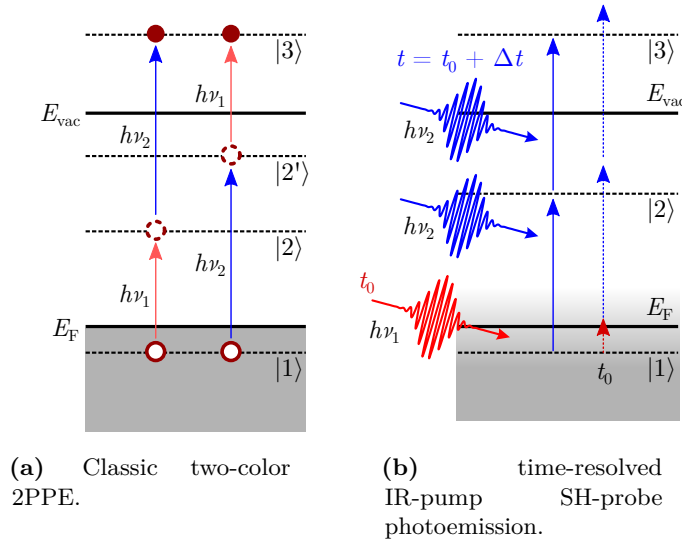


Figure 2.11: (a) A two-color 2PPE experiment usually involves different photon energies, $h\nu_1$ and $h\nu_2$, for the pump and probe pulses.

fundamental emission of the laser and the second harmonic (SH) thereof⁵ with typical photon energies of approximately 1.59 eV and 3.18 eV. Considering the rather high work function of the TMDCs discussed in this work ($\Phi > 5$ eV, see section 3.3), a 1PPE or 2PPE process is not possible using the infrared (IR) photons. Nevertheless, 2PPE is feasible for the SH photons—a three-photon photoemission (3PPE) transition involving one IR and two SH photons or, of course, two IR and one SH photons, as well as higher order processes are also possible. Considering that the photoemission process becomes less likely the higher the order [128], we expect the situation depicted in figure 2.11(b) to yield the dominant contribution to the observed spectra. Please note, that 3PPE processes (dotted arrows) cannot be fully ruled out a priori and need to be considered for the interpretation of the data (see section 6.2) especially at time zero, t_0 , when the pump and probe pulses overlap temporally. This excitation path does not differ from the cross-correlation scheme discussed before considering the convolution of the data by the laser correlation and shall therefore not be discussed here.

Instead, we like to focus on the 2PPE process available using the discussed ratio of photon energy and work function. Figure 2.11(b) visualizes this excitation path (full arrows). Because there is no lower order (< 3) transition possible involving the low energy photons, $h\nu_1$, there is no contribution to the photoemission signal, even at time zero and only $h\nu_2$ generates photoelectrons. The low energy photons thus act as the

⁵For the nomenclature see section 3.2.

pump, and the high energy photons act as the probe pulse [129].

If the low energy pump pulse is absorbed by the sample at $t_0 = 0$ fs it perturbs the electronic system (shading) by, e. g., the generation of a non-equilibrium distribution of the electrons (see section 2.5.4). The probe pulse, $h\nu_2$, which is temporally delayed by Δt , generates photoelectrons and thus yields the 2PPE spectrum of the perturbed electronic system. These data are not modified by the laser cross-correlation of the pump and probe pulses, but rather represent the actual response of the electronic system, as well as the subsequent relaxation thereof, to the pump pulse. In contrast to auto- or cross-correlation measurements the response of the electronic system becomes directly observable. Please note, that while we employ a 2PPE process, the common approach generates photoelectrons via 1PPE by the probe pulses (see, e. g., references [44, 129])—our choice for the 2PPE process is motivated by the requirements on the photon energy with respect to the work function of the sample, as well technical restrictions concerning possible SHG, third harmonic generation (THG), and fourth harmonic generation (FHG) (see section 6.2 for details).

2.5.4 The Typical Stages of the Laser Induced Excitation of the Electronic System

The absorption of a ultrashort laser pulse by a solid surface leads to the excitation of the electronic system, i. e. the energy of the pulse is first deposited into the electronic system. The decay of this excited state exhibits two distinct relaxation steps (see, e. g., reference [130] and references therein), which are shown in figure 2.12.

Initially, the absorbed laser pulse immediately generates a strongly non-equilibrium electron distribution [figure 2.12(a)]. This defines the *time zero* ($t = 0$) in our time resolved experiments. Basically, electronic states up to $E - E_F = h\nu$ are occupied by the laser pulse [131] (shaded red). This is achieved by a quasi-instantaneous redistribution of electrons from $E - E_F = -h\nu$ to 0 eV into the corresponding energetic range above E_F [132, 133].

Within a thermalization time of the electronic system, τ_{th} , the hot electrons reach thermal equilibrium which is characterized by the reestablishment of a Fermi distribution for the electrons [130]. The temperature of the electronic system, T_e , is typically significantly enhanced with respect to the lattice temperature, T_l , i. e. electrons and lattice are not in thermal equilibrium. Thermalization of the electronic system is established by electron–electron interaction by collisions of the excited electrons [130]. Thermal equilibrium of the electronic system is not established within the duration of the pump pulse, i. e. especially for ultrafast pulses of low fluence or at low sample temperatures [133, 134] the thermalization needs considerable time.

Finally, electron–phonon coupling leads to a transfer of the heat to the lattice. The temperature of the electronic system and the lattice equilibrate. The latter temperature is generally much smaller than the initial value of T_e , because of the significantly larger

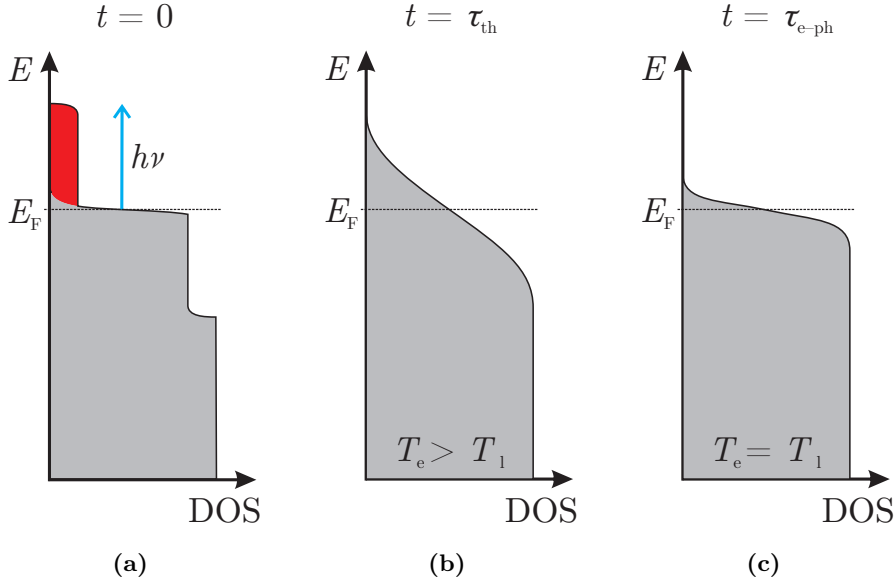


Figure 2.12: The laser induced excitation of the electronic system is characterized by (a) an initial, non-equilibrium electron distribution, followed by (b) thermal equilibrium of the electron system (time constant τ_{th}), and finally (c) thermal equilibrium of the electronic system and the lattice (time constant $\tau_{\text{e-ph}}$) [130]. T_e and T_l are the temperatures of the electrons and the lattice, respectively.

heat capacity of the lattice (see, for instance, reference [110]) for sample temperatures above the Debye temperature, Θ_D , which is about 220 K for TiSe₂ and TiTe₂. The electron–phonon coupling is characterized by a second timescale, $\tau_{\text{e-ph}}$ [130].

The two temperature model is commonly employed for describing the heat transfer process from the electrons to the lattice [135, 136]. This model is successfully used to estimate the laser induced heat-up of the sample in section 5.2.2–a. However, it is only valid *after* thermalization of the electronic system, i. e. after a defined electronic temperature exists. To quantitatively describe the initial non-Fermi distribution, as well as the thermalization of the electronic system, the model needs to be extended. For details on possible additions to the two temperature model refer to, e. g., references [131, 133, 134, 137].

Please note, that the relaxation phases discussed here are not subsequent, well separated exclusive processes. The timescales of the electron–electron and the electron–phonon interaction partially overlap [96], i. e. a heat transfer to the lattice is already expected during the thermalization of the electrons.

3 Experimental Setup

*»Courage, mon ange, courage; souviens-toi que c'est
par les peines qu'on arrive toujours aux plaisirs.«*

Donatien Alphonse François, Marquis de Sade [138]

3.1 UHV Systems for Angle-integrated and Angle-resolved Photoemission Experiments

The experiments presented within this dissertation were performed at two different facilities at the universities of Kiel and Kaiserslautern, due to the particular emphases of the experimental setups. In this chapter both setups will be discussed with respect to their application in the miscellaneous experiments.

The angle integrated two-photon photoemission (2PPE), time-resolved two-photon photoemission (TR-2PPE) and time-resolved IR-pump SH-probe photoemission experiments were performed in a magnetically shielded ultrahigh vacuum (UHV) chamber at the university of Kiel at a base pressure better than 5×10^{-11} mbar. The chamber is equipped with a cylindrical sector analyzer (CSA; *CSA 300*, FOCUS GmbH), featuring a slit-to-slit distance of 298.3 mm in a 90° geometry. The entrance aperture S_1 can be set to 1 mm and 8 mm leading to angular acceptances $\Delta\theta$ of $\pm 6^\circ$ and $\pm 12^\circ$, respectively. The energetic resolution ΔE (full width at half maximum (FWHM)) depends on the pass energy E_{pass} and the angular acceptance. Table 3.1 shows the ratio $\frac{\Delta E}{E_{\text{pass}}}$ corresponding to the entrance apertures used in this work, as well as the energetic resolution in case of the typical pass energy value of $E_{\text{pass}} = 2$ eV. By using the small entrance aperture a theoretical energetic resolution of $\Delta E \approx 10$ meV can be achieved. In case of very low photoelectron emission or if reasonably smooth spectra cannot be acquired fast enough, e. g. in case of the time resolved experiments, the sensitivity of the cylindrical sector analyzer (CSA) is enhanced by employing the wide entrance aperture, reducing the energetic resolution to $\Delta E \approx 96$ meV.

The angle-resolved photoemission spectroscopy (ARPES) and angle-resolved two-photon photoemission (AR-2PPE) as well as time- and angle-resolved two-photon photoemission (TAR-2PPE) experiments were performed at the university of Kaiserslautern in a similar magnetically shielded ultrahigh vacuum chamber using a hemispherical energy analyzer (HSA, *PHOIBOS 150*, SPECS GmbH) with 150 mm mean radius. This analyzer

3 Experimental Setup

Table 3.1: Energetic, ΔE , and angular resolution, $\Delta\vartheta$, of the the angle-integrated and angle-resolved photoelectron energy analyzers at typical pass energies of 2 eV and 20 eV, respectively. Typical values for the entrance apertures, S_1 , the angular acceptance, $\Delta\Theta$, and the ratio, $\frac{\Delta E}{E_{\text{pass}}}$, are included.

setup	S_1/mm	$\Delta\Theta/^\circ$	$\frac{\Delta E}{E_{\text{pass}}}/\%$	$\Delta\vartheta/^\circ$	$\Delta E/\text{meV}$
$E_{\text{pass}} = 2 \text{ eV}$					
angle-integrated	1	± 6	0.501		≈ 10
	8	± 12	4.8		≈ 96
$E_{\text{pass}} = 20 \text{ eV}$					
angle-resolved	0.5	± 13	≈ 0.1	≈ 0.3	≈ 20

is equipped with a two-dimensional detection unit which allows for parallel detection of the photoemitted electrons kinetic energy and emission angle. The detection unit consists of a micro-channel plate (MCP), a phosphor screen (P 43) and a thermo-electrically cooled 12 bit CCD camera (*SensiCam QE*, PCO AG) with extremely low noise. The analyzer features different lens modes, of which only the angular resolved wide angle mode (WAM) with an emission angle range of $\pm 13^\circ$ is used here. The accessible kinetic energy range is typically 2 eV at a pass energy of $E_{\text{pass}} = 20 \text{ eV}$. The energetic resolution ΔE is determined by the sizes of the entry slit, which is set to $S_1 = 0.5 \text{ mm}$ throughout all experiments, and the spatial resolution of the CCD $S_2 = 0.1 \text{ mm}$, the mean radius $R_0 = 150 \text{ mm}$ and the acceptance angle α of the analyzer, which depends on S_1 . Please note, that S_2 and R_0 are fixed. The contribution due to the acceptance angle can be neglected for the entrance slit width used in our case. An energetic resolution of $\Delta E \approx 20 \text{ meV}$ is derived for the typical parameters using the following equation [139]:

$$\frac{\Delta E}{E_{\text{pass}}} = \frac{S_1 + S_2}{4R_0} + \frac{\alpha^2}{4} \approx \frac{S_1 + S_2}{4R_0}.$$

The angular resolution $\Delta\vartheta$ depends on the angular dispersion D of the lens mode ($D = 0.5 \text{ mm}/^\circ$, WAM), the spatial resolution of the imaging system S_2 , the spot size broadening M due to the lateral spread of electrons emitted within an angular range on the detector ($M \approx 0.8$) and the actual spot size of the laser on the sample surface ($d \approx 100 \mu\text{m}$). For the typical parameters used for all experiments presented here an angular resolution of $\Delta\vartheta \approx 0.3^\circ$ is derived using the following equation [139]:

$$\Delta\vartheta = \sqrt{\left(\frac{1}{D} \cdot S_2\right)^2 + \left(\frac{M}{D} \cdot d\right)^2}.$$

Please note, that the energetic resolution of both analyzers presented here (see table 3.1) is calculated from the specifications of these systems. These resolutions are only

3.1 UHV Systems for Angle-integrated and Angle-resolved Photoemission Experiments

achievable under ideal conditions, i. e. experimentally we expect worse values of ΔE . See our discussion in section 3.2 on the actual spectral resolution, especially table 3.4.

Both UHV chambers are equipped with additional components for sample preparation and characterization. A low energy electron diffraction (LEED) system is used to check the surface quality and the alignment of the surface crystalline orientation prior to the photoemission experiments. The samples can be translated, rotated about the sample normal and about the axis perpendicular to the angle dispersive plane of the angle-resolved system, thus allowing a detailed selection of the region of the Brillouin zone to be mapped.

Defined surfaces of the single crystals Ag(111) and Cu(111), as well as a polycrystalline tantalum sheet were prepared by repeated cycles of Ar⁺ sputtering and subsequent annealing. A typical preparation cycle for Ag(111) and Cu(111) consist of sputtering for 2×15 min at 0.8 kV and annealing at 450 °C. Tantalum is sputtered for 2×15 min at 1 kV and annealed at 600 °C. For all photoemission experiments either a sheet of tantalum or a Cu(111) single crystal in electrical contact to the sample was used as Fermi energy reference. For the characterization of the laser pulses and for alignment purposes of the time-resolved IR-pump SH-probe photoemission experiments (see chapter 3.2.1) a Ag(111) crystal has been used.

The preparation of clean and well defined surfaces of the TiSe₂ crystals is achieved by cleavage and heating under UHV conditions. In a dedicated transfer chamber adhesive tape is attached to the surface of the crystal, which removes the top layers of the crystal during the cleaving process while the sample is transferred to the analyzer chamber. Residual adsorbates are removed by a short heating cycle to about 220 °C (details see chapter 3.3). A quadrupole mass spectrometer enables us to monitor the species of the adsorbates desorbing during heating.

Furthermore, sources of different alkali metals produced by SAES Getters S. p. A. (in particular rubidium and cesium) are present within the analyzer chamber. These sources allow a very controlled and pure evaporation of the desired alkali. Finally, to allow the cooling of TiSe₂ below the critical temperature of the charge density wave (CDW) phase transition and to suppress intercalation during alkali adsorption, the samples can be cooled using liquid nitrogen. Our system allows temperatures as low as about 120 K.

3.1.1 Cooling With the Liquid Nitrogen Heat Exchanger

Cooling of samples is implemented by a heat exchanger setup. Liquid nitrogen is filled into an insulated tank in which a copper coil tube serves a first heat exchanger. Gaseous nitrogen is cooled as it flows through the coil. The gas runs into a second heat exchanger inside of the UHV system which is basically a small copper block. A flexible copper wire connects this block to the manipulator right to the holding unit of the sample.

The first heat exchanger is an open system. The liquid nitrogen evaporates constantly and needs to be refilled. The connection of the copper coil to the UHV system needs to

be kept as short as possible to ensure the best cooling. Therefore, the tank is attached directly to the UHV chamber. This leads to a problem: Our samples show homogeneous photoemission spectra only for a limited surface area (tens to hundreds of micrometers in diameter, see addendum A.1.2). Small shifts of the relative position of sample and laser beam already alter the acquired spectra significantly.

The filling level of the liquid nitrogen tank constantly changes because of evaporation. To reduce spatial shifts induced by the different weight of the tank, a desired level is marked inside. After each taken spectrum the tank is refilled to this mark which leads to a very constant filling. The very small differences in weight do not seem to yield any discernible spectral changes.

However, spectral modifications due to such weight induced shifts are indeed observed for spectra taken for empty and filled tank. To circumvent this problem the initial spectroscopy for calibration and optimization is performed with the tank being filled by water compensating the mass of liquid nitrogen later used for cooling. Please note, that these initial experiments are performed over several hours, thus using liquid nitrogen would be a tedious and wasteful approach.

3.2 Laser Systems and Optical Setups

ARPES reference spectra have been recorded using the He-I emission (21.22 eV) of a gas discharge vacuum ultraviolet (VUV) lamp [e. g. figure 3.9(b)]. Additionally, three different mode-locked Ti:sapphire laser systems are used for the experiments of this work. In general, these lasers are tunable over a wide infrared wavelength range. Furthermore, due to mode-locking, ultrashort pulses of a few ten femtoseconds duration can be generated. The high intensity of the short laser pulses allows frequency conversion in an optical non-linear crystal, like for instance β -barium borate (BBO) or lithium triborate (LBO), resulting in the generation of the second harmonic (SH) and third harmonic (TH); a necessity for the 2PPE spectroscopy experiments of this work. Next to initial and final states accessible in conventional photoemission experiments, 2PPE spectra contain in addition information about the unoccupied state distribution between Fermi energy E_F and vacuum energy E_{vac} . The energy scale $E - E_F$ used in this work is determined from the kinetic energy E_{kin} of the photoelectrons analyzed in the spectrometer according to $E - E_F = E_{kin} + \Phi - h\nu$, with the work function Φ and the photon energy $h\nu$.

Figure 3.1 illustrates the excitation scheme of a 2PPE process as well as the different electronic states contributing to the measured signal. Please note, that additionally to the occupied band structure also observed in one-photon photoemission (1PPE) spectroscopy, 2PPE enables us to investigate the unoccupied band structure between E_F and E_{vac} , too. Furthermore, 2PPE can easily be extended to stroboscopic time resolved measurements by introducing a simple temporal delay between the two laser pulses contributing to the 2PPE process. This enables the observation of the population decay of the intermediate

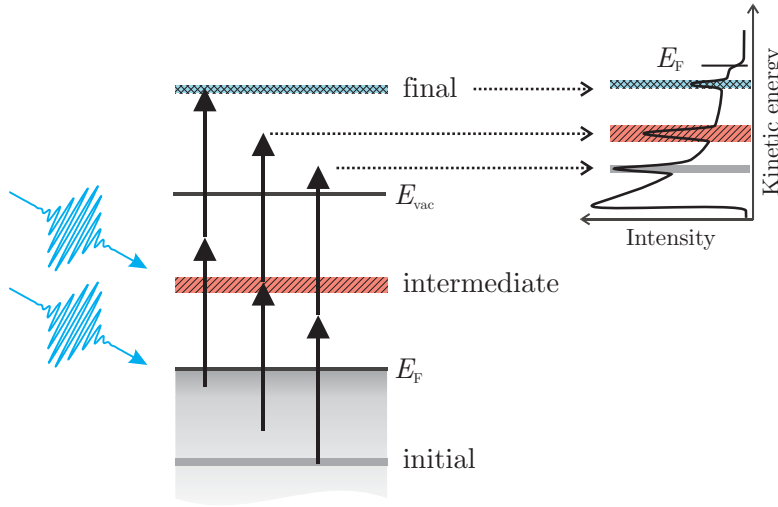


Figure 3.1: Excitation scheme of the 2PPE process. The contribution of initial, intermediate (hatched) and final (cross-hatched) states to the recorded spectrum is visualized.

state of such a two-photon excitation (for details see section 2.5).

The minimum of the temporal pulse width $\Delta\tau$ for a laser pulse is determined by its bandwidth $\Delta\nu$ via the time-bandwidth product $\Delta\nu\Delta\tau$. For a given pulse shape, this product determines the minimal temporal width of a laser pulse achievable for a specific spectral width, yielding a so called transform-limited pulse. Table 3.2 shows the value of this product for two typical pulse shapes. In fact, we expect a mixture of hyperbolic secant (sech) and Gaussian pulse shape for the lasers used in our experiments.

Table 3.2: Value of the time-bandwidth product $\Delta\nu\Delta\tau$ for typical pulse shapes, as well as the corresponding conversion factor for the FWHM of the autocorrelation trace FWHM_{AC} into the temporal pulse width $\Delta\tau$ [106].

pulse shape	$\Delta\nu\Delta\tau$	$\text{FWHM}_{\text{AC}}\Delta\tau^{-1}$
Gaussian	0.441	1.414
sech	0.315	1.543

Two of the laser used for the experiments of this work are located at the university of Kaiserslautern, one at the university of Kiel. Because pulse length and laser bandwidth cannot be optimized simultaneously, different laser systems—meaning the laser and the optical setup—are used for spectroscopy and time resolved experiments. At Kaiserslautern, one system is dedicated to spectroscopy, i. e. optimized for a small bandwidth (laser 1) and one system is optimized for extremely short pulses (laser 2). In Kiel both tasks are realized by only one laser system. It is either optimized for a small bandwidth at

3 Experimental Setup

high pulse intensity, which we will call laser 3_{PES}, or for short pulses by increasing the bandwidth and by using a different optical path further optimized for such short pulses (laser 3_{TR}). The details of the laser systems and optical setups will be discussed in the following. The typical parameters of these laser systems are summarized in table 3.3.

Table 3.3: Typical parameters of the laser systems used in this work, i. e. the repetition rate f_{rep} , the bandwidth $\Delta h\nu$ and the tunable photon energy range $h\nu$ for SH and TH (in brackets). $\Delta\tau_{\text{exp}}$ is the experimentally observed temporal pulse width for the SH pulses for a typical alignment. For reference, $\Delta\tau_{\text{TL}}$ is calculated for a transform limited laser pulse of a central wavelength $\lambda = 390$ nm. The pulse duration is given for Gaussian- and sech-shaped pulses, because a mixture of these shapes is expected for the lasers used.

laser	$f_{\text{rep}}/\text{MHz}$	$\Delta h\nu/\text{meV}$	$h\nu/\text{eV}$		$\Delta\tau_{\text{exp}}/\text{fs}$		$\Delta\tau_{\text{TL}}/\text{fs}$	
			SH, (TH)		Gaussian	sech	Gaussian	sech
narrow bandwidth								
1	82	$\lesssim 20$	2.95 to 3.45 (4.45 to 5.15)				$\gtrsim 89$	$\gtrsim 63$
3 _{PES}	80				as laser 1			
broad bandwidth								
2	76	≈ 91	3.12		31.7	28.0	20.0	14.3
3 _{TR}	80	≈ 50	3.18		43.1	38.0	36.7	26.2

For the 2PPE spectroscopy experiments we utilize the frequency converted output of two different pulsed Ti:sapphire lasers (*Tsunami*, Newport / Spectra-Physics) pumped by either a frequency-doubled solid-state Nd:YVO₄ laser (laser 3, 10 W continuous wave (cw), *Millenia Pro 10sJ*, Newport / Spectra-Physics) or a gas argon-ion laser (laser 1, 10 W cw, *BeamLok*, Newport / Spectra-Physics). The AR-2PPE measurements are performed with the SH and TH of a narrow bandwidth laser system (laser 1, repetition rate: 80 MHz, bandwidth $\lesssim 20$ meV) at the university of Kaiserslautern to ensure a high energy resolution. The bandwidth of laser 1 varies in a range of 7 meV to 20 meV and is usually about ≈ 13 meV. By taking into account the energy resolution of the 2D analyzer of 20 meV and by considering that the given bandwidth of laser 1 is indeed a maximum value which is usually significant smaller, we expect an overall energy resolution of approximately 30 meV. This is well below the width of the spectral signatures probed in our experiment (see chapter 4). Therefore, the bandwidth of the pulses used for the 2PPE spectroscopy experiments will not affect the spectral peak width considerably. The angle-integrated 2PPE experiments at the university of Kiel were performed using a very similar narrow bandwidth laser, which operates at the same repetition rate and is set to a similar bandwidth (laser 3_{PES}). All spectroscopy experiments are performed using the

SH and TH of this laser. The CSA can be setup with a small or big entrance aperture S_1 (see chapter 3.1, table 3.1), leading to an overall energetic resolution of ≈ 22 meV and ≈ 98 meV, respectively. Furthermore, the wavelength of the laser light can be tuned continuously between about 720 nm and 840 nm corresponding to photon energies of the SH light in the range of $h\nu = 2.95$ eV to 3.45 eV, and of the TH light in the range of $h\nu = 4.45$ eV to 5.15 eV.

Time-resolved 2PPE experiments require the broad bandwidth lasers. Thus, the TAR-2PPE experiments are performed using laser 2 (repetition rate: 76 MHz, bandwidth ≈ 90 meV, *FEMTOSOURCE compact 20*, Femtolasers GmbH) at the university of Kaiserslautern. Laser 2 is also pumped by a frequency-doubled solid-state Nd:YVO₄ laser (8 W cw, *Verdi V8*, Coherent Inc.). This laser delivers frequency doubled light pulses of 28 fs (sech-shaped, 32 fs Gaussian-shaped) temporal width at a photon energy of $h\nu = 3.12$ eV. Because of its optimization strictly for short pulses, the photon energy of laser 2 cannot easily be tuned, i. e. this specific photon energy is used throughout this work. The broad bandwidth reduces the overall energy resolution using the 2D analyzer to typically about 93 meV. All TAR-2PPE measurements are performed in the autocorrelation mode using identical, p-polarized laser pulses. The broader bandwidth of laser 2 leads to noticeable broadening of the spectral features in comparison to the AR-2PPE measurements with laser 1. The data was phase-averaged during acquisition using an electric wobbling motor, thus eliminating interference contributions to the signal. A TAR-2PPE scan consists of a series of E - \mathbf{k}_{\parallel} intensity maps recorded with the two-dimensional (2D) energy analyzer at varying temporal delays Δt between the two pulses. Individual 2PPE autocorrelation traces from selected E - \mathbf{k}_{\parallel} areas can later be extracted from these intensity maps and then deconvoluted using calculated autocorrelation traces. For this purpose, the laser autocorrelation is convoluted with a decreasing exponential. The pulse shape of all lasers used in this work is a mixture of Gaussian and sech. For laser 2 the sech-shape seems to describe the shape of the pulses better than the Gaussian, especially considering the lower part of the flanks of the autocorrelation trace. Therefore, we will assume hyperbolic secant shaped pulses for laser 2 throughout this work.

The angle integrated TR-2PPE and time-resolved IR-pump SH-probe photoemission experiments at the university of Kiel are performed using laser 3_{TR} (laser 3 optimized for short pulses). To achieve a reasonable temporal resolution this system is tuned for a broader bandwidth. To further improve the pulse length of the SH of laser 3_{TR}, a thinner LBO crystal (100 μm) is utilized instead of the thicker BBO crystal (1 mm) used for the spectroscopy with laser 3_{PES}. A thinner frequency conversion crystal allows a broader bandwidth of the SH emission, while a thicker crystal generally increases the intensity of the SH emission, allowing higher photoelectron rates in the spectroscopy experiments. In contrast, for laser 1 BBO of 200 μm thickness is used for second harmonic generation (SHG). However, laser 1 is usually optimized for a high spectral resolution, thus the full potential with respect to pulse length is not utilized. The main difference of laser 1 and laser 3_{TR}—both basically identical in construction—are the details of the

alignment of the lasers themselves. Laser 3_{TR} is optimized for maximum bandwidth at the expense of tunability and intensity. For the frequency doubled light pulses at a photon energy of $h\nu = 3.18$ eV (typically used for the time resolved experiments) a bandwidth of about 50 meV is achieved. This yields a temporal width of the pulses of about 38 fs (sech-shaped) to 43 fs (Gaussian-shaped), depending on the actual pulse shape. In case of laser 3_{TR} we find a good agreement of the autocorrelation trace with a Gaussian fit indicating Gaussian-like shaped pulses. The temporal width of the laser pulses at the sample surface is usually determined by a TR-2PPE experiment of either the excitation from the Shockley surface state of Ag(111) (in analogy to the Cu(111) sample), or excitation via an intermediate state far above the Fermi-energy of a polycrystalline tantalum sheet [see e. g. 28, 117, 140]. For the TR-2PPE autocorrelation with laser 3_{TR} we used Ta as reference system for practical reasons. The laser autocorrelation is then acquired right at the Fermi-edge of the spectrum, corresponding to the highest intermediate state reachable. In this case the broadening of the autocorrelation trace due to the lifetime of the intermediate state is negligible.

The high bandwidth reduces the overall theoretical energy resolution when using the CSA to approximately 51 meV or 108 meV depending on the entrance aperture. For the time resolved experiments only the wide aperture can be used to ensure photoelectron rates high enough for feasible experiments, i. e. the worse energy resolution usually applies. The spectroscopy optimized laser 3_{PES} features bandwidths of only 7 meV to 20 meV, supporting pulse durations of longer than about 63 fs and up to 202 fs for sech-shaped pulses [89 fs to 282 fs for Gaussian-shaped pulses], which is significantly too long for time resolved experiments.

Table 3.4 summarizes the total energetic resolutions, ΔE_{tot} , calculated for the different laser systems and the corresponding photoelectron energy analyzers using the data provided by table 3.3 on the FWHM of the typical laser spectra, ΔE_{laser} , and by table 3.1 for the theoretical energy resolution of the analyzers, ΔE_{spec} . This theoretical value of the total resolution is calculated as the root of a sum of squares of both values, $\Delta E_{\text{tot}} = \sqrt{\Delta E_{\text{laser}}^2 + \Delta E_{\text{spec}}^2}$, which corresponds to a convolution of the Gaussian shaped contributions [139]. The *theoretical* values are thus based on the specifications of the analyzers, i. e. on the energetic resolution of these system achieved under ideal conditions. Experimental data is therefore necessary to gain insight into the actual, achievable resolution of the setup—the origin of the deviation being the specifications of the analyzers.

We extract the width of the secondary electron cutoff, ΔE_{cutoff} , of the spectra (normal emission for ARPES) by applying a 90–10-criterion, i. e. by evaluation of the energetic separation of 90 % and 10 % of the plateau intensity of the cutoff; the given uncertainties are standard deviations of different experiments averaged to calculate the width. ΔE_{cutoff} directly corresponds to the energetic resolution of the analyzer as presented in table 3.1 and is not modified by the laser bandwidth or thermal broadening, because it is generated

Table 3.4: The total energetic resolution, ΔE_{tot} , of the laser system and the photoelectron energy analyzer setup is given for laser 1 and 2 combined with the HSA and laser 3_{PES} and 3_{TR} in combination with the CSA. Theoretical values (denoted by “theo.”) are calculated as sum of squares of the energy resolutions of the analyzers (table 3.1) and the typical bandwidth of the lasers (table 3.3). The entry aperture sizes “small” and “big” of the CSA refer to S_1 being 1 mm and 8 mm, respectively. Exemplary experimental data extracted from the width of the low energy cutoff of room temperature spectra, ΔE_{cutoff} , yield a comparable total experimental energy resolution by convolution with the corresponding laser bandwidth (“exp.”, see text for details). Note, that these data serve as a reference point for the spectral resolution to be expected.

laser	$\Delta E_{\text{tot, theo.}} / \text{meV}$	$\Delta E_{\text{tot, exp.}} / \text{meV}$	$\Delta E_{\text{cutoff}} / \text{meV}$
1 ^a	30	47	43
2 ^a	93	100 ± 2	41 ± 4

laser	$\Delta E_{\text{tot, theo.}} / \text{meV}$		$\Delta E_{\text{tot, exp.}} / \text{meV}$		$\Delta E_{\text{cutoff}} / \text{meV}$	
	CSA aperture size:					
	big	small	big	small	big	small
3 _{PES}	98	22				
3 _{TR} ^b	108	51	115 ± 4	100 ± 5	103 ± 5	86 ± 6

^a carefully prepared Cu(111) crystal

^b four independent measurements of Ag(111), all featuring similar bandwidths and pulse durations of the fundamental

by secondary electrons which do not carry information on the band structure (the band they originate from) or the exciting laser anymore—ideally, the cutoff is defined only by the work function of the sample (given the work function of the analyzer is lower) and should be a sharp drop. We estimated the cutoff for well prepared single crystal samples, Cu(111) and Ag(111), only, because the presence of facets on the surface leads to averaging over regions of different work function and thus broadening of the cutoff. The data in table 3.4 is expected to represent the actual resolution of the analyzer. The experimental value of the total energy resolution is calculated by convolution with the laser bandwidth similar to its theoretical counterpart.

The data in table 3.4 demonstrate, that especially the highest resolutions predicted by the analyzer specifications deviate the most from the actual experimental observations. For the low resolution mode of the CSA (“big” aperture) the experimental analyzer resolution of $(103 \pm 5) \text{ meV}$ is just slightly worse than the value expected from the specifications of 96 meV (see table 3.1) which is, of course, also reflected in the total resolution. The HSA on the other hand is expected to provide $\Delta E_{\text{spec}} = 20 \text{ meV}$ in the mode used, however, the experimental data shows a broadening of the spectral

features higher by a factor of about 2. This difference is virtually irrelevant for the broad bandwidth laser 2 for which the laser itself defines the total resolution (deviation about 8%), but is significant for the small bandwidth laser 1 for which ΔE_{tot} is increased by about 57%. For the CSA the difference between the specified best-case resolution of 10 meV and the observed value of (86 ± 6) meV is most distinct. The broadening of spectral structures is not reduced by about 53%, but only by approximately 13%.

We usually employ laser 3_{TR} in combination with the inferior analyzer resolution, because the gain in energy resolution is rather small, yet, the gain in photoelectron count rate and thus spectral intensity is large. Nevertheless, in case of the CSA a bigger entrance aperture also means averaging over a wider angular range which also reduces the spectral resolution of dispersive bands (see section 5.1). Therefore, whenever spectral resolution is a concern for the interpretation of our data we will provide actual experimental estimations as discussed here—the total energy resolution provided here is only a guide to the performance to be expected for the different combinations of lasers and analyzers.

The experimental setup at the university of Kaiserslautern, consisting of lasers 1 and 2 as well as a 2D analyzer system (discussed in section 3.1) is shown schematically in figure 3.2. This setup is used not only for AR-2PPE, but also for TAR-2PPE experiments in this work. The ultrashort pulses produced by the lasers will undergo a temporal broadening by dispersive optical elements and even by the air, if the optical path is sufficiently long. The wavelength dependence of the refraction index results in the introduction of group velocity dispersion (GVD), also referred to as *chirp*, to the laser pulses. To ensure the shortest possible pulses, the GVD needs to be compensated, which we achieve by a pair of two prisms. The first prism disperses the pulses spectrally, leading to a wavelength dependent optical path to and through the second prism. The beam is retro-reflected through both prisms, compensating the spectral division, again. By tuning the geometry of this GVD-compensation setup, the temporal pulse length can be optimized [for details see for instance 106, 107, 141].

A first step is the GVD compensation of the fundamental. This is not only important to reduce the pulse duration of the SHG, but a shorter temporal pulse length also translates into a higher peak intensity of the fundamental pulse, which enhances the efficiency of the SHG process. For the infrared fundamental of laser 2 this is achieved by a pair of chirped mirrors [106, 107]. Laser 3 features a conventional prism pair for GVD compensation of the fundamental, while laser 1 has no such compensation. Afterward, the SH is generated using a BBO crystal for both laser 1 and 2. The temporal pulse length of the SH at the samples position is always optimized by GVD compensation using a pair of prisms in our case. Great care is bestowed on the optimization of the SH GVD compensation of laser 2.

Figure 3.2 shows the details of the optical setup under particular consideration of laser 2. Time-resolved 2PPE experiments are realized by a Mach–Zehnder interferometer. The incident pulse is split into two equal pulses, one proceeding along a static optical

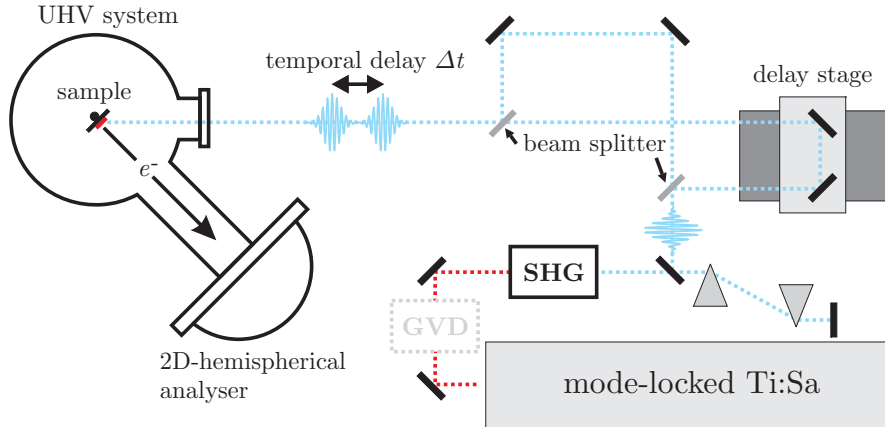


Figure 3.2: Scheme of the experimental setup used for AR-2PPE and TAR-2PPE experiments.

path while the other is directed to a motorized delay stage [*Linear Positioning Stage M-511.DD*, Physik Instrumente (PI) GmbH & Co. KG], which features a direct drive and a linear encoder for positioning. This stage has a travel range of 102 mm and an unidirectional repeatability of $\pm 0.1 \mu\text{m}$. Both pulses are combined at a second beam splitter, thus generating a sequence of two pulses separated by a small, well defined temporal delay Δt . For our experiments the interferometer is generally used in autocorrelation mode, i. e. the p-polarized pulses in both arms are identical. This leads to considerable interferences for small Δt . Furthermore, due to the step width of the delay stage a minimal change in optical path of $\pm 0.2 \mu\text{m}$ corresponding to about $\pm 0.67 \text{ fs}$ is achieved. Neither the step width, nor the overall stability of the interferometric setup is sufficient to capture a phase-resolved autocorrelation trace. At a wavelength of 397 nm ($h\nu = 3.12 \text{ eV}$) the interference fringes are separated by only about 1.3 fs. Actually, considering the Nyquist–Shannon sampling theorem [142], our temporal resolution may be just sufficient for the minimal sampling frequency needed to reproduce the interference fringes. However, although the temporal resolution is quite good, this value is only true for one continuous experimental run. In a time-resolved experiment with the 2D analyzer it is necessary to set discrete temporal delays for a set of AR-2PPE spectra. In this case, the delay stage cannot operate uni-directional¹ leading to an inferior resolution of about $\pm 0.2 \mu\text{m}$ or $\pm 1.33 \text{ fs}$ optical path, which is not sufficient anymore to resolve the interference pattern. We use two electric wobbling motors at the two mirrors of the static arm of the interferometer to phase-average the signal during acquisition by introducing a small, random variation of the optical path (for details see section 2.5.1), thus circumventing the problems arising from the interference and the insufficient resolution of the interferometer.

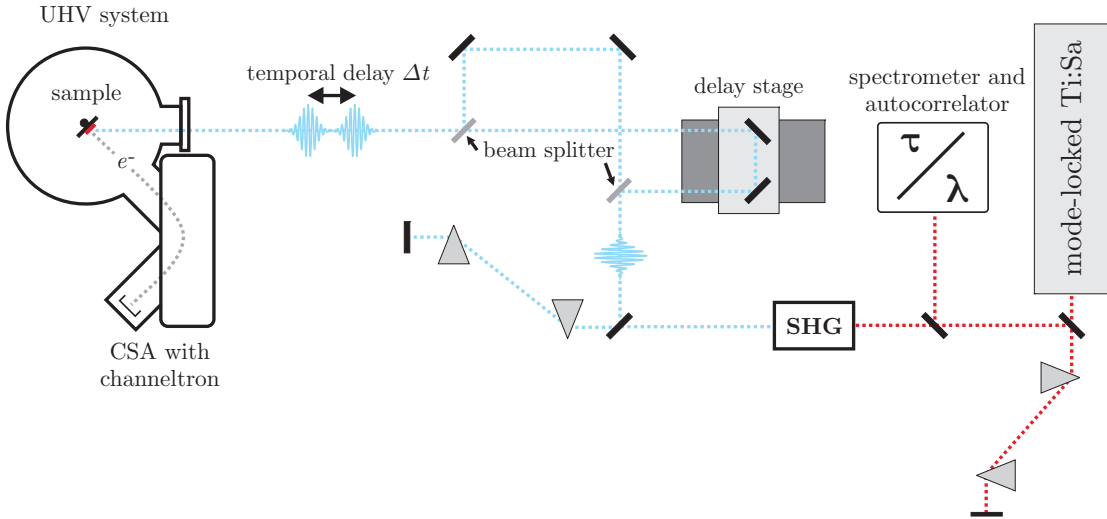
¹The stage needs to correct its position with respect to an internal reference scale, i. e. it needs to drive in both directions to arrive at a specific position.

For the spectroscopic experiments with laser 1, the interferometer is bypassed.

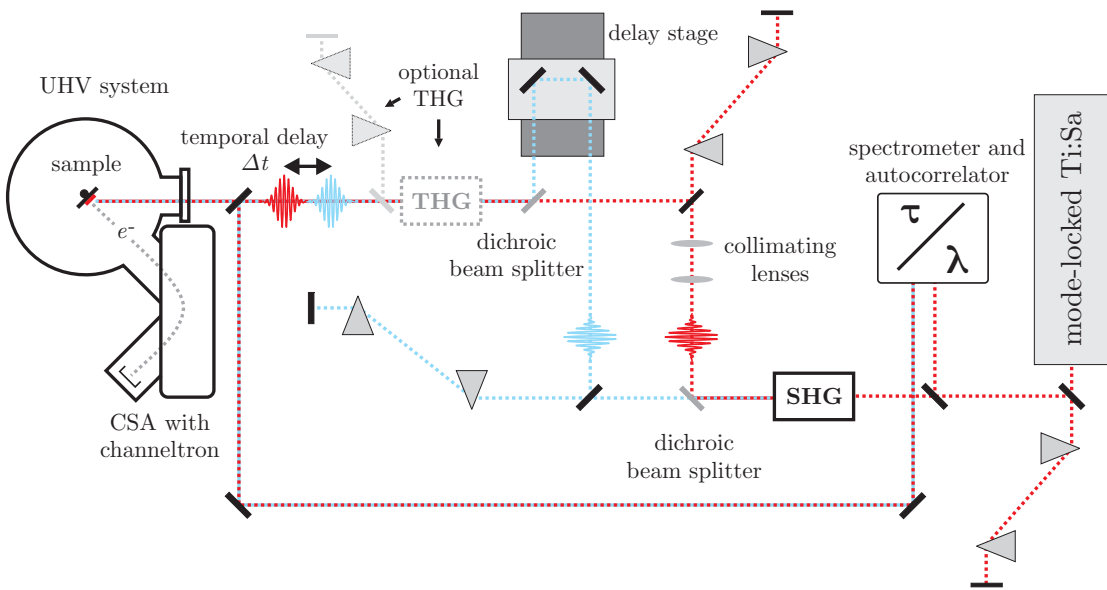
Finally, for both laser systems, the pulses are focused on the surface of the sample using a plano-convex lens, which is carefully centered on the incident beam and which is aligned for optimal focusing. A 2D analyzer detects the emitted photoelectrons and captures intensity maps $I(E_{\text{kin}}, \vartheta)$ depending on the kinetic energy E_{kin} and the emission angle ϑ . Details of the TAR-2PPE measurement process as well as the evaluation of the data are provided in section 3.2.2.

The experimental setup at the university of Kiel consists of laser 3, which will be either optimized for narrow (laser 3_{PES}) or broad (laser 3_{TR}) bandwidth and the angle-integrating CSA analyzer described in section 3.1. The experimental setup used for both angle-integrated 2PPE spectroscopy and TR-2PPE is shown schematically in figure 3.3(a), the setup of the time-resolved IR-pump SH-probe photoemission experiments is shown in figure 3.3(b). The initial setup up to the SHG is the same in both cases. The fundamental of laser 3 is always GVD compensated by a pair of prisms at the position of the frequency doubling crystal by optimization for the highest SH intensity. The fundamental can be characterized using a commercial autocorrelator with integrated spectrometer (*PulseScope*, APE GmbH), i. e. the pulse duration of the fundamental, the spectral width and central wavelength can be monitored. This allows for a good reproducibility of the lasers' characteristics in the day-to-day alignment of the laser in particular with respect to the difference in the alignments we choose to call laser 3_{PES} and 3_{TR}. For the 2PPE spectroscopy a commercial SHG unit including a BBO crystal with a thickness of 1 mm (*Model 3980-4 fs Frequency Doubler*, Newport / Spectra-Physics) is used, allowing, besides an easy alignment, a very efficient second harmonic generation. For laser 3_{TR} a self-constructed SHG-stage with a LBO crystal of only 100 μm thickness is used to ensure a broad bandwidth and correspondingly short pulses of the SH. In both laser 3 setups the GVD of the SH at the position of the sample in the UHV chamber is compensated by a pair of prisms.

The basic principle of the TR-2PPE experiment is very similar to the TAR-2PPE case [see figure 3.3(a)]. A series of two pulses separated by a defined temporal delay Δt is generated in a Mach-Zehnder interferometer using a motorized delay stage of the same model as described for the TAR-2PPE setup. The signal is phase-averaged with two electric wobbling motors at the mirrors of the static arm, too. The beam incident on the sample is carefully aligned through a plano-convex lens and focused on the surface of the sample and the photoelectrons are detected by a CSA analyzer (see section 3.1). For the angle-integrated 2PPE spectroscopy with laser 3_{PES}, the SH bypasses the interferometer. But also in case of the time-resolved experiments with laser 3_{TR}, reference spectra for, amongst others, Fermi-level assignment have to be acquired. This is achieved by blocking one arm of the interferometer and therefore using only single pulses of laser 3_{TR}. Please note, that the negative impact of the broad bandwidth of this laser on the spectral resolution is no concern, as we are solely interested in the energetic position of the Fermi-level needed as reference for the band energies in our time-resolved data. Such reference



(a) Setup used for 2PPE (bypass of interferometer) and TR-2PPE in auto- and cross-correlated mode.



(b) Setup for two color time-resolved IR-pump SH-probe photoemission experiments.

Figure 3.3: Scheme of the experimental setup used for angle-integrated 2PPE and TR-2PPE, as well as pump / probe experiments.

spectra are necessary, because the kinetic energy of the photoelectrons is depending on the photon energy.

Figure 3.3(b) shows the setup of the two-color time-resolved IR-pump SH-probe photoemission experiments and for third harmonic generation using laser 3_{TR} . After passing the self-constructed SHG setup, the residual fundamental is split from the second harmonic by a dichroic beam splitter. The transmitted SH is GVD compensated either for shortest pulse length at the sample position or at the frequency doubling crystal for third harmonic generation (THG). The fundamental is collimated using two lenses and GVD compensated either using the commercial autocorrelator (for details see section 3.2.1) or for optimal THG intensity. The fundamental and SH are combined by a second dichroic beam splitter. The optical path of the SH is varied by the delay stage using one arm of the Mach-Zehnder interferometer. This generates a series of a pump (fundamental) and probe (SH) pulses delayed by Δt with respect to each other. The focusing lens in front of the UHV chamber is optimized for focusing the SH on the surface of the sample, leaving the fundamental partially focused. This is taken into account when evaluating the incident laser fluences of pump and probe.

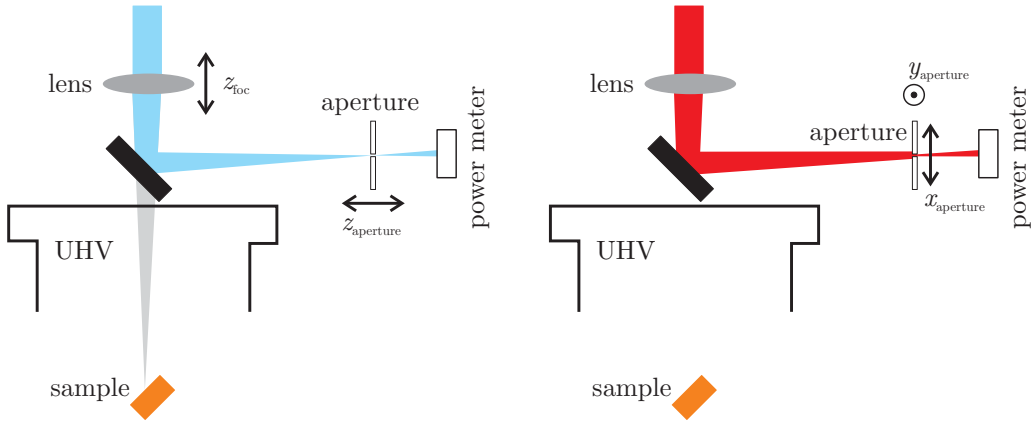
The time-resolved IR-pump SH-probe photoemission setup is easily extended for third harmonic generation by introducing a second frequency doubling crystal (BBO, 100 μm thickness). The fundamental and SH pulses have to be spatially and temporally overlapped at the THG-BBO. In this case the delay stage is bypassed by the SH, while the optical path of the fundamental can be tuned by a manual linear stage. The GVD of the TH is compensated by a dedicated pair of prisms for shortest pulse length at the position of the sample. The beam is focused analogous to the SH on the sample surface using the same lens. We apply the TH for 2PPE spectroscopy.

3.2.1 Details of the Time-resolved IR-pump SH-probe Photoemission Experiment and Evaluation of the Data

3.2.1–a Experimental Setup

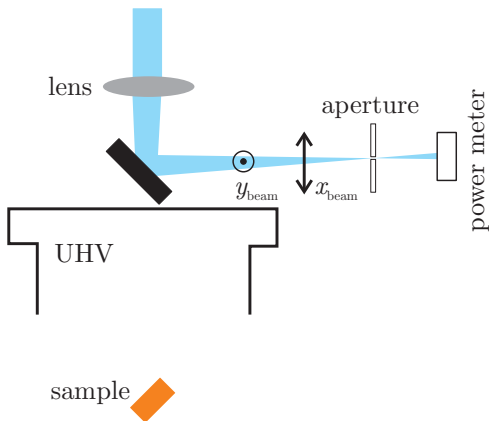
A very good spatial overlap of pump and probe pulses is crucial for the time-resolved IR-pump SH-probe photoemission experiment. Therefore, this section will give a brief overview of the procedure used within this work. Furthermore, we will discuss some considerations for the data evaluation with respect to the experimental part of this dissertation.

A base alignment of the two-color time-resolved experiments first requires the fundamental beam to be aligned into the UHV chamber. It is the reference for all further alignment. The focusing lens is carefully centered and aligned perpendicular with respect to the fundamental. It is necessary that fundamental and SH pass the lens perpendicular at its center to ensure the overlap of both pulses at the sample surface after transmission through the lens. The SH is carefully aligned collinear to the fundamental using two

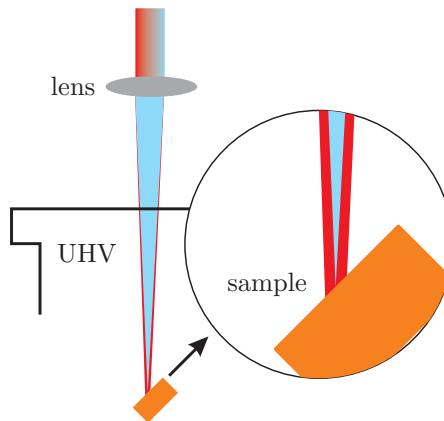


(a) Setting the lens to focus the SH on the sample and finding the position of the aperture corresponding to the distance of the sample from the lens.

(b) Setting the lateral position of the aperture to the fundamental reference beam.



(c) Alignment of the SH through the aperture, i. e. optimization of the spatial overlap at the sample position.



(d) Spatial overlap of pump and probe pulses at the sample position after the alignment procedure.

Figure 3.4: Alignment of the spatial overlap of the pump and probe pulses using an external aperture.

apertures. To further enhance the spatial overlap at the sample surface, i. e. to compensate for inevitable deviations of the alignment, the following procedure (sketched in figure 3.4) is applied:

First of all, the lens (plano-convex, fused silica (FS), $f = 200$ mm) focus z_{foc} is optimized for the SH for best focus on the sample surface [figure 3.4(a)]. The beam is then redirected to a small aperture (diameter: $50 \mu\text{m}$), which is carefully set to the focus of the SH by adjusting its distance from the lens z_{aperture} . The transmitted laser power is monitored by a power meter as a measure of the focal position. This step defines the aperture as the distance of the focus of the SH on the sample surface.

Next, the fundamental is directed to the aperture [figure 3.4(b)]. Only the lateral position of the aperture (x_{aperture} and y_{aperture}) is changed for maximum transmission of the fundamental. This defines the lateral position of the fundamental on the sample surface. The aperture now represents the focal point of the reference beam on the sample.

To improve the alignment of the SH, the lateral position of its focus on the aperture is slightly tuned [x_{beam} and y_{beam} , figure 3.4(c)]. Please notice, that only very little adjustment is necessary, if both beams are sufficiently collinear. This step ensures good spatial overlap of pump and probe pulses at the sample surface, which is shown in figure 3.4(d).

3.2.1–b Estimation of the Laser Fluence

For a quantitative analysis of our data knowledge of the incident pump and probe fluences is necessary. We have to consider that only one of the two pulses can be focused on the sample. By focusing the SH probe pulse we illuminate a larger area with the fundamental pump pulse. The actual diameter of both beams is experimentally estimated using a knife-edge. The knife is carefully aligned into the focus of the SH after completing the alignment procedure of the two-color pump-probe experiment, i. e. after both beams are spatially overlapped at the focal point. The knife is attached to a linear stage which allows us to move it in steps of $5 \mu\text{m}$ through the laser spot. We derive an integral profile of the focused SH. This procedure is repeated for the fundamental yielding a similar integral profile of this beam in its non-focal plane. The actual focus of the fundamental is $\Delta z_{\text{foc}} = (4.53 \pm 0.01)$ mm in the direction of the sample, as checked by focusing the fundamental at the sample surface using the photoemission count rate.

$$I(x, y) = \text{const.} \times \exp \left[-2 \frac{(x - x_0)^2}{w^2} \right] \times \exp \left[-2 \frac{(y - y_0)^2}{w^2} \right] \quad (3.1)$$

We assume a circular beam profile in the focus, therefore beam profiling is only necessary along one, in our case the horizontal axis. We will now show, that by assuming a Gaussian beam, the beam diameter can be extracted from this one dimensional knife-edge beam profile by numerical differentiation. Equation (3.1) shows the intensity profile $I(x, y)$ of a two dimensional circular Gaussian beam [the (x, y) plane is perpendicular to the

direction of beam propagation], with A being the amplitude and w corresponding to the beam radius where the intensity drops to $\frac{1}{e^2}$ of its maximum value at (x_0, y_0) . For the evaluation of the mean fluence of the SH probe pulse we will use this definition of the beam radius. The radius w around the center of the Gaussian contains 86.5% of its area which directly corresponds to the fraction of incident laser power within this beam diameter $P(a_{\text{probe}})$, with the radius of the probe pulse defined as $a_{\text{probe}} = w$. Therefore, the actual laser power contained in the defined area of the probe pulse is $P(a_{\text{probe}}) = 0.865 \cdot \bar{P}$, with \bar{P} being the total incident laser power.

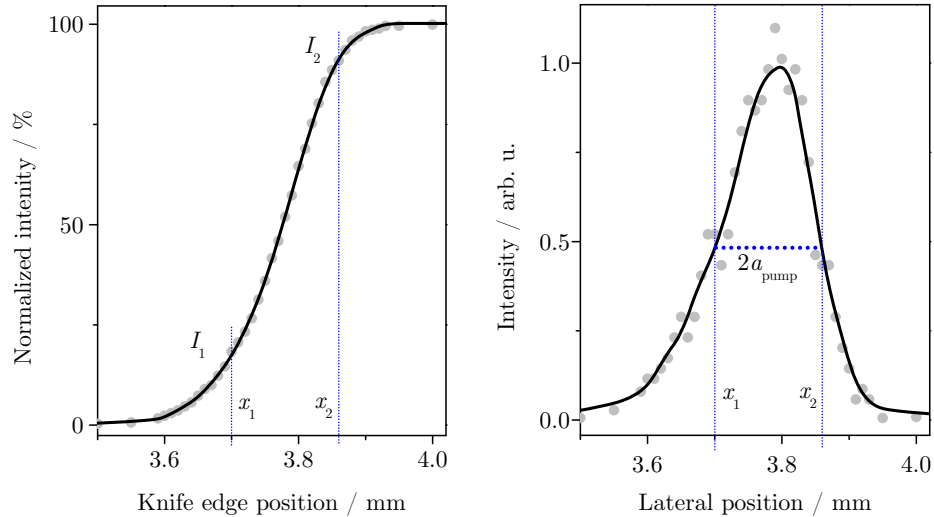
$$\begin{aligned}
 I(x) &= \text{const.} \times \exp \left[-\frac{(x - x_0)^2}{2\sigma^2} \right] \times \underbrace{\int_{-\infty}^{\infty} \exp \left[-\frac{(y - y_0)^2}{2\sigma^2} \right] dy}_{=\sqrt{2\pi}\sigma \text{ [143]}} \\
 &= \sqrt{2\pi}\sigma \times \text{const.} \times \exp \left[-\frac{(x - x_0)^2}{2\sigma^2} \right] \\
 &:= \text{const.} \times \exp \left[-\frac{(x - x_0)^2}{2\sigma^2} \right] \tag{3.2}
 \end{aligned}$$

For the photon energy of $h\nu = 3.18 \text{ eV}$ used for all two-color pump-probe experiments the beam diameter of the focused SH probe pulse is estimated for laser 3_{TR} to be $2a_{\text{probe}} = 26.2 \mu\text{m}$. The integral knife-edge profile [e. g. figure 3.5(a)] yields a symmetric Gaussian beam profile after differentiation. The mean power of the SH is set by defocusing the crystal for second harmonic generation. To eliminate any potential influence of this defocusing on the beam diameter, the beam profiling is carried out at a typical total incident laser power value of 8 mW. However, a significant modification is not to be expected, because we operate in the very focus of the SH beam and the change in position of the SHG crystal is negligible in the power range used for the probe pulses. Overall, the SHG position influences the beam diameter before focusing.

For the infrared (IR) pump beam on the other hand only the part of the spot overlapping with the probe pulse is relevant for the two-color pump-probe experiments. The value of the fluence for a chosen diameter depends on the position within the beam profile. It is the highest in the center and decreases to the edges. Although the spatial overlap of pump and probe pulses is aligned with great care, we cannot guarantee a perfect overlap in the very center of both focused beams. The exact relative position may even change within a series of experiments due to minimal movement of the UHV chamber and the optical table, changes of the sample position for optimization of the photoemission spectrum or due to differences in the weight of the liquid nitrogen used for cooling of the sample, which is attached to the UHV chamber. This uncertainty is considered by a diameter of the fundamental pump pulse four times the diameter of the probe pulse, i. e. $a_{\text{pump}} = 4a_{\text{probe}}$. This corresponds to definition of a mean value of the fluence of

3 Experimental Setup

the pump pulse for the area we expect the probe pulse to reside in. The pump power contained within this radius and centered on its maximum is used to calculate the fluence.



(a) Integral knife-edge beam profile. The intensities I_i corresponding to the edges of the chosen beam diameter x_i ($i \in \{1, 2\}$) define the fraction of intensity within the x_i range

(b) Derivative of (a) as well as smoothed curve. x_i are defined as the position where the chosen beam diameter fits the beam profile.

Figure 3.5: Procedure to extract the percentage of incident pump laser power \bar{P} within the beam radius a_{pump} .

Analogously to our discussion for the probe pulse we evaluate the knife-edge intensity profile of the pump pulse. Figure 3.5(a) shows such a profile. In this case the pump beam radius, a_{pump} , is given and we like to find the corresponding fraction of the total incident laser power residing within this diameter, P_{knife} . Differentiation of the integral profile, shown in figure 3.5(a), leads to the asymmetric beam profile in figure 3.5(b). The beam profile is smoothed and the lateral positions x_1 and x_2 corresponding to the radius a_{pump} are estimated. The intensities I_1 and I_2 corresponding to these lateral positions are evaluated from the integral knife-edge profile in figure 3.5(a), which yields the fraction of laser power residing within the chosen beam diameter, $2a_{\text{pump}} = 104.8 \mu\text{m}$, as $P_{\text{knife}} = I_2 - I_1$. Please note, that the radii a_{pump} and a_{probe} defined in this section will be used throughout this work for all experiments using laser 3.

Figure 3.6 reveals a non-linear dependence of the full beam diameter as defined by a 10% to 90% integral intensity criterion for the knife-edge profile (black, circles). The fundamental is attenuated by a rectangular gray filter which is covered by an absorbing metal coating with a thickness gradient along one axis. The absorbancy of this coating

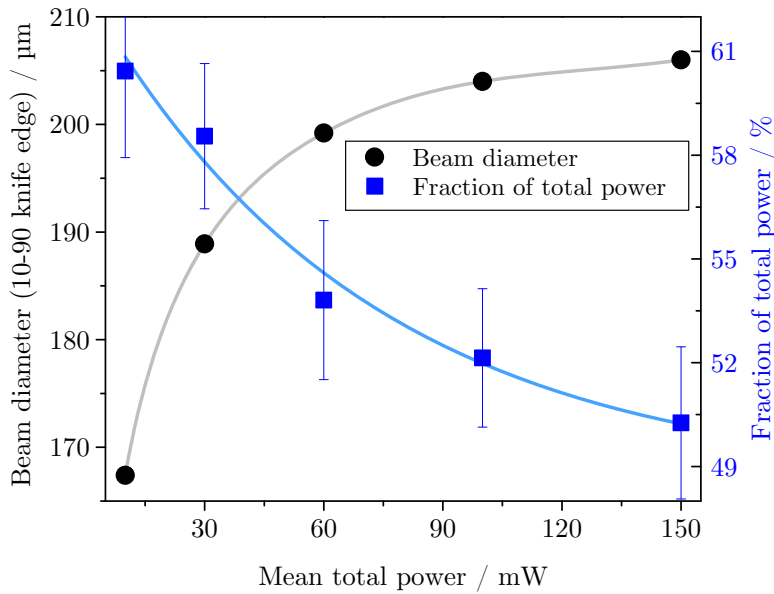


Figure 3.6: Narrowing of the beam diameter with decreasing total laser power (black circles) due to non-uniform attenuation of the filter. The full line is a guide to the eye. The percentage of the area within the chosen beam diameter a_{pump} decreases with increasing beam diameter (blue squares). The full line is an empirical exponential-like fit.

is non-linear, therefore, the beam profile becomes asymmetric, because it is suppressed stronger in one direction [see figure 3.5(b)]. This leads to a stronger asymmetry at small transmitted laser powers and a consequent reduction of beam diameter, which is, by itself, not relevant here, because we always evaluate the same pump pulse diameter. However, the full transmitted laser power is concentrated to a smaller area for low laser powers, i. e. the fraction of power contained within a_{pump} is increased (blue, squares). We find empirically a good agreement of the power dependence of P_{knife} to an exponential function $f(x) = a + b[\exp(cx) - 1]$, with fit parameters a , b , and c . This fit is used to define P_{knife} for a given transmitted laser power.

There is still a considerable deviation from the relevant fraction of laser power contained within a circular laser spot of diameter a_{pump} , P_a , and the fraction estimated from the knife-edge profile, which is a consequence of the integration along one axis in case of the knife-edge profile. Using a 2D Gaussian profile which is normalized to volume of 1, i. e. integration over the whole profile yields 1, corresponding to 100% of the transmitted laser power, we define, following equation (3.1), $I(x, y) = f(x)f(y)$, with $f(x) = \frac{1}{\sqrt{2\pi}\sigma} \exp\left[-\frac{(x-x_0)^2}{2\sigma^2}\right]$ [143]. This yields the fraction of laser power within $r_1 \equiv x_1 = y_1$ (and analogously for r_2) for the knife-edge method and for a circular

integration area:

$$\begin{aligned}
 P_{\text{knife}} &= \int_{r_1}^{r_2} f(x) dx \int_{-\infty}^{\infty} f(y) dy \\
 &= \sqrt{2\pi}\sigma \int_{r_1}^{r_2} f(x) dx
 \end{aligned} \tag{3.3}$$

$$\begin{aligned}
 P_a &= \int_{r_1}^{r_2} f(x) dx \int_{r_1}^{r_2} f(y) dy \\
 &= \left[\int_{r_1}^{r_2} f(x) dx \right]^2,
 \end{aligned} \tag{3.4}$$

which yields:

$$P_a = \frac{1}{2\pi\sigma^2} P_{\text{knife}}^2 =: P_{\text{knife}}^2, \tag{3.5}$$

using the definition, that the integral over the full profile is defined as unity, i. e. $(2\pi\sigma^2)^{-1} =: 1$.

Because the sample surface is aligned perpendicular to the energy analyzer, the angle of incidence of the laser is 45° . The laser spot on the sample surface is therefore elliptical. The beam radius a perpendicular to the plane of incidence is given by the values we extracted for our beam profiling in the focal plane. The beam is, however, horizontally broadened to the radius $b = \frac{a}{\sin(45^\circ)}$. Therefore, by using these two radii we can calculate the spot area of the laser as $A(a) = \sqrt{2}\pi a^2$.

Using these considerations, we are able to calculate the absorbed mean fluence per pulse F_{pp} using equation (3.6). $P(a) = \bar{P} P_a$ (\bar{P} is the full laser power, P_a is the fraction absorbed within beam diameter a) is the laser power incident on the area $A(a)$, f_{rep} is the laser repetition rate. The factor τ_{FS} corresponds to the transmission of the FS lens and the entry window of the UHV chamber. The transmission of the lens is experimentally estimated to be $\tau_{\text{lens}} \approx 93\%$ for the fundamental using a power meter. We expect the same value for the SH, too, because the transmission characteristics of fused silica in a range of about 300 nm to 1000 nm is virtually constant [144]. For the entrance window of the UHV chamber we find $\tau_{\text{window}} \approx 92\%$ [144], leading to a total transmission of $\tau_{\text{FS}} = \tau_{\text{lens}} \times \tau_{\text{window}} \approx 85.6\%$.

$$F_{\text{pp}} = \tau_{\text{FS}} \times \alpha \times \frac{P(a)}{A(a)f_{\text{rep}}} \tag{3.6}$$

The absorption of the laser, α , needs to be calculated by a more complicated procedure. We extracted values of the complex dielectric function $\varepsilon^j = \varepsilon_1^j + \varepsilon_2^j i$ ($j = \parallel, \perp$) for p- and

s-polarized incident laser light from the work of Reshak and Auluck [68]. The complex refraction $\mathbf{n} = n + \kappa i$ for both polarizations is calculated as follows [68, 145]:

$$\begin{aligned} n^2 &= \frac{1}{2} \left(\sqrt{\varepsilon_1^2 + \varepsilon_2^2} + \varepsilon_1 \right) \\ \kappa^2 &= \frac{1}{2} \left(\sqrt{\varepsilon_1^2 + \varepsilon_2^2} - \varepsilon_1 \right). \end{aligned} \quad (3.7)$$

Please keep in mind, that the complex dielectric function and consequently the complex refraction index are dependent on photon energy. The refraction indices for the photon energy of the fundamental and the SH typically used in our time-resolved IR-pump SH-probe photoemission experiments are shown in table 3.5.

Table 3.5: Complex refraction indices for the photon energies typically used for the two-color pump-probe experiments for p- and s-polarized incident light as calculated from the corresponding complex dielectric function presented in reference [68]. The corresponding absorptions α_{TiSe_2} , α_{TiTe_2} , and α_{Ag} for p-polarized light under an angle of incidence of 45° as calculated using equation (3.8) is also given.

photon energy / eV	refraction index		absorption α / %	
	p-pol.	s-pol.	p-pol.	s-pol.
1 T-TiSe ₂				
1.59	2.84 + 1.26i	2.98 + 4.41i	81.56	25.38
3.18	3.66 + 1.30i	2.76 + 1.78i	75.31	51.28
1 T-TiTe ₂				
1.59	3.40 + 1.25i	2.46 + 2.14i	77.63	47.28
3.18	3.14 + 2.22i	2.43 + 2.03i	69.29	48.93
Ag(111)				
3.18	0.095 + 1.87i		9.97	

We cannot directly use the reflectivity values also given in reference [68], because our setup does not feature normal incidence of the laser beams. The reflectivity in dependence of the angle of incidence is calculated by using the Fresnel equations [146, 147], [see also e. g. 145, 148]:

$$r_{\parallel} = \frac{\mathbf{n}^2 \cos(\vartheta) - \sqrt{\mathbf{n}^2 - \sin^2(\vartheta)}}{\mathbf{n}^2 \cos(\vartheta) + \sqrt{\mathbf{n}^2 - \sin^2(\vartheta)}} \quad (3.8)$$

$$r_{\perp} = \frac{\cos(\vartheta) - \sqrt{\mathbf{n}^2 - \sin^2(\vartheta)}}{\cos(\vartheta) + \sqrt{\mathbf{n}^2 - \sin^2(\vartheta)}}, \quad (3.9)$$

with the angle of incidence ϑ . The reflectivity is the square of the absolute value of the Fresnel equations (3.8) and (3.9). It is calculated as $R_j = |r_j|^2$, with $j = \parallel, \perp$. This yields the absorption $\alpha = 1 - R_{\parallel}$. For an angle of incidence of $\vartheta = 45^\circ$, p-polarization, and the complex refraction indices for the two photon energies discussed here, we derive an absorption of $\alpha_{\text{TiSe}_2}(1.59 \text{ eV}) = 81.56\%$ for the fundamental pump pulses and $\alpha_{\text{TiSe}_2}(3.18 \text{ eV}) = 75.31\%$ for the SH probe pulses. An analogous calculation yields the absorption α_{TiTe_2} for our reference system 1T-TiTe₂ (ε_1 and ε_2 extracted from reference [68]). All relevant data is summarized in table 3.5.

For some experiments a Ag(111) single crystal is used. The absorbed fluence can be estimated analogously to TiSe₂ by employing equation (3.6). However, in this case we need to know the absorption of silver α_{Ag} . Stahrenberg et al. [149] acquired the dielectric function of Ag(110) in an ellipsometry experiment and by calculations. We extract $\varepsilon_1 \approx -3.5$ and $\varepsilon_2 \approx 0.36$ at a photon energy of $h\nu = 3.18 \text{ eV}$ from their data. Equation (3.7) enables us to calculate a complex refraction index of $\mathbf{n} \approx 0.095 + 1.87i$. By using this value of \mathbf{n} as an approximation for our Ag(111) crystal, equation (3.8) enables us to calculate an estimated absorption of Ag(111) of $\alpha_{\text{Ag}}(3.18 \text{ eV}) = 9.97\%$, which will be used throughout this work. The data is included in table 3.5.

These calculations finally enable us to calculate the mean fluence per pulse absorbed in our TiSe₂ samples. The typical probe fluence is $5 \mu\text{J cm}^{-2}$, although fluences of up to about $50 \mu\text{J cm}^{-2}$ are applied in section 5.2. For the IR pump pulses, as used in section 6.2, the fluence varies in a range of approximately $0.3 \mu\text{J cm}^{-2}$ to $3.5 \mu\text{J cm}^{-2}$. Please note, that the chosen pump diameter is rather large. However, as we explicitly consider only the laser power contained within this radius the impact on the mean pump fluence value is quite low. We estimate the fluence to increase by about 11%, if the pump diameter is reduced to only two times of the probe pulse diameter.

3.2.1–c Setting the Laser Fluence

Throughout this work we will use three slightly different means of setting a defined value of the laser fluence for three different experimental cases: (i) spectroscopy, (ii) TR-2PPE [see figure 3.3(a)], and (iii) time-resolved IR-pump SH-probe photoemission experiments [see figure 3.3(b)].

For the spectroscopic experiments we use a very simple approach. Two linear gray filters are introduced into the optical setup. The first filter reduces the power of the fundamental beam incident on the LBO crystal [“SHG” in figure 3.3(a)] which allows a coarse setting of the mean SH laser power. Furthermore, this approach reduces the degradation of the non-linear crystal as observed for high laser powers. Reducing the power before SH generation to the necessary value thus enhances the long-term power stability. A second gray filter right in front of the UHV chamber enables fine tuning of

the laser power transmitted to the sample. Using a second filter enables us to change the transmitted laser power without destabilizing the SHG crystal.

For auto- and cross-correlation TR-2PPE experiments we use a slightly different approach. The power incident on the SHG crystal is reduced by a linear gray filter like before. The power is set such, that the maximum SH power needed for the experiment is available. The power incident on the UHV system is then fine tuned by defocussing the fundamental beam at the position of the SHG crystal by slightly moving the crystal itself along the beam axis. Although the SHG needs to be stabilized after each change of crystal position, avoidance of a second linear gray filter in the SH beam line is favorable in case of time resolved experiments. The attenuation of laser power is always performed for a considerable beam waist—the damage threshold of the filter does not allow its application at a focal point—i. e. the filter varies slightly over the beam profile in horizontal direction. We therefore avoid such filters in the time resolved experiments to circumvent any modification of the spatial pulse shape.

Finally, for time-resolved IR-pump SH-probe photoemission experiments a combination of both previous methods is used. The optical setup is slightly different in this case [see figure 3.3(b)] as we use both fundamental (pump) and SH pulses (probe). We need high fluences of the fundamental pulses, i. e. a coarse attenuation before the SHG is not possible. The fundamental power is reduced right after the SHG crystal between dichroic beam splitter and the collimating lenses. We have to use a linear gray filter in this case which is, however, rather unproblematic because of the small beam diameter at this position. The SH power is attenuated analogously to the TR-2PPE setup by defocusing.

3.2.1–d Estimation of the Pulse Duration

The temporal length of the SH laser pulse in case of the two-color pump-probe experiments is measured in-situ at the position of the sample in the UHV chamber by a TR-2PPE reference experiment using a Ag(111) single-crystal (see also chapter 3.2). Ag(111) is used instead of the tantalum sheet for two reasons:

- The position of the surface of the Ag(111) crystal corresponds rather well to the actual surface position of the TiSe_2 crystals. In general, a difference in the optical path may increase the pulse duration due to the additional GVD. This problem, although exceptionally small considering the UHV condition in the chamber, is practically circumvented by ensuring the same sample position.
- Ag(111) is crucial for finding and optimizing the temporal overlap of the pump and probe pulses. We will discuss this procedure in this section shortly.

3 Experimental Setup

For the TR-2PPE reference experiment the optical setup of figure 3.3(a) has to be used, i. e. the optical path of the SH light is slightly different, than in case of the time-resolved IR-pump SH-probe photoemission experiment. Both optical paths feature the same amount of dispersive optical elements (focusing lens and entry window of the UHV chamber), but more mirrors and an overall longer optical path through air are necessary for the pump-probe experiment in comparison to the TR-2PPE reference measurement. Therefore, a difference in pulse length is to be expected due to the additional GVD in case of the pump-probe setup. This difference has to be considered for the correct SH pulse duration. We calculated the temporal broadening of the SH pulses using the *Lab2* package [150] for *LabVIEW* (National Instruments). The effect of GVD and third order dispersion (TOD) on the temporal pulse width is discussed in section 2.3. We considered only the difference in propagation path length, which is $\Delta s_{\text{SH}} = 25.5 \text{ cm}$ longer for the actual pump-probe experiment, than in case of the reference autocorrelation experiment. Broadening of the pulse due to the different amount of mirrors is negligible.

Table 3.6: Exemplary data of the fundamental (central wavelength $\lambda = 780 \text{ nm}$) and SH (390 nm) of a two-color pump-probe experiment. The bandwidth $\Delta\lambda$ is used to calculate the temporal width of the transform-limited pulses $\Delta\tau_{\text{TL}}$. Experimentally, autocorrelation traces are acquired which FWHM FWHM_{AC} is used to calculate the temporal pulse width $\Delta\tau_{\text{exp}}$ using the conversion factors in table 3.2. The difference of $\Delta\tau_{\text{exp}}$ and $\Delta\tau_{\text{TL}}$ is due to uncompensated GVD of the pulses. By assuming a GVD_0 , the experimental FWHM_{AC} is reproducible, leading to a non-transform-limited pulse width $\Delta\tau_{\text{GVD}_0}$. Because the pulse shape is a mixture of Gaussian and sech, all calculations are performed for both shapes using *Lab2* [150].

λ/nm	$\Delta\lambda/\text{nm}$	$\Delta\tau_{\text{TL}}/\text{fs}$	$\text{FWHM}_{\text{AC}}/\text{fs}$	$\Delta\tau_{\text{exp}}/\text{fs}$	GVD_0/fs^2	$\Delta\tau_{\text{GVD}_0}/\text{fs}$
Gaussian						
780	25.1	35.8	58.5	41.4	264.5	41.4
390	6.1	36.9	58.8	41.6	252.5	41.5
sech						
780	25.1	26.1	58.5	37.9	266.6	43.8
390	6.1	26.9	58.8	38.1	266.7	44.0

In figure 3.3(b) a mirror right after the second dichroic beam splitter which recombines fundamental and SH is used to reroute the spatially overlapped fundamental and SH pulses to the commercial autocorrelator and spectrometer. This enables us to not only measure the bandwidth of both pulses, but also to estimate the pulse duration of the fundamental ex-situ. In our setup, it is not possible to perform TR-2PPE using the fundamental, because neither a two fundamental pulses, nor a fundamental and SH pulse are sufficient for photoemission. The pulse duration cannot be measured in-situ

at the sample position for the fundamental, but the external autocorrelator is used instead. The spectral bandwidth $\Delta\lambda_{\text{SH}}$ and the central wavelength λ acquired with the spectrometer are used to calculate the pulse duration of a corresponding transform-limited pulse $\Delta\tau_{\text{TL}}$ for both fundamental and SH. Table 3.6 shows such data measured for an exemplary time-resolved IR-pump SH-probe photoemission experiment. The FWHM of the autocorrelation FWHM_{AC} acquired in-situ (SH) or ex-situ (fundamental) enables us to calculate the temporal width of the pulses $\Delta\tau_{\text{exp}}$ by assuming transform-limited pulses and using the conversion factors in table 3.2.

We expect a mixture of Gaussian and sech pulse shape. Therefore, we perform these calculations for both shapes. In case of the exemplary experiment, the autocorrelation is fitted very well by a Gaussian, i. e. Gaussian shaped pulses are a reasonable assumption². The data in table 3.6 clearly show a significant difference of the calculated transform-limited (i. e. minimal) pulse duration and the duration extracted from the experimental autocorrelation traces. We conclude, that the GVD of the pulses in this exemplary experiment is not compensated completely. By assuming a certain GVD_0 for the simulation of the autocorrelation, the FWHM_{AC} of the non-transform-limited pulse can be reproduced. The actual pulse duration under the assumption of GVD_0 is also included as $\Delta\tau_{\text{GVD}_0}$ in the table. Please note, that $\Delta\tau_{\text{exp}}$, the pulse duration calculated from the experimental FWHM_{AC} values, is only valid for transform-limited pulses, which is clearly not the case here. These values are given to demonstrate the effect of assumed pulse-shape on the temporal pulse widths. For Gaussian-shaped pulses the difference of the pulse duration of the transform-limited and the experimental pulses is negligible, but it is significant for sech-shaped pulses. Therefore, whenever a sech pulse shape is observed and the pulse duration needs to be extracted from an autocorrelation trace, the influence of residual GVD (GVD_0) on the actual pulse width needs to be taken into account. This is especially important in case of TAR-2PPE using laser 2, where we indeed observe sech-shaped pulses (see chapter 3.2.2).

Table 3.7: Broadening of the fundamental ($\lambda = 780 \text{ nm}$) and SH ($\lambda = 390 \text{ nm}$) due to an additional optical path through air Δs_{air} and fused silica Δs_{FS} . The GVD (GVD_{air} and GVD_{FS}) is calculated for the experimental data of table 3.6 under assumption of GVD_0 using reference [150]. The temporal pulse width at the sample $\Delta\tau_{\text{calc}}$ is given for Gaussian and sech pulses.

λ/nm	$\Delta s_{\text{air}}/\text{mm}$	$\Delta s_{\text{FS}}/\text{mm}$	$\text{GVD}_{\text{air}}/\text{fs}^2$	$\text{GVD}_{\text{FS}}/\text{fs}^2$	$\Delta\tau_{\text{calc}}/\text{fs}$	
					Gaussian	sech
780	715	5.3	15.7	200.4	51.9	59.5
390	255	0.0	13.1	0.0	42.0	44.9

²We use laser 3_{TR} for most of our time resolved experiments. In this case, a Gaussian pulse shape is in good agreement.

For the SH pulses we have to consider only the additional optical path which completely passes through air Δs_{SH} . The *Lab2* simulation accounts not only for the corresponding GVD (GVD_{air} , included in table 3.7), but also higher order dispersion like TOD. The latter becomes important in the estimation of the pulse broadening, especially in case of the dispersive optical elements. The interplay of TOD and GVD can lead to sidings of the autocorrelation—the center contribution of the trace may then seem quite narrow, i. e. the pulsewidth seems reduced [106]. The calculated pulse duration at the sample position within the UHV chamber $\Delta\tau_{\text{calc}}$ is given for Gaussian- and sech-shaped pulses. For the fundamental, the optical path of the pump-probe experiment is $\Delta s_{\text{fund, air}} = 71.5$ cm longer than the path used to acquire the ex-situ autocorrelation. Again, the contribution of the different amount of mirrors is negligible, but in this case additional GVD is introduced by dispersive optical elements, the lens and the entry window of the UHV chamber, which are both made of fused silica. Again, by using the spectral bandwidth of the fundamental, we calculate the pulse duration at the sample position analogous to the SH case. A total of $\Delta s_{\text{fund, FS}} \approx 5.3$ mm of FS is additionally passed in the pump-probe path. Again, the calculated GVD is included in table 3.7 as well as the corresponding TOD, which is needed for a correct simulation if FS is introduced into the optical path. The autocorrelation of the SH fits very well to a Gaussian, therefore, we use the $\Delta\tau_{\text{calc}}$ values for a Gaussian-shaped pulse; the values acquired for sech pulses provide an estimate of the uncertainty of our pulse duration values.

We derive the following temporal pulse width at the sample position for these data in the two-color pump-probe experiment: $\Delta\tau_{\text{calc}}(\text{SH}) = (42.0 \pm 2.9)$ fs and $\Delta\tau_{\text{calc}}(\text{fund}) = (51.9 \pm 7.6)$ fs. In case of an unclear pulse shape, i. e. a mixture of Gaussian and sech, we will use the mean value and standard deviation of $\Delta\tau_{\text{calc}}$ for both shapes as an estimate. In summary, the pulse durations specified in this work are either measured in-situ (SH in case of TR-2PPE and TAR-2PPE) or they are measured ex-situ and corrected for the additional GVD and TOD as in case of the fundamental and SH for the two-color pump-probe experiments.

We will finally comment on the necessity of the Ag(111) reference sample for the time-resolved IR-pump SH-probe photoemission experiments. In fact, Ag(111) is an integral part of the alignment process for these experiments. This system is used for the measurement of the SH pulse duration in a TR-2PPE experiment, but more importantly, we can optimize the temporal overlap of fundamental and SH pulses using spectroscopy data of this sample. This is achieved as follows: We use a two-color 2PPE process involving one photon of the fundamental and one photon of the SH. At a wavelength of 780 nm ($h\nu_{\text{fund}} = 1.59$ eV, $h\nu_{\text{SH}} = 3.18$ eV), the usual value employed for the time-resolved IR-pump SH-probe photoemission experiments, the Fermi-edge of the two-color 2PPE spectrum is expected to be 1.59 eV, i. e. one photon energy of the fundamental, below the Fermi-edge of the corresponding SH-2PPE [see figure 3.7(a)]. Such a two-photon process with fundamental and SH is only possible, if the pump and probe pulses overlap temporally, i. e. the spectrum is acquired at time zero, which is the reason, why we are able

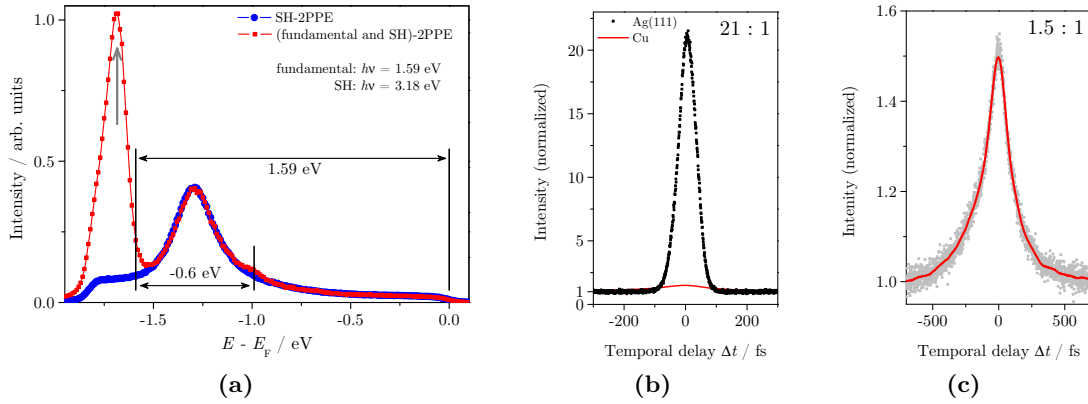


Figure 3.7: Optimization of the temporal overlap of the pump and probe pulses. (a) Ag(111) shows a clear 2PPE signal of fundamental and SH when the pulses overlap temporally. (b) The cross-correlation shows a very strong signature at time zero [acquired at the binding energy shown by a gray arrow in (a)] (c) Cross-correlation on the Cu holder of the TiSe₂ samples used as time zero for the actual pump-probe experiments on TiSe₂. The signal is much too subtle for the initial search of the temporal overlap.

to optimize the temporal overlap of fundamental and SH using this method. Furthermore, the work function needs to be small enough to support such a two-color 2PPE process, which is not true for the polycrystalline tantalum sheet ($\Phi_{\text{Ta}} \approx 5 \text{ eV}$, experimental value) and the TiSe₂ sample ($\Phi_{\text{TiSe}_2} = 5.7 \text{ eV}$ [151]). However, the Ag(111) reference crystal ($\Phi_{\text{Ag}(111)} = 4.74 \text{ eV}$ [152]) fulfills this prerequisite, as well as the polycrystalline copper sample holder ($\Phi_{\text{Cu}(\text{poly})} = 4.65 \text{ eV}$ [152]).

The small bump at about 0.6 eV above the Fermi-edge [see figure 3.7(a)] of the two-color 2PPE from fundamental and SH is also present at the corresponding energy for the SH-2PPE. This feature corresponds to a three-photon photoemission (3PPE) process involving either three SH photons or one fundamental and two SH photons. In this case an image potential state of Ag(111) acts as a second intermediate state. $E - E_F = 0.62 \text{ eV}$ is expected for this state and excitation with photons of 1.59 eV and 3.18 eV is feasible [153].

Figure 3.7(b) shows a cross-correlation of fundamental and SH pulses acquired on Ag(111). It is used to find the temporal overlap of pump and probe pulses for the time-resolved IR-pump SH-probe photoemission experiments on TiSe₂. The small deviation in the actual time zero of the Ag(111) reference sample and the TiSe₂ sample are compensated using a second cross-correlation acquired on the polycrystalline copper sample holder on which the TiSe₂ sample is attached [see figure 3.7(c)]. This cross-correlation is used to define the time zero for the time-resolved IR-pump SH-probe photoemission experiments. Please note, the big difference in signal to noise ratio for both cross-correlations. While a ratio of 14:1 is achieved on Ag(111), the signal acquired

on the Cu holder is barely visible. We cannot identify a dedicated two-color 2PPE signal on Cu, i.e. we observe an increase in intensity for the whole spectrum and virtually no special modifications in the 3PPE range identified for Ag(111). In fact, we just observe subtle modifications of the SH-2PPE signal in time zero. The corresponding cross-correlation curves for Cu and Ag(111) are visualized in figure 3.7(b). Clearly, we see a very distinct difference in the signal to noise ratio, which nicely demonstrates the need to use Ag(111) for searching the temporal overlap. The signal derived from the Cu holder is just too weak.

3.2.2 Evaluation of the TAR-2PPE data

A TAR-2PPE measurement consists of a series of AR-2PPE spectra acquired at varying temporal delays Δt of the pulses involved in the 2PPE process. Figure 3.8 shows such spectra (top) for seven exemplary delays in the range of -100 fs to 100 fs at ± 100 fs, ± 30 fs, ± 17 fs and 0 fs. The spectra show a significant increase of intensity in the delay range of the temporal overlap of both contributing pulses. By selection of a certain kinetic energy and emission angle range (white, hatched box) an autocorrelation curve can be generated by plotting the integrated intensity of the area versus the temporal delay Δt (center). The red dots emphasize the delays in the autocorrelation trace corresponding to the spectra at the top. This procedure can be applied to the whole 2D spectral range, producing a set of autocorrelation traces. Assuming sech-shaped pulses, the autocorrelations are fitted using a sech² function. Although the real laser pulse shape is a mixture of Gaussian and sech, the latter seems to fit the data acquired with laser 2 better. This yields a set of FWHM values. The bottom of figure 3.8 shows the generated FWHM-map, i.e. a 2D representation of the FWHM values of the corresponding energy and angle ranges. The values are color-coded from blue for small to red for broad FWHM. Due to the broadening of the autocorrelation in the presence of intermediate states with non-vanishing lifetime, this representation already maps the relative changes in the lifetime of the spectral range investigated. For instance, the non-dispersive feature at the center is indeed generated by an intermediate band which population decay is probed in this experiment (for details see chapter 4). The lifetime mapping clearly visualizes the decay dynamics of the spectral structures and allows a straightforward access to the lifetime distribution within the electronic structure. Please notice, that the variation of the FWHM is not due to the intensity enhancement at time zero, as one might assume at first glance. The spectra at the top clearly show an intensity enhancement for all spectral features, yet only the intermediate band shows up in the lifetime map.

The lifetime map is already a very powerful tool to get a qualitative impression of the relative lifetime changes within a certain energetic and angular range. Even subtle changes, which are not easily seen in the individual autocorrelation traces, can be easily observed in the lifetime map due to the sheer amount of available lifetime values which compensates for the noise in the individual values. Yet, a quantitative analysis of the

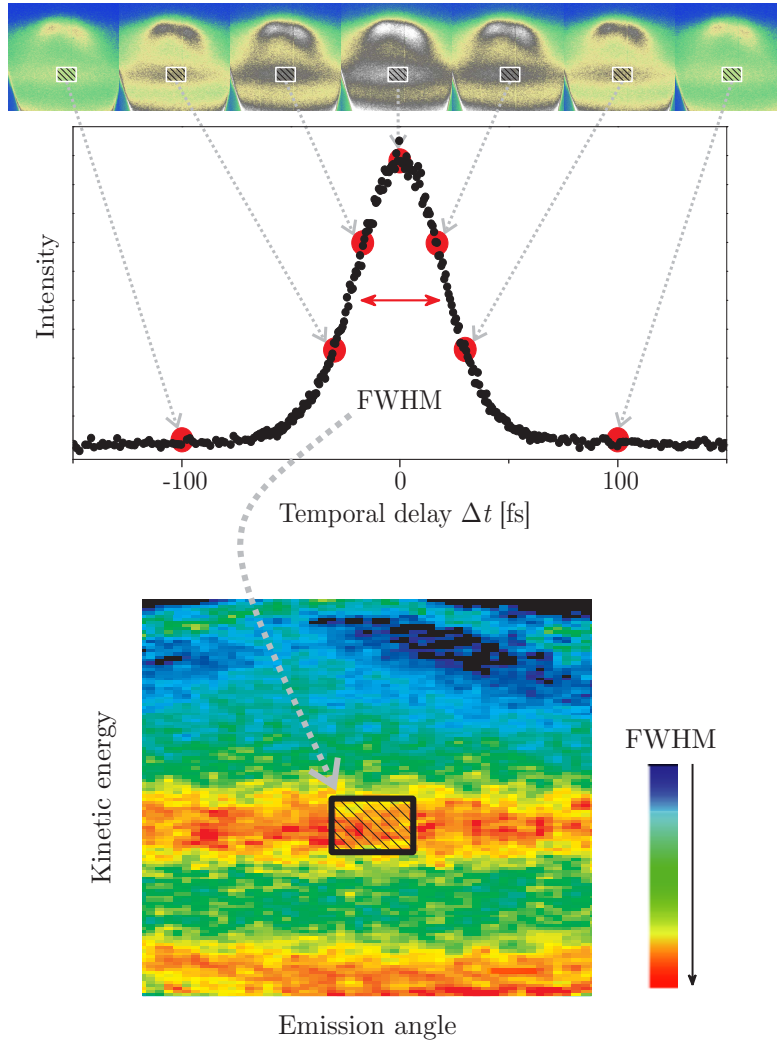


Figure 3.8: A TAR-2PPE measurement consists of a series of AR-2PPE spectra acquired for defined delays Δt (top). For certain ranges of kinetic energy and emission angle an autocorrelation trace is generated by integrating intensity values for each delay (center). The FWHM of these curves are mapped to kinetic energy and emission angle again, yielding a color-coded representation of the FWHM of the autocorrelation for all spectral regions (bottom). The FWHM corresponds to the lifetimes of the states involved.

data is needed to extract the actual lifetime from the FWHM of the autocorrelation traces.

For a quantitative analysis the autocorrelation traces need to be deconvoluted by comparison to simulated autocorrelation traces. We will define a lifetime T_1 of the relaxation of the intermediate states population as proposed by Gauyacq and Kazansky [114]. Our deconvolution method consists of the following steps: First of all, the actual duration of the laser pulses at the sample surface is measured. While this information has to be corrected for a difference in the optical path for the fundamental (see chapter 3.2.1), it can be measured in-situ in a TR-2PPE experiment using the SH. A Cu(111) single crystal serves as a reference for the TAR-2PPE experiments. Because the 2PPE from the initial Shockley surface state proceeds via a strongly off-resonant intermediate state, the resulting autocorrelation trace is not broadened considerably by lifetime effects, i. e. the trace is virtually a convolution of the laser pulse shape with itself [120, 154]. The pulse length can easily be extracted by assuming a laser pulse shape—sech in our case—and subsequent deconvolution of the autocorrelation by simply using the factors in table 3.2. The temporal width of the sech-shaped pulses cannot be extracted reliably from an autocorrelation for non-transform-limited pulses (see discussion in section 3.2.1). This problem can be resolved by the assumption of a certain uncompensated GVD and simulation of the corresponding broadening of the transform-limited pulse using a *Lab2*-based simulation. By optimizing the amount of GVD for reproduction of the experimental autocorrelation, a better value of the pulse duration can be achieved. However, for the deconvolution of the lifetimes the actual pulse duration is not needed. The laser autocorrelation itself is sufficient, because in case of a sech-shaped pulse (sech²-shaped intensity profile), the autocorrelation is also sech²-shaped, because it is just the convolution of a sech² with itself.

Please note, that this is not of concern for this work. For the sech²-shaped autocorrelation we directly use this trace itself for the extraction of lifetime data. Knowledge of the exact pulse duration is not necessary. Furthermore, for most of our experiments the pulses are indeed Gaussian shaped, i. e. the problem discussed before does not apply.

This method can be used to extract lifetimes for individual spectral features, i. e. in case of the non-dispersive signature observed in figure 3.8 its whole energetic and angular range is integrated to generate a single autocorrelation trace for further evaluation. In fact, a single autocorrelation is compared to a set of simulated data to find the best fitting lifetime value. For the 2D lifetime maps this procedure is much too time consuming. In this case only selected areas featuring significant differences of the FWHM_{AC} are evaluated. The extracted lifetimes are then used for linear inter- and extrapolation, thus assigning lifetimes to all the FWHM_{AC} values [53]. Please keep in mind, that this approach does not degrade the quality of the lifetime values for certain spectral features, because the 2D maps are used solely for an overview of the data and never for quantitative statements. Nevertheless, the linear interpolation proves to be a very good assumption.

The autocorrelations acquired for the TiSe₂ samples are broadened by the lifetimes

of the bands involved. The lifetime is extracted from the traces following a procedure described in detail in references [114, 124]:

- First, a sech²-shaped laser autocorrelation is calculated either by using the experimentally determined pulse length and convolution of the sech²-shaped pulse intensity with itself in case of transform-limited pulses, or by calculating a sech²-shaped autocorrelation with the experimentally determined FWHM_{AC} for non-transform-limited pulses. The actual shape of the autocorrelation, i. e. Gaussian or sech², has only minor influence on the lifetime values extracted.
- The resulting laser autocorrelation is convoluted with a decreasing exponential, mimicking the broadening due to the finite lifetime of the intermediate state involved in the photoemission process. By variation of the characteristic time T_1 of the exponential, a set of calculated autocorrelation traces for different lifetimes is derived.
- The experimental and calculated data are quantitatively compared in the delay range of 0 fs to 100 fs by calculation of a χ^2 value [see equation (3.10)], which is commonly used to characterize the goodness of a fit [155]. Basically, the squared deviation of every single measured intensity x_i from the calculated or expected value e_i is summed:

$$\chi^2 = \sum_i \frac{(x_i - e_i)^2}{e_i}. \quad (3.10)$$

- The characteristic time of the calculated trace showing the smallest χ^2 value is the wanted lifetime value T_1 .
- For the 2D lifetime map lifetime values are assigned to the FWHM values by linear interpolation [53].

This procedure finally yields in parallel a complete lifetime value data set $\tau(E_{\text{kin}}, \vartheta)$ easily converted to $\tau(E, \mathbf{k}_{\parallel})$, covering the complete experimentally accessible energy and momentum regime [53, 156].

3.3 Crystal Growth and Preparation of TiSe₂

The 1T-TiSe₂ single crystals used for the experiments were grown in the laboratories of the work group of Prof. Dr. L. Kipp at the university of Kiel by chemical vapor transport using iodine as a transport gas [8, 157, 158]. The crystals were grown at a temperature of 660 °C at a selenium excess of 3 mg cm⁻³. Such a procedure results in the formation of large, homogeneous single crystals with a typical size of 3 × 3 mm² and a typical thickness of approximately 1 mm (usable crystals exhibit sizes of about 1.5 × 1.5 mm²

3 Experimental Setup

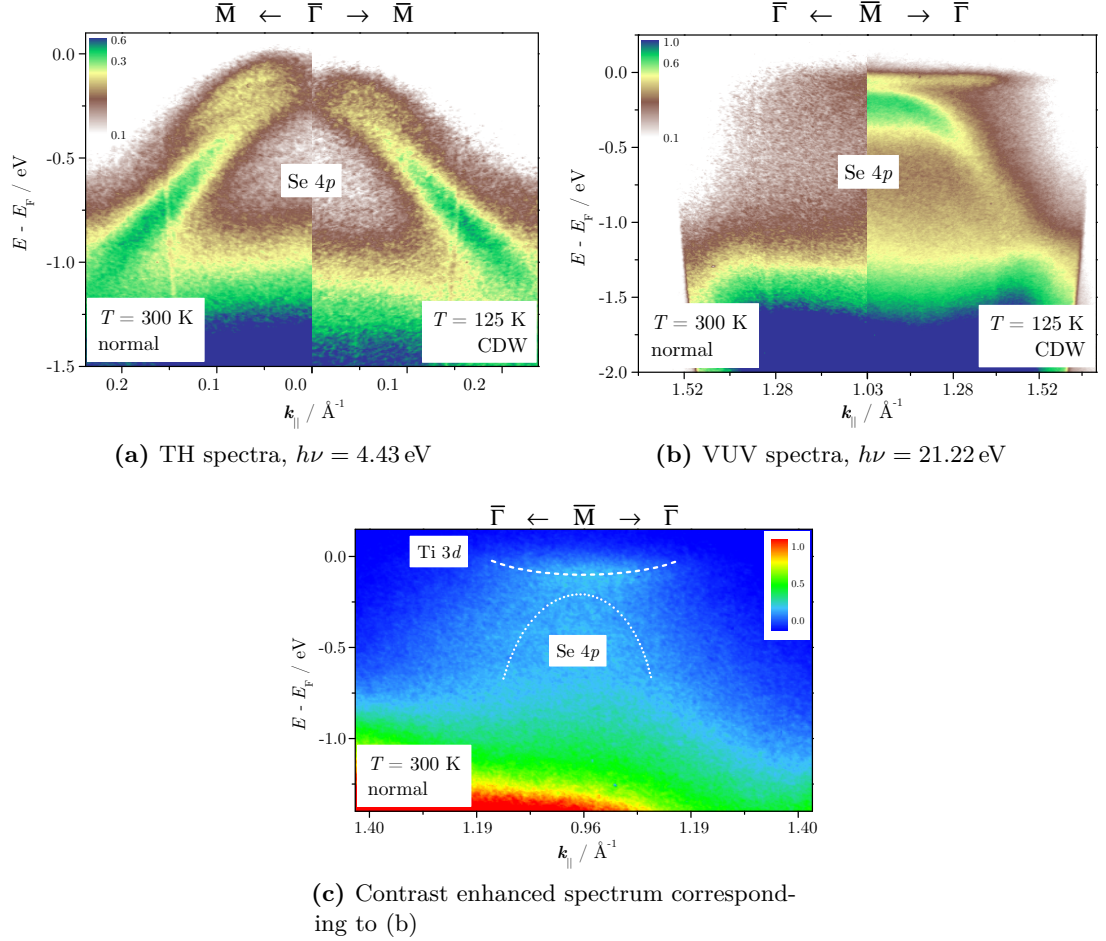


Figure 3.9: Spectra taken in the normal (300 K, left part) and CDW (125 K, right part) phase. (a) AR-2PPE data at the $\bar{\Gamma}$ -point (normal emission). The Se 4p bands shift to higher binding energy upon the CDW transition. Additionally, a reduction of the spectral weight is observed right at the $\bar{\Gamma}$ -point. (b) Analogous ARPES data at the \bar{M} -point of the Brillouin zone (about 28° emission angle). The formation of the CDW ($2 \times 2 \times 2$) superlattice leads to a backfolding of the Se 4p bands, which appear at the \bar{M} -point. The conduction band, which is situated above the Fermi energy at room temperature, shifts into the occupied region during the phase transition. This leads to the appearance of the non-dispersive feature right below the Fermi level upon cooling. (c) Room temperature spectrum corresponding to (b) with enhancement and higher resolution of the spectral features. Clearly some residual Se 4p backfolding (dotted) due to fluctuations of the CDW remains even at room temperature. Furthermore, the Ti 3d band (dashed) is occupied which hints at a certain amount of contamination of the samples.

up to $6 \times 4 \text{ mm}^2$). Such crystals are suitable for photoemission experiments, however, with the drawback of a slight loss in crystal stoichiometry towards an enrichment with titanium atoms [8, 79, 159].

Preparation of a defined surface is achieved by cleavage of the crystal under high vacuum conditions and the subsequent removal of residual adsorbates by a short annealing of the sample to about 493 K under UHV conditions in the experimental chamber. The overall preparation procedure results in flat and shiny (0001) surfaces of the TiSe₂ samples yielding sharp LEED spots and well defined 1PPE and 2PPE spectra. Surface impurities are known to modify the spectral weight of the electronic states of 1T-TiSe₂ considerably [160, 161] and can also completely quench the CDW transition as a result of a net charge transfer between adsorbate and compound. Interestingly, heating of TiSe₂ under UHV conditions is known to remove even certain intercalates [78]. A reliable check of the surface quality in our experiments is the observation of the CDW transition by mapping characteristic changes [7, 10, 11, 14, 94] in the electronic structure, either at the $\bar{\Gamma}$ -point of the Brillouin zone using angle-integrated or -resolved 2PPE spectroscopy [figure 3.9(a)], or at the \bar{M} -point using ARPES [figure 3.9(b)]. The details of the spectral modifications upon the phase transition are briefly discussed in the caption of figure 3.9 and a more detailed experiment is shown in section 5.3.

Nevertheless, we like to point out, that in the room temperature normal conduction phase of TiSe₂ two interesting features are observed in figure 3.9(c): First, the Ti 3*d* band (dashed) is occupied at the L-point and second the backfolded Se 4*p* bands (dotted) are visible, although much less defined than after the phase transition. The persistence of the backfolding even at room temperature is due to fluctuations of the CDW [7, 11, 55]. The observation of an occupied Ti 3*d* band at the L-point clearly indicates a contamination of the sample by adsorbates or intercalates [151, 160–162], because the charge transfer from the contamination to the host crystal leads to a band filling in the simple approach of the *rigid band model* [63, 78, 163]. Even after the removal of the adsorbates by heating of the samples prior to the experiment the Ti 3*d* band stays occupied, i. e. our samples deviate from the ideal crystal. We will show shortly that our samples contain a considerable amount of additional titanium atoms within the van der Waals gap because of self-intercalation, a process well known by previous studies of this system (see e. g. references [95, 164–166]). This is the reason for lowering of the energy of the Ti 3*d* band in our case (see e. g. references [11] and [63, chapter 3.3]).

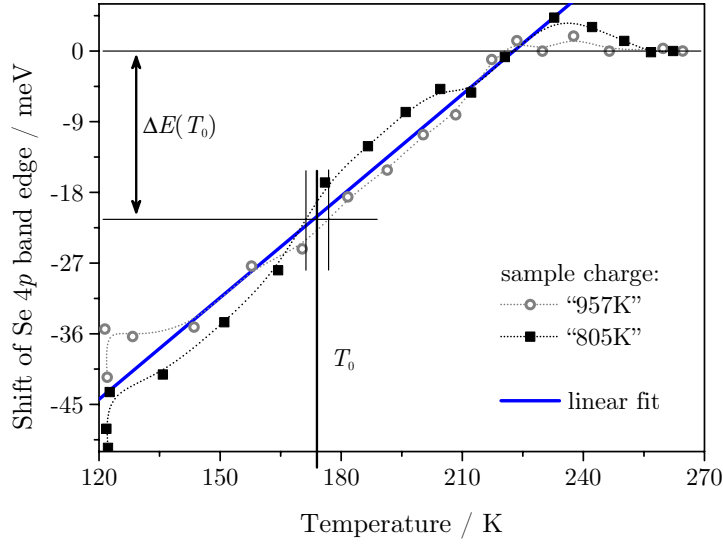
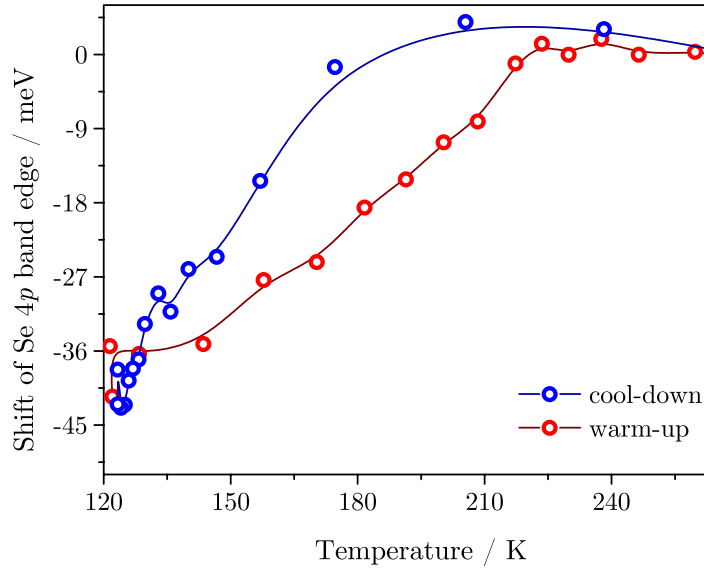
The actual transition temperature of the samples used in this work into the CDW phase is $T_0 = (174 \pm 3) \text{ K}$. The critical temperature was determined from the temperature dependence of the energy of the upper Se 4*p* band edge at the $\bar{\Gamma}$ -point [see figure 3.9(a)] by using the data provided by Rosnagel et al. [7]. In this reference resistivity measurements of similar TiSe₂ samples yielded a transition temperature of about $T_{0,\Omega} = 198 \text{ K}$. The shift of the upper Se 4*p* band at the $\bar{\Gamma}$ -point relative to its energy at room temperature corresponding to the phase transition temperature $\Delta E(T_0)$ is evaluated for $T_{0,\Omega}$ of the resistivity measurement to $\Delta E(T_{0,\Omega}) = -21.43 \text{ eV}$ (all data as per reference [7]). We use

two different sample charges grown at slightly different temperatures and a difference in growth duration of a factor of two (“805K” and “957K”). We acquired a series of 2PPE spectra during cooling of TiSe₂ below the critical temperature T_0 and subsequent warm-up to room temperature. Figure 3.10(a) shows the shift of the upper Se 4*p* band edge, i. e. the energy of the half-maximum of the flank nearest to the Fermi level of the Se 4*p* feature relative to its energy at room temperature. We used the data acquired during warm-up of the sample, because sample and temperature sensor are significantly better in thermal equilibrium than during the cooling process [see figure 3.10(b)]. By assuming $\Delta E(T_0) = -21.43$ eV as the shift indicative for T_0 , we find $T_0 = (174 \pm 3)$ K for our TiSe₂ samples.

This temperature value enables us to estimate the Ti excess concentration in the samples. Di Salvo et al. [8] investigated the effect of non-stoichiometry on the critical temperature of the phase transition. They observed a strong influence of the preparation temperature of the growth process of the crystals on this temperature. A decrease of T_0 in the range of 204 K to 140 K is observed for increasing preparation temperature. Furthermore, a chemical analysis of TiSe₂ for two samples of different preparation conditions by this group showed deviations from stoichiometry—described by Ti_{1+x}Se₂—for high preparation temperatures of up to $x = (1.8 \pm 0.3)$ % in the amount of titanium atoms for the highest preparation temperature used, i. e. the samples contain 101.8 % titanium with respect to the ideal TiSe₂ crystals. By assuming a defect free sample for the highest value of T_0 , the defect concentration in dependency on the transition temperature can be estimated by a linear fit. Although the uncertainty of the defect concentration is rather high, the three given data points fit very well to a line of best fit. For the transition temperature observed for our samples we derive a defect concentration of (0.85 ± 0.38) %. The uncertainty of the defect concentration results from the 0.3 % uncertainty of the values provided by Di Salvo et al. [8] and the uncertainty of T_0 , resulting in an additional uncertainty of 0.08 % of x . To reflect the high uncertainty, we round up to a defect concentration of (1 ± 1) % in this work.

Furthermore, figure 3.10(a) enables us to establish a temperature scale for our experiments. At low temperatures the energy of the cutoff may be used to determine the temperature of the sample. The combined data of both samples is used for a linear fit (gray line). We derive a temperature coefficient of $\Delta E_c = (4.31 \pm 0.15) \times 10^{-4}$ eV K⁻¹. Please note, that this coefficient refers to data acquired upon heating of the sample, because in this case the thermal equilibrium of sample and temperature sensor is better. For similar data taken during the cooling, the equilibrium deviates and a significantly different temperature coefficient is observed [see figure 3.10(b)]. A similar linear fit yields a coefficient of $\Delta E_c = (7.7 \pm 0.4) \times 10^{-4}$ eV K⁻¹ in this case. Our discussion in section 5.3.2 will refer to these coefficients.

A work function of $\Phi = 5.7$ eV has been determined for several AR-2PPE experiments on well prepared 1*T*-TiSe₂ from the low energy onset of the photoemission spectrum. This value is in good agreement with the results of previous measurements [19] and


 (a) Estimation of T_0 .


(b) Different thermal equilibrium.

Figure 3.10: (a) Evaluation of the amount of excess titanium (defect concentration) in TiSe_2 . For two samples of different growth charges the shift of the Se $4p$ upper edge during warm-up from below the temperature of the phase transition T_0 to room temperature is monitored [7]. With the extracted value of T_0 the amount of excess Ti is determined using data published by Di Salvo et al. [8]. A linear fit (blue) defines the temperature coefficient of the high energy cutoff. (b) The different thermal equilibrium of sample and thermal sensor leads to differences of energetic shift of the upper Se $4p$ bands edge. The slope of the data is significantly different.

3 *Experimental Setup*

calculations [151]. For part of the experiments the TiSe_2 surface is covered by a small amount of cesium from a SAES Getters source to reduce the surface work function. To inhibit the intercalation of the alkalis into the van der Waals gap of the TiSe_2 crystal, as reported in several works, we evaporated and performed these experiments at a low sample temperature of 123 K [73, 151, 163, 167, 168].

4 Spectroscopy and Population Decay of a van der Waals Gap State in Layered $1T\text{-TiSe}_2$

We begin the experimental part of this thesis by a detailed investigation of photoemission spectroscopy, specifically in the two-photon photoemission (2PPE) mode, of $1T\text{-TiSe}_2$. We focus on understanding such 2PPE data by comparison to band structure calculations as available from literature. We find an unoccupied, strongly localized van der Waals gap defect state which is, to our best knowledge, experimentally observed for the first time, here. We perform additional time- and angle-resolved two-photon photoemission (TAR-2PPE) experiments which enable us to ascertain our assignment of the new unoccupied state to a van der Waals gap state by comparison of its lifetime to reference bands.

First, we present photoemission spectroscopy experiments, which focus particularly on the 2PPE method. Although there exists a multitude of one-photon photoemission (1PPE) (see for instance references [7, 10, 14, 66, 94, 161, 169, 170]) and inverse photoemission (IPE) [17, 19] data for TiSe_2 , a thorough investigation of the unoccupied band structure, especially using 2PPE, is still missing. Therefore, we need to establish a procedure for acquisition of meaningful spectroscopic data for our samples.

The samples feature a rather high work function; consequently we need to lower the work function for certain ranges of the photon energy. We utilize angle-integrated 2PPE as well as angular-resolved (AR-2PPE) spectra for a series of different photon energies to gain insight into the origin of the spectral features observed.

A direct comparison to band structure calculations available from literature proves to be a valuable tool in this context. We observe unoccupied bands which are all but one well explained by standard band structure calculations. A time resolved approach—TAR-2PPE—finally allows us to assign the additional band to states induced attributed to excess atoms within the van der Waals gap of the layered TiSe_2 crystal.

Please note, that the experimental findings presented in this chapter have been published in *Physical Review B* in 2010 by Wiesenmayer et al. [171], copyright 2010 by the American Physical Society.

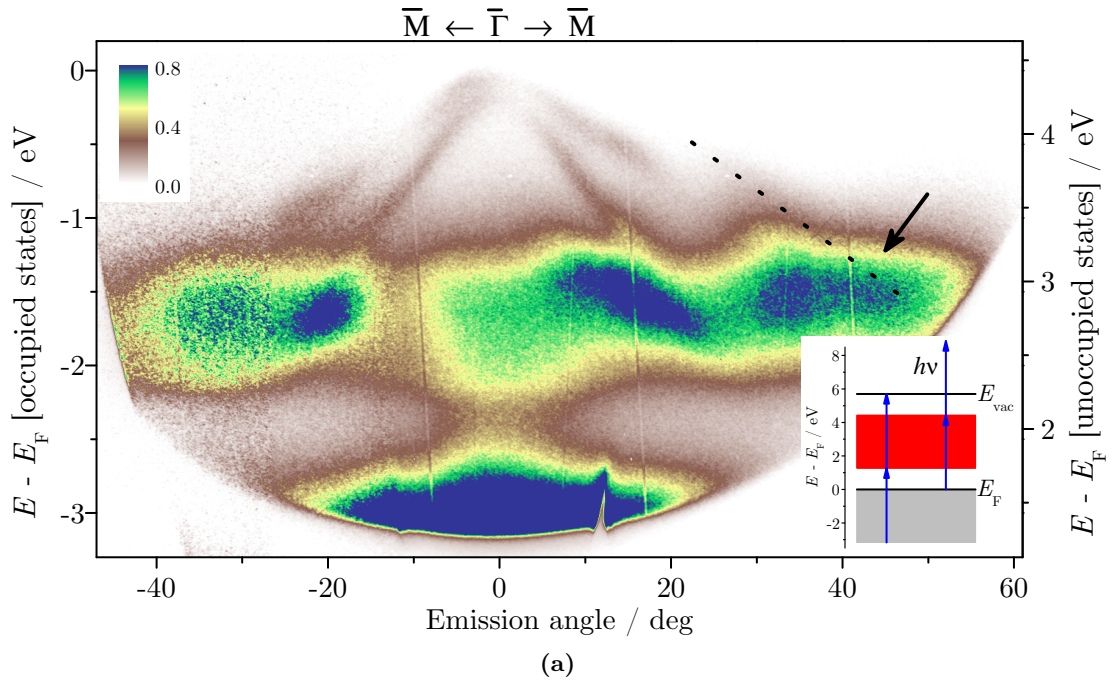
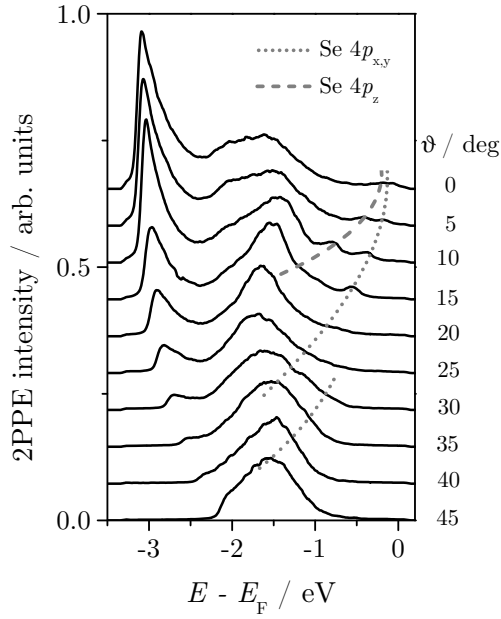
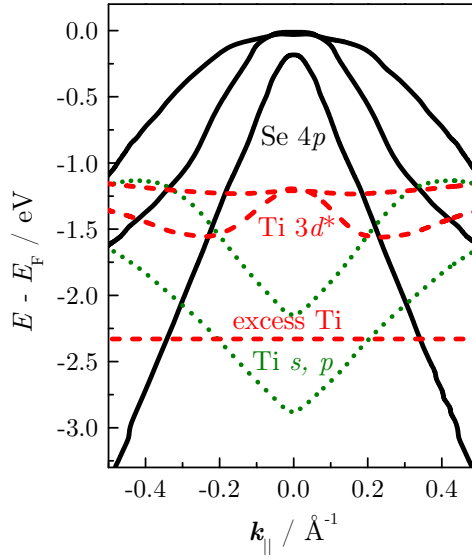


Figure 4.1: (a) AR-2PPE intensity map of pristine 1T-TiSe₂, photon energy $h\nu = 4.43$ eV (TH-2PPE). The map is composed of four partial spectra recorded at different polar angles of the sample relative to the analyzer axis. The partial spectra are shifted in angular direction for best correlation and blended at the seams using a special software (*SpecsComposer*, SPECS, Version 1.0). Normalization is applied to match the intensity as homogeneous as possible. The labeling of the left axis displays the occupied states energy, the labeling of the right axis displays the unoccupied states energy of the 2PPE process. The colorscale corresponds to the mapping of the intensities. The inset shows the occupied and unoccupied states energy span that is sampled in this 2PPE experiment at the $\bar{\Gamma}$ -point. (*continued on page 75*)



(b)



(c)

Figure 4.1: (continued from page 74) (b) EDCs for selected emission angles extracted from the AR-2PPE intensity map. (c) Corresponding 2PPE-energy-reduced band scheme of $1T$ -TiSe₂ following calculations from references [9] and [69]. Initial state bands are shown in black, intermediate state bands (red, dashed) have been shifted by $h\nu = 4.43$ eV, final state bands (green, dotted) have been shifted by $2h\nu = 8.86$ eV. Intersections of different bands indicate possible direct transition within the 2PPE process. The non-dispersive (unoccupied) band labeled *excess Ti* (dashed line) arises from excess Ti atoms located in the van der Waals gap of the layered crystal [69].

4.1 Spectroscopy of the Unoccupied States

Figure 4.1 shows a composite AR-2PPE $E(\mathbf{k}_{\parallel})$ intensity map recorded with the third harmonic of laser 1 (TH-2PPE) at a photon energy $h\nu = 4.43$ eV and at four different polar angles of the sample with respect to the energy analyzer axis. This composite map is used for illustration purposes only. The quantitative analysis of the data was performed using energy distribution curves (EDCs) deduced from the intensity maps as shown in figure 4.1(b) for different emission angles. Normal emission (0° emission angle) corresponds to photoelectron emission from the $\bar{\Gamma}$ -point. At a work function $\Phi = 5.7$ eV of the pristine 1T-TiSe₂ sample, the used photon energy provides spectroscopic access to an overall energy span of 3.16 eV [see inset of figure 4.1(a)]. This span covers an energy range for occupied states between -3.16 eV and the Fermi level E_F and an energy range for unoccupied states between 1.27 eV and 4.43 eV between E_F and the vacuum level E_{vac} . The energy scale used throughout this work is referred to the Fermi energy E_F . By providing two energy scales for the 2PPE spectra for both occupied and unoccupied spectral signatures, the corresponding energies are assessed in a simple, direct manner.

The work function is determined from a 2PPE-EDC of the normal emission [a sample of such an EDC can be seen, for instance, in figure 4.1(b)]. Using Einstein's photoelectric equation, the work function is easily calculated as $\Phi = 2h\nu - \Delta E$, with the photon energy, $h\nu$, and the width of the spectrum defined by the low energy onset and the Fermi edge, ΔE .

The sharpest and therefore most distinctive features appearing in the TH-2PPE intensity map in figure 4.1(a) are the two parabolas at the top of the spectrum, exhibiting a strong, hole-like dispersion in the vicinity of the $\bar{\Gamma}$ -point. The parabolas are well known from conventional angle-resolved photoemission spectroscopy (ARPES) data [7, 10, 94, 170] and can be attributed to the occupied Se $4p$ bands of the composite. The upper visible parabola corresponds to one of the two spin-orbit split Se $4p_x$, $4p_y$ valence bands [66]. The second split-off band is only barely visible at about 30° emission angle [indicated by the dashed line in figure 4.1(a)] and as a resonance feature at about 45° emission [arrow, see EDCs at different emission angles shown in figure 4.1(b)]. The lower parabola can be assigned to the Se $4p_z$ band.

4.1.1 Analysis of the Band Dispersion

Our assignment of the two parabolas in the angle resolved TH-2PPE spectrum to two different Se $4p$ bands is supported by the dispersion of these bands. A multiple Gaussian fit to the EDCs presented in figure 4.1(b) yields the energies for different surface parallel momenta, as shown in figure 4.2. A parabolic fit as described by $E - E_F = a + b\mathbf{k}_{\parallel} + c\mathbf{k}_{\parallel}^2$ with the parallel momentum \mathbf{k}_{\parallel} and the fit coefficients a , b and c . The effective mass m^*

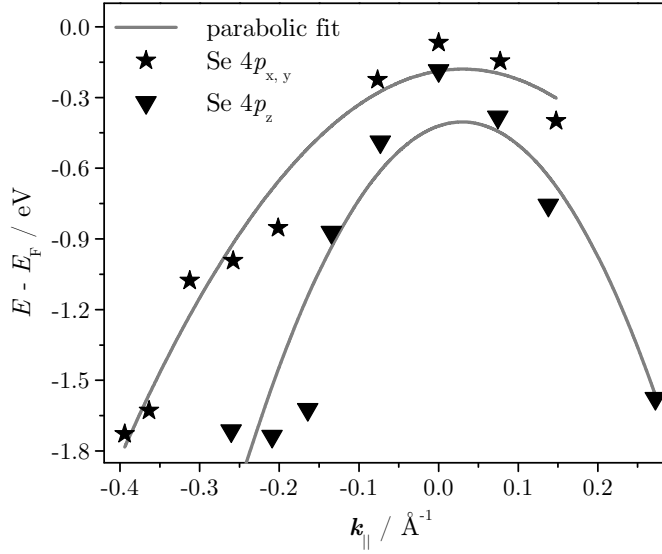


Figure 4.2: Fitted energies of the two clearly visible Se $4p$ bands, Se $4p_x$, $4p_y$ and Se $4p_z$, in figure 4.1. These data are extracted by a multiple Gaussian fit (as discussed later in this chapter, see figure 4.8) of the corresponding EDCs. The gray lines represent parabolic fits of these data.

can be calculated [110, 172] using

$$m^* = \hbar^2 \left[\frac{\partial^2(E - E_F)}{\partial k^2} \right]^{-1}.$$

In our case, using

$$\frac{\partial^2(E - E_F)}{\partial k_{\parallel}^2} = 2c,$$

we derive

$$m^* = \frac{\hbar^2}{2c}.$$

Table 4.1: Effective masses of the two clearly visible Se $4p$ bands.

band	m^*/m_e
Se $4p_x$, $4p_y$	-0.43 ± 0.08
Se $4p_z$	-0.19 ± 0.04

From the data in figure 4.2 we extract an effective mass of $m_{x,y}^* = -0.43 \pm 0.08 m_e$ for the Se $4p_x$, $4p_y$ band. This is in very good agreement with ARPES data published

earlier, like e. g. $-0.36 \pm 0.10 m_e$ [7] and $-0.44 \pm 0.02 m_e$ [94]. For the Se $4p_z$ band we derive an effective mass of $m_z^* = -0.19 \pm 0.04 m_e$, which is also in very good agreement with $-0.23 \pm 0.01 m_e$ [94] and $-0.21 m_e$ [10]. Note, however, that reference [10] deviates quite significantly from our value of the effective mass of the Se $4p_x, 4p_y$ band, although the trend is still supported. Table 4.1 summarizes our findings.

4.1.1–a Discussion of the Spectral Signatures

The main spectral feature dominating the TH-2PPE data in figure 4.1 is the broad, weakly dispersive intensity band located in the occupied state energy regime $E - E_F$ between -2.25 eV and -1.25 eV. In the following, we will show that this spectral feature has a complex origin, and contains contributions from five different bands. For a direct comparison with the experimental data, figure 4.1(c) shows an energy band diagram of 1T-TiSe₂ deduced from band structure calculations of Zunger and Freeman [9]. These data cover the full energy regime probed in our experiment. The data are completed by results from Pehlke and Schattke [69] which particularly consider the effect of defect states on the electronic structure. More recent band structure calculations are also available from literature [58–62]. The band structure calculations mainly differ in the vicinity of the Fermi energy, especially concerning the actual energy of the Se $4p$ bands. The more sophisticated calculations yield a smaller binding energy and even a crossing of the Fermi level of these bands at the Γ -point. Although such a crossing is not experimentally observed, the bands' energy acquired for samples of good stoichiometry is rather small [10], but increases in the presence of contaminations [15]. In comparison to our experimental findings this is a first indication for the deviation of our TiSe₂ samples from the ideal crystal composition. We will indeed show that a small amount of additional titanium atoms are intercalated into the van der Waals gap of our crystals which leads to a reduction of the energy not only of the Se $4p$, but also to a lowering of the first Ti $3d$ conduction band at the L-point [3, 11, 15, 66] which renders this band occupied; it is expected to be unoccupied with an energy slightly above the Fermi level for the ideal crystal [7, 14]. The Ti $3d$ band feature is clearly visible at the \bar{M} -point in the ARPES spectrum in figure 3.9(c) on page 68 and in the data presented in chapter 7.

We will therefore compare our data to the band structure calculations of Zunger and Freeman [9], because they agree very well to the energies observed for the Se $4p$ bands in our experiments. Furthermore, the other calculations are restricted with respect to the energy range addressed. They usually focus on the occupied electronic structure. In particular, in most cases only the energy regime in the vicinity of the Fermi energy is investigated. We need, however, a wide energetic range for the interpretation of our spectral data which restricts us to the calculations in reference [9]. We like to emphasize, that the band energies and band dispersions provided by these data do not considerably deviate from data of more recent references. Additionally, we will refer to the calculations of del Pilar Ramírez García [61], because, to our knowledge, they provide the only band

structure containing at least the lower final Ti band and the energy of the Ti $3d^*$ band agrees very well to our experimental data (it is indeed very similar to reference [9]; the most significant being the details of the Se $4p$ bands).

The data in figure 4.1(c) are shown in a representation that we refer to as a 2PPE energy-reduced band scheme. In this representation all energy bands which are potentially involved in the 2PPE process (initial, intermediate, and final state bands) are projected to the initial state energy level under consideration of the experimentally used photon energy, i. e. $h\nu = 4.43$ eV in the present example. Final state bands are shifted down in energy by $2h\nu$, intermediate state bands are shifted down by $h\nu$, and initial state bands are not shifted at all. This representation allows for the comparison of experimental data and calculations in an intuitive and direct manner. In particular, band intersections in the reduced band scheme are indicative of potential resonant transitions within the 2PPE process.

Four main features are predicted by the calculations and the corresponding 2PPE energy-reduced band scheme: First of all, the above mentioned parabolic Se $4p$ bands ($4p_x$, $4p_y$ and $4p_z$) which are shown in black and are clearly identified in the TH-2PPE intensity map. Secondly, the intermediate (unoccupied) states labeled in red which exhibit two distinct contributions. The two higher lying energy levels are derived from a mixture of Ti $3d_{x^2-y^2}$, $3d_{xy}$, $3d_{xz}$ and $3d_{yz}$ orbitals and will in the following be referred to as Ti $3d^*$ bands in accordance with Fang et al. [60]. The lower lying non-dispersive feature marks the energy of a band arising from the presence of Ti excess atoms in the van der Waals gaps of the layered crystal structure (excess Ti state) and was predicted by Pehlke and Schattke [69]. At last, the two final state bands marked in green are derived from high energy titanium orbitals of s and p character [9, 19].

4.1.2 SH-2PPE Spectroscopy—Analysis of the Unoccupied Bands

The broad intensity band in the experimental TH-2PPE data extends over an occupied states energy range of -2.25 eV to -1.25 eV. Note that these two energy values agree rather well with the energies of the Ti $3d^*$ band (-1.2 eV) and the excess Ti state (-2.3 eV) in the energy reduced band scheme of figure 4.1(c). However, only the resonance features, due to the crossing of the Se $4p$ bands, can be assigned unambiguously from the experimental TH-2PPE data. AR-2PPE intensity maps recorded with second harmonic light (SH-2PPE data) enable us to distinguish and identify further contributions to this intensity band.

Figure 4.3 shows a SH-2PPE intensity map recorded at a photon energy of $h\nu = 3.44$ eV. As in the case of the TH-2PPE intensity map, figure 4.3(a) includes scales for occupied states energy (left) and unoccupied states energy (right). Figure 4.3(b) is the corresponding 2PPE related energy-reduced band scheme [9, 69]. A meaningful 2PPE intensity map of a 1T-TiSe₂ sample recorded in the second harmonic photon energy regime ($h\nu = 3.00$ eV to 3.44 eV) requires a specific sample treatment which will

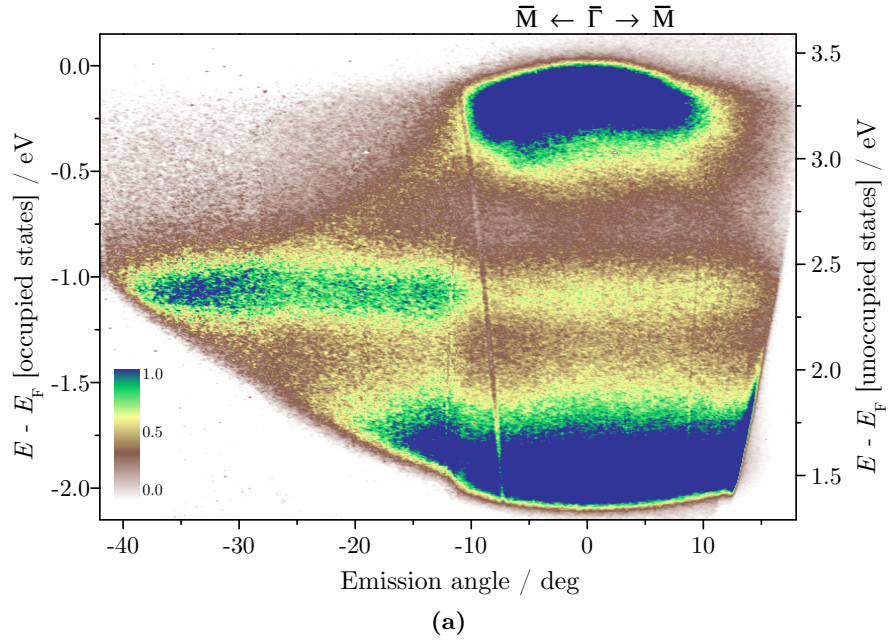


Figure 4.3: (a) AR-2PPE intensity map of 1T-TiSe₂ covered by a small amount of cesium recorded with p-polarized laser light at a photon energy of $h\nu = 3.44$ eV. The map is composed of three partial spectra, angularly shifted and blended as described in figure 4.1(a). The intensity of the two non-normal emission spectra is amplified to enhance the visibility of the Se 4p bands. Otherwise, the structure of the Se 4p bands—enhanced due to a resonant excitation near normal emission—is barely visible in the higher emission angle regime. The energy labeling corresponds to occupied states energy (left axis) and unoccupied states energy (right axis). (*continued on page 81*)

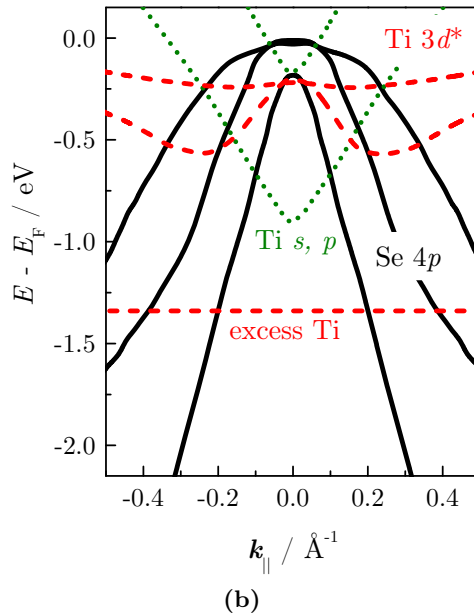


Figure 4.3: (continued from page 80) (b) 2PPE energy reduced band scheme ($h\nu = 3.44$ eV) corresponding to the spectrum in (a).

be described and commented on in the following and prior to the discussion of the actual SH-2PPE data.

Due to the high work function value of 5.7 eV of the pristine 1T-TiSe₂ surface, the accessible energy span in a 2PPE experiment recorded at $h\nu \approx 3.0$ eV to 3.5 eV is limited to a width of about 1.3 eV and below. To extend this energy span, the samples have been covered, in our study, with a small amount of cesium atoms [$\vartheta < 0.27$ monolayer (ML)], a procedure, which is well known to be very effective in reducing the surface work function [151, 162, 173]. Figure 4.5(b) shows 2PPE EDC of the TiSe₂ sample taken at increasing Cs coverages up to a maximum of 0.34 ML. The successive shift in the low energy onset of the spectrum is indicative for the lowering of the surface work function. This shift is used to calibrate the cesium coverage by monitoring the work function decrease during evaporation at room temperature. We followed a procedure described by Boehme [174] and references therein, especially references [175] and [176]. Figure 4.4 shows this coverage calibration for Cs on TiSe₂ evaporated at room temperature. We estimated the work function for different evaporation durations (upper scale). If we assume a constant flux of Cs atoms from the alkali source—a valid assumption considering the rather short duration of the evaporation and the low and stable flux of the source as checked by monitoring the emission current—we can convert the evaporation time linearly into the corresponding coverage. The references assign the transition from a linear to a non-linear work function decrease to a coverage of 0.4 ML. This behavior is also observed

for sodium on Cu(111)—no specific dependence on the alkali as well as the metallic substrate, especially concerning the occurrence of a minimum of the work function at 0.38 ML to 0.5 ML, are reported [173]. Indeed, we observe such a linear behavior for low coverages. A linear fit to those data is included in figure 4.4 (red dotted). The onset of the non-linear behavior determined in correspondence with Boehme [174] is emphasized by a vertical black line. All Cs coverages quantified in this work are determined by relating the work function shift to the coverage using the data in figure 4.4. Obviously, this is only feasible for coverage below 0.4 ML, i. e. for the linear range of these data.

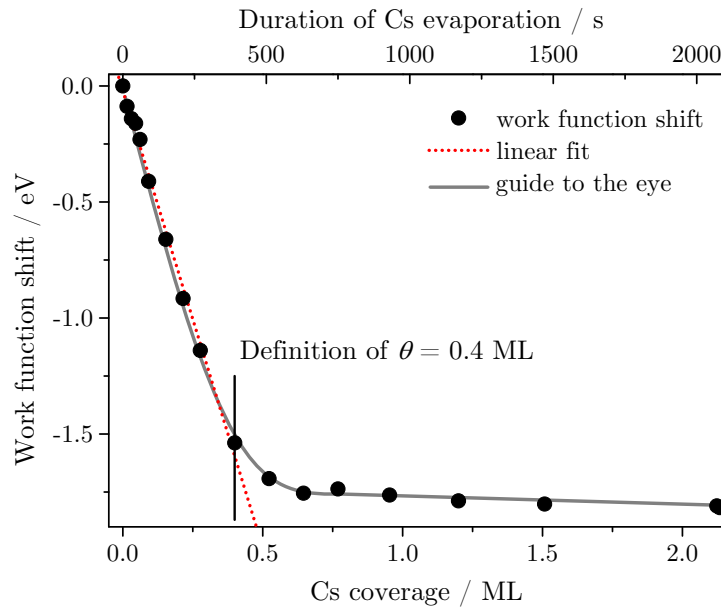


Figure 4.4: Calibration of the Cs coverage of TiSe₂ at room temperature. The decrease of the work function $\Delta\Phi$ is monitored in dependence of the time of Cs evaporation (upper scale). In correspondence to reference literature [174–176] we define the deviation from the initial linear decrease (red dotted, linear fit) of the work function to 0.4 ML (black vertical line) under the assumption of a proportionality of Cs coverage and evaporation time. The gray line is a guide to the eye.

The work function exhibits a rather unique trend considering the usual characteristics observed for alkalis on metal surfaces. We do not observe a distinct minimum followed by a plateau for the highest coverages [173], but the linear decrease of the work function is directly completed by saturation into a plateau. Similar experiments on MoS₂ have shown, that for a sufficiently low temperature during adsorption of the alkali this typical minimum is reproduced [175]. The absence of the minimum at room temperature is explained by the presence of two different ionic adsorption states for

high and low temperature [176]. At high temperature larger clusters of Cs are formed which leads to an early saturation of the work function, while at low temperature more, but smaller clusters are present, leading to a larger decrease of the work function [175]. Calculations for Li/TiSe₂ have shown a similar behavior of the work function for lithium intercalation, while adsorption yielded the usual minimum in the coverage dependence [151].

The interaction between alkali atoms and transition metal dichalcogenides (TMDCs) substrate can be rather complex. Alkalies tend to intercalate into the van der Waals gap in between the crystal layers [73, 151, 163, 168]. Therefore, to thermally inhibit alkali intercalation, the sample temperature is kept at 123 K during evaporation, as well as during the consequent spectroscopic and time-resolved experiments of this work [73, 167, 168]. Indeed, our room temperature data presented in figure 4.4 exhibits a final work function of the high coverage plateau of about 4 eV which is significantly higher than the expected value for metallic Cs layers [177]. This strongly indicates a coexistence of adsorbed and intercalated Cs [167]. This emphasizes the importance of cooling of the samples during our experiments. Acquisition of a corresponding coverage calibration data set at liquid nitrogen temperatures is not feasible due to limitations of the experimental setup and due to the long duration of the experiment. Because the intercalation is a thermally activated process, it is only slowed down at low temperatures and not completely suppressed, i. e. for long experimental runs intercalation is still to be expected [73].

Please note, that due to the expected stronger decrease of the work function for evaporation at low temperature [175, 176] our coverage values are slightly exaggerated by comparison to the room temperature data in figure 4.4, i. e. the given coverage is a upper limit of the actual Cs coverage. We do not expect significant deviations, because the linear part of the coverage dependence (low coverage regime) of the work function is in fact influenced very little by the sample temperature. Only when approaching the 0.4 ML limit of the data notable deviations are expected.

4.1.2–a ARPES Study of the Adsorption of Alkali Atoms

Furthermore, electron transfer from the adsorbed alkali species to the substrate can give rise to a successive filling of the 1T-TiSe₂ bands and results in an increase of the electron binding energies [162, 178]. In particular, the energy regime close to E_F , governed by the Se 4*p* and the Ti 3*d** bands, is considerably affected by the adsorbed Cs [see figure 4.5(b)]. Three-peak fits to this spectral region (see figure 4.8) show that the different spectral signatures exhibit an energy shift ΔE of up to approximately -30 meV for the maximum Cs coverage used in this work. Additionally, the relative photoemission yield becomes clearly reduced due to the adsorption of Cs. Figure 4.6(a) shows the shift in energy for different Cs coverages relative to the pristine crystal. The spectral feature we assign in the following to the Ti 3*d** (red, circles) band shows a significant shift upon

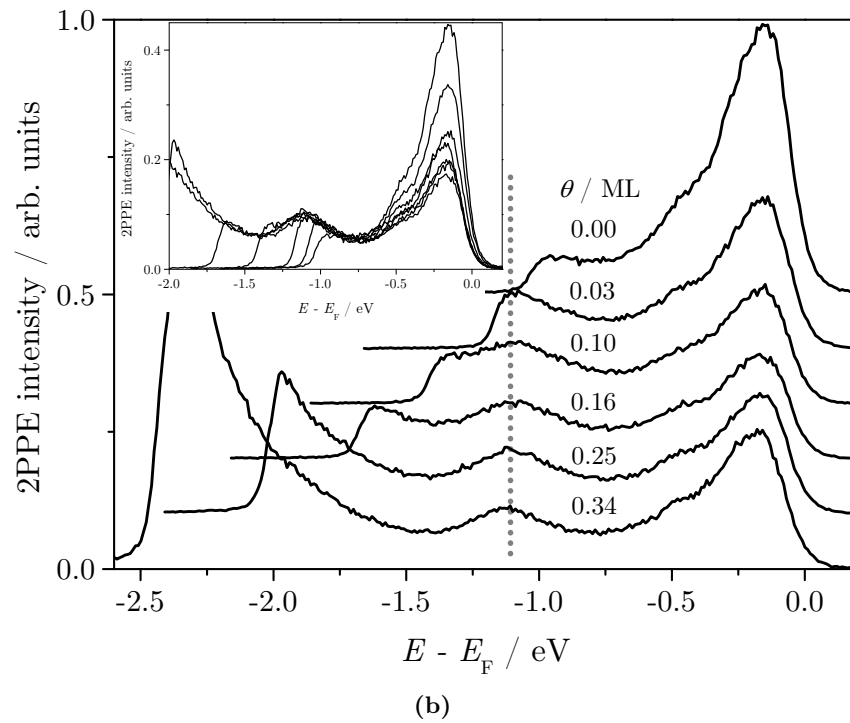
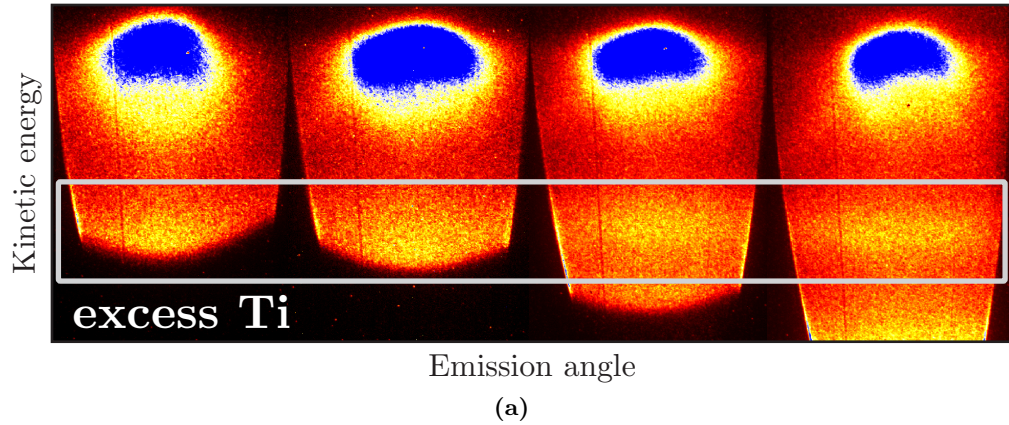


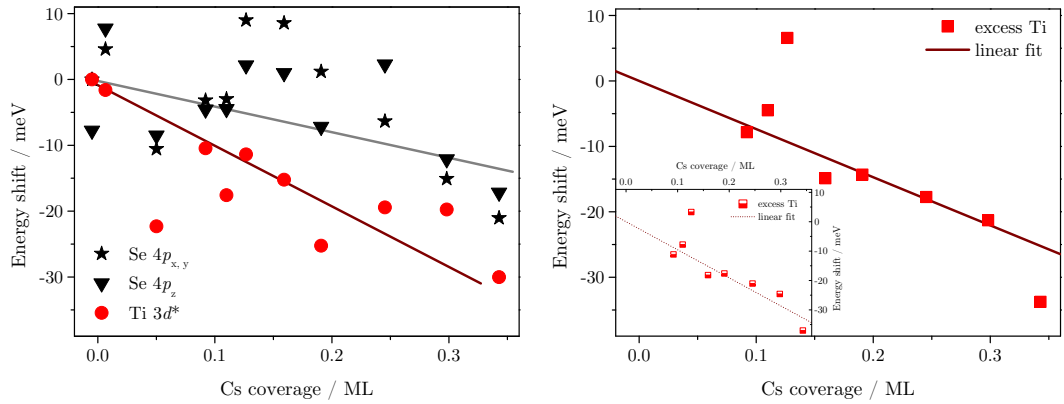
Figure 4.5: (a) A series of AR-2PPE spectra for increasing Cs coverage (left to right, beginning at 0 ML). Clearly the excess Ti state is already visible for vanishing Cs coverage (gray box). The intensity is enhanced for best visibility of the excess Ti state, i. e. the Se 4*p* bands are overexposed. (b) Series of SH-2PPE EDC ($h\nu = 3.42$ eV, normal emission) for different cesium coverages ϑ up to 0.34 ML. The position of the excess Ti band is emphasized by a dotted line. Inset: Spectra plotted without normalization of the intensity. This representation clearly shows the appearance of the excess Ti state, as well as its insensitivity to the cesium coverage.

Cs deposition of up to about -30 meV. The Se $4p$ bands seem to be less affected and only shift about -10 meV to -20 meV. The spread of the single measurements leads to an uncertainty of about ± 10 meV. Especially in case of the Se $4p$ bands the exact shift is not easily extracted due to the multi-peak fit procedure, which is more critical in the range of these bands. In the quantitative analysis of the experimental data, this energy shift was circumvented by discarding the data of the cesiated samples for these spectral features, i. e. only pristine samples were used to evaluate the energy of the Se $4p$ bands and the Ti $3d^*$ band. Interestingly, for similar Cs adsorption experiments on $2H$ -TaSe₂ the Se $4p$ bands show a comparable, small shift of approximately -15 meV [167].

For other surface systems the appearance of new, surface localized electron states due to the adsorption of alkalis has been reported [173, 179–183]. In this 2PPE study such an alkali derived state could not be observed. The peak at $E - E_F \approx -1.1$ eV ($E - E_F \approx 2.3$ eV unoccupied states energy) that becomes accessible due to the decrease in the work function is already present at zero Cs coverage—even so spectrally merely accessible at this coverage—as evidenced by the inset in figure 4.5(b) [see also figure 4.5(a)]. Figure 4.6(b) shows the relative shift of the energy of this feature in dependence of the Cs coverage. The data is much more defined than in case of the Ti $3d^*$ and the Se $4p$ bands. The two stronger deviations are most certainly due to the variations of the fit of the three other bands just below the Fermi level. In the coverage range of about 0.1 ML to 0.3 ML used in our experiments, i. e. from the coverage needed to observe the feature with the second harmonic (SH) photon energies to the maximum coverage we used, this state is extremely robust against Cs-adsorption and exhibits no significant change in energy ($|\Delta E| < 15$ meV) and no detectable change in photoemissivity. This is in contrast to the low energy part of the spectrum near E_F .

The change in energy of the excess Ti state in the coverage range of 0.1 ML to 0.3 ML suggest a linear characteristic, which seems very reasonable at least for low coverages concerning the usual behavior for alkalis on metals [173, 184], especially considering the work function at low coverages [185–187]. Therefore, if we assume a linear shift of the energy of this state for low alkali coverages, we derive a maximum shift in energy of about -20 meV to -30 meV. Please note, that we can directly observe a shift of less than -15 meV; our estimation of the extremal shift relies on its linearity for the whole Cs coverage up to about 0.3 ML, which we cannot access experimentally. The findings of Fischer et al. [173], however, support such a linear behavior only for coverages significantly below about 0.2 ML. Our estimate of the potential shift—or more precisely the ideal value of the energy without contaminations—of the excess Ti state using linear extrapolation is thus strictly speaking problematic. We can only comment on a shift of less than -15 meV with certainty.

The linear fit in figure 4.6(b) omits the data points strongly deviating from the overall trend, but the inset shows a fit of all data points, which is used to estimate the range of the actual shift. For the quantitative analysis of the data a maximum Cs coverage of 0.3 ML is used. The extremal coverage defines a worst case value of the maximal



(a) The change in energy relative to the pristine sample for the spectral features visible without cesium. All lines are guides to the eye.

(b) Energy of the non-dispersive feature. The reference energy is extrapolated, because the feature is not observable without Cs. A linear fit (line) is included.

Figure 4.6: Cesium coverage dependence of the energetic shift $\Delta(E - E_F)$ of the spectral features of TiSe₂.

shift of -30 meV, which is comparable to the overall energetic resolution of our setup (see sections 3.1 and 3.2). We will reconsider this extremal shift in the discussion of the experimental energies with respect to earlier experiments and band structure calculations. However, please note that the scatter of the data in figure 4.7 is of the order of the maximum of the shift we expect for the excess Ti band and that different coverages of alkali or random adsorbates have been used in this case.

A lowering of the work function by other adsorbates (i. e. non-alkalies), for instance, because of contamination by the residual gas in the ultrahigh vacuum (UHV) chamber over days, will also render this feature visible with no significant changes in its energy, width or photoemission yield. This insensitivity to modifications in the surface properties hints to a state that exhibits no or only negligible wave function amplitude in the TiSe₂ top layer, but that is buried underneath—within the van der Waals gap of the crystalline structure. We will see later that this feature considerably contributes also to the broad intensity band in the TH-2PPE intensity map of the non-cesiated sample. The insensitivity of the 2PPE data to adsorbates/surface contaminations proves that this state is not due to surface localized states such as adsorbate states, surface states or image potential states, but that it is indeed an unoccupied electron state located within the bulk. Surface localized states usually show a significant sensitivity to surface contaminations. The image potential states and the alkali induced state of sodium on Cu(111) for instance both show a shift of energy of more than -2 eV for Na coverages up to about 0.3 ML [173] and the Shockley surface state shifts about -0.4 eV within

only the first 0.15 ML. The shift in energy even for the highest Cs coverages of about 0.3 ML in our experiments is only in the range of a few -10 meV for all bands. This clearly shows, that we are observing bulk electronic states. Note also that a pronounced dependence of the photoemission yield on the polarization of the non-dispersive state, as one would expect particularly in the case of surface states and image potential states, is not observed.

4.1.2–b Discussion of the Observed Unoccupied Defect State

Considering, that the 2PPE method is usually applied to the investigation of surface localized states (e. g. adsorbate, surface and image potential states) it may seem surprising that we observe strong contributions from a bulk state. Yet, there exists a multitude of experiments, where bulk states were not only clearly identified in 2PPE spectra, but also the focus of investigation:

- In Ag(111) a direct *sp*-transition between two bulk bands produces a feature dominating the spectrum [188, 189].
- Contributions of the *d*-bands were observed in 2PPE experiments of polycrystalline molybdenum [123].
- The *d*-bands of noble metals also influence the decay dynamics of optically excited bulk electrons, as observed by time-resolved two-photon photoemission (TR-2PPE) experiments [118, 190, 191].
- Finally, quantum well states (QWSs) in thin metallic films are of particular interest to our 2PPE study of TiSe₂ [192–195]. In these systems, the electron wave function is localized in the direction perpendicular to the films, i. e. within the metallic film. The energy–momentum dispersion perpendicular to the surface is therefore reduced, rendering the dispersion parallel to the surface of the QWSs directly accessible in photoemission experiments. The electronic bands in the focus of our study of TiSe₂ show no or very little dispersion perpendicular to the surface, too (see figure 4.10). This is caused by the decoupling of the individual crystal layers due to the layered structure of TiSe₂.

Let us now briefly discuss the experimental evidence supporting our assignment of the non-dispersive unoccupied feature to a bulk state within the van der Waals gap and thus refuting the relevance of surface localized states in this case:

- (i) The Se 4*p* bulk bands are clearly identified and their energies as well as dispersion probed by 2PPE are in very good agreement with conventional photoemission data published in numerous earlier works (see, e. g., [7, 10, 94, 170]) and band structure calculations [9, 61].

- (ii) The spectral features in our 2PPE data are very insensitive to surface contamination by residual gas, like oxygen and water, or deliberately applied adsorbates, like alkali atoms. The contamination over hours and days under UHV conditions is easily monitored by the suppression of the transition into a low temperature charge density wave (CDW) phase, due to the consequent lowering of the critical temperature. Additionally, contamination of the surface of the crystal reduces the photoemissivity of the Se 4*p* bands in agreement with reference literature (e. g., [15, 162, 196]). In contrast, the band we assign to an excess Ti state proves to be extremely robust against contamination with adsorbates, considering peak position, width and intensity (see figures 4.5 and 4.6). Surface localized states on the other hand are known to be very sensitive to such contaminations of the surface. Surface states, for instance, undergo significant broadening and energetic shift and they are typically completely quenched as a full monolayer of contaminants is reached. In case of highly ordered adsorption layers image potential states may survive [197–199], but they will undergo a clear energetic shift due to their pinning to the vacuum level [200]. These behaviors are clearly not observed for the non-dispersive feature of TiSe₂.
- (iii) However, even bulk bands should exhibit at least some response to adsorbates, as long as these bands are also supported by the top layer of the crystal. The occupied Se 4*p* and the unoccupied Ti 3*d** bulk bands are striking examples for this behavior. They exhibit a slight shift in energy and they feature a distinct loss in photoemissivity. The extreme robustness of the non-dispersive unoccupied band—especially in comparison to these bands—strongly indicates that the associated electron orbital is indeed buried underneath the top layer of TiSe₂ and that this state is not a bulk feature at least of the top layer. This indicates location of this state within the van der Waals gap of the crystal, especially considering that it does not seem to be a regular electronic feature of the ideal crystal.
- (iv) A strong dependence on the polarization of the incident light is typical for the photoemission signal of surface states which are visible under illumination with p-polarized light only. Yet, the excess Ti state does not exhibit such a polarization sensitivity; it is well visible with p- and s-polarized light.
- (v) Band structure calculations for single layers of TiSe₂ do not exhibit significant differences in comparison to corresponding calculations for bulk crystals, although the band overlap at E_F may be reduced for the single slab [60] (and references therein). Considering that the TiSe₂ crystal is basically a compound of weakly, van der Waals bound layers, this is not very surprising. This evidences that the surface of the crystal does not deviate significantly from the bulk, i. e. it does not support strong surface bands—except image potential states. However, the electron-like dispersing $n = 1$ image potential state reported in IPE experiments features an

energy of $E - E_F \approx 5$ eV [19] which is just beyond the energy range accessible in a 2PPE experiment even with the highest photon energies provided by our third harmonic.

In summary, we conclude, that (i) we can exclude an interpretation in terms of a surface or image potential state or an adsorbate resonance contribution to the photoemission signal of TiSe₂ and that (ii) the 2PPE spectra of this work are indeed dominated by bulk band contributions. Especially the unoccupied excess Ti state can be convincingly attributed to a bulk band.

4.1.3 Spectroscopy at Varying Photon Energy

Let us now consider in detail the SH-2PPE intensity map displayed in figure 4.3. At first glance the data exhibit the same general spectral features as the TH-2PPE spectrum: Parabolas exhibiting hole-like dispersion just below the Fermi level due to photoemission from the Se 4*p* bands and additional (non-dispersive) features at somewhat lower energies that become fully accessible due to the reduction of the work function by cesium adsorption. A closer inspection shows, however, clear differences in the spectral characteristics. The Se 4*p* signal in the SH spectrum appears somewhat blurred, yet strongly enhanced in the vicinity of the $\bar{\Gamma}$ -point. Furthermore, the non-dispersive feature appears to be much narrower than in the TH-2PPE spectrum. The energy-reduced band scheme in figure 4.3(b) gives an obvious explanation for both characteristics. The change in photon energy has shifted initial, intermediate and final state contributions with respect to each other in the initial state energy projection. Therefore, for 2PPE excitation with $h\nu = 3.44$ eV, the unoccupied excess Ti state is now expected to be rather isolated and well separated from the final state titanium *s* and *p* orbitals (green parabolas). In fact, the energy of the excess Ti state as derived from the calculations fits rather well to the energy of the narrow band in the SH-2PPE data. This interpretation is corroborated by the robustness of the state against surface contamination indicating a localization within the van der Waals gap as expected for the Ti excess state. Furthermore, the Se 4*p* parabolas now show significant overlap with the intermediate Ti 3*d**-band particularly at $\bar{\Gamma}$, and therefore explain the experimentally observed resonant enhancement and overall spectral broadening. We will discuss the differences observed in the third harmonic (TH) and SH spectra, especially concerning the articulate separation of the two unoccupied Ti bands in the SH spectra in more detail in section 4.2.

The quantitative analysis of AR-2PPE data recorded at a number of different photon energies supports our assignments and enables us to explicitly extract the respective band energies and dispersions from the experimental data. Figure 4.7 shows the kinetic energy position (corresponding to the final state energy) of all spectral features identified in the SH-2PPE maps at the $\bar{\Gamma}$ -point as a function of the applied photon energy ($h\nu = 3.00$ eV to 3.45 eV). This graph is completed by corresponding TH-2PPE data ($h\nu =$

4.40 eV to 4.75 eV). The data points were extracted from the 2PPE EDCs deduced from the intensity maps and after subtraction of a secondary background mimicked by an exponential decay function. Peak positions were determined from multiple, sufficiently separated Gaussian fits. These fits delivered unambiguous peak energies from all SH-2PPE EDC. In the case of the TH-EDC the extraction of peak positions is however somewhat critical in the energy regime of the broad intensity band. Figure 4.8 compares a SH- and TH-EDC recorded at $h\nu = 3.44$ eV and 4.43 eV, respectively, with the result of the multiple Gaussian fit. As can be seen, while two Gaussians are sufficient to fit the unoccupied features (dashed, peak A and C) in the SH-EDC, a satisfactory fit to the dominating broad feature in the TH-EDC requires the assumption of a third Gaussian (dotted, peak B). We assign these three Gaussians to three different bands.

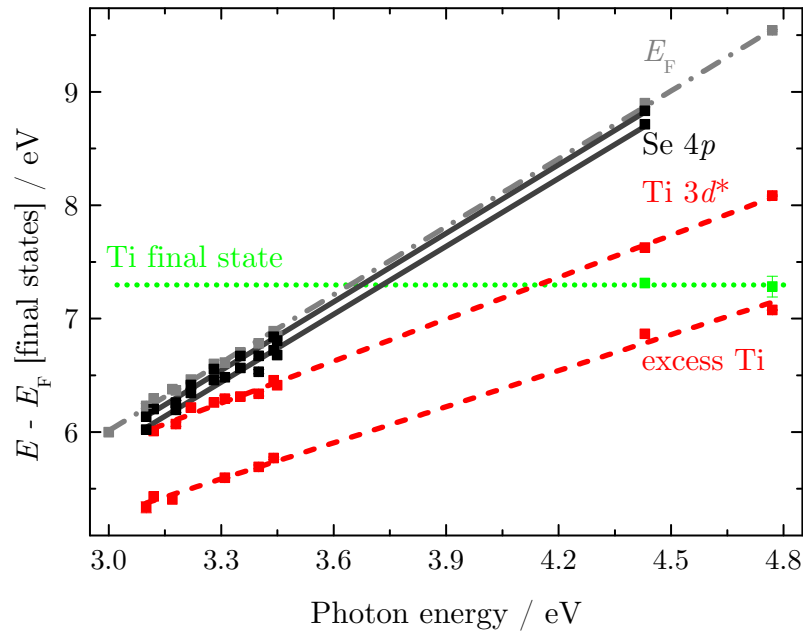


Figure 4.7: Shift in the kinetic energy of the relevant spectral features observed in the 2PPE experiments as a function of the excitation photon energy (p-polarized). The respective slope of the shift is characteristic for the nature of the probed electron state (see text). This dependence allows us to assign the data points/lines labeled in red (dashed) to the unoccupied Ti $3d^*$ band and a state associated with the excess Ti atoms.

The slope of the peak positions in figure 4.7 allows for distinguishing initial, intermediate and final state contributions to the spectrum. A slope of $2\Delta h\nu$, two times the change in photon energy, is characteristic for an initial state, $\Delta h\nu$ is characteristic for an intermediate state and final states exhibit a vanishing slope [113]. The two parabolas in the vicinity of the Fermi edge, which we already assigned to the occupied (initial) Se $4p$

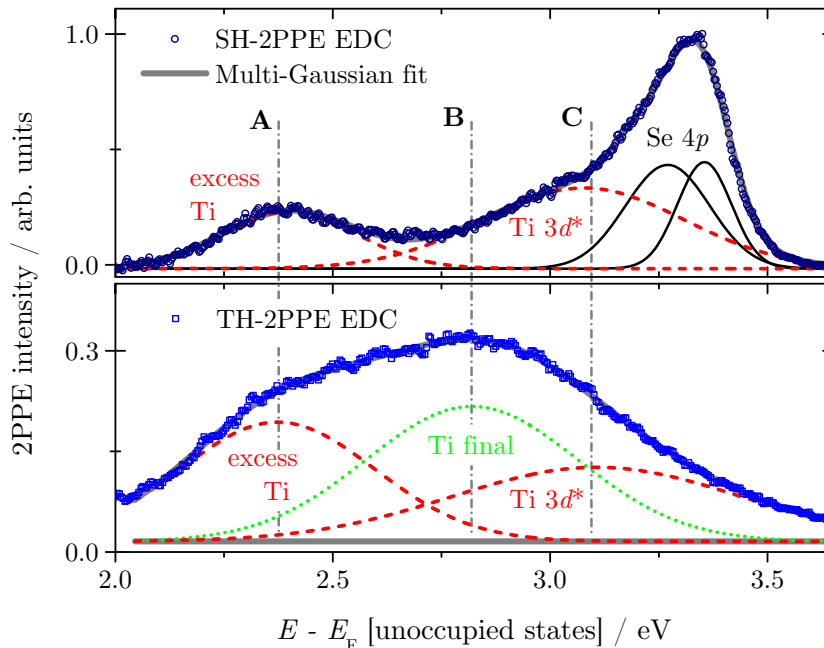


Figure 4.8: Comparison of an experimental SH- and TH-2PPE EDC ($h\nu = 3.44$ eV and 4.43 eV, respectively, normal emission) with the result of a multiple Gaussian fit. Line style and color as per figure 4.1(c).

states, show indeed a slope of 2.0 ± 0.1 and 2.0 ± 0.2 as expected. They are shown in figure 4.7 by full black lines in correspondence to the color coding and line style used in the energy-reduced band schemata [figures 4.1(c) and 4.3(b)]. Another peak (labeled in red and dashed, C in figure 4.8) which evolves slightly below the Se $4p$ parabolas in the SH-2PPE spectra as the photon energy increases exhibits a slope close to one 1.2 ± 0.1 and fades into the upper edge of the broad band feature in the TH-2PPE spectrum. Due to the energy of this state in comparison to the band structure calculations, we assign the peak to the unoccupied Ti $3d^*$ bands. The deviation of the slope from one is likely due to the fit of the broad feature in the TH-EDC, as described above. Except for the Se $4p_z$ band all bands exhibit a small or even vanishing band dispersion in \mathbf{k}_\perp , due to the weak coupling between the TiSe₂ layers (see the band structure calculations by Zunger and Freeman [9] shown in figure 4.10). Therefore, the experimentally determined photon energy slopes are not affected by the \mathbf{k}_\perp dispersion as reported before for instance in the case of a resonant interband excitation in Ag(111) [188, 189]. With respect to the Se $4p_z$ band the observed slope of two just confirms the assignment on the basis of the \mathbf{k}_\parallel dispersion and the comparison with 1PPE measurements and the band structure calculation. In this case the pronounced \mathbf{k}_\perp dispersion does not seem to affect the photon energy dependence of the 2PPE signature. The data points at the lowest energy values

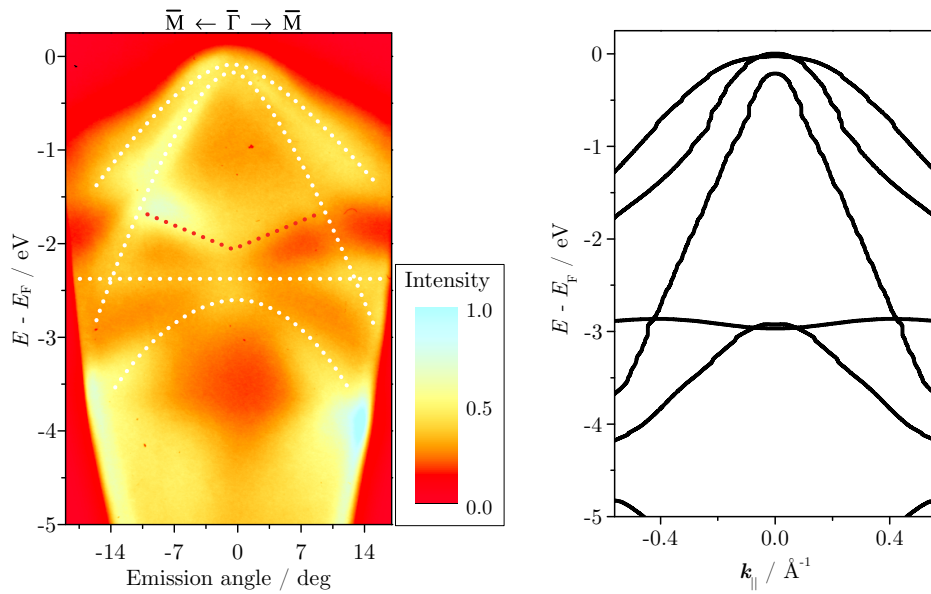
(also shown in red and dashed, A in figure 4.8) correspond to the separated non-dispersing band in the SH-2PPE intensity map. These data points also exhibit a slope close to one 1.1 ± 0.1 and further support our previous assignment to the non-dispersive unoccupied excess Ti atom state.

Let us finally consider the slope of the center Gaussian fitted to the broad band feature in the TH-2PPE EDC (figure 4.8) and displayed in figure 4.7 in green (dotted). This peak does not exhibit any change in position with excitation energy and is therefore characteristic for a final state contribution. Extrapolation of these data to the second harmonic photon energy regime 3.0 eV to 3.5 eV (see also figure 4.7) shows that this state is located well above the final state cut-off energies in these spectra (labeled by the gray dash-dotted line) and therefore cannot contribute to the SH-2PPE signal. In comparison with the reduced band scheme, the energy of this state fits approximately to the energy of the upper of the two final state Ti bands of *s* and *p* character. We do not observe any contribution of a second final state band to the photoemission in any of the 2PPE data, although we will show that the second band suppresses the photoemission from the Ti 3*d** band under certain conditions (see section 4.2). Such final state contributions to the 2PPE spectrum are not new. They have been observed, for instance, in 2PPE spectra of Ag(111) which show a pronounced peak due to the resonant excitation into a *sp* final band [188, 189]. Also adsorbate–surface systems, like C₆H₆/Cu(111) [201], C₆₀/Au(111) [202] and tetra-*tert*-butyl-azobenzene (TBA) on Au(111) [203], exhibit such final state effects. However, the feature we assign to a Ti final band is rather weak and different alternative assignments are imaginable. Furthermore, the energy of the feature is too high with respect to E_F , an observation, we will discuss later (see also figure 4.10).

4.1.3–a Comparison to VUV Spectra—the Influence of the Se 4*p_z* Band

Figure 4.9(a) shows an ARPES spectrum of TiSe₂ acquired at a photon energy of $h\nu = 21.22$ eV; this 1PPE spectrum contains information only about the occupied (and final) electron states. Such data is particularly interesting in comparison to the AR-2PPE experiments shown before [figures 4.1(a) and 4.3(a)]. A closer look at the contribution only from the occupied bands allows for a better interpretation of the 2PPE data.

Direct comparison to the band structure calculation by Zunger and Freeman [9] shown in figure 4.9(b) enables us to understand almost all features (white, dotted lines serve as a guide to the eye). Right below the Fermi energy the parabolas of the Se 4*p_x*, 4*p_y* and the stronger dispersing Se 4*p_z* bands are clearly visible and they agree very well to the band structure. At an energy of $E - E_F \approx -2.5$ eV at the Γ -point we see a non-dispersive and a hole-like dispersing band, both derived from Se 4*p_x*, 4*p_y* orbitals [60]. An electron-like dispersing band at about -6 eV at the Γ -point, which is observed at about -5 eV and $\mathbf{k}_{\parallel} > \pm 0.4 \text{ \AA}^{-1}$ in the spectrum, is of Se 4*p_z* character [60]. Newer band structure calculations exhibit an energy of the two lower Se 4*p_x*, 4*p_y* bands experimentally observed at about -2.5 eV which is up to about 0.8 eV higher (closer to E_F , see, e. g.,



(a) ARPES spectrum of TiSe_2 acquired with a gas discharge VUV lamp operating at a photon energy of $h\nu = 21.22$ eV.

(b) Corresponding calculated band structure of Zunger and Freeman [9] for the energy and angle range of (a).

Figure 4.9: The main spectral features in (a) are emphasized by white, dotted lines. A very good agreement to the band structure calculations in (b) is observed. Both data show the $\bar{\Gamma}\bar{M}$ -direction. We discuss the deviating feature (red, dotted) in the text.

reference [60–62]). Therefore, our assignment of the corresponding spectral features to these bands is valid, although the energy is higher by about 0.5 eV with respect to reference [9]. In the lower part of the spectrum (below about -4 eV) even some hints at the electron-like Se $4p_z$ band are observed. Overall, the spectral features can be easily assigned to the expected band structure. Nevertheless, one spectral feature cannot be explained by such a simple, straightforward comparison to band structure calculations: the electron-like structure marked in red.

In this case we need to consider the surface projected band structure as provided, e. g., by Stoltz et al. [73]. The Se $4p_z$ band just below the Fermi level features a significant perpendicular dispersion—in contrast to most of the other bands of TiSe₂ which show only negligible dispersion in this direction (see figure 4.10). Also, the parallel dispersion of this band varies along the perpendicular direction. Therefore, the Se $4p_z$ band provides electronic states in an energy range of about -2 eV to 0 eV below E_F at the Γ -point. Close to the Brillouin zone center the lower limit of this projected band reveals the triangular shape also observed in our spectrum in figure 4.9(a) (red line). The projected Se $4p_z$ band is thus defined by a parabolic, hole-like dispersion in the ΓM - and a triangular shape in the AL-direction¹ [60–62].

What can we learn from the comparison to this ARPES spectrum? First, the non-dispersive occupied Se $4p_x$, $4p_y$ band coincides with the unoccupied excess Ti state as observed in the TH-2PPE spectra. We like to point out that this band cannot explain the feature we assign to the excess Ti state, because photon energy dependent spectroscopy (figure 4.7) clearly proves its unoccupied character. Especially concerning the SH-2PPE data, shown e. g. in figure 4.3(a), it is obvious that an additional unoccupied non-dispersive state is present, because the occupied non-dispersive band is not accessible using SH photon energies. However, this occupied band increases the smearing out of the broad feature in the TH-spectra. This may be one of the reasons, why we cannot separate excess Ti and Ti $3d^*$ band in these data (another contribution to this problem will be discussed in section 4.2). The electron-like dispersion of the Se $4p_z$ band at $E - E_F \approx -2.5$ eV in the AL-direction on the other hand provides an alternate explanation of the electron-like dispersing resonance feature we attributed to the Ti final band. Figure 4.9(a) shows an energy range of about -2.0 eV to -1.5 eV for a contribution of the triangularly shaped band edge near the A-point. This agrees reasonable well with the energetic region of the resonance in the TH spectrum. Nevertheless, the Se $4p_z$ band as the source of this spectral feature seems less likely than a final state contribution, because

- its kinetic energy is not depending on the photon energy (see figure 4.7) which is a strong indication for a final state contribution.
- The energy of the Se $4p_z$ band at the A-point is $E - E_F \approx (-1.8 \pm 0.1)$ eV—it is

¹Please note, that an older band structure calculation yields a flat dispersion in the AL-direction [9], i. e. it does not agree with our experimental observation.

a rather broad structure with high intensity in the range of -1.9 eV to -1.7 eV— which is considerably higher, than the corresponding value fitted for the resonance feature of about -1.6 eV.

- Also, the Se $4p_z$ band is well resolved in figure 4.1(a), its parabolic characteristic agrees very well with the expected dispersion (see figure 4.2 and table 4.1, as well as references [10, 94]). The ARPES spectrum in figure 4.9(a) on the other hand shows a stronger emphasis of the characteristic of this band in the AL-direction. The parabola observed in the Γ M-direction appears somewhat attenuated. Considering the strong perpendicular dispersion of this band it seems, that we are probing the band structure near the Brillouin zone border using the VUV source, while we are operating closer to the Brillouin zone center for the SH and TH photons.

In conclusion, the Se $4p_z$ band increases the smearing of the broad feature in the TH spectra. Although we favor a final state contribution as the source of the resonance feature, we cannot ultimately rule out a Se $4p_z$ contribution. The Se $4p_z$ band complicates the assignment of an energy to this resonance feature.

4.1.4 Discussion of the Surface Projected Band Structure

Here, we evaluate the peak positions of 2PPE EDCs at different, finite k_{\parallel} values along the Γ M-direction. The results are summarized in figure 4.10 and are directly compared with the band structure calculations of Zunger and Freeman [9] under consideration of the findings of Pehlke and Schattke [69]. The first conduction band of the TiSe₂ compound, exhibiting a Ti $3d^*$ and Ti $3d_{z^2}$ character with admixtures of Se $4p$ bands [60], is located at an energy between 0 eV and 1 eV above the Fermi level and is therefore experimentally not accessible with the photon energies available to our 2PPE study. For the upper unoccupied Ti $3d^*$ band (full red circles) the experimental data show only a weak dispersion and an energy of $E - E_F = (3.0 \pm 0.1)$ eV at the $\bar{\Gamma}$ -point, as derived from figure 4.7. This result is in good agreement with the calculated band structure, which yields a corresponding value of 3.2 eV [9, 61] and 3.1 eV [60] respectively. For comparison, in previous IPE studies a value of 3.1 eV [18] and 3.2 eV [19] was reported. We would like to point out that the energy of the Ti $3d^*$ band is not influenced by the adsorption of Cs, because the corresponding photoemission data was solely acquired on pristine TiSe₂ crystals.

The data points located approximately 0.7 eV below the Ti $3d^*$ band (open and filled red squares) correspond to the band that we assigned to the excess Ti atom states. The absence of any dispersion in the experimental data supports the localized character of this state and an energy of $E - E_F = (2.3 \pm 0.1)$ eV agrees well with the calculated value of 2.1 eV [69]. Please note, that for the maximum Cs coverages of this work a linear extrapolation to vanishing Cs coverage yields a worst case shift of the excess Ti states' energy of about 30 meV, i. e. the energy of this state is expected to be

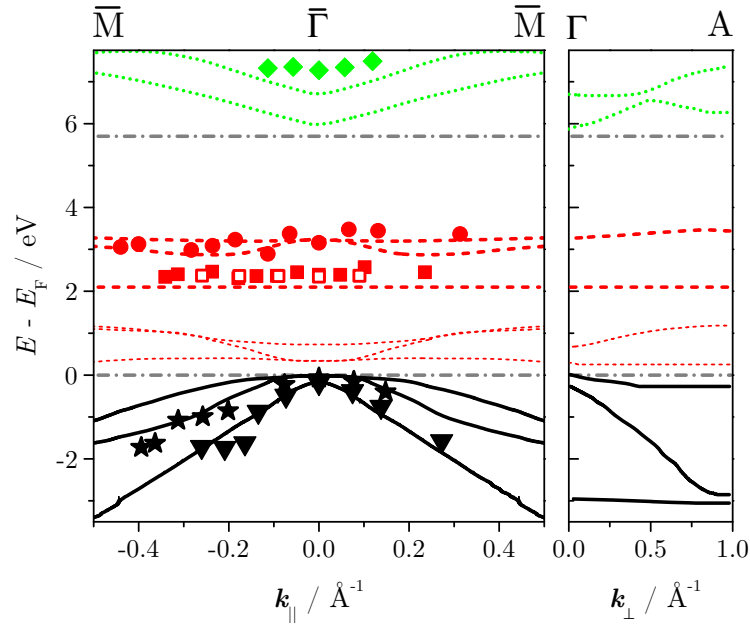


Figure 4.10: Left: Calculated band structure along the $\Gamma\bar{M}$ -direction (k_{\parallel}) [9] in comparison to the experimental results of this 2PPE study. The lower lying red line is the unoccupied non-dispersive excess Ti atom band ($E - E_F = 2.1$ eV [69]). Filled symbols correspond to experimental TH-2PPE data, open symbols correspond to SH-2PPE data. Right: Calculated band dispersion data perpendicular to the surface plane along the ΓA -direction (k_{\perp}).

$E - E_F < (2.33 \pm 0.10)$ eV (if we omit the uncertainty of the shift). Considering the uncertainty of the energy, the effect of the small shift upon Cs adsorption is indeed negligible. The energy of the state is rather close to the regular Ti $3d^*$ bands which is not very surprising considering the rather similar octahedral coordination site proposed for both Ti species, within the regular TiSe₂ layers and within the van der Waals gap of the crystal, respectively [73, 151]. At first glance it may be surprising that the Ti excess peak shows up in the spectra at a significant intensity even though only 1% of all Ti-atoms contribute to this signal. However, as we will see later, this state exhibits a rather long lifetime which enhances the probability for the second 2PPE excitation step and consequently the efficiency of the overall 2PPE process. The relatively long lifetime of this band is indeed in further support of our interpretation, because for a decoupled band within the van der Waals gap such an increase in lifetime is to be expected.

Please keep in mind, that the band structure calculations for the ideal TiSe₂ crystal [9] in general reproduce our experimental findings very well. Yet, they do not provide any indications for the non-dispersive unoccupied band we observe experimentally very clearly. This leads us to the conclusion that the appearance of this band in the 2PPE spectra of TiSe₂ has to be related to a distortion of the ideal crystal, like a substitution

of regular bulk atoms, vacancies or additional atoms intercalated within the van der Waals gap. The overall very good agreement of our data to band structure calculations further supports our assignment of this state to excess Ti atoms.

The observed final state energy in the 2PPE experiment (green diamonds) agrees within about 0.6 eV with the predictions for the Ti-band of s and p character [9]. However, this result is worse than for the other bands. Both final state bands of TiSe_2 show significant dispersion perpendicular to the layers (see figure 4.10), which may already explain to some extent the observed deviations. Furthermore, recent band structure calculations by del Pilar Ramírez García [61] show a significant deviation of about 0.5 eV in the binding energy of the lower Ti final band (not observed here) with respect to the data of Zunger and Freeman [9]. They do not provide any data for the final band observed here, but considering the deviation of the other band, the difference in energy observed in our case does not seem unlikely. Furthermore, the expected band dispersion cannot be confirmed experimentally. Nevertheless, the final state contribution is only a very side aspect of our experiments and we focus on the intermediate states contribution. In particular, considering the time-resolved experiments of this work, the final state contribution is irrelevant, because it does not modify the SH-2PPE spectra used in this case (see also figure 4.7).

4.1.5 The Origin of the Ti Excess Atoms

We will now comment in more detail on the actual origin of the Ti excess atoms in our samples. Pehlke and Schattke [69] considered in their theoretical work titanium atoms that have been removed from a crystalline layer, leaving vacancies within the layer, and occupying empty sites within the interlayer van der Waals gap. These kinds of defects have been referred to as *Frenkel-type defects*, characterized by additional occupied and unoccupied localized states. The results of their calculations give evidence for a vacancy state at $E - E_F = -1.5$ eV, and states localized at the Ti excess atom at energies of -7 eV, 0.5 eV and 2.1 eV. The existence of the non-dispersive vacancy state at an energy of -1.5 eV has been previously observed in a conventional photoemission experiment [66, 69]. Such intercalate localized states are not uncommon. Upon the intercalation of $3d$ -metals, like e. g. iron, the appearance of a narrow $3d$ -like band has been reported [204]. A narrow, non-dispersive occupied band derived from Fe $3d$ states is observed, for instance, in ARPES measurements of the system $\text{Fe}_{0.25}\text{TiTe}_2$ [205]. Here, we present, for the first time, experimental evidence for the unoccupied state induced by Ti excess atoms at the predicted energy of 2.1 eV.

From a preparational point of view, it is likely that the Ti excess atoms were embedded into the van der Waals gap during the growth process of the TiSe_2 crystal. As already discussed in the experimental setup section 3.3 of this work, our TiSe_2 samples exhibit a considerable amount of excess Ti atoms. Indeed, TiSe_2 tends to grow at a non-stoichiometric surplus of titanium atoms, even if the usual compensating excess of

selenium is applied for the growth process [8, 159, 206]. Yet, the presence of a surplus of titanium is not an indication for inferior quality of the samples. The growth process has been explicitly optimized for such a slight excess of Ti, because it supports the growth of sufficiently large single crystals—a prerequisite for photoemission experiments. A Ti surplus of approximately 1% for the samples used in this work guarantees TiSe₂ single crystals large enough for photoemission experiments (refer to section 3.3 for the typical crystal dimensions). However, the acceptable drawback of this procedure is a Ti excess dependent lowering of the CDW phase transitions' critical temperature. In fact, this lowering enables us to estimate the amount of excess Ti atoms (see section 3.3). We find that the typical transition temperature of $T_0 = (174 \pm 3)$ K corresponds to a defect concentration of about $x = 1\%$ in Ti_{1+x}Se₂. In other words, about one out of 101 Ti atoms occupies an excess atom site within the van der Waals gap. In comparison, another considerable contamination of the crystals is due to the iodine atoms which are used as a transport gas during the growth process. Iodine is assumed to substitute selenium atoms on regular lattice sites. Typically 0.3 at. % (atomic percent) of iodine are observed for TiSe₂ grown by chemical vapor transport. This translates to about one iodine atom per about 1000 selenium atoms (1.5 : 1001.5) or about 0.3 iodine atoms per 101 titanium atoms. This ratio has been reported to be rather insensitive to the growth conditions (especially growth temperature) [8]. Therefore, we expect the iodine concentration in our samples to be at maximum one third of the density of excess Ti atoms, i. e. we do not expect significant contributions to the photoemission spectra.

We stated earlier in the cause of our argumentation, that the otherwise very good agreement of the photoemission data to band structure calculations strongly suggests, that a deviation from the ideal crystal is the source of the non-dispersive state observed. The fact, that our TiSe₂ crystals indeed show a slight surplus of Ti already renders a state associated with these defects a likely candidate for the spectral feature observed. On the other hand, the appearance of vacancies is not expected in our case. Experimentally we neither observe a vacancy state at $E - E_F = -1.5$ eV in conventional ARPES, nor in the 2PPE intensity maps (figures 4.1 and 4.3), supporting this view.

Considering our findings so far, ideally experiments for different excess Ti concentrations should be performed to support our conclusions. If our assignment of the non-dispersive feature to a state localized at excess titanium atoms is correct, changes, for instance, of the intensity of this peak are to be expected for varying defect concentrations. Therefore, we attempted to experimentally provide such data. However, we had to learn that these experiments are most likely not possible. Even the samples *optimized* with respect to the crystal size as used throughout this work exhibit strong inhomogeneities in the peak intensity of the spectral signatures of up to about 25% on a

- (i) single, specific sample,
- (ii) between different samples of one charge of growth,

(iii) and between different samples of different growth charges.

The dominating problem we are facing is the presence of structural inhomogeneities of the TiSe₂ crystals which pronounce or weaken different spectral reference signatures, such as the Se 4*p* bands and/or the low energy onset of the spectra in different ways. These structural issues will be even more critical for samples of a significantly lower excess of titanium, because such samples typically tend to be too small to perform photoemission spectroscopy experiments at all. A certain amount of excess titanium seems to be necessary to support the growth of sufficiently large crystals. This is due to the observation, that the growth temperature strongly influences the size of the grown crystals. In particular a certain minimum of the temperature has to be surpassed to prevent the growth of microcrystallites [157, 158], but the deviations from stoichiometry also increase with the growth temperature [8]. In summary, we cannot study virtually defect free or ideal 1T-TiSe₂, because of the dimensions of the corresponding crystals. Additionally, the distinct structural inhomogeneities of the samples prevent a meaningful comparison of measurements of different crystals with, for instance, different concentrations of excess Ti. The expected variation of the peak intensity within the feasible concentration range is just too subtle considering the influence of the inhomogeneities.

Even though such a concentration dependent data set would further support our interpretation, unfortunately we cannot provide these data. However, the points we discussed above clearly show that the non-dispersive feature observed experimentally arises (*i*) from an unoccupied state located within the van der Waals gap (*ii*) and that this state originates from intercalated Ti excess atoms.

In the following section we will focus on the ultrafast decay dynamics associated with the population of the unoccupied Ti 3*d** band and the excess Ti atom state. Both bands originate from titanium 3*d*-orbitals. Since the unoccupied state associated with the excess Ti is much stronger localized at the corresponding atoms, one can expect a clear distinction between both excitations with respect to their lifetime.

4.2 Decay Dynamics of the Unoccupied States of 1T-TiSe₂

The time resolved experiments were performed using the second harmonic light of laser 2 ($h\nu = 3.12$ eV, 28 fs). The left part of figure 4.11(a) shows a SH-2PPE intensity map from a sample recorded with this light source. Note that for these measurements the work function of the 1T-TiSe₂ sample was lowered by 1.2 eV by the adsorption of cesium ($\vartheta = 0.27$ ML). Clearly visible and marked by the dotted box is the non-dispersing excess Ti atom state at an energy of about 2.3 eV. The Se 4*p* band just below the Fermi edge shows—at this photon energy—a distinct structure exhibiting a maximum at about -4° emission angle and marked in the figure by a dotted ellipse. This intensity maximum arises from the resonant excitation of the weakly dispersing Ti 3*d** intermediate state band from the strongly downward dispersing Se 4*p* initial state band at finite k_{\parallel} values

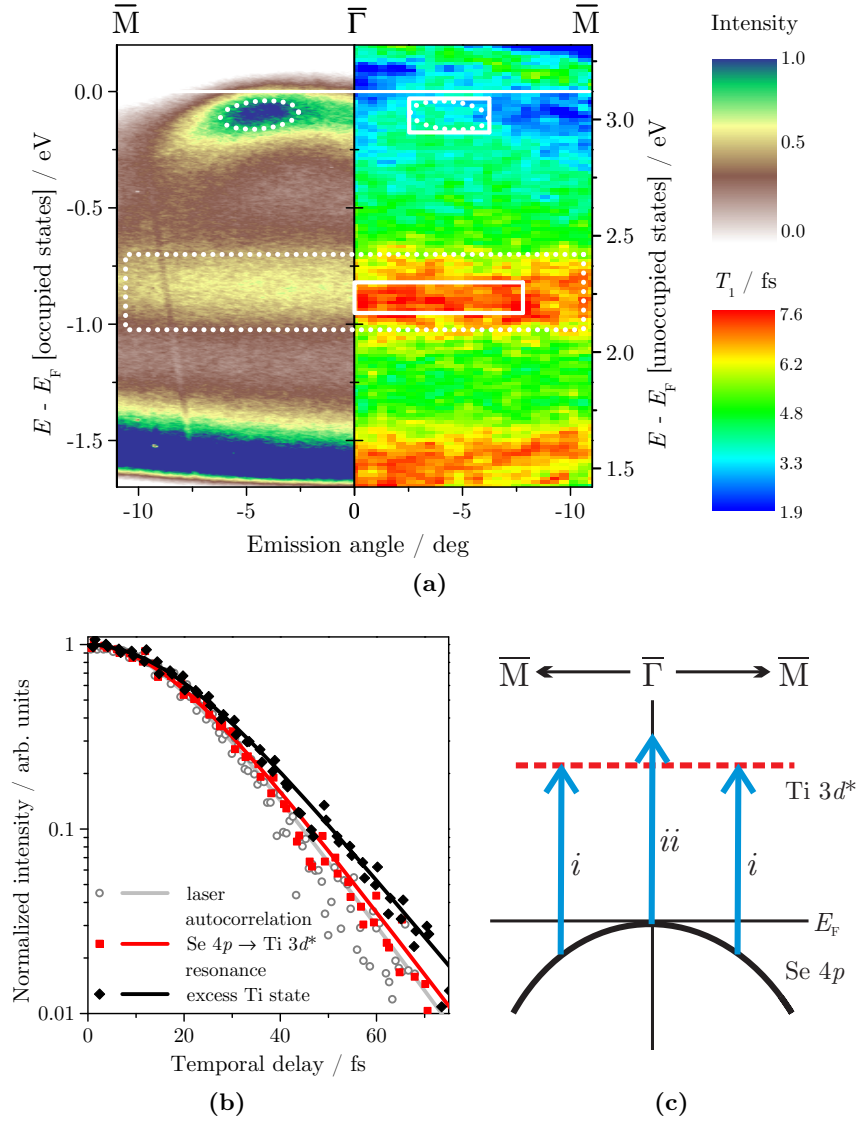


Figure 4.11: (a) Left: SH-2PPE spectrum of 1T-TiSe₂ recorded with laser 2 at $h\nu = 3.12$ eV (p-polarization). Right: Corresponding lifetime map deduced from a time-resolved 2PPE scan. Lifetimes are color coded as labeled in the inset. The left scale shows occupied states energy and the right scale unoccupied states energy with respect to E_F . The dotted lines highlight the distinct spectral features. The full boxes mark the integration areas that have been used to extract the 2PPE autocorrelation traces shown in (b). (c) Scheme of the resonant excitation pathways at $h\nu = 3.12$ eV. (b) Comparison of the 2PPE autocorrelation traces related to excess Ti atom state and Ti 3d* band, respectively. The laser autocorrelation is also shown. (continued on page 101)

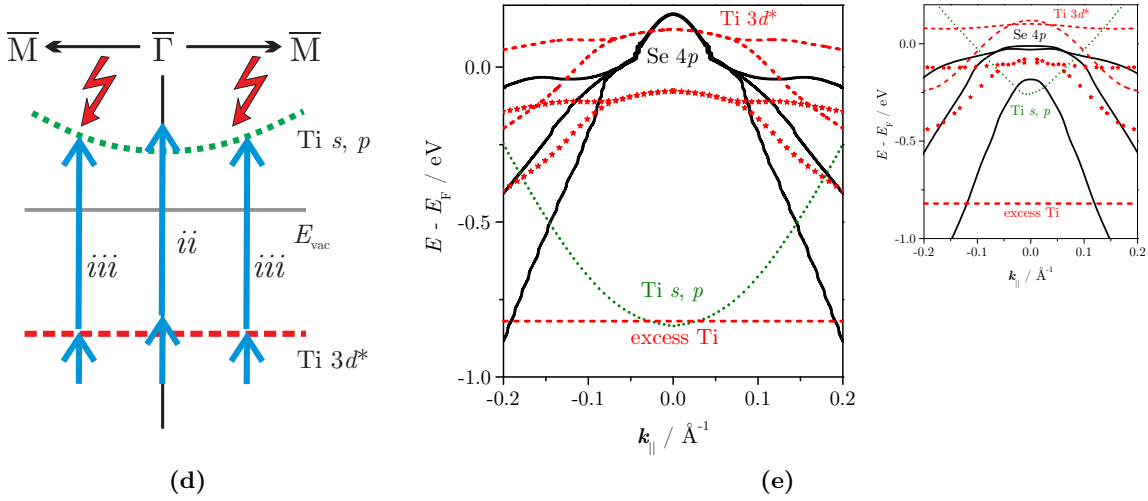


Figure 4.11: (continued from page 100) Explanation of the missing Ti 3d* emission between the excess Ti state and the Fermi level; (d) and (e) show only a qualitative representation of our interpretation (see text). (d) Schematic representation of the second excitation step of the 2PPE process. For a certain momentum range the excitation from the Ti 3d* becomes resonant with the lower final Ti band. This transition is forbidden by dipole selection rules. (e) Energy reduced band structure corresponding to a photon energy of $h\nu = 3.12$ eV (energies of the bands as per reference [61]). Clearly, for momenta beyond the Brillouin zone center the Ti 3d* and the lower final band overlap, resulting in a suppression of photoemission from these bands. The corresponding energy reduced band structure using the data of Zunger and Freeman [9] is shown in the inset. For details see text.

[see figure 4.11(c), excitation path *i*]. At a photon energy of $h\nu = 3.12$ eV a resonant excitation is not possible at the $\bar{\Gamma}$ -point, due to the higher energetic separation of the Ti $3d^*$ and Se $4p$ bands [see figures 4.11(a) and 4.11(c), excitation path *ii*]. The 2PPE process enables us to selectively address two distinct unoccupied states of the 1T-TiSe₂ compound, both derived from Ti $3d$ orbitals. In the following we will focus on the population lifetime T_1 of these two unoccupied states, Ti $3d^*$ and Ti excess state, as probed by means of time-resolved 2PPE.

Before we discuss the TAR-2PPE experiments in detail, we would like to comment on a specific characteristic of the spectra acquired with the second harmonic. Interestingly, the excess Ti state is much more defined than in case of the TH spectra, because Ti $3d^*$ and excess Ti bands do not overlap in one broad spectral feature anymore. Figures 4.11(c)–(e) will help us to understand this phenomenon in a qualitative manner. The first step of the 2PPE process is shown schematically in figure 4.11(c). The band structure calculations of Zunger and Freeman [9] are the basis for the schematics shown in figure 4.11. The schematic representation has been chosen for clarity and to compensate for the little deviations of experimental and calculated data. Please note, that we assume an energy about 200 meV lower than the value calculated for the Ti $3d^*$ band in agreement with our experimental data. Basically, this figure shows, that a resonant excitation from the Se $4p$ into the Ti $3d^*$ band is not possible at the Brillouin zone center (see path *ii*), but requires a certain parallel momentum (see path *i*). This explains the resonance enhancement in the spectrum in figure 4.11(a).

Figure 4.11(d) shows the second step of the 2PPE excitation. Again, this is a simplified scheme inspired by band structure calculations [9]. The second step of excitation path *ii* starts off-resonant slightly above the Ti $3d^*$ band and ends off-resonant between the lower and the upper Ti s and p final band. For a certain parallel momentum the Ti $3d^*$ and the lower final band can be coupled resonantly (excitation path *iii*). Such a resonant optical transition using linearly polarized light from Ti $3d^*$ into the lower final band is forbidden by dipole selection rules [e. g. 172] due to the same positive parity of both bands [9, 60]. This explains, why we do not observe significant intensity of the Ti $3d^*$ band outside the two resonances, in particular considering the very defined and clearly separated excess Ti state.

Actual energy reduced band structures are presented in figure 4.11(e). However, such schemes do not quantitatively represent our experimental data using the otherwise well fitting band structure calculations [9, 61]. Although the calculation of del Pilar Ramírez García [61] does not reproduce the Se $4p$ bands as well as the data of Zunger and Freeman [9], both derive a very similar energy of the Ti $3d^*$ band important to this work. Furthermore, both provide data for at least the lower one of the Ti s and p final bands. To enhance the agreement to our experimental data, the energy of the Ti $3d^*$ band is shifted by 200 meV to lower energies (red stars), i. e. nearer to E_F . Please note,

that the experimental energy and dispersion of the higher final band is not reproduced very well by the band structure of reference [9] (see also figure 4.10). We cannot decide, whether the more recent calculations of del Pilar Ramírez García [61] are better fitting in this case as we do not observe the lower final band, but these calculations yield a significantly lower energy of the lower final band. A lowering of the lower final bands' energy would increase the agreement to our spectroscopy data, as we will see shortly. The inset of figure 4.11(e) shows the corresponding energy reduced band structure using the calculations of Zunger and Freeman [9]. Although the Se 4*p* bands fit better to our experiment, the lower Ti final band features an energy significantly too high. We expect this final band to reside between these two extrema, by trend nearer to the newer calculation [61]. Overall, the energy reduced band structure shows qualitative how the lower final band masks the emission from the Ti 3*d** band for certain parallel momenta, especially in between the apex of the Se 4*p* parabolas and the excess Ti state.

In summary, beginning at the Brillouin zone center, we do not observe the Ti 3*d** band because of the off-resonant first excitation step. After the first transition becomes resonant, but the second transition is still off-resonant, we observe a strong resonance feature in the spectra. Finally, if the second transition of Ti 3*d** band into the lower final state becomes resonant, the Ti 3*d** intensity is suppressed due to dipole selection rules.

The right part of figure 4.11(a) also shows a color-coded lifetime map derived from a TAR-2PPE scan as described in detail in section 3.2.2 and in an earlier publication [124]. A blue, green, and red color coding corresponds here to short, medium, and the longest lifetimes measured within this experiment, respectively. The actual lifetime values have been deduced from the measured 2PPE autocorrelation traces following an analysis procedure suggested by Gauyacq and Kazansky [114] and under the assumption of rapid dephasing conditions within both excitation steps of the 2PPE process [125, 126] (see section 2.5.2). The lifetime map covers the identical energy and momentum range shown in the 2PPE intensity map on the left of figure 4.11(a). Once again the $E(\mathbf{k}_{\parallel})$ areas related to the excitation of the excess Ti atom state and the Ti 3*d** band are marked by the dotted box and the dotted ellipse, respectively. Evident from these data is a distinct maximum in the unoccupied state population lifetime of about 7 fs at the energy of the excess Ti atom state, which is independent of the probed momentum vector \mathbf{k}_{\parallel} . By contrast, in the energy region of the Se 4*p* band, autocorrelation traces are measured, which closely follow the laser autocorrelation. In the lifetime map this behavior gives rise to the pronounced minimum, mimicking the parabolic downward dispersion of the Se 4*p* band in correspondence to the 2PPE spectroscopy data. Only at the $E(\mathbf{k}_{\parallel})$ -area, which is indicative for the resonant excitation of the Ti 3*d** band (see dotted ellipse), the color coding of the lifetime map points to an increase in the measured lifetime to values of about 3.0 fs. We assign this local maximum to the actual population lifetime T_1 of the Ti 3*d** band. On the other hand, the minimum lifetime value along the rest of

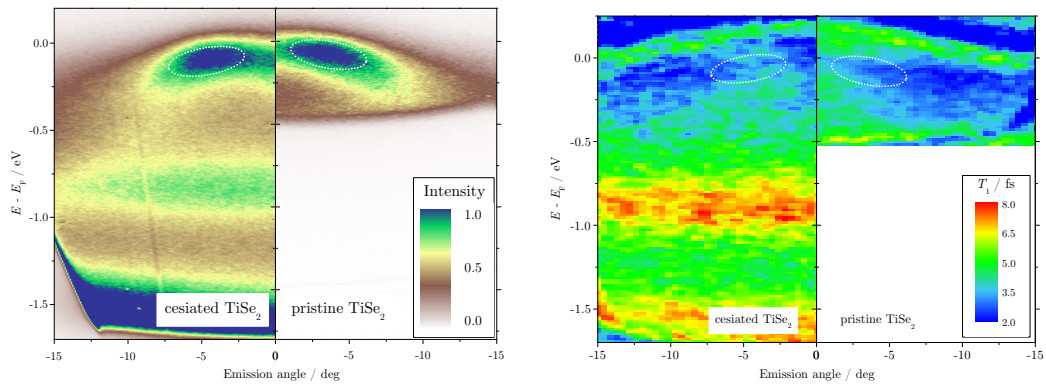
the Se 4p parabola, i. e. outside the area of the resonant excitation, arises from the off-resonant character of the 2PPE process [120, 154].

4.2.1 The Influence of Alkali Adatoms

Before we continue with our comparative discussion of the decay dynamics of the Ti 3d* and excess Ti band, we will address a problem arising from the alkali adsorbate used to lower the work function of the sample. The electronic structure as well as the dynamics can be affected by alkali adsorption, if a significant contribution from the surface layer to the photoemission signal is present. 2PPE spectra for different Cs coverages are shown in figure 4.5, the actual shift in energy of the relevant features is presented in figure 4.6. These data clearly illustrate that the electronic structure of the system is barely affected by the Cs adsorption and that the minor changes in energy can be well compensated by a Cs coverage dependent analysis for the consecutive experiments. Furthermore, the focus of our time resolved studies is the Ti excess band which associated spectral feature is highly robust against adsorption (with respect to energy, peak width and intensity), especially in comparison to the Se 4p and Ti 3d* bands. This proves that particularly this state cannot be surface located, but it needs to be buried underneath the surface layer. And indeed, the Ti excess atoms are actually expected to reside within the van der Waals gap. We are therefore convinced that the electron dynamics of this state is also unaffected by Cs adsorption—additional decay channels as offered by the Cs adsorbate are well decoupled by the interstitial TiSe₂ layer.

In case of the regular Ti 3d* band, which acts as a reference band with respect to the electron dynamics, an interaction with the Cs adsorbate cannot be excluded a priori. However, the lifetime of this band is also measured in a corresponding TR-2PPE experiment of the pristine (uncesiated) sample (see figure 4.12). The results of such measurements show no significant differences of the electron dynamics in comparison to the data of the cesiated sample, although the electronic structure is—especially concerning the relative intensity of this band—significantly altered, as can be seen in figure 4.12(a). By simply calculating the mean value of the lifetimes within the resonant part of the Ti 3d* band (the ellipses are only a guide to the eye in figure 4.12) we derive a lifetime of (3.2 ± 0.7) fs for the pristine TiSe₂ crystal, which is in good agreement to the lifetime observed for the Cs covered sample. However, we have to emphasize that our statement about the lifetime of the Ti 3d* band of < 3 fs is meaningful only to a limited extent due to the limited time-resolution of the experimental setup. A more precise statement is, that the influence on the dynamics of the Ti 3d* band cannot be temporally resolved, i. e. the deviation induced by the adsorbate is sufficiently small to neglect it.

To illustrate the difference in the depopulation dynamics between excess Ti atom state and Ti 3d* band, we compare in figure 4.11(b) the corresponding 2PPE autocorrelation traces. These traces have been generated by signal integration of the respective areas marked in the lifetime map in figure 4.11(a) by full boxes. The result of the quantitative



(a) AR-2PPE spectra for the same sample before and after Cs adsorption. The resonant excitation of the Ti $3d^*$ band is clearly visible.

(b) Lifetime maps corresponding to (a). The lifetime scale is identical in both cases. No significant influence of the adsorbed Cs on the lifetime is observed.

Figure 4.12: Comparison of the spectral and time resolved data acquired for pristine and Cs covered TiSe₂. Laser system, photon energy and sample are identical to the data presented in figure 4.11; especially the data of the pristine samples was acquired within the same experimental run using the same sample before and after adsorption of cesium. The region of the resonant excitation of the Ti $3d^*$ band is emphasized by dotted ellipses.

analysis of the two Ti autocorrelation traces is displayed as a full line. For reference the laser autocorrelation has also been added to figure 4.11(b) (open symbols), which has been determined from the time-resolved 2PPE signal of the Shockley Surface state of a well-prepared Cu(111) single crystal surface [120, 154]. The broadening of both unoccupied Ti state autocorrelation traces in comparison to the laser autocorrelation is indicative for the finite lifetime T_1 of the Ti intermediate states involved in the 2PPE process. The quantitative analysis delivers a lifetime $T_1 = (7.1 \pm 3.3)$ fs for the excess Ti atom state and a lifetime $T_1 < 3$ fs for the Ti $3d^*$ band. The population decay of the excess Ti state happens on a timescale which is about 2.5 times slower than the population decay of the Ti $3d^*$ band.

We suggest that the difference in the population lifetime of the two unoccupied Ti states arises from the characteristic differences in the electronic coupling of the corresponding layer and interlayer titanium sites to the TiSe₂ bulk electronic structure. As mentioned above, both the regular Ti atoms embedded within the crystal layers (layer Ti atoms), as well as, the excess Ti atoms located within the van der Waals gap, exhibit octahedral coordination sites with respect to the selenium atoms [73, 151]. Furthermore, the unoccupied states probed in our time resolved experiment are very similar with respect to the involved atomic orbitals. The inelastic population decay of these states, which is mainly governed by the coupling to the electronic environment, is, however, expected to differ significantly. Within the crystal layers the large orbital overlap with the layer electronic structure provides a multitude of efficient channels for the inelastic decay of the unoccupied Ti $3d^*$ band via electron hole pair excitation. These decay channels are less efficient for the spatially decoupled excess Ti state. The experimentally observed increase in the lifetime of the Ti excess state is a direct consequence of this decoupling.

4.2.2 Discussion of the Observed Time Resolved Data

Efficiently decoupled unoccupied states in solid state systems have been observed particularly in the context of surface-localized unoccupied states in the past: Examples are, for instance, image potential states [21–25] and adsorbate resonances on noble metal surfaces [26–30]. The characteristic lifetimes of these states, which are also governed by the coupling to the substrate electronic structure, cover the low femtosecond to picosecond regime. The long lifetime of the Ti excess atom state, in comparison to the layer Ti atoms shows, that in a similar manner a stabilization of electronic resonances is also possible within the bulk.

Our study of the decay dynamics of the excess Ti and the Ti $3d^*$ band finally enables us to understand an apparent discrepancy in our discussion of the origin of the non-dispersive feature in section 4.1. Considering the low concentration of excess Ti atoms (only about 1%) it is rather surprising that we observe a feature of these defect states in the 2PPE spectra at all. Yet, this band exhibits a photoemission intensity comparable to the crystal intrinsic bulk band, in particular in comparison to the Ti $3d^*$ reference band.

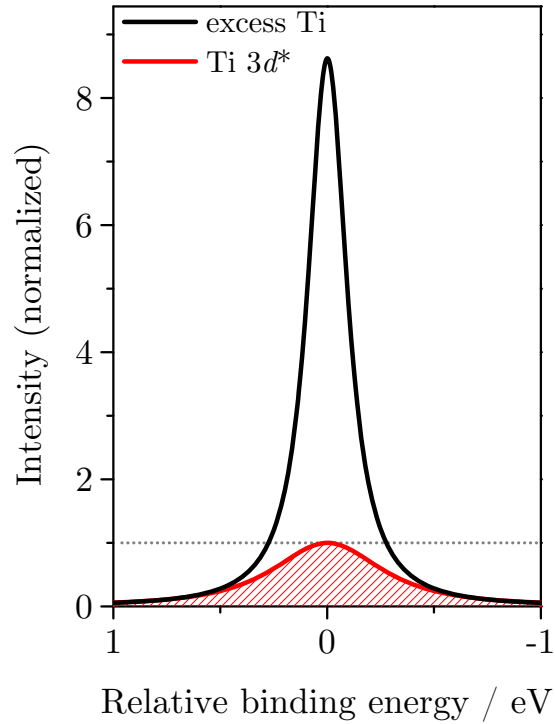


Figure 4.13: Calculated 2PPE spectra involving the transient population of the Ti $3d^*$ band (red, hatched area for emphasis) and the excess Ti state (black). The lifetimes were chosen to fit the experimental results obtained for these bands. The intensity is normalized to the peak intensity of the simulation of the Ti $3d^*$ band. The energy is given relative to the center of the corresponding spectral feature. Due to the higher lifetime of the excess Ti state, its spectral intensity is significantly enhanced. For details see text.

For instance, X-ray photoelectron spectroscopy (XPS) of core-level photoemission is generally used to quantify the element concentration in compound systems by comparing the relative intensities (see, e. g., references [207] and [108]). For ultraviolet photoelectron spectroscopy (UPS), i. e. the energetic regime of the valence bands, such a relation of spectral intensity and elemental concentration is also expected [208, 209]. So why do we observe such a strong contribution from a spectral feature associated with a low-concentration defect?

We need to consider, that we are dealing with unoccupied electron states—here, the situation becomes more complex, mainly for two reasons: (i) The 2PPE process involves three energy levels—initial, intermediate and final state—instead of only two levels as in case of conventional 1PPE (no intermediate state). Effects of resonant and off-resonant excitation become important and more complex. Therefore, 2PPE intensities are expected to be less related to the actual concentration of the compound species. (ii) The comparatively long lifetime of the excess Ti state with respect to the other features can considerably enhance the 2PPE intensity of this state. This important aspect will be discussed in the following in more detail.

Intuitively, the influence of the lifetime of an unoccupied state on the 2PPE photoemission signal is understood qualitatively as follows: After a normally unoccupied state is populated by excited electrons, a second photon can lift such an electron into the vacuum where it is detected. The longer this excited electron population exists, i. e. the longer the lifetime of the intermediate state, the higher the probability for the second photoexcitation process. For illustration of the efficiency of this lifetime effect, we performed model calculations of 2PPE spectra within the density-matrix formalism using the framework of the Liouville–von Neumann equations. This approach is typically used to model 2PPE data; details of the numerical method are discussed, for instance, in references [115, 210]. We consider intermediate state lifetimes T_1 as determined from TAR-2PPE for the Ti $3d^*$ and the excess Ti bands. Figure 4.13 shows the calculated 2PPE intensities as a function of the energy relative to the maximum of each band, i. e. the spectra are centered at the corresponding peak maximum. The calculated unoccupied bands are characterized by a lifetime of 2.0 fs and 7.1 fs, respectively.

The model assumes excitation from a homogeneous, broad band—the initial state—into a homogeneous, broad band—the final state—for the intermediate state considered. The lifetime of this intermediate state is set to the corresponding value to simulate a spectrum of the Ti $3d^*$ or excess Ti band. However, an open tuning parameter we cannot determine accurately from our time-resolved experiments, is the dephasing time characteristic for the individual states. The two broad bands (initial and final state) can be treated in the rapid dephasing limit. For the response of the unoccupied intermediate state we assume a dephasing time equal to the corresponding lifetime, i. e. the parameter Γ_{23} of the calculation is set in accordance to the intermediate states' lifetime to $\Gamma_{23} = \frac{1}{T_1}$ [115]. This is a compromise between the two extremal possibilities determined by the width of the spectral peak on the one hand and a dephasing time twice the states' population

lifetime on the other hand.

The spectral feature of the Ti $3d^*$ bands (red and hatched for better visibility) exhibits an articulate difference in the peak area with respect to the simulation of the excess Ti state (black). The maximum peak intensity in this example is enhanced by almost a factor of ten because of the increase in lifetime. Note, that the parameters chosen here are moderate. It is not difficult to tune the simulation for an enhancement of up to a factor of one hundred or even more under maybe less likely, but not completely unrealistic assumptions. Overall, we can safely state that the comparatively long lifetime of the unoccupied excess Ti state itself increases the spectral weight of this signature into the 10 % to several 10 % regime in comparison to other spectral features, even though the atomic concentration is only about 1 %. This result is indeed in reasonable agreement with the experimental data shown in figure 4.8, particularly if the 2PPE intensity of the excess Ti state is compared to the *intrinsic* 2PPE intensities of the Se $4p$ and the Ti $3d^*$ bands of the pristine TiSe_2 samples which are not modified by adsorbed Cs. A rather strong 2PPE signal from a low concentration constituent is not new; such an effect has also been observed for other systems before, like, e. g., the $6sp_z$ resonance state observed for Cs adsorbed on Cu(111) [26, 27, 30, 124, 180, 211, 212]. Even at Cs coverages in the low percentage regime, the 2PPE intensity of this Cs-localized state is comparable to the Shockley surface state of the Cu(111) substrate—the latter being attributed to all the surface atoms of the bulk crystal.

Overall, the data in figure 4.13 clearly shows that the lifetime of the intermediate state of a 2PPE process is crucial for the an understanding of the spectral intensity of this state. We believe that this lifetime effect is responsible for the comparably high intensity of the excess Ti state with respect to the Ti $3d^*$ band.

4.3 Summary and Conclusion

In summary, in this chapter we presented novel 2PPE spectroscopy data for the system $1T\text{-TiSe}_2$, with section 4.1 focusing on an angle resolved two-photon photoemission study of the transition metal dichalcogenide $1T\text{-TiSe}_2$. In addition to the well known spectral signatures of the occupied Se $4p$ valence bands, we are able to identify two different unoccupied bands in the system: The Ti $3d^*$ conduction band, which has been observed before in an IPE experiment. Comparison to band structure calculations as available from literature and corresponding measurements of our reference system $1T\text{-TiTe}_2$, our spectroscopic data is well explained, if considering contributions from the unoccupied electronic states. An additional non-dispersive band, which we assign to the excitation of excess Ti atoms within the van der Waals gap of the crystal, is observed, too. In a theoretical study by Pehlke and Schattke [69], this band was predicted before. To our best knowledge, this work provides the first experimental proof for the existence of this excess Ti band. Especially AR-2PPE proved to be a very valuable method for gaining

detailed insights into the electronic structure of such systems.

The time resolved 2PPE data, acquired using a *conventional* TR-2PPE setup, are presented in section 4.2. They give insight into the coupling efficiency of the Ti excess state to the electronic environment. In comparison to the interlayer Ti $3d^*$ band we observe an increase in the population lifetime of the excess Ti state by more than a factor of two, up to a value of $T_1 = (7.1 \pm 3.3)$ fs. This difference is attributed to the reduction in the coupling of the excess Ti state to the electronic band structure of the TiSe₂ layers. Our results particularly show that besides surface-localized unoccupied states also bulk-embedded states can exhibit an efficient decoupling from the residual decay channels. Therefore, these experiments enabled us to draw important conclusions about the origin of the localized unoccupied band we assigned to excess Ti atoms in the van der Waals gap. We would like to emphasize, that the spectroscopy and the conventional time-resolved experiments presented in this chapter all served the understanding of the actual electronic structure of our samples.

5 Static Response of 1*T*-TiSe₂ to Thermal and Laser Excitation

So far, our investigation focused on a detailed understanding of the electronic structure of two transition metal dichalcogenides (TMDCs)—1*T*-TiSe₂ and 1*T*-TiTe₂—mapped by two-photon photoemission (2PPE) spectroscopy at the photon energies relevant for this work. This detailed investigation was necessary, because only little 2PPE data is available for TiSe₂.

The application of 2PPE, however, implies the usage of higher photon fluences, as multi photon processes are significantly less likely to appear than photoexcitation by only one photon. It is therefore necessary to investigate the reaction of the system to such high fluences, especially considering, amongst others, the electronic system of 1*T*-TiSe₂ which is strongly influenced by correlation effects (see section 2.2). Furthermore, the two-dimensional (2D) character of the layered TMDCs may hinder the dissipation of the energy deposited by the laser pulses. This could lead to an enhancement in laser induced heat-up of the sample. A closer look into the thermally induced spectral modifications is thus very instructive to discriminate laser induced effects and sample heat-up. We therefore begin with a thorough analysis of thermal and laser induced modifications.

Additionally, a detailed understanding of the fluence dependence is vital with respect to our time resolved experiments presented in chapter 6. If not stated differently, all spectra presented in this chapter are therefore acquired using the p-polarized second harmonic (SH) emission of laser $\mathfrak{3}_{\text{TR}}$ at a photon energy of $h\nu = 3.18$ eV. The laser optimization for short pulses leads to spectral broadening degrading the energetic resolution of the photoemission spectra to typically $\Delta E \lesssim 108$ meV (theoretical value, see section 3.2). Yet, it is still sufficient for a quantitative analysis of the data and the inferior energy resolution is acceptable considering the direct comparability to the time resolved data which is an important result of this chapter. Also, direct comparison to higher resolution data of our reference system 1*T*-TiTe₂ compensates for these shortcomings to a certain degree.

This chapter is structured as follows:

- First, we investigate the temperature dependence of the 2PPE spectrum of TiSe₂ and identify the occurring changes, especially focusing on the suppression of the spectral intensity of the Se 4*p* bands, which is also observed in our time resolved investigations. The chalcogen *p* bands react strongly to perturbations of the charge density wave (CDW)—or rather the fluctuations thereof at room temperature [3, 7, 8, 38]. This section aims at separating such laser induced perturbations

from thermal effects by providing a detailed understanding of the pure thermal modifications. In this context comparison to the reference system 1T-TiTe₂ proves to be very valuable, because:

- TiTe₂ does not feature any phase transition to a CDW state.
- The band structures of the titanium based TMDCs, TiS₂, TiSe₂, and TiTe₂, are very similar, exhibiting differences mainly in the vicinity of the Fermi energy. The degree to which the chalcogen p bands cut the Fermi level varies [68]. For TiTe₂ the chalcogen bands of p_x , p_y character are energetically well separated from the p_z bands which enables the study of contributions to the thermal behavior from bands of strong and weak 2D character.
- Finally, these data are acquired with a better energetic resolution of the photoelectron analyzer which is, as we will see, unfavorable in case of the CDW dominated TiSe₂.

The quantitative analysis of the temperature dependence of prominent spectral features yields a scale for the (relative) sample temperature at the laser spot position which is very useful to quantify laser induced heat-up.

- The second part of this chapter presents a detailed look into laser induced changes. For TiSe₂ we observe a loss of spectral weight of the Se 4*p* bands. Comparison to the data on the temperature dependence enables us to distinguish heat-up and additional laser induced effects. We find, beside the thermal signatures, an additional signal by a non-equilibrium distribution of electrons and modifications of the transfer of spectral weight of the Se 4*p* bands. The absence of a CDW transition for the TiTe₂ reference system allows for additional insights into contributions which originate from the correlation of the electronic system of TiSe₂. This section is completed by angle-resolved two-photon photoemission (AR-2PPE) data which help identifying the range of energy and momentum relevant for the observed intensity suppression. These data confirm, that the loss of intensity is not due to an energetic shift of the Se 4*p* bands and a real intensity reduction localized at these bands is indeed observed. These findings are important for the discussion of the mechanism of the low temperature CDW phase transition of TiSe₂, especially considering the work of Cercellier et al. [11].
- Finally, we complement these data by analogous fluence dependent experiments within the low temperature CDW phase of 1T-TiSe₂. We present spectra for temperatures below room temperature which show modifications induced by the phase transition (see section 3.3) at the $\bar{\Gamma}$ -point. Afterward, we present indications for a laser induced partial transition from the CDW to the normal conducting phase (see section 6.2.3 for corresponding time resolved data).

5.1 Spectroscopy Within the Normal Phase

With respect to the data analysis presented in this chapter we are primarily tasked with a detailed understanding of laser induced spectral modifications. The absorbed energy of the laser pulses ultimately dissipates via excitation of the lattice, i. e. by a laser induced heat-up of the samples. The first step of our investigation is thus the general discussion of thermal effects by performing a series of 2PPE experiments at room temperature and above (low temperature data is presented in section 5.3).

To discriminate laser and thermally induced modifications a very low absorbed fluence per pulse, F_{pp} , of only about $5.3 \mu\text{J cm}^{-2}$ is applied when investigating TiSe_2 . This value is experimentally motivated (see section 5.2) and ensures that laser induced spectral modifications are insignificant. For details on the chosen fluence refer to the spectroscopic investigation in section 3.2.1–c.

The TiTe_2 reference data presented in this section, however, are acquired using a higher absorbed fluence. Following our findings on the count rate stabilization in photoemission experiments with the cylindrical sector analyzer (CSA) (see appendix A.3) in this case we initially increase the absorbed laser fluence to about $49 \mu\text{J cm}^{-2}$ and then perform the experiments at a fluence of $F_{\text{pp}} \approx 24.5 \mu\text{J cm}^{-2}$. Although the higher fluence leads to an offset of the temperature scale with respect to TiSe_2 because of the laser induced heating (see section 5.2), we derive a better quality of the spectral data, as the significantly enhanced photoelectron count rate allows for a higher energy resolution mode of the CSA. The loss of absolute comparability to the TiSe_2 data is acceptable, because the fluence is not varied during the experiment and the relative thermal behavior still remains observable.

By complementing the TiSe_2 data with reference measurements of TiTe_2 we enhance the informative value of our investigation, because (i) strong correlation effects are absent for TiTe_2 and thus their influence on the behavior of TiSe_2 may manifest in a direct comparison, i. e. the presence of modifications for both systems strongly hints at a pure thermal effect, and (ii) the sub-bands forming the spectral feature assigned to chalcogen p bands are well separated in case of the Te $5p$ bands. By using an enhanced spectral resolution we can thus study contributions from bands with strong (p_x, p_y) and weak (p_z) 2D character to the thermal modifications. Furthermore, by using a very low absorbed laser fluence for acquisition of the 1 T - TiSe_2 data we can effectively suppress laser induced effects (see section 5.2) and thus focus on thermal modifications, while using the TiTe_2 spectra to gain qualitative insights into spectral features only accessible with a higher energetic resolution—the details of the electronic structure near E_F also help. Table 3.4 in section 3.2 summarizes theoretical values of the energetic resolution. The analyzer setting used for TiTe_2 supports $\Delta E \approx 51 \text{ meV}$ by specifications, however, such high resolution is not easily accessed experimentally. By evaluating the secondary electron cutoff of the spectra acquired at room temperature using a 90–10-criterion (see section 3.2) we find $\Delta E_{\text{TiSe}_2} \approx 90 \text{ meV}$ and $\Delta E_{\text{TiTe}_2} \approx 66 \text{ meV}$, which corresponds to total energy resolutions

of 103 meV and 83 meV, respectively, using a laser bandwidth of 50 meV¹ [see table 3.3, page 42]. The broadening of the spectral structures of the TiSe₂ spectra induced by the resolution of the system (laser and analyzer) is thus reduced by about 19% for TiTe₂, i. e. the spectral resolution of the latter data is indeed significantly enhanced.

The sample temperature is increased using resistive heating at the backside of the sample holder. Limitations of the experimental setup lead to modifications of the bias voltage applied to the sample while the heating power supply is connected which shows as a shift of the kinetic energies of the photoelectrons. Therefore, the power supply is disconnected during acquisition of the spectra. Temperatures given in this chapter are averaged for the slowly cooling sample. This defines an uncertainty of the temperature of about ± 6 K [typical range observed ± 2 K to ± 13 K] which is rather independent on the mean temperature of the sample. Please note, that the temperature sensor is not attached directly to the sample surface, but to the base of the sample holder. Thus, a systematic offset of the actual sample temperature is to be expected; we are concerned with relative changes in this chapter and usually do not rely on the more uncertain absolute temperatures.

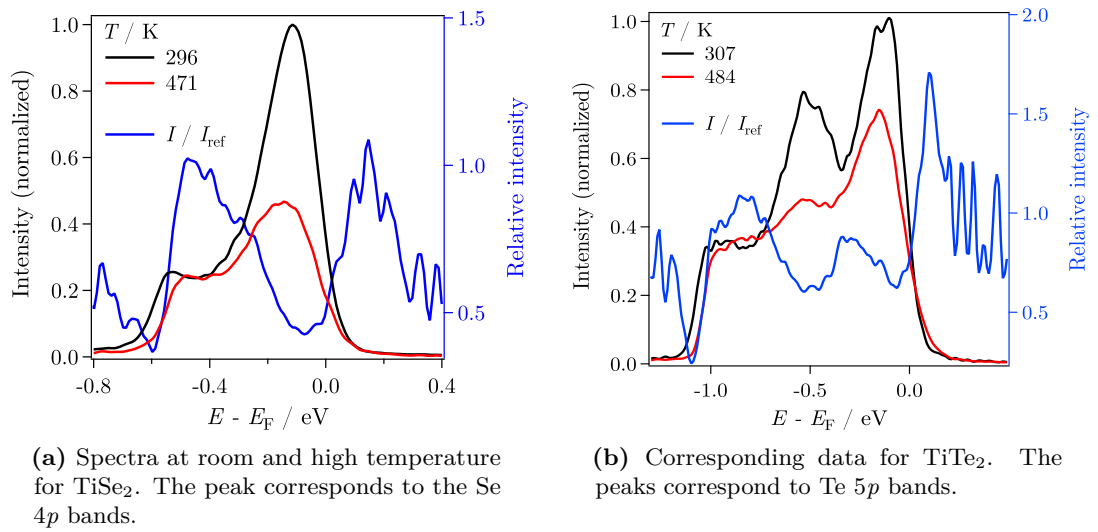


Figure 5.1: The reference spectrum acquired at room temperature (black, I_{ref}) and a spectrum corresponding to the highest temperature investigated (red, I) are normalized to the plateau level. The relative intensity $\frac{I}{I_{\text{ref}}}$ (blue) emphasizes the the strongest changes. Spectra for TiSe₂ (a) and TiTe₂ (b) are shown.

¹Please note, that the bandwidth of the SH emission is estimated from the bandwidth of the fundamental, which is about 54 meV. The latter defines an upper limit for the frequency doubled emission. ΔE_{tot} may thus increase by about 2 meV, if this extremal value is assumed.

Let us take a first glance at a 2D representation of the relative modifications observed in the spectra. Such data is very intuitive for a qualitative understanding of the thermal effects. Before we focus on the 2D mappings presented in figure 5.2 we give a short introduction to their construction. Figure 5.1 shows data acquired for TiSe₂ and TiTe₂ at room temperature (TiSe₂: 296 K, normal emission; TiTe₂: 307 K, 10° emission angle²) as black curve and an exemplary high temperature of about 475 K in red. The presented data is smoothed (binomial smoothing) and normalized to the *plateau level* [TiSe₂: (-0.46 ± 0.04) eV, TiTe₂: (-0.90 ± 0.07) eV]—this normalization procedure will be motivated and discussed in section 5.1.2. In this representation we already observe strong thermal effects, the most prominent being a strong reduction of the amplitude of the Se 4*p* and Te 5*p* bands, respectively, and an increase of the work function.

To visualize these modifications the spectral intensity, I , at high temperature (red) is normalized to the room temperature data, I_{ref} , (black), i. e. we calculate a relative spectrum (blue), $\frac{I}{I_{\text{ref}}}$, which shows the relative intensity changes upon heating.

Such relative spectra are generated for different temperatures—a subset of these data is presented in figures 5.2(b) and (d)—which enables us to visualize the thermal modifications in a 2D energy–temperature map. Please note, that the data provided in figure 5.2 is given relative to the room temperature spectrum. We use a very simple interpolation procedure which repeats each relative spectrum up to half-way to the adjacent spectrum, i. e. the thermal resolution is not artificially enhanced. Figures 5.2(a) and (c) show such 2D maps. Intensities are color coded: white representing virtually unchanged regions (thus the white stripe at room temperature), red/yellow indicates an increase and blue/black emphasize a reduction of intensity.

In these relative intensity maps we directly observe the shift of the low energy cutoff of the spectra corresponding to the work function increase as an increasingly broadened blue/black strip at $E - E_{\text{F}} \approx -0.6$ eV and -1.1 eV, respectively. Furthermore, the suppression of the amplitude of Se 4*p* and Te 5*p* bands is also directly visible (TiSe₂: about -0.1 eV, TiTe₂: about -0.1 eV and -0.45 eV). We see a continuous reduction of the *p* bands’ signal with temperature visualized by the increasing blue/black hues in this energetic range. Figures 5.2(b) and (d) show a selection of the spectra used for the 2D maps which allow for another interesting observation: for both systems, TiSe₂ and TiTe₂, the *p* bands amplitude drops continuously, yet, significantly stronger in case of the Se 4*p* bands which, as we will see in the discussion in section 5.1.4, is well explained by the reduced energetic separation of the TiSe₂ sub-bands.

Please note, that the ambiguous relative intensity observed for $E - E_{\text{F}} > 0$ is caused by numeric artifacts. The spectral intensity in this range is almost zero, thus, small deviations of the noise level of consecutive spectra leads to large relative changes—the noisy character of this signal is obvious considering the converse behavior for both samples, i. e. intensity increase for TiTe₂ and decrease for TiSe₂. However, in case of TiTe₂ we

²The reason for the difference in emission angle is discussed in section 5.1.1.

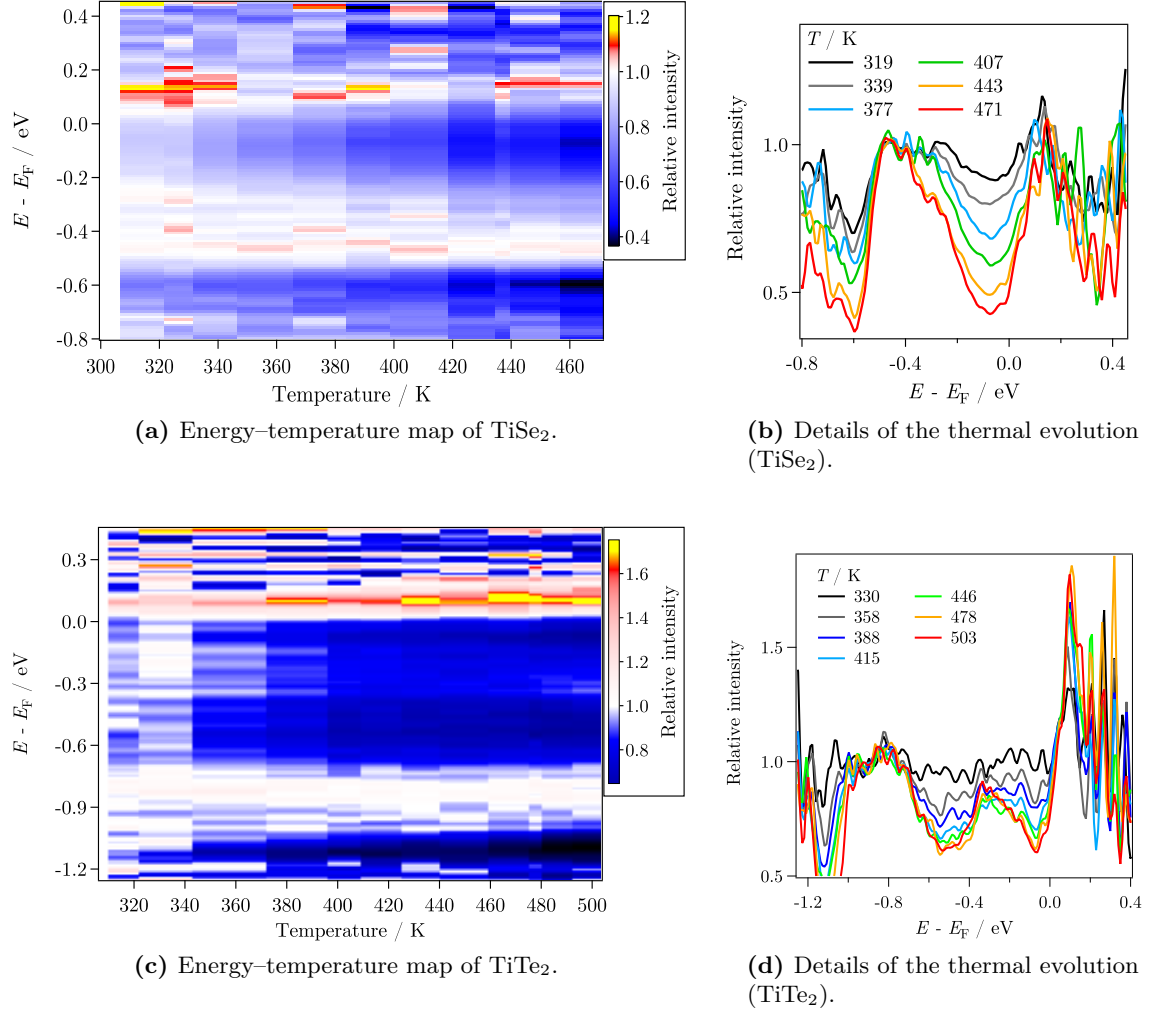


Figure 5.2: By normalization to a reference spectrum at room temperature and using interpolation, a 2D energy–temperature map is generated. Blue hues represent a reduction of intensity, reds and yellows show increases for increased temperature. (a) shows such data for TiSe₂, (c) features the corresponding data for TiTe₂. (b) and (d) show the corresponding data used for the generation of the 2D maps.

actually observe a slight increase of intensity just above the Fermi energy in the energy–temperature map ($E - E_F \approx 0.1$ eV) which is not present for TiSe_2 . The difference is even better visible when comparing figures 5.1(a) and (b)—the high temperature spectrum crosses the room temperature curve exhibiting increased intensity in named energy range in case of TiTe_2 only. In section 5.1.4–c we will see that this is not a systematic difference of these two TMDCs, but rather a consequence of the higher energetic resolution in case of the TiTe_2 data: the thermal broadening of the Fermi edge becomes visible (see discussion in section 5.1.4).³

In summary, we observe two prominent thermal modifications of the SH-2PPE spectra: (i) a reduction of the chalcogen p bands’ amplitude, and (ii) an increase of the work function. We will now discuss the temperature effects in detail, beginning with a short overview followed by subsequent discussions focusing on the different features.

5.1.1 Detailed Overview of the Thermal Modifications

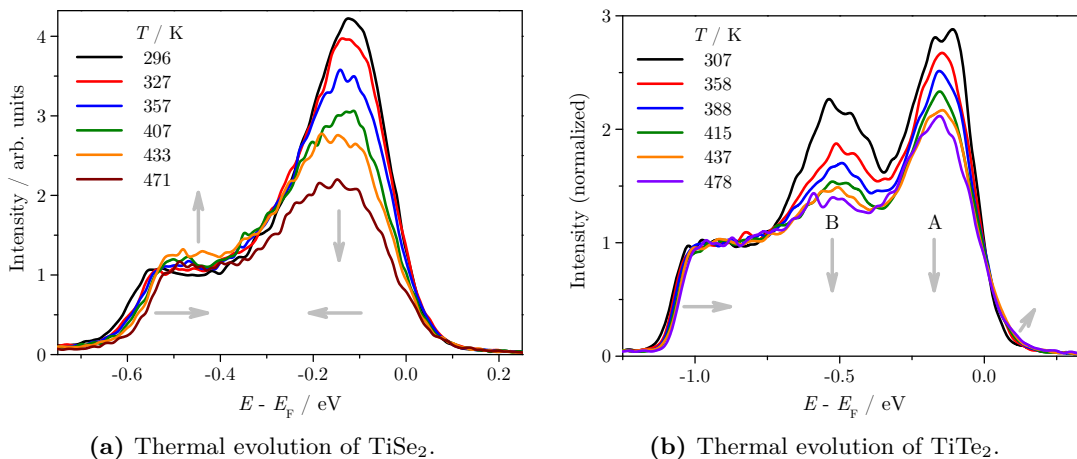


Figure 5.3: SH-2PPE spectra acquired with p-polarized photons of $h\nu = 3.18$ eV (laser 3_{TR}) at absorbed fluences of $F_{\text{pp}} \approx 5.3 \mu\text{J cm}^{-2}$ (TiSe_2) and $24.5 \mu\text{J cm}^{-2}$ (TiTe_2) for different temperatures. Arrows emphasize the spectral modifications. The data presented in (b) is normalized to the plateau level and acquired for off-normal emission. A and B mark the two sub-band contributions.

³The discussion in section 5.1.4–c focuses on the apparent increase of intensity just above E_F induced by thermal broadening. This is by itself no interesting effect, however, we quantify this behavior for comparison to the fluence dependent experiments presented in section 5.2 (refer to figure 5.27) which show a systematic enhancement of intensity in this energetic range not attributed to simple heating and significantly stronger even using the inferior energy resolution of the TiSe_2 data than in case of the TiTe_2 data presented here.

Figure 5.3 shows SH-2PPE data acquired at different temperatures for 1T-TiSe₂ and 1T-TiTe₂. Before we discuss the spectral modifications (arrows). We like to point out two experimental differences in the acquisition of these data sets:

First, the TiTe₂ spectra presented in figure 5.3(b) are acquired for off-normal photoemission (emission angle with respect to surface normal: 10°)—in contrast to the TiSe₂ data. We discuss this for the AR-2PPE spectroscopy in section 5.1.1-a. The off-normal emission leads to a separation of the Te 5*p_x*, 5*p_y* and the Te 5*p_z* bands in the spectra and establishes the resonant excitation of an unoccupied Ti 3*d* band from the Te 5*p_z* band (peak B).

The band structure of 1T-TiTe₂ is very similar to that of 1T-TiSe₂. Corresponding to the Se 4*p* bands of TiSe₂ this system shows a set of Te 5*p* bands in the vicinity of E_F , as well as Ti 3*d* contributions. The TiTe₂ spectra are very useful for the interpretation of our TiSe₂ data in section 5.1.4, because the Te 5*p_x*, 5*p_y* (peak A) and the Te 5*p_z* (peak B) contributions are energetically well separated even at the Γ -point. However, we cannot investigate TiTe₂ at the Brillouin zone center, because the chalcogen *p_x*, *p_y* bands cut E_F there, rendering them unoccupied for normal emission [79, 91, 213, 214].

Second, the TiSe₂ data discussed here was acquired with great care concerning the stability of the incident laser power. We monitored a reflex of the laser beam for in-situ estimation of the actual fluence.⁴ This enables us to directly compare the absolute count rate values without the necessity of any intensity normalization. We use this data set to derive valuable information on the temperature dependence of the mean intensity of the plateau level (see section 5.1) which enables us to quantify the influence of normalization to this level on the temperature coefficients of the intensity derived spectral features (see sections 5.1.2 and 5.1.4). This is necessary as we need a means of normalization to compensate for small drifts of the laser fluence. We like to stress, that while our in-situ power monitoring is sufficient to evaluate the stability, the alignment requires a level of accuracy not provided by the setup.

The spectra presented in figure 5.3(a) feature spectral intensities that are directly comparable which shows, that we achieve very stable fluences at the position of the sample using this method. Especially the plateau level changes only slightly and, as we will see in section 5.1.2, in a linear manner. Please note, that the deviation observed for the spectrum at 433 K is caused by a small increase of the laser fluence by about 0.24 $\mu\text{J cm}^{-2}$ resulting from a power outage; such data is, however, useful to qualitatively assess the applicability of plateau normalization for compensation of power fluctuations in section 5.1.2. Please note, that the fluence increase is nearly compensated using the reflected intensity, as demonstrated by the spectrum at 471 K. However, the TiTe₂ data is significantly influenced by drifts of the incident laser fluence and normalization to the

⁴We use a reflex of the second gray filter right in front of the ultrahigh vacuum (UHV) chamber, therefore a constant reflected power also indicates stability of the horizontal pointing along the gradient of the filter.

plateau intensity is necessary in this case (see section 5.1.2–b).

We need to keep the systematic differences of TiSe₂ and TiTe₂ data in mind for the discussion of our findings, although no fundamental modification of the thermal behavior is observed. Before we start our detailed analysis of the data we want to emphasize the regions of interest in figure 5.3 (gray arrows). Upon increasing the sample temperature, we find three prominent spectral modifications:

- the amplitude of the chalcogen p bands decreases significantly already for rather small temperatures,
- simultaneously, their binding energy increases slightly, and
- the work function increases considerably.

Additionally, we will discuss the following modifications:

- the plateau level increases slightly—comparably small with respect to the chalcogen p bands intensity—, and
- the thermal broadening of the Fermi edge leads to a small increase of spectral intensity just above E_F ,

which are interesting as references. The plateau level will be used for normalization for compensation of laser drifts, i. e. the TiSe₂ data enable an estimation of the deviations introduced by normalization; it is not used for temperature estimation (see discussion in section 5.1.2). The broadening of the Fermi edge is only visible for TiTe₂, as we are using a better energy resolution in this case (see section 5.1.4–c). Especially in comparison to data on the absorbed laser fluence dependence of the spectra presented in section 5.2 this data is very interesting.

Before we begin our detailed analysis of these data, we will check, whether the thermally induced spectral modifications are reversible. Figure 5.4 shows spectra acquired during the cool-down of TiSe₂ after the maximum temperature was reached. It includes the initial room temperature curve (black) and the final heating stage (dark red) corresponding to the data presented in figure 5.3(a). The red curve ($T = 307$ K) is taken after the slow cooling of the sample. We did not apply active cooling using liquid nitrogen, thus the sample reaches almost room temperature within about an hour, however, the cooling is increasingly slower at low temperatures, i. e. a small offset to slightly higher temperatures cannot be eliminated within reasonable time. On the other hand, the slow passive cool-down ensures thermal equilibrium of sample and temperature sensor, enhancing the comparability of the acquired temperatures. The cooling of the sample may be sped up using active cooling with liquid nitrogen, however, reaching equilibrium with the room temperature—the initial sample temperature—is still the most time consuming task. Therefore, the final spectrum features a slight temperature offset with respect to the initial one.

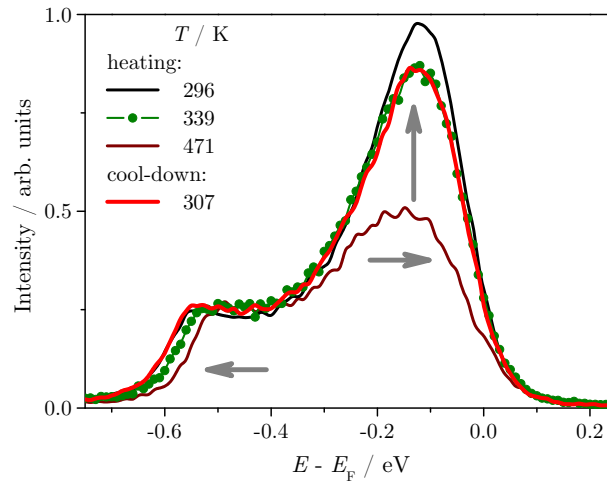


Figure 5.4: The thermal spectral modifications are reversible upon cool-down to room temperature.

After the heating of the sample and subsequent cool-down its temperature does not reach the initial room temperature value which is manifested by the comparison shown in figure 5.4 where the overall spectral shape agrees best with data acquired at $T = 339$ K during the heating experiment (red and green). Considering the spatial separation of thermal sensor and sample it is not surprising, that both are not at the same temperature and that the thermal equilibrium during heat-up and cool-down may differ, i. e. the relative temperature of sample and sensor can be different for both cases. Considering that we are only interested in the relative changes with temperature the incomparability of data acquired during cooling on an absolute temperature scale is acceptable. Nevertheless, comparison of the spectral shape proves to be a valid means of assigning a common temperature scale. However, one deviation remains: the work function seems to be lowered by about 15 meV after cool-down. We find adsorption of residual gas during the slow cooling phase to be the most likely explanation for the change of work function. Spatial instability of the surface area probed by the laser can be ruled out, because our findings in appendix A.1.2 clearly show, that the otherwise almost perfect reproduction of the overall spectral shape contradict a significant shift of the work function—indeed, these data may actually be considered a strong indication for good spatial stability.

In summary, we conclude that the observed thermal effects are reversible (see gray arrows). In the following sections we present a detailed analysis of these modifications. The prerequisites and methods of data evaluation are described in appendix A.1.1. Here, we focus on the actual interpretation of the data as well as the implications for a temperature estimation in the context of fluence dependent and time resolved pump-probe experiments.

To allow for direct comparability of such data, the same temperature (290 K to 491 K) versus intensity (76 % with respect to the room temperature value) or energy (75 meV), respectively, ranges are used. The scales may be shifted, but span the same ranges if not noted otherwise. Room temperature is defined as $T_{\text{RT}} = 296 \text{ K}$ in this section. A linear fit is used for the normalization of the intensity data to the T_{RT} value and for the definition of zero energetic shift.

5.1.1–a Photoemission Spectroscopy of $1T\text{-TiTe}_2$ —Specific Differences to $1T\text{-TiSe}_2$

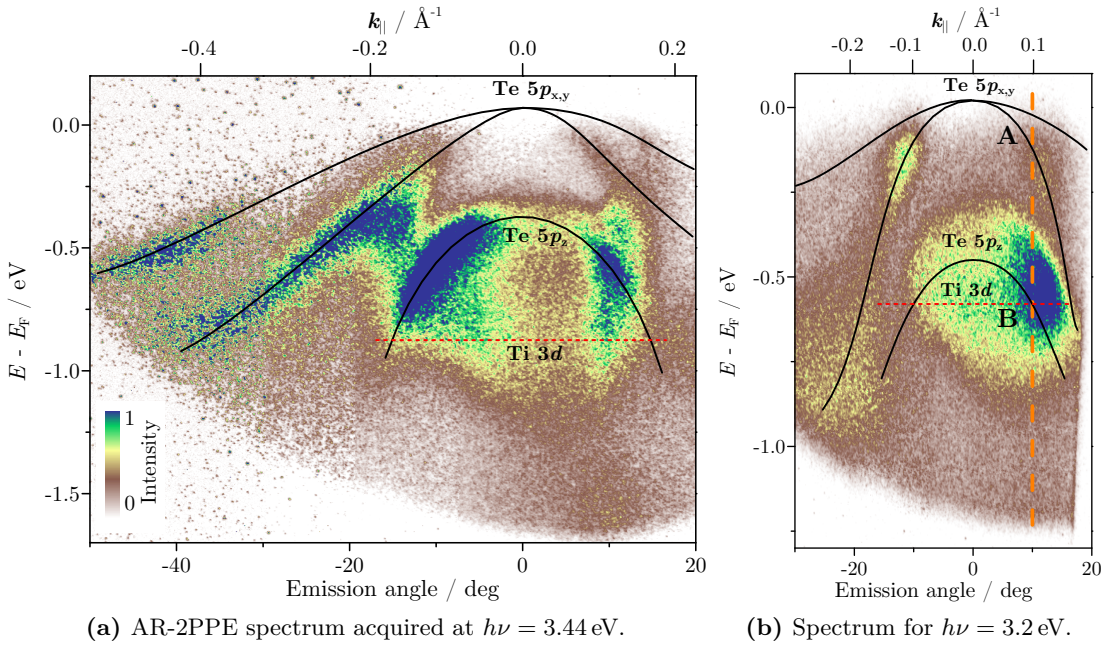


Figure 5.5: Composite AR-2PPE spectra generated by blending several spectra acquired for different emission angles (see figure 4.1, section 4.1 for details). Lines emphasize certain spectral features, like the occupied Te $5p$ bands (black) and the unoccupied Ti $3d$ band (red, dashed)—these lines are guides to the eye only. A vertical line (orange, dashed) shows the emission angle of 10° chosen for TiTe_2 spectra, the peaks observed in angle integrated spectra [see figure 5.3(b)] are marked “A” and “B”.

Figure 5.5 shows typical AR-2PPE spectra of $1T\text{-TiTe}_2$ acquired using laser 1 (see section 3.2). The spectra are taken for pristine samples, i. e. adsorption of a small amount of alkali metal atoms was not necessary, because the work function of TiTe_2 is lower than for TiSe_2 , being about $\Phi = 5.3 \text{ eV}$ in good agreement with literature [19, 214]. The spectra are acquired for the $\overline{\Gamma\text{M}}$ direction of the surface. All spectra are composed from

partial spectral taken at different angles of the sample surface with respect to analyzer and laser (see also figure 4.1 in section 4.1) which enables access to a wider range of emission angle. The partial spectra are shifted in angular direction and blended together which is the reason for the slight inconsistencies of spectral intensity and noise level in the figure.

The spectrum shown in figure 5.5(a) is acquired using the SH emission of laser 1 at a photon energy of $h\nu = 3.44$ eV. We identify the occupied Te $5p_x$, $5p_y$ and the Te $5p_z$ bands which feature hole-like dispersion. Black lines emphasize these spectral structures—note, however, that all lines are only a guide to the eye. Additionally, we identify an unoccupied contribution from a Ti $3d$ derived band which shows only little dispersion parallel to the surface (red, dashed). In contrast to our very detailed investigation of the 2PPE spectrum of 1T-TiSe₂ presented in chapter 4, the interpretation of the corresponding TiTe₂ data is straightforward. All spectral structures are well explained considering earlier band structure calculations and one-photon photoemission (1PPE) spectroscopic experiments [71, 73, 79, 213, 214]. Therefore, we do not interpret the the TiTe₂ spectra here, but rather refer to the detailed analysis of these data in the diploma thesis of Hilgenfeldt [215]. Especially a careful variation of the photon energy (compare to figure 4.7, section 4.1) enabled the identification of the unoccupied Ti $3d$ band.

With respect to the TiSe₂ spectra we find an obvious difference in case of the prominent parabolas of the chalcogen p bands: The Te $5p_x$, $5p_y$ bands are clearly cut by the Fermi energy, i. e., in contrast to the corresponding Se $4p$ bands, they are unoccupied at the $\bar{\Gamma}$ -point. Please note, that the rather high binding energy of the Te $5p_z$ band is in accordance with its perpendicular dispersion. Our experiments are generally performed at a photon energy of 3.18 eV and it is therefore instructive to use a similar photon energy for the TiTe₂ reference data, too. Figure 5.5(b) shows such data. The unoccupied character of the Ti $3d$ band leads to a reduction of its separation from the Te $5p_z$ band (see also section 4.1) because of the difference in the energetic shift of occupied and unoccupied spectral features upon variation of the photon energy. This leads to a resonant excitation from the Te $5p_z$ via this Ti $3d$ as an intermediate state of the 2PPE process.

The orange, dashed vertical line in figure 5.5(b) marks the emission angle of 10° used for the acquisition of angle integrated 2PPE spectra as show, for instance, in figure 5.3(b). At this angle we are able to map the Te $5p_x$, $5p_y$ bands (peak “A”). Simultaneously, we find a second spectral peak (“B”) at a higher binding energy corresponding to the resonant excitation of a Ti $3d$ band from the Te $5p$ band. This situation is qualitatively very similar to the spectra observed for TiSe₂ at this photon energy as we discussed in detail in section 4. Therefore, a slight tilting of the TiTe₂ sample to off-normal photoemission at 10° establishes spectral conditions analogous to corresponding TiSe₂ data. The spectral features, especially the Te $5p_x$, $5p_y$ and the $5p_z$ bands are, however, energetically more separated, which enables a more detailed analysis of the spectral structures we mark peak A and B.

5.1.1–b General Remarks on the Structure of This Section

Our detailed discussion of the thermal modifications observed for the TMDCs investigated is split into three subsections, dealing with different aspects of the experiments and spectral characteristics:

- A very detailed discussion of the thermal behavior of the spectral plateau focuses on its application for normalization of the spectra. The temperature dependence intrinsic to the plateau will also be investigated, however, with respect to the influence thereof on the normalized data.
- The work function features a distinct dependence on temperature and is a valuable, easily estimable property which enables the assignment of a relative temperature scale.
- The most prominent spectral features, the chalcogen p bands, also exhibit the most articulate thermal modification. The extraction of the relevant properties—area, amplitude, binding energy and full width at half maximum (FWHM)—requires different numerical methods. Thermal broadening of the Fermi edge needs a closer inspection, too, because the p bands cut E_F .

This chapter provides a reference for thermally induced spectral modifications, necessary for the interpretation of fluence dependent (section 5.2) and time-resolved IR-pump SH-probe photoemission experiments (chapter 6) with respect to the definition of a relative temperature scale for the experiments. The work function and primarily the amplitude of the chalcogen p bands enable the assignment of an instantaneous sample temperature, i. e. the quantification of the laser induced heat-up of the crystal. Furthermore, a detailed understanding of thermally induced spectral modifications is necessary to discriminate laser induced contributions.

In this context, section 5.1.2 presents preliminary investigations. The temperature dependence of the plateau range is discussed and the findings of the corresponding section 5.1.2–d are valuable also for the investigation of the thermal modifications observed for the chalcogen p bands. However, with respect to the scope of this work—we aim at contributing to the discussion on the origin of the CDW phase of 1T-TiSe₂—the most relevant spectral signatures are the chalcogen p bands, especially considering the laser induced effects. The relevance of the plateau in the context of this work is its application for normalization of spectra which intensities are influenced by laser fluence drifts and/or instabilities of the CSA, i. e. the correction of external influences which do not alter the spectral shape. Its intrinsic temperature dependence, however, renders a very detailed investigation necessary, especially considering the data analysis, as intensity derived properties are modified by the normalization.

The reader may skip section 5.1.2 for the initial study of our findings, because the other sections refer thereto whenever appropriate. This section is relevant mostly considering

the potential of the plateau for normalization, i. e. in context of generating a consistent data set and less with respect to the physical properties of the TMDCs investigated here. The level of detail chosen here is justified by the importance of the impact of the procedure on virtually all data discussed in this work.

5.1.2 The Mean Plateau Intensity—Thermal Behavior and Applicability for Normalization

A detailed look at the TiTe₂ reference spectra in section 5.1.1 revealed a significant drift of the general spectral intensity, rendering direct comparison of absolute intensities futile. However, as figure 5.8 emphasizes, normalization to the plateau level provides a powerful means of correcting such drifts of the photoelectron count rate. Ideally, these intensity modifications are induced by instabilities of the absorbed laser fluence, in which case our simple normalization approach is sufficient to correct for them. We may disregard the influence of surface inhomogeneities (see appendix A.1.2), but, especially with respect to the thermal behavior of the other spectral signatures, a sample intrinsic temperature dependence of the electronic features contributing to the plateau level cannot be eliminated a priori. Although the absolute changes of the plateau level are insignificant in comparison to, e. g., the amplitude of the chalcogen *p* bands, they still feature an articulate relative modification. If the thermal changes of the plateau level are not induced solely by laser fluence drifts, if any actual sample intrinsic modification is superimposed, normalization tampers with all the other intensity derived spectral features in such a way that the respective temperature coefficients are in-/decreased by the corresponding coefficient of the plateau, i. e. instead of the value of the investigated feature a combination with the temperature dependence of the plateau level is observed. A close look at the plateau level is thus crucial before we focus on the more prominent spectral modifications.

We are basically facing two tasks in the quantitative analysis of the spectral data: the evaluation of energies and intensities (see appendix A.1.1). In contrast to the energetic features like, for example, the work function or the binding energy of the chalcogen *p* bands, spectral signatures derived from intensities like, e. g., the amplitude and area of the chalcogen *p* bands, are delicately influenced by fluctuations of the absorbed laser fluence. We see in section 5.2 that the spectral intensity is even quadratically depending on the fluence for 2PPE processes, thus small deviations in the fluence may lead to significant intensity changes. In this section we will discuss the applicability of the plateau level for compensation of such instabilities.

In the first part of this section we evaluate the thermal behavior of the plateau level of the spectrum with respect to the influence of the secondary electron background of the spectrum. The second part analyzes the fitness of this spectral signature as a means of normalization—our focus being the utilization of this feature for correction of slight drifts of the incident laser fluence. In this context we use data acquired under very stable

conditions concerning the laser fluence (TiSe_2) which allow us to observe the changes of the plateau dominated by real thermal effects, while the TiTe_2 experiment is dominated by fluence drifts and therefore serves as a benchmark for the normalization procedure. An estimation of the magnitude of the modification introduced by normalization to the plateau will be given.

Analysis of the thermal behavior of the mean plateau intensity is necessary for understanding its applicability for normalization. The temperature dependent 2PPE spectroscopy data is analyzed using the methods described in appendix A.1.1. A set of mean plateau intensities for $1T$ - TiSe_2 (filled triangles) and $1T$ - TiTe_2 (open triangles) is presented in figure 5.6 for averaged energetic ranges of $E - E_F = -0.50 \text{ eV}$ to -0.42 eV and -0.97 eV to -0.83 eV , respectively.

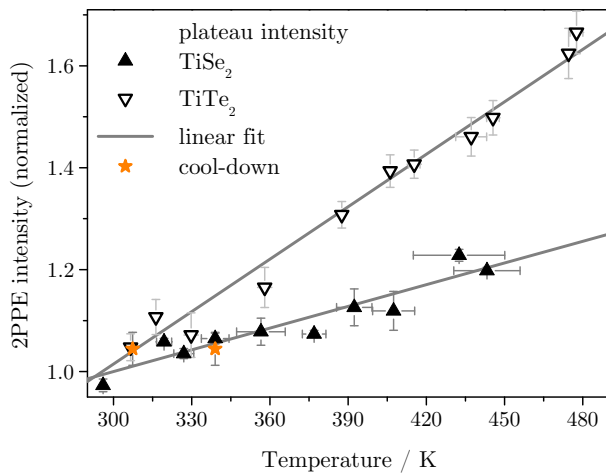


Figure 5.6: The mean intensity of the plateau range of TiSe_2 (full triangle) and TiTe_2 (open triangle) shows a linear increase with temperature. The line is a linear fit. Corresponding data acquired after cool-down is included for TiSe_2 at the measured and at a more likely (see figure 5.4) temperature as stars.

For both sample systems the increase of the plateau intensity with temperature agrees well with a line fit (gray line). For TiSe_2 we observe an increase by about 20 % of the mean plateau intensity in the temperature range investigated here. Interestingly, the slope of the TiTe_2 data fit is steeper by a factor of 2.4 in comparison to TiSe_2 . We show shortly, that this deviation is explained by a laser fluence increase. The temperature coefficient (see appendix A.2.1) of the TiSe_2 plateau level, I_{PL} , referenced to the room temperature value is $\Delta \tilde{I}_{\text{PL, RT}} = (14.2 \pm 1.7) \times 10^{-4} \text{ K}^{-1}$ which is of the order of magnitude of the amplitude of the Se $4p$ bands [see table 5.5 in section 5.1.4], although the opposite sign and a value smaller by a factor of 2.5 are observed.

Please note, that the absolute intensity of the plateau does not react strongly on temperature variations [see figure 5.3(a)] especially considering the strong reduction of the Se 4*p* amplitude. Naturally, the plateau presents itself as a possible means of compensation of laser fluence fluctuations. The photoemission intensity depends on the absorbed fluence; changes thereof modify the general spectral intensity, i. e. if the actual momentary fluence is known, the data can be normalized by multiplication with a single factor. We apply this method successfully to our fluence dependent investigation in section 5.2. Here, however, we do not deliberately change the laser fluence, but rather focus on stable conditions. Subtle fluctuations of the laser fluence and/or small in-/decreases over hours cannot be unambiguously detected by the thermopile power meter used, because of unavoidable thermal drifts.

Although the plateau level dependence on temperature seems rather insignificant considering absolute intensities, the relative change is huge and obviously affects the spectral intensity as a whole if used for normalization. This is important, because we discuss only relative modifications for the intensities to circumvent variations or spreading between the samples.

A careful discussion of possible physical reasons for the dependence of the plateau level on temperature enables us to distinguish contributions from laser instabilities and system intrinsic thermal modifications. If this effect is not entirely induced by fluence fluctuations, normalization to the plateau level indeed modifies the temperature coefficients of all other intensity derived spectral characteristics (see appendix A.2.1). Nevertheless, the contribution of the laser fluctuations often dominates (see discussion of figure 5.8) and can be compensated by such a normalization. This is especially necessary for the very time consuming time resolved experiments for which such drifts are not avoidable. We will estimate the magnitude of deviation induced by normalization. Please note, that by normalizing all data we still preserve comparability which puts these trade-offs into perspective.

5.1.2–a Inhomogeneities of the Sample Surface and Spatial Drifts of the Laser

The TMDC sample surfaces are generally not very homogeneous which is not surprising considering their preparation by cleaving (see section 3.3). Therefore, a spatial shift of the surface area probed by photoemission induced by, for example, a movement of the UHV system or a change in pointing of the incident laser can lead to significant changes of the spectral shape. The homogeneity of the probed area is always checked prior to the experiments. Furthermore, thermal expansion of the crystals as well as the mounting assembly might lead to such shifts.

In addendum A.1.2 we present a detailed estimation of the homogeneous area especially with respect to thermal expansion (appendix A.1.2–a) for the TiSe₂ sample discussed in this section. Please note, that the reproducibility of the spectral shape after cool-

down (see section 5.1.1) shows that no significant changes of laser pointing are observed. Furthermore, our investigation in named appendix revealed, that thermal expansion does not lead to a crossing of the boundaries of the homogeneous area.

Although we cannot rule out some contribution of surface inhomogeneities to the increase of the plateau level. However, the magnitude of the effects observed upon heating is much too significant to allow an explanation in terms of such drifts only, especially for the work function and the amplitude of the Se 4*p* bands (see appendix A.1.2–a). We therefore conclude, that any contribution of inhomogeneities in these investigations is only minor.

5.1.2–b Compensation of Fluctuations of the Laser Fluence—Finding a Spectral Characteristic for Normalization

Small fluctuations of the absorbed laser fluence are one of those extrinsic effects which can easily be compensated by normalization, because they do not alter the spectral shape. Larger fluence variations lead to changes of the spectral shape as discussed in section 5.2. In this section we investigate how such drifts manifest in photoemission spectra and how they may be compensated. Note, that careful monitoring of the laser power as applied for the TiSe₂ data discussed here is not feasible for all experiments, especially in time resolved mode (see section 5.1.1), however, generally the laser power is rather stable (see section 5.1.2–c) and only small drifts are to be anticipated. We like to point out, that the main extrinsic modification is an instability of the analyzer used which is investigated in section 5.1.2–c. The detection of small drifts of the laser fluence using a thermopile power meter is very difficult, because of its sensitivity, resolution and susceptibility to changes of, for instance, room temperature and air movement. Stable and comparable laser powers cannot be guaranteed for very small differences.

The spectral intensity on the other hand is highly sensitive to variations of the absorbed laser fluence, more so for the 2PPE process employed here. The non-linearity of 2PPE leads to a quadratic dependence of the spectral intensity on the absorbed laser fluence. This sensitivity can be used to compensate the fluence induced intensity changes by simply multiplying all intensities of a spectrum by one factor—the square of the fluence ratio—which is successfully practiced in section 5.2 to generate comparable data acquired at different fluences. Nevertheless, we cannot apply this approach here, because we anticipate only small fluence variations which cannot be assessed with the necessary accuracy using the thermopile power meter.

To compensate the extrinsic intensity modification we therefore need a measure for its change; normalization to the intensity of a thermally stable part of the spectrum is the simplest possibility. Typical 2PPE spectra of TiSe₂ are presented in figure 5.7. We labeled four candidates for such a measure as *i–iv*. The Se 4*p* bands cannot be used for normalization, because they feature the most prominent thermal modification observed (see section 5.1.4–a). The Fermi edge is also unusable as it thermally broadens.

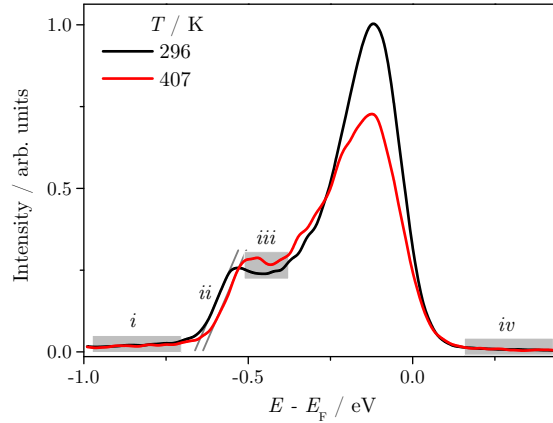


Figure 5.7: Typical 2PPE spectra of TiSe₂ acquired at two different temperatures. Possible characteristics for normalization are marked by boxes or lines and labeled i – iv .

The energy range labeled i (gray box) is actually below the secondary electron cutoff, i. e. the signal in this range is not directly linked to photoemission, but most likely to effects intrinsic to the energy analyzer, like, e. g., characteristics of the electronics or stray reflexes of the laser beam directly into the analyzer. Normalization thereto indeed does not yield consistent data. Region iv may be a suitable choice for normalization as higher order photoemission yields a small signal actually strongly dependent on the incident laser fluence. However, this is not a good choice, too, for three reasons: first, the signal right above E_F actually exhibits a strong fluence dependence induced by the creation of a non-thermal electron distribution (see section 5.2) which renders it useless in most of our experiments, second, thermal broadening of the Fermi edge does not allow to use the significant intensities right above E_F even at sufficiently low fluence, and finally, the intensities are generally very small in this energy range, rendering data normalized thereto prone to even the most subtle noise levels.

The only spectral range sufficiently featureless is iii . However, the energetic range we refer to as the *plateau* throughout this work is also flawed by its intrinsic temperature dependence (see section 5.1.2-d), but its thermal modification is much less pronounced than in case of the Se 4*p* bands. The slope of the low energy cutoff of the spectra, labeled ii , is also a good means of assessing an extrinsic intensity modification. In this case the slope at both temperatures agrees very well, confirming the comparability of the absolute intensities in this case. Although this slope is a good means to qualitatively estimate whether extrinsic effects are to be considered, quantitatively employing this property for normalization seems futile. Evaluation of these slopes is much less stable as a simple calculation of the mean plateau intensity. Additional noise may be introduced thereby. Furthermore, the slope is altered very subtle after normalization to the plateau in case of the TiSe₂ data, because the intensity is changed only slightly. For the small deviations

we usually have to deal with the slope is not a good means of compensation.

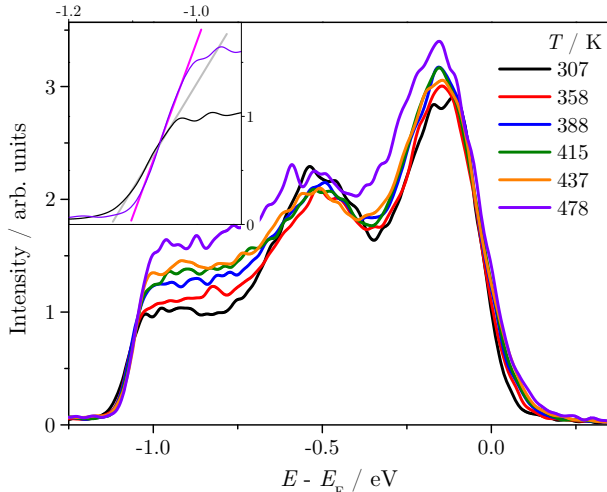


Figure 5.8: 2PPE data corresponding to figure 5.3(b) showing absolute intensity values, i. e. no normalization to the plateau level is applied. The inset emphasizes the necessity of normalization.

However, the characteristics *ii* and *iii* need to be considered simultaneously if normalization is applied. We will discuss this necessity using data acquired for 1 *T*-TiTe₂ which is presented in figure 5.8. The absolute spectral intensity at different temperature is presented. We observe a strong increase on spectral intensity, accompanied by a distinct change of slope of the secondary electron cutoff (inset). This proves, that the increase of the plateau level in this case is not entirely induced by its intrinsic temperature dependence, but extrinsic effects play a key role here—the TiSe₂ data discussed in section 5.1.2–c are much more stable as they show similar drifts only if the CSA is destabilized. Normalization to the plateau intensity actually compensates the increase and the slope of the cutoff; figure 5.3(b) on page 117 demonstrates this nicely. This is an indication, that we compensated a dominant extrinsic intensity modification. The good agreement of the slopes, however, also proves that although they clearly indicate an extrinsic modification, they cannot be used for compensation—the temperature dependence of the plateau is completely compensated after normalization and due to the small magnitude of this effect it cannot be deduced from the slopes (see section 5.1.2–d).

A higher absorbed laser fluence of $F_{pp} \approx 24.5 \mu\text{J cm}^{-2}$ is used in case of the TiTe₂ experiments. Considering our findings in appendix A.3 this should assure stability of the CSA system, because the instabilities discussed in section 5.1.2–c are generally observed at low fluences. The intensity variation of the plateau is, however, too big to be explained solely by fluence drifts. Monitoring during the experiments only supports an increase of laser power by about 1.6 % which supports about 3.2 % increase of spectral intensity.

Please note, that this value is a rather conservative estimation, because the SH emission was rather unstable. Realignment, usually not necessary, of the lithium triborate (LBO) and loss of the defined measurement position of the power meter are reasons which render the acquired laser powers uncertain. However, even if we take into account the temperature coefficient observed for the plateau of TiSe₂ (see section 5.1.2–e), for which an intensity increase of about 24 % for a temperature range of 171 K is estimated, laser fluence increase and temperature support only a plateau increase of about 28 %. The laser power is not very defined, but the observed strong increase of plateau intensity of about 59 % for temperatures up to 478 K would suggest an increase of the laser power by approximately 28 %.

We believe an instability of the photoelectron energy analyzer system, in this case a CSA, to contribute to the plateau intensity. The thermal dependence of the slope of the low energy cutoff of the spectra clearly shows, that additionally to the intrinsic thermal modification which does not change the slope, an extrinsic contribution is observed. These data emphasize, that drifts of the laser fluence are most likely small, even under non-optimal conditions. The instability of the CSA, however, cannot be controlled and may lead to big changes of the observed photoelectron count rates (see appendix A.3).

In conclusion, the spectral plateau is the only reliable spectral feature for normalization of the data. The TiTe₂ spectra show convincingly that even very significant intensity drifts can be compensated. To decide, whether the intrinsic temperature dependence of the plateau is observed or extrinsic contributions dominate, the slope of the secondary electron cutoff provides valuable insights, however, only qualitative information can be extracted thereby. Our investigation further shows, that the incident laser fluence is rather stable, however, an additional instability needs to be taken into account: drifts of the CSA which lead to long-term modifications of the photoelectron count rates. We will focus on the latter effect in section 5.1.2–c. Please note, that fluence drifts are actually compensated by plateau normalization due to their spectral shape conserving nature. However, a significant modification induced by instability of the laser power cannot be dismissed generally. The power meter is highly sensitive to external influences (e. g. temperature and drafts) and reacts strongly on alignment, i. e. the sensor is not homogeneous. At low fluences which are used for most experiments a small uncertainty of ± 1 mW corresponds to a ± 20 % variation of the actual laser power which modifies spectral intensity by a factor 1.44 for an increase. Please note, that laser fluence and analyzer instabilities modify the spectra similarly—discrimination of these effects is not necessary.

5.1.2–c Compensation of Instabilities of the CSA

Besides fluctuations of the absorbed laser fluence instabilities of the CSA system (see appendix A.3) are to be expected during an experimental run. Such effects are best studied for the 1T-TiSe₂ data presented in this section, because the stability of the

incident laser fluence was monitored very carefully which allows to rule out fluctuations thereof in this case. For low laser fluences, as used for the TiSe_2 experiment, drifts of the CSA are observed which lead to a long-term modification of the general spectral intensity. This is analogous to our findings in section 5.1.2–b on the effect of small variations of the laser fluence and suggests that normalization to the plateau level also compensates such drifts of the analyzer. In this section we demonstrate that plateau normalization allows for a compensation of CSA intrinsic instabilities of the spectral intensity at low photoelectron count rates similar to compensation of *reasonably small* variations of the absorbed laser fluence. For fluences small enough, variation of the fluence leads to destabilization of the CSA (see appendix A.3), i. e. the spectral intensity is significantly modified even after the initial fluence is applied again. We like to point out that even under ideal conditions, i. e. in the absence of any variations of the absorbed laser fluence, instabilities of the analyzer are still to be expected at low incident fluences—a suitable means of compensation is therefore crucial.

The CSA can be destabilized considerably by deliberately applying a significant change of the absorbed fluence. Laser induced modifications like heat-up of the sample induced by the absorbed pulse energy (see section 5.2) are expected at higher fluences. The spectral shape is altered in this case, i. e. a simple normalization procedure cannot compensate this. After resetting to the initial fluence the spectral shape is reestablished within a few minutes. However, a long-term suppression of the general spectral intensity remains after such a fluence increase (see figure 5.10), slowly regenerating the initial intensities in the course of hours. Such intensity drifts which are indiscriminate with respect to the spectral shape can very well be compensated by normalization. We will use such induced destabilization of the CSA as a benchmark for the applicability of our normalization scheme, as well as the limitations thereof.

Figure 5.9 demonstrates the effect of destabilizing the CSA by increasing the absorbed laser fluence from $F_{\text{exp.}} = 5.3 \mu\text{J cm}^{-2}$ to about $F_{\text{destab.}} = 15.9 \mu\text{J cm}^{-2}$ for a few minutes. We complement the TiSe_2 data already presented in figure 5.6 (full line) by additional data acquired under unstable conditions. After the last “stable” experiment (red circle) the laser fluence is increased to $F_{\text{destab.}}$. The following measurements yield significantly lowered plateau intensities (dashed boxes), actually lowered to the initial, room temperature value, however, still featuring qualitatively the same thermal behavior (dashed line, guide to the eye) if acquired fast enough (within about 10 min) with respect to the long-term re-stabilization. This experiment is repeated at room temperature. The initial mean plateau intensity (star) agrees well with the data acquired during heating if we consider the systematic temperature offset as discussed for figure 5.6. Because cooling takes rather long time (about 1 h) it is safe to assume re-stabilization of the CSA; indeed no general reduction of the spectral intensity is observed anymore. The same cycle of the absorbed fluence (increase to $F_{\text{destab.}}$, then decrease to $F_{\text{exp.}}$) is repeated at room temperature. The plateau intensity after destabilization of the CSA (pentagon) is decreased by about $(26 \pm 9) \%$ which is in good agreement to the reduction observed for the corresponding

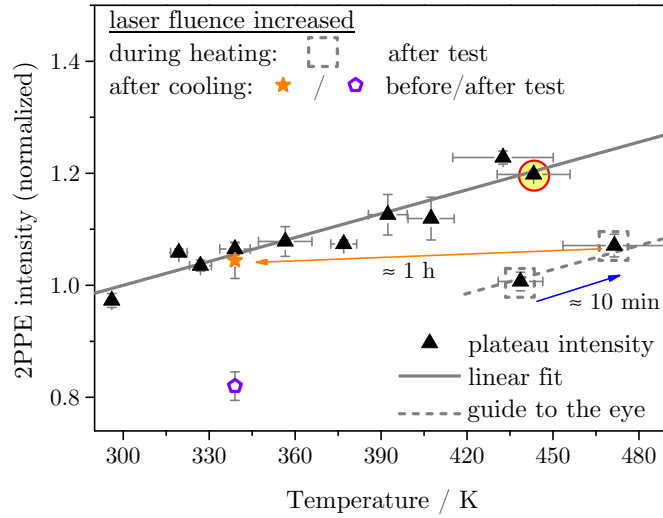


Figure 5.9: The temperature dependent plateau intensity (see figure 5.6) is complemented by additional data acquired during the heating of the sample (dashed boxes) and after cool-down to room temperature (star, pentagon, refer to legend for details) which were taken after inducing instabilities of the CSA by variation of the incident laser fluence (see appendix A.3). Arrows emphasize the relevant time scales.

destabilization during heating of $(21 \pm 11)\%$ (average of data in dashed boxes), the slightly higher reduction in case of the former experiment being attributed to the shorter delay between high and low fluence measurement (about 20 min versus 35 min) leading to slightly different phases of the re-stabilization of the analyzer being probed. In summary, by a short increase of the incident laser fluence we can reproducibly induce an instability of the CSA system which allows for a detailed analysis.

Figure 5.10 compares the spectrum acquired right after the destabilization of the CSA ($T \approx 439$ K, red) to spectra taken just before (black, green). The inset of the figure shows absolute values of the intensity, i. e. non-normalized data. After destabilization the intensity is significantly reduced over the whole energetic range. Please note, that this is not a new, stable state of the system, but still recovers slowly. After cool-down of the sample to room temperature (orange star in figure 5.9) the offset in spectral intensity is fully recovered after about one hour as demonstrated strikingly by figure 5.4. Of course, if the analyzer is destabilized by such significant fluence changes the most obvious and straightforward countermeasure is to wait for the system to recover—the time scale of approximately one hour definitely allows for this approach. However, experimental experience indicates that the CSA is prone to instability at small incident laser fluences which can typically lead to a slow reduction of photoelectron count rate over time; it is this case we aim to compensate for.

After normalization to the plateau intensity (main figure 5.10) the consistency of the

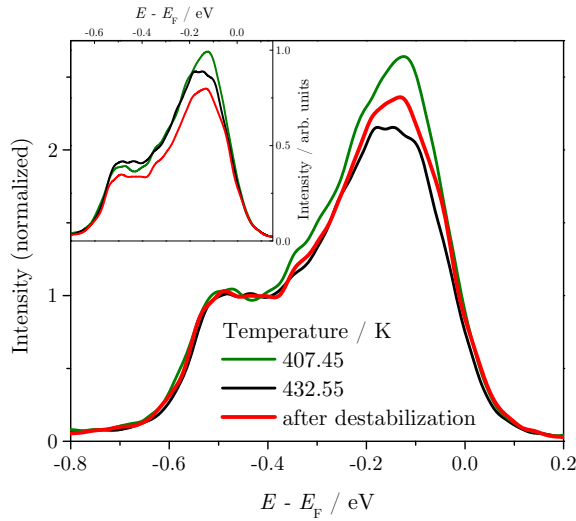


Figure 5.10: Spectrum acquired after destabilization of the CSA by an intermediate increase of the incident laser fluence (red) which leads to an energy independent lowering of the spectral intensity (inset). Plateau normalization enables us to qualitatively compare the spectra before (black, green) and after the destabilization. These data show, that the spectral shape is not altered, i. e. the spectral intensity is reduced. Comparison to data taken during heating reveals an actual sample temperature below 433 K—the measured temperature is thus slightly too high.

spectral shape becomes obvious—the remaining differences are, as we discuss shortly, in agreement with an altered sample temperature. This is emphasized by the fact, that energetic features like, for example, the work function are not influenced by the suppression of intensity as shown exemplary in figure 5.11(a). Within the uncertainties the work function after destabilization of the analyzer (dashed boxes) still agrees to the extrapolation of the heating experiment. This is also true for the second test at room temperature (star, pentagon) where no influence of the CSA stability on the work function is observed, too. The systematic deviation after cool-down is discussed in section 5.1.1. Intensity derived spectral features like the amplitude and area of the chalcogen p bands, shown for TiSe_2 in figure 5.11(b), are of course directly influenced by extrinsic variations of the photoelectron count rate. The inset of the figure presents the absolute, non-normalized values of the data. Especially the area is strongly reduced with respect to the linear extrapolation and does not agree within the limit of the uncertainties. However, after normalization to the plateau intensity (main figure) this deviation is rectified. The data for the amplitude on the other hand is ambiguous and does fit equally dis-satisfactory before and after normalization.

We discussed the problematic indirect assignment of a temperature of the sample earlier in section 5.1.1 and concluded that comparable values can only be obtained under

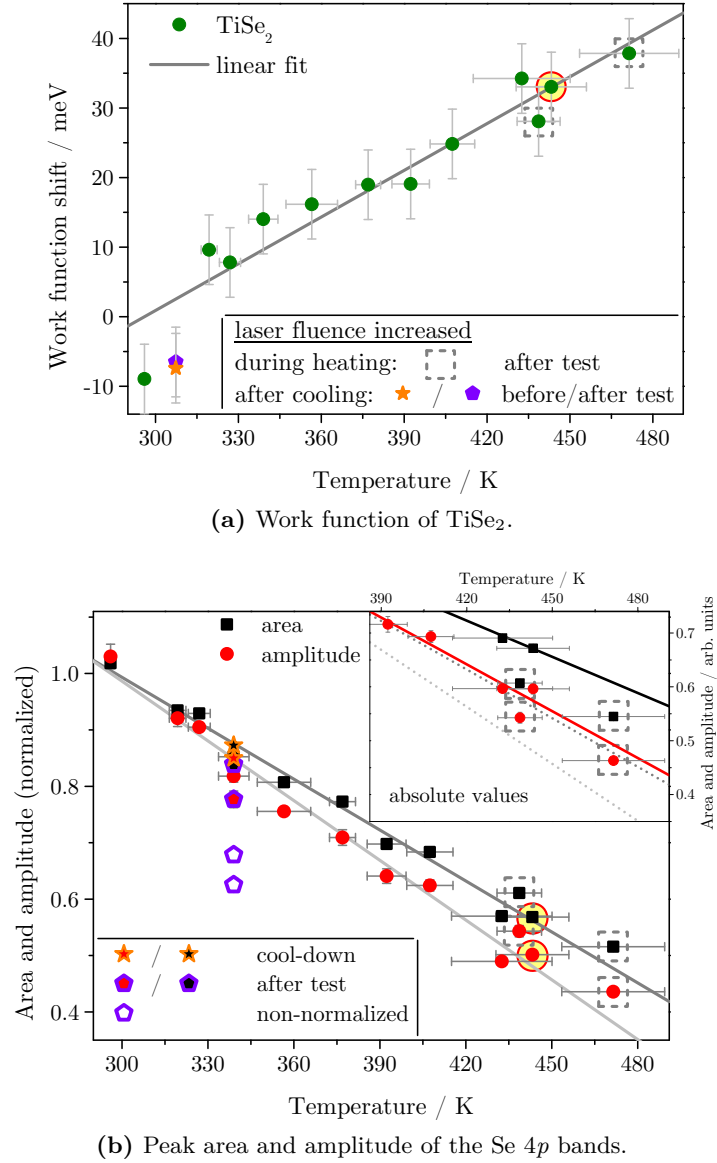


Figure 5.11: Effect of the CSA instability on energetic and intensity derived features exemplified by complementary data for (a) the work function and (b) the area and amplitude of the Se 4p bands (see also figures 5.15 and 5.16). (b) shows amplitude and area after normalization of the spectra to the plateau level; the inset contains the corresponding non-normalized data and both are featuring the same scale. For the marking of the additional data points refer to figure 5.9 and the text.

equilibrium conditions of sample and thermal sensor—once this balance is disturbed, the absolute temperature may become incomparable. Such a deviation from equilibrium is actually observed (red circle in figures 5.9 and 5.11) as a failure of heating power and subsequent restart may have altered thermal equilibrium of sample and sensor. The temperature of the first data point right after destabilization of the analyzer (left dashed box) may also feature an incomparable temperature value. $T \approx 439$ K was measured, yet, the data in figure 5.10 suggest a temperature below 433 K. Using the line fits presented in figure 5.11(b) for the normalized area and amplitude a temperature of about (427 ± 28) K and (426 ± 32) K, respectively, is estimated. Obviously, the non-normalized data suggests a higher temperature because of the generally reduced intensity after destabilization which is, however, not supported by the spectral shape. Figure 5.11(a) clearly is compatible with a lower temperature of the sample—a value of (421 ± 72) K is in good agreement to the estimation for amplitude and area of the Se 4*p* bands—, but does not support a higher value. Temperature measurements using the thermo couple are only relevant for the experiments presented in section 5.1, all other experiments refer to these data for defining a temperature scale using spectral signatures.

In conclusion, normalization to the plateau yields a consistent set of data. The inconsistency observed here arises from the problematic assignment of sample temperature. This is not an issue considering laser fluence dependent or time resolved pump-probe experiments as discussed in section 5.2 and chapter 6. By normalization of the spectra to the plateau level instabilities of the CSA system are compensated.

Nevertheless, it is very important to check, whether normalization can be applied to a dataset. Figure 5.11(b) shows the destabilization test at room temperature after cool-down of the sample (stars, pentagons), using open symbols for data non-normalized to the plateau intensity and filled symbols for normalized data. Even after normalization the area and amplitude do not agree to the expected values and rather suggest an increased sample temperature by about 20 K; the work function deviates as discussed in section 5.1.1, and agrees very well with the value before destabilization, i. e. no indication for a significant heat-up of the sample is derived from the work function. Generally, the suppression of Se 4*p* band intensity—or in other words the modification of the spectral shape observed here— can be attributed to heat-up of the sample, in this case because of the absorbed laser pulses. This is most likely the reason for the short-term spectral modification observed upon destabilization of the CSA by increased incident laser fluence. However, heat-up of the sample is most unlikely in this case, not only because of the contradictory behavior of the work function, but also considering the time scale of the experiment. These data are indeed acquired faster after destabilization of the analyzer (about 20 min later instead of 35 min), yet, appendix A.3 shows that short-term modifications are only observed within a few minutes; the time scale investigated here is too long. Figure 5.12 compares the initial spectrum after cool-down (orange) with the

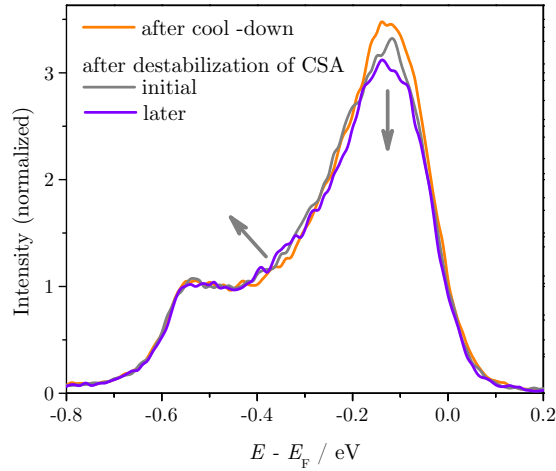


Figure 5.12: Comparison of the spectrum after cool-down (orange) and two consecutive spectra after destabilization of the CSA (gray, violet). The data is normalized to the plateau intensity. Work function, area and amplitude of the Se 4*p* bands as discussed in this section are averaged for these two spectra. Gray arrows emphasize the modifications of the spectral shape which contradict the applicability of plateau normalization.

first spectrum after the destabilization of the analyzer (gray) and a spectrum acquired shortly afterward (violet). These spectra further eliminate warm-up by the laser as the reason for the observed deviation, because after such a warm-up the sample needs to cool-down again at a lower incident laser fluence, yet, the intensity of the Se 4*p* bands does not recover, although non-normalized spectra actually show the slow long-term recovery of the general intensity.

Indeed, the spectral shape after the destabilization test is altered. Gray arrows emphasize the decrease of the amplitude of the Se 4*p* bands and an increase of intensity at about $E - E_F \approx -0.35$ eV. This could be explained, for instance, by a change of the laser pointing or sample position—the spectral shape agrees well with the expectations for probing a slightly different emission—or could hint at degeneration of the sample. We cannot conclusively decide why the spectral shape is altered and in fact we do not need to discuss this. In terms of the analysis of our experimental data it is important to state for the record that these data confirm the importance of a careful evaluation of the spectral shape whenever plateau normalization is applied: the procedure cannot yield consistent data, if additional, shape-modifying effects are to be considered.

5.1.2–d Thermal Origin of the Spectral Intensity Increase of the Plateau

The discussion on the actual origin of the observed thermal modification of the spectra in the energetic range of the plateau is best performed for the 1T-TiSe₂ data, because

this data set was acquired carefully monitoring the stability of the laser system by in-situ measurement of the incident laser power (see section 5.1.1). Additionally, the very low absorbed laser fluence chosen suppresses modifications induced by the laser itself (see section 5.2). These data are thus well suited to investigate the sample intrinsic thermal modifications of the spectral plateau.

First, we need to discuss the stability of the incident laser power. This is important to decide, whether extrinsic intensity modifications as discussed in section 5.1.2–b need to be considered. Indeed, the monitored laser power slightly increased during the several hours of the heating experiment (about 0.2 mW, corresponding to approximately $0.24 \mu\text{J cm}^{-2}$, refer to section 5.1.1). The quadratic dependence of spectral intensity on laser fluence for the 2PPE process employed here yields a corresponding increase of spectral intensity of about 8% which is too small to explain the thermal behavior of the plateau level solely by a fluence increase (the observed effect is about twice). Additionally, the observed laser power drift is of the order of magnitude of the resolution of the thermopile power meter used here which is about a tenth of a milliwatt— considering the sensitivity of this type of power meter to variations of the temperature of its environment and to stray radiation even the small change of fluence proposed seems unlikely and the fluence increase, if any, may actually be much smaller. This is further supported by the last data point acquired under stable conditions of the CSA (see section 5.1.2–c, figure 5.9, red circle) which is actually acquired after correcting for the increase of the incident laser fluence, i. e. the laser power was decreased by 0.2 mW. Obviously, within error bars, this measurement still agrees very well with the overall linear increase of the mean plateau intensity and no significant reduction is observed. In conclusion, the laser fluence may be considered constant for this experiment.

The initial data on the temperature dependence of the plateau intensity presented in figure 5.6 in the introduction of this section also contains a measurement made after cool-down of the sample subsequent to the last heated experiment (stars). In this case the higher temperature ($T \approx 339 \text{ K}$, see section 5.1.1) is correct, but for both temperatures the plateau intensity after cool-down agrees very well (for the corrected T even better) with the observation during the heating experiment. Please note, that these are absolute intensities, i. e. the plateau intensity can be reproducibly changed with temperature which is a strong indication for an intrinsic thermal modification.

The mean plateau intensity thus increases with temperature and the initial value is reproduced upon cooling. Indeed, the linear behavior is analogous to the observation for the amplitude of the Se $4p$ bands (see section 5.1.4–a). It is therefore tempting to discuss a contribution from these bands. The Se $4p_z$ band contributing to named spectral feature exhibits considerable perpendicular dispersion (ΓA -direction, e. g. references [9, 60–62], see also figure 4.10, page 96). This dispersion yields states originating from this band in the surface projected band structure, which is the $\bar{\Gamma}\text{M}$ -direction investigated in our spectroscopy experiments, within a broad energetic range beginning at $E - E_F \gtrsim -3 \text{ eV}$ up to about E_F , depending on the sample stoichiometry (see section 4.1). The energy

range we refer to as the “plateau” therefore coincides with the projected Se 4 p_z band.

Nevertheless, at first glance the Se 4 p_z band seems to be a rather unlikely candidate to explain our observation. In section 5.1.4–a the thermal modification of the Se 4 p_x , p_y on the one hand and the Se 4 p_z band on the other are discussed. Spectra acquired for the reference system 1T-TiTe₂ enable the most easy access, because while featuring a very similar band structure with respect to TiSe₂, the corresponding Te 5 p_x , p_y and the Te 5 p_z bands are energetically well separated. These data show that the chalcogen p_z band decreases significantly stronger with temperature than its p_x , p_y counterpart (sections 5.1.4–a and 5.1.1). For TiSe₂ these different contributions cannot be spectrally resolved but the substructure of the feature of the Se 4 p bands is investigated using a multi Gaussian fit which is, however, much less defined. Nevertheless, these data also show a clear reduction of the amplitude of the Se 4 p_z band with temperature. This behavior seems to contradict an explanation using the Se 4 p_z band.

To understand the thermal modification of the spectral plateau we need to take electron–phonon coupling into account. Figure 5.13 shows the band structure perpendicular to the crystal surface for TiSe₂. These curves are based on calculations of Zunger and Freeman [9] and Pehlke and Schattke [69]. The shape of the bands is approximated, but energies near the high symmetry points represent the calculations well. The coloring of the lines emphasizes the potential involvement of the corresponding bands in a 2PPE process: black for initial, red for intermediate and green for final states. 2PPE transitions are visualized for a photon energy of $h\nu = 3.18$ eV by blue arrows. The wave vector of photons of such energy is about 0.002 \AA^{-1} which is negligible in comparison to the photoelectrons. Photoemission thus proceeds via direct transitions (see e. g. reference [96, 216]) which is represented by two vectors of $|\Delta\mathbf{k}| = 0$ in figure 5.13; optical excitation connects states of the same momentum as the photons do not provide significant momentum.

Of the two contributions to the observed Se 4 p bands only the Se 4 p_z band features a significant perpendicular dispersion—it spans a broad energy range below E_F and provides states within the spectral plateau.⁵ Figure 5.13 shows the direct 2PPE transition which resonantly connects initial and final bands (path i). This resonant contribution provides the slight asymmetry in the high binding energy flank the distinct Se 4 p peak observed right below the Fermi energy in our spectra (for details see section 5.1.4). Note, that the actual details of the band structure deviate from the calculation presented in this figure, because different approaches generally yield discrepancies especially in the vicinity of E_F , see discussion in section 4.1—the band structure as well as the included transitions are schematic.

⁵Although the Se 4 p_x , 4 p_y band exhibits virtually no perpendicular dispersion, it still may contribute to the spectral plateau, because the CSA is an angle-integrating analyzer which, in combination with the strong dispersion of these bands parallel to the surface, leads to some contribution to the spectra. However, photoelectrons originating from the p_z derived band are expected to dominate.

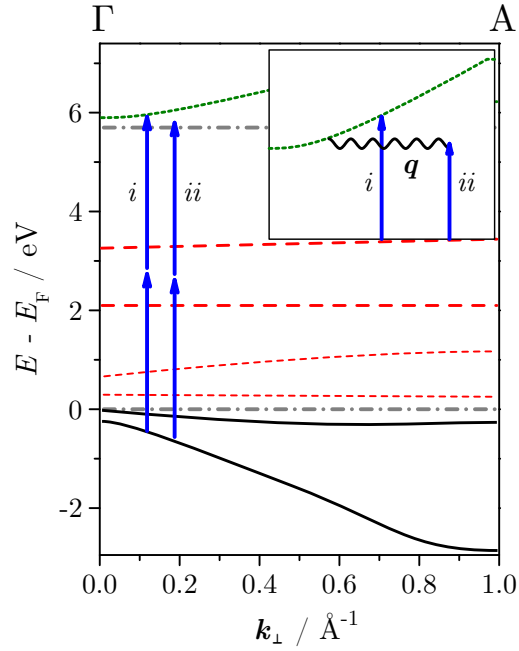


Figure 5.13: Band structure of 1T-TiSe₂ perpendicular to the surface (see section 4.1, figure 4.10), i. e. in k_{\perp} direction. The band shape and energetic positions are based on the calculations of Zunger and Freeman [9], complemented by the excess Ti state at $E - E_F = 2.1$ eV as suggested by Pehlke and Schattke [69]. Black lines represent occupied and broken lines unoccupied bands; red emphasizing potential intermediate and green final states of the photoemission processes discussed here. Vacuum and Fermi energy are included (dash-dotted). Blue arrows correspond to the energy of one photon, $h\nu = 3.18$ eV, and represent the two steps of the 2PPE process. The inset shows a detail of the final step of the excitation, including the wave vector of a phonon, q , visualized by a wiggly line.

We began our discussion with the assumption, that the Se $4p_z$ band is a rather unlikely candidate for the plateau emission, because of its contrary thermal behavior with respect to the plateau which raises the following question: What is the reason for the difference in magnitude and sign of the thermal behavior of the Se $4p_z$ band and the spectral plateau, if both are basically derived from the same band? While the direct transition leads to the dominant signal from the p_z derived band with the observed peak, additional non-direct paths of photoexcitation are also possible. Excitation path *ii* is such an exemplary transition contributing to the spectral plateau. We discuss the temperature dependence of the chalcogen p bands in some detail in section 5.1.4—a focusing on the direct transition and showing that the negative temperature coefficient is well understood. Here we shall analyze the non-direct contribution.

Non-direct transitions, like path *ii* in figure 5.13, do not directly excite a photoelectron into a final band, i. e. the direct path associated therewith does not end in an energetic state but rather a band gap. However, if final states at this energy do exist at a different momentum, i. e. if $\mathbf{q} = \Delta\mathbf{k}$ is provided by a phonon—the phonon assisted excitation path (Drude absorption) is characterized by scattering of the photoelectrons in perpendicular direction [96, 189, 217]—the transition is still feasible. This is shown schematically in the inset. For the spectral plateau observed in the TiSe₂ spectra discussed here, such non-direct phonon mediated excitation is compatible with the observed thermal behavior.

Following the analysis of Pontius et al. [189] of non-direct excitation paths between bulk bands of Ag(111), the involvement of phonons in the process leads to a temperature dependence of the photoelectron signal, because the electron–phonon scattering rate depends on the energy of the electron and temperature (becoming linear in T for sufficiently high temperatures). Matzdorf et al. [217] evaluated the thermal modification of the spectral intensity following a Debye–Waller ansatz and deduced a parabolic dependence on temperature for $T \ll \Theta_D$ and a linear dependence for $T \gg \Theta_D$, with Θ_D being the Debye temperature. Considering $\Theta_D = 221$ K for TiSe₂ [83] we indeed expect a linear modification of spectral intensity with temperature, which is very well confirmed by the data presented in figure 5.6 as well as for the amplitude of the chalcogen p bands as presented in section 5.1.4; comparable data for Ag(111) at sufficiently high temperatures also exhibit a clear linear temperature dependence of the spectral background [189].

In conclusion, the temperature dependence of the electron–phonon scattering rate is the reason for the observed linear dependence of the plateau intensity. Although the expected linear modification is reproduced well, our discussion remains qualitative. This is because the spectral intensity cannot be related quantitatively to the scattering rate [189], although a proportionality seems reasonable as these scattering processes provide the necessary momentum for the photoemission, i. e. enhanced electron–phonon scattering corresponds to enhanced photoemission. However, the thermal broadening of the observed peaks corresponding to direct transitions from the chalcogen p bands is well reproduced quantitatively by these calculations (see section 5.1.4).

5.1.2–e Implications for Normalization

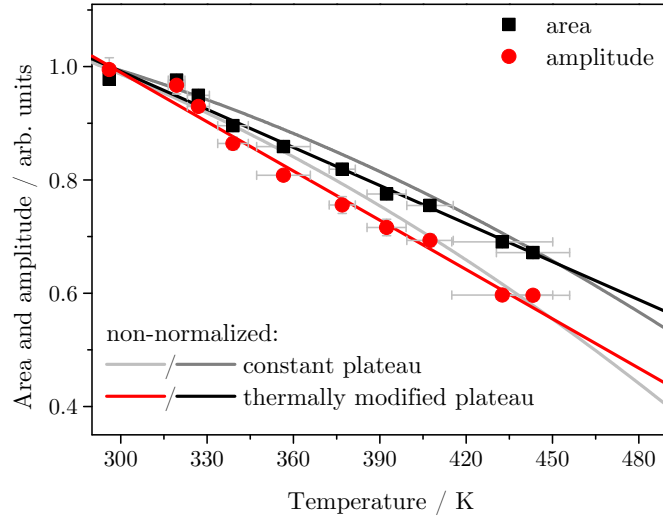
We would like to point out that the findings discussed in this section are important with respect to the interpretation of our investigation of the fluence dependence of the spectral shape (section 5.2) as well as time resolved experiments thereof (chapter 6). We are not focused on the actual temperature dependence of the spectral plateau—after all the effect is very small in comparison to, e. g., the modification of the chalcogen p bands—, but rather on finding a practical solution for compensation of inevitable drifts of the incident laser fluence and the CSA analyzer. Our goal is the compensation of any instability modifying the spectral intensity while conserving the shape of the spectrum. This is all the more important, as especially the time-resolved IR-pump SH-probe photoemission experiments take several hours for preparation and performance. It is impossible to prevent small drifts of the laser power—and in fact we aim at compensating only such minor changes— over this time scale which, additionally, require the laser to be slightly realigned leading to inevitable changes of the laser power, too.⁶ Furthermore, the destabilization of the CSA at low photoelectron rates cannot be suppressed and must also be compensated. Even if the laser fluence could be stabilized perfectly, the long-term stability of the analyzer cannot be guaranteed.

Therefore, consistent data cannot be acquired without a means of compensation for the drifts to be expected. We have shown in section 5.1.2–b that using angle integrated SH-2PPE spectra this can only be achieved by normalization to the plateau level. The normalization procedure is, however, flawed by the intrinsic temperature dependence of this spectral range (see section 5.1.2–d) and we therefore need to discuss the deviations introduced to intensity derived features thereby. The inset of figure 5.11(b) shows linear fits to the amplitude and area of the Se $4p$ bands of TiSe_2 before (full lines) and after (dotted lines) plateau normalization. Indeed, the slope is significantly increased in both cases.

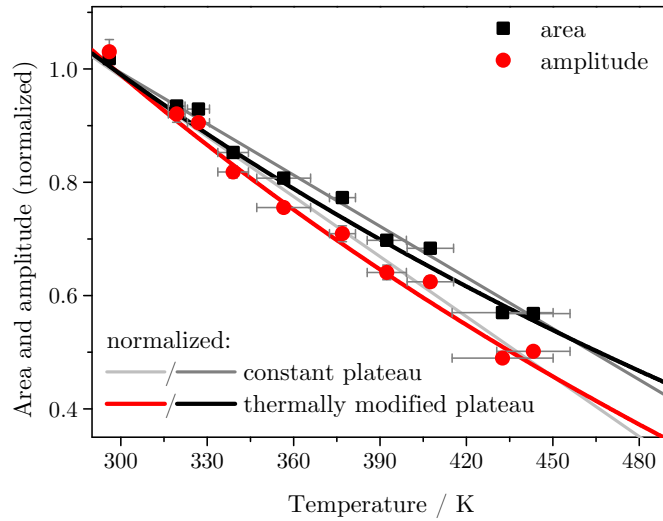
Table 5.1: Slopes of line fits of the area and amplitude of the Se $4p$ bands as presented in figure 5.11(b) with and without normalization to the mean plateau intensity.

feature	normalized / 10^{-4} K^{-1}	non-normalized / 10^{-4} K^{-1}
area	-30.1 ± 1.5	-22.4 ± 1.1
amplitude	-35.3 ± 2.0	-29.0 ± 1.3

⁶Of course, such realignments can also change the laser pointing, thus, careful determination of the spectral shape is necessary. Please note, that we face deviations on a sub-1 mW to 1 mW range of the laser power because of realignments which is implied by the accuracy of the thermopile power meter used.



(a) Before plateau normalization.



(b) Normalization to the plateau intensity.

Figure 5.14: Area and amplitude (symbols) of the Se 4p bands of $1T$ -TiSe₂ (a) before and (b) after normalization to the plateau intensity (see figure 5.11). The data are presented relative to the reference value at room temperature. There are line fits and theoretical estimations included for the area (black, dark gray) and the amplitude (red, light gray). We assume two extremes: constant plateau intensity over the whole temperature range (gray shades) and a linear temperature dependence thereof (black, red), assuming that the thermal behavior intrinsic to area and amplitude is actually linear. For details see text.

Table 5.2: Quality of the linear fit data presented in table 5.1 estimated by a χ^2 value (see section 3.2.2).

feature	normalized $\chi^2 / 10^{-3}$	non-normalized $\chi^2 / 10^{-3}$
area	3.37	1.98
amplitude	7.09	3.65

The thermal behavior intrinsic to the spectral plateau range modifies not only the slope of the other intensity derived features after normalization thereto.

The significant influence on the slope of the line fits is rather obvious considering that we discuss relative changes here. Although with respect to the absolute value of the amplitude of the Se 4*p* bands and the plateau the corresponding changes with temperature are much more prominent for the amplitude—the plateau intensity variation is subtle—, yet, the relative changes with respect to the room temperature values are in fact of the same order of magnitude. The temperature coefficients of the relative area and amplitude are presented in table 5.1; they are before normalization only about 2 to 2.5 times bigger (absolute values) than the corresponding value of $(14.2 \pm 1.7) \times 10^{-4} \text{ K}^{-1}$ in case of the plateau.

In appendix A.1.1–a we discuss, how the thermal behavior of the plateau modifies the spectral features investigated if plateau normalization is applied. To understand, how a sample intrinsic temperature dependence of the plateau intensity may modify intensity derived spectral features normalized to the plateau we take a closer look at two extremal cases:

- (i) the actual plateau intensity is constant with respect to temperature and its observed thermal modification is induced solely by external effects (laser fluence drift, analyzer instability) modeled by a function $f_{\text{ex}}(T)$, and
- (ii) extrinsic effects are absent (laser and analyzer are perfectly stable) and the temperature dependence of the plateau intensity is a sample intrinsic effect.

In the first case, the plateau intensity is constant with respect to the temperature and its modification is of a purely sample extrinsic nature, i. e. the real thermal behavior of all intensity derived spectral features is multiplied by a temperature dependent factor, $f_{\text{ex}}(T) \neq 0$. Then, the experimentally observed linear increase of the plateau intensity with temperature indeed corresponds to $f_{\text{ex}}(T) \propto T$. In this case, normalization to the plateau level compensates the external drifts fully (see addendum A.1.1–a). Our findings in section 5.1.3 reveal a linear thermal expansion of the crystal which suggest an intrinsic linear temperature dependence of the intensity derived spectral features. Before normalization to the plateau level the observed thermal behavior for intrinsically linearly

modified spectral features is non-linear, because the corresponding intensity is multiplied by a factor $f_{\text{ex}}(T)$ which is a linear function of T .

Normalization to the plateau intensity reveals the intrinsic temperature dependence after referencing the data to the room temperature value [see equation (A.4) in appendix A.1.1–a]. Figure 5.14 shows experimental data (symbols) referred to room temperature for the area and amplitude (a) before and (b) after normalization to the plateau. The gray shaded lines show a linear fit to the normalized data [figure 5.14(b)]. By multiplying the line fit of the amplitude and area with the linear behavior of the plateau intensity (figure 5.6) we can recreate the non-normalized data [figure 5.14(a)].

Assuming that the system was sufficiently stabilized during the experiment we expect $f_{\text{ex}}(T) \approx 0$. In this case, the plateau intensity is not constant, but the measured linear temperature dependence is an intrinsic property. Because no additional extrinsic linear temperature dependence needs to be considered, the proposed linear behavior of area and amplitude should be observed in the non-normalized data [line fits; black, red; figure 5.14(a)]. Plateau normalization thus does not compensate for an inexistent external modification, but does rather lead to division by the linear function modeling the thermal behavior of the plateau, yielding the black and red curves in figure 5.14(b).

The second scenario fits better to our experimental data (black, red). Calculation of the χ^2 value for each linear fit, summarized in table 5.2, supports this, as the line fit to the non-normalized data agrees significantly better to a linear function, than after normalization. This agrees with the prerequisite of this measurement: the stabilization of the system, especially of the laser fluence, was a prime concern in this case. However, our investigation here is qualitative. We cannot deduce reliable data on the actual ratio of intrinsic and extrinsic contributions to the plateau intensity. The simple line fit used after normalization [figure 5.14(b)] definitely deviates from the actual expected curve, however, the difference is sufficiently small in the temperature range investigated here; the linear fits still agree very well with the experimental data which is also shown by the small value (10^{-3} , table 5.2) of χ^2 . We need to consider the non-linearity induced by our normalization routine, but we do not expect significant deviations to arise from this, especially considering the rather strong extrinsic effects often observed, like in case of the 1T-TiTe₂ data discussed in section 5.1.2–b.

In summary, we discussed that neither the incident laser fluence, nor the CSA system can be stabilized perfectly. We need to anticipate small drifts of the laser power which cannot be reliably measured with our thermopile power meter. Additionally, the instability of spectral intensity using this analyzer seems to be rather uncontrollable—experimental experience suggests that it cannot be circumvented and its actual extent seems to vary. Please note, the latter instability is the prime reason for the normalization. Monitoring of the laser power revealed a high stability thereof, yet, using low fluences the analyzer is easily destabilized.

Generally, if the system could be sufficiently stabilized for the long time needed to perform our experiments, normalization to the plateau intensity would be unnecessary. This is advantageous, for instance, in case of the investigation of the temperature dependence of the spectral features, because the plateau intensity is clearly temperature dependent, too. Our normalization method therefore superimposes this thermal behavior on all intensity derived spectral features. In case of TiSe_2 , the absolute value of the temperature coefficient of the relative area of the Se $4p$ bands increases by about 34% and the corresponding amplitude increases by approximately 22% (see table 5.1). Even more, the temperature dependence itself is altered and the expected linear behavior is modified.

However, sufficient stability cannot be guaranteed and it is not possible to reliably isolate extrinsic and intrinsic contributions to the spectral intensity. In section 5.1.2–b we used the steepness of the secondary electron cutoff to qualitatively determine to what degree extrinsic contributions are observed. This cannot be applied in a quantitative investigation, because the absolute intrinsic changes of the plateau are just too subtle.

For consistency of all data discussed in this work we therefore generally apply plateau normalization. Although this leads to intensity derived spectral features to be often exaggerated considering their thermal modification, the overall trend and most important the comparability between different data sets is ensured. Most important, extrinsic contributions to spectral intensity are compensated—degeneration of the sample and positional shifts need of course to be carefully checked—, i. e. the resulting data show only sample intrinsic properties.

The deviation from the intrinsic thermal behavior of certain spectral features induced by normalization, however, needs to be considered, especially when unusual thermal behavior is encountered. Also, we need to take into account the significant modification of the temperature coefficient if, e. g., different TMDCs are to be compared.

5.1.3 The Work Function Increase

In this section we focus on the origin of the observed thermal work function shift. The corresponding experimental data is presented in figure 5.15. We like to point to appendix A.1.2 which gives a detailed analysis of the homogeneity of our TiSe_2 samples. These data illustrate that inhomogeneities of the sample surface, especially under consideration of thermal expansion of the crystal, cannot explain the articulate increase of work function observed here. Also, the very similar behavior of our reference system TiTe_2 (open symbols) supports a sample intrinsic effect in contrast to an artifact.

Interrelation of work function and temperature is not surprising at all. Smoluchowski [218] investigated the origin of the dependence of the work function on the crystal plane which yielded a dependence on the lattice constant. As the inter-atomic spacing of the lattice changes with temperature, also a modification of the work function is expected. Indeed, calculations predict a linear response of the work function to the temperature by

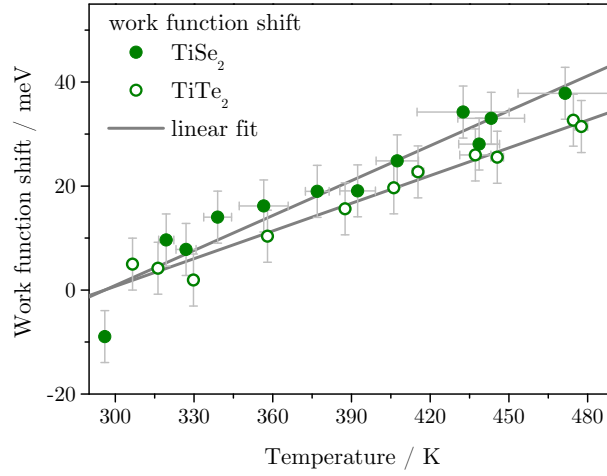


Figure 5.15: The relative change of the work function with temperature with respect to its room temperature value, $\Phi(296\text{ K})$, agrees well with a linear fit (lines) which is consistent with equation (5.1).

considering, amongst others, the typical linear expansion of metals [219–221]:

$$\Phi(T) = \Phi_0 + \Delta\Phi T, \quad (5.1)$$

with the work function at absolute zero, Φ_0 , and the temperature coefficient $\Delta\Phi = \frac{d\Phi}{dT}$ (see appendix A.2.1).

For both TiSe₂ and TiTe₂ the linear behavior expected from equation (5.1) is reproduced very well—except for the very first work function value of TiSe₂ which deviates significantly and is attributed to residual adsorbates present at room temperature, rapidly evaporating upon heating. This explains the step between the first two values and is consistent with our observation in figure 5.4, section 5.1.1.

The linear fits yield the work function at room temperature, Φ_{RT} , the corresponding temperature coefficient, $\Delta\Phi$, and via extrapolation the work function at absolute zero, Φ_0 (note, that the fit is performed on the data relative to Φ_{RT}). Table 5.3 presents the outcome of these fits for both systems. The calculation of the work function requires knowledge of the spectral width and the photon energy ($2h\nu$ in case of 2PPE, see section 3.2). Assuming an accuracy of one energy channel (10 meV) for the low and high energy cutoff of the spectrum, we derive an uncertainty of 20 meV for Φ_{RT} (presuming $h\nu$ to be exact). Φ_0 is calculated from Φ_{RT} and extrapolation to $T = 0\text{ K}$ using $\Delta\Phi$.

The work function at room temperature Φ_{RT} and the temperature coefficient $\Delta\Phi$ are both defined by a linear fit. These values enable us to extrapolate to absolute zero temperature, yielding Φ_0 . The work function agrees well with literature values for both TMDCs [19]. In the following sections we discuss the physical source of the observed

Table 5.3: The room temperature ($T = 296\text{ K}$) work function, Φ_{RT} , the extrapolation of the work function to $T = 0\text{ K}$, Φ_0 , and the corresponding temperature coefficient, $\Delta\Phi$, are presented for $1T\text{-TiSe}_2$ and $1T\text{-TiTe}_2$. All data are defined by linear fits and the uncertainties are rounded up. See text for details.

sample	$\Phi_{\text{RT}} / \text{eV}$	Φ_0 / eV	$\Delta\Phi / 10^{-4} \text{eV K}^{-1}$
$1T\text{-TiSe}_2$	5.76 ± 0.02	5.70 ± 0.03	2.24 ± 0.22
$1T\text{-TiTe}_2$	5.27 ± 0.02	5.22 ± 0.03	1.78 ± 0.10

work function changes, especially focusing on the corresponding temperature coefficient $\Delta\Phi$.

5.1.3–a Origin of the Thermal Work Function Modification

For both systems investigated here, $1T\text{-TiSe}_2$ and $1T\text{-TiTe}_2$, we observe two interesting facts:

- the work function increases with temperature ($\Delta\Phi > 0$), and
- the absolute value of the temperature coefficient [$|\Delta\Phi| \approx 1 \times 10^{-4} \text{eV K}^{-1}$, see table 5.3] is of the order of magnitude of the Boltzmann constant ($k_{\text{B}} = 8.6 \times 10^{-5} \text{eV K}^{-1}$ [222]).

The former is, at first, puzzling, as similar investigations as well as calculations for metals often exhibit a negative temperature coefficient in the temperature range investigated [220, 223–226], i. e. a reduction of the work function with temperature ($\Delta\Phi < 0$, [227]) is expected. For the absolute value we find $|\Delta\Phi| \sim k_{\text{B}}$ which agrees with literature [220]—there is, however, some indication that this value may be to some degree enhanced (see in section 5.1.3–b).

Experimentally observed temperature coefficients of the work function are known to be often contradictory [228] considering magnitude and sign, because the structural quality of the surface and impurities like, e. g., adsorbates can significantly contribute to $\Delta\Phi$. In the following we analyze the effects contributing to the work function, especially focusing on the temperature dependence thereof. Both Φ and $\Delta\Phi$ depend on the crystallographic plane investigated [220, 229, 230] which can also explain the seemingly unusual sign of the latter. Section 5.1.3–b discusses the influence of adsorbates and impurities which also strongly modify the thermal behavior of the work function [219, 224, 227].

Before we begin our detailed analysis we like to give a few remarks on the comparability of work functions. In general, the term “work function” is used for quantities acquired by different experimental methods and which are in fact not always equivalent physical properties [219, 225]. In this section we refer to earlier works which used the Kelvin contact potential method for all relevant data—in part data acquired by other methods,

like field emission techniques, are mentioned (e. g. references [223, 231]). The contact potential and photoemission methods are known to yield comparable work function data [232], thus, we do not expect relevant, systematic deviations considering our qualitative discussion in this section.

What is the expected thermal modification of the work function? Herring and Nichols [219] discussed several temperature dependent contributions to the work function, the significant being:

- the thermal expansion of the crystal lattice,
- atomic vibrations, and
- an effect of the electronic specific heat.

The other contributions—most notably the surface dipole layer⁷—only yield insignificant contributions to the thermal modification of the work function for metals.

The third effect is generally negligible, because its magnitude only becomes comparable to the other effects if the top or bottom of a band is close to the Fermi energy. Transition metals, like titanium which comprises the TMDCs investigated here, feature narrow d bands close to E_F and in our case also provide p bands which cut the Fermi energy at the Γ -point of the Brillouin zone. In this case, the electronic specific heat—which contributes to the temperature dependence of the chemical potential—may be modified and yield an either positive or negative, significant contribution $\Delta\Phi_{\text{ESH}}$ to the total temperature coefficient. Herring and Nichols [219] show that this part of the temperature dependence of the work function is linear in T :

$$\Delta\Phi_{\text{ESH}} = \frac{\pi^2}{3} k_B^2 \left(\frac{d \ln \nu}{dE} \right)_{E=E_F} \times T, \quad (5.2)$$

with the density of states $\nu(E)$, the energy E and the Boltzmann constant k_B . Thus, if a band edge is close to E_F , the value of the derivative of $\ln \nu$ is big at the Fermi energy, i. e. for TiSe₂ and TiTe₂ $\Delta\Phi_{\text{ESH}}$ may become relevant.

However, except for the calculations presented in reference [233] cited by Herring and Nichols, to our knowledge no data on the actual magnitude of its contribution exists, especially for the TMDCs discussed here. Nevertheless, we can still deduce qualitative insights from equation (5.2). For a certain density of states at E_F the contribution to the temperature coefficient is described by $\Delta\Phi_{\text{ESH}} \propto T$, i. e. if this effect actually modifies the thermal behavior of the work function for our samples, this modification is linear. This fits nicely to the observed linearity in figure 5.15.

⁷For semiconductors the contribution of the surface dipole layer may be relevant [227].

Probably the most self-evident explanation for the thermal modification of the work function is given by the thermal expansion of the sample crystals. The work function change with temperature can be expressed as:

$$\frac{d\Phi}{dT} = 3\alpha V \frac{\partial\Phi}{\partial V} + \frac{\partial\Phi}{\partial T}, \quad (5.3)$$

consisting of thermal expansion (first term) and thermal excitation at constant volume (second term) as discussed by Crowell and Armstrong [223] (see also reference [219]), with the volume V and the linear thermal expansion coefficient α .

Solids generally exhibit a change of volume upon variation of the temperature. This is described by the volumetric thermal expansion coefficient $\alpha_V = \frac{1}{V} \left(\frac{\partial V}{\partial T} \right)_p$ (homogeneous, isotropic solid [234]) with the volume V , evaluated at constant pressure p . For solids this value is constant within certain temperature ranges, i. e. the thermal expansion is linear in temperature, which enables the definition of the coefficient by:

$$\begin{aligned} V(T) &= V_0 (1 + \alpha T)^3 \\ &\approx V_0 (1 + \alpha_V T), \quad \alpha_V = 3\alpha, \end{aligned}$$

with the volume $V(T)$ at a specific temperature and its value at absolute zero, $V_0 = V(0 \text{ K})$, and the linear thermal expansion coefficient α [234].

It is not surprising that the linearity of the thermal expansion of the volume of a solid also reflects in the volume dependent part of the work function shown in equation (5.3). Kiejna et al. [230] evaluated the work function contribution independent of the crystallographic direction at a specific temperature, $\Phi(T)$, to be linear in temperature:

$$\Phi(T) = \Phi_0 - \alpha_V f_0 T, \quad (5.4)$$

with the work function at absolute zero temperature, Φ_0 , and a function of the temperature evaluated at $T = 0 \text{ K}$, f_0 . An alternative analysis by Seely [235] also concludes a linear behavior of $\Phi(T)$:

$$\Phi(T) = \Phi_0 + \alpha \left(\text{const.} \times N_0^{\frac{2}{3}} - \Phi_0 \right) T, \quad (5.5)$$

with the density of free electrons at absolute zero temperature, N_0 . Physically, the linear dependence of the volume of the solid also leads to the work function being linear in temperature. The thermal expansion influences the work function twofold: first, it lowers the free electron kinetic energy because of the reduction of density, and second, the potential barrier height of the surface decreases [230].

The second term in equation (5.3) is attributed to atomic vibrations. An estimation of its contribution is given by Kiejna [220] (see also reference [223]) which reveals a non-linear dependence of the work function on temperature if atomic vibration is considered. The vibrational contribution tends to enhance the absolute value of the thermal effect

(dependent on the crystallographic direction, as we discuss shortly) by an order of magnitude in most cases. The calculations also showed that this contribution can be almost linear in the temperature range used here for the investigation of our TMDCs (see, e. g., aluminum). Our data do not provide indications for a significant non-linearity which is compatible with either a very small contribution or almost linear behavior in our temperature range. The calculations of Kiejna [220] show, that the pure effect of thermal expansion leads to a temperature coefficient which absolute value is rather small, generally being a fraction of the Boltzmann constant, i. e. $|\Delta\Phi| \lesssim 1 \times 10^{-4} \text{ eV K}^{-1}$. The inclusion of vibrations, however, increases $|\Delta\Phi|$ up to about $10 \times 10^{-4} \text{ eV K}^{-1}$; positive values of up to $\Delta\Phi \lesssim 1.7 \times 10^{-4} \text{ eV K}^{-1}$ are observed.

The work function and its temperature coefficient depend on the crystallographic plane which is studied in great detail in two works by Kiejna et al. [220, 230]—the latter simultaneously including the effect of thermal vibrations of the atoms—and Swanson and Crouser [231]. To investigate this effect, Φ is separated into a part depending on the crystallographic direction and an independent contribution, the “jellium part”. The latter is found to yield $\Delta\Phi < 0$ for all metallic systems investigated by Kiejna et al. Choosing a certain crystal plane yields either a negative or a positive temperature coefficient. Although the most total coefficients are still negative, the contribution of the direction dependent part can be big enough to render the total $\Delta\Phi$ induced by thermal expansion positive. The occurrence of either sign seems to be a consequence of the difference in work function of the different crystallographic planes. Upon melting, the work function needs to be equal for the whole system, thus for planes of high work function it decreases with temperature and vice versa [226].

The dependence of the work function on the crystal face and the corresponding change of the sign of the temperature coefficient provide an explanation for the observation of a positive $\Delta\Phi$. However, this has to be carefully considered for our samples. 1T-TiSe₂ and 1T-TiTe₂ are layered TMDCs which surfaces are formed by the (0001) plane of the hexagonal lattice. This is the densest of the planes of these systems, thus, considering above argument, an increase of work function with temperature seems unlikely. Furthermore, the total $|\Delta\Phi|$ tends to increase for decreasing density of the crystal faces [220], although the part attributed to the crystal direction may increase or decrease with plane density; it can even virtually vanish for the most dense packed plane [230]. The effect of the actual crystal plane may therefore not be sufficient to exclusively explain the observed sign of $\Delta\Phi$ in our experiments.

A positive temperature coefficient of the work function is also observed for other systems. The work of Ibragimov and Korol’kov [228] on p band metals, for instance, yielded a positive value of $\Delta\Phi$ below the melting point of the crystals, i. e. the work function increases with temperature. Values of $1.2 \times 10^{-4} \text{ eV K}^{-1}$ to $7.4 \times 10^{-4} \text{ eV K}^{-1}$

are observed. Considering, that the band structure of TiSe_2 and TiTe_2 consists of Se $4p$ or Te $5p$, respectively, and Ti $3d$ bands in the vicinity of the Fermi energy, some similarities to these data is expected. However, Ibragimov and Korol'kov also state, that $\Delta\Phi$ is positive for loosely packed faces and negative for dense packing which is explained by the fact that the dense planes increase atomic distance upon heating, leading to compression of their loose counterparts. Considering the plane investigated for the two TMDCs discussed here (see section 2.1) being the densest, comparability of these data is rather questionable.

Bachmann [227] performed similar experiments on Si(111) and also observed a positive temperature coefficient of $1 \times 10^{-4} \text{ eV K}^{-1}$ for the clean surface. Although the semimetallic character of TiSe_2 may suggest comparability to some degree to the semiconductor silicon, the sign of $\Delta\Phi$ for Si is attributed to effects which are rather unlikely in case of our samples: For semiconductors the Fermi energy at the surface resides within the band gap and deviates from its bulk value. Depending on the doping of the silicon, E_F may increase or decrease with temperature, allowing either sign of $\Delta\Phi$.

The thermal modification of the work function of TiSe_2 and TiTe_2 is consistent with the general behavior of other metallic systems. To our knowledge we provide the first estimation of the temperature coefficient of these two systems, thus we can only comment on the plausibility of our observation in the context of investigations of other systems.

Calculations and earlier experiments show linear behavior of the work function with temperature which is consistent with our data. The temperature coefficient of the work function agrees with the expected order of magnitude, however, we cannot preclude the presence of impurities which can significantly influence the absolute value of $|\Delta\Phi|$. Indeed, considering especially the other metallic systems used for comparison, our value of the temperature coefficient seems rather large to such an extent that it signifies the upper range observed.

Although there exist a multitude of explanations for the increase of work function with temperature, neither fits satisfyingly to our actual system. The following section discusses the influence of impurities on the modification of the work function with temperature, yielding an additional contribution to our observation.

5.1.3–b Changes Induced by the Presence of Adsorbates

It is well known from earlier works that adsorbates significantly modify the work function and also the corresponding temperature coefficient [219, 220, 224, 227] with respect to the magnitude of its absolute value and possibly even its sign. The absolute value of the temperature coefficient of the work function can be significantly enhanced in the presence of impurities, adsorbates, or films at the surface with respect to a clean metal or semiconductor [219, 226, 227].

Bachmann [227], for instance, investigated the semiconductor Si(111) which features a work function variation in a range of 4.47 eV to 4.9 eV accompanied by temperature coefficients of $-1 \times 10^{-4} \text{ eV K}^{-1}$ to $1 \times 10^{-4} \text{ eV K}^{-1}$. These experiments demonstrated that adsorbates which lower the work function also lead to an increase of the temperature coefficient and vice versa; surface impurities were also able to change the sign of the coefficient. In section 5.1.1 we observed the effect of adsorbed residual gas on the work function of TiSe₂. Our experiments showed, that upon adsorption of common residual contaminations (like, e. g. water) the work function of this system is reduced (see also 4.1). If we assume a small coverage by adsorbates which lower the work function, an increase of $|\Delta\Phi|$ is expected from these considerations, explaining the rather big values of the temperature coefficients observed for the TMDCs investigated here.

How do adsorbates influence the temperature dependence of the work function? In section 5.1.3–a we mentioned that the surface dipole layer itself does not contribute significantly to the temperature coefficient of the work function for metals. In the presence of adsorbates, however, Bachmann [227] discussed the following mechanism influencing Φ and $\Delta\Phi$: The strongest modification per adatom is expected for ionic bonds. Each adsorbed atom is associated with a mirror charge within the surface which induces a dipole moment. The work function change is quantized by the mean normal component of this dipole moment and the area density of adatoms. The linear thermal expansion of the surface reduces the area density of the these adatoms. The mean dipole moment is temperature dependent, too, because the orientation of the dipoles fluctuates stronger with increasing temperature. Thus, the modification of the work function induced by the adsorbates can be significantly modified depending on the actual temperature and the magnitude of $\Delta\Phi$ additionally depends on the change of work function induced by the adatoms, leading to an increase of the effect with adsorbate density at low coverages.

The presence of impurities on the TMDC samples is indeed a very possible scenario. The preparation of these crystals by cleaving under high vacuum conditions and subsequent heating (see section 3.3) is prone to leave residual adsorbates on the surface. Because heating to very high temperatures destroys the crystals integrity and we thus need to limit this temperature, for practical reasons the sample preparation is a trade-off for structural integrity, surface purity, and time restrictions. Indeed, our findings in section 5.1.1 (see figure 5.4) hint at the presence of a small coverage by residual adatoms.

Furthermore, in section 4 we employed spectroscopic and time resolved experiments to confirm an excess of titanium atoms within the van der Waals gap of 1T-TiSe₂, i. e. our samples deviate from the ideal stoichiometry by a small excess of titanium. Such intercalates modify the expansion of the crystal perpendicular to the surface, leading to a local increase of the interlayer spacing [70, 71, 151, 178] and a consequent decrease of the work function [151, 162]. It is reasonable that these excess interlayer atoms modify the temperature dependence of the work function in a similar way, as discussed for the

adsorbates—they are actually the analog of adsorbates, however, located between the crystal sheets. Even if the intercalates situated at the other side of the surface layer do not modify the mean surface dipole moment significantly, they will modify the expansion of the surface crystal layer. A contribution of excess Ti to $\Delta\Phi$ seems therefore reasonable.

An evaluation of to which extent adsorbates contribute to the observed temperature coefficient is enabled by the work of Seely [235]. It combines the temperature dependent work function with the density of free electrons at $T = 0$ K, N_0 , which yields a temperature coefficient of:

$$\Delta\Phi_{\text{calc.}} = \alpha \left(N_0^{\frac{2}{3}} 3.62 \times 10^{-15} \text{ eV} - \Phi_0 \right), \quad (5.6)$$

with $\Phi_0 = \Phi(T = 0 \text{ K})$, the linear thermal expansion coefficient α , and the density of free electrons at absolute zero temperature, N_0 .

Due to the layered structure of the TMDCs investigated here a strong anisotropy of the thermal expansion is to be expected. Indeed, the linear expansion coefficients parallel, α_a , and perpendicular, α_c , to the crystal layers are different (see appendix A.1.2–a) which is considered by using a mean value, $\bar{\alpha} = \frac{1}{3}(2\alpha_a + \alpha_c)$ [234], presented in table 5.4.

Table 5.4: Literature values of the mean linear expansion coefficient, $\bar{\alpha}$, calculated using data of references [236, 237], and the carrier concentration per unit of volume for stoichiometric crystals, $N_{0, \text{ideal}}$, and for titanium self-intercalation, $N_{0, \text{excess}}$. See also table 2.1 in section 2.1.

sample	$\bar{\alpha} / 10^{-6} \text{ K}^{-1}$	$N_{0, \text{ideal}} / 10^{20} \text{ cm}^{-3}$	$N_{0, \text{excess}} / 10^{20} \text{ cm}^{-3}$
1 T-TiSe ₂	18.67	2.8 to 7.1 ^b	9 to 10 ^d
1 T-TiTe ₂	22 ^a	13 ^c	18.0 ^e

^a polycrystalline powder sample

^b [5, 63]

^c [79, 80]

^d 2 at. % to 4 at. % excess Ti [164, 165]

^e 1 at. % Ti over-doping [79]

Using the experimental values of $\bar{\Phi}_0$ presented in table 5.3 and literature values for the electron density summarized by table 5.4, equation (5.6) allows us to calculate the temperature coefficient of the work function. We derive, for stoichiometric TiSe₂, a value of $\Delta\Phi_{\text{calc.}} = (-1.02 \pm 0.02) \times 10^{-4} \text{ eV K}^{-1}$ and for TiTe₂ we find $(-1.05 \pm 0.01) \text{ eV K}^{-1}$ which are both very reasonable considering magnitude and sign in comparison to other metallic systems. If we assume this value $\Delta\Phi_{\text{calc.}}$ to be the “real” coefficient for the clean, stoichiometric samples, our experimental data might indicate the presence of adsorbates and/or surface impurities. In other words: the observed magnitude and sign of $\Delta\Phi$ might also be explained by impurities alone.

However, the approach of Seely leading to equation (5.6) may be too simplified, because it tends to yield positive values of the temperature coefficient for electron densities typical for metallic systems (a few 10^{22} electrons/cm³ [110, 238]) although more sophisticated calculations [220, 223] and experiments [223, 226, 228] often exhibit negative values (see the discussion in reference [219]). Using equation (5.6) to calculate the free electron density of our samples from the experimental $\Delta\Phi$ we derive values about three orders of magnitude too high, i. e. the range of a few 10^{23} electrons/cm³, which is much too high even for metals, especially considering the semimetallic character of TiSe₂⁸. However, as the more sophisticated calculations rely on complicated, numerical approaches exceeding the scope of this section, this simple approach may still provide a hint at the relevance of adsorbates.

In conclusion, we like to point out that the linear increase of the work function is very well understood and explained by theoretical considerations. The positive sign of the temperature coefficient may be typical for the crystal plane and the specific TMDCs investigated here, however, considering the influence of adsorbates we find either the presence of a slight residual coverage of adatoms or the intercalated excess titanium a reasonable source for the magnitude and sign of the experimentally observed value of $\Delta\Phi$.

5.1.4 The Thermal Modifications of the Chalcogen p Bands

Finally, after establishing the necessary methods of data analysis in the preceding sections 5.1.2 and 5.1.3, we now focus on the most prominent feature of the SH-2PPE spectra of 1T-TiSe₂: the Se $4p$ bands. Again, we evaluate data acquired for TiSe₂ and the reference system TiTe₂ simultaneously. Considering the chalcogen p bands, the reference data prove very valuable, because the p_x , p_y and the p_z derived sub-bands forming the Se $4p$ feature observed for TiSe₂ (two spin-orbit split p_x , p_y derived bands and one p_z band [66, 161, 240]), yield two distinct, well resolved bands, the Te $5p_x$, p_y and the Te $5p_z$ bands, for TiTe₂. A difference in the thermal modification of the sub-bands needs to be considered, because they are derived from either p_x , p_y orbitals or p_z orbitals. The p_x , p_y orbitals reside within the crystal layers, i. e. the resulting band features strong 2D character which is demonstrated by its virtually vanishing dispersion perpendicular to those layers. The p_z orbitals reach out of the crystal planes, into the van der Waals gap and consequently the corresponding band features strong perpendicular dispersion and

⁸Adsorbates and intercalates can increase the density of electrons by providing additional free electrons [6, 70, 89, 162, 178, 239] (the hole concentration can also be decreased [88]). However, equation (5.6) does not explicitly include the effect of adsorbates and the additional free electrons alone do not change $\Delta\Phi_{\text{calc}}$. considerably. Even for intercalates like (N₂H₄)_x which increase the free carrier concentration to 0.5×10^{22} cm⁻³ to 1.5×10^{22} cm⁻³ [78] the temperature coefficient would still be negative.

shows a more 3D-like character.

We will analyze the chalcogen p bands with respect to amplitude, area, FWHM, and binding energy. Evaluation of energetic spectral properties like the binding energy and the FWHM is not hindered by drifts of the spectral intensity (see section 5.1.3), however, we need to define these characteristics in a suitable manner, a task complicated by the fact, that the peak associated with the Se $4p$ bands is cut by the Fermi edge. The very small binding energies with respect to E_F are shown by different band structure calculations [9, 60–62] as well as experimental data [10, 15]. Plateau normalization is necessary to evaluate the intensity derived amplitude and area, because comparison to the TiTe_2 data would be hindered otherwise (see section 5.1.2). As the TiSe_2 data are sufficiently stable with respect to extrinsic intensity modifications, the deviations introduced by normalization can be evaluated.

A numerical method is introduced for the extraction of named spectral characteristics. This method is suitable for the analysis of a single spectral peak. The analysis of the substructure of the observed chalcogen p bands will be performed using two methods: the TiTe_2 data can be numerically evaluated as the sub-peaks are sufficiently separated, additionally the Se $4p$ peak is fitted by a double Gaussian. The numerical evaluation of the whole Se $4p$ band feature is important for the interpretation as its quality is much better than that of the fitted sub-bands—the fit procedure is not very stable because of the insufficient spectral resolution of the evaluated data, i. e. the sub-band analysis of TiSe_2 can only provide insights into the trends expected for the sub-bands. Only by comparison to the TiTe_2 reference quantitative statements are derived.

The methods of data evaluation applied in this section are discussed in appendix A.1. The numerical methods are presented in appendix A.1.1, the addendum A.1.1–b focuses on the multi Gaussian fit used for the substructure analysis of the Se $4p$ bands.

This section is divided into four parts:

- (i) Section 5.1.4–a presents data on the intensity derived spectral characteristics, i. e. amplitude and area of the spectral features.
- (ii) Energetic properties, like the FWHM and energy of the observed bands, are investigated in section 5.1.4–b.
- (iii) We are focused on spectral structures in the vicinity of the Fermi energy and thus a detailed look on the influence of thermal broadening especially of the Fermi edge is necessary for the interpretation of our data (see section 5.1.4–c).
- (iv) Finally, in section 5.1.4–d we will discuss how the observed thermal modifications can be understood in terms of sample properties.

In this section we therefore first introduce the results of our thorough data analysis for the thermal behavior of the chalcogen p bands (sections 5.1.4–a to 5.1.4–c) and

afterward provide an interpretation of the relevant spectral characteristics (section 5.1.4–d). The latter section also summarizes the relevant features which allow for identification of temperature induced modifications—the corresponding temperature coefficients are tabulated for reference for the other experiments discussed in this work.

5.1.4–a Reduction of the Spectral Weight

Upon increasing the sample temperature we observe a strong change in the spectral weight of the chalcogen p bands for the TMDCs investigated here. First, we discuss the behavior of the photoemission amplitude and area, especially with respect to the question, which of these properties is best suited for quantitative comparison of different data. Afterward, we investigate the substructure of the chalcogen p bands using a multi peak fitting procedure.

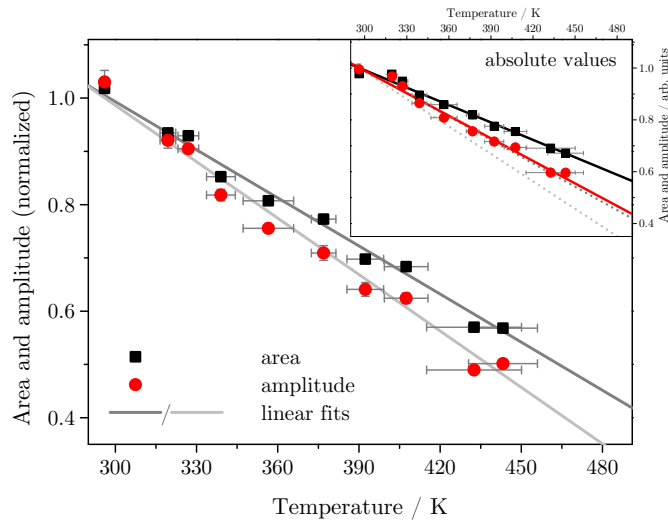


Figure 5.16: Peak area (black) and amplitude (red) of the Se $4p$ bands of TiSe₂ decrease linearly with increasing temperature. The data is calculated applying the numerical method to plateau normalized spectra. The inset shows absolute count rates, i. e. without plateau normalization. The slope is about 2 to 2.5 times steeper than in case of the plateau level (see section 5.1.2). Linear fits are included.

Evaluation of the photoemission amplitude and area of the broad peak originating from the Se $4p$ bands is performed by applying the numerical evaluation methods described in addendum A.1.1. The temperature dependence of the photoemission amplitude (red circles) and area (black squares) is presented in figure 5.16.

In general, the numerical methods of data analysis are more reliable than their multi peak fit counterpart. However, they cannot be applied to analyze the two peaks observed

in the TiTe_2 spectra because the energetic separation is not big enough. A direct comparison of the compound features of the chalcogen p sub-bands is not instructive, as the details of the overlap of the sub-bands strongly influence, e. g., the peak area. A comparison needs a closer look to the details of this substructure which we discuss later in this section.

Following our discussion in section 5.1.2 we use plateau normalization to enable direct comparison to all data presented in this work. Non-normalized data is included in the inset for reference. Please note, that the enhancement of the temperature coefficient introduced by normalization (dotted lines, see section 5.1.2–e) is relevant for the quantitative interpretation of the temperature dependence presented in section 5.1.4–d and is only of minor concern in the context of the qualitative comparison of the two TMDCs here. The thermal modification of area and amplitude is referenced to the corresponding room temperature value (\tilde{x} or \tilde{x}_p , respectively, in addendum A.1.1–a), i. e. the ordinate represents the ratio of the properties with respect to room temperature.

We observe a very strong reduction of the amplitude within the temperature range investigated—about 40 % to 50 % within 147 K—the temperature coefficient of the corresponding area is, however, smaller which leads to a reduction thereof which is approximately 7 % smaller in the same temperature range. The observed difference is fully explained by thermal broadening of the spectral features which we will discuss now.

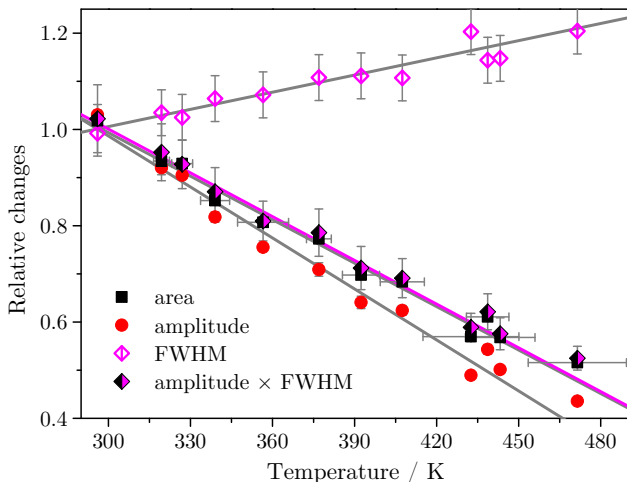


Figure 5.17: Area (black squares), amplitude (red circles) and FWHM (magenta diamonds) normalized to the corresponding value at room temperature. The black/magenta diamonds show the product of amplitude and FWHM which features the same slope as the area. For details see text.

Which spectral characteristic is best suited to describe the observed loss of spectral weight? A closer look at figure 5.16 reveals an interesting detail: the data for photoemission amplitude and area are qualitative extremely similar exhibiting only subtle differences. Indeed, a Gaussian curve is fully described by its amplitude, FWHM, and center and, using the FWHM, the area is defined by the amplitude (see appendix A.2.2). Discussing both amplitude and area is thus redundant as these measures are equivalent. Considering the relative data presented in 5.16, the relative area is the product of the relative FWHM and amplitude for a Gaussian peak. Figure 5.17 combines the data presented in figure 5.16 (squares and circles) with the temperature dependence of the FWHM (open diamonds, see section 5.1.4–b). The latter is given relative to its room temperature value, i. e. the ratio of FWHM and the reference value is given, in contrast to the broadening discussed later in this chapter. Multiplication of FWHM and amplitude (full diamonds) yields a very good agreement to the area directly extracted from the spectra; even a line fit of the calculated area agrees very well with the corresponding fit of the numerically extracted data (magenta and gray lines).

Addendum A.2.2 is especially interesting with respect to the multi Gaussian fit method applied for the substructure analysis which we also discuss in this chapter—the provided values for the amplitudes are in fact calculated from the area provided by the fitting routine. However, the applicability of these arguments to the asymmetric peak of the Se 4*p* bands is not obvious as it is clearly not described by a single Gaussian—the assumption of a single Gaussian is actually a rather crude approximation (for a baseline corrected spectrum see figure A.1, appendix A.1.1). Nevertheless, no significant deviations of the experimentally observed peak area and the one defined by the amplitude is observed—focusing the discussion on the amplitude alone is thus justified.

The small deviation of the two areas presented in figure 5.17 is of course explained by the deviation of the actual peak shape. The experimental area is systematically smaller which we attribute to the crossing of the Fermi energy which cuts the spectrum off and reduces the area in the vicinity of E_F . However, this deviation is very small and an artifact, therefore the amplitude is sufficient even to discuss the numerical evaluation of the compound feature of the Se 4*p* bands.

Analysis of the substructure of the spectral features of the chalcogen *p* bands.

To gain insight into the substructure of the spectral peaks originating from chalcogen *p* bands (two spin-orbit split p_x , p_y derived bands and a p_z band, see, e. g., reference [66]) we apply the multi Gaussian fit method discussed in addendum A.1.1–b. Following our findings in that appendix we use the superposition of two Gaussians for both TiTe₂ and TiSe₂; typical spectra and fits are presented there, too. These fits are manually checked for consistency and the parameters of the fits as well as the corresponding uncertainties yield a set of temperature dependent data. We define two spectral features, peak A and B, as shown for TiTe₂ in figure 5.3b (section 5.1.1) and analogously for TiSe₂ the

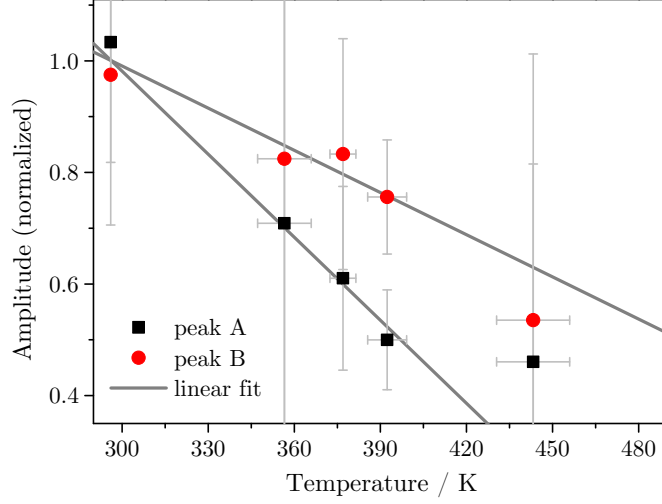
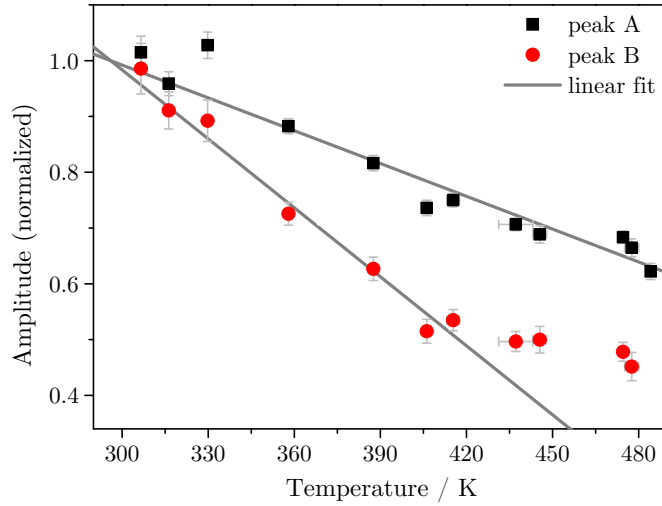

 (a) Amplitude of the Se $4p$ bands of $1T$ -TiSe $_2$.

 (b) Amplitude of the Te $5p$ bands of $1T$ -TiTe $_2$.

Figure 5.18: Amplitude of the two chalcogen p bands (peak A and B) along a linear fit (lines, error bars are adhered to) as extracted by a double Gaussian fit. The fits for TiSe $_2$ are significantly worse than for TiTe $_2$ because of the overlap of peak A and B in the former case. For TiTe $_2$ the linearity of the amplitude is lost for $T_{\text{linear}} \lesssim 415$ K and a plateau is reached (the linear fit discards this data). This is explained in terms of numerical issues in the text.

two partial peaks forming the asymmetric spectral feature are also labeled A and B for increasing binding energy [see figure A.2a, appendix A.1.1–b]. Figure 5.18 presents the temperature dependence of the amplitude of two sub-bands relative to the room temperature value. Please note, that the uncertainty of both amplitudes is much larger for TiSe₂ than for TiTe₂ which is obviously a consequence of the sub-band overlap—for TiTe₂ two clearly distinguishable features are observed, while for the Se 4*p* bands a broad asymmetric peaks needs to be fit and consequently only a small subset of the fits yields consistent data. This demonstrates nicely, why TiTe₂ is an important reference system for a detailed understanding of the sub-band contributions; the TiSe₂ data is significantly less reliable in this case.

Both TMDCs show considerable differences in the thermal behavior of the two sub-bands featuring temperature coefficients different by a factor of about 2, however, the relative behavior of peak A and B is reversed for both samples—peak A of TiSe₂ behaves like peak B of TiTe₂ and vice versa. Although the thermal behavior observed here seems quite different, the spectral structures are very alike: peak A is attributed to the spin-orbit split p_x , p_y bands, and peak B results from a resonant excitation of a Ti 3*d* band from the p_z band (see section 5.1.1). We need to discuss this surprising deviation in section 5.1.4–d for the interpretation of our data. Please note, that the uncertainties of the TiSe₂ double peak fit are generally very high, i. e. the quality of these data is much worse, than in case of TiTe₂.⁹ The differences in the behavior of both peaks presented here are induced by the rather delicate analysis of the TiSe₂ data and basically emphasize the necessity of a clearer spectral structure, as available for TiTe₂. Especially from the TiTe₂ data we conclude, that we indeed observe a difference in the loss of spectral weight of both spectral features.

Finally, we like to point out the non-linearity observed, especially in case of peak B of TiTe₂, for high temperatures ($T > 415$ K). The normalization to the plateau level is known to introduce non-linearity to otherwise linear data (see section 5.1.2–e), however, this does not seem to be the case here. Yet, only peak B shows such a strong deviation while the temperature dependence of peak A remains virtually linear. Because the normalization procedure modifies all intensities by the same factor, both relative representations should be equally modified. Indeed, a closer look at the background corrected spectra fitted for these data reveals a clear reduction of both peak amplitudes with temperature and no stagnation for peak B. However, because of peak B's stronger loss of spectral weight and the tendency of both peaks to energetically shift closer to each other [see figure 5.21(b)] the two peaks are less defined at higher temperatures and peak B turns into something more like a shoulder of peak A in the spectra. We identify

⁹A weighted fit using the big uncertainties of the amplitude values yields a factor of 2 between the corresponding temperature coefficients. If the individual uncertainties are discarded the line fit yields a temperature coefficient which error is reduced by an order magnitude, i. e. the uncertainty of the fit is significantly reduced. The absolute value of the coefficient of peak A is slightly reduced and of peak B slightly increases, reducing the ratio of both to 1.4.

this deviation in the double Gaussian fits as the source of the observed stagnancy—the incomparable data for $T > T_{\text{linear}}$ is discarded for the interpretation of the experiments.

The temperature coefficients defined by the linear fits presented in figure 5.18 are summarized in table 5.5 in section 5.1.4–d. The data show, that the temperature dependence of the amplitude of peak B of TiSe_2 agrees within the errors with the corresponding feature of TiTe_2 . Peak A of TiSe_2 , however, clearly exhibits a significantly enhanced loss of intensity with temperature. We attribute this to the additional reduction of intensity of peak A in case of TiSe_2 , because of thermal broadening of the Fermi edge—the corresponding spectral feature of TiTe_2 shows a higher energetic separation and is thus less influenced by the Fermi edge.

5.1.4–b Binding Energy of the Chalcogen p Bands

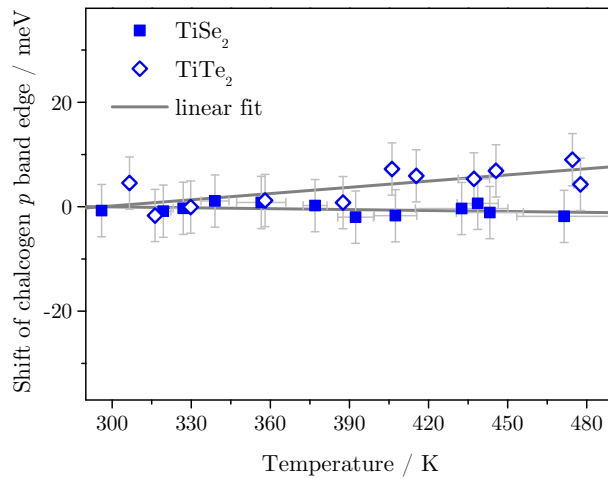


Figure 5.19: Energy of the upper edge of the spectra near E_F corresponding to the high energy flank of the Se $4p$ bands. No dependence on the temperature is observed for TiSe_2 within error bars. Line fits are included.

To understand the thermal modification of the flank of the chalcogen p bands, we need to analyze the high energy cutoff of the spectra. The cutoff is defined by the intersection of the chalcogen p band of the lowest binding energy with with the Fermi edge. It is estimated, using the numerical analysis approach as described in appendix A.1.1, and its thermal behavior is shown in figure 5.19 both for $1T$ - TiSe_2 and $1T$ - TiTe_2 . The spectral features associated with the chalcogen p bands exhibit a rather complex substructure (see the introduction of this section) which cannot be energetically resolved. In case of TiSe_2 an asymmetric Se $4p$ feature is observed, which is actually a superposition of all three contributions. The substructure is considered later in this subsection where we present multi peak fits of the chalcogen p bands and compare them to a center of mass estimation

for TiSe₂. The data on the cutoff presented here is also interesting in context of section 5.1.4–c which focuses on the influences of the thermal Fermi edge broadening on the analysis of the energetic positions of the peaks—the energy of the cutoff is basically the energy of the p band of the lowest binding energy modified by the Fermi edge.

Why do we investigate the thermal modification of the upper flank here, if more reliable data on the actual energies of the chalcogen p bands are also discussed in this section? The energetic position of the high energy cutoff is a good measure for gaining an overview of the thermal behavior of the chalcogen p bands binding energies. It is probably the spectral signature which is the most simple and least prone to details of the spectral structure—the actual band structure is modified by, e. g., the stoichiometry of the samples, especially in the energetic region of the Fermi level [11, 78, 166]. Great care has to be exercised when performing a fit of features close to the Fermi-energy [14]. Therefore, the multi peak fit and the calculation of the center of mass of the chalcogen p bands is intrinsically susceptible to the discussed effects; the high energy cutoff, which basically marks the energy the Fermi level, is less influenced. However, the opening of a band gap, for example, can be well observed using just this characteristic and its simplicity yields very reliable data.

Data on the energetic position of the high energy cutoff is very instructive considering the thermal modification thereof upon cooling of the sample. For 1T-TiSe₂ this flank is known to undergo a shift upon the transition into the low temperature CDW phase [7]. Section 5.3 investigates this behavior in detail and a comparable set of data above room temperature is provided here in figure 5.19 (squares).

The relative energy of the cutoff is virtually constant for TiSe₂ and varies in a range of about ± 1.6 meV, which is very small, especially considering the error of ± 5 meV for these data. A linear fit yields a temperature coefficient of approximately -6×10^{-3} meV K⁻¹. This is all the more obvious, if these data are compared to the temperature behavior of the work function in section 5.1.3, because figure 5.15 uses the same range of the energy scale, i. e. the energetic shifts of both features is directly comparable. We conclude, that the cutoff of the Se $4p$ bands does not exhibit any shift upon heating of the sample—in striking contrast to the cooling experiments shown in section 5.3. Please note, that an increase of energy cannot be observed using the flank center of the Se $4p$ bands, because of the intersection with E_F which fixes the observed energy—we compare this to the case of TiTe₂ shortly.

Additionally, figure 5.19 contains similar data acquired for TiTe₂ (diamonds). These data show a small increase of the high energy cutoff with temperature with a corresponding temperature coefficient of $(40 \pm 13) \times 10^{-3}$ meV K⁻¹. This means, considering the absolute values, that in case of TiTe₂ the thermal shift of the cutoff is about 6.7 times larger than for TiSe₂. The work function shows a temperature coefficient of about 200×10^{-3} meV K⁻¹ [see table 5.3, section 5.1.3], 5 times the value observed for the energetic shift of the cutoff. The cutoff of TiTe₂ therefore exhibits a clear, yet, small temperature dependence leading to an increase of energy of only $\Delta(E - E_F) \approx 7.2$ meV

for a temperature increase of about 170 K.

We conclude, that in case of the TiTe_2 data a real shift of the high energy cutoff is observed, which seems to be a difference with respect to our observation for TiSe_2 . Considering that the TiTe_2 spectra are acquired at a different emission angle which leads to a slightly higher binding energy of peak A with respect to the TiSe_2 data, the separation of peak A from E_F might just be big enough to actually observe an upward shift with increasing temperature. A closer look at the spectra shown in figure 5.3(a) in section 5.1.1 reveals a clear shift of the mean peak position of the Se $4p$ bands feature by about -40 meV to lower values of $E - E_F$ and also for TiTe_2 even the naked eye suggests a shift of the chalcogen p bands to higher binding energy. In fact, the higher energetic resolution—and to some degree also the higher binding energy of peak A—in case of the TiTe_2 spectra leads to a perceived shift of the broadened peak flank and the broadened Fermi edge, the broadening of peak A further enhancing the effect. This cannot be resolved for TiSe_2 because of the inferior spectral resolution (we come to this difference in more detail in section 5.1.4–c).

In summary, the expected consistency of the energetic position of the high energy cutoff of the spectra is supported by our experimental data. Small deviations as observe in case of TiTe_2 can be attributed to thermal broadening, the effect thereof much less than the strong energy shifts observed upon the phase transition at low temperatures (see section 5.3). Our analysis of the detailed thermal behavior of the substructure of the chalcogen p bands is complicated by the broadening of the Fermi edge. It is thus necessary to take a careful look at the complex interplay of the three partial bands forming the chalcogen p features, their intersection with E_F , thermal broadening, and even the behavior of the amplitudes (see section 5.1.4–a) to understand the observed behavior—not only at the high energy cutoff, but of the whole set of sub-bands. With respect to binding energy this is done in the remainder of this section.

The energetic shift of the chalcogen p bands is observed as a clear shift of the center of mass of the spectral features in temperature dependent spectra. Figure 5.20 shows such data for TiSe_2 . Spectra at different temperatures (black: room, red: higher temperature) are shown in the inset of the figure. By rescaling of both to the same amplitude the spectral changes are emphasized. We observe a broadening of the Fermi edge which we will discuss shortly and a shift of the low energy flank of the Se $4p$ bands to higher binding energy. The TiSe_2 data are, however, not conclusive: the observed modification is compatible with a broadening of the spectral feature which is cutoff by the Fermi edge, but also with an actual energetic shift of the bands involved. In this context the TiTe_2 spectra may provide valuable input as peak B is not influenced by the Fermi edge.

The binding energy of the spectral features is investigated here to provide a complete picture of the thermal modifications. These data contribute to the interpretation of the

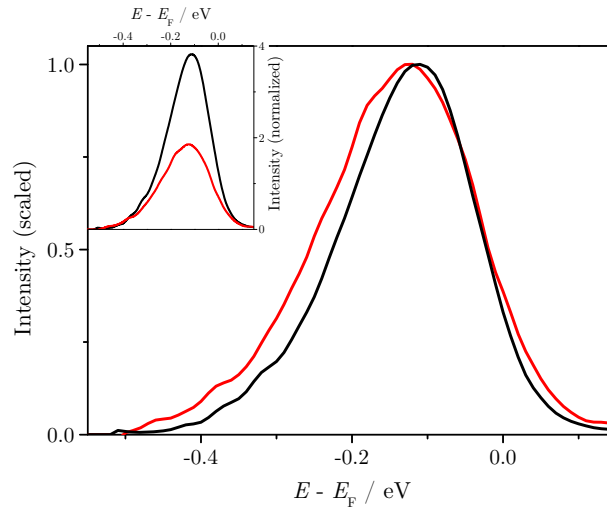
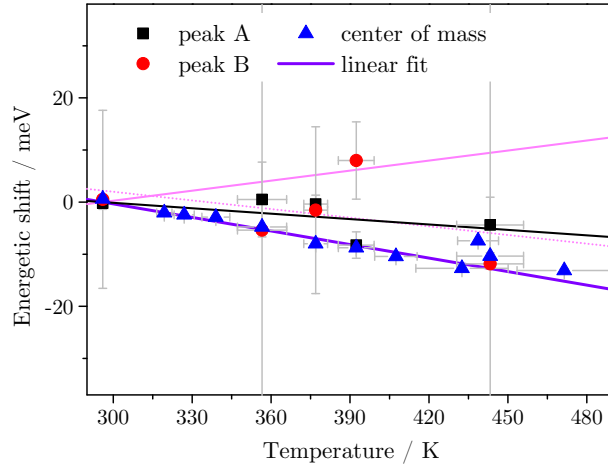


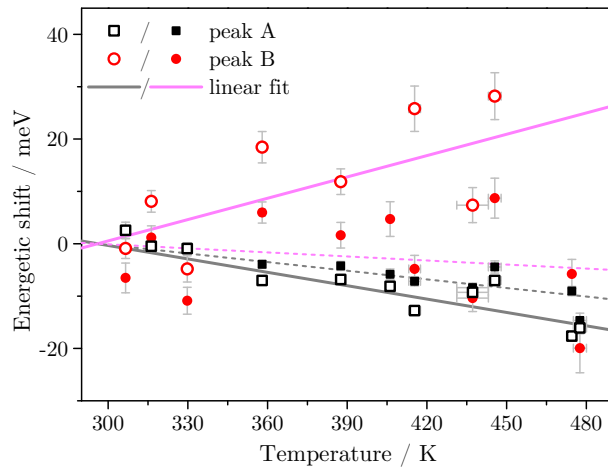
Figure 5.20: Spectra acquired at room temperature ($T = 296$ K, black) and at $T = 443$ K (red) are shown in the inset. The main figure presents these data scaled for a similar amplitude, visualizing the energetic shift of the center of mass of the peak to higher binding energy with temperature.

observed changes of the peak of the Se 4*p* bands given in section 5.1.4–d in a qualitative manner. We like to point out, that neither the binding energy of the center of mass, nor that of the substructure is suitable for defining an instantaneous sample temperature.

The experimental spectra shown in figure 5.3(b) in section 5.1.1 clearly show a small—yet, visible to the naked eye—energetic shift to higher binding energy of peak B. After Shirley background correction this shift vanishes and the binding energy seems to be constant or to decrease very slightly which is observed for the extracted energies provided by figure 5.21(b) [see also figure A.2(b) in addendum A.1.1–b]. This emphasizes a problem arising for the definition of the binding energies here. The thermal changes, if any, are rather small and the energy of the spectral features is additionally modified by the spectral background of secondary electrons (see appendix A.1.1). The intensity of this background signal increases with binding energy, reaching a maximum at the low energy cutoff. Additionally, the plateau observed in the spectra is dominated by indirect, phonon-assisted photoelectron transitions (see section 5.1.2–d) which yield a distinct temperature dependence of the plateau. If a spectral structure is overlaid by a spectral background which increase to higher binding energies, the structure shifts in this direction, too. The shift of peak B may therefore be a consequence of the intensity increase of the plateau. The Shirley background correction compensates for this effect, however, the correction is empirical and may therefore also modify the real binding energies. A small shift to higher binding energies or uniformity agrees with the background corrected data, as we see in the following, which seems reasonable considering these possible modifications.



(a) Energy of the center of the Se $4p$ bands of $1T$ - TiSe_2 .



(b) Energy of the center of the Te $5p$ bands of $1T$ - TiTe_2 .

Figure 5.21: The temperature dependence of the relative energy of peak A and B is defined by the center energy of a double Gaussian fit (full symbols) and referenced to room temperature. Linear fits are included (lines). For the TiTe_2 data in (b) a fit by two separated single Gaussians (open symbols, full line, see appendix A.1.1–b) is compared to a double Gaussian fit (full symbols, dashed line). For TiSe_2 a fit omitting the individual uncertainties [see discussion of figure 5.24(a)] is included as well (dotted line).

Figure 5.21(b) includes two different fits, the double Gaussian fit (full symbols) and a fit by two single Gaussians (open symbols) as described in appendix A.1.1–b. Qualitatively, the double Gaussian seems to fit the spectra better at high temperatures, while the single Gaussian fits agree better to the data near room temperature, although the latter is relevant especially in case of peak A. The single Gaussian fit seems to overestimate the energy of peak B for higher temperatures, i. e. the slope of the full magenta line fit may be too steep. The data for TiSe₂ and TiTe₂, as presented in figure 5.21, unambiguously supports an increase of binding energy of peak A (gray line fits), which can be understood in context of the broadening of the Fermi edge of the spectrum (see section 5.1.4–d). Please note, that again the single Gaussian fit overestimates the energy of peak A for TiTe₂, i. e. the peak center seems to be shifted into the spectrum, away from the cutoff. In this case the double Gaussian fits very nicely at higher temperatures. We conclude, that our data supports a vanishing or small negative temperature coefficient for peak B which is in line with our interpretation in section 5.1.4–d.

The TiSe₂ data presented in figure 5.21(a) include a numerical center of mass calculation which shows the downward shift of the Se 4*p* bands as observed in figure 5.20. While peak A exhibits a clear shift to higher binding energy, the quality of the data for peak B is not sufficient to conclusively decide on a possible energetic shift. We included two fits, one adhering to the uncertainties of the individual data points (full line) and one omitting them (dotted line). We see when discussing the broadening of the peaks [see figure 5.24(a)] that these uncertainties are rather questionable considering their relevance. The thermal behavior of peak B may therefore very well be in accordance with the observation for TiTe₂.

Before we conclude our investigation, we like to discuss an additional contribution to the increase of binding energy of the center of mass of the Se 4*p* bands in case of TiSe₂. In section 5.1.4–a we presented data on the temperature dependence of the amplitude of the substructure of the Se 4*p* bands and observed a significantly stronger suppression of peak A—the feature closer to the Fermi energy. Figure 5.22 compares two spectra at low (squares) and high (circles) temperature to simulated spectra. The simulations are superpositions of two Gaussians which parameters are derived by the double Gaussian fits applied in this section, however, the center energies of the simulation for $T = 443$ K (red) are fixed at the value fitted for room temperature (black) version, i. e. the FWHM and amplitude of the corresponding fit is used, but the energy is fixed at the room temperature value.

We observe, that the change in peak width in combination with the asymmetric reduction of spectral weight alone leads to a shift of the peak maximum position (see also inset), however, and the calculation of the center of mass yields a shift of about 25 % of the experimentally observed change. Normalization to the amplitude (inset) reveals that the simulated curve at high temperature broadens in both signs of the energy, while the experimental data is cutoff at the Fermi energy (see figure 5.20) leading to an articulate asymmetry in the broadening—as we see in section 5.1.4–c the temperature dependence

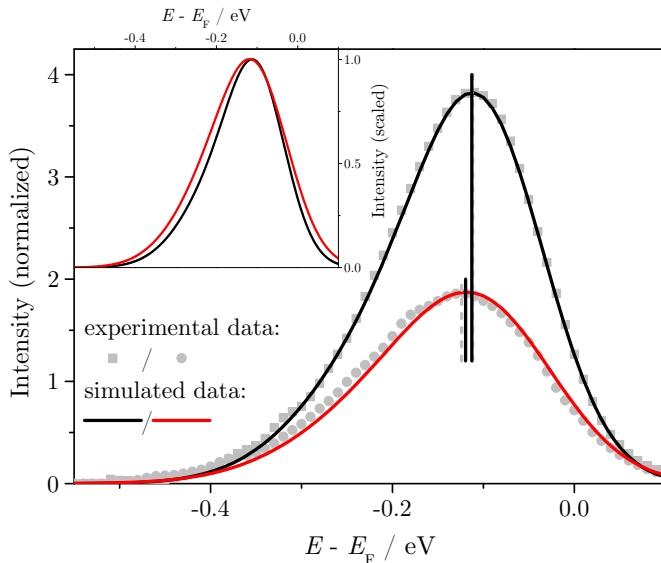


Figure 5.22: Simulated (lines) spectra are compared to experimental (symbols) data. Two Gaussians of the experimentally observed FWHM and area at room temperature and 443 K at a fixed central energy of the room temperature experiment are summed. The inset emphasizes the energetic shift by rescaling.

of the Fermi edge itself contributes to the intensity loss of peak A, as well as its energetic shift. The energy of the amplitude of the Se 4*p* bands is a better measure of the energetic shift induced by the asymmetric loss of peak intensity. It is fitted by a single Gaussian in the energy range of about ± 0.15 eV and yields a shift of about 56 % of the experimental observation. These fitted amplitude energies are included for the simulations (full lines) and the experiment (dotted lines) in figure 5.22.

These simulations show a reduction of $E - E_F$ of the Se 4*p* bands induced exclusively by the asymmetric loss of intensity which basically leads to an increase of intensity outside of the center of peak A. In other words: the shift of the binding energy of the Se 4*p* bands to higher values is partially—by about 50 %—explained by this artifact.

In conclusion, we observe an increase of binding energy with temperature for peak A. The proximity to the Fermi energy suggest an influence thereof as discussed in section 5.1.4-c and our interpretation consequently focuses on the modifications of peak A by the broadening of the Fermi edge. The data for peak B is rather inconclusive, however, the more reliable data indicate either a slight increase of binding energy or a virtually constant energy with temperature. The simulation presented in figure 5.22 further supports a very small or vanishing temperature coefficient for peak B, because the additional energetic shift needed to explain the magnitude of the measured energy shift of the numerical center of mass is provided by the difference in suppression of the spectral intensity of both

peaks. Please note, that the difficulties in identifying a clear temperature dependence even for the well resolved peak B of TiTe₂ disqualify the binding energy as a means of temperature definition.

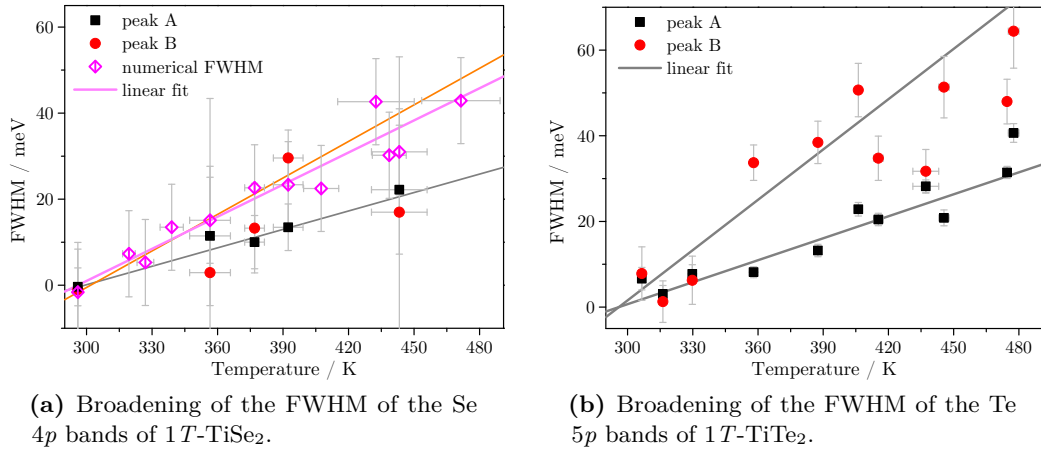


Figure 5.23: Temperature dependence of the FWHM of peak A and B extracted by a double Gaussian fit (full symbols), given relative to the room temperature value. Linear fits are included (lines). (a) also includes numerically fitted data (open diamonds) which exhibit better consistency.

Thermal broadening of the chalcogen p bands is probably the most straightforward thermal modification of the photoemission spectra (refer to section 5.1.4–d for details). The FWHM is easily evaluated numerically for the background corrected TiSe₂ spectra and the corresponding data is presented in figure 5.23(a) as diamonds. Although the uncertainty of such data is worse than for other energy derived data, like, for instance, the binding energies, because two energies need to be evaluated, the increase of FWHM is clearly observed and well fitted by a line (magenta).

The fit of the substructure of the chalcogen p bands is less defined for peak B (see figure 5.23) which is the weaker spectral feature. For the TiSe₂ spectra the FWHM of peak B varies strongly rendering a conclusive statement on its temperature coefficient futile—these data is in agreement with a stronger or similar temperature coefficient with respect to peak A. The scatter of the data is, again, induced by the overlap of both peaks within the broad spectral feature of the Se 4p bands. Consequently, the TiTe₂ data exhibit more scatter at high temperatures for peak B, because due to broadening and energetic shift both peaks become increasingly less separated. Please note, that the numerical method cannot be applied to the TiTe₂ data, because both features are not separated sufficiently with respect to their binding energies [see background corrected

spectrum in figure A.2(b) in appendix A.1.1–b], i. e. it is not possible to extract the half-intensity of both flanks of each peak.

Although, the absolute values of the broadening given in figure 5.23 suggest a stronger effect for peak B, this spectral feature is also broader to begin with. Figure 5.24 presents the ratio of the broadening of the FWHM with respect to the room temperature value. We estimate a temperature coefficient of about $1 \times 10^{-3} \text{ K}^{-1}$ [see table 5.6 in section 5.1.4–d] which is virtually identical not only for peak A and B, but also for both TMDCs investigated here. Both sub-figures include a line fit for peak A (gray) which also agrees well for peak B, because the temperature coefficients deviate by only about $1 \times 10^{-5} \text{ K}^{-1}$. The fit of peak B of TiSe_2 (orange) shows a significantly steeper slope if the fit adheres to the individual uncertainties of the data. However, these errors depend, amongst other origins, on slight deviations in the quality of the smoothing of the spectra and the corresponding remaining noise. The severe differences in uncertainty of subsequent spectra is thus most likely an artifact. If the uncertainties are omitted for the fit altogether, a slightly smaller temperature coefficient with respect to peak A (dashed) is observed. The rather delicate double Gaussian fit in case of the Se $4p$ bands therefore does not allow for assignment of a reliable temperature coefficient of peak B, however, there is no indication for any considerable deviation from the thermal behavior of peak A.

The relative temperature dependence of the numerical FWHM of TiSe_2 [not shown, see figure 5.23(a)] reveals a bigger value of the temperature coefficient which is evaluated to be $(1.19 \pm 0.14) \times 10^{-3} \text{ K}^{-1}$ —the corresponding line fit resides in between the full orange and the gray line in figure 5.24(a). The deviation of these data is explained by the substructure of the spectral feature of the Se $4p$ bands. The superposition of sub-bands which show different energetic shifts (see earlier in this section) obviously leads to a modification of its FWHM.

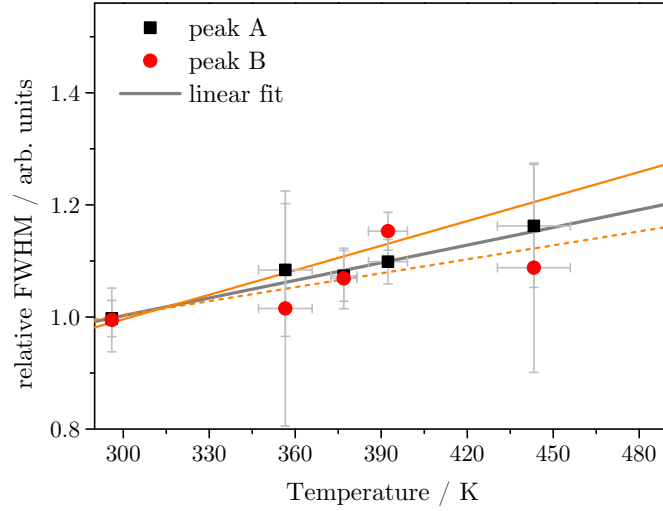
Overall, we observe good agreement of the substructure analysis of both samples. The ratio of the broadening of the FWHM with respect to room temperature of both evaluated spectral peaks (A and B) is virtually identical for both TMDCs (TiSe_2 and TiTe_2) and about $1 \times 10^{-3} \text{ K}^{-1}$.

5.1.4–c The Thermal Broadening of the Fermi Edge

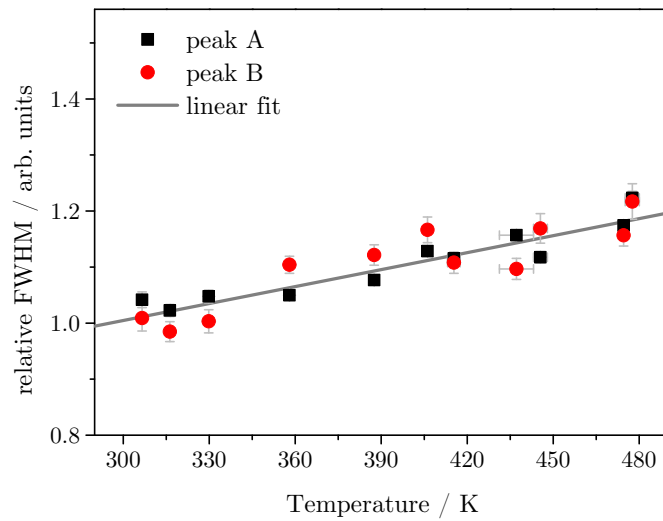
The Fermi edge of a photoemission spectrum features a characteristic dependence on temperature which is described by the Fermi-Dirac distribution $f_{\text{FD}}(E)$ [110]:

$$f_{\text{FD}}(E) = \left(1 + e^{\frac{E-E_{\text{F}}}{k_{\text{B}}T}} \right)^{-1}, \quad (5.7)$$

with temperature T and the Boltzmann constant k_{B} . At very low temperatures the Fermi edge becomes step-like, yielding a sharp cutoff, for increasing temperature this cutoff broadens and the Fermi edge reveals the typical S-shape of a sigmoid function. This thermal broadening leads to an increase of spectral intensity above E_{F} within the



(a) Relative FWHM of the Se $4p$ bands of $1T$ -TiSe₂.



(b) Relative FWHM of the Te $5p$ bands of $1T$ -TiTe₂.

Figure 5.24: The data presented in figure 5.23 is referenced to the room temperature value, i.e. the ratio of the FWHM with respect to T_{RT} is given. Line fits are included for peak A gray. For TiSe₂ a fit of peak B is given adhering full line and omitting dashed line the individual uncertainties of the data.

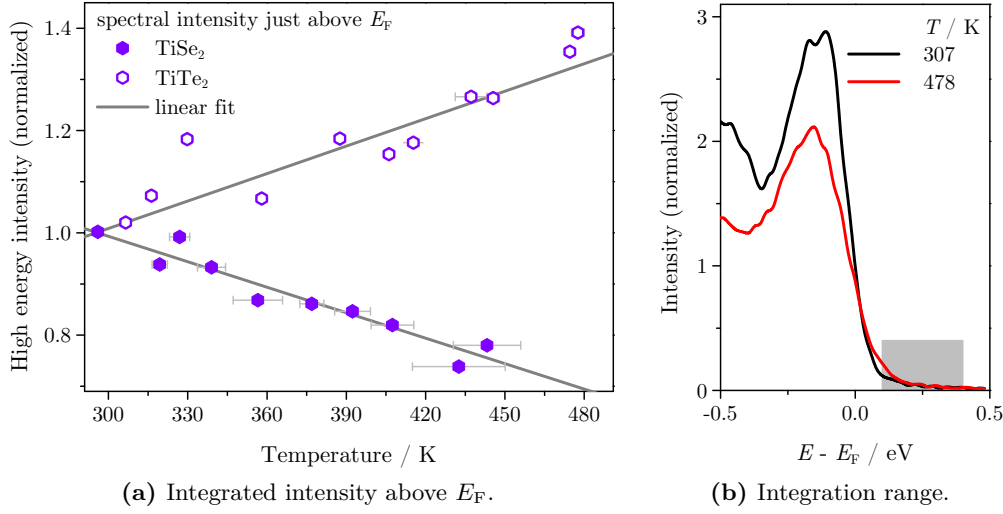


Figure 5.25: 5.25a Relative change of the spectral intensity observed above the Fermi energy for TiSe₂ (filled hexagons) and TiTe₂ (open hexagons). The spectra are normalized to the plateau level. Linear fits are included (line). 5.25b Detail of TiTe₂ spectra acquired at low and high temperature. The intensity is integrated in a fluence range of 0.1 eV to 0.4 eV for comparison to section 5.2.2. A similar offset is used for TiSe₂, as no crossing appears in this case.

high energy cutoff flank of the spectra as visualized by the gray box in figure 5.25(b). A closer look at this spectral range is instructive for two reasons: *(i)* comparison to laser induced effects, and *(ii)* estimation of the influence of the thermal broadening of the Fermi edge on the spectral characteristics. Our investigation of laser fluence induced spectral changes discussed in section 5.2 revealed a very significant signal in this energetic range, especially in the 2D representation corresponding to the thermal data shown in figure 5.2 in section 5.1. However, the temperature coefficient of the TiTe₂ data in figure 5.25(a) is only $(0.96 \pm 0.02) \times 10^{-3} \text{ K}^{-1}$. The data presented here are a reference for the fluence dependent experiment and clearly shows, that the strong enhancement of signal above E_F is not thermally induced (see discussion in section 5.2). Consequently, the coefficient for these fluence dependent data is much bigger, about $(11 \pm 1) \times 10^{-3} \text{ K}^{-1}$ [after stabilization, $(7.7 \pm 0.7) \times 10^{-3} \text{ K}^{-1}$ during the fluence increase], i. e. the fluence induced effect observed for TiSe₂ is about 8 to 11 times stronger, than the thermal effect discussed here. Such a small thermally induced effect is most likely concealed by the worse energy resolution and the thermal broadening of the Se 4*p* bands.

For TiSe₂ the intensity in the chosen energy range decreases with temperature [see figure 5.25(a)], while for TiTe₂ a small increase of the relative intensity is observed. This is no indication for a systematic difference of both TMDCs, but rather a consequence of

the difference in spectral resolution (see section 5.1). Figure 5.3 in section 5.1.1 shows a series of spectra acquired for TiSe₂ and TiTe₂ for increasing temperature. The better energetic resolution of the TiTe₂ data renders the broadening of the Fermi edge visible which leads to the observed increase in signal just above the room temperature Fermi edge for spectra at higher temperatures which is observed by the increase of intensity in figure 5.25(a). The lower resolution of the TiSe₂ data conceals this broadening and because the amplitude of the Se 4*p* bands is decreasing with temperature, the loss of intensity within the high energy flank of the spectra leads to the decrease observed in figure 5.25(a) for TiSe₂. The Te 5*p* bands are shifted by about -50 meV with respect to the Se 4*p* bands which additionally renders the Fermi edge broadening more accessible. Please note, that this thermal broadening yields a photoemission signal just above the Fermi energy much smaller than what is induced by the laser in section 5.2—the latter effect is not thermally induced and the data presented here will be relevant in the discussion presented there.

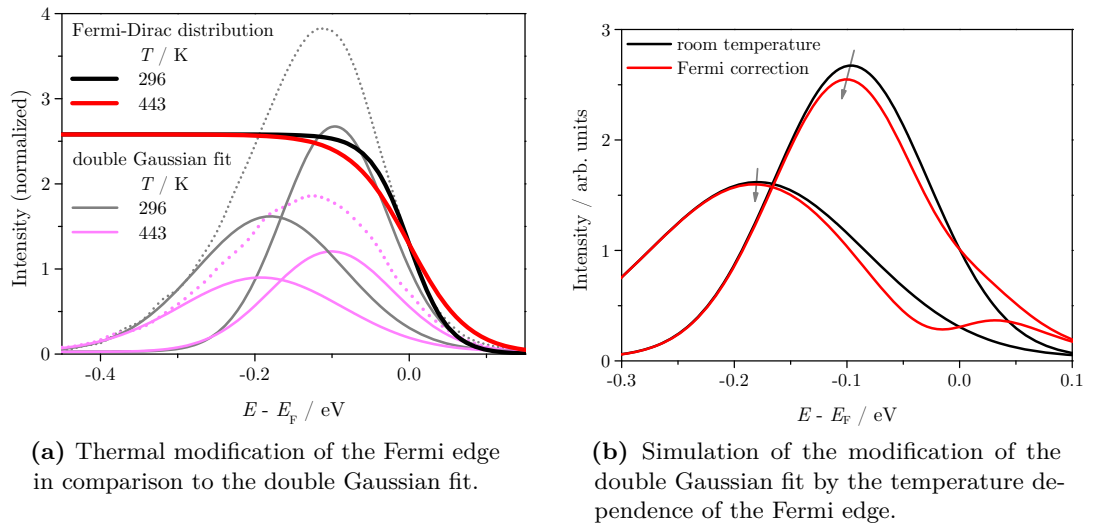


Figure 5.26: (a) Comparison of the Fermi-Dirac distribution at room temperature and at 443 K to the corresponding double Gaussian fit. (b) Simulation of the influence of the broadened Fermi-Dirac distribution on both peaks by subtraction of the difference of this distribution at high and low temperature from the Gaussians corresponding to peak A and B (black: fitted Gaussians at room temperature, red: after subtraction of the differences in the Fermi edge itself).

However, these data demonstrate the necessity to include broadening of the Fermi edge into the discussion of spectral characteristics in the vicinity of E_F . Please note, that the Shirley background correction used here cannot include a correction for the Fermi edge (see appendix A.1.1). The thermal broadening of the Fermi-Dirac distribution needs to be considered especially for spectral characteristics closest to E_F , like, peak A of our

double Gaussian fit. Figure 5.26(a) shows the Fermi-Dirac distribution as calculated using equation (5.7) at room (black) and a typical high temperature (red) alongside background corrected spectra of TiSe_2 (dotted) and the corresponding double Gaussian fits (gray, magenta). This representation reveals, that thermal broadening of the Fermi edge alone explains the slight increase of intensity just above the Fermi energy with increasing temperature.

Furthermore, the intensity for energies up to about -200 meV below E_F is considerably reduced. Especially peak A is thus modified considering its amplitude and, because of the asymmetric reduction of intensity which influences the high energy flank of peak A stronger than its low energy flank, an additional change of the binding energy is also expected. A direct influence on the peak's FWHM is not expected—indirectly the change of binding energy might alter the FWHM of peak A which is not observed at all in the data presented in figure 5.24. Because peak A lies within the energy range of maximum thermal modification of the Fermi level, especially the upper edge of this peak is reduced. If the intensity modification close to E_F is superimposed on the multi peak fit in figure 5.26(a), it can quantitatively yield the whole observed shift of peak A. Figure 5.26(b) presents such a calculation. Here, the difference of the Fermi-Dirac distribution at 443 K and room temperature is subtracted from the double Gaussian fit. Depending on the actual maximum height of the Fermi edge, which is assumed quite high in this case, the fit at room temperature (black) features the observed energetic shift of peak A after this correction (red). The position of peak B is, however, virtually unchanged [$\Delta(E - E_F) < -1$ meV in case the shift of peak A is fully established]. Thermal broadening of the Fermi edge thus does not influence peak B significantly. This results in a net shift to higher binding energy—and, of course, a modification of its amplitude which manifests in the rather big temperature coefficient thereof of peak A. In section 5.1.4–d we thus need to consider the broadening of the Fermi edge for the discussion of the thermal behavior of the amplitude and binding energy especially of all spectral features sufficiently close to E_F , which is in our case peak A of the double Gaussian fit.

5.1.4–d Interpretation of the Origin of the Thermal Modification of the Chalcogen p Bands

In this section we focus on the interpretation of the observed thermal modifications of the chalcogen p bands, which are the FWHM, the binding energy and the amplitude. We discuss these temperature dependences with respect to their physical origin. Our goal is to show that all observed effects are indeed thermally induced, which is important to discriminate laser induced modifications in section 5.2. Please note, that the substructure analysis is not usable to quantitatively define a scale for the instantaneous sample temperature, because these fitting methods are much too delicate, resulting in a rather bad quality of the evaluated data. We use the numerical methods for this purpose and find the amplitude of the chalcogen p bands to be the most reliable characteristic. In

combination with the thermal behavior of the work function (see section 5.1.3) we derive a set of two spectral characteristics to monitor the relative temperature changes of the two TMDCs investigated in this work.

All relevant temperature coefficients assigned to the chalcogen p bands investigated in this section are summarized in tables 5.5, 5.6, and 5.7. The data on the amplitude is referred to a room temperature value of $T_{\text{RT}} = 296$ K which is used throughout this work. This ensures comparability to all photoemission experiments discussed. For the FWHM both the absolute relative shift, Δw , and the ratio with respect to the room temperature value, $\Delta \tilde{w}_{\text{RT}}$, are given, because the latter demonstrates that actually all peaks broaden thermally by the same factor, while the absolute increase of FWHM enables us to quantitatively compare our observation to calculations within the Debye model. The energetic shift, E_c , is provided to complete these data and is employed only qualitatively in the following discussion.

Thermal broadening of the spectral structures is the most straightforward modification of the photoemission spectra and we shall therefore begin our discussion with the FWHM data presented in section 5.1.4–b and the corresponding temperature coefficients shown in table 5.6. In general, three processes contribute to the broadening of a spectral feature: *(i)* electron–electron, *(ii)* impurity or defect, and *(iii)* electron–phonon scattering [241]. The first two contributions can be modeled by a constant, temperature independent term $\Gamma_{\text{const.}}$, because the electron–electron interaction leads to negligible thermal broadening and the impurity contribution acts mainly in terms of momentum integration similar to the limited angular resolution of the setup [86, 241].

In the limit of sufficiently high temperature ($T \gg \Theta_{\text{D}}$, with the Debye temperature $\Theta_{\text{D}} = 221$ K for TiSe₂ [83]) the temperature dependence of the electron–phonon scattering induced broadening is described within the Debye model by:

$$\Gamma_{\text{e-ph}} = 2\pi\lambda k_{\text{B}}T, \quad (5.8)$$

with the Boltzmann constant, k_{B} , and the electron–phonon coupling constant, λ [86, 241–243]. Thermal broadening of the spectral peaks is therefore expected to be linear in temperature T with a temperature coefficient $\Delta w = 2\pi\lambda k_{\text{B}}$ which is defined by the electron–phonon coupling constant alone. Please note, that only the electron–phonon interaction leads to a temperature dependent broadening, because all other contributions are virtually constant. Indeed, our experimental data supports such a linearity.

To analyze, whether the thermal broadening of the spectral structures is indeed explained by electron–phonon scattering, we calculate the electron–phonon coupling parameter using the temperature coefficients of the FWHM, Δw , extracted from our experimental data and compiled in table 5.6. Using equation (5.8) we derive:

$$\lambda = \frac{\Delta w}{2\pi k_{\text{B}}}.$$

Table 5.5: The temperature coefficients of the amplitude defined by line fits of data extracted by a double Gaussian fit (peak A and B) and the numerical method. The table contains the coefficient of the ratio with respect to room temperature ($T_{\text{RT}} = 296 \text{ K}$), $\Delta\tilde{I}_{\text{max,RT}}$.

sample	$\Delta\tilde{I}_{\text{max,RT}} / 10^{-3} \text{ K}^{-1}$		
	peak A	peak B	numerical
TiSe ₂	-5.0 ± 2.2	-2.5 ± 2.8	-3.56 ± 0.17
TiTe ₂	-1.96 ± 0.09	-4.12 ± 0.26	

Table 5.6: The temperature coefficients of the FWHM defined by line fits of data extracted by a double Gaussian fit (peak A and B) and the numerical method. The fit of peak B of TiSe₂ is additionally performed omitting the uncertainties of the individual FWHM values (brackets). The table contains the coefficient of the absolute FWHMs, Δw , and for the ratio with respect to room temperature, $\Delta\tilde{w}_{\text{RT}}$.

sample	$\Delta\tilde{w}_{\text{RT}} / 10^{-3} \text{ K}^{-1}$		
	peak A	peak B	numerical
TiSe ₂	1.05 ± 0.45	1.46 ± 0.66 (0.83 ± 0.47)	1.19 ± 0.14
TiTe ₂	1.01 ± 0.05	1.02 ± 0.11	

sample	$\Delta w / 10^{-5} \text{ eV K}^{-1}$		
	peak A	peak B	numerical
TiSe ₂	14.3 ± 6.1	28.3 ± 12.7 (16.0 ± 9.2)	24.9 ± 3.0
TiTe ₂	17.1 ± 1.7	39.1 ± 5.1	

Table 5.7: The temperature coefficients of the energy $E - E_{\text{F}}$ of the peak center, E_{c} , defined by line fits of data extracted by a double Gaussian fit (peak A and B) and the numerical method. The fit of peak B of TiSe₂ is additionally performed omitting the uncertainties of the individual binding energies (brackets). For TiTe₂ the coefficients fitted by a single Gaussian fit are given in square brackets

sample	$\Delta E_{\text{c}} / 10^{-5} \text{ eV K}^{-1}$		
	peak A	peak B	numerical
TiSe ₂	-3.5 ± 2.0	6.4 ± 18.9 (-5.5 ± 7.2)	-8.7 ± 0.1
TiTe ₂	-5.5 ± 0.8 [-8.5 ± 0.5]	-2.6 ± 1.5 [13.6 ± 2.0]	

Table 5.8: The electron–phonon coupling constant, λ , is calculated from the temperature coefficient of the FWHM, Δw , given in table 5.6 using equation (5.8). For the additional “numerical” value in table 5.6 we derive $\lambda = 0.46 \pm 0.06$ for TiSe₂.

sample	λ	
	peak A	peak B
TiSe ₂	0.26 ± 0.11	0.52 ± 0.23 (0.30 ± 0.17)
TiTe ₂	0.32 ± 0.03	0.72 ± 0.09

Table 5.8 shows the values of the electron–phonon coupling constant calculated from our experimental data. First of all, we like to point out, that the values for peak B are generally more reliable than for peak A, because the binding energy of the latter is closer to the Fermi edge, i. e. peak A tends to be partially cutoff by E_F . The corresponding modification of the FWHM is not compensated (see discussion in section 5.1.4–d). Although the agreement of the values of λ in case of TiSe₂ is still sufficiently well considering the uncertainties, the disagreement of the values for peak A and B for TiTe₂ is rather significant. We expect the temperature coefficient of the FWHM—and thus the calculated electron–phonon coupling parameter—to be more reliable for peak B, because this spectral feature is less modified by E_F .

Table 2.1 in section 2.1 compiles different values of λ which are reported in different publications; unfortunately, the spread of these data is quite significant. For TiSe₂ values of $\lambda = 0.37$ and 0.8 have been reported. In this case, the higher value is derived using assumptions more complex than the simple Drude model employed here (refer to table 2.1, section 2.1) and we thus expect a better agreement to the smaller value. Indeed, within the uncertainty of the calculations in table 5.8 our data agrees well to $\lambda = 0.37$. Please note, that the value given in brackets in table 5.8 is derived from a different fitting approach. The quality of this fit seems better, as the uncertainty is smaller. Additionally, the agreement of the values of λ is also better. Please note, that using the numerical approach discussed in appendix A.1.1 does, as expected, yield a slightly exaggerated FWHM, as both peaks are superimposed¹⁰. Overall, our experimental data supports the lower value of the reported electron–phonon coupling constants, while a value thereof as high as 0.8 is not reproduced within the uncertainties. Please note, that the “numerical” evaluation of the FWHM of the whole, asymmetrically shaped superposition of peak A and B (see caption of table 5.8) overestimates λ —a direct consequence of the dependence of the thermal broadening of the asymmetric spectral feature on the energetic separation of peak A and B. The numerical FWHM value is not suited for comparison to a calculation following equation (5.8), because the temperature dependence of both sub-peaks differs

¹⁰The different thermal behavior of the binding energies of peak A and B (see table 5.7) also modifies the numerically evaluated FWHM of the whole feature.

(see table 5.7).

TiTe₂ exhibits a very similar Debye temperature of $\Theta_D = 225$ K [82] in comparison to TiSe₂. Electron–phonon coupling constants of 0.22, 0.67 and 0.83 are reported, see 2.1 in section 2.1. Here, we expect the two lower values to fit better to our data, as they are derived—via application of a Debye model—from angle-resolved photoemission spectroscopy (ARPES) data. Table 5.8 provides the values of λ for our experiments. Within the uncertainties we find good agreement of the value for peak B to $\lambda = 0.67$. Although the value for peak A is rather small, it does not fit to $\lambda = 0.22$ within the errors. Again, peak A is cutoff by the Fermi edge, i. e. the temperature coefficient of the FWHM is most likely reduced thereby. Instead of assuming two electron–phonon coupling constants for TiTe₂, we find the rather small value observed for peak A to be a strong indication for a severe influence of the Fermi edge, even in case of the well separated spectral features observed for TiTe₂.

In conclusion, the thermal broadening of the spectral features of TiSe₂ and TiTe₂ is well explained using a simple Debye model—at least considering peak B, which is less influenced by the Fermi edge. Using the experimental temperature coefficients of the FWHM we are able to calculate the electron–phonon coupling parameters of these TMDCs and find good agreement to published data. Our data suggests a bigger value of λ for TiTe₂ than for TiSe₂. However, this is to be taken with a grain of salt. Although we can attribute the experimentally observed thermal broadening to electron–phonon scattering using a simple model, our analysis is not sophisticated enough to be conclusive with respect to λ . We do not compensate for the Fermi edge in close proximity to the spectral features (see addendum A.1.1). While our data suggest a bigger value of the electron–phonon coupling constant for TiTe₂, a decision on the actual value is therefore beyond the scope of this work.

Understanding the origin of the thermal shift of the chalcogen p bands is complicated for the whole peak of the Se $4p$ bands and peak A in case of TiTe₂ because of the close proximity to the Fermi energy. The analysis of the TiSe₂ data is additionally complicated by the significant overlap of peak A and B. Even the well separated peak B of the TiTe₂ spectra does not allow for an unambiguous extraction of its energetic shift because of the rather delicate double Gaussian fit involved, as well as the influence of the necessary correction for spectral background (see section 5.1.4–b). There is, to our knowledge, no quantitative data available on the temperature effects on TiSe₂. Our discussion with respect to the observed changes in binding energy therefore focus on a qualitative understanding thereof. We intent to show that such modifications are fully explained by the differences in sample temperature.

In section 5.1.4–b we present data on the thermal modification of the binding energies of the spectral peaks observed for both TMDCs. We derive a clear shift to higher binding energy for the numerical center of mass of the whole feature of the Se $4p$ bands and also

for the substructure feature we named “peak A”. The data for peak B at higher binding energy is inconclusive, but seems compatible with vanishing temperature dependence or a slight decrease of binding energy. Considering analogous temperature dependent photoemission experiments [32] and corresponding calculations [34] for gold, as well as ARPES spectra of copper [33], the behavior observed for our samples is unexpected, because those data show a reduction of the binding energy of the bulk bands. This reduction is understood in terms of the thermal expansion of the sample crystals which induces a linear energy shift [33].

The energetic shift of the center of mass of the broad peak of the Se 4*p* bands is mainly an artifact generated by the different loss of spectral weight of the bands contributing thereto; for a detailed analysis see section 5.1.4–b. However, the shift of peak A, i. e. the contribution of the chalcogen *p_x*, *p_y* derived sub-bands, still features a clear shift to higher binding energy which actually contributes significantly to the shift of the center of mass of the whole spectral peak derived by peaks A and B for TiSe₂. Table 5.7 shows a compilation of the relevant temperature coefficients of the energetic shifts of peak A and B. These data show, that considering the absolute value the temperature dependence of the binding energy of peak A is less than for peak B, i. e. the effect is actually rather small. To understand, why the unexpected shift is observed, we need to consider thermal broadening of the Fermi edge. Figure 5.26 in section 5.1.4–c shows, how the temperature dependent changes of the Fermi-Dirac distribution lead to an intensity reduction mainly within one flank of peak A which results in shift of its center of mass. Knapp et al. [33] found a comparable energetic shift of a bulk band similarly close to E_F for Cu(100) and attributed it, at least partially, to the broadening of the Fermi cutoff, too. They provide a temperature coefficient for the copper feature of $(-5 \pm 1) \times 10^{-5} \text{ eV K}^{-1}$ [33] (the uncertainty is an estimate considering the typical uncertainty of the energy values in this reference and should be considered to be a lower limit) which agrees within the uncertainties very well to our data on both TiSe₂ and TiTe₂. We conclude, that the observed shift of peak A is fully explained by its interaction with the Fermi cutoff.

Peak B, however, is not influenced considerably by the temperature dependence of the Fermi edge. Its thermal behavior is understood if considering the special composition of the SH-2PPE spectra of TiSe₂ and TiTe₂ at a photon energy of $h\nu = 3.18 \text{ eV}$ and the fact that 2PPE maps contributions of unoccupied bands to the photoelectron spectra. Our spectroscopic investigation of both TMDCs in section 4 revealed that the occupied Se 4*p_z*/Te 5*p_z* bands become resonant with an unoccupied Ti 3*d* intermediate band, therefore peak B actually represents a mixture of the occupied chalcogen *p_z* and an unoccupied Ti 3*d* band.

Two interesting temperature dependences of the binding energies of electronic bands need to be considered: (i) experimental data [32, 33] and calculations [34] demonstrate, that the temperature coefficients of the bands increases with binding energy, i. e. only a very small value is expected close to E_F , and (ii) bands with $E - E_F < 0$ generally decrease in binding energy as a consequence of the thermal increase of lattice spacing

while bands with $E - E_F > 0$ show the inverse behavior—the bands therefore tend to shift towards the Fermi energy [33]. Knapp et al. [33] found, that the temperature coefficient of the binding energy of spectral features depends not only on the initial state, but also on all states involved in the photoemission process, i. e. they also observed that those contributions cancel each other. Our experimental observations for peak B indeed is compatible with a very small or vanishing temperature coefficient which is well explained in the context discussed here. A small increase of binding energy is compatible with the expectations for the occupied initial p_z band. However, this change is either very small—which is also expected near the Fermi energy—or vanishes altogether. Considering the excitation path via an unoccupied intermediate band and the rather big scatter of the data for peak B, we prefer to assume a more or less constant binding energy thereof. In conclusion, the observed energetic shift of the Se $4p$ bands are an artifact induced by thermal broadening of the Fermi edge in interplay with the asymmetric changes of the amplitudes of the substructure peaks A and B.

The significant loss of spectral weight of the chalcogen p bands is well described by the decrease of the corresponding spectral amplitude (see appendix A.2.2). Nevertheless, the magnitude of this effect is surprising at first. Particularly with regard to the laser induced modifications discussed in sections 5.2 and 6, which also strongly influence the peaks' amplitude, it is crucial to understand the pure thermal effect to be able to distinguish both contributions—both for the evaluation of an instantaneous sample temperature and the identification of laser induced processes.

We already discussed the increase of the FWHM of the spectral peaks with increasing temperature within this section. Interestingly, the decrease of the amplitude is often much more pronounced which leads to a decrease of the photoemission peak area with temperature [244], i. e. an increase of sample temperature often leads to an actual loss of spectral weight of a feature. The reduction of the amplitude is thus not a mere consequence of the broadening of the FWHM at otherwise constant area. Please note, that we indeed observe a reduction of the area of all chalcogen p bands discussed here (see also figure 5.16 in section 5.1.4-a). The very strong reaction of the peak amplitude on temperature renders this property, as Matzdorf et al. [244] state, in general the lowest order thermal effect.

Comparison to similar data on the temperature dependence of photoemission spectra of gold, copper, and silver single crystals [32, 37, 244] reveals another interesting parallel to our data on $1T$ -TiSe₂ and $1T$ -TiTe₂: for bulk band transitions the amplitude shows a linear temperature dependence—at least in the temperature range investigated in this work—, while surface states exhibit nonlinear behavior [refer to appendix A.3 for data of Ag(111)]. In case of our TMDCs we investigate the chalcogen p bulk bands and indeed our data supports such linear changes.

The temperature coefficients presented in tables 5.5 and 5.6 are extracted from relative

Table 5.9: Temperature coefficients of TiSe₂ similar to tables 5.5 and 5.6, but referred to absolute zero temperature instead of room temperature. Nomenclature as per appendix A.2.1.

$\Delta\tilde{w}_0 / 10^{-3} \text{ K}^{-1}$			
sample	peak A	peak B	numerical
TiSe ₂	1.3 ± 0.1	2.28 ± 0.17	1.83 ± 0.22

$\Delta\tilde{I}_{\text{max},0} / 10^{-3} \text{ K}^{-1}$			
sample	peak A	peak B	numerical
TiSe ₂	-1.25 ± 0.06	-1.78 ± 0.10	-1.72 ± 0.09

data which provide the ratio with respect to the room temperature, T_{RT} , value. Referring the data to T_{RT} is an obvious choice, because the initial state of the sample at the beginning of an experimental series is usually also characterized by the room temperature and is thus used throughout this work. However, direct comparison of the temperature coefficients to literature values requires a reference temperature of 0 K. Please note, that extrapolation to absolute zero temperature is problematic in the context especially of 1T-TiSe₂ because of this system’s peculiar behavior at low temperatures (see addendum A.2.1). Table 5.9 shows the corresponding temperature coefficients referred to $T = 0$ K.

The table enables comparison of $\Delta\tilde{I}_{\text{max},0}$, the temperature coefficient of the amplitude, to corresponding data for Cu(100) provided by Matzdorf et al. [244]. Our experimental data agree in sign and the order of magnitude with those observations for bulk bands. Please note, that the generally higher value of the temperature coefficient of the amplitude (the area) of our data is most likely a consequence of the stronger broadening of the FWHM [$\Delta\tilde{w}_0$ in table 5.9], but the data on the Shockley surface state of the (111) faces of copper, silver, and gold reported by Paniago et al. [37] agree very well with respect to the magnitude for Ag(111) and Au(111). The temperature coefficient of the amplitude is therefore in good agreement to the expectations for other metallic systems and seem—lacking reference data for our TMDCs—reasonable.

Qualitatively, the observed linear loss of amplitude intensity with increasing temperature is in good agreement with similar investigations of metallic single crystals. In the following we now focus on understanding the origin of this behavior. Although we cannot quantitatively calculate the expected temperature coefficients for the chalcogen p bands, we can qualitatively discuss the differences observed for peak A and B, as well as the reason for this behavior. Please note, that in the context of this work we focus on identifying thermal effects and on providing a means of defining the instantaneous sample temperature. These goals are not put into question by the lack of a quantitative evaluation.

The origin of the thermal reduction of the amplitude of the chalcogen p bands and the implications on the differences observed for the substructure of the spectral peaks is discussed in the following. The loss of spectral weight of all chalcogen p bands in the photoemission spectra presented here can be understood analogously to the increase of intensity within the spectral plateau, which we discussed in section 5.1.2–d.

We analyzed the origin of the structures observed within our SH-2PPE spectra in section 4. Especially in case of the chalcogen p_z band which features a strong surface perpendicular dispersion the energy of the observed spectral peak changes with excitation photon energy as the conditions for a direct transitions are changed. The observed spectral features presented here are derived from direct transitions between states within the chalcogen p bands, the intermediate Ti $3d$ and/or Ti derived final states.

Matzdorf et al. [217] observed a strong loss of intensity for such a direct transition peak on Cu(110) accompanied by an increase of intensity elsewhere in the spectrum, i. e. the spectrum became similar to the expectation for a polycrystalline sample, which is due to the relevance of additional phonon-assisted excitation paths at elevated temperatures. The phonons, as Matzdorf et al. [217] state, provide additional momentum to the photoexcitation process, which leads to changes of the momentum of the photoelectrons contributing to the direct transitions—in consequence, these electrons are removed from the direct transition, leading to a reduction of the corresponding signal. In the context of our data, the loss of intensity of the chalcogen p bands in our spectra and the simultaneous increase of the phonon-assisted transitions yielding the spectral background is consistently understood. However, as mentioned in section 5.1.2–d for the discussion of named background, a quantitative calculation is not possible. Please note, that those calculations propose a linear dependence of the intensity of the direct transition peak on temperatures above the Debye temperature (this is true for both TMDCs investigated here) which is in agreement with our experimental data.

We observed in figure 5.16, section 5.1.4–a a difference in the relative thermal behavior of peak A and B. As both originate from analogous photoexcitation paths this is unexpected, but is it a real difference of the chalcogen p_x , p_y (peak A) and chalcogen p_z (peak B) derived bands? Considering the fitted temperature coefficients of peak B presented in table 5.5 both values agree well within the uncertainties—the quality of the TiSe₂ double Gaussian fit is rather bad, after all. The most striking deviation is observed for peak A.

The broadening of the Fermi edge does not reduce the amplitude of peak A significantly [see figure 5.26(b) in section 5.1.4–c]. Even if we assume the maximum reduction of intensity within the Fermi-Dirac distribution, a temperature coefficient of only about $-0.8 \times 10^{-3} \text{ K}^{-1}$ is derived which is much too small to explain the deviation.

Following the argument of Matzdorf et al. [217] again, the difference in the momentum range investigated in case of TiSe₂ and TiTe₂ may explain the differences in the temperature coefficients. The TiSe₂ data is acquired for normal emission, while the TiTe₂ spectra are taken off-normal under an emission angle of about 10° for the photoelectrons. The rate of this scattering depends, amongst others, on the dispersion of the bands. The

hole like dispersion of the chalcogen p bands thus leads to scattering of the electrons to lower values of $E - E_F$. For normal emission therefore the effect leads to photoelectrons being scattered out of the range observed by the CSA, while for off-normal emission those electrons are scattered into the investigated spectral range. This effect leads to a smaller absolute value of the temperature coefficient for off-normal emission from a hole-like dispersing band than for normal-emission—a characteristic clearly observed for peak A. The fact that such an effect is not observed for peak B may be attributed to the virtually vanishing dispersion of the intermediate Ti $3d$ band.

5.2 Spectroscopy at Varying Incident Laser Fluence

After we discussed the effect of the sample temperature on the photoemission spectra in the preceding section 5.1, we now focus spectral modifications induced by the absorbed laser pulses themselves. We are able to identify an overall very similar behavior of the photoemission signal, regardless of temperature or laser fluence variation and we will therefore show that the main laser induced modification is a temperature increase of the sample. However, we also identify distinct differences between both experimental approaches. In combination with the AR-2PPE data in section 5.2.4, which show the localization of the laser induced modifications on the apex of the spectral feature of the Se $4p$ bands, these data motivate the time resolved experiments presented in chapter 6.

We would like to stress, that in contrast to our analysis of thermal modifications in section 5.1, which focuses on the interpretation of the observed spectral changes, our investigation of the absorbed laser fluence dependence is more phenomenological. Because most of the laser induced effects are well explained in terms of thermal modifications, our primary task is the identification of deviations from the pure temperature dependence. Such laser induced modifications are investigated in detail in chapter 6 where we focus on the corresponding temporal evolution of the spectral changes after the excitation by the laser pulse—it is there that we are finally able to provide an interpretation of these effects.

Please note, that the data presented are not meant to be used as a reference (e. g. for the time resolved experiments). While we expect similar laser induced effects for different samples, the thermal changes of the spectral characteristics are expected to deviate considerably between different samples. We will see, that the temperature increase induced by the absorbed laser pulses depends on the establishment of a thermal equilibrium which is basically derived from the energy deposited in the crystal, i. e. the absorbed fluence, and the dissipation thereof. The static increase of sample temperature leads to a heat-up of the whole system consisting of sample and sample holder and is thus depending on, e. g., the sample size and the contact of the sample to the holder. In other words, comparability of the static heat-up cannot be expected for different samples. Please note, that we do not present similar TiTe₂ data here for this reason.

This section therefore pursues the following objectives:

- The energy of the absorbed laser pulses ultimately dissipates by heating the crystal lattice [130, 133, 134, 137]. Although the laser induced excitation is fundamentally different from heating of the sample—we will discuss this in some detail in this section—a comparison of the temperature and fluence dependent data enables the identification of a warm-up of the samples. Additionally we find spectral modifications associated with the initial, non-equilibrium electronic distribution characteristic for the laser excitation.
- In section 5.1 we discussed, how the sample temperature relates to the modification of certain spectral structures. These data enable us to establish an instantaneous temperature scale—relevant especially for the time resolved experiments (see chapter 6)—which allows the quantification of the laser induced warm-up of the sample. This section serves as a benchmark for this approach.
- Knowledge about the spectral modifications to be expected at a certain laser fluence is very instructive for time resolved experiments such as presented in chapter 6. Especially for the investigation of the low temperature CDW phase of $1T$ -TiSe₂ (see section 5.3.2) it is crucial to choose suitable fluences for the observation of the temporal evolution of the laser induced phase transition.¹¹
- We face additional, energetically non-selective drifts of the photoemission intensity within a certain laser fluence range (see discussion in section 5.1.2–c) which we attribute to instabilities of the CSA system. These are briefly discussed with respect to how such drifts modify the experimental data and how they may be compensated and/or circumvented. Most important, we identify the fluence ranges which should be avoided for the acquisition of static and time resolved data. Only the main considerations are presented and a detailed investigation of the experimental artifact is presented in addendum A.3 where we shall also provide a motivation for our interpretation in terms of an instability of the analyzer. A fluence value of about $5 \mu\text{J cm}^{-2}$ for the SH pulses enables virtually unmodified and stable spectra and is thus used throughout this work whenever laser induced effects are to be minimized.

First, some remarks on the specifics of the experimental method in this section. To enable an accurate and stable setting of the absorbed laser fluence over a broad range, we employ two linear gray filters, one in front of the LBO crystal and one just in front of the entrance window of the UHV chamber. The first gray filter reduces the incident fundamental on the LBO, thus preventing degradation of the crystal, the second gray filter allows for fine-adjustment of the SH fluence. The mean laser power

¹¹Please note, that in section 5.3.2 we show that the CDW phase of $1T$ -TiSe₂ can even be fully perturbed by a sufficiently strong laser pulse.

transmitted through the second filter is carefully adjusted and monitored repeatedly during the experiment. Please note, that the use of laser setup laser 3_{TR}, the short pulse duration optimization, is chosen for better comparability to the time resolved experiments. All experiments in this section are performed at room temperature; for the low temperature CDW phase see section 5.3.2.

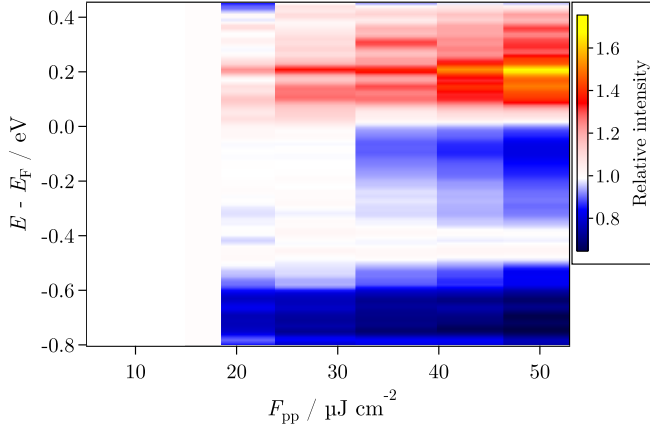
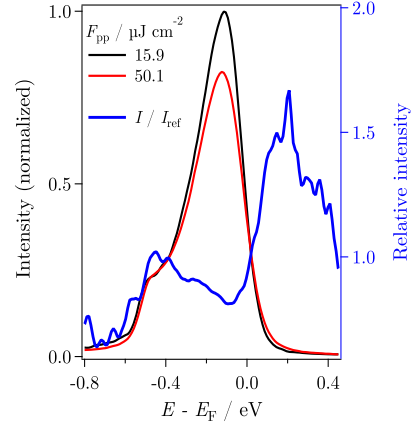
5.2.1 Overview of the Laser Induced Modifications

In section 5.1 we prefix our introduction of thermal modifications of the spectroscopic data by 2D energy–temperature maps. We found this representation very instructive for gaining a first impression of the laser induced effects to be expected. Figure 5.27 shows two corresponding 2D energy–fluence maps. Refer to section 5.1 for details on the generation of these maps. These maps emphasize the relative changes of the spectral intensity with fluence by referring the spectral intensity, I , at each fluence to a reference spectrum, I_{ref} , acquired at $F_{\text{pp}} = 15.9 \mu\text{J cm}^{-2}$ or $5.3 \mu\text{J cm}^{-2}$, respectively. The construction of the relative spectra is shown in figures 5.27(b) and (d), the blue curve basically being the ratio of the intensities of the spectra with respect to the reference data.

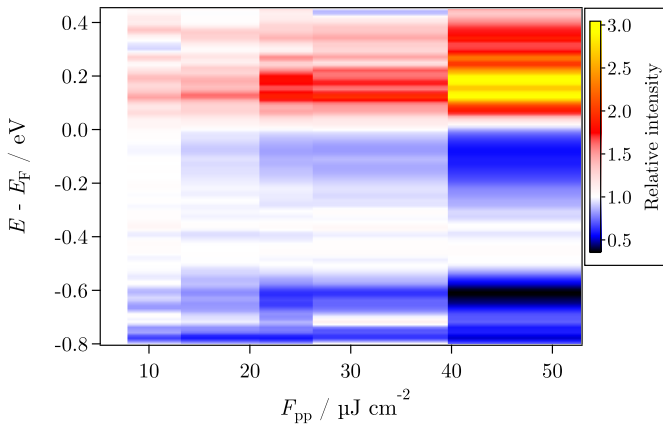
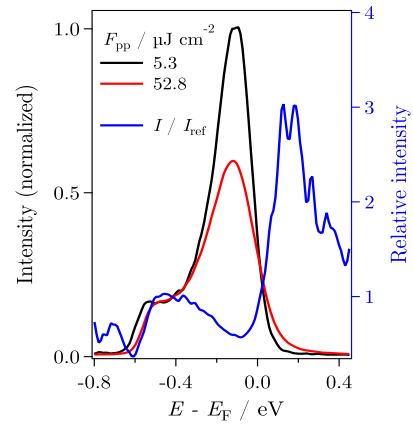
Figures 5.27(a) and (b) show data derived from an experiment starting at the lowest fluence. The absorbed laser fluence, F_{pp} , is slowly increased, carefully waiting for stabilized photoemission. The instabilities of the CSA system are discussed in detail in appendix A.3. Up to $F_{\text{pp}} \approx 25 \mu\text{J cm}^{-2}$ the spectra are influenced by this effect and we therefore only include data for fluences above the onset of the stabilization at approximately $15 \mu\text{J cm}^{-2}$. Figures 5.27(c) and (d) present corresponding spectra acquired under the most stable conditions experimentally accessible using the CSA. In this case the system is stabilized at the highest fluence investigated and then a series of spectra for decreasing fluence from about $52.8 \mu\text{J cm}^{-2}$ to $5.3 \mu\text{J cm}^{-2}$ is recorded—this time spectra are taken in fast succession to suppress the reestablishment of instabilities at low fluences as far as possible. For a discussion on the acquisition of stable spectroscopic data refer to appendix A.3.5.

The energy–fluence maps of 1T-TiSe₂ are most instructive in direct comparison to the corresponding energy–temperature map of this TMDC in figure 5.2(a), section 5.1. For better comparability all three figures show the same energy range. First of all, both datasets feature distinct similarities: (i) a significant reduction of spectral weight in the energetic range of the Se 4*p* bands (blue, $E - E_{\text{F}} \approx -0.1 \text{ eV}$), (ii) the energetic shift of the secondary electron cutoff of the spectrum which corresponds to an increase of the work function yields a reduction of intensity (blue, black) at $E - E_{\text{F}} \approx -0.6 \text{ eV}$, and (iii) the white stripe at an energy of about -0.45 eV represents the spectral plateau used for normalization of the spectra. We discuss in section 5.2.2 that these laser induced spectral modifications are well explained by a temperature increase of the sample crystal.

Nevertheless, we additionally identify a striking difference to the thermal data. The relative intensity just above the Fermi energy, up to $E - E_{\text{F}} \approx 0.4 \text{ eV}$ exhibits a very


 (a) Mapping of the relative intensity (F_{pp} increases).


(b) Construction of (a)


 (c) Mapping of the relative intensity (F_{pp} decreases).


(d) Enhanced signal with respect to (b)

Figure 5.27: A 2D energy–fluence map shows the relative change in spectral intensity with fluence (red for increase, blue for decrease) for (a) increasing fluence (count rate stabilized) and for (c) decreasing fluence (after stabilization at the highest value). Interpolation as per section 5.1. (b) and (d) present the reference spectrum (black, I_{ref}) acquired at the lowest fluence included and the spectrum corresponding to the highest fluence (red, I). The relative intensity is calculated as $\frac{I}{I_{\text{ref}}}$ (blue).

significant increase with fluence, especially for the carefully stabilized data in figure 5.27(c). This signal seems to be less pronounced [by a factor of 2, see figures 5.27(b) and (d)] for the data acquired for increasing F_{pp} , however, this is a consequence of referring the data to a significantly higher fluence—the low fluence regime is governed by severe intensity instabilities which render a comparison to the spectra included in figure 5.27(a) futile. Please note, that even the smaller effect for increasing fluence [figure figure 5.27(a)], i. e. for the less stabilized data, is distinctively different from the small increase of intensity above E_F in case of TiTe₂, see figure 5.2(c) in section 5.1, which we attributed to thermal broadening of the Fermi edge. We use the same color mapping for these TiTe₂ data and the TiSe₂ experiment for increasing fluence, i. e. a direct comparison of the 2D maps is possible.

The 2D energy–fluence and –temperature maps of TiSe₂ and TiTe₂ reveal two distinctively different relative intensity features. In case of TiTe₂ we observe the gain and loss of spectral intensity for $E - E_F \approx \pm 0.1$ eV, respectively, i. e. only close to the Fermi energy the intensity is modified. This is expected for the thermal broadening of the Fermi edge which is not observed for the temperature dependent TiSe₂ data because of insufficient spectral resolution. Furthermore, the temperature dependent data for both TMDCs in figure 5.2 exhibit a small intensity increase localized at an energy of about 0.1 eV which is not surprising as it is an effect within the flank of the Fermi edge. The laser induced modification presented in figure 5.27, however, reveals a maximum intensity increase at approximately 0.2 eV and the intensity increases within the spectral range of roughly 0.1 eV to 0.4 eV.

Additionally, figure 5.28 shows a selection of the relative spectra used for the generation of the maps in figure 5.27. The corresponding temperature dependent data is presented in figure 5.2(b) [the TiTe₂ data is shown in (d)] in section 5.1. This representation reveals in case of the stable experiment [decreasing F_{pp} , figure 5.28(b)] a laser induced reduction of the spectral weight of the Se 4*p* bands similar to the temperature induced effect to about 50 %, i. e. the same, severe spectral modification can be established by the laser itself. Furthermore, figure 5.28 shows the strong increase of intensity above E_F , up to about 0.4 eV in striking contrast to the corresponding thermal data. We observe a clear and well defined increase of spectral intensity with increasing fluence in this energetic range. In contrast to the intensity increase at $E - E_F \approx 0.1$ eV for TiTe₂ [figure 5.2(d), section 5.1], the TiSe₂ data discussed here show a much more defined signal in this energy range. The TiTe₂ data are governed by noise and artifacts of the calculation of the ratio of the spectra, because there exists virtually no real signal above the broadened Fermi edge. The clarity of the laser induced changes, however, is a consequence of the presence of a real photoemission signal up to about 0.4 eV above the Fermi energy—and thus well exceeding the energetic range of the Fermi edge.

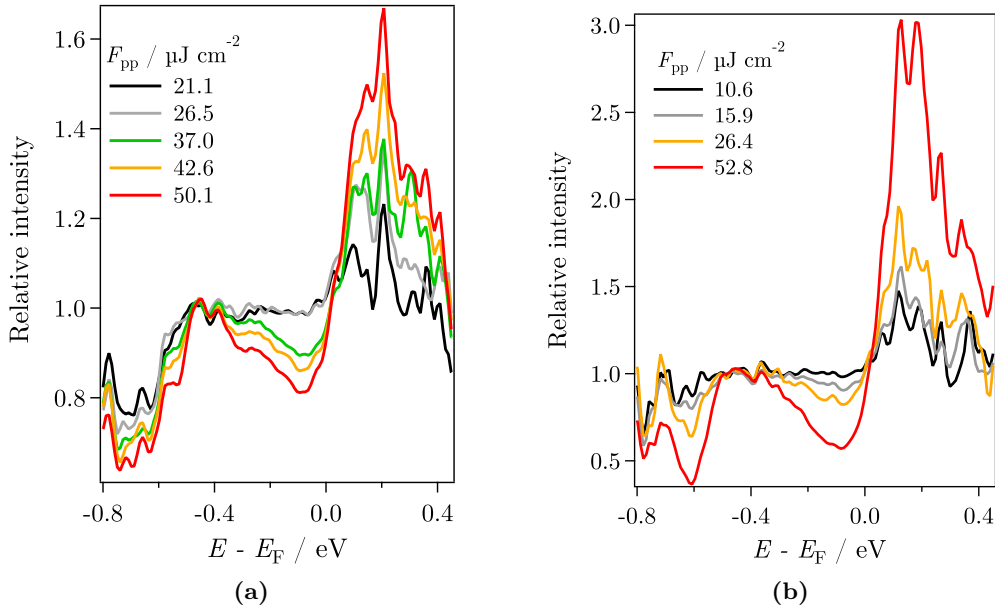


Figure 5.28: (a) relative intensity spectra acquired during the slow subsequent increase of laser fluence, i. e. the count rate stabilized at about $15.9 \mu\text{J cm}^{-2}$ which is used as reference. (b) shows analogous data taken after stabilization at the highest fluence and subsequent reduction of the fluence normalized to $F_{\text{pp}} = 5.3 \mu\text{J cm}^{-2}$.

5.2.2 Laser Induced Modifications of the Spectral Shape

We would like to begin our detailed investigation of laser induced modifications of 2PPE spectra of $1T\text{-TiSe}_2$ with a brief look at a peculiar instability of the photoemission signal which we attribute to unstable conditions of the CSA—we provide an extensive discussion in addendum A.3. In summary, at low absorbed fluences, which correspond to low photoelectron count rates, the spectral intensity is unstable. After a certain fluence is applied, the detected photoemission signal decreases slowly within hours. At sufficiently high fluence the intensity is stable, i. e. no long-term variation is observed, however, as the fluence is reduced again, the intensity slowly increases. Our primary objective is the introduction of stable conditions during the experiment. We therefore need to discuss, to what extent the CSA instability may influence our experiment, if we reduce the fluence to values prone to the instability.

Figure 5.29(a) shows spectra acquired for increasing fluence, beginning at the lowest fluence. These data are shown for reference and are not as thoroughly stabilized as those presented in figure 5.27(a)—or as the experiment presented in appendix A.3. After normalization to a reference fluence with respect to the quadratic dependence of the

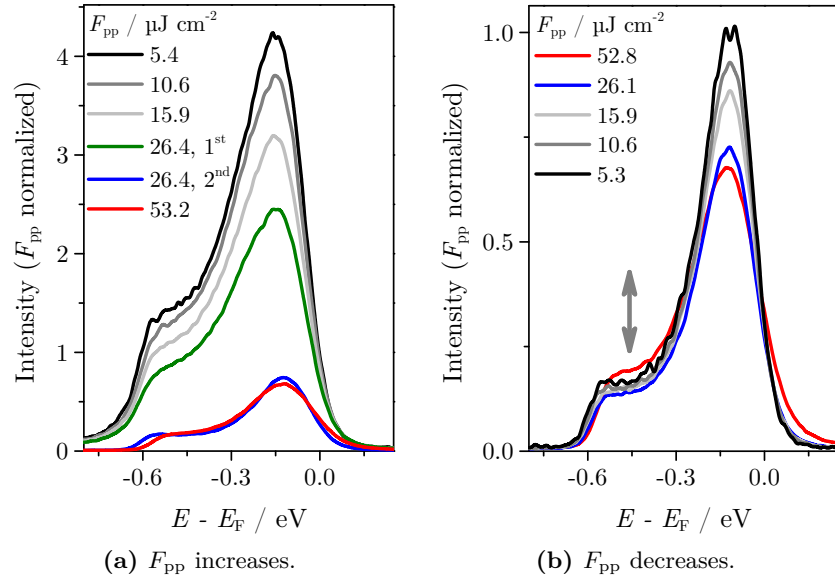


Figure 5.29: 2PPE spectra acquired for increasing fluence (a) and decreasing fluence after stabilization at the highest fluence (b). All spectra are normalized with respect to the quadratic dependence of spectral intensity on absorbed fluence. The same scales are used for both figures. (b) presents spectra corresponding to the data in to figures 5.27 and 5.28 for decreasing F_{pp} . The arrow points out an interesting behavior of the plateau, see text.

intensity on the fluence we observe the typical loss of intensity with fluence (refer to appendix A.3.1). The spectra stabilize at fluences of about $25 \mu\text{J cm}^{-2}$ and indeed at $F_{pp} = 26.4 \mu\text{J cm}^{-2}$ we find stabilization within two consecutive measurements.

If we, however, begin the experiment at the highest fluence, in this case $52.8 \mu\text{J cm}^{-2}$, ensuring stability of the photoemission signal, we derive well comparable spectra using only normalization with respect to the fluence. Such data is presented in figure 5.29(b). Note, that the intensity scales are identical in figure 5.29. Nevertheless, a quantitative comparison of the spectra is still not feasible. The two curves for $F_{pp} \geq 26.1 \mu\text{J cm}^{-2}$, which is the stable range of the CSA, exhibit the increase of intensity of the plateau range expected for a higher temperature (see section 5.1.2-d) with increasing fluence; this increase is, however, exaggerated as demonstrated by the difference in slope of the secondary electron cutoff of the spectra (see section 5.1.2-b). Additionally, the plateau intensity slowly increases for $F_{pp} \leq 15.9 \mu\text{J cm}^{-2}$ which is obviously not a thermal effect, but an indication for the onset of the long-term instability of the CSA. After reduction of the fluence the photoemission signal slowly recovers (see addendum A.3.2).

To compensate for the remaining deviations from spectral intensity we apply normalization to the plateau intensity as discussed in appendix A.1.1; figure 5.30 shows the result.

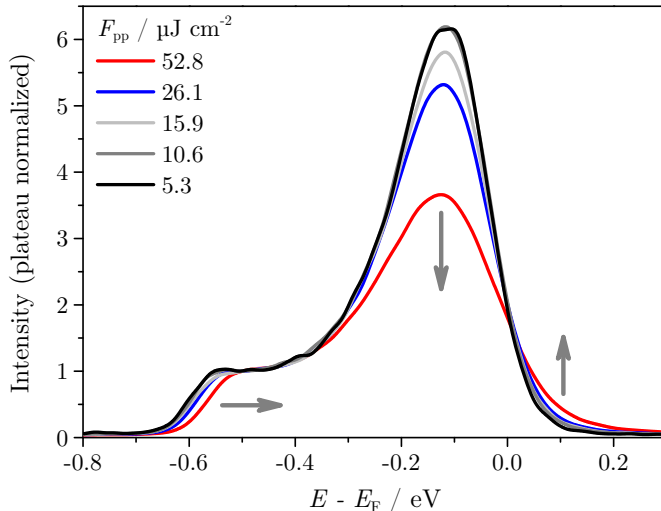


Figure 5.30: The spectra presented in figure 5.29(b) are normalized to the plateau intensity. Arrows emphasize the main laser induced modifications.

Comparison to the temperature dependent experiment shown in figure 5.3 in section 5.1.1 we identify a very similar loss of spectral weight of the Se 4*p* bands accompanied by an increase of the work function which suggests a predominantly thermal origin of the laser induced modification. Nevertheless, these spectra exhibit a significant increase of intensity around $E - E_F \approx 0.1$ eV. Please note, that these spectra are acquired using the higher resolution mode of the CSA (closed aperture, see section 3.1), like in case of the temperature dependent data for TiTe₂. Still the laser induced signal above the Fermi energy is more significant (refer also to section 5.2.1).

5.2.2–a Thermal Modifications Induced by the Laser

Numerically fitted data enables a detailed analysis of the relevant spectral characteristics modified by the absorbed laser. We use the carefully stabilized data for increasing fluence shown in section 5.2.1—not the reference data presented here—and the spectra acquired for decreasing fluence after stabilization at a high F_{pp} as discussed here and in the preceding section. The data presented for increasing F_{pp} was taken under “quasi-stable” conditions, i. e. the observed drift of the photoelectron count rate could be considered stabilized—the count rate decrease was not completed, especially in case of the lowest fluences, but rather slow enough to be tolerable. For a discussion of the numerical fitting method refer to addendum A.1.1. We present fits of the work function, the high energy cutoff of the spectrum, the amplitude of the Se 4*p* bands, and we evaluate the increase of spectral intensity above E_F by intensity integration of a suitable energetic range.

Figure 5.31 shows the relative change of the work function with absorbed laser fluence.

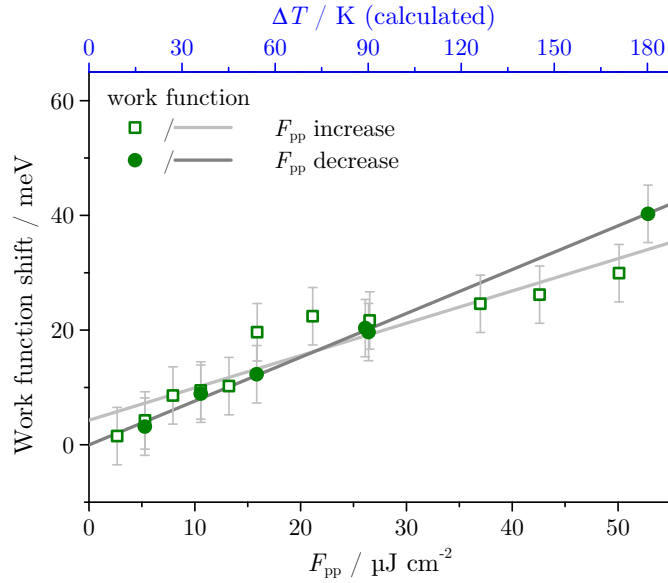


Figure 5.31: Relative increase of the work function of TiSe₂ with increasing absorbed laser fluence for the experiment starting at the lowest fluence (unstable, open symbols) and the highest fluence (stable, full symbols); the uncertainty of ± 5 meV corresponds to one energy channel of the CSA. Linear fits (lines) are included. The top scale (blue) shows the relative temperature, ΔT , corresponding to the work function change of the stable data (F_{pp} decrease).

For increasing fluence (open symbols), i. e. unstable spectroscopic conditions especially at low fluences, the work functions exhibits considerable deviation from a linear behavior in the fluence range of the vanishing of the instability of the CSA—we will discuss this shortly later in this section. After stabilization at a high fluence, i. e. for an experiment for decreasing F_{pp} , the work function shows a linear dependence on the fluence—very similar to its thermal modification observed in section 5.1.3. For the stable experiment (full symbols) the line fit, $\Phi = \Phi_0 + \Delta\Phi_{F_{pp}} F_{pp}$, yields a fluence coefficient of $\Delta\Phi_{F_{pp}} = (7.64 \pm 0.18) \times 10^{-4} \text{ eV } \mu\text{J}^{-1} \text{ cm}^2$. The corresponding temperature coefficient is $\Delta\Phi_T = (2.24 \pm 0.22) \times 10^{-4} \text{ eV K}^{-1}$ (see table 5.3, section 5.1.3). This enables us to calculate the temperature increase associated with a certain absorbed fluence:

$$T = \text{const.} + \frac{\Delta\Phi_{F_{pp}}}{\Delta\Phi_T} F_{pp} = \text{const.} + \Delta T_{F_{pp}} F_{pp} . \quad (5.9)$$

We calculate $\Delta T_{F_{pp}} = (3.41 \pm 0.41) \text{ K } \mu\text{J}^{-1} \text{ cm}^2$ using this equation. This calculation of course assumes that the change in work function is fully explained by the heat-up of the sample. Considering that the energy of the absorbed laser pulses dissipates by heating of the crystal lattice (see section 2.5.4 and, e. g., references [130, 137]) and an actual

temperature increase induced by such laser absorption is experimentally reported, for instance, in references [245, 246], we find this assumption a sound one. Our following discussion of different spectral characteristics establishes—in a phenomenological manner—the similarity of almost all laser induced effects to the temperature dependent data. This discussion is supported by an estimation of the expected laser induced temperature increase. For now, we use $\Delta T_{F_{pp}}$ to establish a relative temperature scale corresponding to the absorbed fluence. We chose the relative work function as reference for establishing a temperature scale, because it is not influenced by normalization (see section 5.1.2–c) and because we do not find any ultrafast laser induced modification which renders non-thermal effects very unlikely in this case (see section 6.2).

Figure 5.31 includes this scale of the relative temperature increase, ΔT , at the top in blue. This scale is also used in the following discussion of different spectral features for reference. Please note, that the fluence range investigated here is roughly comparable to the temperature range applied in section 5.1. This scale is included in the following figures to enable direct comparison to the temperature dependent data.

Another typical thermal modification of a photoemission spectrum is the broadening of the spectral features. For the Se $4p$ bands we find that the numerically evaluated FWHM of the whole peak (compare to section 5.1.4–b), $w(F_{pp})$, is very well described by a linear function (not shown) for the data acquired for decreasing F_{pp} .¹² Such a linear behavior is also observed in a temperature dependent experiment and it is fully explained in terms of thermal modifications in section 5.1.4–b. Analogously to our investigation of the work function, we define a fluence coefficient of the FWHM, $\Delta w_{F_{pp}} = (11.9 \pm 0.9) \times 10^{-4} \text{ eV } \mu\text{J}^{-1} \text{ cm}^2$. Using $\Delta T_{F_{pp}}$ we can now calculate a temperature coefficient $\Delta w'_{F_{pp}} = \Delta w_{F_{pp}} \Delta T_{F_{pp}}^{-1}$. We derive $\Delta w'_{F_{pp}} = (3.5 \pm 0.7) \times 10^{-4} \text{ eV K}^{-1}$. Indeed, this value agrees reasonably well within the uncertainties to the corresponding temperature coefficient of TiSe₂ given in table 5.6 in section 5.1.4–d of $\Delta w = (2.5 \pm 0.3) \times 10^{-4} \text{ eV K}^{-1}$. Please note, that an enhanced broadening in case of the fluence dependent data can be understood considering the increase of intensity above E_F as discussed in section 5.2.2–a. The typical fluence coefficients for TiSe₂ are summarized in table 5.10 in the summary presented in section 5.2.3. We will now focus on understanding, how the fluence dependence of these two spectral characteristics is understood in terms of a temperature increase.

Is the linear behavior of the spectral modifications in agreement to a heating of the sample by the absorbed laser pulses? The laser induced processes expected after absorption of a pulse are discussed in some detail in section 2.5.4 under consideration of the time resolved experiment in section 6.2. The absorbed laser pulse initially excites the electronic system, generating a highly non-thermal electron distribution (see e. g.

¹²The data for increasing fluence exhibit deviations at small fluences similar to the other spectral characteristics discussed here.

[130, 132, 137]), i. e. the system is excited into a non-equilibrium state. Please note, that we probe this initial condition in our static 2PPE experiment—this is discussed for figure 5.33(a) shortly. Afterward, the internal thermalization of the electronic system proceeds on a time scale longer than the duration of the laser pulses, i. e. the thermalized, equilibrium state of the system is not accessible here as photoelectrons can only be excited within the temporal duration of the pulses, introducing the expected Fermi-Dirac distribution of the electrons corresponding to their temperature. The energy introduced into the electronic system is finally transferred to the lattice which is consequently heated.

Ultimately, the absorbed pulses therefore lead to a temperature increase of the crystal lattice which may accumulate if not dissipated fast enough—the sample temperature is thus statically increased [245, 246]. We assume that such a static heat-up leads to the change of work function observed in figure 5.31. Please note, that the layered structure of the TMDCs investigated in this work may also lead to a hindered dissipation of heat (see addendum A.3.4). The linear behavior in this case is thus a consequence of the thermal nature of the effect, because the thermal modifications lead to linear effects which we discussed in section 5.1 in detail.

The linear dependence of the work function on the absorbed fluence is therefore an indication for a linear dependence of the temperature increase of the crystal lattice on F_{pp} . The temperature of electronic system and lattice after excitation by a laser pulse is described within the two temperature model [135, 136] (see also section 2.5.4) by:

$$c_e(T_e) \frac{dT_e}{dt} = G_{\text{el}} [T_l(t) - T_e(t)] - \kappa_e \nabla^2 T_e(t, \mathbf{r}) + p(t) \quad (5.10)$$

$$c_l \frac{dT_l}{dt} = G_{\text{el}} [T_e(t) - T_l(t)] - \kappa_l \nabla^2 T_l(t, \mathbf{r}) , \quad (5.11)$$

with the temperature of electronic system and lattice, T_e and T_l , the corresponding specific heat capacities, $c_e(T_e)$ and c_l , a coupling constant G_{el} modeling electron–phonon interaction, the thermal diffusion constants, κ_e and κ_l , a corresponding spatial coordinate, \mathbf{r} , for the diffusion, and a source term, $p(t)$, modeling the initial heating introduced by the laser pulse. In our experiment we observe the static heat up of the sample lattice by the shift of the work function, because this feature is closely related to characteristics of the crystal surface, which we discuss in section 5.1.3–a. Indeed, we find no dynamics on a femto- to picosecond timescale of the work function in the corresponding time resolved experiments (see section 6.2) which shows, that this spectral feature represents a thermal equilibrium condition of the sample, i. e. the effect of heat diffusion can be considered equilibrated, the corresponding term is constant. The first term of equations (5.10) and (5.11) models the coupling of electronic and phononic system and governs the energy transfer from the electrons to the lattice. In our case the transfer of energy from the electrons to the lattice is assumed to be fully completed and the first term is thus irrelevant here.

In summary, the change in work function is induced by a static increase of the sample

temperature. This is described by the heat-up of the lattice alone using its specific heat capacity, c_1 , and the definition thereof, $c_1 = \frac{\Delta Q}{m \Delta T}$ [172], with the heated mass, m , the temperature difference, ΔT , and the heat, ΔQ , necessary for this temperature change. For the temperature range discussed here (roughly $T_{\text{RT}} \dots T_{\text{RT}} + 200$ K, with room temperature T_{RT}) c_1 can be considered constant [137], because for $T \gg \Theta_{\text{D}}$ with the Debye temperature, Θ_{D} , ($\Theta_{\text{D}} = 221$ K for TiSe₂ [83]) the phonon heat capacity becomes constant [172, 247]. Indeed, experimental data show, that the specific heat capacity exhibits only small variations below room temperature [248, 249]. The mass of the sample which is heated is a function of the volume in which the laser beam is absorbed. This volume results from the penetration depth of the laser which depends on its wavelength, because of the wavelength dependence of the complex dielectric function [250]. The heat deposited in the crystal by the laser pulses is defined by the fluence, the surface area illuminated by the laser and the reflectivity of the sample (see table 3.5 in section 3.2.1–b) yielding $\Delta Q \propto F_{\text{pp}}$. Assuming that the equilibrium reached for the heat up of the sample is not governed by significant differences in heat dissipation for different fluences, we find $\Delta T \propto F_{\text{pp}}$. The linear fluence dependence of the work function is thus consistent with its linear temperature dependence.

Finally, we like to estimate the expected temperature increase of the sample.

First, we need the depth of penetration, d , of the absorbed laser pulses, i. e. the entry depth of the laser into the crystal, where the intensity is decreased to $\frac{1}{e}$ of its initial value. At $h\nu = 3.18$ eV ($\lambda = 390$ nm) and for p-polarization table 3.5 in section 3.2.1–b gives $\kappa = 1.3$ of the complex refraction index for TiSe₂, which yields, using reference [250]:

$$d = \frac{\lambda}{4\pi \kappa}, \quad (5.12)$$

a value of $d \approx 23.9$ nm. The laser spot on the sample surface is elliptic (radii $a = 13.1$ μm and $\sqrt{2}a$, see section 3.2.1–b). The Volume, V , in which the laser is absorbed is half of an ellipsoid, i. e. $V = \frac{4\sqrt{2}}{6}\pi da^2$ which yields $V = 1.21 \times 10^{-17}$ m³. We assume that all the energy of the absorbed laser pulse is transferred to the lattice, i. e. the lattice is heated within the volume V . Using the molar mass $M = 205.8$ g mol⁻¹ [251], the mass density $\varrho = 5.2 \times 10^3$ kg m⁻³ [252] and the molar volume $V_{\text{M}} = \frac{M}{\varrho}$, we derive number of moles of the sample in which the laser is absorbed, $N_{\text{M}} = 3.07 \times 10^{-13}$ mol.

The specific heat capacity of the lattice is $c_1 \approx 71$ J mol⁻¹ K⁻¹ (at $T = 300$ K) [248], which enables the calculation of the sample heat-up, ΔT , for a specific absorbed heat, Q , which is the absorbed energy of the laser, by $\Delta T = \frac{Q}{N_{\text{M}} c_1}$. A laser fluence of $F_{\text{pp}} = 50$ $\mu\text{J cm}^{-2}$ corresponds to a heat per pulse of $Q_{\text{pp}} = 0.38$ nJ. The heat-up per pulse is therefore $\Delta T_{\text{pp}} = 17.5$ K.

Considering the repetition rate of about 80 MHz (pulse separation 12.5 ns) of this laser and the dissipation of the heat introduced to the small, specified volume, a temperature increase of the whole sample of the order of approximately 150 K after thermal

equilibration of sample and surroundings seems very reasonable. Please note, that heat diffusion is a process on a nanosecond timescale [246, 253] which further supports a slow heat accumulation for absorption of pulses separated by a few nanoseconds—after all we observe heat-up within a few minutes (see appendix A.3.4).

5.2.2–b Spectral Modifications Originating From a Non-Equilibrium State of the Electronic System

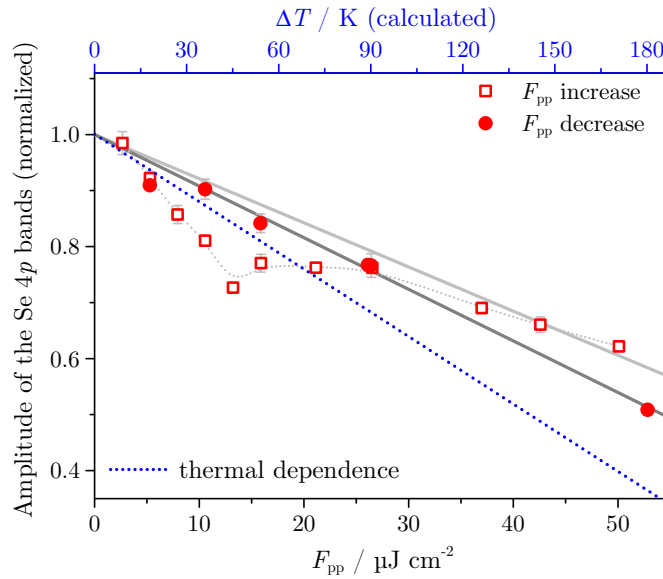


Figure 5.32: Relative decrease of the amplitude of TiSe₂ with increasing F_{pp} for the experiment starting at the lowest fluence (unstable, open symbols) and the highest fluence (stable, full symbols). A linear fit (line) is included for the stable data (full symbols). The top scale (blue) shows the relative temperature, ΔT , corresponding to the work function change in figure 5.31. The temperature dependence of the amplitude (see section 5.1.4–a) is included for reference (dotted line).

Figure 5.32 shows the laser induced modification of the amplitude of the Se 4p bands. The stable data (decreasing F_{pp}) is again included as full symbols, the corresponding data for increasing fluence is shown by open symbols. We focus on the stable amplitude values (full) for a further discussion of the observed fluence dependence. The unstable data are presented for reference as they exhibit a peculiar fluence dependence for fluences $F_{pp} \lesssim 25 \mu\text{J cm}^{-2}$. We interpret this deviation from the stable data in terms of the instability of the CSA (initial, rapid drop below about $15 \mu\text{J cm}^{-2}$) and the stabilization thereof in between (plateau-like region) which we discuss in addendum A.3.3. These data show, that even by carefully stabilizing the photoemission signal during the slow increase

of fluence modifications of the spectral shape are to be expected, i. e. stable acquisition of fluence dependent spectra is only possible by beginning the experiment at a sufficiently high fluence to stabilize the photoelectron analyzer system.

Such stable amplitude values are well reproduced by a linear fit; the deviation at the lowest fluences is partially attributed to the onset of the photoemission instability encountered at low fluences. By switching to a low fluence after a high fluence was used, the spectral intensity slowly increases as shown in figure 5.29(b). However, we use normalization to the plateau intensity which in combination with the modification of the spectral shape induced by the instability of the CSA (see appendix A.3.3) leads to a stronger suppression of the amplitude within the unstable fluence range—this is also clearly observed for the data for increasing F_{pp} (open symbols). Additionally, we observe a threshold for the onset of the laser induced modification of the spectrum (see appendix A.3.5) which, however, seems to change for different samples. We attribute this to the effect of heat accumulation in the layered crystals, i. e. to the formation of a thermal equilibrium of the sample and its surroundings. For the lowest fluences the heat introduced by the laser seems to be able to still dissipate.

The fluence coefficient, $\Delta I_{\max, F_{pp}} = (-9.37 \pm 0.29) \times 10^{-3} \mu\text{J}^{-1} \text{cm}^2$, is estimated by a line fit for the stable data. Table 5.5 in section 5.1.4-d provides the corresponding (numerical) temperature coefficient of $\Delta \tilde{I}_{\max, RT} = (-3.56 \pm 0.17) \times 10^{-3} \text{K}^{-1}$. The coefficient referenced to the room temperature value of the amplitude is a good choice for our fluence dependent experiment as the sample is kept at room temperature while the laser pulses are absorbed, i. e. analogously to the thermal experiment the sample temperature is increased beginning at the room temperature. Using $\Delta T_{F_{pp}}$ we are able to calculate a temperature coefficient, $\Delta I'_{\max, F_{pp}}$, corresponding to $\Delta I_{\max, F_{pp}}$ by $\Delta I'_{\max, F_{pp}} = \Delta I_{\max, F_{pp}} \Delta T_{F_{pp}}^{-1}$. We derive $\Delta I'_{\max, F_{pp}} = (-2.75 \pm 0.42) \times 10^{-3} \text{K}^{-1}$

Within the uncertainties of the line fits, the laser induced decrease of the amplitude of the Se 4*p* bands is less pronounced, than the thermal effect. This is not unexpected, because we already discussed that we probe the initial, non-equilibrium state of the electronic system in our static photoemission experiment. In contrast to the work function the amplitude of the Se 4*p* bands is less defined by the lattice temperature than by the specifics of the electronic system. The deviation may therefore be an indication for specific laser induced modifications. Indeed, the time resolved experiments in chapters 6 and 7 show a complex temporal evolution of the Se 4*p* bands. It is in these chapters, where we interpret the laser induced effects. However, a notable finding in these chapters is a delayed reduction of the amplitude of the Se 4*p* bands after the laser excitation at room temperature. The reduction is therefore not fully established in these static experiments and the deviation from the temperature dependent experiment hints at additional laser induced effects in this case.

Furthermore, the fact that we probe a non-equilibrium state of the electronic system in case of the amplitude of the Se 4*p* bands also supports a smaller reduction. In this case,

we do not probe a system in thermal equilibrium—like in case of the work function which is basically defined by the lattice (see section 5.1.3–a)—but the electronic system within its non-thermal, initial phase, i. e. instead of $t \gg 0$ in equations (5.10) and (5.11) we focus on $t \approx 0$. In this case, the energy of the laser pulse is initially deposited in the electron system leading to an increase of its temperature, T_e . The electronic temperature is, however, not a linear function of F_{pp} , because the specific heat capacity of the electronic system, c_e , is a function of T_e —usually a linear dependence of the form $c_e = \gamma T_e$ with a proportionality constant, γ , is a good assumption [132, 134, 135, 137]. In this case we find $\Delta T_e(T_e) \propto \frac{F_{pp}}{T_e}$ which yields a reduction of the temperature increase of the electronic system, ΔT_e , with increasing temperature thereof, i. e. the increase of temperature of the electrons for a certain absorbed heat decreases with increasing fluence.

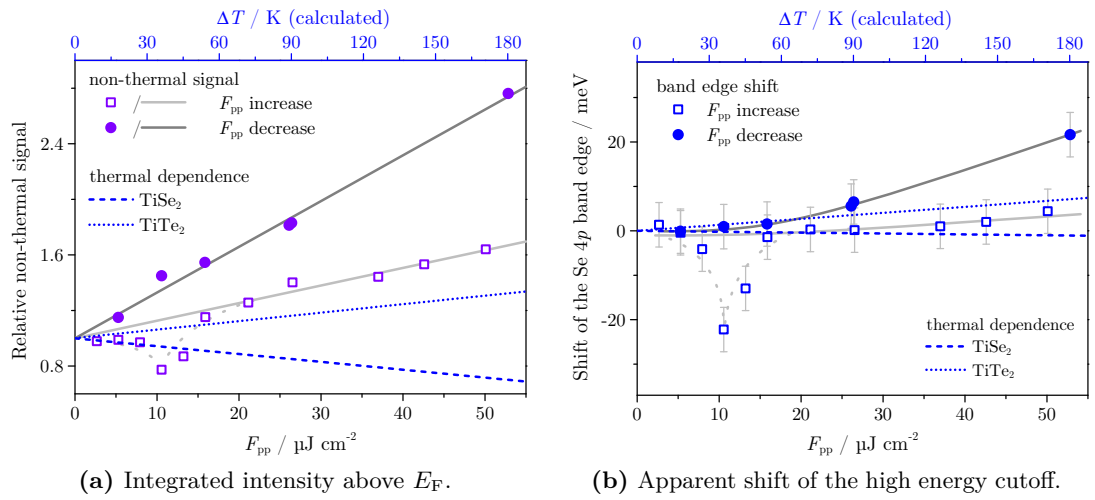


Figure 5.33: (a) Within an energetic range of about 0.1 eV to 0.4 eV above E_F the intensity increases significantly with F_{pp} (open/full symbols as per figure 5.32). Line fits (line) are included (a subset of the open symbol data is fitted). The top scale (blue) shows the relative temperature, ΔT , corresponding to the work function change in figure 5.31. A fit of the corresponding temperature dependent data (see section 5.1.4–a) is included for reference (dotted line). (b) Apparent shift of the high energy cutoff of the spectra with fluence. Lines are guides to the eye only.

A direct observation of a spectral characteristic of the electron system in non-equilibrium is possible right above the Fermi energy. We integrated the intensity for $E - E_F = 0.1$ eV to 0.4 eV and present the results in figure 5.33(a). The corresponding thermal data discussed in figure 5.25(a) in section 5.1.4–c uses the same integration range for direct comparability. Again, the fluence dependent data is referenced to zero fluence and the temperature dependent data is referred to room temperature, which enables

direct comparability of both data. The figure includes linear fits (gray lines) for the data acquired upon increasing (open, the data for $5 \mu\text{J cm}^{-2} < F_{\text{pp}} < 15 \mu\text{J cm}^{-2}$ is omitted for the fit) and decreasing absorbed fluence.

The line fit of the temperature dependent data from section 5.1.4–c is included as well (blue dotted lines, top scale). Both the TiSe_2 (negative slope, low spectral resolution) and the TiTe_2 (positive slope, high spectral resolution) experiment are included, because they correspond to the two resolution modes of the CSA. Interestingly, the intensity seems to decrease for the inferior spectral resolution, while a small increase is observed for the better resolution. The latter is attributed to thermal broadening of the Fermi edge which leads to a contribution to the integration area. This broadening is not visible very well for data acquired with the worse resolution (see section 5.1.4–c and our discussion of the 2D energy–fluence maps earlier in section 5.2.1).

The fluence induced increase of intensity above E_{F} is significantly enhanced with respect to the thermal data. The difference between in-/decreasing fluence of the enhancement is attributed to the different spectral resolutions used, because it is consistent with the temperature dependent case. Furthermore, the temperature dependent data exhibits a high uncertainty for the line fit, i. e. the scatter of the individual data is quite pronounced, which is clearly seen in figure 5.25(a), section 5.1.4–c. This demonstrates, that for the temperature dependent spectra the signal above E_{F} is strongly influenced by noise—the representation by relative intensities amplifies an absolutely small signal. In case of the fluence dependent data, however, the scatter of the data is much less which is a consequence of the comparatively strong signal in this spectral range, as demonstrated by figures 5.27(d) and 5.30.

The increasing intensity above E_{F} also influences the numerically fitted energy of the high energy cutoff of the spectra shown in figure 5.33(b). The data derived from the experiment for decreasing F_{pp} exhibits virtually no energetic shift for small fluences and a significant shift for high fluences. While the temperature dependent data do not show any significant change in energy (blue lines), the fluence dependence seems rather strong. However, the observed shift is most likely an artifact explained by the increase of spectral intensity above the Fermi energy—the strong increase of intensity leads to an apparent shift of the high energy cutoff. While a shift of the binding energy of the chalcogen p bands to higher values leads to a corresponding shift of the high energy cutoff (see section 5.1.4–b), these bands are cut by E_{F} at room temperature, i. e. the binding energy of the cutoff is defined by E_{F} . The temperature dependence of the distribution of electrons in the vicinity of E_{F} is described by the Fermi-Dirac distribution, i. e. the Fermi edge of the spectrum broadens with temperature, but does not change the value of E_{F} itself [172, 247]—in this context the additional intensity above E_{F} leads to the apparent shift.

However, is strictly speaking, this argument only true for metals, for which the valence electrons are well described by a Fermi gas [172]. For semiconductors, a temperature dependence of the Fermi energy is indeed expected, because the carrier density is temperature dependent [247]. Considering the semimetallic to semiconducting character

of TiSe₂ [12–15], a shift of E_F may therefore be attributed to changes of the carrier density, which is, for instance, reported for the intercalation of alkali atoms [160, 162, 167]. We thus need to discuss, why our fit of the high energy cutoff of the spectra is indeed, as proposed, an artifact and does not support an actual change of the Fermi energy.

For our experiment on thermal modifications in section 5.1.4–b we also observed a slight increase of the energy $E - E_F$ of the high energy cutoff of the spectra in case of TiTe₂. We interpreted this shift in terms of broadening of the Fermi-Dirac distribution which reduces the intensity within the spectral peak, while simultaneously increasing intensity above (see especially figure 5.26, section 5.1.4–c). However, the shift observed for $F_{pp} \gtrsim 25 \mu\text{J cm}^{-2}$ significantly deviates from this rather small thermal shift. The deviation is a consequence of the fact, that we map the highly non-equilibrium state of the electronic system in our static 2PPE experiments, for which the electron distribution in the vicinity of E_F is much stronger perturbed [130, 137], than in the purely thermal case—additionally, the Fermi energy is not defined until thermalization of the electrons.

To investigate the strong influence of the additional intensity for $E > E_F$ we take a look at the center of the Se 4*p* and the highest Te 5*p* (peak A) bands of the thermal data presented in figure 5.21 in section 5.1.4–b, and compare it to the fluence dependent data for decreasing F_{pp} . We use a numerically estimated center of mass, E_c , which weights each energy within the peak with the corresponding intensity. We choose integration areas beginning at the base of the peak after background correction¹³ (see addendum A.1.1) at $E - E_F \approx -0.47 \text{ eV}$ for TiSe₂ and -0.34 eV for TiTe₂, up to 0.2 eV or 0.5 eV. For the thermal data shifts of $\Delta E_c \approx (-13.5 \pm 0.5) \text{ meV}$ ($\Delta T = 137 \text{ K}$) for TiSe₂ and $\Delta E_c \approx (7 \pm 5) \text{ meV}$ ($\Delta T = 139 \text{ K}$) for TiTe₂ are observed, independent of the integration area chosen. In contrast, for the fluence dependent data the shift of the high energy cutoff clearly depends on the integration area. We find a shift of $\Delta E_c \approx 6 \text{ meV}$ for the smaller and $\Delta E_c \approx 12 \text{ meV}$ for the bigger integration area for $\Delta F_{pp} = 47.6 \mu\text{J cm}^{-2}$ for the TiSe₂ data discussed here, i. e. the shift of the cutoff is more pronounced, if we consider more and more of the signal above the Fermi energy. This is a clear indication for a strong, laser induced increase of intensity above E_F which is not present for the temperature dependent data. Additionally, it demonstrates, that the observed strong shift is a consequence of the non-equilibrium electron distribution and not of a change of E_F .

5.2.3 Summary

In summary, our investigation of the laser induced modifications of the 2PPE spectra of 1T-TiSe₂ at different absorbed laser fluences leads to very instructive findings, especially with consideration of the time resolved experiments discussed in chapter 6. We are able

¹³This method is problematic in case of TiTe₂, because peak A and B (see figure 5.3, section 5.1.1) are not well separated. We chose a fixed beginning of the integration range such, that mainly peak contributes to the signal.

to identify thermal effects, like the change in work function and the broadening of the chalcogen p bands, which are most likely attributed to a static heat-up of the sample crystal induced by the heat deposited by the absorbed laser pulses. We do not expect any specific dynamics of such features on a femto- to picosecond timescale, because the relevant temperature of the sample is established—probably within minutes, see appendix A.3.4—by slow thermal equilibration of the sample and its surrounding, balancing the heat introduced to the system and the dissipation thereof.

Table 5.10: A compilation of the fluence coefficients of the work function, $\Delta\Phi_{F_{pp}}$, the FWHM, $\Delta w_{F_{pp}}$, and the amplitude of the Se $4p$ bands with respect to the value at $F_{pp} = 0 \mu\text{J cm}^{-2}$, $\Delta I_{F_{pp}}$, is compiled in this table. These data are given for increasing (beginning at the lowest F_{pp}) and decreasing fluence (starting at the maximum F_{pp}). The fluence coefficient are summarized in sub-table (a) and the corresponding factors for fluence to temperature conversion are shown in sub-table (b).

(a) Fluence coefficients.				
F_{pp}	$\Delta\Phi_{F_{pp}} / \text{meV } \mu\text{J}^{-1} \text{cm}^2$	$\Delta w_{F_{pp}} / \text{meV } \mu\text{J}^{-1} \text{cm}^2$	$\Delta I_{F_{pp}} / 10^{-3} \mu\text{J}^{-1} \text{cm}^2$	
increase	0.56 ± 0.07	0.56 ± 0.04	-7.9 ± 0.6	
decrease	0.76 ± 0.02	1.19 ± 0.09	-9.2 ± 0.6	

(b) Temperature–fluence conversion.				
F_{pp}	work function	$\Delta T_{F_{pp}} / \text{K } \mu\text{J}^{-1} \text{cm}^2$		
		FWHM	amplitude	average
increase	2.52 ± 0.58	2.24 ± 0.42	2.21 ± 0.29	2.38 ± 0.50
decrease	3.41 ± 0.41	4.78 ± 0.94	2.59 ± 0.30	4.10 ± 0.68

For further reference, table 5.10(a) compiles the fluence coefficients of the work function, the FWHM, and the amplitude of the Se $4p$ bands as observed for increasing and decreasing laser fluence. Table 5.10(b) shows the corresponding conversion factors for assigning a temperature to the respective modification of the spectral signatures. The latter are calculated using the temperature coefficients presented in sections 5.1.3 and 5.1.4–d and equation (5.9) from section 5.2.2–a.

These conversion factors allow for a direct calculation of the temperature from the value of F_{pp} . Of course, if a spectral signature is modified by a purely thermal effect, i. e. if the observed change corresponds to a temperature change, we expect the temperature scales established by comparison to the thermal behavior (see section 5.1) to be equal. The temperature–fluence conversion factors in table 5.10(b) show, that in agreement to our findings in this section 5.2 this is indeed the case for the work function and the FWHM. Our discussion for the amplitude in section 5.2.2–b revealed non-thermal influences and

consequently its $\Delta T_{F_{pp}}$ does not agree to the other evaluations within the errors for the experiment with decreasing F_{pp} . Furthermore, as expected from our findings in addendum A.3, we find a difference in the fluence dependence for in-/decreasing fluence. This needs to be considered whenever the fluence coefficients of the conversion factors are to be used.

Please note, that the simple calculation of the temperature from the absorbed laser fluence is only possible for a sample in thermal equilibrium, i. e. in case of static experiments like the spectroscopy discussed in this chapter 5. Especially in case of time resolved experiments this is not feasible, because a sample temperature is not necessarily defined at all times. In this case, comparison of thermally modified signatures, like the work function, to the other spectral modifications may yield insight into potential non-thermal effects.

Additionally to thermal modifications, we observe laser induced changes of the spectral shape which seem to be exclusive for the laser excitation of the sample. Considering that we only access the state of the sample within the temporal range defined by the duration of the pulses contributing to the 2PPE signal, we basically map the initial non-equilibrium distribution of the electrons right after/during absorption of the laser. This non-thermalized electron distribution is visible by distinct spectral modifications. We observe significant intensity in an energy range of roughly 0.1 eV to 0.4 eV which is a direct consequence of the non-thermalized electron system. Furthermore, the fluence dependence of the amplitude of the Se 4*p* bands does not agree to the thermally expected behavior—or more precisely: it does not agree to the other spectral characteristics, which we attribute to thermal modifications.

We have therefore observed indications for laser induced spectral modifications—the non-equilibrium electron distribution for $E > E_F$ and the difference of the reduction of the amplitude of the Se 4*p* bands with respect to the thermal data—but a conclusive distinction of laser induced and thermal effects is not possible using static photoemission data. This is, however, not the purpose of this section. The data presented here allows us to identify potential laser induced effects which we investigate in detail in chapter 6. Those time resolved experiments enables the observation of the temporal evolution of the spectral changes on an ultrafast timescale which finally allows to distinguish the different contributions.

5.2.4 The Momentum Range of the Laser Induced Modification of Spectral Weight

So far we discussed the loss of spectral weight of the Se 4*p* bands of TiSe₂ in dependence on the laser fluence as observed in angle integrated spectra. Yet, these data does not allow us to draw any conclusions concerning the following questions: Is this effect present along the whole Se 4*p* parabola? Is it really a decrease in the intensity of a distinct spectral feature or is it just a shift of the band with respect to the Fermi energy?

To address these questions, we performed AR-2PPE experiments using laser 2 at a photon energy of $h\nu = 3.12$ eV. The experimental setup is shown in figure 3.2 on page 47. The data discussed in this section was acquired prior to a time-resolved experiment, which has the advantage that after careful alignment of the interferometer for spatial and temporal overlap of the pulses at the sample surface, we can easily switch between low and high (i. e. about two times the low) fluence of the laser by simply blocking one arm of the interferometer.

Figures 5.34(a) and (b) show such AR-2PPE spectra. The intensity is normalized to the plateau region ($E - E_F \lesssim -0.2$ eV, emission angle about -5° to 0°), rendering the intensities in both spectra directly comparable. Please note, that otherwise the difference in intensity would be significant due to its quadratic dependence on the laser fluence in a 2PPE process. The fluences per pulse used here are $F_{pp} \approx 36 \mu\text{J cm}^{-2}$ (low fluence) for only one opened arm of the interferometer and $F_{pp} \approx 78 \mu\text{J cm}^{-2}$ (high fluence) for both arms opened. By comparison of the intensities in both normalized spectra, a clear suppression of the emission from the Se $4p$ parabolas is observed for the high laser fluence.

To gain insight into the energy and momentum distribution of the loss of spectral weight, we calculated a map of the intensity ratio, $Q(E, \vartheta)$, by using the intensity values of the spectrum at low incident fluence, $I_{\text{low}}(E, \vartheta)$, as reference for the quasi-undisturbed system. With the intensities, $I_{\text{high}}^*(E, \vartheta)$, for the excited system at high laser fluence, we define:

$$Q(E, \vartheta) = \frac{I_{\text{low}}(E, \vartheta)}{I_{\text{high}}^*(E, \vartheta)}. \quad (5.13)$$

Please note, that I_{low} and I_{high}^* are normalized, as discussed in this paragraph. The intensity ratio Q has a high value in energy and momentum regions of strong modifications, because the spectral intensity is reduced there for high laser fluences ($I_{\text{high}}^* < I_{\text{low}}$). The corresponding map is shown in figure 5.34(c). This representation enables us to conclusively answer our two initial questions.

5.2.4–a Is the observed Loss of Intensity Just a Shift of the Energy of the Se $4p$ Bands?

Concerning a possible energetic shift of the bands, angle-integrated 2PPE exhibits some drawbacks. Because the Se $4p$ bands graze or even cut the Fermi energy at the Brillouin zone center—depending on the stoichiometry and preparation of the sample, see section 3.3—a shift in energy may be mistaken for a variation of the spectral intensity of the corresponding feature. The extraction of the actual energy of a state at the Fermi level is not straightforward. A careful deconvolution of the Fermi distribution at E_F is necessary to extract meaningful energies in this energetic region of the photoemission spectra. However, AR-2PPE experiments allow us to decide, whether or not such a shift lies at the core of the observed change of intensity of the Se $4p$ bands, without the need for a difficult and delicate evaluation of the exact energies. Using the two-dimensional detection

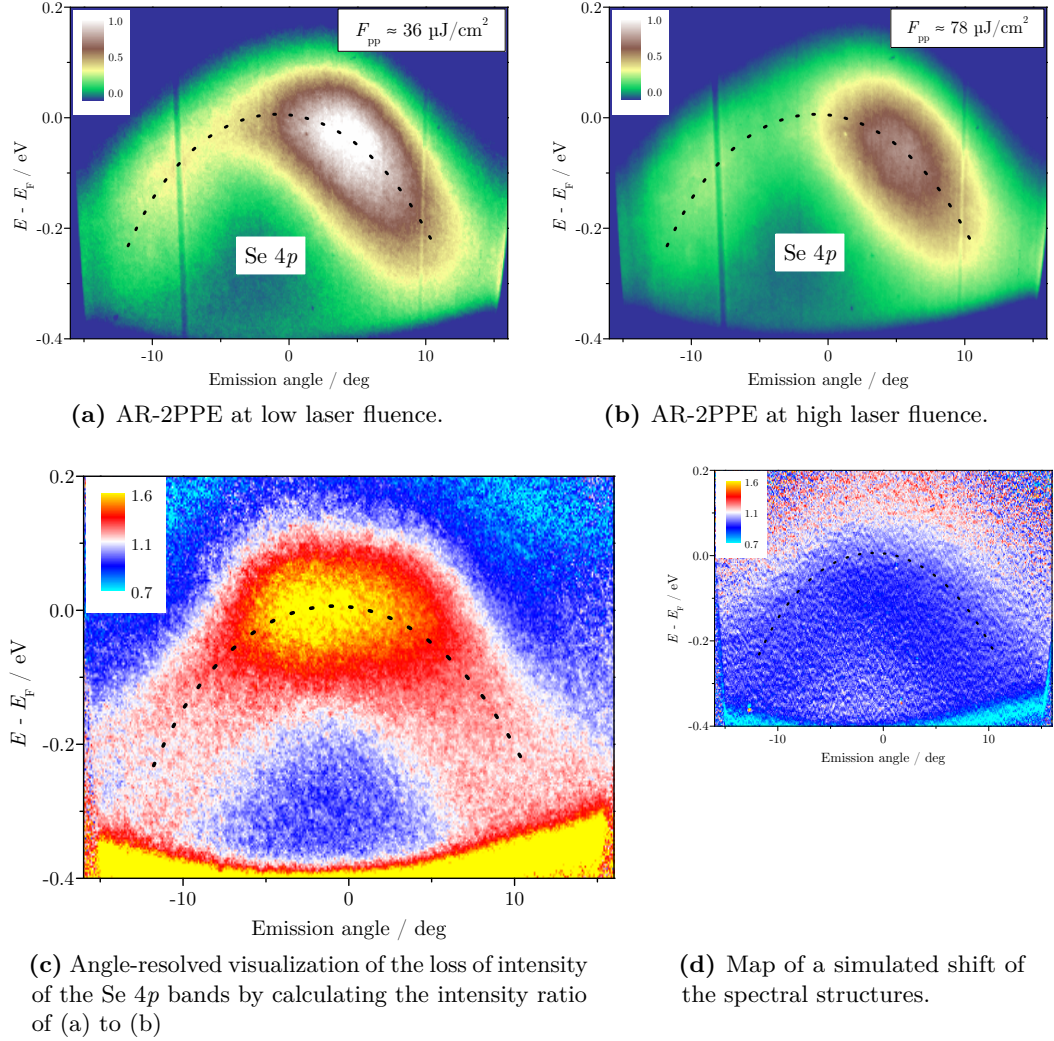


Figure 5.34: (a) and (a) Normalized AR-2PPE spectra of TiSe₂ acquired with laser 2 at $h\nu = 3.12$ eV. We see the Se 4p parabolas and the resonance enhancement due to the Ti 3d* band. Upon increase of the laser fluence, a distinct intensity reduction of the Se 4p feature is observed. (c) By calculating the ratio of the normalized spectra in (a) and (b) an energy and momentum resolved representation of the strength of intensity variations is derived. Clearly, the strongest modification is localized at the $\bar{\Gamma}$ -point, i. e. at the apex of the Se 4p parabolas. (d) The spectrum in (a) is shifted by about 9 meV. A mapping of the intensity ratio analogous to (c) is calculated. Please refer to the black dotted lines as a guide to the eye; they feature the same coordinates in (a)–(c).

unit described in section 3.1 significantly simplifies the task at hand. Please note, that the alternative acquisition of angle-integrated spectra at different polar angles of the sample also yields angular information. Yet, the experimental setup of the angle-integrated photoemission experiments is not well suited for such experiments, i. e. the position of the laser spot on the surface of the samples cannot be reproduced defined enough. Due to inevitable inhomogeneities of our samples, a definite statement on a potential energetic shift and even more on the ratio Q is not possible. The parallel acquisition of spectral intensity for a certain energetic and the range of momentum by the two-dimensional system on the other hand enables us to conclusively compare certain areas with respect to energy and intensity.

Figure 5.34(c) shows such data. This intensity ratio map contains high numerical values wherever the quasi-undisturbed intensity of the sample I_{low} is significantly higher than the corresponding intensity of the excited system I_{high}^* and vice versa. A shift of a spectral feature increases the intensity in the area the feature is shifted into, while simultaneously decreasing the intensity in the area it vacates. Therefore, for a spectral shift, we expect areas of high and low ratio following the spectral shape of the feature.

Please note, that the low-energy cutoff of the spectrum indeed shifts a little, most likely due to desorption of some residual adsorbates or due to a small shift of the work function by an increase in the crystal temperature induced by heating with the high powered laser. A hint of the expected seam-like structure is already observed in the intensity ratio map for this feature, however, the data in this case is not very convincing. Therefore, we simulated a shift of the Se $4p$ bands by shifting the quasi-undisturbed spectrum for low incident laser power, shown in figure 5.34(a), by approximately 9 meV to higher values of $E - E_{\text{F}}$. By calculating a corresponding map of the intensity ratio for the shifted and the original spectrum, we derive an analogous map to figure 5.34(c), yet, uninfluenced by a real loss of spectral weight.

This simulation is shown in figure 5.34(d). Indeed, we clearly observe the expected seam-like structure. Please note, however, that the Se $4p$ parabolas are shifted, only. If we take the cutoff of these bands at the Fermi level upon the shift into account, an increase in the intensity ratio at the Brillouin zone center would still occur. Nevertheless, a closer look at the maps in figures 5.34(c) and (d) reveals some fundamental differences. Please note, that both mappings feature the same color scale, thus making the presented values directly comparable. As confirmed by the simulated data in figure 5.34(d), we expect a lowering of the ratio below the original position of the band and an increase above. In particular for the off-normal photoemission ($\mathbf{k}_{\parallel} \neq 0 \text{ \AA}^{-1}$), which is well separated from the Fermi energy, a shift of this band should be easily observed. Yet, we do not observe such a structure in figure 5.34(c). If any, this data may even suggest a shift in the opposite direction.

In conclusion, we are able to rule out a shift of the Se $4p$ bands energy as the source for the strong suppression of spectral weight for increasing incident laser fluence.

5.2.4–b Does the Se 4p Band Loose Intensity Homogeneously?

The map of the intensity ratio in figure 5.34(c) clearly exhibits a localization of the effect at the apex of the parabolas of the Se 4p bands. The yellow color coding corresponds to the strongest modification observed in this investigation. For off-normal emission the effect is significantly weaker, but clearly observed (red color coding). It is very interesting, that the Se 4p bands seem to be better resolved in the intensity ratio map. In particular, the resonance with the Ti 3d* band strongly influencing the spectral intensity does not modify the intensity ratio at all. The complete absence of the Ti 3d* band is also supported very visually by the fact, that the spectral intensity are asymmetrically distributed around normal emission, yet the intensity ratio is very symmetrical. Also, the region of the lowest spectral intensities resides within the area of the maximum modification, while the dominating resonance lies partially within the flanks of the Se 4p band which feature only a subtle change.

We can summarize our observations as follows: The whole Se 4p band seems to loose spectral intensity, at least in the energetic and the range of momentum investigated here. Obviously, the effect is strongest for near normal emission. In fact, the change is considerably enhanced at the apex of the parabolas of the Se 4p bands.

5.2.4–c Comparison to Simulations within the Model of the Excitonic Insulator

Cercellier et al. [11] presented calculations within the model of the excitonic insulator—one of the possible mechanisms to explain the CDW—which show a very interesting resemblance to our experimental findings. Amongst others, they presented simulated ARPES spectra for the normal conducting room temperature phase of 1T-TiSe₂, as well as data for the low temperature CDW phase. The most distinct difference of this data at the Γ -point is a reduction of the spectral intensity right at the apex of the Se 4p bands' emission upon the phase transition, i. e. these simulations show virtually the same loss of spectral weight in a similar energetic and momentum regime as our experiment.

However, in case of the simulations the effect is induced by the phase transition itself, i. e. the formation of the charge density wave is accompanied by a transfer of spectral weight between certain bands (see section 2.2.1). The transfer of spectral weight leads to a visible decrease of the Se 4p bands at the Γ -point upon the formation of a CDW. This effect is explained exclusively by a excitonic insulator process by the simulations in reference [11].

In contrast, our data feature a very similar spectral modification, although we perform our investigations at room temperature, i. e. within the normal conduction phase of the TiSe₂. Because TiSe₂ features a second order phase transition [3, 8, 248], we expect a continuous onset of the CDW instead of abrupt changes. As already discussed, the charge density wave fluctuations exist even at room temperature [see figure 3.9(c), page 68 and

section 3.3]. Therefore, it is rather tempting to assign the observed reduction of spectral intensity to modifications of the CDW fluctuations. However, our data until now is not sufficient to make any unambiguous decisions, especially concerning the involvement of an excitonic isolator.

5.3 Spectroscopy in the CDW Phase

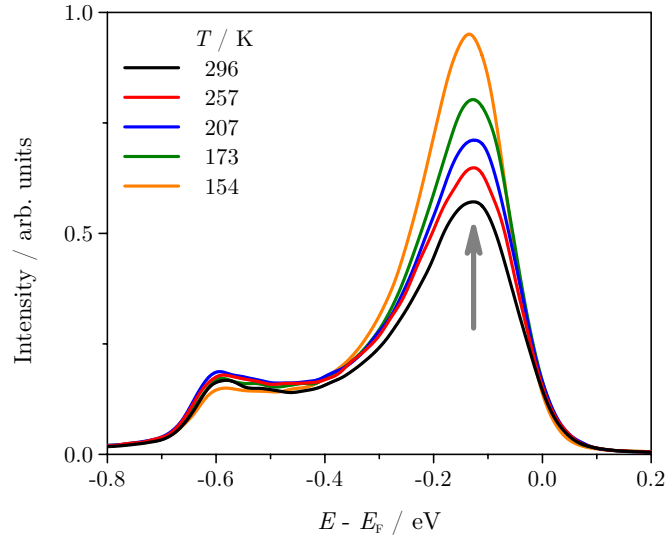
5.3.1 Thermal Dependence

In section 5.1 we discussed in detail the thermal modifications of the spectral shape for the TMDCs investigated in this work. Those experiments focused only on the effect of a temperature increase within the normal conduction phase. Until now we do not know, how the temperature dependence is modified within the low temperature regime, i. e. within the CDW/PLD phase, of $1T$ -TiSe₂. Here we present data acquired upon cooling of the sample below the critical temperature, T_0 , of the phase transition, focusing on potential differences with respect to the normal phase. Our analysis is restricted to TiSe₂, because our reference system TiTe₂ does not show any phase transition and deviations attributed to a CDW/periodic lattice distortion (PLD) are therefore not expected.

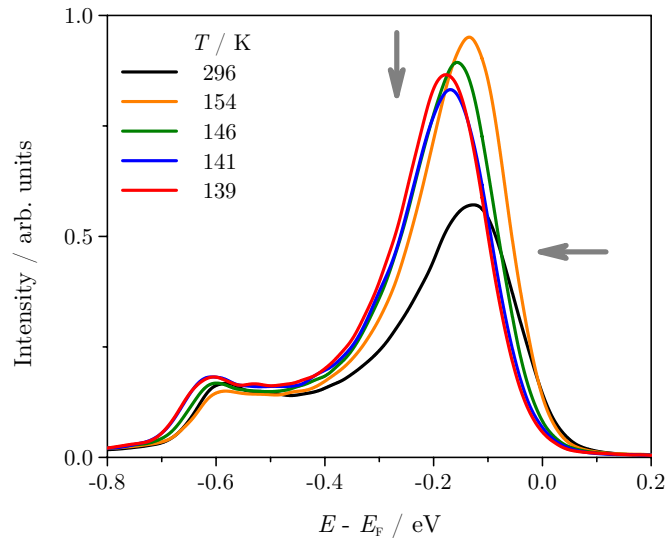
We employ the same laser system, optimized for the same photon energy, energetic resolution, and incident laser fluence, F_{pp} , as given in section 5.1 for the normal conducting phase. The laser fluence is set using two gray filters. The stability during the photoemission experiments performed while cooling the sample (see section 3.1.1) is strikingly demonstrated by the very good comparability of the absolute count rates of the spectra in figure 5.35—no normalization of the spectral intensity is necessary. The stability is emphasized by the plateau area at $E - E_F = -0.5$ eV to -0.4 eV which features intensity variations of only about 5%. The laser power transmitted to the UHV chamber was further checked between different experimental runs and no adjustment was necessary.

Figure 5.35 allows for a first overview of the observed thermal modifications upon approaching the critical temperature of the CDW transition. Initially, the decrease of temperature leads to an increase of the spectral weight of the Se $4p$ bands (arrow) which is exactly what we expect from our previous experiments in section 5.1. However, if the temperature is further decreased and nearing the critical temperature ($T_0 = 202$ K, see table 2.1 in section 2.1) the behavior changes: the Se $4p$ bands reveal a small reduction of the amplitude and a simultaneous, articulate increase of the binding energy (arrows). The latter is clearly visible as a shift of the high energy cutoff of the spectrum.

A quantitative analysis of the data corresponding to the methods described in section 5.1 is presented in figure 5.36. The amplitude and area of the spectral peak of the Se $4p$ bands are given relative to their room temperature value ($T_{RT} = 296$ K). The spectra were only smoothed, but not normalized to the plateau level, except for figure 5.36(d) (see section 5.1.2–e), we will comment on this shortly. Above T_0 we expect a behavior



(a) Initially, upon cooling the spectral weight of the Se 4p bands increases.



(b) Further cooling leads to the formation of a CDW phase and a characteristic shift of the energy of the Se 4p bands.

Figure 5.35: SH-2PPE EDCs corresponding to the data in figure 5.3(a) ($h\nu = 3.18 \text{ eV}$, $F_{\text{pp}} \approx 5 \mu\text{J cm}^{-2}$). (a) and (b) show a series of EDCs for decreasing sample temperature. The most prominent spectral modifications are visualized by arrows.

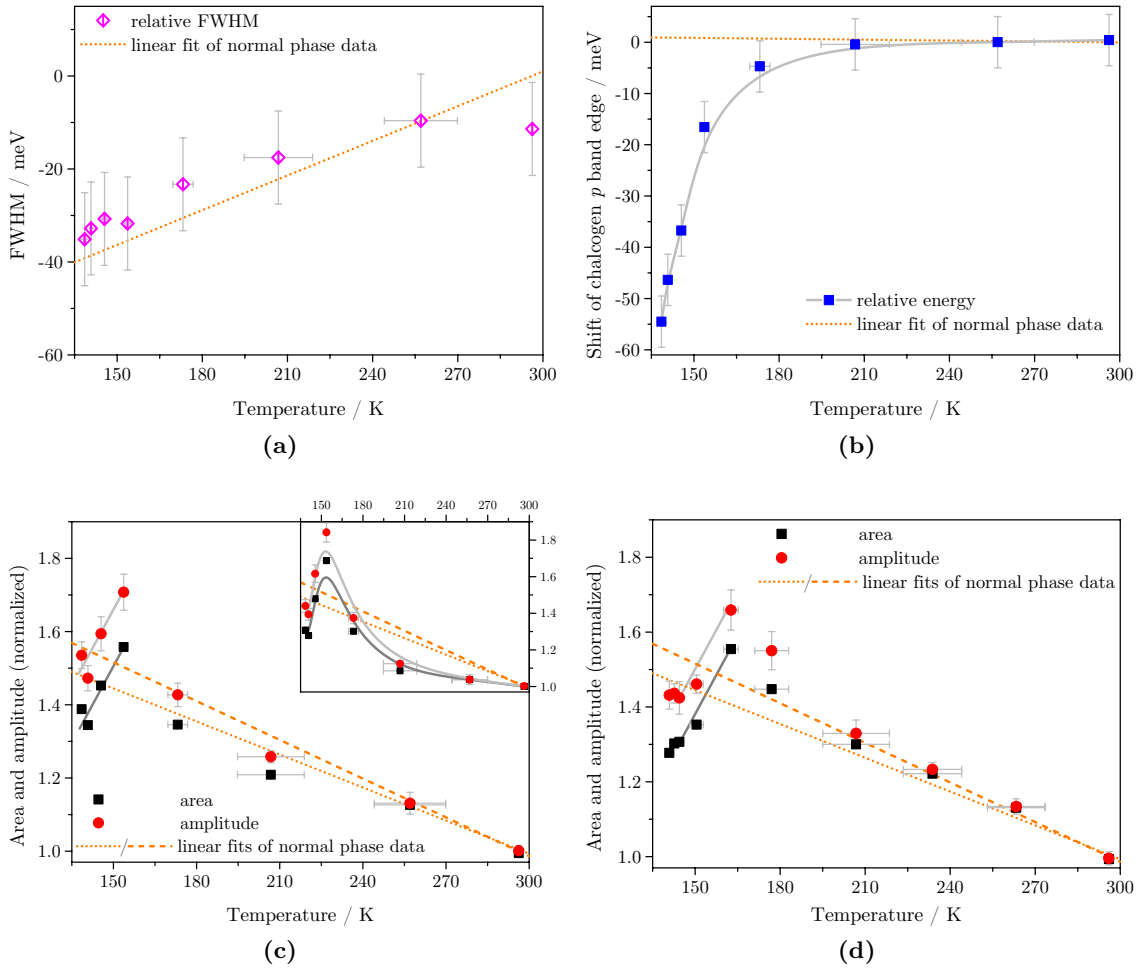


Figure 5.36: The numerically evaluated (a) FWHM and (c) amplitude/area of the Se $4p$ bands and the (b) energy of the high energy cutoff of the spectra is shown. The orange lines represent linear fits to the data acquired within the normal conducting phase which are presented in section 5.1. In (c) the dashed (dotted) line corresponds to the amplitude (area). Gray lines are a guide to the eye. The inset shows data normalized to the plateau intensity. (d) is similar to (c), but features a different set of experimental data. The non-linearity just above T_0 is visible better in this case.

similar to our previous investigation at room temperature, because the sample is still within the normal conducting phase; this is indeed the case.

The numerically evaluated FWHM of the whole spectral peak of the Se 4*p* bands is shown in figure 5.36(a). We find a good agreement of the FWHM for the whole temperature range investigated here to the temperature coefficient presented in section 5.1.4-d. The orange line is a linear fit to the room temperature data from section 5.1.4-b. The modification of the FWHM is well described by the temperature coefficient and therefore consistent with a purely thermal effect. No influence of the phase transition is observed even below T_0 .

The CDW instability, however, modifies quite prominently the energy of the high energy cutoff of the spectra, as well as the amplitude of the Se 4*p* bands. Figure 5.36(b) shows the temperature dependent energy of the spectral cutoff. In section 5.1.4-b we observed, that within the normal conducting phase of TiSe₂ the high energy cutoff of the spectrum is virtually constant with respect to temperature. The corresponding linear fit is again included in the figure (orange). If the critical temperature is approached, the energy of the cutoff decreases, i. e. the binding energy of the Se 4*p* bands increases by a few tens of meV. Please note, that the offset of T_0 (about 25 K) with respect to the typical value presented in figure 3.10 in section 3.3 is a consequence of the difference in the thermal equilibrium. The data presented here was taken during the cooling of the sample, while the other data set was acquired during the warm-up. The latter is supposed to allow for a better thermal equilibrium of the sample and the temperature sensor. The experiment is nevertheless performed during the cool-down, because only then a specific behavior of the amplitude of the Se 4*p* bands can be observed in our experiment—we will discuss this shortly. Although these two acquisition modes yield an offset and a difference of the temperature coefficient, the qualitative behavior is still observed.

The energetic shift of the Se 4*p* bands is a consequence of the opening of a band gap induced by the formation of a CDW/PLD (refer to section 2.2 for details). The increase of binding energy of the Se 4*p* bands is well known from experimental and theoretical data [7, 10, 11]. The temperature dependent shift investigated here is therefore a clear marker of the formation of a CDW. Furthermore, the energy of the cutoff is easily evaluated with good precision, i. e. this energy allows for an quantification of the transition into the CDW phase.

Finally, figures 5.36(c) and (d) present the numerical evaluation of the amplitude and area of the peak of the Se 4*p* bands (see addendum A.1.1 for details) for two different experimental runs. For our discussion, we need to consider only the amplitude (see section 5.1.4-a), however, we provide both equivalent data for comparison to the linear fits from section 5.1.4-d (dashed: amplitude, dotted: area). The data is normalized to the room temperature value, i. e. the line fits cross at room temperature. Consequently for lower temperatures the amplitude features now the higher magnitude than the area (see appendix A.2.1). Please note, that figure 5.36(c) shows data extracted from spectra

containing absolute photoemission intensities, i. e. no normalization to the plateau was applied. The inset features plateau normalized data. The plateau normalization mainly modifies the linear decrease of the amplitude/area for $T > T_0$. In this case the linearity is lost after normalization.

Comparison to our discussion in section 5.1.2–e reveals, that this behavior is in agreement to a plateau intensity which is temperature dependent, i. e. the assumption of a more or less constant plateau level is not appropriate anymore. While plateau normalization is necessary to compensate instabilities of the laser fluence and the experimental setup, it modifies the shape of the normalized data. Here, the spectra exhibit virtually no extrinsic drifts (see figure 5.35), therefore, normalization to the plateau is not required and the distortion of the normalized data can be circumvented. In conclusion, the data show the expected linear behavior in good agreement to the room temperature data and the shape of the corresponding curves clearly indicates a vanishingly small influence of sample extrinsic drifts of the photoemission intensity. In contrast, the second data set presented in figure 5.36(d) yield a better consistency of the data especially at the lowest temperatures with plateau normalization—this indicates the relevance of drifts of the spectral intensity. It is therefore crucial to analyze the applicability of plateau normalization.

Upon the phase transition, the simple linear behavior does not hold anymore. The amplitude reveals a maximum close to the critical temperature, followed by a decrease of the spectral intensity upon lowering of the temperature within the CDW phase. This loss of spectral weight is not a thermal effect. The CDW formation is accompanied by a transfer of spectral weight. In case of TiSe_2 the Se $4p$ bands at the Γ -point lose spectral weight [55] (see also section 6.2). The decrease of the amplitude and the increase of the binding energy of the Se $4p$ bands are both spectral modifications attributed to the CDW transition of this system and consequently the data deviate from the thermal modifications observed within the normal conducting phase. Please note, that the loss of spectral weight is observed for different experimental runs. Figures 5.36(c) and (d) show two such exemplary runs. Figure 5.36(d) also demonstrates, that the enhanced increase of the spectral weight just above T_0 is indeed not an artifact. The temperature coefficient of the amplitude is thus not valid close to T_0 (range about 30 K). We attribute this enhancement to the onset of the increase of binding energy of the Se $4p$ bands. These bands are cut by the Fermi energy, therefore, initially, the energetic shift reveals the full, uncut peak of these bands and consequently the spectral intensity of this feature increases.

We do not show data on the thermal behavior of the work function, because of its bad quality and reproducibility. Cooling to the temperature range of liquid nitrogen renders the sample prone to adsorption of residual gas which modifies the work function significantly and it is thus not a good measure of the sample temperature. The work function becomes more of an indicator for the surface quality. However, our data hint at a small drop of the work function coinciding with the phase transition which we

attribute to modifications of the sample surface, probably induced by the formation of a superstructure. In section 6.2.3 we present a detailed time resolved investigation of this effect.

Which of these spectral signatures can be employed for assigning a temperature of the sample? Because of the cooling of the sample the work function cannot be used at all as it is very susceptible to adsorbates on the sample surface. Cooling leads to enhanced adsorption of residual gas, in contrast to heating of the sample, which actually removes such impurities.

The FWHM does not seem to be influenced by the CDW phase transition and its temperature coefficient is well defined and in very good agreement to our room temperature experiment. It proves to be a valuable means of estimation of the temperature, especially in combination with the other spectral characteristics. For the remaining spectral features we need to discuss the normal conducting state above the critical temperature and the CDW phase below T_0 separately, because the thermal evolution of some of these signatures changes drastically.

For $T > T_0$ we find a good agreement to our data acquired during heating of the sample. The FWHM and the amplitude (or area) of the Se 4*p* bands are well suited for monitoring the temperature of the sample using the thermal coefficients of section 5.1.4–d. However, the amplitude is also sensitive to instabilities of the experimental system and adsorbates of the sample, i. e. it is very sensitive on sample extrinsic influences, like the incident laser fluence. Normalization to the spectral plateau—necessary in case of such extrinsic effects—further complicates the analysis. Nevertheless, our analysis in this section shows, that even close to T_0 the system exhibits still the same temperature dependence, as analyzed for the normal conducting phase. Although we need to take care considering the amplitude of the Se 4*p* bands, in combination with the FWHM a sufficiently precise evaluation of the relative temperature changes is possible using temperature coefficients.

Below the critical temperature the thermal modifications of TiSe₂ differ significantly. Again, the FWHM of the Se 4*p* bands serves as a reference criterion for the relative change in temperature. We observe two distinct thermal effects which are only present within the CDW phase: a loss of spectral weight and an increase of binding energy of the Se 4*p* bands for decreasing temperature. These are very prominent temperature dependent modifications which are characteristic for the CDW/PLD of TiSe₂. The energetic shift of the high energy cutoff of the spectrum is indeed well suited for finding small, relative changes of the sample temperature; even small energetic shifts of the cutoff within the CDW phase are identified with good precision. Please note, that data acquisition during the cool-down and warm-up of the sample leads to a

differences in the thermal equilibrium of the sample and the temperature sensor which results in an offset of the corresponding temperature scales and different temperature coefficients. The data presented in this section is thus not suitable for the definition of a temperature scale for our time resolved experiments for which we expect a laser induced heat-up of the sample (see section 5.2). Therefore, we use the temperature coefficient as defined in section 3.3 (see figure 3.10) using a very precise temperature dependent experiment performed during the sample warm-up. The reference temperature coefficient is $\Delta E_c = (4.31 \pm 0.15) \times 10^{-4} \text{ eV K}^{-1}$. We discuss the applicability of ΔE_c in the following section 5.3.2 with respect to time resolved experiments.

A closing remark on the temperature dependence in the vicinity of T_0 . The loss of spectral weight of the Se $4p$ bands is not easily observed experimentally. It is only visible upon cooling of the sample for an extended period of time, because this modification is only established within the CDW phase. The temperature range in which this modification occurs is already close to the minimum temperature reachable by our setup. The thermal equilibrium is established slowly at the lowest temperatures. We cannot observe this effect during the warm-up of the sample, because it seems to proceed too fast. Nevertheless, the discontinuity of the spectral weight is clearly observed in several experiments.

A quantitative analysis in terms of a temperature coefficient of the amplitude for $T < T_0$ is futile. At the lowest temperatures the temperature of the sample and the sensor slowly equilibrate thermally, i. e. the measured temperature changes. The temperature dependence of the amplitude is, however, very instructive for understanding our time resolved experiments in section 6.2. They enable a qualitative understanding of the low temperature behavior below the critical temperature.

The energetic shift of the spectral cutoff provides a good measure for the formation of the CDW/PLD. TiSe_2 features a second order phase transition at T_0 [3, 8, 248], i. e. the phase transition proceeds gradually. This process can be monitored using the energy of the cutoff. The data thus allow for a qualitative understanding of our time resolved experiment presented in section 6.2. By a careful perturbation or variation of the sample temperature, for instance, by the absorbed laser fluence (see also section 5.3.2) the observation of the transfer of spectral weight and the changes in binding energy in the CDW phase are accessible.

5.3.2 Laser Fluence Dependence

In the previous section 5.3.1 we focused on thermally induced spectral modifications. Analogously to section 5.2 we expect, of course, similar modifications upon variation of the absorbed laser fluence, F_{pp} . Here, we complement the normal phase experiments by measurements of the TiSe_2 crystals within the CDW phase. We investigate, whether increasing F_{pp} indeed leads to an increase of the sample temperature. Additionally, we

are interested in the degree to which the CDW/PLD may be perturbed by the absorbed laser pulses. Is it possible, to fully destroy the CDW and establish the normal conducting phase solely with the laser? This is of relevance with respect to our time resolved investigations in chapter 6.

Our experimental approach is again analogous to section 5.2 using the same laser system, set for the same photon energy, and the energetic resolution of the experimental setup is also comparable. Great care was taken to ensure the stability of the setup by employing the method described in section 3.1.1. The sample was stabilized to thermal equilibrium at the minimum temperature reached and constant cooling ensured a stable temperature. A series of photoemission spectra was taken for different values of F_{pp} .

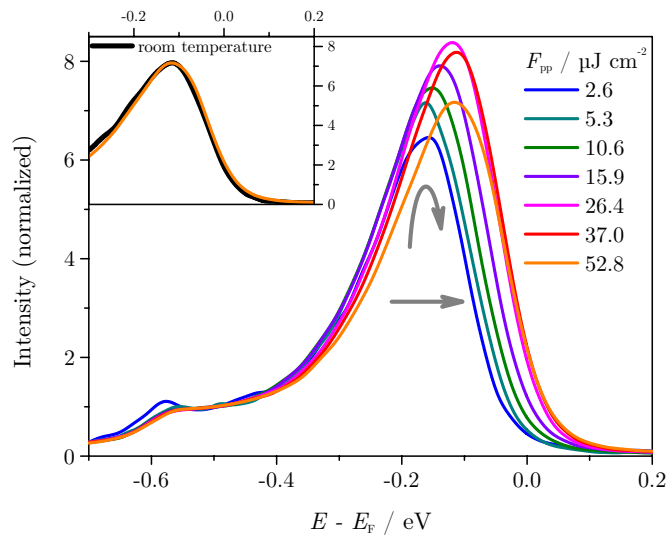


Figure 5.37: Dependence of the spectral shape on the absorbed laser fluence, F_{pp} . The changes of the binding energy and spectral weight of the Se 4*p* bands is emphasized by gray arrows. The data is normalized to the plateau intensity. The inset compares the spectrum acquired at $F_{pp} = 52.8 \mu J cm^{-2}$ to a spectrum taken at room temperature.

Figure 5.37 presents such a set of fluence dependent spectra. The main modifications of the spectral shape (arrows) are an increase of the amplitude and a decrease of the binding energy of the Se 4*p* bands. Our investigation in section 5.2 revealed that an increase of the absorbed laser fluence leads to a heat-up of the sample which results in spectral modifications qualitatively comparable to temperature dependent experiments. An interesting and important finding is visualized in the inset: for $F_{pp} \approx 53 \mu J cm^{-2}$ the spectrum is consistent with the room temperature case. The energy of the cutoff agrees very well with the value observed at room temperature, i. e. it is possible to drive a transition from the low temperature CDW phase into the high temperature normal conducting phase solely by the absorbed laser fluence.

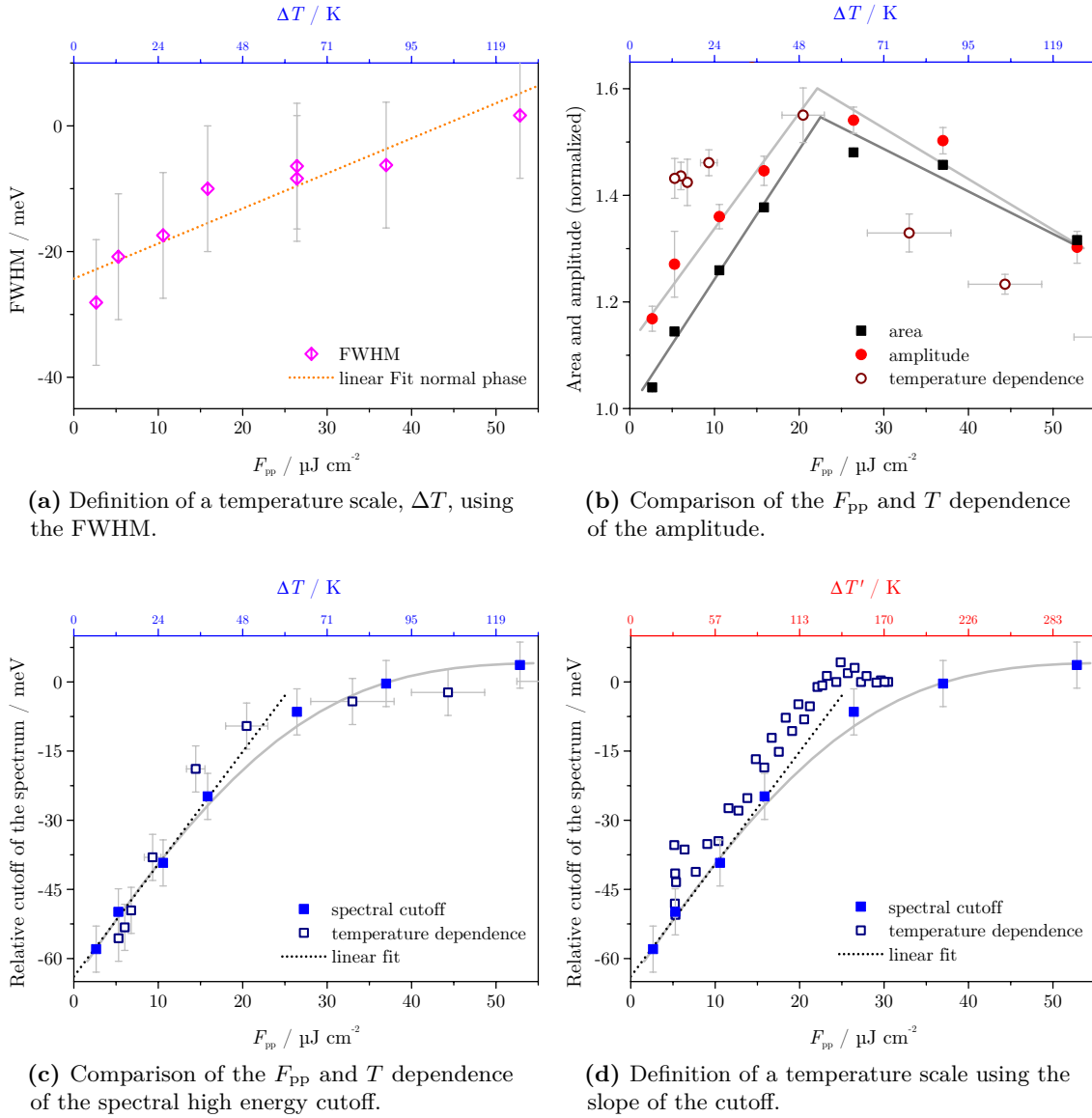


Figure 5.38: (a) The fluence and temperature coefficients of the FWHM allow for the calculation of a relative temperature scale, ΔT , (blue). The temperature–fluence conversion factor given in section 5.2.3 is used. (b) and (c) compare F_{pp} dependent data on the amplitude/area of the Se $4p$ bands and the spectral high energy cutoff to the T dependent data from section 5.3.1 (open symbols). The latter are rescaled to the relative scale. Gray lines are guides to the eye. (c) also features a fit of the slope of the low fluence data (dotted line). This fit is used in (d) to define an alternative relative T -scale (red) from the line fit to the cutoff by comparing its slope to the corresponding data in section 3.3.

Figure 5.38 compiles the fluence dependence of the FWHM, the amplitude (area) of the Se 4*p* bands, and the spectral high energy cutoff. The fluence range is $F_{pp} = 2.6 \mu\text{J cm}^{-2}$ to $52.8 \mu\text{J cm}^{-2}$ and the fluence is increased, beginning at the lowest fluence after cool-down of the sample. The system is initially well within the CDW phase, i. e. well below the critical temperature.

First, we compare these low temperature data to the corresponding experiment at room temperature (section 5.2) and to the temperature depended behavior during the phase transition (section 5.3.1). In the normal conducting phase experiments we found the work function and the FWHM of the Se 4*p* bands to be reliable spectral signatures for the assignment of a sample temperature for different F_{pp} . However, the work function cannot be evaluated for a sample cooled by liquid nitrogen, because of its sensitivity to adsorbates.

We therefore focus on the FWHM which is presented in figure 5.38(a). The figure shows a linear fit (dotted line) with a fixed slope at the fluence coefficient, $\Delta w_{F_{pp}}$, for increasing F_{pp} , as estimated from normal phase experiments [see table 5.10(a), section 5.2.3]. Please note, that a difference is observed for the fluence coefficients, depending on whether the fluence is in- or decreased; see section 5.2.3. The fluence dependent FWHM for the experiment within the CDW and the normal conducting phase is very well described by one fluence coefficient. Additionally, the temperature dependent FWHM in section 5.3.1 [see figure 5.36(a)] also fit well to the same temperature coefficient for both phases of TiSe₂. Therefore, the average temperature–fluence conversion factor¹⁴, $\Delta T_{F_{pp}}$, provided by table 5.10(b) for the normal phase data (section 5.2.3) is also valid for the low temperature data, too.

In other words, the fact that the normal phase temperature and fluence coefficients fit very well to the CDW phase data means, that the conversion factor deduced from the normal phase data still holds at low temperatures. $\Delta T_{F_{pp}}$ thus allows for a direct calculation of a temperature scale from F_{pp} for the whole temperature range. The static temperature increase of the sample, ΔT , for a certain F_{pp} is shown in the top scale (blue) of figures 5.38(a) to (c).

Let us now analyze, whether the relative temperature defined in this way really corresponds to the static heat-up of the sample. Figures 5.38(b) and (c) provide additional data on the amplitude/area of the Se 4*p* bands and the spectral high energy cutoff. The general fluence dependent behavior is strikingly similar to the thermal modifications (see section 5.3.1):

- the reversed magnitude of amplitude and area with respect to the data for the

¹⁴The temperature–fluence conversion factor is calculated using equation (5.9) in section 5.2.2–a:

$$\Delta T_{F_{pp}} = \frac{\Delta w_{F_{pp}}}{\Delta w_T},$$

with the fluence and temperature coefficients, $\Delta w_{F_{pp}}$ and Δw_T , respectively.

normal conducting phase is observed,

- the spectral weight of the Se $4p$ bands increases initially and then decreases with increasing F_{pp} , exhibiting a maximum close to the phase transition, and
- the spectral cutoff reveals the simultaneous decrease of the binding energy of the Se $4p$ bands during the phase transition.

Therefore, an increasing F_{pp} leads to spectral modifications qualitatively very similar to a sample heat-up. The calculated ΔT -scale¹⁵ allows for a quantitative comparison to the thermal data (open symbols). We find a good agreement of the fluence and temperature dependent data.

Figure 5.38(b) exhibits strikingly consistent maxima of the amplitude of the Se $4p$ bands. The fluence dependent data reveal the laser induced phase transition at a value of $F_{pp} \approx 20 \mu\text{J cm}^{-2}$ which corresponds to an increase of the sample temperature calculated using $\Delta T_{F_{pp}}$ of approximately 50 K. Note, that ΔT is referred to $F_{pp} = 0 \mu\text{J cm}^{-2}$, i. e. considering the temperature dependent data there is an offset for the incident laser fluence of $\Delta T \approx 10$ K. These findings are in very good agreement to the temperature dependence presented in figure 5.36 (section 5.3.1).

Furthermore, the energy of the spectral cutoff, presented in figure 5.38(c), also reveals a consistent onset of the shift of the binding energy associated with the phase transition. Assuming the relative temperature scale defined in this section, the energetic shift of the cutoff thus agrees well to the fluence dependent data, i. e. both data reveal a similar fluence/temperature range for the transition.

We summarize two important findings:

- (i) The shift of the high energy cutoff of the spectrum and the changes in spectral weight of the Se $4p$ bands are both markers for the phase transition of TiSe_2 (see section 5.3.1). The consistent ΔT at which they occur for both datasets shows, that the temperature–fluence conversion factor defined for the normal conducting phase still holds within the CDW phase. We therefore conclude, that the fluence induced static heating of the sample is the same for the cooled sample, too. The fluence coefficients and the corresponding conversion factor (see section 5.2.3) are applicable for experiments at low and at room temperature. The static thermal behavior induced by changes of F_{pp} is described by $\Delta T_{F_{pp}}$ only and is not considerably modified within the CDW phase.
- (ii) It is indeed possible to transfer the system from its low temperature CDW state into the normal conducting phase solely by the absorbed laser fluence. However,

¹⁵Note, that the temperature dependent data are offset by $F_{pp} = 5.3 \mu\text{J cm}^{-2}$, because they were taken at this value of the absorbed fluence.

this is mainly induced by the strong heat-up of the TMDC investigated here. The absorbed laser yields a temperature increase high enough to drive the phase transition.

However, we observe interesting deviations from the thermal behavior. The “markers” of the phase transition—the binding energy and spectral weight of the Se 4*p* bands—both deviate from the simple thermal effects associated with the static heat-up of the sample. This is in agreement to our observations in section 5.2.2–b where we found a distinct deviation of the fluence dependent amplitude from the behavior expected from the temperature scale derived from the other spectral signatures. The static spectra correspond to coinciding pump and probe pulses in a time resolved experiment, i. e. the initial, highly non-thermal state of the electronic system is probed in such an experiment. Additional laser induced modifications (beside the static heating of the sample) therefore manifest in such fluence dependent data. The observation of these deviations is very instructive with respect to the time resolved experiments presented in chapter 6, because they reveal spectral signatures, which may exhibit ultrafast dynamics after the excitation by the laser.

Such deviations are observed for the two spectral characteristics which are closely related to the CDW/PLD phase transition:

- (i) The amplitude of the Se 4*p* bands does not fit well to the thermal behavior [see figure 5.38(b)] if the single values are compared, only the general trend is observed in both cases. Both data are normalized to the corresponding room temperature values, thus, we do not expect this normalization itself to deviate. Generally, the intensity derived spectral signatures are sensitive to adsorbates (see section 5.3.1), which can lead to considerable modifications—a quantitative evaluation of the differences is thus futile.

Nevertheless, the observed deviations are also in agreement to non-thermal laser induced effects as described in section 5.2.2–b. Above the critical temperature, these room temperature fluence depended data feature a similarly enhanced amplitude/area with respect to the temperature dependent experiment. This suggests, that initially¹⁶ the absorbed laser pulses do not reduce the amplitude as much, as expected from a simple, static heating of the sample. Below T_0 the amplitude reveals a significantly stronger reaction to the laser fluence with respect to the thermal data. This hints at a strong laser induced perturbation of the CDW/PLD phase.

- (ii) A close look at the cutoff data in figure 5.38(c) shows a mismatch of the slopes of the thermal and the fluence dependent curves. Although the occurrence of the phase

¹⁶Please note, that the static experiment corresponds to the zero delay case of a time resolved experiment (see section 5.2.2–b).

transition is well reproduced, the slopes do not agree. Indeed, the temperature and fluence dependent data are not expected to be in perfect agreement. The thermal data was acquired during cooling of the sample, while an increase of the fluence leads to a warm-up, i. e. these data should compare better to the temperature coefficient deduced from an experiment starting at the lowest temperature. The different thermal equilibrium of sample and temperature sensor for cooling and heating leads to differences in the absolute temperature—this is not relevant here, as we investigate only relative changes—and the temperature coefficient (see discussion in section 5.3.1).

In comparison to the thermal behavior of the cutoff, the fluence dependent data reveals a reduced slope. This is compatible with the differences observed for experiments performed during cooling and heating of the sample below T_0 (see section 3.3). However, if we calculate a temperature–fluence conversion factor from the temperature coefficient of section 3.3 and the fluence coefficient of the data discussed here, we derive the relative temperature scale $\Delta T'$ (red) in figure 5.38(d). This scale is not to be understood in terms of an static sample temperature, because it predicts a phase transition at clearly too low fluences. It emphasizes the enhanced laser induced perturbation of the CDW phase. The systems reacts stronger, than estimated from the thermal data.

Finally, we like to comment on the quality of the temperature scale assigned to the absorbed laser fluence. The characteristic markers of the phase transition are very well reproduced using the suggested conversion factor: the maximum of the amplitude of the Se $4p$ bands and the center of the flank of the energetic shift of the spectral high energy cutoff do not deviate from their temperature dependent counterpart.

The details of the fluence dependence, however, reveal significant deviations from the thermal data. Therefore, while the static laser induced heat-up of the sample can be estimated, the deviations suggest an additional laser induced perturbation of the CDW/PLD phase. This enables the identification of interesting spectral signatures for a detailed time resolved investigation.

5.4 Summary and Conclusion

Chapter 5 focused on static spectral modifications, induced either by a variation of the sample temperature or the absorbed laser fluence. Both the temperature and fluence dependence of the relevant spectral signatures were investigated thoroughly and quantified by the definition of temperature and fluence coefficients, as well as a conversion factor for the calculation of the static increase of the sample temperature corresponding to a certain absorbed fluence (see sections 5.1.4–d, 5.2.3, and 5.3.2).

The foundation of our investigation is the behavior of the TMDCs discussed here with temperature. Our experiments yield a multitude of findings:

- First of all, the temperature dependent spectra reveal characteristic modifications, for instance, of the work function, and the FWHM and amplitude of the chalcogen p bands. A careful analysis in terms of thermal effects fully explains these observations.
- Furthermore, we find a linear temperature dependence for some of these spectral features—or at least a thermal behavior well estimated by a line fit in case of the amplitude or area of the chalcogen p bands. This enables the definition of temperature coefficients, which describe the linear change of a spectral signature with the temperature.
- In case of TiSe₂ a phase transition at the critical temperature $T_0 = 202$ K (see section 2.1) from the normal conducting ($T > T_0$) into a CDW/PLD phase ($T < T_0$) is observed. The temperature coefficients are valid for $T > T_0$, at least up to approximately 500 K, which is the maximum accessed in our experiments.
- Within the CDW/PLD ($T \leq T_0$) we observe the typical spectral signatures of the phase transition: an increase of the binding energy and a loss of the spectral weight of the Se $4p$ bands (see section 2.2). These data are, however, not suitable for the definition of a temperature scale below T_0 . For reasons discussed in section 5.3 the experiment needed to be conducted under thermal equilibrium conditions incomparable to our usual experimental approach. Nevertheless, a qualitative approach is possible and the fluence dependence we discuss shortly allows for a quantitative evaluation of the time resolved data.

In case of the time resolved experiments discussed in the following chapters 6 and 7 we investigate the temporal evolution of the spectral shape after excitation of the system by a pump laser pulse. This pump pulse obviously modifies the sample system by deposition of its energy. We therefore investigated the effects of a variation of the absorbed laser fluence on the spectral shape in a static photoemission experiment, leading to the following observations:

- We find, that the laser induced spectral modifications are mainly described by thermal effects, i. e. by a static heat-up of the sample, leading to a new thermal equilibrium. This is true for the whole temperature range of our experiments ($T \approx 120$ K to 500 K).
- The static heat-up is quantified by a single temperature–fluence conversion factor (see section 5.2.3), i. e. the temperature increase induced by a certain absorbed fluence is easily calculated. This approach is, of course, only valid for a sample in thermal equilibrium. It can only describe the static heat-up, but not the instantaneous effects during a time resolved experiment.
- We identify distinct deviations for the spectral signatures associated with the phase transition. The amplitude of the Se $4p$ bands and the energetic shift of the spectral

cutoff at low temperatures are not well described by the static heat-up of the sample. This hints at additional, non-thermal modifications induced by the laser which are the subject of our time resolved experiments.

- For the interpretation of the time resolved data our static findings are very valuable. They provide a qualitative overview of the expected spectral modifications. The markers of the phase transition—the energy of the spectral high energy cutoff and the amplitude of the Se $4p$ bands—allow for an evaluation of the degree to which the pump pulse perturbs the CDW/PLD phase.
- Finally, our experiments show, that the static heat-up of the sample induced by the absorbed laser pulses is already enough to drive the phase transition into the room temperature state.

It will be therefore very instructive to investigate in the following chapters, whether the phase transition can also be driven non-thermally, i. e. without statically heating the sample by the absorbed laser. Can we observe an ultrafast laser induced perturbation of the electronic system which also leads to the typical spectral modifications associated with the phase transition? Our findings in this chapter 5 are very valuable for the interpretation of such data and will enable us, to identify and quantify a laser induced perturbation of the low temperature phase of TiSe_2 .

6 Ultrafast Dynamics of the Laser Induced Modifications of the Se $4p$ Bands of $1T$ -TiSe $_2$

In the preceding chapters we presented static spectroscopic experiments on two transition metal dichalcogenides (TMDCs). In the course of our investigations we observed strong spectral modifications which can be induced either thermally or by the absorbed laser—the temperature and fluence dependent spectra revealing interesting differences (see chapter 5). Time resolved photoemission methods provide a means of monitoring the temporal evolution of the electronic system after excitation by a laser pulse on a femtosecond timescale. Such methods are presented in the in section 2.5. Earlier time resolved photoemission works, for example, by Perfetti et al. [4] and Schmitt et al. [31] have shown, that the detailed study of the non-equilibrium dynamics of the electronic system can provide valuable insight into systems with strong electronic correlations. In the specific case of $1T$ -TiSe $_2$ a peculiar correlated electronic ground state is observed at low temperatures, characterized by a charge density wave (CDW) which even persists in form of fluctuations at room temperature, see, e. g., references [3, 7, 8, 38] and section 2.2. There is still an ongoing discussion on the actual mechanism of the CDW phase transition which basically focuses on the question, as to what degree the transition originates from the electronic system or the lattice [3, 7–11], different possible mechanism are presented in section 2.2.1. The fundamental timescales of the processes involved may particularly contribute to the identification of the origin of this correlated phase [4].

In this chapter we first present conventional one-color time-resolved two-photon photoemission (TR-2PPE) autocorrelation experiments (cf. section 2.5.1) performed on $1T$ -TiSe $_2$ and $1T$ -TiTe $_2$. Although this method has some drawbacks concerning the interpretation of the data, which we will discuss in detail shortly, it enables us to draw first conclusions about the potential processes underlying the observed effects. In particular, we discuss the data acquired for TiSe $_2$ in comparison to the reference system TiTe $_2$.

A two-color pump–probe setup is better suited for this investigation as it disentangles the pump and probe event; section 2.5.3 presents the method in detail. In this work, we take a rather unconventional approach: the time-resolved IR-pump SH-probe photoemission setup which combines an IR-pump with a probe pulse photon energy suitable for two-photon photoemission (2PPE). Similar pump–probe schemes are generally employed, however, often a significantly higher photon energy in the ultraviolet (UV) range is used

for the probe pulse. This enables one-photon photoemission (1PPE) spectroscopy which features a higher photoelectron yield than 2PPE. Our choice of a lower photon energy and consequently a 2PPE scheme is motivated twofold: first, sufficiently high photon energies for 1PPE are not available to our experiment even by generation of the fourth harmonic, and second, the pulse duration and thus the temporal resolution is considerably better than for the fourth harmonic which is very important for our studies. We discuss our approach in detail in section 6.2.

The pump–probe experiments consist of two stages: first, a high powered pump pulse of the fundamental (IR) photon energy is used to excite the sample and afterward a second harmonic (SH) probe pulse generates photoelectrons. In contrast to the pump, the probe pulse actually contributes to the 2PPE spectrum. The fluence of this second laser pulse is chosen such, that it does not lead to considerable additional excitation of the sample—an important difference to the TR-2PPE method mentioned earlier, where both pulses act as pump and probe simultaneously. The temporal evolution of excitation and relaxation of the sample is accessed upon tuning the delay of pump and probe pulses (see section 2.5).

This chapter concludes with a detailed investigation of the different processes identified in our time-resolved experiments. Because of the rather small photon energy needed for the 2PPE process, these experiments focus on a small part of the Brillouin zone near its center¹; we typically investigate normal emission at the $\bar{\Gamma}$ -point. In the following chapter 7 we provide an outlook on an experiment which uses very high photon energies and thus is capable of monitoring the whole first Brillouin zone simultaneously.

6.1 One-color TR-2PPE experiments in autocorrelation mode

In section 4.2 we investigated the ultrafast dynamics of excited electronic states using conventional TR-2PPE and time- and angle-resolved two-photon photoemission (TAR-2PPE) experiments in the autocorrelated mode. These data enabled us to investigate the lifetime of the unoccupied Ti 3d* band of TiSe₂.

Our findings in section 5.2 lead us now to a fundamentally different approach for the investigation of ultrafast dynamics in the systems TiSe₂ and TiTe₂. A set of *static* SH-2PPE experiments performed at different absorbed laser fluences reveals peculiar, laser induced and fluence dependent modifications of the photoemission spectra which are related to the *occupied* electronic structure. These spectral changes are in part

¹This is a consequence of the fact, that a photoelectron needs a non-vanishing surface perpendicular momentum in the direction of the vacuum, i. e. $|\mathbf{k}_\perp| > 0 \text{ \AA}^{-1}$, to be transmitting into the vacuum and into the analyzer. Equation (2.10) in section 2.4 shows, that this leads to a quadratic increase of the minimum kinetic energy of a detectable photoelectron with parallel momentum, i. e. to enable the generation of photoelectrons at high momenta, the photon energy needs to be high.

similar to data acquired upon increasing the sample temperature, yet, we also observe distinct deviations which are a consequence of the thermal non-equilibrium condition after laser excitation. Furthermore, in section 5.3 we discussed a corresponding experiment performed within the low temperature CDW phase of TiSe_2 . Again, distinct spectral modifications are observed upon an increase of the absorbed laser fluence. The changes of the spectral shape indicate a perturbation and consequent weakening of the CDW phase of this system. Our approach enables a detailed investigation of the dynamics of this perturbation.

In general, the time resolved experiments of this work provide access to the ultrashort dynamics of excitation and relaxation of the electronic system, allowing the identification of different processes and their corresponding timescales. These timescales are quite instructive, because the excitation of the electronic system proceeds on a femtosecond timescale, while the subsequent thermalization with the crystal lattice is a significantly slower process (see, e. g., reference [96]). The absorption of the pump pulse initially leads to excitation of the electronic system, generating a highly non-thermal electron distribution (see, e. g., references [130, 132, 137]). The static photoemission experiment presented in section 5.2 corresponds to “time zero”, i. e. temporal overlap of both pulses in the TR-2PPE scheme. The time resolved method is, however, capable of monitoring the temporal evolution of the induced non-equilibrium state, as well as its thermalization. Ultimately, the energy passed to the electronic system by the laser pulse is transferred to the crystal lattice. The different time constants of such processes allow to discriminate their contributions. Please refer to section 2.5.4 for a detailed discussion of the typical dynamics of the excitation of the electronic system by a laser pulse.

The TR-2PPE method, used for the study of the relaxation dynamics of the population of unoccupied states (see section 4.2), is employed here for the investigation of the occupied chalcogen p bands. Usually, TR-2PPE monitors the population of an unoccupied intermediate state after excitation (see section 4.2) by an absorbed laser pulse. We use the p -polarized SH emission of laser 3_{TR} at a photon energy of $h\nu = 3.18 \text{ eV}$ and the TR-2PPE setup [figure 3.3(a) in section 3.2]. Here, we observe distinct spectral modifications after increasing the laser fluence which reduce, for instance, the spectral weight of the occupied Se $4p$ bands significantly (see section 5.2). A TR-2PPE autocorrelation trace is basically a representation of the spectral intensity recorded within a certain energy and momentum range and thus a laser induced drop of intensity is also visible in such an experiment—of course the time scale of the modifications needs to be in the order of femto- to picoseconds, the typical temporal range of our time resolved experiments.

Here, the single pulse fluence is chosen such, that for temporal overlap of pump and probe pulse (“time zero”, pulse delay $\tau = 0 \text{ fs}$) the combined absorbed fluence leads to a modification significantly enhanced with respect to the single pulse fluence. The temporal evolution of these spectral changes induced at time zero is then monitored in an autocorrelation trace. This method is, however, flawed, because both temporally separated pulses contribute to the photoemission and to the spectral modifications. This

complicates quantitative statements.

Therefore, the data presented in this section are a precursor to the more sophisticated approach presented later in section 6.2. The first goal of these experiments is the identification of any ultrafast laser induced dynamics, as well as their corresponding timescales. TR-2PPE is well suited for this task, because it is a simple approach for the identification of interesting temporal modifications. Furthermore, it allows for an overview of the expected energy and momentum ranges of interest, as well as the identification of the relevant parameters to be tuned in a more detailed investigation. We do not present a detailed analysis of the data in this section, because the interpretation of such data is complicated severely by the coupling of pump and probe process—the time-resolved IR-pump SH-probe photoemission experiment presented in section 6.2 is much better suited.

These data also enable the comparison of the two TMDCs with respect to the temporal evolution of the excitation of both electronic systems under variation of the relevant parameters. We are able to identify characteristic differences. This investigation shows, that the modifications observed for TiTe₂ are much less pronounced and lack certain of the processes involved. Overall, TR-2PPE in autocorrelation mode already enables us to understand the peculiarities of TiSe₂ with respect to the reference system TiTe₂ using a much faster and simpler experimental approach. Our findings enable us to focus on the more interesting behavior of TiSe₂ applying the much more complicated and time-consuming experiments in section 6.2. We will refer to our observations here during our conclusion in section 6.3.

Section 6.1.2 completes our presentation of TR-2PPE data by showing exemplary data acquired within the low temperature CDW phase of TiSe₂ (see section 2.2). Even from the autocorrelation traces we can already deduce interesting properties. However, considering our investigation in section 5.3, changes of temperature and laser fluence both result in characteristic modifications of the binding energies of the spectral features, which are only indirectly accessible with auto-/cross-correlation traces. A set of full spectra acquired at different delays of pump and probe pulse is more suitable and we briefly discuss such spectra in context of the TR-2PPE experiments in section 6.1.2–a. Nevertheless, instabilities of the cylindrical sector analyzer (CSA) system (see appendix A.3) complicate the interpretation of such data. Our two-color approach presented in section 6.2 circumvents these problems by using high powered pump pulses which do not yield photoelectrons. The two-color experiment focuses on the acquisition of full spectra at different delays and we shall discuss these data in great detail.

6.1.1 Ultrafast Laser Induced Effects in the Room Temperature Phase

The experiments discussed in this section are inspired by the observation of distinct laser induced modifications in static photoemission data which are presented in section 5.2. A more detailed investigation of the potential ultrafast dynamics is presented in the

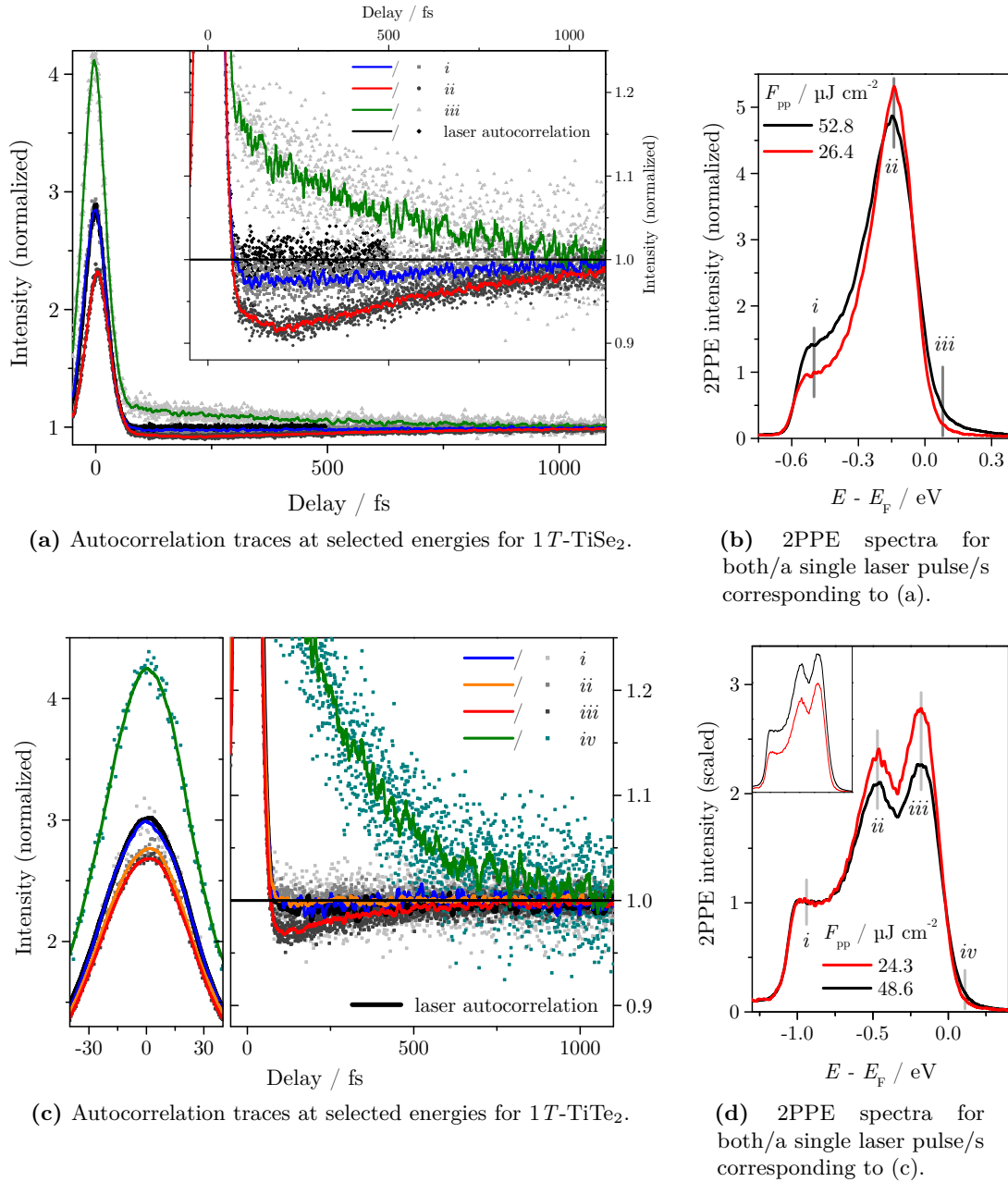


Figure 6.1: (a) and (c) present a comparison of autocorrelation traces acquired for the TMDCs at different characteristic energies [see *i*–*iii*/*iv* in (b) and (d)] to a laser autocorrelation measured on polycrystalline tantalum (black). The actual experimental data is presented by symbols (typically about 100 runs averaged), lines represent smoothed curves (averaging over ten adjacent data points). The inset shows a detail of the characteristic deviations from the laser autocorrelation right after absorption of both pulses (delay $\tau = 0$ fs). (b) and (d) show two spectra acquired using both optical paths of the interferometer (black; see section 3.2) and using only one path (red). These spectra enable to identify the energetic ranges of interest.

following section 6.2.

Here we show TR-2PPE experiments—a very simple and fast approach—which enable us to identify whether the observed laser induced spectral modifications actually feature any ultrafast dynamics at all. The comparison of 1T-TiSe₂, which exhibits a low temperature phase transition, and 1T-TiTe₂, which does not, reveals interesting differences of the temporal evolution of certain spectral features already in the room temperature phase. Finally, the simplicity of the TR-2PPE enables a fast overview of the expected behavior upon changing certain parameters of the experiment. The data presented here thus provide a first outlook on the ultrafast dynamics to be expected for these TMDCs.

We use the time resolved TR-2PPE laser setup in autocorrelation mode, as presented in figure 3.3(a) in section 3.2. In this case, an interferometer generates double laser pulses with a defined delay, τ . Although both pulses are identical and the excitation of the system (pump pulse) cannot be separated from the generation of photoelectrons (probe pulse, see also section 6.2), the absorbed fluence is the highest for temporal overlap of both pulses ($\tau = 0$ fs) which corresponds to the sum of the single pulse fluences—the temporal overlap of both pulses thus marks the “pump” event. The fluence is reduced to the value for only one pulse at sufficiently high delay. Considering Gaussian shaped pulses, which agrees very well to the shape of the experimental laser autocorrelation acquired on polycrystalline tantalum, the pulse duration is estimated to be about 40 fs (FWHM). The laser autocorrelation is basically a convolution of both pulses, i. e. only for overlapping pulses the signal is increased with respect to its value for separated pulses (the latter is normalized to unity). Calculating the 3σ width of a Gaussian corresponding to about 99.7% of its area [254] we derive a temporal range of about ± 70 fs in which we expect considerable overlap of the two pulses. Therefore, our experiment excites/pumps the sample system close to time zero—as long as both pulses overlap significantly—and then probes the temporal evolution afterward. In other words, the laser induced effects are enhanced near $\tau = 0$ fs and are expected to relax to lesser intensity for higher delays.

Figures 6.1(b) and (d) show 2PPE spectra of TiSe₂ and TiTe₂, respectively, acquired using both pulses (black) and after blocking one arm of the interferometer (red), which corresponds to single pulses. The spectra are normalized by considering of the quadratic dependence of the 2PPE intensity on the absorbed laser fluence. Please note, that the normalization does not yield consistent spectra for TiTe₂ in the inset of figure 6.1(d) which we attribute to the instabilities of the CSA under variation of the incident laser fluence (see appendix A.3). The main figure therefore shows spectra normalized to the plateau intensity. We will discuss the implications of the instability of the CSA on the autocorrelation traces shortly.

At the chosen peak fluence of approximately $50 \mu\text{J cm}^{-2}$ the spectra show distinctive changes between two- and one-pulse fluence and we identify the following energetic ranges for a closer inspection: the plateau (*i*), the chalcogen *p* bands (TiSe₂: *ii*, TiTe₂: *ii*, *iii*) and the increase of intensity right above the Fermi energy (TiSe₂: *iii*, TiTe₂: *iv*). Figures 6.1(a) and (c) present the corresponding autocorrelation traces. The phase

averaged laser autocorrelation of Gaussian shaped pulses is also Gaussian shaped and the maximum is observed at three times its value for fully temporally separated pulses (see section 2.5.1). This is very well reproduced by our laser autocorrelation (black). Please note, that differences in the actual maximum value thereof are a consequence of slight differences in the laser alignment as the theoretical maximum to minimum ratio of 3 implies perfect alignment. An ordinary TR-2PPE experiment probes the decay dynamics of an intermediate state, populated by the pump pulse. The corresponding autocorrelation is broadened with respect to the laser autocorrelation because of the lifetime of the intermediate state (see sections 2.5.1 and 4.2). However, such curves are considerably altered in case of the two TMDCs investigated here and deviate significantly from the expected Gaussian-like shape.

These deviations are indeed intrinsic to the investigated TMDC as we did not observe similar autocorrelation shapes for polycrystalline tantalum and Ag(111) and Au(111) single crystals. Furthermore, a detailed investigation of Ag(111) at different absorbed fluences revealed spectral modifications induced by instabilities of the CSA system very similar to our observation for TiSe₂ (see addendum A.3), however, the autocorrelation acquired for a *sp* band which is significantly influenced by such instabilities does not show any deviation from the expected Gaussian shape (not shown here). Although the maximum absorbed fluence in case of silver is only about $15 \mu\text{J cm}^{-2}$, this fluence is still high enough for distinct modifications in case of TiSe₂ as shown in figure 6.2(a). Yet, autocorrelation curves of Ag(111) do not show any deviation—besides the possibility of broadening of the full width at half maximum (FWHM)—from the laser autocorrelation shape. We conclude, that our observation is not induced by the analyzer itself and that it is characteristic for the TMDC investigated here.

Figures 6.1(a) and (c) present autocorrelations acquired at the energies corresponding to *i-iv*. For TiSe₂ the main figure presents the whole trace for reference. It shows strong modifications of the autocorrelations at $\tau = 0$ fs and for delays of up to about 1 ps. The latter are shown in more detail in the inset. The TiTe₂ data focus on the vicinity of time zero and the modifications within the first picosecond in two detailed sub-figures. The latter uses the same scales as the inset of the TiSe₂ data for better comparability. First, we find virtually no deviation of the trace corresponding to the spectral plateau for TiTe₂. We attribute the slight undershoot of the trace for $\tau \gtrsim 70$ fs in case of TiSe₂ to the closer vicinity to the Se *4p* bands which feature a well defined undershoot of the corresponding autocorrelation (red) as well as considerable reduction of the intensity at $\tau = 0$ fs. A detailed investigation of these bands by a set of autocorrelations for different energies within the peak (not shown here) reveals that the deviations from the laser autocorrelation are the most defined at the peak center and diminish for higher or lower energies. Finally, the spectral weight right above E_F increases with the absorbed laser fluence. Indeed, the corresponding autocorrelation (green) features a strong increase at time zero which relaxes within similar timescale as the intensity reduction of the chalcogen *p* bands. The reduction/enhancement of spectral weight is directly observed

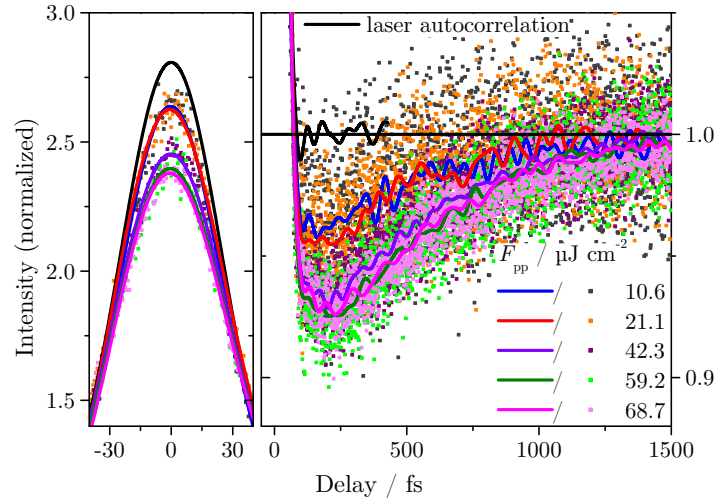
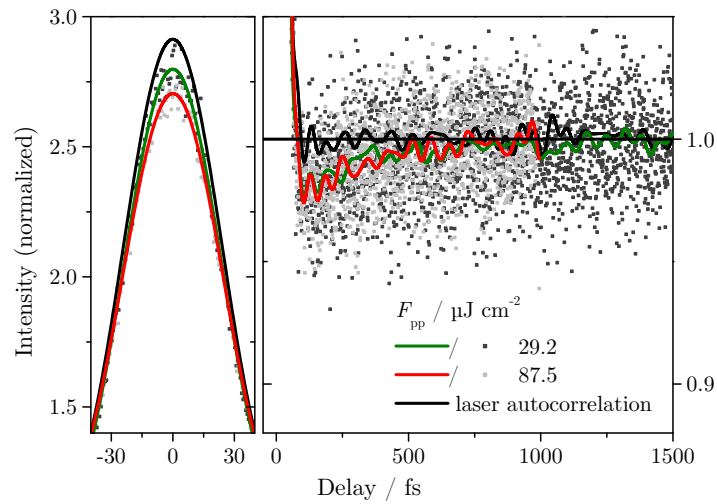
(a) Fluence dependence of the autocorrelation for 1T-TiSe₂.(b) Fluence dependence of the autocorrelation for 1T-TiTe₂.

Figure 6.2: Autocorrelation traces acquired at the energy of the peak (path *ii* for TiSe₂, *iii* for TiTe₂, see figure 6.1), i.e. for the energetic region of the most significant deviation from the laser autocorrelation, for several absorbed peak fluences. The given values of the fluence correspond to pump and probe in temporal overlay. The experimental data (symbols) is smoothed (lines) using a FFT algorithm. For better comparability the same scales are used in (a) and (b).

in the autocorrelations, because the theoretical 3:1 ratio of maximum to minimum is reduced to about 2.3:1 for the Se 4*p* bands and increased to about 4.1:1 for the green trace.

The TiTe₂ data shown in figure 6.1(c) feature similar deviations, however, much less pronounced in case of the chalcogen *p* bands. At $\tau = 0$ fs the reduction of the autocorrelation ratio is only approximately 2.7:1, but the increase above the high energy cutoff is similar at about 4.2:1. The difference in the magnitude of the signal right above the Fermi energy (green) cannot be assessed using the data presented here, because it strongly varies with the chosen binding energy and the data is thus not comparable for both samples. We can, however, conclude that the observed behavior is consistent. The autocorrelations of the two chalcogen *p* bands (*ii*, *iii*) are significantly less reduced at $\tau = 0$ fs and the peak of higher binding energy (orange, *ii*) does not exhibit the undershoot for $\tau \gtrsim 70$ fs observed for the other peak (red, *iii*). The band structure of TiTe₂ requires off-normal emission for mapping the chalcogen *p* bands (see section 5.1.1–a), i. e. the observed spectrum in figure 6.1(c) clearly indicates a tilting of the sample surface. We show in section 6.2.2–b that the reduction of spectral weight of the Se 4*p* bands is less pronounced for off-normal emission in case of TiSe₂. The decreased deviations of the autocorrelations shown here may therefore be attributed to off-normal emission. Please note, that we observe the maximum modification of the autocorrelation—manifesting itself in, e. g., the lowest minimum of the curves—at an off-normal angle corresponding to the highest photoemission signal from the Te 5*p* band of the lowest bind energy, i. e. the situation presented here. Additionally, the data in figure 6.1 clearly shows a significantly faster relaxation for TiTe₂ which is visible to the naked eye; a different representation of the data, discussed shortly for figure 6.3, also reveals distinct differences. We will return to these issues in section 6.2.

So far, we observe a peculiar shape of the autocorrelations in certain energetic ranges for both TMDCs investigated here. Comparison to similar data of occupied bulk bands of other metallic systems show no such deviations. Furthermore, these data also show, that the instability of the CSA induced by laser fluence variations (refer to appendix A.3) is not the source of the observed modification of the autocorrelation, because even in case of significant spectral modifications induced by such instabilities, the corresponding autocorrelation traces are not altered with respect to the expected Gaussian-like shape.

Both samples exhibit a very fast loss of spectral weight of the chalcogen *p* bands at zero delay followed by a relaxation on a sub-picosecond timescale. Simultaneously, the spectral intensity above the high energy cutoff increases and relaxes on roughly similar timescales. Furthermore, the deviation from the laser autocorrelation is much weaker for TiTe₂, however, similar modifications are still present. In section 6.2.3–a we provide full spectra for each temporal delay for TiSe₂. We will see, that the observed modifications of the autocorrelation at room temperature is consistent with the initial generation of a

non-equilibrium electron distribution (see section 2.5.4), i. e. in case of TiTe₂ fluctuations of the CDW phase at room temperature are not relevant.

TR-2PPE enables fast access to the influence of different, relevant experimental parameters. Figure 6.2 shows data on the fluence dependence of the autocorrelation of the center of the Se 4p bands of TiSe₂ [*ii* in figure 6.1(b)] and the Te 5p bands of lowest binding energy [*iii* in figure 6.1(d)] in comparison to the laser autocorrelation (black). The figures for both TMDC use the same scales for direct comparability. For TiSe₂ we increase the absorbed fluence up to about 68.7 $\mu\text{J cm}^{-2}$ and observe a reduction of the maximum intensity at time zero to about 84 %. The undershoot reaches a minimum of about 93 %. Even for an absorbed fluence of 87.5 $\mu\text{J cm}^{-2}$ in case of TiTe₂, about 1.3 times the fluence employed for TiSe₂, the autocorrelation is reduced to only about 93 %, the undershoot reaches only approximately 98 %. Furthermore, the TiTe₂ autocorrelations are virtually identical for both fluences, while we observe a significant development for TiSe₂. Especially the undershoot becomes more pronounced at higher fluences. However, the intensity instability of the CSA (see addendum A.3), which leads to long-term changes of the spectral intensity, may modify the shape of the autocorrelations.² The consequence is incomparability of curves acquired at different fluences, if the system is not sufficiently stabilized. This is the reason for the step-like decrease of the minimum intensity observed in the figure.

Nevertheless, in contrast to the TiTe₂ data we also observe modifications of the temporal evolution. The minimum of the trace is reached with a delay and the relaxation to the laser autocorrelation shape proceeds slower for higher fluences (see also figure 6.3 and section 6.2.3–b). These very qualitative observations are investigated in detail in section 6.2 using a more intuitive set of data.

Additionally, we investigated the influence of inhomogeneities on the shape of the autocorrelation (not shown here) by acquiring autocorrelations for the Se 4p bands for different areas of the sample surface which yielded different spectral shapes. We observe a reduction of the modification of the autocorrelation if the binding energy of the Se 4p bands is increased, i. e. if we actually observe off-normal emission due to tilting or corrugations of the surface. This is expected, because the strongest loss of spectral weight exists for normal emission (see discussion in section 6.2.2–b and also section 5.2.4). If areas of similar spectral shape are investigated, the autocorrelation shapes agree well.

Please note, that another experimental parameter, the temperature of the sample, is discussed in section 6.1.2 where we give a brief overview of the behavior of TiSe₂ in the low temperature CDW phase.

²Typically about 100 autocorrelations are averaged. The CSA instability slowly reduces the detected photoemission signal. Because the linear stage of the interferometer (see section 3.2) moves unidirectional for best positional accuracy, the CSA instability establishes a subtle intensity gradient which can manifest in modifications of the shape of the curve, especially for averaged data.

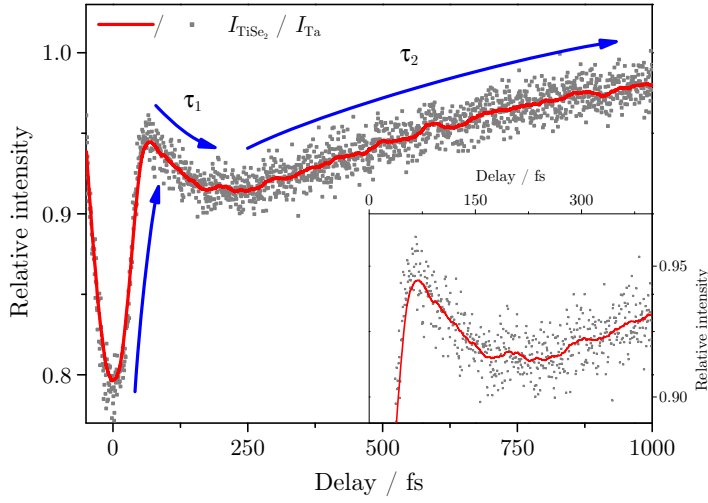
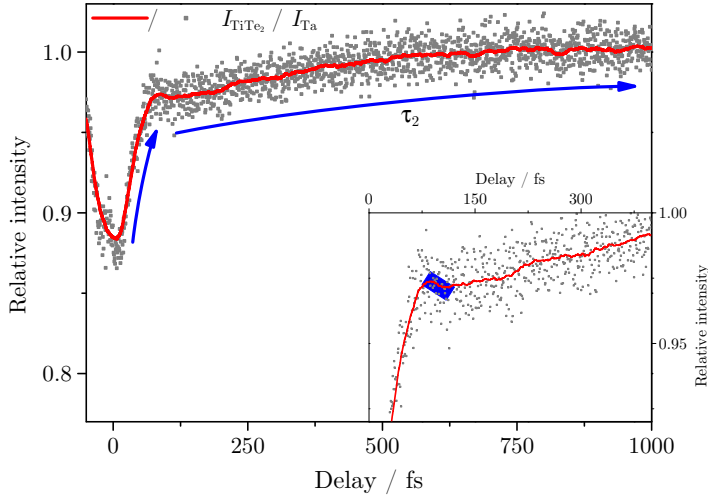

 (a) Relative autocorrelation trace for 1T-TiSe₂.

 (b) Relative autocorrelation trace for 1T-TiTe₂.

Figure 6.3: The intensities of autocorrelation traces corresponding to the peak right below E_F (path *ii* for TiSe₂, *iii* for TiTe₂, see figure 6.1), I_{TiSe_2} and I_{TiTe_2} , are normalized to the laser autocorrelation acquired on tantalum, I_{Ta} . This yields relative intensities which correspond to the deviation from the laser autocorrelation. To reduce noise a careful Gaussian fit of the laser autocorrelation is used. The calculated relative data (symbols) is presented along smoothed data (averaging of 50 adjacent data points). Blue arrows emphasize the different observed processes and their timescales, τ_i . The insets emphasize the region of the main difference between the two TMDCs. For better comparability the same scales are used in (a) and (b), the insets showing a shifted, but similar intensity range.

The extraction of the temporal evolution of the laser induced spectral changes of the investigated TMDCs is improved by emphasizing the deviations from the laser autocorrelation. This is achieved by normalizing the autocorrelations to the laser autocorrelation which yields a relative intensity scale of the ratio of modified and unmodified autocorrelation, i.e. it directly shows the deviation from the laser autocorrelation. For example, in case of conventional TR-2PPE the lifetime of an intermediate state broadens the autocorrelation. The relative intensity is thus unity, except for the delays around time zero where the intensity of the broadened trace is always higher than that of the laser autocorrelation—this leads to a “M”-shaped curve.

Figure 6.3 compares relative intensities for TiSe₂ and TiTe₂. Please note, that the laser autocorrelation is carefully fitted with a Gaussian and this fit function is then used as the reference intensity, $I_{\text{ref}}(\tau)$, for the calculation of the relative intensity, $\tilde{I}(\tau)$, by $\tilde{I}(\tau) = \frac{I(\tau)}{I_{\text{ref}}(\tau)}$ [$I(\tau)$ being the autocorrelation intensity of the investigated sample]. Using a Gaussian as reference reduces the noise of the resulting data considerably.

Both TMDCs show a reduction of the intensity at time zero which shows the significant reduction of spectral weight during the temporal overlap of the two laser pulses. This initial process is thus very fast and proceeds on time scales below 70 fs. The increase of the relative intensity does not necessarily correspond to an actual relaxation of the initial reduction of chalcogen p band intensity, but is a consequence of the shape of the autocorrelation. Please note, that we circumvent such complications by using a time-resolved IR-pump SH-probe photoemission setup in the following section 6.2. For TiSe₂ figure 6.3(a) demonstrates that the loss of spectral weight actually continues after the two laser pulses do not overlap anymore, i.e. the reduction is still enhanced after “pumping” by both pulses. This process is characterized by a time constant τ_1 . Please note, that the actual time constant of the initial loss of spectral weight cannot be accessed in an autocorrelation experiment, because this process is partially masked by the laser autocorrelation near time zero. The reduction is followed by a slower relaxation with a time constant τ_2 .

Comparison to the TiTe₂ data in figure 6.3(b) reveals an interesting difference: the process with time constant τ_1 is not observed for this TMDC. The observed loss of spectral weight of the Te 5p bands is thus fully established within the temporal overlap of the two laser pulses and the system directly proceeds with the relaxation thereof. The insets of figure 6.3 show a detail of the relevant temporal range using equivalent scales. For TiTe₂ we observe, although covered by the noise level of the signal, a very subtle hint of additional chalcogen p band reduction (blue box, inset), i.e. the process with time constant τ_1 observed for TiSe₂. However, the relative intensity reacts strongly on small changes of the reference curve and a very similar apparent initial enhancement of the loss of spectral weight can be induced by such numerical instabilities. The τ_1 process is always observed prominently for TiSe₂, even using the experimental autocorrelation as reference, while the TiTe₂ data only reveals a very subtle relative intensity feature if a fitted

Gaussian is used as reference and this structure vanishes completely for experimentally acquired reference data. Because the visibility of the τ_1 -feature significantly depends on the reference data chosen, we conclude that TiTe₂ does not show this initial process with time constant τ_1 .

In conclusion, both TMDCs exhibit a clear, ultrafast dynamics of the changes in spectral weight. Furthermore, the observed loss of spectral weight of the Se 4*p* bands of TiSe₂ is not only much stronger than the corresponding effect of TiTe₂, but the reduction of the intensity of these bands is also further enhanced well after the fluence increase induced by the temporal overlap of both laser pulses vanishes. These findings, although of a qualitative nature, already provide interesting details to our interpretation in section 6.2.3–a, especially considering the temporal evolution, as well as the processes involved, of the excitation of the TMDCs investigated here.

6.1.2 The Low Temperature CDW Phase

Reducing the temperature of 1*T*-TiSe₂ below about 200 K leads to a phase transition into a new, coherent ground state of the electronic system characterized by a CDW (refer to, e. g., references [7, 8] and section 3.3). Using the liquid nitrogen cooling system of our ultrahigh vacuum (UHV) system (see section 3.1.1) temperatures of $T \lesssim 140$ K are reached for the data discussed here, ensuring that the samples are well within their low temperature CDW phase. The system TiSe₂ features a second order phase transition [3, 8, 248] which results in continuous, non-abrupt changes of the sample characteristics upon the transition. Within 2PPE spectra acquired using the SH emission of our laser system, i. e. for momenta in the vicinity of the $\bar{\Gamma}$ -point, the phase transition manifests as an increase of the binding energy of the Se 4*p* bands which increases with decreasing temperature (see figure 5.36 in section 5.3.1). This energetic shift is easily observed by fitting the half-intensity of the high energy cutoff of the spectrum, E_{flank} . At $T = 140$ K we observe a shift of the energy of about $\Delta E_{\text{flank}} = (-56 \pm 5)$ meV which is within uncertainties in good agreement to the observations reported by Rosnagel et al. [7].

The energy E_{flank} is quite sensitive on the continuous second order phase transition, i. e. this energy is a measure for the establishment of the CDW (see e. g. references [7, 55]). In section 5.3 we showed, that, by increasing the absorbed laser fluence, this energetic shift can be compensated—the CDW is perturbed by the absorbed laser pulses. In this section we focus on the non-equilibrium dynamics of TiSe₂ within the low temperature CDW phase, i. e. on the temporal evolution of the perturbation of the CDW by the laser which is also our primary question in section 6.2.

We learned in section 6.1.1—see especially figures 6.1(b) and (d)—that it is very instructive to precede a time resolved experiment by the acquisition of two static spectra, one taken with only one pulse passing the interferometer (i. e. one path is blocked) and one for the full fluence of both pump and probe pulse overlapping temporally. Similar to the

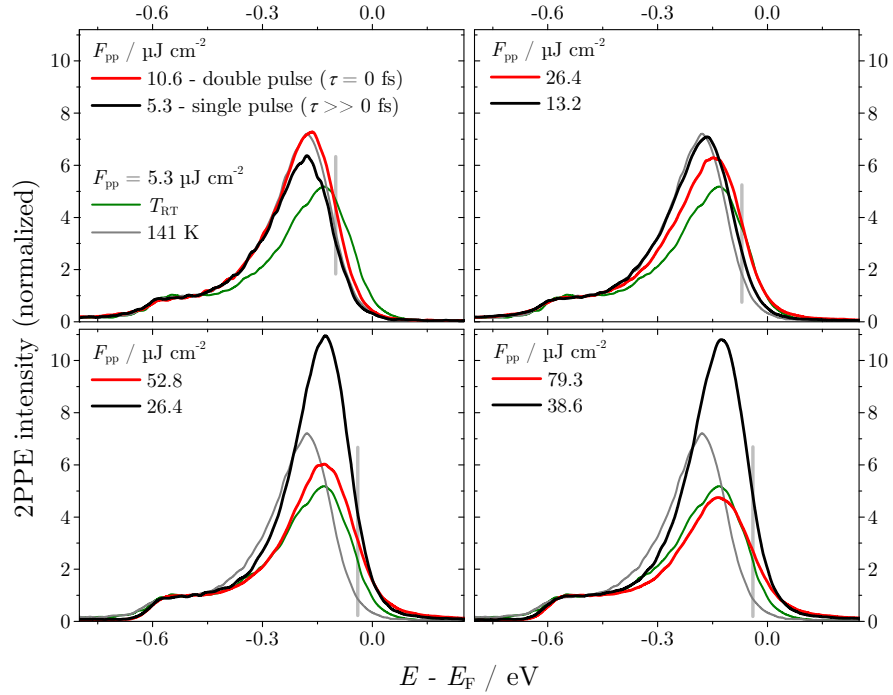


Figure 6.4: Finding interesting laser fluences for the time resolved investigation of TiSe₂ in the low temperature CDW phase. The 2PPE spectra are acquired using both paths (red) and only one (black) path of the interferometer (see figure 6.1), emphasizing the spectral modifications to be expected in a TR-2PPE experiment (note the effect of changing the absorbed laser fluence, presented in section 5.3). These data are normalized to the plateau intensity ($E - E_F = -0.54$ eV to -0.45 eV). A gray line visualizes the energy chosen for acquisition of an autocorrelation. For all four fluences the same reference spectra (dashed) acquired using $F_{pp} = 5.3 \mu\text{J cm}^{-2}$ at room temperature (T_{RT} , green) and after the phase transition ($T \approx 141$ K, gray) are included. The reference data is scaled to the plateau level of the red curve by the same factor. All four graphs feature the same scales.

static experiment presented in section 5.3 we observe an increase of E_{flank} up to its room temperature value for increasing absorbed laser fluence. Figure 6.4 shows a compilation of such spectra for four different laser fluences. Spectra corresponding to the full fluence of both optical paths of the interferometer are included in red, while black is used for the case of half of the maximum fluence. The same scales are used in all graphs. For reference, a spectrum acquired at room temperature (green, T_{RT}) and at the low temperature (gray, $T = 141$ K) is included as well; a very low absorbed fluence ($F_{\text{pp}} = 5.3 \mu\text{J cm}^{-2}$) is used to suppress laser induced perturbation of the CDW. All spectra presented in this figure and in the remainder of this section are normalized to the plateau intensity to enable comparison which is necessary here for two reasons: (i) Although a ratio of the fluence of 2 is expected for the one- and two-pulse fluence, leading to a ratio of photoemission intensity of 4 for 2PPE, normalization under consideration of the absorbed fluence (see section 5.1.2) does not yield consistent data. We attribute this to an instability of the CSA (see appendix A.3). (ii) In case of the acquisition of a series of spectra for different temporal delays of pump and probe pulse (see section 6.1.2-a) the total absorbed fluence varies in the vicinity of time zero. The absolute intensities are rendered incomparable—normalization to the plateau intensity circumvents this problem for the whole temporal range.

Figure 6.4 shows the four fluences chosen for the time resolved experiments, ranging from $10.6 \mu\text{J cm}^{-2}$ to $79.3 \mu\text{J cm}^{-2}$ absorbed two-pulse (maximum) fluence at $\tau = 0$ fs. For $F_{\text{pp}} \lesssim 26.4 \mu\text{J cm}^{-2}$ we observe a clear energetic shift of E_{flank} —the binding energy of the Se $4p$ bands is visibly reduced at the higher fluence (red) and the initial, low temperature spectrum (refer to the gray line) transforms into the room temperature spectrum (green). Above approximately $26.4 \mu\text{J cm}^{-2}$ the room temperature value of E_{flank} is virtually re-established. Consequently, we observe the characteristic reduction of the spectral weight of the Se $4p$ bands with increasing fluence which is typical for the room temperature phase for $F_{\text{pp}} = 52.8 \mu\text{J cm}^{-2}$ and above (see section 5.2). The CDW seems to be maximally perturbed and virtually reduced to the room temperature fluctuation in this case. The behavior of the amplitude and the binding energy upon changing the absorbed fluence is in good agreement to our observations in section 5.3—the binding energy significantly decreases until the room temperature value is reached while the amplitude first increases and then decreases during the transition.³

The simple TR-2PPE experiment discussed in section 6.1.1 enabled us to identify an ultrafast dynamics of the laser induced loss of spectral weight of the Se $4p$ bands at room temperature. The spectra in figure 6.4 reveal a significant modification of the energy of these bands within the low temperature CDW phase of TiSe_2 . The acquisition of an autocorrelation trace at a carefully chosen energy can identify, whether the observed, laser

³The difference in shape of spectra acquired at $26.4 \mu\text{J cm}^{-2}$ (maximum and minimum fluence) observed in figure 6.4 is a consequence of the resolution settings of the CSA. Two different entrance apertures are used which inevitably yield deviating spectral shapes. This is, however, irrelevant for the acquisition of TR-2PPE data.

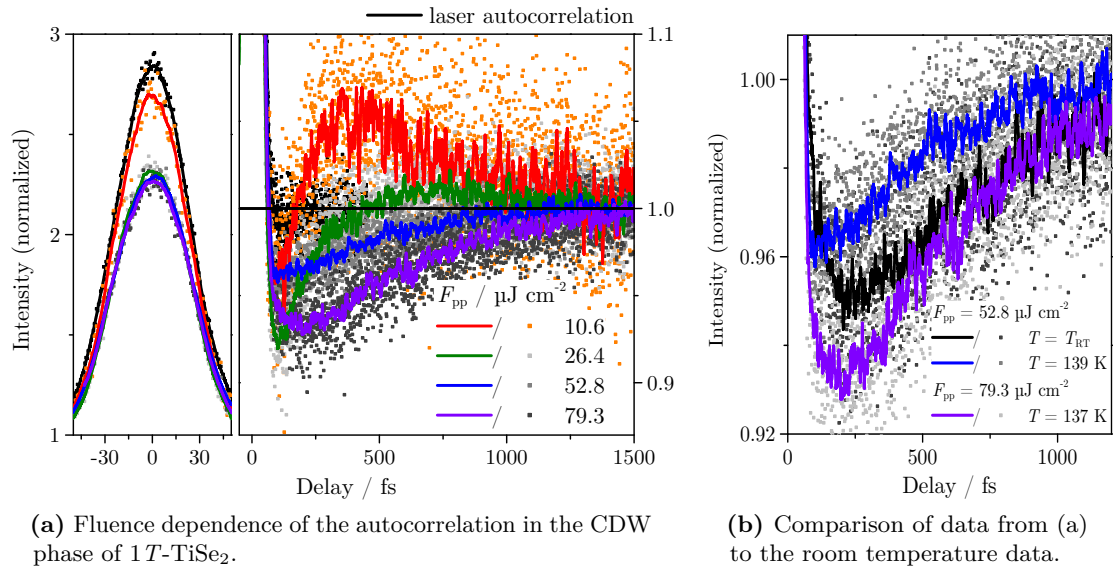


Figure 6.5: (a) presents autocorrelation traces acquired for different absorbed laser fluences (maximum) corresponding to the spectra presented in figure 6.4. The energy investigated is defined by the mean value of the half-intensity of the high energy cutoff of the two spectra shown in figure 6.4 and marked by a vertical line. The laser autocorrelation (black) recorded on polycrystalline tantalum is included for reference. Symbols represent the experimental data and lines are smoothed curves (averaging over ten adjacent data points). (b) compares the autocorrelations measured for the two highest absorbed fluences within the low temperature CDW phase to the corresponding autocorrelation acquired at room temperature using the same energy (within 10 meV, i. e. one channel of the CSA).

induced modification of E_{flank} proceeds on a femto- to picosecond timescale, too, in a fast and simple way. We like to emphasize that this method is capable of identifying indirectly, whether the energetic shift of the Se 4p bands shows any ultrafast dynamics at all. In combination with the spectra presented in figure 6.4 we can also decide on which laser fluences are most promising for a detailed investigation. However, it will be necessary to acquire a more comprehensive set of full 2PPE spectra at different temporal delays for a quantitative analysis of this effect. We discuss, although rather qualitative, such data later in this section (see section 6.1.2-a)—a quantitative analysis of the energetic shift is performed in section 6.2.

Figure 6.5(a) shows autocorrelation traces acquired at the four chosen fluences (see figure 6.4) at the mean value of E_{flank} of the spectrum for the one- and two-pulse fluence (gray lines), i. e. the energy corresponding to the strongest modification of E_{flank} . For better visual accessibility we use a split graph as introduced in figure 6.1.

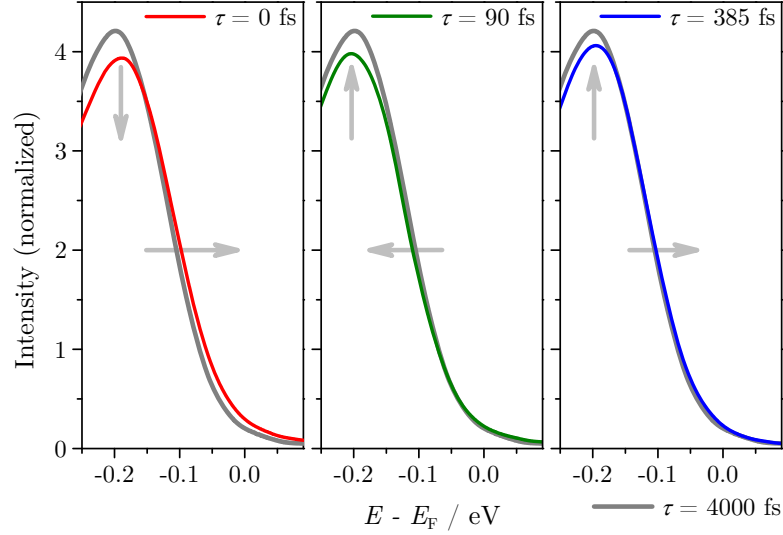
The autocorrelations taken within the CDW phase feature a distinctively different shape from their room temperature counterparts [black, figure 6.5(b)]. For low fluence

(red) the sample remains within the CDW phase for both maximum and minimum fluence. The peculiar shape of the corresponding autocorrelation is a consequence of the energetic shift of E_{flank} which passes the energy monitored by the TR-2PPE experiment, i. e. the maximum of the autocorrelation at $\tau \approx 400$ fs hints indirectly at a delayed shift of E_{flank} closer to its room temperature value. Nevertheless, by increasing the maximum fluence we observe a change of the shape of the autocorrelation curves. The peculiar local maximum is lost and the distinct minimum at $\tau \approx 200$ fs becomes stronger and temporally broader (blue and violet)—the full reduction is thus established with a delay. Figure 6.5(b) compares the autocorrelations for the two highest fluences (blue, violet) to data acquired at room temperature (black).

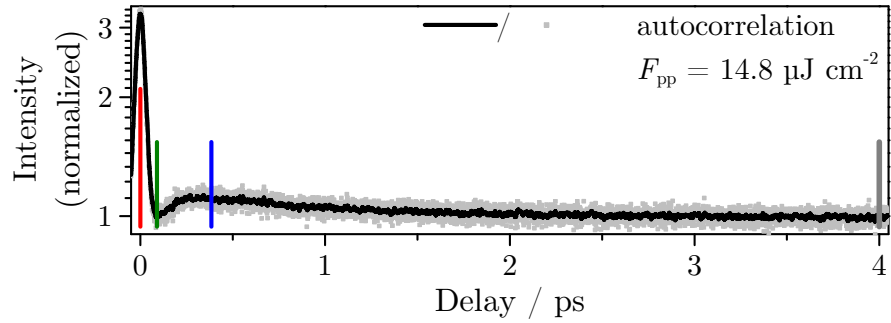
We recapitulate our findings so far: The study of the perturbation of the CDW of TiSe_2 requires sufficiently low absorbed laser fluences, because with increasing fluence the spectral characteristics indicating that the CDW phase gradually vanishes (see also section 5.3). This is also observed in static spectroscopic data. Autocorrelation traces acquired for different absorbed fluences at an energy chosen such, that a possible temporal evolution of E_{flank} should manifest in the autocorrelations, reveal an interesting fluence dependence. For the highest investigated fluence the behavior is similar to the room temperature data presented in section 6.1.1 which is indeed induced by the loss of spectral weight of the Se $4p$ bands upon increasing the laser fluence. The energetic shift of these bands to the room temperature value is already fully established in this case. At low fluences the autocorrelation trace is altered. Although we cannot extract E_{flank} quantitatively from these data, they already confirm an interesting ultrafast dynamics in this energetic range of the spectrum. The observed increase of intensity at about $\tau \approx 400$ fs suggests a delayed shift of the Se $4p$ bands to lower binding energies. Please note, that the room temperature data, as well as the autocorrelations taken for high fluences show a strong, initial drop of intensity at $\tau = 0$ fs which is not observed at the lowest fluence. This is in line with our findings on the fluence dependence of the amplitude of the Se $4p$ bands in section 5.3.

6.1.2—a Temporal Evolution of the 2PPE Spectra in the CDW Phase—a First Look

Autocorrelation traces are not very instructive for gaining insight into the temporal evolution of E_{flank} , because they monitor the temporal evolution of the photoemission intensity at a *specific* energy and momentum—energetic shifts are only observed using full 2PPE spectra for different temporal delays. Figure 6.6(a) presents such data for four characteristic temporal delays and (b) shows the corresponding autocorrelation along vertical lines marking the delays chosen for the spectra. Of course, these data are not sufficient for a detailed analysis of the ultrafast dynamics, yet, they enable us to identify, whether and to which extent E_{flank} is modified on a femtosecond timescale. Such



(a) Spectra acquired for selected temporal delays in comparison to time zero.



(b) Reference autocorrelation showing the selected delays.

Figure 6.6: (a) compares 2PPE spectra acquired at delays of 0 fs, 90 fs and 385 fs to a reference spectrum taken at $\tau = 4$ ps. Gray arrows emphasize the relevant spectral modifications. (b) shows an autocorrelation acquired within the high energy cutoff of the spectra [dashed line in (a)] for TiSe₂ in the low temperature CDW phase. Characteristic temporal delays are visualized by colored lines. The combined absorbed laser fluence of pump and probe pulse is $F_{pp} = 14.8 \mu\text{J cm}^{-2}$ and the sample temperature was (134.7 ± 0.5) K throughout acquisition of the spectra.

information is very valuable especially considering the extensive experiments presented in section 6.2, as they help us in understanding the magnitude of the effects to be expected and to identify suitable fluences for further investigation.

The spectra are presented in figure 6.6(a) in three graphs, each comparing a spectrum of a certain delay of 0 fs, 90 fs and 385 fs (red, green, and blue) to reference data acquired at $\tau = 4$ ps (gray). This reference is chosen, because in this case the minimum, i. e. single pulse, fluence is absorbed by the sample and the enhanced excitation of the electronic system is expected to be relaxed. This spectrum is the closest we get in our experiment to the unperturbed system. This is indeed a rather good approach, because comparison to static spectra shows, that the spectrum acquired at time zero fits to one taken for the two-pulse fluence, while the spectrum at large temporal delay agrees very well with the one-pulse case which shows, that the TR-2PPE experiment does not differ from the static experiment at least for such low fluences. In general, the layered structure of TiSe₂ may lead to heat accumulation (see section 5.2 and experimental data by Roth et al. [246]) and thus to an increase of the sample temperature. This should be observed as a difference between the two one-pulse fluence spectra. Note, that the small entrance aperture (see section 3.1) of the CSA is used for an enhanced energetic resolution. Analogously to 5.1 we estimate the width of the secondary electron cutoff of the spectra using a 90–10-criterion (see section 3.2) to (61 ± 1) meV. The laser bandwidth of the fundamental is approximately 54 meV, yielding a total energy resolution of about 82 meV by calculation of the root of a sum of squares (refer to section 3.2).

The behavior observed in figure 6.6 is the following:

- (i) At $\tau = 0$ fs a reduction of the amplitude and an increase of energy of the Se 4*p* bands (emphasized by gray arrows) is observed. The laser induced spectral modification closer to the room temperature spectrum therefore proceeds very fast within the temporal overlap of both pulses.
- (ii) At $\tau = 90$ fs, corresponding to the minimum of the autocorrelation trace, the suppression of the amplitude already relaxes and E_{flank} is actually reduced with respect to its value at the highest temporal delays. This may be an indication for an enhancement of the CDW in TiSe₂ right after the perturbation of the electronic system.
- (iii) For the local maximum of the autocorrelation at $\tau = 385$ fs the spectrum shows an still higher amplitude, nearing the value observed at 4 ps delay, and a subtle increase of E_{flank} .

Especially the temporal evolution of E_{flank} , which is observed for two independent experiments, is very interesting. These data suggest a possible oscillatory behavior of the Se 4*p* binding energy after the excitation by both laser pulses. The energy E_{flank} is an indicator not only for the CDW transition, but also for the degree of to which this CDW

is established (see discussion in section 6.2.4 and, e. g., reference [55]). Oscillations of E_{flank} may occur if the perturbation of the CDW by the laser pulse leads to collective vibrations of the lattice similar to the investigation presented by Perfetti et al. [4] and Schmitt et al. [31].

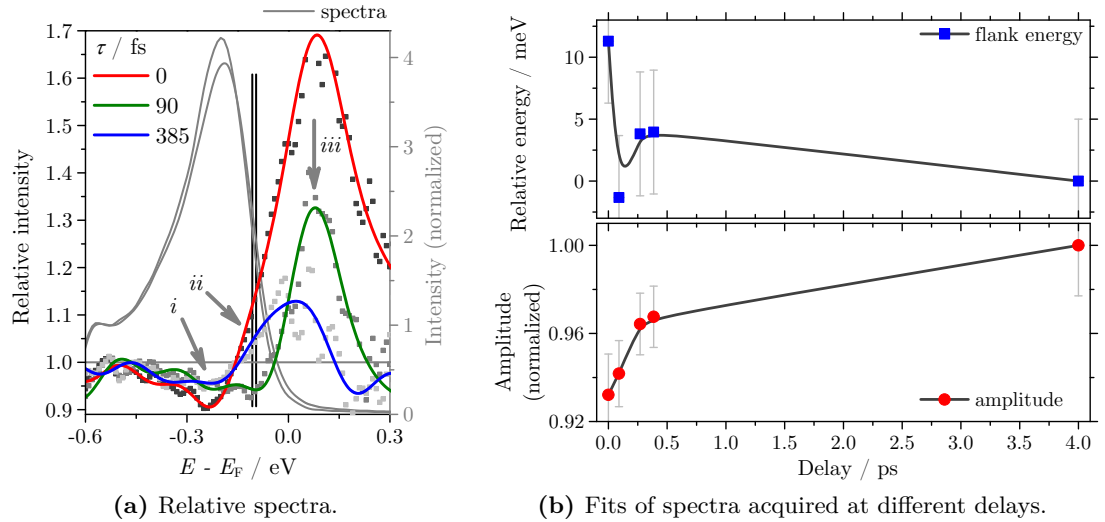


Figure 6.7: (a) presents relative spectra referred to the spectrum taken for $\tau = 4$ ps by calculation of the ratio of intensities. This representation emphasizes the relative spectral modifications and gray arrows point out the most distinctive ones (*i-iii*). For reference the spectra at 0 fs and 4000 fs are included (gray) and the energy of the corresponding E_{flank} is included shown by two black lines. The data (symbols) is smoothed (lines) using FFT filtering. (b) shows numerical fits of the amplitude of the Se 4p bands (circles) and the energy of the high energy cutoff of the spectrum (squares, “flank”); the gray lines are a guide to the eye. All data is referred to the value at $\tau = 4$ ps which is the highest temporal delay investigated.

The more subtle changes are revealed by calculating relative spectra which show the ratio of the intensities of each spectrum with respect to reference data—in our case a spectrum acquired at 4 ps. Figure 6.7(a) presents such data for the spectra discussed in figure 6.6(a). We observe a reduction of the amplitude of the Se 4p bands which relaxes for increasing temporal delay (see *i*). Furthermore, the initial generation of a non-thermal electron distribution by the absorbed laser pulse (see section 5.2) leads to a characteristic increase of spectral intensity right above the Fermi energy—an effect, also observed here (see *iii*)—which also relaxes for increasing delay (see also section 6.1.1). Additionally, the low temperature data reveal characteristic, time dependent changes of E_{flank} which show at energies of about -100 meV (see *ii*). The relative spectra demonstrate what actually happens at the three chosen delays:

- (i) At $\tau = 0$ fs the significant peak right above E_F indicating the non-thermal electron distribution features a shoulder at $E - E_F \approx -0.1$ eV which is a consequence of the shift of E_{flank} to lower binding energies.
- (ii) For $\tau = 90$ fs the thermalization of the electron distribution is advanced. Additionally, the signal at $E - E_F \approx -0.1$ eV is strongly reduced which emphasizes the increase of binding energy of the high energy cutoff of the spectra in this case.
- (iii) Finally, at $\tau = 385$ fs the electron distribution in the vicinity of the Fermi energy is fully thermalized (note the difference of energy of this feature with respect to both the other relative spectra). The peak observed at E_F is a consequence of the thermal broadening of the Fermi edge. The asymmetry of this peak is explained by a small remaining lowering of the binding energy of the Se 4*p* bands.

Figure 6.7(b) shows the amplitude of the Se 4*p* bands (circles) and the relative change of E_{flank} (squares). In both cases the data is referred to the value at $\tau = 4$ ps. These data are numerically fitted using the algorithm described in appendix A.1.1. Please note, that the uncertainty of the delay is only ± 0.67 fs (see section 3.2), for the energetic shift the width of one energetic channel of the analyzer is assumed (± 5 meV) and the uncertainty of the amplitude is defined by the standard deviation of the numerical calculation. The lines are a guide to the eye. Although only little data is available, this quantitative evaluation shows the continuous relaxation of the amplitude and the unexpected, oscillation-like shift of E_{flank} for small delays. Nevertheless, the TR-2PPE experiments do not provide the level of detail necessary to conclusively identify an oscillatory reaction of E_{flank} to the laser excitation, but rather motivate a thorough investigation in section 6.2.

In conclusion we identified very interesting laser induced ultrafast dynamics of the electronic system of 1*T*-TiSe₂ both in the room temperature, normal conducting and the low temperature CDW phase. Our findings enable us to focus on the relevant parameters for our detailed and more sophisticated experiments in the following section 6.2. Especially the investigation of the CDW at low fluences seems to be instructive for understanding the temporal evolution of the laser induced perturbation of the correlated electronic state of TiSe₂. We need a set of full 2PPE spectra with a good temporal resolution especially at the local extrema of the autocorrelation traces ($\tau \lesssim 1$ ps). The TR-2PPE data indicate a possible oscillatory behavior of the binding energy of the Se 4*p* bands after excitation, however, much better temporal resolution is necessary to conclusively identify such an effect.

Additionally, we presented a comparison of autocorrelation curves acquired at room temperature for the relevant spectral structures of TiSe₂ and TiTe₂. Both reveal deviations from the laser autocorrelation which are attributed to the initial non-equilibrium phase of the laser excitation. Furthermore, for TiSe₂ stronger modifications are observed which

indicate additional effects of the correlations of the electronic system, which is discussed in section 6.2.3–a.

6.2 Two-color pump-probe experiments on TiSe₂

The investigation of the temporal evolution of the laser induced non-equilibrium dynamics of the electronic system necessitates suitable experimental methods. We like to point out, that we focus on laser induced modifications of occupied electronic bulk bands. In the preceding section 6.1 we presented an application of conventional TR-2PPE to this task, however, this approach is complicated by the usage of identical pump and probe pulses. In this case, a significant laser induced modification of the spectra for the whole temporal range of the experiment is observed. It renders the interpretation of the data very challenging, because the “pump” event is basically the short enhancement of incident laser power, while the two pulses overlap. Nevertheless, these TR-2PPE data provide a valuable overview of interesting experimental parameters which we investigate in more detail in this section using an experimental setup methodically more suited.

The difficulty of a quantitative interpretation of the TR-2PPE autocorrelations is basically a consequence of the coupling of pump and probe process in the experiment and the obvious improvement of the experiment is decoupling the two processes. In this section we present a time-resolved IR-pump SH-probe photoemission setup (see section 3.2) which uses two different, well adapted laser pulses for pump and probe. The pump pulse is derived from the fundamental infrared (IR) emission of the laser system. At this photon energy the generation of photoelectrons is only possible by a second (or higher) order process. Because of the high work function of the TMDCs discussed in this work the excitation of photoelectrons requires four photons of the fundamental energy, i. e. a four-photon photoemission (4PPE) process. In combination with the probe pulses—we discuss these shortly—a three-photon photoemission (3PPE) involving two SH and one IR photon are also possible. However, the contribution of photoemission originating from the pump pulses to the photoemission spectra is expected to be insignificant in comparison to the contribution of the probe pulses, i. e. in contrast to the experiment in section 6.1 the pump pulse may induce non-equilibrium conditions of the sample but does not yield any contribution to the photoemission spectra. Furthermore, we generally observe, that the instabilities of the CSA system are reduced here (see appendix A.3)—probably because the photoelectron count rate is not directly increased by the absorbed pump pulses. The absorbed pump fluence of our experiments on TiSe₂ can be tuned in a range of up to about $3.5 \mu\text{J cm}^{-2}$.

In contrast to the pump, the photon energy of the probe pulse is chosen such, that significant photoemission is observed. It is generally good to employ a 1PPE process for the probing process of a two-color pump–probe experiment, because in this case a higher photoelectron count than for multi-photon processes (i. e. 2PPE and higher) is expected.

Nevertheless, our experiment uses the rather low photon energies accessible by second harmonic generation (SHG) which do not enable 1PPE for the TMDCs investigated here. We thus use IR-pump pulses and probe the temporal evolution of the electronic system by 2PPE spectra using SH-probe pulses.

What are the advantages of the IR pump and SH probe experiment presented here? Generally, with respect to the autocorrelation experiment discussed before in section 6.1, the cross-correlation experiment discussed here employs pump and probe pulses which are distinguishable, i. e. the pump pulse leads to the excitation of the system and the probe pulse exclusively generates the photoemission signal. The interpretation of the data is thus significantly simplified, because pump and probe event are now clearly different.

Furthermore, using SH probe pulses instead of UV pulses proves to be advantageous, too. Although the 2PPE process associated with SH pulses leads to a lower photoemission yield with respect to the 1PPE emission of the UV pulses, the duration of the SH pulses is generally shorter. The UV pulses are generated in a fourth harmonic generation (FHG) process involving two subsequent SHG stages. The frequency doubling crystals used in our setup do not allow photon energies above approximately 6.05 eV, corresponding to a wavelength of 205 nm. The limited wavelength range of the crystals leads to a reduction of the laser pulse bandwidth, which corresponds to an increase of the pulse duration (see section 3.2, especially table 3.2).

Other time resolved photoemission experiments using FHG for the UV pulses report a pulse duration of about 80 fs to 90 fs [4, 31] for this reason, thus limiting the temporal resolution of the experiment. A short pulse duration is crucial for our time resolved experiments—using SH pulses yields therefore the best temporal resolution in our setup.

Finally, the limitation of the UV photon energy is also problematic with respect to the high work function of our samples (see section 3.3). The resulting spectral width is reduced to about 350 meV for TiSe_2 , which does not allow to acquire meaningful spectral data without using alkali adsorbates (see sections 3.3 and 4.1).

Please note, that the absorbed fluence of the probe pulse is set to $5.3 \mu\text{J cm}^{-2}$ for TiSe_2 within this section, if not explicitly stated otherwise. This fluence enables reasonably high photoelectron counts for the acquisition of 2PPE spectra, while simultaneously minimizing static laser induced spectral modifications. The decrease of spectral weight of the chalcogen p bands is reduced to a negligible amount (see section 5.2). Also, at low fluences the instability of the CSA (see addendum A.3) is suppressed, however, changes of the general photoelectron count rate are still observed sometimes and normalization to the spectral plateau is thus still necessary (see section 5.1.2).

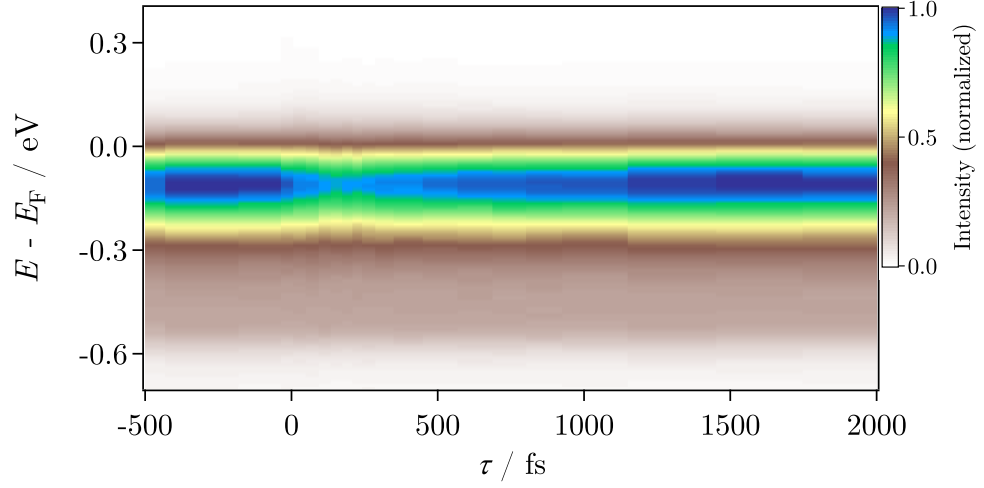
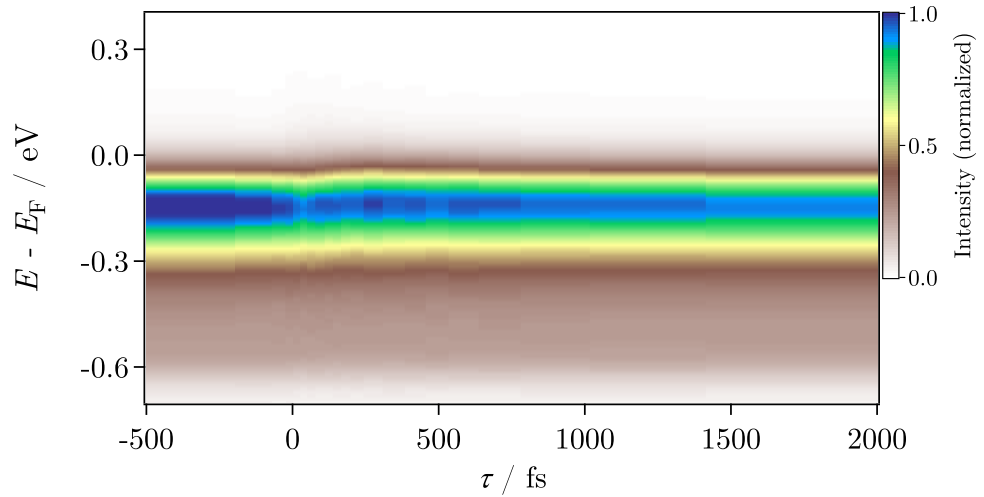
(a) Energy–delay map at $T = T_{\text{RT}}$ with $F_{\text{pp}} = 2.7 \mu\text{J cm}^{-2}$.(b) Energy–delay map at $T = (122.4 \pm 0.5) \text{ K}$ with $F_{\text{pp}} = 1.9 \mu\text{J cm}^{-2}$.

Figure 6.8: Intensity of spectra of 1T-TiSe₂ acquired at different temporal delays of pump and probe pulse in 2D energy–delay maps. The data are acquired within the normal conducting room temperature and the CDW low temperature phase. The interpolation method described for figure 5.2 in section 5.1 is applied. Positive Delays correspond to the probe arriving after the pump pulse. The maps show the suppression of the intensity of the Se 4p bands after absorption of the pump at T_{RT} , as well as their energetic shift within the low temperature phase.

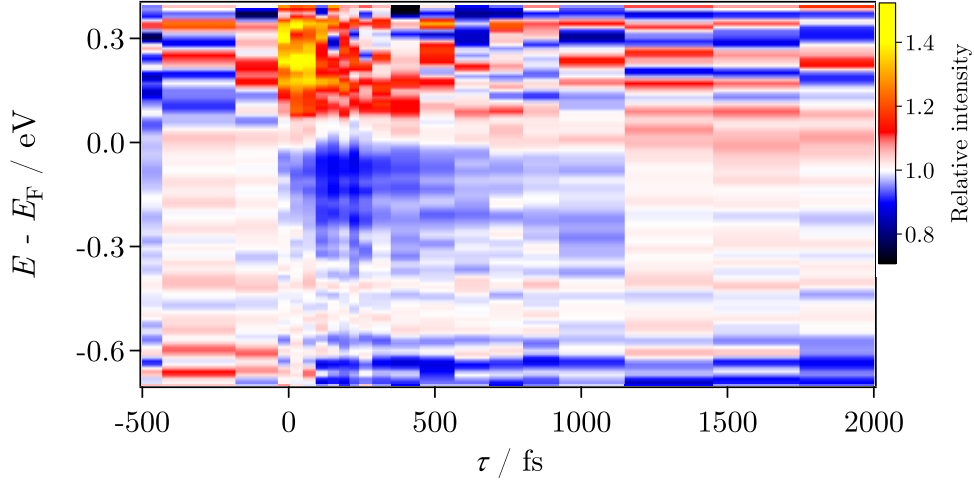
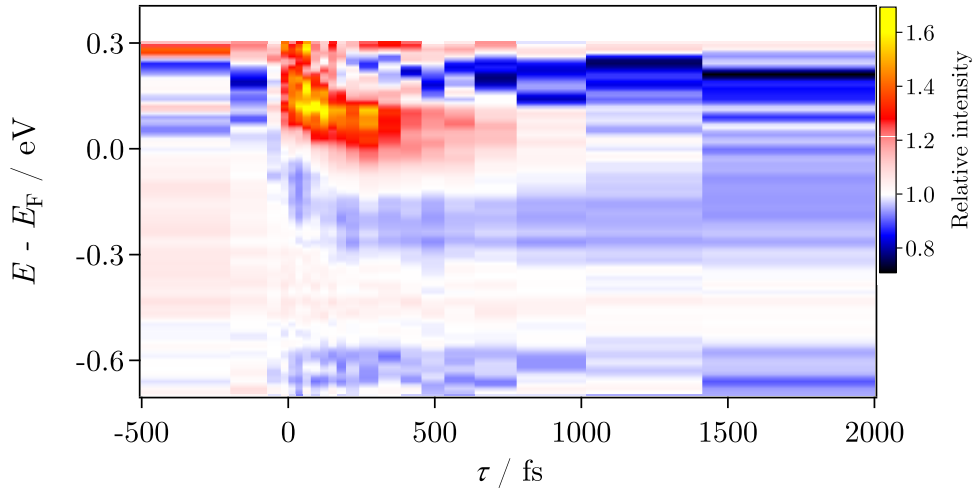
(a) Energy–delay map at $T = T_{\text{RT}}$ with $F_{\text{pp}} = 2.7 \mu\text{J cm}^{-2}$.(b) Energy–delay map at $T = (122.4 \pm 0.5) \text{K}$ with $F_{\text{pp}} = 1.9 \mu\text{J cm}^{-2}$.

Figure 6.9: Intensity ratio 2D energy–delay map corresponding to figure 6.8. Here the intensity ratio with respect to the average spectrum before the pump event is plotted. This representation emphasizes intensity in- and decreases. The spectral modifications discussed for figure 6.8 are better visible—especially the energetic shift is obvious to the naked eye in (b). Please note the non-equilibrium electron distribution at time zero above E_{F} (near about $E - E_{\text{F}} = 0.3 \text{eV}$) shown in red/yellow.

6.2.1 Overview of the Ultrafast Dynamics to be Expected in the Two-Color Experiment

Figures 6.8 and 6.9 show two-dimensional (2D) energy–delay maps of spectral data and a corresponding map showing the intensity ratio with respect to a reference spectrum, respectively. The latter uses a reference spectrum generated by averaging several spectra acquired for negative delays, corresponding to delays before the pump pulse arrives at the sample, i. e. these spectra represent the “unperturbed” sample state (see also section 6.2.2–a). Similar to the 2D mappings presented in section 5.1 we use a very simple interpolation method—each intensity or ratio spectrum is repeated for the additional delays up to halfway to the next spectrum. The data correspond to normal emission.

Figure 6.8 shows the spectrum of 1T-TiSe₂ for different pump–probe delays, acquired at (a) room temperature and (b) at $T \approx 122$ K (CDW phase). Time zero is defined using a cross-correlation acquired at the polycrystalline copper sample holder (see section 3.2.1–d). The 2D map shows the Se 4p bands (blue hues, $E - E_F \approx 0.0$ eV to -0.3 eV) and the plateau (brown tones, $E - E_F \approx -0.3$ eV to -0.6 eV). The data is smoothed and normalized to the plateau intensity. At room temperature we observe the distinct loss of spectral intensity of the Se 4p bands shortly after time zero, which recovers within a few hundred femtoseconds, which is expected from the time resolved experiments presented in section 6.1.1. We speculated in this section on a possible delay of the maximum suppression of the Se 4p bands after the excitation. This is indicated by the autocorrelation traces, but a conclusive extraction of this effect is not possible from those data.

Comparison to the intensity ratio with respect to the spectrum before absorption of the pump pulse in figure 6.9(a) enables the clear identification of the delay in the establishment of the amplitude reduction of the Se 4p bands. Here, red and yellow show a relative increase of spectral intensity, blue and black a reduction, and white signifies unchanged intensity. At time zero the non-equilibrium electron distribution just above the Fermi energy (see sections 5.2.2–b and 6.2.3), which is established during the temporal overlap of pump and probe pulse, is clearly observed. This map emphasizes the increase of signal above E_F , which cannot be observed this clearly in figure 6.8(a), while showing the loss of intensity by a blue spot at $\tau \approx 150$ fs. The loss of intensity of the Se 4p bands is clearly not “instantaneous” and takes a certain time. Further investigation of the temporal evolution of the amplitude of the Se 4p bands is therefore promising and will be discussed both for the normal and the CDW phase in section 6.2.3.

At low temperatures, TiSe₂ enters the CDW phase. Preliminary experiments presented in section 5.3.2 revealed, that absorption of a sufficiently intense laser pulse can perturb this phase. This is observed as a decrease of binding energy of the Se 4p bands, easily monitored by the energetic shift of the high energy cutoff of the spectrum. Indeed, figure 6.8(b) suggests that the modifications of the amplitude are also accompanied by an energetic shift closer to E_F , i. e. closer to the room temperature value. The intensity

ratios in figure 6.9(b) emphasize such spectral changes. In the vicinity of time zero we again observe the non-equilibrium electron distribution, leading to an intensity increase up to about 0.3 eV above E_F , and a slight decrease of amplitude of the Se 4*p* bands. Close to time zero there is no significant difference between the room and the low temperature data. For $\tau \gtrsim 100$ fs, however, we clearly observe an energetic shift of the Se 4*p* bands. Beginning at this delay the map shows a blue and a red stripe centered at approximately -0.2 eV and 0.05 eV. The white, unmodified region in between ($E - E_F \approx -0.1$ eV) corresponds to the high energy cutoff [see figure 6.10(b)], which center is at about -0.05 eV in this case. The increase above and the corresponding decrease below the cutoff energy thus show the energetic shift of this feature to lower binding energies. This ultrafast dynamics of this energetic shift is consequently also investigated in detail in section 6.2.3.

6.2.2 Considerations Concerning the Two-Color Experiment

The two-color time resolved experiment discussed in this section uses—in contrast to all experiments discussed in the preceding chapters—the IR fundamental of the laser for the pump pulses. Such photon energies were not used before in our experiments. First, we therefore need to investigate, whether the laser induced spectral modifications discussed in section 5.2 are still observed. Also, the necessary fluence range needs to be established.

Furthermore, in section 6.2.2–b, we provide data on the momentum localization of the laser induced spectral changes. This experiment complements the static data provided in section 5.2.4. We discuss, whether the laser induced ultrafast dynamics of the electronic system is also localized.

6.2.2–a Static Heat-up of the Sample by the Absorbed Pump Pulses

Before we focus on time resolved experiments for different absorbed pump fluences, it is instructive to investigate, how excitation of the sample by an IR pump pulse differs from excitation by SH pulses, as discussed in detail in section 5.2. Figure 6.10 shows fluence dependent 2PPE spectra acquired using the SH probe pulses at room temperature T_{RT} , shown in figure 6.10(a), and within the low temperature CDW phase at $T = 121$ K, presented in figure 6.10(b), both pumped using IR pulses.

We present data acquired at a pump–probe delay, τ , of about -2 ps, i. e. long before the pump pulse excites the sample and at approximately 100 fs to 250 fs after the excitation by the pump pulse, i. e. within the region of (roughly) the most distinct spectral modification after excitation as observed in cross-correlation data [see figures 6.9 and 6.8, as well as figure 6.11(b)].

We switched to IR pulses for pumping to avoid a contribution of these pulses to the photoemission signal, which obviously is achieved. However, the pump pulses modify the spectral shape constantly for all pump–probe delays, which is demonstrated by the data

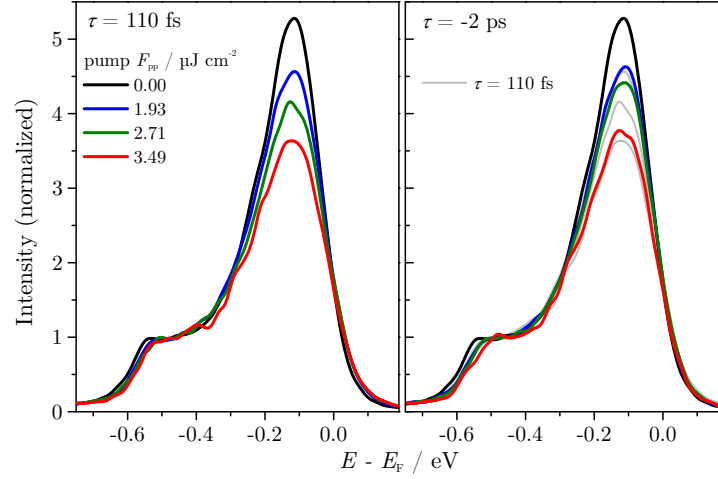
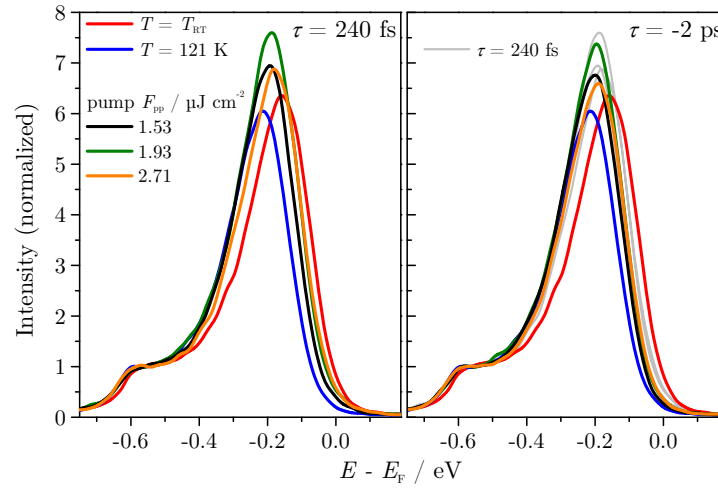
(a) Pump fluence variation at room temperature, T_{RT} .(b) Pump fluence variation at $T = 121$ K.

Figure 6.10: Spectra taken well before the pump (right, $\tau = -2$ ps) and at the delay of the strongest spectral modification after pumping (left, 110 fs or 240 fs). (a) presents data in the normal conducting phase. In the left the maximum effect upon increasing pump fluence is shown, the right reveals the offset due to sample heat-up by comparing the spectrum before pump to the maximum change after pump (gray). (b) shows the corresponding data for the CDW phase. The spectra at room and low temperature without pump are shown for reference.

compiled in figure 6.10. Even two picoseconds before the pump pulse is absorbed (right), the spectral shape is significantly altered with respect to the initial spectrum without any incident IR emission [(a) black, (b) blue]. The curves included in gray correspond to the spectrum acquired after pumping. The observed spectral modifications are compatible with the corresponding fluence dependent data for the SH pulses discussed in sections 5.2 and 5.3.2.

We like to stress the following observation from figure 6.10, which needs to be considered for all the two-color time resolved experiments discussed in this section: the pump pulses do modify the sample system statically, i. e. in a time resolved experiment we expect that the temporal evolution of an investigated spectral characteristic after excitation by the pump pulse is superimposed by a static offset. We attribute this offset to a static heat-up of the sample by the absorbed laser pulses, similar to our observations in section 5.2.2–a on an increase of sample temperature induced by heat accumulation of the absorbed pulse energy.

The absorbed pump fluence, F_{pp} , of the IR pulses seems very small ($F_{\text{pp}} \leq 3.5 \mu\text{J cm}^{-2}$) compared to the corresponding SH pulses employed in chapter 5 (F_{pp} being tens of $\mu\text{J cm}^{-2}$) considering the significant modifications observed—especially since the spectra are virtually unchanged for $F_{\text{pp}} \lesssim 5 \mu\text{J cm}^{-2}$ (see addendum A.3.2–a). Therefore, a closer look at this apparent discrepancy is necessary.

In the following we compare the spectral changes induced by the absorption of the IR pump pulses to the effects of thermal heat-up (see section 5.1), similar to our approach for the SH probe pulses in section 5.2. This is, of course, a phenomenological method. We will see shortly, that, although the pump fluences are rather small, the thermal effects are unexpectedly strong. This is a consequence of the unfocused pump spot on the sample surface, which leads to a small value of F_{pp} . Nevertheless, a significantly higher laser power is absorbed within a larger surface area of the sample. For a quantitative evaluation of the sample warm-up we therefore need to consider the heat diffusion into the sample crystal—the corresponding long-term thermal equilibrium yields the observed sample temperature (see, e. g., reference [246] and section 5.2.2–a).

For a qualitative estimate of the sample warm-up induced by the absorbed pump pulses, we follow the method employed in section 5.2. There, the work function, Φ , proved to be a good measure of the instantaneous sample temperature (see section 5.1.3). Indeed, Φ increases linearly with the laser fluence as expected for a temperature increase of the sample (see section 5.2). The fluence coefficient of the work function is $\Delta\Phi_{F_{\text{pp}}} = (58 \pm 2) \times 10^{-4} \text{ eV } \mu\text{J}^{-1} \text{ cm}^2$ for both chosen delays. This value is about 7 times higher than in case of the SH experiment (see section 5.2.2–a). Following the method presented in section 5.2.2–a, we use the temperature coefficient $\Delta\Phi_T = (2.24 \pm 0.22) \times 10^{-4} \text{ eV K}^{-1}$ (see table 5.3, section 5.1.3) to calculate $\Delta T_{F_{\text{pp}}} = (26 \pm 3) \text{ K } \mu\text{J}^{-1} \text{ cm}^2$. The work function increase thus supports a heat-up of $(91 \pm 12) \text{ K}$ at pump fluence of $3.5 \mu\text{J cm}^{-2}$. This temperature increase is indeed consistent with the observed loss of intensity of the amplitude of the Se $4p$ bands. The temperature coefficient of the amplitude (referred to

room temperature) in table 5.5 in section 5.1.4–d yields a reduction of the amplitude to $(68 \pm 6) \%$ for $\Delta T = 91$ K, which is in very good agreement to the amplitude reduction observed at $\tau = -2$ ps of $(69.2 \pm 0.8) \%$. The amplitude at $\tau = 110$ fs is slightly lower at $(66.8 \pm 0.5) \%$.

To check the plausibility of the estimated heat-up, we calculate the temperature increase of the sample induced by the absorption of one single laser pulse (see section 5.2.2–a). Table 3.5 in section 3.2.1–b yields $\kappa = 1.26$ at $h\nu = 1.59$ eV ($\lambda = 780$ nm) which corresponds to a penetration depth of $d = 49.3$ nm of the IR pulses. A beam radius of $a \approx 206 \mu\text{m}^4$ (see figure 3.6 in section 3.2.1–b) corresponds to a pump fluence of $3.5 \mu\text{J cm}^{-2}$. The laser is thus absorbed by $N_M = 4.98 \times 10^{-11}$ mol of the sample, which is about 162 times the amount of sample compared to the case of the SH probe pulses. The pump fluence discussed here corresponds to an absorbed heat of $Q_{\text{pp}} = 1.75$ nJ per pulse. We estimate a heat-up of $\Delta T = 0.5$ K per pulse. Although ΔT is approximately 35 times smaller than the heat-up for one probe pulse, the heated portion of the crystal is more than two orders of magnitude bigger. This renders the estimated static temperature increase of the sample—under consideration of heat diffusion and accumulation—plausible.

In conclusion, the absorbed IR pump pulses lead to an increase of the sample temperature in agreement to our observations in sections 5.2 and 5.3. After excitation by the pump, the spectrum is further modified on a femtosecond timescale. However, the observed heat-up is much stronger than expected from the experiments using SH pulses.

A final remark on the significant difference in the fluence coefficients for excitation with IR and SH laser pulses. The deviation from our earlier experiments is understood considering the definition of the IR pump fluence in section 3.2.1–b and the experimental setup, especially the beam alignment, as presented in section 3.2.1–a. Only one lens is used for focusing the incident laser beams onto the sample to reduce temporal broadening of the pulses (see section 2.3), i. e. only pump *or* probe pulses can be focused on the sample surface. We decided for focusing the SH probe pulses for direct comparability to our investigations in chapter 5 and—most importantly—to ensure, that the probe pulse always resides within the pumped area of the sample. The IR pulses therefore exhibit a large diameter of approximately $200 \mu\text{m}$, of which only a diameter of four times the probe pulse diameter is considered⁵, i. e. the sample absorbs the full pump beam within a larger area. The fluence, being dependent on the illuminated area, is

⁴Note, that the linear gray filter leads to an asymmetric shape of the laser spot, as the attenuation is significantly stronger in one direction of the filter. This inhomogeneity is less pronounced at smaller attenuation, i. e. the observed beam diameter becomes independent on the filter position. This is a consequence of the fact, that the “linear” filter seems to be not very linear, especially for high attenuations.

⁵The fluence depends on the area of the laser spot, because of the Gaussian intensity profile. The fluence is therefore highest at the beam center. We consider a larger area for evaluation of the pump fluence to include a slight mismatch of pump and probe pulse pointing (see section 3.2.1–b).

rather small, because of the large spot size, however, the IR pulses feature a significantly higher mean power which is absorbed within a larger sample surface area. It is reasonable to assume, that heat accumulation (see section 5.2.2–a) leads to a stronger heat-up of the sample in this case. Furthermore, the small fluence of the pump pulse leads to a less strong induced ultrafast dynamics. The laser induced modifications are more subtle, while the static background is more pronounced (compare figure 6.6 in section 6.1.2–a to figure 6.16).

Future experiments might therefore profit from a better focusing of the IR pump pulses to circumvent this problematic observation. The beam diameter can be safely reduced to 2 to 4 times the diameter of the probe pulses. We expect less background induced by sample warm-up and a stronger laser induced effect because of the higher fluences. Nevertheless, using such low fluences enables the observation of coherent dynamics in section 6.2.4.

Please note, that we circumvent the need of a detailed simulation of the effects of heat diffusion for the estimation of the static long-term equilibrium temperature of the sample established by heat accumulation by comparison of certain spectral features to the temperature dependent data in section 5.1.

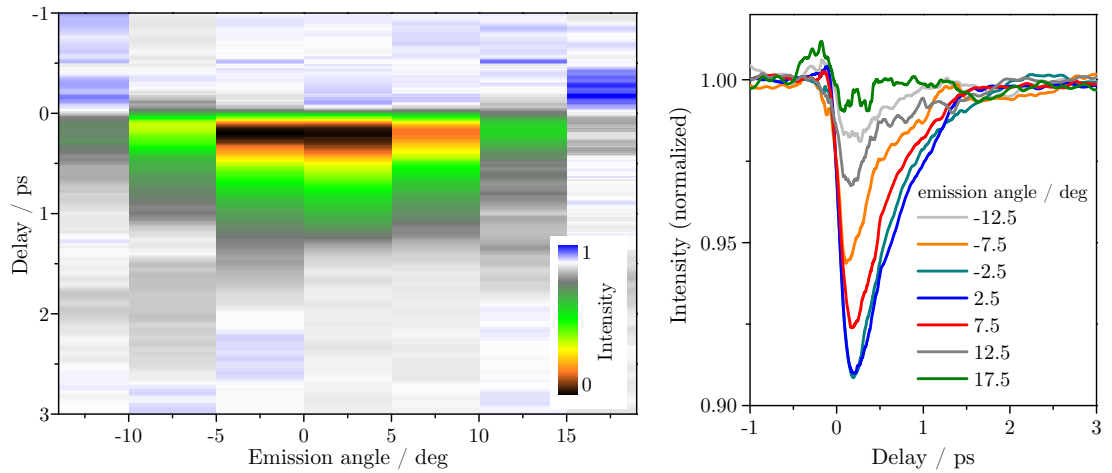
6.2.2–b Dependence of the Ultrafast Dynamics of TiSe_2 on the Parallel Momentum

In a static spectroscopic experiment on TiSe_2 , the variation of the absorbed laser fluence leads to a reduction of the spectral weight of the Se $4p$ bands (see section 5.2). Interestingly, this modification reveals a distinct momentum dependence—the strongest changes are observed for normal incidence, i. e. at the apex of the Se $4p$ parabolas (see section 5.2.4). In this section we provide additional, time resolved data on the momentum dependence of the laser induced dynamics of the electronic system.

Figure 6.11(b) presents cross-correlation traces acquired for an IR pump fluence of $2.7 \mu\text{J cm}^{-2}$ using our typical SH probe pulses for different emission angles. These data are taken at the energy of the maximum intensity of the Se $4p$ bands. Figure 6.11(a) shows a corresponding, more intuitive 2D delay–emission angle map, generated by the simple interpolation method described for figure 5.2 in section 5.1.

From figure 6.11 we find a strong angle dependence of the cross-correlation signal. The strongest suppression of Se $4p$ photoemission signal is observed in the vicinity of $\mathbf{k}_{\parallel} = 0 \text{ \AA}^{-1}$, in agreement to the static data discussed in section 5.2.4.

Please note, that the observed emission angle dependence of the magnitude of the drop of the cross-correlations is not solely induced by the change of absorbed pump fluence. The emission angle is varied by about $\pm 15^\circ$ by a rotation of the sample with respect to the incident laser and the entrance aperture of the CSA, i. e. the size of the laser spot on the sample surface varies. The laser spot is elliptical (see section 3.2.1–b) and thus the radius within the plane of incidence, b , changes if the sample is rotated



(a) 2D delay-emission angle map of cross-correlations.

(b) Cross-correlations taken at the maximum of the Se 4p bands at selected emission angles.

Figure 6.11: Emission angle dependence of the cross-correlation shape of time-resolved IR-pump SH-probe photoemission experiments performed for the maximum of the Se 4p bands at room temperature. The probe fluence is $5.3 \mu\text{J cm}^{-2}$ ($h\nu = 3.18 \text{ eV}$), the pump fluence is $2.7 \mu\text{J cm}^{-2}$ ($h\nu = 1.59 \text{ eV}$). The cross-correlations are normalized and linearly drift corrected (see text) and smoothed by averaging 15 adjacent data points. (a) shows a 2D representation of these data generated by repeating of the data for $\pm 5^\circ$.

like $b = \frac{a}{\cos \alpha}$. The laser radius, a , and the angle of sample surface and incident laser, α , are parameters. For the default angle of 45° this corresponds to $b = \sqrt{2}a$ (see section 3.2.1-b). Rotation of the sample leads to $\Delta\alpha = \pm 15^\circ$, which corresponds, because of $F_{\text{pp}} \propto (\pi ab)^{-1}$, with the laser spot area πab , to an increase or decrease of the absorbed fluence to approximately 123% or 71%, respectively. This explains the asymmetry of the drop of the cross-correlation in figure 6.11 for negative and positive angles.

The sample rotation therefore leads to variations of F_{pp} of below 30% ($1.9 \mu\text{J cm}^{-2} \lesssim F_{\text{pp}} \lesssim 3.3 \mu\text{J cm}^{-2}$). In section 5.2.2-b we observed a linear decrease of the amplitude of the Se 4p bands with increasing F_{pp} . Our findings in section 6.2.2-a show, however, that the absorbed IR pulses lead to a static heat-up of the sample, i. e. the spectral shape is significantly modified even before the pump pulse arrives (see spectra for $\tau = -2 \text{ ps}$). Figure 6.11(b) presents cross-correlation traces acquired at the peak of the Se 4p bands, which are normalized to the signal for big temporal delays. This corresponds to normalization to the amplitude at, e. g., $\tau = -2 \text{ ps}$ in case of the spectroscopic data. The normalized amplitudes yield a fluence coefficient of $\Delta I_{\text{max}, F_{\text{pp}}} = (1.1 \pm 1.0) \times 10^{-2} \mu\text{J}^{-1} \text{ cm}^2$ which corresponds to a laser induced in-/decrease by $(0.7 \pm 0.6) \%$ and $(0.9 \pm 0.8) \%$,

respectively, of the Se 4*p* bands.⁶

We therefore conclude, that the observed angular dependence of the cross-correlation signal is not explained solely by the fluence changes resulting from differences of the angle of incidence, because this contribution is too small.

Both the static spectroscopy and the time resolved cross-correlation data therefore support a localization of the laser induced modifications at the $\bar{\Gamma}$ -point. This finding proves valuable for the interpretation of our data in the following sections. In section 5.2.4-c we presented a preliminary interpretation of the static data using the theoretical work of Cercellier et al. [11] (see especially [55, 103]) which provides calculations of angle-resolved photoemission spectroscopy (ARPES) spectra within the model of the excitonic insulator (see section 2.2.1). Those calculations predict strong intensity changes within the Se 4*p* bands right at the Γ -point, i. e. within the momentum range of the strongest modification in the experimental cross-correlations presented here.

However, our experiment is performed at room temperature, i. e. within the normal conducting phase of TiSe₂, while the calculations in reference [11] investigate the spectral changes upon the phase transition into the low temperature CDW phase. Nevertheless, we observe a striking resemblance of the laser induced modifications to these calculations under the absorption of a strong laser pulse. This similarity may be a consequence of the persistence of the CDW phase of this system in the form of fluctuations even at room temperature (see section 5.2.4-c). Our data in section 6.2.3 shows, that the CDW phase is perturbed by the absorption of the IR pump laser pulses. The data discussed in this section suggests a similar laser induced perturbation of the room temperature fluctuations.

We will investigate the ultrafast dynamics of such perturbations in the following sections—such data enable more sophisticated conclusions on the origin of the observed laser induced effects. Nevertheless, the localization of the modification of the amplitude of the Se 4*p* bands observed in static spectroscopic and time resolved experiments itself hints at the relevance of the electronic correlation in TiSe₂ for the understanding of the observed effect. The detailed calculations of Monney et al. [55] within the model of the excitonic insulator for TiSe₂ reveal a significant loss of spectral weight especially at $\bar{\Gamma}$ (see also reference [11]). The proposed mechanism is based on the formation of an “exciton condensate phase” [55], i. e. the good agreement of the experimental and theoretical spectra, especially with respect to magnitude of the loss of spectral weight [11], is an indication for a purely electronic mechanism underlying the CDW transition.

Of course, the data shown here is only a very qualitative hint at a potential transition

⁶A direct linear fit to the data acquired at $\tau = 110$ fs yields a bigger fluence coefficient of $\Delta I_{\max, F_{pp}} = (1.01 \pm 0.04) \times 10^{-1} \mu\text{J}^{-1} \text{cm}^2$, because in this case we do not compensate for the rather strong offset induced by static warm-up of the sample. In this case an in-/decrease by $(6.0 \pm 0.3) \%$ and $(8.1 \pm 0.3) \%$, respectively, would be expected. Nevertheless, a direct comparison of the plateau-normalized spectra and the cross-correlations is not correct.

mechanism. The detailed discussion of the timescales of the processes involved is much more instructive. Nevertheless, the angular dependence of the laser induced modifications provides an interesting aspect to the discussion of the time resolved data in the following.

6.2.3 The Laser Induced Dynamics and Fluence Dependence

This is a two-part section. First, we discuss the temporal evolution of the relevant spectral signatures, then we investigate the pump fluence dependence thereof. In contrast to our time resolved approach using autocorrelation traces (see section 6.1) we are not restricted to the time dependence of the spectral intensity of a fixed energy range anymore. The main advantage of the data discussed in this chapter is, that we retain the full spectral information—this allows for access to, e. g., binding energies and the work function, too.

In sections 5.2 and 5.3 we investigated, how the absorbed laser fluence modifies the spectral shape in a static experiment. Although the laser induced temperature increase of the sample leads to thermal modifications of the spectra, some spectral signatures hint at potential non-thermal effects. The experiment discussed in this section features the full spectral information and thus enables us to investigate the temporal evolution of these signatures after the absorption of the pump pulse.

Furthermore, the pump fluences accessible in our experiment are sufficient to drive a static transition into the normal conducting phase solely by the laser induced temperature increase, if the 1T-TiSe₂ sample is initially within its CDW/PLD phase (see section 6.2.2–a). The experiments with equal pump and probe pulses in section 6.1.2 revealed, that this static heat-up allows for choosing a certain range within the continuous, second order phase transition (see figure 6.4 in this section). At time zero, i. e. when pump and probe pulse overlap temporally, additionally spectral modifications are observed. Therefore, the selection of the pump/probe fluences allows for the investigation of this dynamics well within the CDW, within the phase transition, and under normal conducting conditions.

Before we investigate the fluence dependence of the characteristic modified spectral features, we first focus on the dynamics of the spectral changes typically observed.

6.2.3–a Characteristic Laser Induced Spectral Modifications and their Corresponding Temporal Evolution

Figure 6.12 shows two characteristic spectra acquired during a time resolved experiment within the CDW/PLD phase of TiSe₂. The gray spectrum is taken well before the pump pulse arrives at the sample surface ($\tau = -3.01$ ps) and the magenta spectrum shows the maximum shift of the high energy cutoff which is experimentally observed shortly after excitation by the pump pulse ($\tau = 0.27$ ps). We are going to discuss the temporal evolution of the following spectral signatures: *(i)* the work function (green arrow) and *(ii)* the position of the spectral high energy cutoff (blue arrow) which are

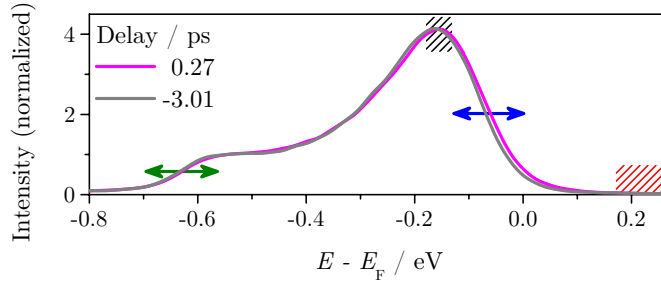


Figure 6.12: Spectra taken at temporal delays of $\tau = -3.01$ ps and 0.27 ps for a sample temperature $T = (122.4 \pm 0.5)$ K and with a pump fluence of $F_{\text{pp}} = 1.9 \mu\text{J cm}^{-2}$. Our analysis yields the work function (green) and the position of the high energy cutoff (blue) fitted by the center of the corresponding spectral flank (arrows). Furthermore, we extract the amplitude of the Se 4p bands (black) and the intensity of the non-equilibrium distribution of the electrons above E_{F} (red) by integration of the intensity for a certain energy range, visualized by the hatched areas. The spectra are normalized to the plateau intensity. For details see text.

defined by the energies of the centers—or half-maxima—of the corresponding spectral flanks. Additionally, we extract the *(iii)* amplitude of the Se 4p bands (black hatched), and *(iv)* the average intensity of the non-equilibrium photoelectron signal well above E_{F} (red hatched).

The data evaluation follows the procedures described in appendix A.1.1. The energetic ranges, averaged for the intensity derived features, i. e. for the amplitude and the intensity well above the Fermi energy, are visualized by hatched areas (the ranges are to scale). The amplitude is derived by averaging the intensity within an energetic range of ± 20 meV around the maximum of the Se 4p bands' peak. For the evaluation of the non-equilibrium electron distribution a range of $E - E_{\text{F}} = 0.17$ meV to 0.27 meV is used. The significant separation from the Fermi edge is necessary, as closer to E_{F} the intensity is dominantly modified by the energetic shift of the Se 4p bands, i. e. the observed intensity changes are mainly attributed to these bands.

Figure 6.13 compiles the temporal evolution of the laser induced modifications of characteristic spectral signatures observed (a) within the normal conducting and (c) starting from the CDW/PLD phase. We present a signal attributed to a non-equilibrium distribution of the electronic system (red circles), the amplitude of the Se 4p bands (black squares) and the relative energy of the high energy cutoff the spectrum (blue triangles)—the latter only for the CDW/PLD phase.

The initial, non-thermal electron distribution is observed by the intensity above the Fermi energy (red) which increases only within a small delay range close to time zero, i. e. this signal is only observed while pump and probe pulse coincide.

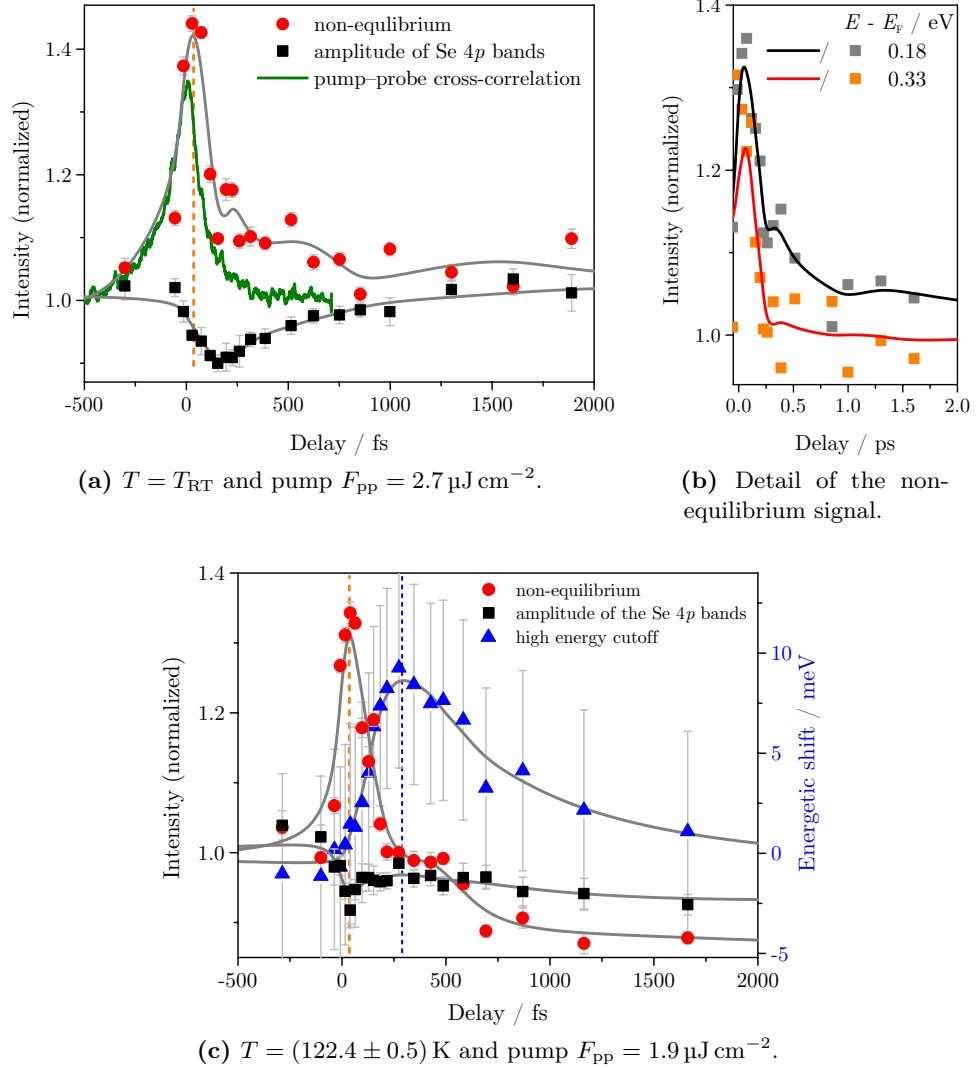


Figure 6.13: A numerical analysis of the spectra presented in figure 6.8 yields the temporal evolution of the signal above E_F ($E - E_F \approx 0.2 \text{ eV}$ to 0.3 eV) of the non-equilibrium distribution of the electrons (red circles), the amplitude of the Se 4p bands (black squares), and the energetic shift of the high energy cutoff (blue triangles). Gray lines are smoothed data (FFT) and provide a guide to the eye. A cross-correlation trace of the pump and probe pulse is shown in green. (b) presents the energy dependence of the signal attributed to a non-equilibrium electron distribution.

The cross-correlation of the pump and probe pulses taken on the copper sample holder (green) is included in figure 6.13(a)—it is used to define the zero delay of the experiment. The signal above E_F fits well to the cross-correlation for negative delays, however, it is broadened for $\tau > 0$ fs.

The signal observed for $E > E_F$ is attributed to the initial non-equilibrium electron distribution expected as the first stage of the laser excitation (see section 2.5.4). The IR pump pulse ($h\nu = 1.59$ eV) generates this non-equilibrium electron distribution by exciting electrons from below E_F up to $h\nu + E_F$, i. e. from the occupied Se $4p$ bands just below, into the unoccupied Ti $3d$ bands right above E_F —refer to figure 4.10 in section 4.1.4 for the corresponding band structure. The initial, laser induced non-thermal electron distribution should therefore reflect in a reduction of the spectral weight of the Se $4p$ bands corresponding to the population of the unoccupied Ti $3d$ bands.

Indeed, a closer look at the amplitude of the Se $4p$ bands in figure 6.13(c) reveals a drop of this value simultaneous with the enhanced intensity above E_F (orange line). However, although this observation is consistent with the expected transfer of spectral weight, the dip in the amplitude of the Se $4p$ right at the occurrence of the maximum signal above E_F is rather subtle and virtually non-present for the room temperature data in figure 6.13(a). This is not surprising, considering the dependence of the amplitude of the Se $4p$ bands on the absorbed laser fluence as discussed in section 5.3.2: if the sample is initially within the CDW phase, an increase of the absorbed laser fluence leads to an increase of the amplitude, while the behavior is inverted within the normal conducting room temperature phase. Therefore, the decrease of the amplitude is well observed for the experiment performed within the CDW phase, because the laser induced thermal effects⁷ are reversed—in contrast to the room temperature phase, where the thermal effect covers the small initial decrease.

Furthermore, using a pump photon energy of $h\nu = 1.59$ eV, the Ti $3d$ bands can be populated within their full energetic range up to $E - E_F \approx 1.2$ eV—the Se $4p_z$ band provides the corresponding initial states (see section 4.1.4). Figure 6.13(b) shows the non-equilibrium signal for different energetic ranges with center energies of 0.18 eV and 0.33 eV above E_F and integration for ± 25 meV. Although the low intensity of the photoemission above E_F renders the temporal curves rather noisy, we still observe a clear broadening closer to the Fermi energy, i. e. the intensity is increased after the excitation by the pump pulse for longer periods of time, the smaller the energy.

The increase in photoemission signal is visible better in the 2D maps presented earlier in this chapter in figures 6.8 and 6.9, section 6.2.1. Especially at room temperature the relative spectrum clearly reveals a longer increase of intensity right above E_F . We attribute this to the broadening of the Fermi edge of the spectrum which reflects an increased sample temperature. This broadening enhances the spectral intensity just above E_F .

⁷We will discuss the temporal evolution of the amplitude shortly.

The second step in the temporal evolution of the excited electronic system is the thermalization thereof. As discussed in section 2.5.4, the initial non-equilibrium electron distribution generated by the absorbed laser equilibrates, i. e. a thermal equilibrium of the electronic system is reestablished. The thermalization time, τ_{th} , characterizes when the temperature of the electrons is described again by the Fermi distribution.

In sections 5.2 and 5.3.2 we discussed laser induced spectral changes within the normal conducting and the CDW phase, respectively. These modifications were well explained by thermal changes, i. e. the observed characteristics generally agreed to thermally induced effects.

In figure 6.13 we therefore analyze the temporal evolution of the amplitude of the Se 4p bands (black) and the position of the high energy cutoff of the spectrum (blue)—both feature a distinct temperature and absorbed laser fluence dependence which is analyzed in detail in chapter 5. During the thermalization process, signified by the decay of the non-equilibrium photoelectron signal (red), i. e. within roughly the first 250 fs, a distinct reduction of the amplitude is established at room temperature, while the cutoff reaches a maximum shift at low temperature. In the following we discuss, how these changes can be understood.

Chapter 5 revealed some distinct deviations between purely thermal and laser induced spectral modifications. The static fluence dependent experiments in sections 5.2 and 5.3.2 correspond to the zero time in our time resolved experiments here. Keeping this in mind, the differences observed for the laser induced modifications are understood considering the temporal evolution shown in figure 6.13: At $\tau = 0$ fs we only observe a significant increase of intensity above the Fermi energy, the “non-equilibrium” data in figure 6.13, and a corresponding reduction of the spectral weight of the Se 4p bands, visible especially at room temperature [see figure 6.13(a)].

At low temperature, within the CDW phase, the energetic shift of the high energy cutoff with increasing laser fluence indicated an increase of temperature (see section 5.3.2). In both cases, the magnitude of the spectral modification deviated from the thermally induced modifications. This is explained as follows: the absorbed laser leads to an increase of the sample temperature, i. e. it provides an offset or background in our time resolved experiments, as well as in their static counterpart, which corresponds to purely thermal effects. Additionally, the time resolved data presented here show laser induced effects, which are already beginning to be established at time zero. It is this onset of the modifications which leads to stronger changes of the amplitude Se 4p bands or the cutoff for the fluence, than the temperature dependent data.

The reduction of the Se 4p bands’ amplitude and the shift of the high energy cutoff of the spectrum are obviously delayed, i. e. they are not instantaneously established; only after thermalization of the electronic system these effects are fully developed. To investigate this delayed reaction of the system further, we present in figure 6.14 two additional spectral signatures which are identified as good benchmarks for thermal effects in chapter 5: the FWHM of the Se 4p bands and the work function.

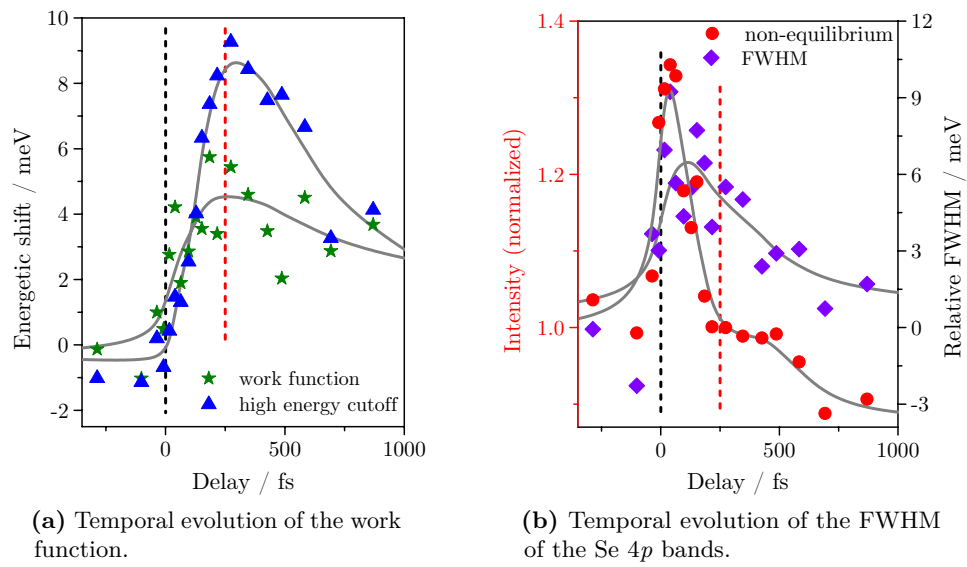


Figure 6.14: Temporal evolution of typical spectral signatures for thermal modifications of the sample, taken at $T = (122.4 \pm 0.5) \text{ K}$ with $F_{\text{pp}} = 1.9 \mu\text{J cm}^{-2}$ [corresponding to figure 6.13(c)]. The relevant delays of 0 fs and 250 fs are marked by dashed lines to emphasize time zero and the approximate temporal delay of the maximum spectral changes.

Generally, the behavior shown in figure 6.14 is observed for the normal and the CDW phase of TiSe₂ at different pump fluences, however, the observed changes are too small with respect to noise to be evaluated for the smallest fluences. Figure 6.14(b) shows the temporal evolution of the FWHM of the Se 4p bands in comparison to the intensity above the Fermi energy. The FWHM increases shortly after the excitation by the pump pulse. The full increase of the FWHM therefore seems to be established very fast, almost during the generation of the non-equilibrium electron distribution. We attribute the strong increase right at $\tau = 0$ fs more to the initial drop of the amplitude of the Se 4p bands, than a real thermal effect. Because of the removal of spectral weight, the FWHM seems to increase—it is thus not a good property to evaluate a corresponding sample temperature.

The work function, however, shows a clear increase as expected for a heat-up of the sample (see section 5.1.3). It is furthermore not expected to be strongly modified by the initial non-equilibrium state of the electronic system. Indeed, figure 6.14(a) reveals qualitatively a very similar behavior of the work function and the high energy cutoff of the spectrum. Please note, that these data do not show a shift of the whole spectrum as expected, for instance, in case of charging of the sample [255]. The cutoff shifts almost two times the value of the work function. Both energetic changes are established within about 250 fs.

We observe a maximum broadening of the FWHM of (6 ± 3) meV and a maximum increase of the work function of (5 ± 1) meV. Both are in agreement with a temperature increase. Using the temperature coefficients from section 5.1.3 for the work function and from table 5.6, section 5.1.4-d, we find a temperature increase of $\Delta T_{\text{FWHM}} = (27 \pm 14)$ K and $\Delta T_{\Delta\phi} = (20 \pm 4)$ K corresponding to the FWHM and the work function, respectively. The maximum shift of the spectral cutoff [see figure 6.14(a)] is approximately (9 ± 1) meV. This corresponds to a thermal effect of $\Delta T_{\text{cutoff}} = (21 \pm 3)$ K using the temperature coefficient for increasing temperature in section 3.3 [$\Delta E_c = (4.31 \pm 0.15) \times 10^{-4}$ eV K⁻¹]. The agreement, especially to the work function, which shows less noise, is very good. Furthermore, as we suggested in section 5.3.2, the temperature coefficient of the spectral cutoff defined by temperature dependent data acquired during slow warm-up of the sample fits indeed better to the laser induced effect observed here.

So far, our experiment revealed, that after thermalization of the excited electrons, i. e. after the reestablishment of a thermal electron distribution, typical thermal spectral modifications are observed: an increase of the work function and the high energy cutoff which both agree quantitatively very well and which are also both expected upon a temperature increase.

Although the agreement to thermal modifications is very good, it reveals a surprising question: Why do we seem to observe thermal spectral modifications which are established during the thermalization of the electronic system? After the equilibration of the electrons we basically derive a hot electronic system. The heat is, however, mainly not transferred to the lattice, yet. While a broadening of the FWHM of an electronic state could still

be motivated by the elevated electronic temperature and the break-down of the CDW—observed by the energy of the cutoff—could be of purely electronic origin, the simultaneous modification of the work function is rather surprising. The work function’s dependence on the temperature is mainly attributed to the thermal expansion of the lattice (see section 5.1.3–a), i. e. to an effect associated with an increased lattice temperature.

Furthermore, although the lattice will already be heated during the electronic thermalization (see section 2.5.4), the modification peaks at the time of the electronic equilibrium, i. e. despite the further heat transfer to the lattice, the effect already diminishes.

We will fully understand the driving mechanism of the observed temporal evolution of these signatures when discussing the oscillatory behavior of the high energy cutoff in section 6.2.4. These data show, that it is feasible to perturb the CDW/periodic lattice distortion (PLD) phase such, that a oscillation of the superstructure can be induced. The CDW is associated with the occurrence of a corresponding phonon mode [256], the amplitude mode of the CDW. We will show, that the laser induced perturbation of the CDW in our experiment leads to the excitation of this phonon mode in the following section. Holy et al. [256] argued from symmetry considerations, that this mode corresponds to a relative movement of the selenium atoms perpendicular to the plane of the crystal layers—refer to section 2.1 for the details of the crystal structure of $1T\text{-TiSe}_2$. The CDW is therefore connected to an oscillation of the Se sheets which build the outer layers of the Se–Ti–Se tri-layers of TiSe_2 , i. e. the distance of these Se sheets varies.

Considering our findings in section 5.1.3–a, the work function is expected to react significantly to a change in atomic distance perpendicular to the surface, especially to vibrations of the ions. The oscillatory behavior discussed in section 6.2.4 vanishes within a fraction of a picosecond. It is observed after thermalization of the electronic system and then vanishes much faster, than the duration of the heat transfer to the lattice [see figure 6.16(a)]. Figure 6.14(a) also shows such a behavior for the work function. It reaches a maximum right at the thermalization of the electrons and then relaxes to its initial value. The work function therefore reacts to the vibrations of the lattice ions induced by the perturbation of the CDW/PLD.

At first, such a fast response of the lattice within only a few hundred femtoseconds may seem unexpected. However, reflectivity measurements basically probe the transient refraction index which depends on the movement of the ions [257]. The CDW is a collective phenomenon where an electronic modulation is coupled to the lattice (see, sections 2.2). Because of the possibility to induce oscillations of the phonon mode associated with the CDW such a fast reaction of the lattice is feasible.

Finally, the temperature of the electron system and the lattice equilibrate. The temperature of the electronic system decreases, while the lattice is heated (see section 2.5.4). The relaxation of the electronic system is mediated by electron–phonon coupling [130]. The final temperature of the sample is significantly smaller than the

temperature reached by the electronic system—described by the broadening of the Fermi edge—because of the much larger heat capacity of the lattice [110]. This leads to the typical decay of the laser induced spectral modifications on a picosecond timescale. In case of the data presented in figure 6.13 the initial spectrum is almost fully reestablished after about 2 ps.

In summary, we observe two distinct time scales of the temporal evolution of the spectral signatures of interest: the formation of a thermalized electronic system, described by the time constant τ_{th} and the transfer of the heat from the electrons to the lattice via electron–phonon coupling, introducing a time constant $\tau_{\text{e-ph}}$. In the following we estimate these time constants. We focus on their dependence on the absorbed pump fluence.

6.2.3–b The Typical Time Constants and Their Fluence Dependence

In the following we present a quantitative analysis of the temporal evolution of the high energy cutoff for different absorbed pump fluences, F_{pp} , for the low temperature CDW/PLD phase of 1T-TiSe₂. Generally, both the amplitude of the Se 4p bands, as well as their binding energy serve as markers for the formation of the CDW (see, e. g., references [7, 55]). However, intensity derived spectral signatures are rather sensitive to adsorbates and laser drifts (see appendix A.1.1–a) and indeed the quality of such data for our low temperature time-resolved IR-pump SH-probe photoemission investigation proved to be insufficient for any quantitative findings. The spectral cutoff, however, is estimated with good stability. It is the most prominent of the CDW-associated spectral signatures at the $\bar{\Gamma}$ -point investigated here.

Figure 6.15(a) presents the temporal evolution of the energetic shift of the high energy cutoff of the spectra for four absorbed pump fluences of $1.28 \mu\text{J cm}^{-2}$, $1.53 \mu\text{J cm}^{-2}$, $1.93 \mu\text{J cm}^{-2}$ and $2.71 \mu\text{J cm}^{-2}$ (scatter plots), along a fit of these data (line plots). To establish a common, well defined delay scale, all data are referred to the maximum of the intensity above E_{F} which is attributed to the non-equilibrium electron distribution, because it is established virtually instantaneously after the pump excitation.

We employ a fitting routine inspired by source code kindly provided by Hellmann [258]. This function proceeds as follows:

- A first parameter, t_0 , defines two distinct temporal ranges for the fit.
- For temporal delays below t_0 we assume a constant behavior, described by c_1 .
- For delays above t_0 a double exponential decay is assumed, see equation (6.1).
- This piecewise function is numerically convoluted with the Gaussian temporal shape of the cross-correlation of pump and probe pulse. This models the temporal broadening of the signal by the non-vanishing duration of the laser pulses generating the photoemission signal.

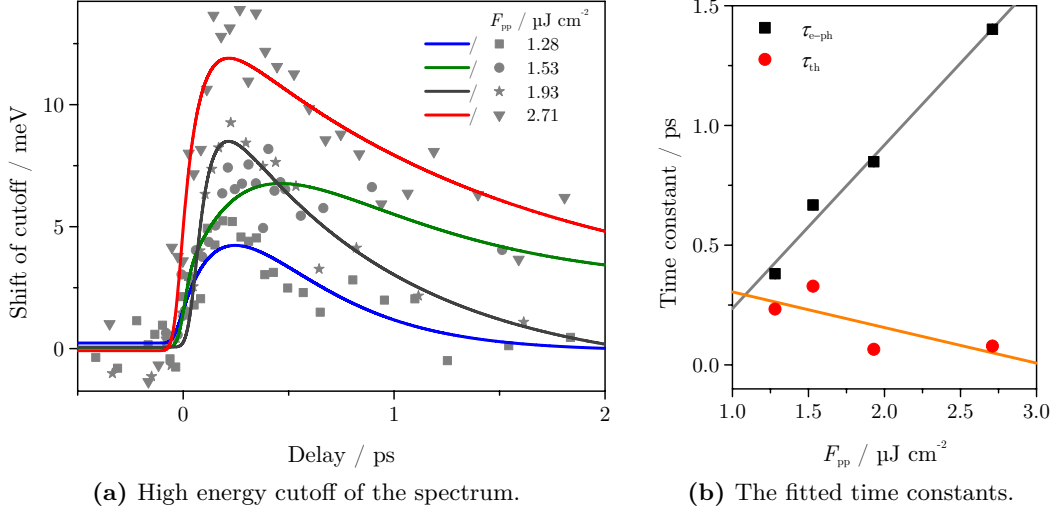


Figure 6.15: (a) Temporal evolution of the spectral high energy cutoff at $T \approx 123$ K, acquired at varying pump fluences, F_{pp} , of $1.28 \mu\text{J cm}^{-2}$, $1.53 \mu\text{J cm}^{-2}$, $1.93 \mu\text{J cm}^{-2}$ and $2.71 \mu\text{J cm}^{-2}$. (b) The fluence dependence of the time constants τ_{th} and $\tau_{\text{e-ph}}$ as fitted to (a).

The piecewise fit function is defined by:

$$f(\tau) = \begin{cases} c_1, & \text{if } \tau \leq t_0 \\ c_2 + c_3 \left\{ \exp\left[\frac{-(\tau-t_0)}{\tau_{\text{e-ph}}}\right] - \exp\left[\frac{-(\tau-t_0)}{\tau_{\text{th}}}\right] \right\}, & \text{if } \tau > t_0, \end{cases} \quad (6.1)$$

with six free and one fixed parameters. The time of the transition from a constant to a double exponential, t_0 , the initial and final values, c_1 and c_2 , the two time constants, τ_1 and τ_2 , and a scaling factor, c_3 , are free. The convolution with a Gaussian of this function is defined by the fixed value of the FWHM. We are interested in the two time constants, τ_{th} and $\tau_{\text{e-ph}}$, of the temporal evolution of the high energy cutoff.

Figure 6.15(a) compiles the temporal evolution for different fluences (symbols) along the corresponding fits (lines) using equation (6.1). First, with increasing fluence we find an increase of the relative shift of the cutoff from approximately 4.4 meV to 11.9 meV upon increasing the pump fluence from $1.3 \mu\text{J cm}^{-2}$ to $2.7 \mu\text{J cm}^{-2}$. Beside the stronger modification for higher fluence, the shape of the temporal traces also exhibits a qualitative change after $F_{\text{pp}} = 1.53 \mu\text{J cm}^{-2}$. We attribute this change to the increasing perturbation of the CDW/PLD phase upon laser excitation. We will see in section 6.2.4 that it is possible only at low temperatures and for small pump fluences to excite the amplitude mode of the CDW [39, 256]. For higher pump fluences the system is already perturbed too much.

The CDW transition is a continuous, second order process [3, 8, 248], i. e. we expect a smooth transition from the CDW into the normal conducting state upon excitation of the system. Our investigation of autocorrelation traces of TiSe₂ at low temperature in section 6.1.2 revealed, that the shape of such curves changes with varying absorbed fluence—the characteristics observed at low temperature vanish and the trace becomes more like its normal phase counterpart. In case of the data presented here we believe the oscillatory behavior, investigated in detail in section 6.2.4, to provide the difference. The maximum of the curves seems to be broadened significantly at lower pump fluences, revealing almost a plateau like structure. This is compatible with the prolonged oscillatory behavior of the CDW. Please note, that in no case the excitation was strong enough to drive the system fully into the normal conducting state, because the high energy cutoff does not reach its room temperature energy. However, at the highest fluence the shift is almost compensated, i. e. the CDW phase is severely weakened.

The time constants of the temporal evolution are extracted using a fit by equation (6.1). We derive the time constant of the thermalization of the electronic system, τ_{th} , and the time constant of the heat transfer to the lattice by electron–phonon interaction, $\tau_{\text{e-ph}}$, for different pump fluences. The corresponding data is presented in figure 6.15(b). We find, that τ_{th} decreases with stronger pumping, while $\tau_{\text{e-ph}}$ increases significantly. In the following, we discuss, how this observation can be interpreted.

The time needed for the thermalization of the excited electronic system decreases from approximately $\tau_{\text{th}} \approx 300$ fs to 70 fs, while simultaneously the heat transfer to the lattice slows significantly, yielding time constants of about $\tau_{\text{e-ph}} \approx 400$ fs to 1400 fs. These data seem to fit well to a simple linear function (lines).

How is this behavior to be understood? First, the higher the pump fluence, the higher the amount of energy deposited into the electronic system and consequently the temperature reached after thermalization thereof also increases (see section 2.5.4). This process leads to the static warm-up of the crystal, because the heat deposited by the laser into the electron system is ultimately transferred to the lattice. The high repetition rate of the laser and the bad thermal conductivity of TiSe₂ lead to the generally observed increase of crystal temperature (see appendix A.3.4). The heat transfer is mediated by electron–phonon coupling, thus, using the two temperature model—discussed in detail in section 5.2.2–a—the increase of $\tau_{\text{e-ph}}$ with the fluence is explained:

For the electronic system, which we probe using our photoemission experiment, the temporal evolution of the temperature is, following equation (5.10), section 5.2.2–a:

$$c_e(T_e) \frac{dT_e}{dt} = G_{\text{el}} [T_l(t) - T_e(t)] - \kappa_e \nabla^2 T_e(t, \mathbf{r}) + p(t) ,$$

for the parameters, see the mentioned section. We assume, that T_e is proportional to the absorbed pump fluence. With increasing pump fluence, $\tau_{\text{e-ph}}$ also increases [135], because

in contrast to the specific heat of the lattice, $c_e(T_e) \approx \gamma T_e$ increases linearly with the temperature of the electronic system [259].

Let us now discuss the decrease of the time needed for the thermalization of the electronic system, τ_{th} , with increasing pump fluence. Such a behavior is already reported for a continuative experiment corresponding to the data presented in chapter 7 and published in reference [54]. In contrast to these experiments, however, the pump fluences used here are three to four orders of magnitude smaller. Rohwer et al. [54] attributed the very fast thermalization to a purely electronic process. The laser induced increase of free carriers enhances the screening which destroys the correlated CDW phase. In the excitonic insulator model of the phase transition an increase of the screening would hinder the formation of excitons [11, 14, 38], necessary for the correlated state. The characteristic time scale for the formation of screening is the plasma oscillation period, τ_{plasma} [260, 261].

The times observed for τ_{th} are, very qualitatively, at least compatible with the observation in reference [54]. We therefore estimate the plasma period for the minimum, $F_{\text{pp}} = 1.28 \mu\text{J cm}^{-2}$, and maximum, $F_{\text{pp}} = 2.71 \mu\text{J cm}^{-2}$, pump fluence used in our experiments. Following the methods described in supplementary information S5 of reference [54], we estimate the density of free carriers as follows:

- (i) Using the pump fluence and the photon energy of $h\nu = 1.59 \text{ eV}$ we derive at $5.0 \times 10^{12} \text{ photons/cm}^2$ to $10.6 \times 10^{12} \text{ photons/cm}^2$ for the two extremal values of F_{pp} .
- (ii) The penetration depth of the IR pulses is $d = 49.3 \text{ nm}$ (see section 6.2.2-a). This yields a density of free carriers, $n = n_e + n_h$, with n_e being the electron and n_h being the hole density, of $1.0 \times 10^{18} \text{ cm}^{-3}$ to $4.2 \times 10^{18} \text{ cm}^{-3}$. We assume, that all photons generate electron-hole pairs.

Reference [54] provides the following equation for the unscreened plasma oscillation period:

$$\tau_{\text{plasma}}^{-1} = \sqrt{\frac{e^2}{4\pi^2 \varepsilon_0} \times \left(\frac{n}{m^*}\right)}, \quad (6.2)$$

with the elementary charge, e , the permittivity of free space, ε_0 , the density of free carriers, n , and the effective mass of the carriers, m^* . For best comparability, we assume like reference [54] an effective mass of $m^* = 6.4 m_e$ for both electrons and holes.

This yields unscreened plasma oscillation periods of 197 fs for $F_{\text{pp}} = 1.28 \mu\text{J cm}^{-2}$ and 136 fs for $F_{\text{pp}} = 2.71 \mu\text{J cm}^{-2}$. The agreement to the values observed for τ_{th} of approximately 300 fs to 70 fs, respectively, is rather good. The magnitude and the fluence dependence is reproduced very well, especially considering the uncertainty of the fit presented here [see the scatter in figure 6.15(b)]. The values of τ_{plasma} shown here are calculated for the unscreened case. Rohwer et al. [54], however, included the effect of

screening by the dielectric background of TiSe₂ using a factor of 9 [5], rendering τ_{plasma} 9 times bigger. In our case, the absorbed laser pulses lead to a significant heat-up of the sample, which we suppose is a bigger issue in this work, because we use a laser system with a very high repetition rate. By increasing the temperature of TiSe₂ from below 150 K to room temperature, the unscreened plasma frequency increases by a factor of about 3 [5] which corresponds to a decrease of τ_{plasma} to a third. Therefore, the given unscreened oscillation periods may increase by a factor of 3 to 9—we expect a factor close to the lower limit of this range, because of the heat-up. The calculated τ_{plasma} are thus of the same order of magnitude, as our experimental data.

Qualitatively, our observation agrees with the high fluence data by Rohwer et al. [54], who reported the breakdown of the CDW even for the lowest pump fluence—it is just increasingly delayed (up to 80 fs). Here, we observe only a relatively small laser induced perturbation of the CDW which is significantly delayed by about 250 fs—bigger modifications or the complete breakdown of this phase are only possible thermally in our case.

In contrast to the high pump fluence experiments [54], the time constants observed for the delayed perturbation of the CDW/PLD are well above the lower limit set by one quarter of the oscillation period of the amplitude mode of the CDW [262], $\frac{\tau_{\text{AM}}}{4}$. This amplitude mode has a frequency of $f \approx 3.4$ THz [39] which corresponds to $\frac{\tau_{\text{AM}}}{4} \approx 74$ fs. The consequence of this is, that while this phonon mode cannot be relevant at high fluences, it may contribute at low fluences, because the observed effects are well within the temporal range, where modifications of the lattice are possible.

However, if the amplitude mode was the only contribution to the perturbation of the CDW/PLD phase at low fluence, we would expect a virtually constant value for τ_{th} . The value of $\frac{\tau_{\text{AM}}}{4}$ shows some fluence dependence. It increases only to about 83 fs, if the fluence is increased to about $50 \mu\text{J cm}^{-2}$ [39], which is a order of magnitude above our fluence range! Even considering such an extreme case, the observed variation of the time constant is not explained by the amplitude mode alone.

We therefore propose a combination of both contributions in the low fluence regime. The amplitude mode of the CDW provides the necessary lattice distortion for the observed oscillatory behavior (see section 6.2.4) and the modification of the work function (see section 6.2.3–a). The screening by the laser excited free carriers contributes to the observed destabilization of the CDW phase, but the timescale for this process may be too long, because of the rather big value for the screened plasma oscillation period. The CDW phase is thus most likely perturbed by a combination of the screening by the generated free carriers and the excitation of the amplitude mode of the CDW. Therefore, for low fluences, both the electronic system and the lattice seem to contribute to the perturbation of the CDW phase—we do not observe a purely electronic effect, as in case of the high fluence data in reference [54].

Please note, that the data presented here is, however, not conclusive. The scatter of the τ_{th} data in figure 6.15(b) is to significant, to ascertain a constant or slightly decreasing

character without doubt.

6.2.4 Oscillatory Behavior of the Intensity and Energy in the Vicinity of the Fermi Energy

A closer inspection of the time resolved data acquired for 1T-TiSe₂ within its low temperature CDW state reveals an oscillatory behavior of certain spectral features. These oscillations are well resolved within cross-correlation traces taken for the energetic range of the strongest spectral modifications, i. e. within the high energy cutoff of the spectrum where the laser induced changes of the binding energy of the Se 4*p* bands (see sections 6.2.1 and 6.2.3) are the most pronounced.

Before analyzing these data, we shall discuss the experimental method employed in this section. It may seem odd that we resort to cross-correlations for the investigation of these oscillations—we used full spectra taken at relevant temporal delays in the preceding sections, because only such data contain provide insight into the complex laser induced dynamics. Cross-correlated data provide information only about the temporal evolution of the spectral intensity at a certain energy. However, section 6.2.3 clearly shows a significant change of the binding energy of the Se 4*p* bands. A cross-correlation acquired within the high energy cutoff of the spectrum can only account indirectly for a band shift by the transfer of spectral weight into or out of the monitored energy window.

The reason for using a less direct experimental method is the need for a better signal to noise ratio. The aforementioned acquisition of full spectra at each temporal delay is very time consuming, i. e. the amount of temporal delays is rather limited and each spectrum is typically taken only once. This leads to a rather high noise level (see figure 6.17). We reduce the noise by focusing on only one energy, i. e. by acquiring a cross-correlation trace. In this case we increase the integration time of the intensity for each temporal delay to 12 s instead of 100 ms in case of the full spectra, while the amount of delays, especially in the relevant range of 0 ps to 1 ps, can be increased⁸.

In the following, we use cross-correlation data to extract quantitative values of the period of the observed oscillations, while full time resolved spectral data yields information necessary for the interpretation of the observed signal, i. e. for distinguishing intensity and binding energy effects.

Figure 6.16 presents cross-correlations acquired for different pump fluences of 1.5 $\mu\text{J cm}^{-2}$ to 2.7 $\mu\text{J cm}^{-2}$ within the high energy cutoff of the spectrum of 1T-TiSe₂

⁸The method described here is called “step-mode” because each delay is set only once and the intensity is integrated rather long. In contrast, cross-correlations are often acquired in the “continuous-mode” where a set of rapidly acquired full correlations is averaged; the intensity at each delay is integrated only very shortly.

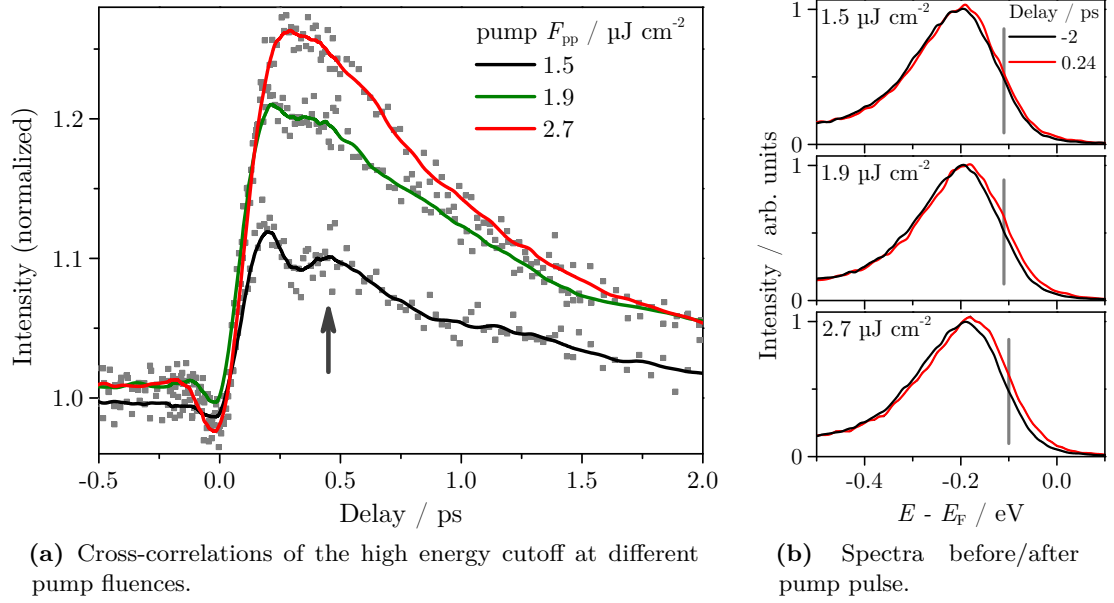


Figure 6.16: (a) Cross-correlations acquired within the high energy cutoff of the spectrum for different pump fluences of 1.5 $\mu\text{J cm}^{-2}$, 1.9 $\mu\text{J cm}^{-2}$ and 2.7 $\mu\text{J cm}^{-2}$ within the CDW phase [$T = (122.6 \pm 1.4)$ K]. The probe fluence is 5.3 $\mu\text{J cm}^{-2}$. The cross-correlations are normalized, linearly drift corrected (see text), and smoothed by averaging 10 adjacent data points. The data is acquired using the step-mode of the time resolved experiment (see text). For the lower pump fluence we observe an oscillation of the high energy cutoff of the spectrum after excitation by the pump pulse.

in the low temperature CDW phase. Figure 6.16(b) shows spectra taken before the pump beam excites the system (black) and for the delay of the—supposedly—strongest spectral modification (red). The chosen energy for the cross-correlations presented in figure 6.16(a) is marked by gray, vertical lines. The full lines are derived from the data by averaging 10 adjacent data points. The step-mode of the cross-correlation experiment employed here is prone to intensity drifts, because the first and last data are separated by a rather long time (about 50 min), i. e. drifts, e. g., of the laser intensity modify the signal strongly. These drifts are corrected by plotting the intensity values against a uniformly spaced time axis, because it takes roughly the same time to acquire each data point. A drift is thus best visible, if the data is plotted versus the time of acquisition, which is approximated by a uniform time axis. In this representation we correct for a linear drift for the parts of the cross-correlation which are expected to be constant. The data is normalized to this fit in accordance to the procedure introduced in section 5.1.2–b.

Figure 6.16(a) reveals a small oscillatory signal right after excitation by the pump pulse for delays of up to 1 ps which is superimposed on the *normal* cross-correlation trace (arrow). It is only observed for low pump fluences; the oscillation vanishes very fast if the pump fluence is increased above $F_{\text{pp}} = 1.5 \mu\text{J cm}^{-2}$, i. e. already at $1.9 \mu\text{J cm}^{-2}$ only a subtle hint of this signal remains. Before we analyze this signal in detail, we need to discuss its origin—it is not obvious, which spectral modifications lead to the observed cross-correlation, because of the missing spectral information.

Full spectra acquired at different temporal delays enable us to identify the source of the observed oscillations. Analogously to our earlier approach in section 6.2.1, figure 6.17(a) presents an energy–delay mapping acquired at the relevant pump fluence of $1.5 \mu\text{J cm}^{-2}$ under conditions similar to figure 6.16. The relative spectral intensity for normal emission is sampled from the intensity ratios with respect to the spectral shape before the pump pulse hit the sample. White represents no changes, blue/black corresponds to a reduction and red/yellow to an increase of spectral intensity with respect to the unperturbed spectrum. Using this representation the subtle spectral modifications become visible to the naked eye. Please refer to figure 6.17(c)—we discuss the details of this figure shortly—for an overview of the spectral shape. Note especially the maximum of the Se $4p$ bands at $E - E_{\text{F}} \approx -0.15 \text{ eV}$.

Comparison to the corresponding map in figure 6.9(b) (see section 6.2.1), which is acquired at a higher pump fluence, reveals some unsurprising similarities. In both cases we observe the initial generation of a non-equilibrium electron distribution which is observed only close to time zero for high energies of roughly $E - E_{\text{F}} \approx 0.2 \text{ eV}$ (see discussion in section 6.2.3). Furthermore, the color “bands” within the range of the Se $4p$ bands show the energetic shift of this feature. The intensity is reduced within the high binding energy flank of this band (blue) and increased within its low binding energy flank (red), i. e. the spectral weight of the Se $4p$ bands is transferred to lower binding energies, as expected

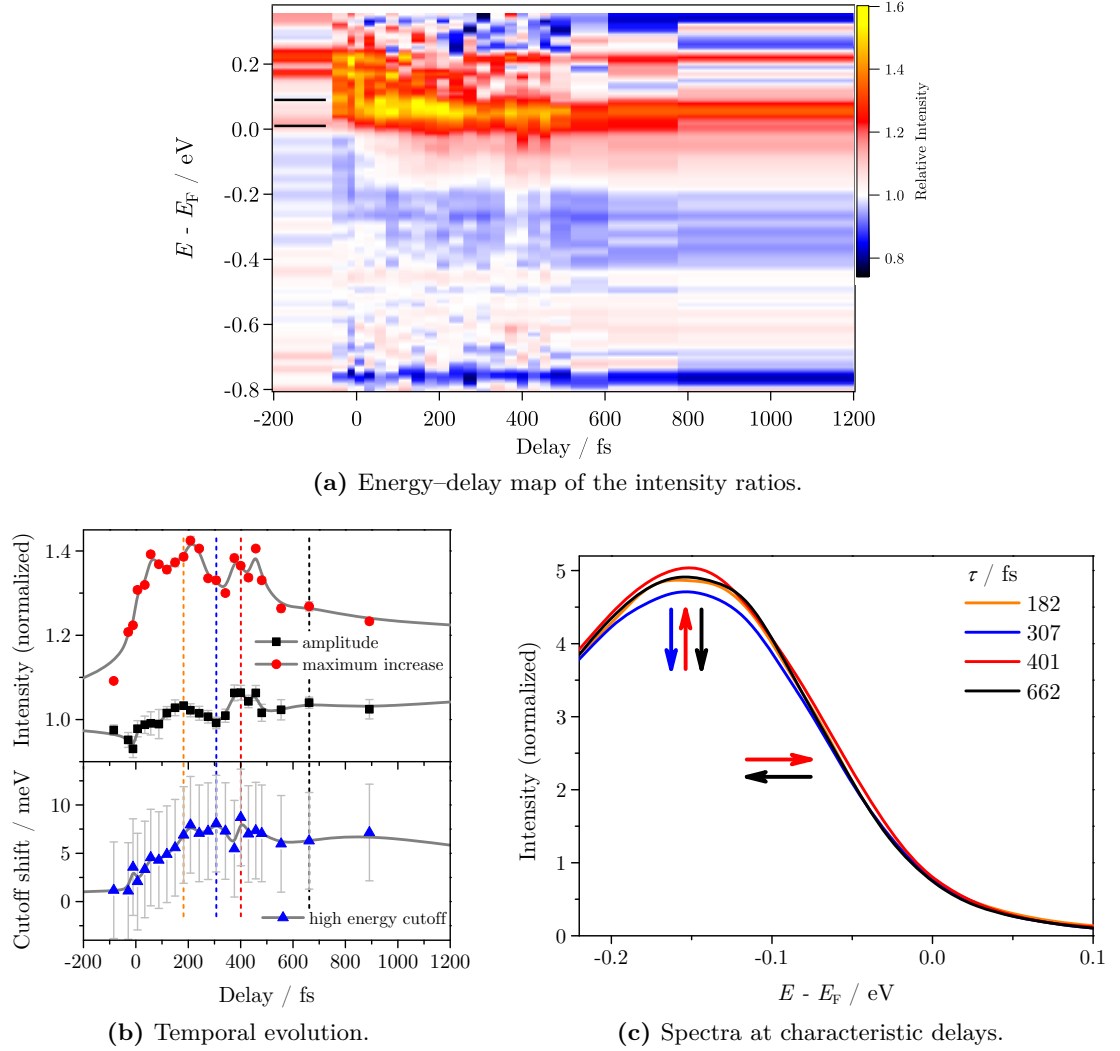


Figure 6.17: A time resolved experiment within the CDW phase [$T = (122.0 \pm 0.4)$ K] is performed at a pump fluence of $1.5 \mu\text{J cm}^{-2}$ (see figure 6.16) by acquiring full spectra at different pump–probe delays. (a) shows an energy–delay map of the relative intensities with respect to the spectrum before absorption of the pump pulse. A fit of the amplitude of the Se 4p bands, the energetic shift of the high energy cutoff, and the spectral range of the maximum intensity increase [$E - E_F = 10$ meV to 90 meV, black lines in (a)] are shown in (b). Spectra for characteristic delays within the oscillatory behavior are presented in (c).

for a weakened CDW phase (see section 6.2.3 for details).

Overall, figure 6.17(a) shows the same temporal behavior which we already discussed in section 6.2.3, however, it also reveals a more pronounced structure associated with the oscillatory behavior at the lowest pump fluences. Right above the Fermi energy—two horizontal black lines on the left mark the relevant energetic range—the intensity strongly increases right after time zero and then oscillates slightly. Furthermore, the in- and decrease “bands” surrounding the peak of the Se $4p$ bands (blue and red, $E - E_F \approx -0.4 \text{ eV}$ to 0.0 eV) indicate a small oscillation of the binding energy of this band—note the variations especially within the color of the blue stripe which indicates a transfer of spectral weight.

A quantitative analysis of the amplitude (black squares) and the high energy cutoff (blue triangles) of the Se $4p$ bands is shown in figure 6.17(b). These data are not very conclusive, because we observe too much noise and too little data is available. This is no problem here, because these data are only used to identify delays of interest for a detailed look into the spectral shape. An oscillatory behavior is observed in the amplitude and cannot be derived from the binding energy of the high energy cutoff, for which the uncertainty is too high. By integrating the energetic range of the maximum intensity increase in the relative spectra (black lines, $E - E_F = 0.1 \text{ eV}$ to 0.9 eV) we derive an even clearer oscillating signal (red circles) than in case of the amplitude.

While the oscillatory behavior is rather subtle in the fitted data, especially for the delicate fit of the energy of the high energy cutoff of the spectra, we are still able to identify four temporal delays of interest, 182 fs, 307 fs, 401 fs and 662 fs, shown by the dashed vertical lines. They correspond to the first and second maximum of intensity (orange and red) and two minima (blue and black). Figure 6.17(c) compares the corresponding full spectra—we focus on the Se $4p$ bands and their high energy cutoff for better detail of the characteristics of interest—with the changes emphasized by arrows which color corresponds to the temporal delay⁹.

Figure 6.17(c) reveals distinct spectral modifications: By increasing the temporal delay from its first value (orange), corresponding to the initial maximum in the amplitude, to the second value (blue), which coincides with the first minimum of the amplitude, we observe a clear drop of the amplitude of the Se $4p$ bands. However, an increase of the binding energy of these bands, visible as a shift of the high energy cutoff, cannot be unambiguously derived from the spectra, as it is rather small. For higher delays the second maximum of the amplitude of the Se $4p$ bands is observed (red) and this maximum is also visible very well within the spectra. Furthermore, the binding energy of the high energy cutoff is clearly reduced. For even bigger delays (black) the binding energy increases again and the initial amplitude is reached.

In summary, we observe a prominent oscillation of the amplitude of the Se $4p$ bands and a less pronounced oscillation of the binding energy of the high energy cutoff of these

⁹A black arrow, for instance, emphasizes the change from $\tau = 401 \text{ fs}$ to $\tau = 662 \text{ fs}$.

bands.

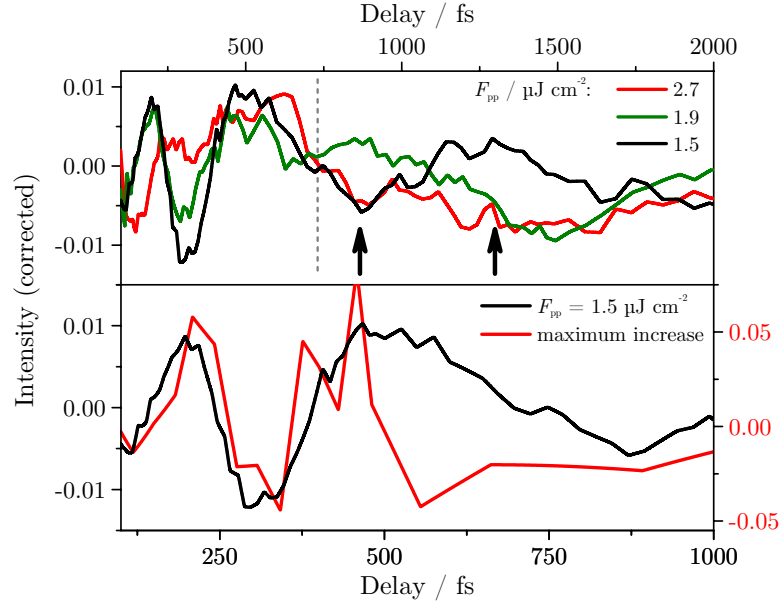


Figure 6.18: Top: The cross-correlations from figure 6.17 are background corrected using the fit function applied to the data in section 6.2.3 [258]. The observed oscillation vanishes for increasing pump fluence. For higher delays (gray, dashed line) the different data show inconsistent oscillations, i. e. in this case we most likely observe artifacts of the background correction. Bottom: For small delays two clear oscillations are observed. The background corrected “maximum increase” data from figure 6.17(b) is also included.

A detailed analysis of the cross-correlation traces enables us to derive the period of the oscillations. We make use of the fact, that the observed oscillatory behavior is superimposed on the temporal evolution already observed in section 6.2.3. We therefore employ the fit routine introduced in this section which is based on a program code kindly provided by Hellmann [258]. The fit function is subtracted from the cross-correlations. This background corrected data from figure 6.16(a) is presented in figure 6.18 (top); it now shows only the oscillatory part of the curves. This representation already allows for two interesting observations:

- We can only identify roughly one period of the oscillation. For $\tau \gtrsim 730$ fs (gray dashed line) the position of the extrema of the data for different pump fluences do not agree anymore (see especially the arrows). We attribute these deviations to artifacts of the background correction, i. e. to the noisy experimental data and difficulties of the background fit.

- For small delays (gray dashed line), i. e. right after time zero, we observe a clear oscillatory signal for the smallest pump fluence. This oscillation vanishes for increasing pump fluence. The amplitude of the oscillation decreases, if we increase F_{pp} from $1.5 \mu\text{J cm}^{-2}$ to $1.9 \mu\text{J cm}^{-2}$. At the highest value of F_{pp} shown here only remnants of this oscillatory signal are still present, strongly masked by the noise of the signal.

Finally, as shown exemplary in the bottom of figure 6.18, the oscillatory behavior is qualitatively similar in different experimental runs. It can be observed in experimental data acquired at comparable pump fluences when using the continuous mode of the experiment to take the cross-correlation, as well as in the fitted data from the full spectral data of figure 6.17. However, the level of detail of the latter data (red) is much worse, i. e. although the oscillations agree qualitatively very well with the cross-correlation (black), a quantitative analysis is futile in this case.

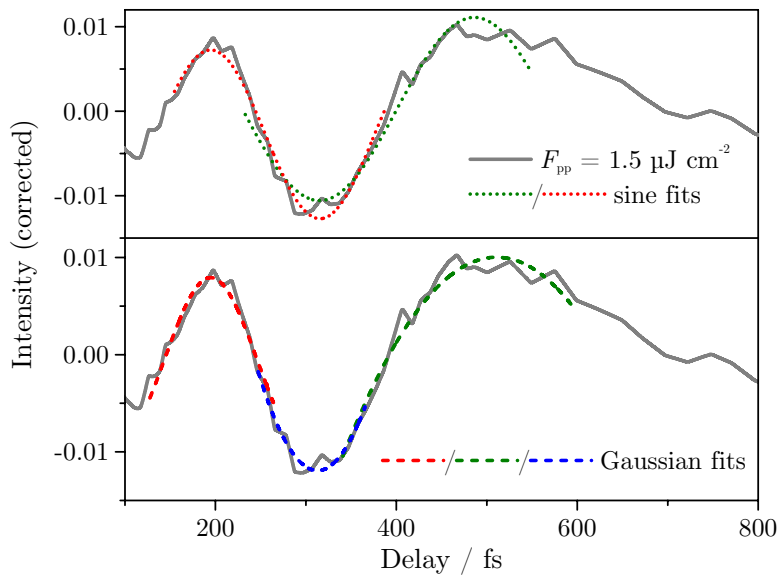


Figure 6.19: Fit of the oscillatory part of the cross-correlation trace acquired at $F_{\text{pp}} = 1.5 \mu\text{J cm}^{-2}$. Top: Fit of two separate sine functions. Bottom: Three independent Gaussians are fitted to the Extrema.

Even our best data set with respect to the observed oscillations—the background corrected cross-correlation in figure 6.18 corresponding to the lowest pump fluence—does not allow for an unambiguous fit. In general, we expect a sinusoidally or damped sinusoidally shaped fit function to reproduce the data. However, a stable fit of such a function to the full experimental curve is not possible. Obviously, the first peak in figure 6.18 is significantly smaller than the second one. This may be a consequence of the fact,

that the onset of the oscillation coincides with the excitation by the pump pulse at time zero, i. e. the oscillation may be distorted. Furthermore, the background correction leads to some distortion, too, which may lead to the asymmetry of the second maximum.

To extract some meaningful information on the period of the oscillation we resort to a simple fitting routine. Figure 6.19 shows our two fitting approaches. We either fit the first maximum and minimum or the minimum and second maximum by a sine function (dotted) or we fit the two maxima and the minimum by single Gaussian functions (dashed). Please note, that the peak of the first maximum is considered to appear reduced in FWHM as its coinciding with the excitation by the pump pulse, while the asymmetric second peak is probably broadened by the background correction, i. e. by evaluating the the first maximum and the minimum we expect to find a shorter period, than for evaluation of the second maximum and the minimum. We provide both values of the period of the oscillation as a limit for reference.

From the fit by two sine functions we derive periods of the oscillation of about 242 fs and 342 fs. The Gaussian fits lead to periods of about 236 fs and 396 fs. We intentionally do not provide the uncertainties of these fits here¹⁰, because they are much too small. The fits themselves are rather well defined, however, the outcome depends on the chosen data range for each fit. If we take a look at the single fitted values above, which mark the limits of the expected period, we find an uncertainty of the mean value of approximately ± 65 fs more realistic. Indeed, comparison of the two data sets in the bottom of figure 6.18 is compatible with an uncertainty of about 25 fs for the delay of the extrema, which yields a similar uncertainty for the period.

Table 6.1: The mean values of the period of the oscillations, t , observed at $F_{pp} = 1.5 \mu\text{J cm}^{-2}$ for the two fit methods. The corresponding frequency, f , of the oscillation is included as well.

fit method	t/fs	f/THz
Gaussian	316 ± 65	3.2 ± 0.7
sine	292 ± 65	3.4 ± 0.8

How can these oscillations be understood? Although our data is rather noisy and we do not have a detailed analysis of all relevant parameters, we find the following characteristics:

- Both fit methods yield compatible oscillation frequencies of (3.2 ± 0.7) THz and (3.4 ± 0.8) THz which are summarized in table 6.1.

¹⁰The center of the three Gaussians is well defined by the fit ($\Delta x_c \approx 1$ fs) and therefore only a very small uncertainty of the period of $\Delta t \approx 4$ fs would result. The sine fit is even better defined, yielding $\Delta t \approx 2$ fs.

- The oscillatory signal is the strongest at the lowest pump fluence investigated here. It rapidly vanishes with increasing F_{pp} as demonstrated by the reduced amplitude of the oscillation.
- The amplitude of the Se $4p$ bands shows a clear oscillation—this is the most easily observed within cross-correlation traces—and also the energy of the high energy cutoff of the spectrum oscillates. The latter is associated with a variation of the CDW induced energy gap, however, it is experimentally observed more subtle.

A recent time resolved optical reflectivity study by Möhr-Vorobeva et al. [39] revealed at low temperatures oscillations with $f \approx 3.4$ THz which is in striking agreement to our observation. They used comparable pump pulses, although the central wavelength and the pulse durations deviates to some degree. Keeping this in mind, the difference in pump fluence can be understood. The value of the absorbed pump fluence strongly depends on the chosen area of the surface and the absorption coefficient. The given pump fluence in this experiment is higher ($F_{\text{pp}} = 3 \mu\text{J cm}^{-2}$), yet, still in agreement to our value. The differences of the laser systems, especially the different laser pulse durations, may lead to deviations in the reaction of the system. Furthermore, the references does not explicitly state, that the absorbed laser fluence is given. We expect only about 82 % of the incident power to be absorbed by TiSe_2 at this wavelength, which reduces the fluence to about $2.4 \mu\text{J cm}^{-2}$; overall, we believe our experiment to be consistent with these data considering the pump fluence.

Möhr-Vorobeva et al. [39] find the observed oscillations to be depending on sample temperature and pump fluence. The latter is irrelevant in our case, because within the range of F_{pp} accessible by our experiment the frequency of the oscillation does not vary considerably. Yet, in our case these oscillations already vanish at comparably low laser fluences. We attribute this to two differences: First, our experiments are performed at a significantly higher sample temperature, i. e. we are only just within the CDW phase. Second, our laser systems features about 276 times the repetition rate (80 MHz instead of 290 kHz). The process of sample heat-up discussed in section 5.2.2-a can thus explain, why in our case the sample heats-up more. Indeed, we observe considerable temperature changes upon variation of the fluence which even drive the phase transition into the normal conducting phase (see section 5.3.2).

The temperature, however, has a strong impact on the visibility of the oscillatory signal and the frequency thereof. This is not uncommon, even for other systems [40, 263]. Our data is taken at a temperature of about 123 K at which only about three minima or maxima of the oscillation are observed which is in good agreement to our data. The frequency of the oscillation decreases with temperature. At 123 K a value of $f \approx 3$ THz is expected. Considering that the temperatures in case of our data and reference [39] cannot be absolutely compared, the agreement of the frequency to our experiment is reasonable.

The frequency of the observed oscillation enables its assignment to the A_{1g} amplitude mode of the CDW (see reference [39] and references therein). The symmetry of this mode corresponds to a relative movement of the Se atoms along the axis perpendicular to the crystal layers, either closer to each other or further away [256]. Upon the phase transition into the CDW a new A_{1g} phonon mode at higher frequency appears [256].

So far we discussed optical reflectivity data of TiSe₂ which show an oscillatory behavior associated with the CDW amplitude mode. Such behavior is also reported for other systems [40–42]. Oscillatory behavior was also reported by, e.g., Perfetti et al. [4] and Schmitt et al. [31] for photoemission data. However, can we compare these data to our photoemission experiment? In general, transient modifications of the optical reflectivity correspond to changes of the refraction index [257] induced by the ion movement. Nevertheless, the effects of such collective excitations on the band structure can also be observed in photoemission data. Perfetti et al. [4] observed the band gap which changes upon the Mott transition of their system. They were able to laser-induce oscillations of this gap which were associated to the amplitude mode of the CDW by the frequency. They reason, that the induced amplitude mode leads to a spectral oscillation of the coupled electronic modes. Schmitt et al. [31] state, that the amplitude mode cannot be directly linked to the band gap. However, a careful analysis of the temporal evolution of the gap after excitation of the amplitude mode and the localization at the momenta at which the CDW modifies the band structure allow to attribute the observed oscillations to this CDW mode.

In our case we observe the oscillatory behavior only at the very top of the Se 4p bands at the $\bar{\Gamma}$ -point. Our analysis revealed the changes of the binding energy and the amplitude of these bands which are expected for modulations in the strength of the CDW phase. Furthermore, the frequency of the oscillatory part agrees well with the expected value for the CDW amplitude mode of this system. Nevertheless, a more detailed analysis, preferably at lower sample temperature, and a full ARPES experiment featuring the whole first Brillouin zone (see chapter 7) may further support our interpretation.

6.3 Summary and Conclusion

This chapter provided a detailed insight into the temporal evolution of the CDW/PLD phase of 1T-TiSe₂ after its perturbation by an absorbed laser pulse. We discussed one-color autocorrelation and two-color cross-correlation data, which provided information about the relevant experimental parameters, as well as first insights into the laser induced ultrafast temporal evolution of the TMDCs.

The one-color autocorrelations of TiSe₂ and TiTe₂ revealed interesting differences. For TiTe₂ we observe small modifications to the autocorrelation shape. The intensity is reduced at time zero—this is later attributed to the generation of an initial non-equilibrium electron distribution in the two-color experiments. Afterward, we observe

a relaxation to the normal shape. For TiSe_2 the behavior is different, as it reveals an additional process. The maximum of the deviation from the normal autocorrelation shape is reached after a delay, i. e. the intensity is still further reduced, even after the temporal overlap of pump and probe pulses. Therefore, these experiments already revealed distinct ultrafast modifications which are exclusive to TiSe_2 . Our two-color experiments enabled us to attribute this feature to the perturbation of the CDW/PLD phase.

Furthermore, the acquisition of two-color cross-correlations enabled us to identify optimal pump fluences for the study of the temporal evolution of the system. The main contribution of these experiments to the interpretation of our data is, however, the investigation of the momentum dependence of the cross-correlations. We find a significant localization at the $\bar{\Gamma}$ -point, i. e. the strongest laser induced modification of the spectra is observed there. This is very instructive, because this observation agrees nicely to the calculations of Monney et al. [55] using a model based on an excitonic insulator. Furthermore, we observed oscillations of the cross-correlation intensity for small pump fluences which we discuss shortly.

In a second step, we acquired full spectra using a two-color time resolved scheme. Additionally to information we got from the cross-correlations, we gain access to changes of the binding energy, especially to the high energy cutoff of the spectra, which is a marker for the formation of the CDW phase. A careful analysis of the spectral signatures revealed two timescales: we observe the thermalization of the electronic system, accompanied by the perturbation of the CDW phase within tens to hundreds of femtoseconds and the subsequent transfer of the heat from the electronic system to the lattice within picoseconds.

The pump fluence dependence of the time constants of the two relaxation processes was also investigated. The second process, the heat transfer to the lattice, becomes slower with increasing fluence. This is a consequence of the linear increase of the specific heat of the electronic system, i. e. the temperature of the electronic system increases less and the temperature difference of the electronic system and the lattice, relevant for the speed of the heat transfer, decreases. The first process, the thermalization of the electronic system and the perturbation of the CDW, gets faster, the higher the fluence.

To understand the processes involved in the first thermalization step, we need to consider two contributions: screening by the laser generated carriers and the excitation of the amplitude mode of the CDW. At very high pump fluences the first time constant is very small, only a few tens of femtoseconds [54]. In this case, the CDW phase is fully destroyed by the absorbed laser by a purely electronic process: screening by the generated charge carriers. In the excitonic insulator model of the CDW (see section 2.2.1) the occurrence of this phase is described in terms of the condensation of excitons into a common ground state. The spontaneous generation of excitons is crucial for this mechanism, i. e. a small density of free carriers is important—the Coulomb interaction of electrons and holes must not be screened. By generating additional free carriers, the screening is enhanced which suppresses the CDW. For the comparably low excitation

densities in our case, due to the much smaller fluences, the density of free carriers generated is significantly smaller. Consequently, the plasma oscillation period, which defines the timescale of the screening, is significantly longer.

Our time constants are in qualitative agreement with the screening timescale estimated by the density of free carriers in our case. However, the observed perturbation—or partial suppression—of the CDW proceeds faster, than estimated from screening alone. Considering the oscillatory signal and the ultrafast reaction of the work function—a dedicated lattice property—we attribute these effects to the excitation of the amplitude mode of the CDW [39]. Because the plasma oscillation period is long for our low fluences, the amplitude mode becomes important here. In case of reference [54] the screening proceeded sufficiently fast, that the lattice reaction did not play any role.

We conclude, that for the low pump fluences the perturbation of the CDW is partially attributed to purely electronic process, the screening of the excitons necessary for the excitonic isolator transition. The contribution of this screening leads to the observed fluence dependence of the corresponding time constant. The localization of the observed spectral modifications at $\bar{\Gamma}$ further supports the excitonic isolator model.

Additionally, the lattice is also very important for the observed perturbation, as we observe the excitation of the corresponding amplitude mode of the CDW. Furthermore, this process is indeed faster for the low fluences. A phononic contribution in terms of a Jahn-Teller instability (see section 2.2.1) is expected to contribute to the transition mechanism in 1T-TiSe₂ [76]. Indeed, in this fluence regime, such a mechanism seems to contribute considerably.

7 Investigation of the Ultrafast Dynamics of the Backfolded Se $4p$ Bands at the \bar{M} -point

In this chapter we give a short outlook on a new and powerful time resolved approach using the generation of high harmonics as a probe pulse. The method is very similar to the two-color time resolved pump-probe experiment presented in section 6.2, however, instead of probe pulses of only a few electronvolts, suitable for two-photon photoemission (2PPE) spectroscopy, we now employ a high harmonic (HH) probe pulse of $h\nu = 43$ eV. A photon energy this high enables access to a wider momentum range and even the full first Brillouin zone becomes accessible in only one angular resolved spectrum (see references [53, 54] and section 2.4). Furthermore, the high harmonic generation (HHG) yields ultrashort laser pulses of typically below 10 fs duration, which enables a high temporal resolution in a time resolved photoemission experiment. In this chapter we present an outlook on the first time resolved experiments on $1T$ -TiSe₂. These experiments were performed during this work in a cooperation with the work group of Prof. Dr. L. Kipp of the university of Kiel. A comprehensive discussion and analysis of these and additional, complete experiments is published in *Nature* in 2011 by Rohwer et al. [54].

First, some remarks on the experimental setup used here. The pump pulses are provided by a Ti:sapphire amplifier (*Dragon*, KMLabs) with a repetition rate of 3 kHz, $h\nu = 1.57$ eV, a pulse duration of about 32 fs and an absorbed fluence of up to about 5 mJ cm^{-2} . A part of this fundamental emission is used to generate high harmonic probe pulses in a hollow-fibre waveguide (*XUUS*, KMLabs) filled with argon. For a detailed discussion of the generation of high harmonics using such a device see, for instance, references [43, 44]. These extreme ultraviolet (EUV) pulses are ultrashort (< 10 fs) and a photon energy of 43 eV (27th harmonic) is selected using a mirror monochromator [54]. The setup of the IR-pump-EUV-probe cross-correlation experiment is analogous to the time-resolved IR-pump SH-probe photoemission setup discussed in section 3.2 in figure 3.3(b), although in this case the infrared (IR) pulses are delayed by a motorized linear stage (see reference [44] for a similar setup).

Figure 7.1(a) shows an angle-resolved photoemission spectroscopy (ARPES) spectrum acquired using p-polarized EUV probe pulses. This spectrum is directly comparable to the one-photon photoemission (1PPE) angle resolved data presented in chapter 4 in figure 4.9 acquired with a vacuum ultraviolet (VUV) lamp. However, using the roughly two

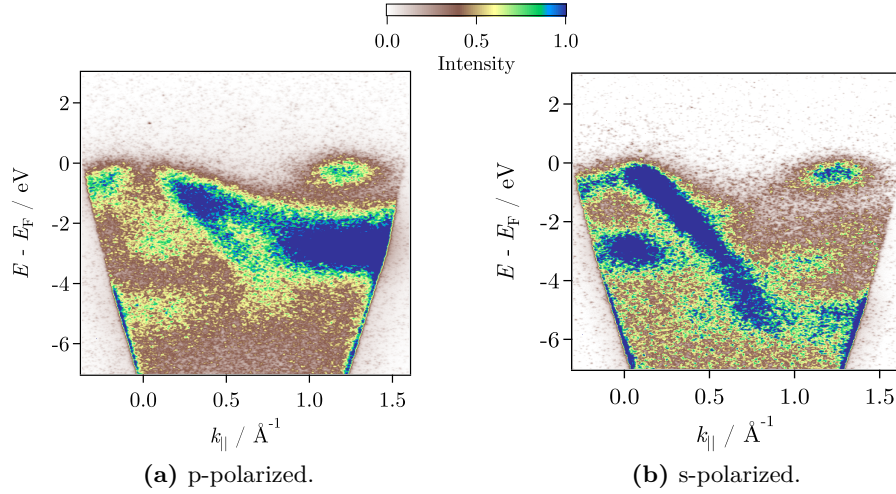


Figure 7.1: ARPES spectra of $1T$ -TiSe₂ acquired during a time resolved experiment within the CDW phase for p- and s-polarized EUV probe pulses and p-polarized IR pump pulses for a delay a few hundred femtoseconds before temporal overlap of pump and probe, i. e. well before the pump event. With s-polarized light the Se $4p_x$, $4p_y$ bands are less intense, while the Se $4p_z$ band is enhanced (see text).

times higher photon energy of the EUV source, we gain access to a significantly broader momentum range. Indeed, more than the full first Brillouin zone is mapped within a spectrum featuring the same emission angle range, as in case of the data acquired using the VUV. First, we like to discuss the spectrum presented in figure 7.1(b) in more detail.

This spectrum is taken using s-polarization for the EUV probe pulse. This is advantageous for the detailed analysis of the temporal evolution of the spectral structures especially at the $\bar{\text{M}}$ -point. The Se $4p_x$, $4p_y$ bands and the Se $4p_z$ band are derived from different orbitals which reside more within or more normal to the surface plane, respectively [16, 56, 60, 66]. The symmetry of a band is crucial for its excitation in a photoemission process using p- or s-polarized light (see, e. g., reference [35, 264–268]). Indeed, we observe much less intensity from the Se $4p_x$, $4p_y$ bands at the $\bar{\text{M}}$ -point with s-polarized pulses, which enables a better visibility of the changes close to E_F we discuss in the following.

The spectral structure at the $\bar{\Gamma}$ -point in figure 7.1 is well understood by comparison to our detailed discussion in chapter 4. We identify the prominent hole-like dispersing Se $4p$ bands right below the Fermi energy, as well as a virtually non-dispersive structure at about -3 eV which is also derived from Se $4p$ orbitals. The data presented here is acquired at a temperature $T \approx 125$ K, i. e. well within the low temperature CDW phase of TiSe₂. The phase transition leads to characteristic spectral changes, like, the increase of binding energy of the Se $4p$ bands at the $\bar{\Gamma}$ -point (see section 3.3)—this subtle change

at $\bar{\Gamma}$ is the only spectral feature directly accessible in our 2PPE experiments presented until now, which is a consequence of the low photon energies used. The spectrum is, however, much more significantly changed at the \bar{M} -point, because the doubling of the lattice periodicity induced by the periodic lattice distortion (PLD) associated with the CDW leads to a backfolding of the Se 4*p* bands at $\bar{\Gamma}$ to \bar{M} [7, 8, 10, 11, 14, 55, 94] (see figure 3.9 in section 3.3 and section 2.2). Please note, that the feature observed at \bar{M} also contains contributions of an electron-like dispersing Ti 3*d* band, which is partially occupied and visible in the room temperature phase (see section 3.3 for details).

By monitoring the full first Brillouin zone within one spectrum we therefore have access in a time resolved experiment, not only to laser induced modifications at the $\bar{\Gamma}$ -point, but also at the \bar{M} -point, i. e. we can now monitor both regions of the Brillouin zone which are strongly affected and modified by the establishment of the CDW phase simultaneously. Because the observed backfolding is a direct consequence of the CDW phase, we expect experimental access to the laser induced perturbation of the CDW, especially to the corresponding dynamics and timescales.

Figure 7.2 shows a series of ARPES spectra acquired within the CDW phase of TiSe₂ using s-polarized EUV probe pulses and a pump fluence of 2 mJ cm⁻². The experiment yields a set of ARPES spectra for different temporal delays of pump and probe pulses—it is similar to the method discussed in section 3.2.2. The figure shows four such spectra (left) at selected, characteristic delays along a corresponding relative intensity map (right). The relative mapping emphasizes spectral changes with respect to a reference spectrum, which is generated by averaging several spectra for negative delays (the probe arrives at the sample before the pump) chosen such, that the pump did not yet perturb the sample. The difference of the spectra at different delays to the reference spectrum is calculated by subtraction. These spectra show intensity increases in red and decreases in blue hues with respect to the unperturbed system, i. e. the effect of the pump pulse is directly visible.

The first delay, $\tau = -500$ fs, represents the unperturbed sample. We observe a well established signal of the backfolded Se 4*p* bands at \bar{M} , the corresponding relative map reveals some noise. At $\tau = -20$ fs, the onset of the overlap of pump and probe pulse, we already observe some instantaneous spectral changes, which are marked in the corresponding relative map by *i-iv*, and which are fully established at time zero ($\tau = 0$ fs). We will not discuss these effects in detail here—please refer to reference [54] for a detailed discussion. Nevertheless, we like to point out several interesting spectral modifications. Features *i* and *iv*, which are significantly enhanced at time zero, are generated by the laser-assisted photoelectric effect [46, 47] which is based on the simultaneous absorption or emission of an IR photon along the EUV pulse if both temporally overlap. The effect is thus only observed in the vicinity of time zero for overlapping pump and probe. It leads to the strong “ghosting”-like bands at time zero which are separated by $h\nu = 1.59$ eV, the IR photon energy, from their corresponding bands, i. e. the Se 4*p* bands at $\bar{\Gamma}$ and \bar{M} , as well as the new structure *ii*. The modifications *ii* and *iii* are fully established at

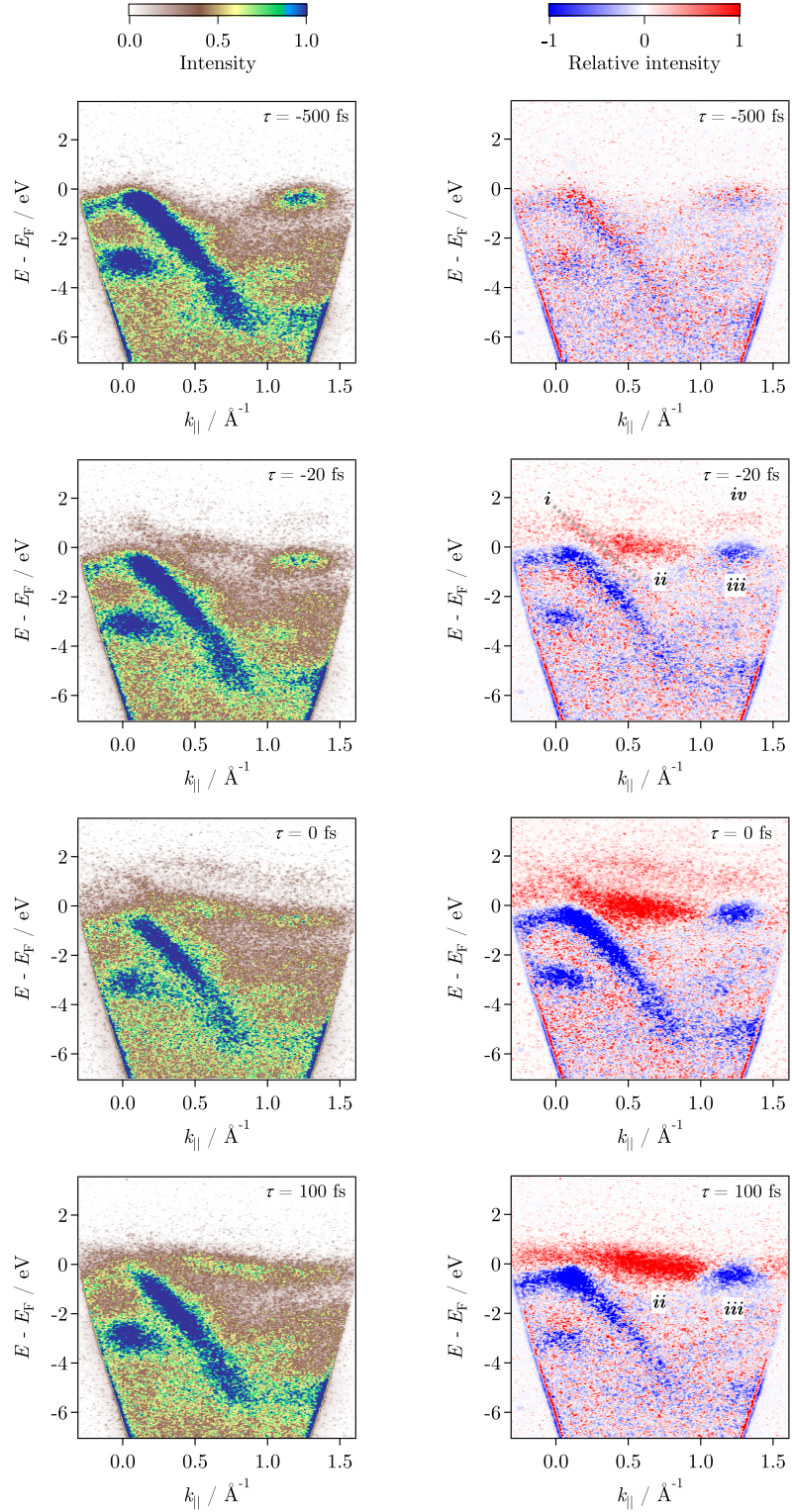
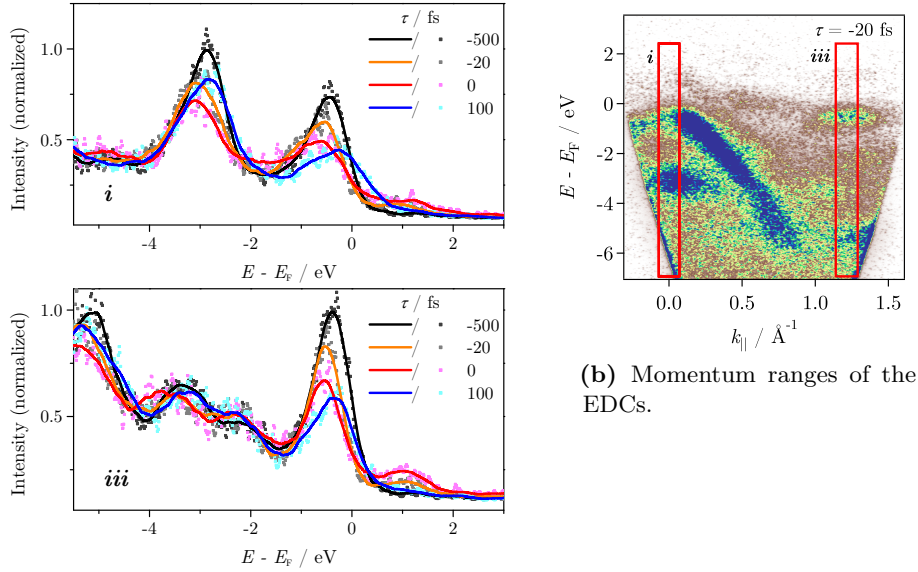


Figure 7.2: Left: ARPES spectra of $1T$ -TiSe₂ acquired within the CDW phase in a time resolved two-color pump-probe experiment using s-polarized EUV probe pulses ($h\nu = 43$ eV) and p-polarized IR pump pulses ($h\nu = 1.59$ eV, $F_{pp} = 2$ mJ cm⁻²) for different temporal delays of pump and probe, τ , of -500 fs, -20 fs, 0 fs and 100 fs. Right: Relative spectra emphasizing the intensity changes (see text). Red and blue hues show intensity increases and decreases, respectively. Roman numerals mark regions of interest.



(a) EDCs at different delays for three distinct momenta.

(b) Momentum ranges of the EDCs.

Figure 7.3: EDCs extracted at two different momentum ranges [*i* and *iii*, see (b)] of the spectra presented in figure 7.2. The ARPES spectrum is averaged along the momentum axis (about $\pm 0.07 \text{ \AA}^{-1}$). The data (symbols) is smoothed (lines). The four characteristic pump-probe delays, τ , are presented.

about $\tau = 100$ fs and they are attributed to the occupation of a Ti 3*d* band (*ii*) close to E_F and the loss of intensity of the backfolded Se 4*p* bands at \bar{M} (*iii*) [54].

These time resolved experiment thus enable us to monitor the ultrafast response of the Se 4*p* bands at the $\bar{\Gamma}$ -point and at the \bar{M} -point simultaneously, i. e. we gain access of the dynamics induced by the perturbation of the CDW phase which is closely connected to these spectral shapes. Please refer to figure 7.3 which presents a set of energy distribution curves (EDCs) for *i* and *iii*, i. e. for the signal at $\bar{\Gamma}$ and at \bar{M} in (a). In this representation the ultrafast loss of spectral intensity at both high symmetry points of the first Brillouin zone of the Se 4*p* bands becomes obvious. It is accompanied by a simultaneous population of a Ti 3*d* band (*ii*). These experiments strikingly show the capabilities of this new setup. By investigating both symmetry points of the first Brillouin zone which are influenced the most by the CDW phase transition, much better insight into the response of the electronic system in this phase may be gained—the first results using this method are published in reference [54].

8 Summary

In this work the transition metal dichalcogenide (TMDC) $1T$ -TiSe₂ was investigated by photoemission studies considering four different key aspects: *(i)* we analyzed the structure of angle resolved two-photon photoemission (2PPE) spectra, *(ii)* we investigated the modification of such spectra upon a variation of the incident laser fluence or the sample temperature, *(iii)* we provided a detailed look into the temporal evolution of the laser induced perturbation of the CDW/PLD phase of this TMDC, and *(iv)* we present a first look into the full first Brillouin zone of this system in an outlook. Our investigation focuses on the low temperature phase transition of TiSe₂. The system $1T$ -TiTe₂ was used as a reference system without any phase transition throughout these investigations.

In the first part, we discussed in detail the findings of angle-integrated 2PPE and angle-resolved two-photon photoemission (AR-2PPE) spectroscopy—to our knowledge, no such data is available for TiSe₂. Using a two photon process for the photoemission, the spectra contain contributions from occupied and unoccupied states, simultaneously. We performed thorough experiments using different photon energies, we lowered the work function using an alkali adsorbate, and evaluated the lifetime of the unoccupied bands using time-resolved two-photon photoemission (TR-2PPE). Our findings are carefully compared to band structure calculations available from different references.

All spectral signatures but one were identified. For the typical photon energies used in this work we attributed them to the occupied Se $4p$ bands, an unoccupied Ti $3d^*$ band and Ti derived final states using the band structures. For higher photon energies, additional bands were mapped and identified in these band structures.

However, we also observed an unoccupied, non-dispersive state at $E - E_F \approx 2.3$ eV in our spectra which is not in agreement to the band structure calculations available. Its unoccupied character was clearly identified in a time- and angle-resolved two-photon photoemission (TAR-2PPE) experiment which revealed a lifetime of about 7 fs. Our experimental data and the calculations of Pehlke and Schattke [69] enabled us to identify the origin of this state. It is attributed to Frenkel-like defects of the crystals, specifically to excess titanium atoms within the van der Waals gap of the crystals. The defect concentration was evaluated to be only about 1%. This data nicely demonstrates, that 2PPE spectroscopy is capable of mapping spectral signatures even for constituents of very low concentration. The comparably long lifetime of this state significantly enhances its photoemission yield in the 2PPE process.

Afterward, we focused on spectral modifications observed upon changes of *(i)* the temperature and *(ii)* the absorbed laser fluence. We observed a very strong reaction of TiSe₂ on these two parameters.

To understand the laser induced effects, we first studied purely thermal modifications of the spectra. We found a linear increase of the full width at half maximum (FWHM) of the Se 4*p* bands, as well as a linear increase of the work function with temperature which are both well explained by thermal effects. The Se 4*p* bands also revealed changes of the amplitude and binding energy; the latter was conveniently monitored by the shift of the spectral high energy cutoff. However, the phase transition of TiSe₂ needs to be considered, because the observed modifications change in the vicinity of the critical temperature.

Above the temperature of the phase transition the chalcogen *p* bands exhibit a linear reduction of spectral weight with increasing temperature. The binding energy did not change significantly in the temperature range discussed here, i. e. the high energy cutoff is virtually constant. Close to the critical temperature, the cutoff, and thus the Se 4*p* bands, showed an increase of binding energy which decreasing temperature of a few tens of electronvolts for our temperature range. Simultaneously, the spectral weight of the Se 4*p* bands decreased. The amplitude of these bands therefore features a maximum close to the critical temperature. These are typical effects of the establishment of the CDW/PLD phase.

We presented a thorough analysis of all thermal effects observed in the 2PPE spectra of both TMDCs. All modification are explained by thermal effects. TiSe₂ reveals distinct low temperature deviations which mark its phase transition.

Additionally, we compared the data on purely thermal changes to laser induced modifications. The absorbed laser pulses lead to a significant heat-up of the sample which we were able to evaluate by comparing the fluence dependence of the spectral features to the corresponding temperature dependence. Because the thermal modifications are linear, we derived a fluence–temperature conversion factor which enables a direct estimation of the sample heat-up for each absorbed fluence—this is, of course, only true for a certain wavelength, as well as comparable samples and experimental conditions for a system in thermal equilibrium.

While most spectral signatures agree well with temperature changes, we also observed distinct deviations: *(i)* the amplitude of the Se 4*p* bands decreases stronger, than expected from the estimated heat-up and *(ii)* we observe additional photoemission from the energy range just above E_F . Time resolved experiments revealed, that these differences are a result of the initial generation of a non-equilibrium electron distribution by the absorbed laser pulses, i. e. in this case we observed a contribution of the non-thermalized electronic system.

For the time resolved experiments we employed two different approaches: *(i)* we acquired one-color autocorrelation data using a standard TR-2PPE setup and *(ii)* we performed two-color time-resolved IR-pump SH-probe photoemission experiments which yield a set of full spectra for different pump-probe delays. The first approach enabled us to gain very fast access to the general laser induced dynamics of our samples in its low temperature CDW/PLD phase. We identified distinct modifications of the expected autocorrelation shape which revealed two distinct timescales, one in the order of a few hundreds of femtoseconds, the other in the picosecond regime. Furthermore, the temporal evolution was distinctly altered for the reference system TiTe_2 , which shows no phase transition. In this case, the deviations were much smaller and in agreement with the expected dynamics: initially we just generate a non-equilibrium electron distribution, which thermalizes within the pump-probe overlap. On a longer timescale, electronic and lattice system then thermalize as well.

TiSe_2 , however, featured a pronounced initial modification of the autocorrelation shape—the shape was still further modified after the temporal overlap of pump and probe pulses. It exhibits a laser induced dynamics which is established within a few hundreds of femtoseconds after the pump-event. The two-color experiments allowed us to attribute this behavior to the excitation of the charge density wave (CDW) amplitude mode and to screening by the laser generated carriers. This was not observed for TiTe_2 .

The two-color experiments proved to be very advantageous. In contrast to the one-color case, the excitation of the system by the pump-pulse is separated from the generation of the photoelectrons by the probe-pulse. The interpretation of the data is thus much easier. We used cross-correlations to determine suitable pump fluences and some general properties of the ultrafast dynamics of 1 *T*- TiSe_2 . These experiments revealed, that the spectral modification is mainly localized at the $\bar{\Gamma}$ -point—the system reacts much less for off-normal photoemission. This behavior is in agreement, for instance, with calculations using the excitonic insulator model and is reported in several experiments.

Finally, we performed time resolved experiments which yielded the full spectral information, i. e. we acquired a full spectrum at each temporal delay of pump and probe pulse. This method provides not only information about intensity changes, like the cross-correlations, but also about energetic changes. Specifically, we gained insight into the variation of the binding energy of the Se $4p$ bands, as well as the corresponding amplitude upon the laser induced perturbation of the CDW/PLD.

Again, we identified two characteristic timescales for our data: an initial process corresponding to the thermalization of the electronic system within tens to hundreds of femtoseconds and the heat transfer to the lattice on a picosecond timescale. The latter process is not specific to the correlated electronic system we investigated here, however, the first dynamic step revealed a surprising behavior. Within the thermalization of the electronic system which establishes the observed spectral modifications, we also observed a work function change. The work function is mainly attributed to lattice parameters, nevertheless, its temporal evolution shows a response within tens to hundreds

of femtoseconds. We attributed this to the excitation of the amplitude mode of the CDW. The observed changes correspond to variations of the lattice distances induced by the perturbation of the CDW state by the absorbed pump pulse. This was supported by the observation of corresponding oscillations in cross-correlation curves at sufficiently small pump fluences.

Additionally, we investigated the dependence of the observed time constants, as well as the occurrence of the oscillatory behavior for different absorbed pump fluences. The thermalization of the electronic system proceeded faster with increasing pump fluence, while the heat transfer took increasingly longer with increasing fluence. The increase of the latter process was attributed to the linear increase of the specific heat of the electronic system. The decrease of the thermalization time of the electronic system was attributed to increased screening at higher fluences which results from the generation of more free carriers by the pump pulse. The CDW phase is thus perturbed stronger and faster at higher fluences.

Our presentation concludes with an outlook. We presented our first time resolved experiments which combine an infrared (IR) pump- with an extreme ultraviolet (EUV) probe-pulse. This experimental approach provided the opportunity to monitor the full first Brillouin zone of 1T-TiSe₂ within a single angle-resolved photoemission spectroscopy (ARPES) spectrum. So far, our time resolved data has been restricted to the $\bar{\Gamma}$ -point only. The most prominent spectral modification induced by the CDW/PLD phase is observed, however, at \bar{M} , the border of the first Brillouin zone. At the \bar{M} -point we observed the appearance of the backfolded Se 4*p* bands which results from the doubling of the periodicity due to the superstructure, the periodic lattice distortion (PLD).

We used s-polarized high harmonic (HH) probe-pulses, because this suppresses the contribution of the Se 4*p_x*, 4*p_y* bands, while enhancing the Se 4*p_z* bands. This is advantageous for the observation at the \bar{M} -point: for p-polarization there is a strong spectral signature of the non-backfolded Se 4*p_x*, 4*p_y* bands at $E - E_F \approx -3$ eV which superimposes the backfolded bands partially. For s-polarization we got a much clearer view of the temporal changes at \bar{M} .

We presented a series of such spectra acquired for characteristic pump-probe delays. At time zero we observed laser-assisted photoemission (LAPE)—the high pump fluences provided by the laser system used for the high harmonic generation (HHG) enabled this effect. This signal is very useful to identify the temporal overlap of pump and probe, because it only exists during the pump pulse. Within about 100 fs additional modifications were established: the unoccupied Ti 3*d* band close to E_F became populated while the backfolded Se 4*p* bands vanished.

Future experiments focus on the pump fluence dependence of these modifications, as well as an elaborate method of data evaluation. The ultrafast temporal evolution of the backfolded Se 4*p* bands and the population of the Ti 3*d* band become accessible. The

first data is already published in reference [54]. Furthermore, considering our findings in chapter 6, measurements at very low pump fluences could be interesting. At sufficiently low fluences the amplitude mode of the CDW can be excited, as the screening becomes a slower process. With HH probe pulses the effect of this phonon mode could be observed within the whole first Brillouin zone.

A Supplementary Information

In this addendum we will discuss methods and considerations necessary for the evaluation of our experimental data presented in chapters 4–7. We present additional experimental data which motivate the decisions made in the course of the main experiments. The analysis in the mentioned chapters refers to this supplementary section whenever suitable.

A.1 Prerequisites for the Analysis of Spectral Modifications

In the following, we introduce the methodology for analyzing the spectral changes observed upon a temperature or laser fluence modification of the transition metal dichalcogenides (TMDCs) investigated here.

In section 5.1 we present data on the temperature dependence of two-photon photoemission (2PPE) spectra acquired for $1T$ -TiSe₂ and $1T$ -TiTe₂. For the detailed analysis of these data a set of numerical methods is needed. Furthermore, with respect to the spatial stability of the laser beam on the sample surface the homogeneity of that surface needs to be checked thoroughly.

A.1.1 Methods of Data Analysis

For the quantitative analysis of the temperature dependent 2PPE spectra we need two different methods: one for the assignment of reliable energies to the spectral features and one for extracting meaningful information on the spectral weight.

In both cases, the first step of data evaluation is smoothing. We are using a binomial smoothing method to reduce noise as it conserves the spectral shape which is checked carefully for each curve. Such algorithms generally act like low-pass filters which calculate each point of the smoothed data by summing some of the original data in the vicinity of this point. Here we use a commercial filter based on the application of a series of binomial coefficients for the summation [269]. The effect of the filter is presented in figure A.1.

The smoothed data is then analyzed by an automated script. We will now discuss the numerical evaluation of the data. A detailed look at a more sophisticated multi-Gaussian fit of the substructure of the chalcogen p bands is presented in appendix A.1.1–b. Although the numerical approach cannot be fully applied to the TiTe₂ spectra, it is very useful for extracting very precise information, because the automated approach leads to

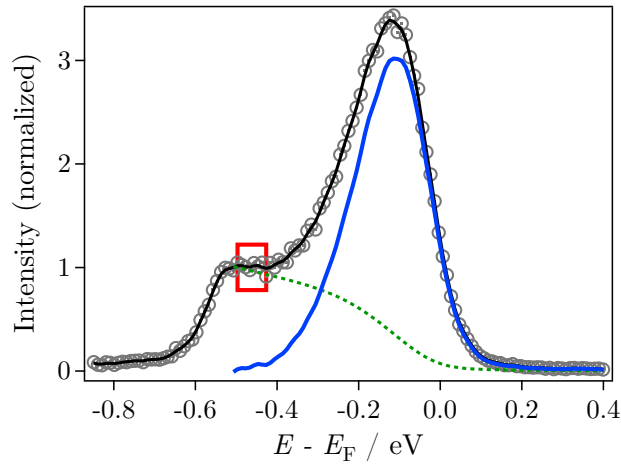


Figure A.1: The experimental data (circles) is normalized to the plateau level and smoothed (black). The plateau level is evaluated by averaging the data points within the energetic range shown by the red rectangle. Calculation of the Shirley background (green dotted) enables a baseline correction of the spectra (blue).

a good reproducibility along good statistics due to the vast amount of averaged data. The multi Gaussian fit is intrinsically prone to deviations between different data sets which leads to significantly higher uncertainties.

Our numerical approach basically consists of several different tasks: *(i)* a fit of edge energies, *(ii)* evaluation of the full width at half maximum (FWHM) of the p bands, *(iii)* their amplitude, *(iv)* area, and *(v)* center of mass. We will now discuss these methods in detail.

Fits of the energetic position of edges are applied to the high and low energy cutoffs of the spectra. This enables the extraction of the work function and the upper flank of the chalcogen p band right at E_F as discussed in sections 5.1.3 and 5.1.4-b. The low energy cutoff is well approximated by a sigmoidal fit which minimum and maximum are fixed at the spectral background level, i. e. the mean intensity of the signal at the lowest kinetic energies, and the plateau level (which we will discuss shortly); the center of the sigmoid yields the energy of the center of the low energy cutoff. The upper flank of the spectrum is generated by the chalcogen p bands which are cut at the Fermi energy. A sigmoid does not reproduce this feature very well. We calculate the half value of the bands' amplitude and search for the energy corresponding to this value. The energy channels of the cylindrical sector analyzer (CSA) are 10 meV wide, therefore, linear interpolation is applied, if the half value is not matched exactly. The width of the energy channels also defines the uncertainty of the extracted energy values as ± 5 meV. The

edge fits are not influenced by variations of the laser fluence, as their center does not shift upon a general increase of count rate, i. e. these data are stable with respect to instabilities of the laser system—so long as spatial shifts are negligible.

The calculation of the plateau level is straightforward. First, a flat region of the spectrum is chosen which should be observed for the full dataset (red box in figure A.1). The intensities in this region are averaged. The standard deviation is used as an estimate of the uncertainty. This method can also be applied to other energetic ranges of the spectrum like, for instance, the signal just above the Fermi energy, but it is most useful in determining the plateau level.

The evaluation of amplitude, area, FWHM, and center of mass of the chalcogen p bands requires a more sophisticated approach. First, the smoothed spectra are baseline corrected using the method proposed by Shirley [270], the “Shirley background correction”. The data can—if necessary—be normalized to the plateau level to enable comparability of the data extracted from the background corrected data even for fluctuating laser fluence. We omit correction for a constant background as our data does not support the extraction of a Fermi edge. Because the chalcogen p bands cut E_F , a detailed simultaneous fit of the bands substructure (multi Gaussian) and a Fermi-Dirac distribution would be necessary. An exact value of the absolute sample temperature is needed which we cannot assign to our data (see discussion in section 5.1). Furthermore, we present a multi Gaussian fit in appendix A.1.1–b to complement the numeric method discussed here which yields rather difficult and unstable results. Overall, subtraction of such a Fermi-Dirac distribution would introduce additional uncertainty to the data. It is, however, necessary to keep in mind the influence of the thermal broadening of the Fermi edge on the spectra, especially considering the discussion in sections 5.1.4 and 5.1.4–c.

We have applied one iteration of the Shirley background correction algorithm to calculate the baseline of our spectra. Figure A.1 shows such a Shirley background (green dotted), as well as the baseline subtracted spectrum (blue). From the corrected curve the amplitude is calculated by averaging the maximum and four vicinal data points. The standard deviation yields the uncertainty of the amplitude. The maximum is defined by the zero crossing of the differentiated spectrum.

The peak area is calculated by integration over the full background corrected spectrum within an energetic range of $E - E_F \approx -0.47$ eV to 0.32 eV. This range is chose to exclude artifacts at the low energies and to include the full spectral feature at the high energy flank. As the baseline corrected curve rapidly approaches zero intensity, the exact range does not influence the area significantly. Furthermore, we do not need to consider the energy scale for the integration, as the corresponding analyzer channels are all of the same width and we are not interested in the actual value of the area, but on relative changes. The uncertainty of the value is evaluated by comparison to the non-smoothed

data.

The *center of mass* E_c of the chalcogen p bands feature is calculated parallel to the area. The energies E_i of each channel are weighted by the corresponding 2PPE intensity I_i following:

$$E_c = \frac{\sum_i I_i E_i}{\sum_i I_i}.$$

The sum over all intensities, $\sum_i I_i$, corresponds to the peak area as defined here. We derive a value of the center energy E_c of all chalcogen p bands. The uncertainty is calculated analogously to the area.

To fully characterize the spectral feature, we finally calculate the FWHM using the same method, as in case of the fit of the energy of the spectral edges. We have already discussed in the beginning of this section, how the upper flank of the spectrum right at E_F can be numerically estimated using the half value of the amplitude and linear interpolation. By applying this method to the background corrected data and by estimating the energies of the upper and lower flank of this spectrum, the FWHM can be extracted. Each flank fit of the spectral peak features an uncertainty of ± 5 meV corresponding to the width of one energy channel of the CSA. Therefore, the uncertainty of the FWHM adds up to ± 10 meV, because two such flanks are fitted to derive the FWHM.

These methods will be applied to the data analysis, for instance, in section 5.1.4.

A.1.1–a On the Influence of the Thermal Behavior of the Spectral Plateau Its Applicability for Normalization

Especially the time resolved mode of experiment is very time consuming and thus requires adequately stable conditions for the whole set of measurements—otherwise the data cannot be compared. However, perfectly stable laser fluences are hard to guarantee over the course of several hours and under certain conditions the CSA system is known to introduce instabilities altering spectral intensities (see addendum A.3). In section 5.1.2 we discussed a powerful means of compensation for instabilities which preserve the spectral shape. As the spectral range used for normalization actually seems to depend on temperature itself, we need to discuss, how the temperature dependence of intensity derived spectral features are modified thereby.

Shall the mean intensity of the spectral plateau be $p(T)$ and an intensity derived spectral feature $x(T)$, both calculated from the non-normalized, absolute spectral intensities. In appendix A.2.1 we discuss that absolute values are not useful for comparison of different data sets (different sample charges, experimental runs, TMDCs, etc.) and therefore relative changes with respect to a reference temperature, $\tilde{x}(T)$, are used. These values are derived by normalization to the reference value, i. e. for example $\tilde{x}(T) = \frac{x(T)}{x(T_{\text{RT}})}$, with the room temperature T_{RT} . We employ two equivalent approaches for the plateau normalization: either $\tilde{x}(T)$ and $\tilde{p}(T)$ are calculated separately and used for calculation of the normalized intensity of the spectral feature, $\tilde{x}_p(T) = \frac{\tilde{x}(T)}{\tilde{p}(T)}$, or the plateau normalization

is applied first, yielding $x_p(T) = \frac{x(T)}{p(T)}$, which is again referenced to its room temperature value, yielding $\tilde{x}_p(T)$. For practical reasons both procedures may be used (the second most often) and they are equivalent, because calculation of the relative values involves multiplication with a fixed factor.

Now, we compare two different extremal situations: first, the intensity of plateau range might be independent of temperature and second, a thermal dependence may be observed. Even the careful stabilized conditions ensured for the investigation of 1 T-TiSe₂ in section 5.1.2 show some indication for slight drifts of the incident laser fluence. We therefore cannot experimentally decide, to what degree these two contributions participate in the observed increase of the plateau, although there are strong indications, that the effect is mostly intrinsic to the plateau and only little influenced by fluence drifts.

For a temperature independent plateau intensity, the observed mean plateau level is modified by extrinsic effects only. The changes which do not alter the spectral shape can be modeled by multiplication with a factor, $f_{\text{ex}}(T)$. This factor needs not to be directly temperature dependent, but for each experiment at each temperature it might be different. For the spectral features we thus find:

$$\hat{x}(T) = f_{\text{ex}}(T) x(T) \qquad \hat{p}(T) = f_{\text{ex}}(T) p(T) , \qquad (\text{A.1})$$

with the observed spectral features $\hat{x}(T)$ and $\hat{p}(T)$ and the corresponding intrinsic values $x(T)$ and $p(T)$ not modified by the external effects modeled by $f_{\text{ex}}(T)$. Referencing to the room temperature value yields:

$$\hat{\tilde{x}}(T) = \tilde{f}_{\text{ex}}(T) \tilde{x}(T) \qquad \hat{\tilde{p}}(T) = \tilde{f}_{\text{ex}}(T) , \qquad (\text{A.2})$$

with $\tilde{p}(T) = 1$, because of the constant value of the plateau. Using equation (A.1), normalization to the plateau yields:

$$\hat{x}_p(T) = \frac{\hat{x}(T)}{\hat{p}(T)} = \frac{x(T)}{p(T)} \\ \hat{x}_p(T) \equiv x_p(T) . \qquad (\text{A.3})$$

Equation (A.3) shows, that in this case the extrinsic effect can be fully compensated. Furthermore, because the plateau intensity does not change with temperature itself, $\tilde{p}(T) = 1$ after referencing to the room temperature value. Because there is no difference, whether the data is referenced to its room temperature value before or after normalization to the plateau intensity, we conclude:

$$\tilde{x}_p(T) \equiv \tilde{x}(T) , \qquad (\text{A.4})$$

i. e. plateau normalization corrects for the extrinsic modifications without altering the intrinsic thermal dependence of the spectral feature investigated which is already supported by equation (A.2). If the plateau range exhibits no temperature dependence at

all, the actual relative temperature dependence of intensity derived spectral features is accessible.

If the plateau intensity depends on temperature, the situation becomes more complicated and by plateau normalization intensity derived spectral features are modified with respect to their intrinsic value. All investigations of the thermal behavior of the different spectral characteristics of the TMDCs discussed in section 5.1 show, that it can be estimated using a linear function. This is not surprising, because the discussion of the thermal modification of the work function in section 5.1.3 revealed a linear behavior which is deduced from the linear thermal expansion of the crystal. We therefore assume line fits to be a reasonable estimation of our data. The intrinsic thermal modifications, i. e. uninfluenced by any external instabilities, are expressed by:

$$x(T) = \Delta x T + x_0 \qquad p(T) = \Delta p T + p_0 , \qquad (\text{A.5})$$

with the temperature coefficients Δx and Δp and the values at zero temperature $x_0 = x(0\text{ K})$, p_0 analogous. If external, intensity modifying influences are present, this becomes similar to equation (A.1):

$$\hat{x}(T) = f_{\text{ex}}(T) (\Delta x T + x_0) \qquad \hat{p}(T) = f_{\text{ex}}(T) (\Delta p T + p_0) . \qquad (\text{A.6})$$

Like in case of a constant, temperature independent plateau intensity normalization to the plateau compensates for the extrinsic effect:

$$\hat{x}_p(T) = \frac{x(T)}{p(T)} \equiv x_p(T) . \qquad (\text{A.7})$$

Again, plateau normalization compensates for all energy indiscriminate external effects affecting spectral intensity, however, $x_p(T)$ is generally different from $x(T)$, the value we are interested in. We are interested in the relative change $\tilde{x}(T)$ of the spectral characteristic. Following the definition earlier in this section, we derive:

$$\begin{aligned} \tilde{x}_p(T) &= \frac{x_p(T)}{x_p(T_{\text{RT}})} \\ &= x_p(T) \frac{p(T_{\text{RT}})}{x(T_{\text{RT}})} \\ &= \text{const.} \times x_p(T) , \end{aligned} \qquad (\text{A.8})$$

referencing to the room temperature value (in fact any value) is equivalent to multiplication by a constant factor, const., of the normalized spectral feature. Using equations (A.5), (A.7) and (A.8), we find:

$$\begin{aligned} \tilde{x}_p(T) &= \frac{1}{\tilde{p}(T)} \tilde{x}(T) \neq \tilde{x}(T) \\ &= \text{const.} \times \frac{\Delta x T + x_0}{\Delta p T + p_0} . \end{aligned} \qquad (\text{A.9})$$

Equation (A.9) demonstrates, that generally $\tilde{x}_p(T) \neq \tilde{x}(T)$. The thermal behavior of the spectral characteristic investigated is thus altered and even the linear behavior is lost. In conclusion, these findings need to be carefully considered, if plateau normalization is applied. Please note, considering equation (A.2), that in case of a temperature independent plateau intensity and for linear behavior of a spectral feature, the measured thermal dependence of the feature after referring to room temperature ($\hat{\tilde{x}}$) is non-linear and linearity is observed only after plateau normalization.

A.1.1–b Analysis of the Substructure of the Chalcogen p Bands

Section A.1.1 presents methods we refer to as *numerical* in the context of this work, because the extracted spectral characteristics are directly calculated from the spectra by integration, i. e. summation of intensities, and by interpolated searching the energy associated with certain intensity values. These methods are very simple, but also rather stable considering the spread of the results. In this section we discuss a more sophisticated fitting procedure which is referred to as the *multi Gaussian* method. The terminological distinction is, of course, superficial—both methods are basically numerical. However, the simple approach we refer to as numerical yields properties which are directly connected to the actual spectral shape, like, e. g., the area of a peak or the energetic position of its flank center. Multi peak fits are based on a superposition of elemental functions, i. e. assumptions about these functions need to be made and the superposition of them is not necessarily unique. Such a fitting procedure is a significantly more sophisticated method.

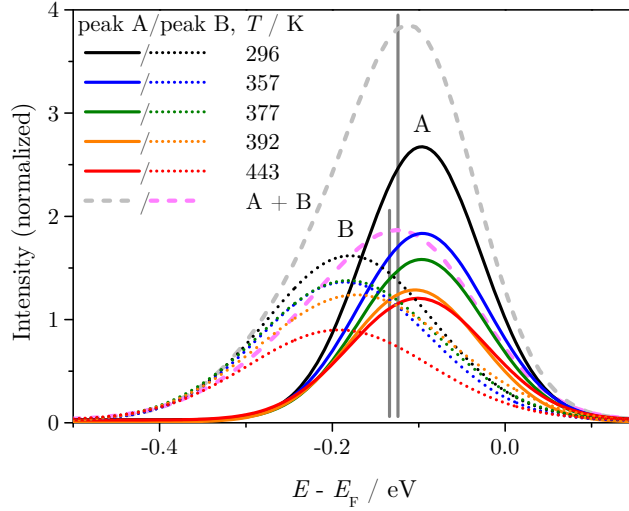
The first step of data evaluation is smoothing and background correction using the method of Shirley as shown in figure A.1. If the fit is performed on spectra after the application of plateau normalization before the background subtraction, this is expressed by denoting the data as *normalized*. This procedure is analogous to the numerical evaluation discussed in section A.1.1 and basically yields a set of spectra consisting only of the contribution of the Se $4p$ bands which can be fitted by a sum of appropriate functions.

A detailed analysis of the chalcogen p bands is thus not possible without a multi peak fit. In case of TiTe_2 the two Te $5p$ derived bands (spin-orbit split p_x, p_y derived bands on the one and a p_z band on the other hand; see reference [66] for TiSe_2) are energetically well separated, yet, too close for application of our numerical methods. TiSe_2 actually features one broad Se $4p$ derived spectral feature consisting of partial bands which are energetically so close that the substructure is only visible as a slight asymmetry of the peak. Quantitative data on the substructure is therefore only available using a method based on a functional fit. Strictly speaking, a superposition of three peaks should be fitted simultaneously. A good assumption for the expected shape of spectral peaks is the Voigt profile, a convolution of a Lorentz and a Gaussian profile which model broadening due to the lifetime intrinsic to the band and additional thermal broadening and the effect of the experimental energy resolution [271]. This is a rather complex fitting function with

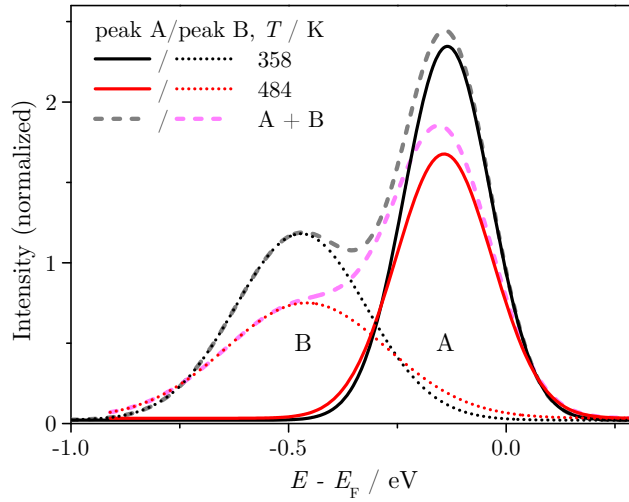
a lot of free parameters. In order to enhance the reliability and stability of the fitting procedure, we apply the *KISS* principle (“keep it simple, stupid” [272]) and simplify the method considerably. We will see that our assumptions enable the extraction of meaningful data, even using a delicate multi peak fit:

- First, we expect thermal contributions—after all we perform a heating experiment—and the low spectral resolution induced by the analyzer and the bandwidth of the laser to yield a dominantly Gaussian-like peak shape. Indeed, the spectra are well fitted by Gaussian shapes only (see figure A.2) which reduces the parameter space of a multi peak fit significantly. In consequence, the simpler multi Gaussian fit is also more reliable.
- Second, especially at higher temperatures, i.e. in case spectral peaks are well described by Gaussians, a double Gaussian fit is sufficient to reproduce the spectra reasonably well [figures A.2(b) and A.3 show a good and a bad fit, respectively]. Close to the room temperature (small thermal broadening/good spectral resolution) a triple Gaussian fit is generally better than its double Gaussian counterpart, considering the reproduction of the experimental data. Overall, the deviation of the double Gaussian fit at low temperature is less for TiSe_2 than TiTe_2 and the peak amplitude and area are extracted with sufficient accuracy—the implications for the quality of the data is discussed in the experimental section 5.1.4. The better quality in case of the TiSe_2 data is explained by the lower energetic resolution which increases the Gaussian-like contribution. We therefore use a double Gaussian fit to extract amplitude, area, and FWHM of the two partial peaks. Consistent estimation of the binding energy is discussed shortly.
- Finally, the Shirley background does not include a correction for the Fermi edge by the temperature dependent Fermi-Dirac distribution, because of the systematic problems discussed in section A.1.1. This leads to some difficulties for the fits discussed here—we will investigate this shortly—and also introduces broadening to the feature of lowest binding energy as the temperature dependence of the Fermi-Dirac distribution is basically added to the fitted width of this band (this is considered for the analysis in section 5.1.4).

Figure A.2 shows the results of our simplified *double Gaussian* fit routine for both TiSe_2 and TiTe_2 . The two expected spectral signatures of the spin-orbit split p_x , p_y derived bands (peak A) and the p_z band (peak B) are best observed for TiTe_2 [see figure A.2(b)]. The figure shows only the two Gaussian fits (dashed, A + B) and the two curves contributing to the fit (A: full, B: dotted)—the quality of the fit is discussed shortly with respect to figure A.3. Two gray vertical lines represent the center of mass calculated for the sum traces per section A.1.1 and show the shift to higher binding energy with temperature; the length emphasizing to which of the dashed curves they apply.



(a) Double Gaussian fit of 1T-TiSe₂.



(b) Double Gaussian fit of 1T-TiTe₂.

Figure A.2: Double Gaussian fit of the Se 4*p* and Te 5*p* bands. The lower binding energy feature is called “peak A” (full lines), the other “peak B” (dotted lines). The sum of both Gaussians yields a good representation of the background corrected spectra (dashed lines).

Figure A.2(a) contains only a subset of all TiSe_2 fits. Even using the simplified approach discussed here we find it impossible to generate a set of consistent fits for all spectra if all parameters of the fit are allowed to vary, i. e. if no restrictions defined. We decided on an all-free-parameter fit to exclude human influences on the analysis—although the fits become more delicate, the outcome is based solely on a mathematical measure of agreement to the spectra. However, small deviations in the spectra induced, for instance, by noise can lead to significant differences in the outcome of such multi peak fits. It is therefore necessary to compare the fits visually to categorize them. We derive three groups of qualitatively similar fits, deviating in the relative weight of the two partial peaks; we pick the biggest subset. The ratio of peak A and B agrees well with the data for TiTe_2 which is an indication for the validity of the chosen fits. Please note, that all three classes of fits show qualitatively the same thermal behavior. The chosen one is simply the most comprehensive. Generally, the multi Gaussian fit discussed here yields consistent data sets which exhibit, however, much higher uncertainties of the extracted data (see section 5.1.4) in comparison to the numerical method.

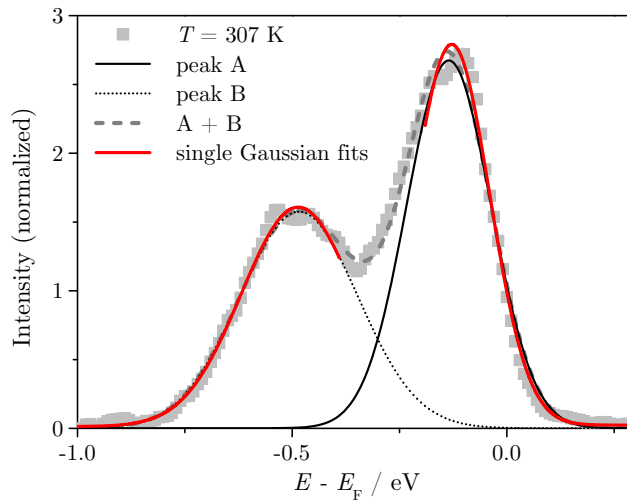


Figure A.3: The double Gaussian fit (dashed line) as presented in figure A.2(b) for TiTe_2 does not fit well to the experimental spectrum (squares) near room temperature, especially in the vicinity of E_F (full line). In this case two separate Gaussian fits for only the energetic range of the corresponding peaks (red lines) yield consistent binding energies. Similar to the calculated center of mass in case of TiSe_2 , energies defined this way allow for much better data on the relative energetic shifts.

Finally, we like to comment on a problem arising from the unavailability of a good estimation of the Fermi edge of the spectra. Figure A.3 compares a double Gaussian fit as discussed in figure A.2(b) to actual experimental data (squares). While these fits match the experimental data well at higher temperatures, close to room temperature

the quality is worse, especially in case of TiTe_2 . The figure shows, that the multi peak fit (dashed) does not reproduce peak A—in the vicinity of $E - E_F = 0 \text{ eV}$ the whole peak flank deviates significantly and the binding energy seems to be reduced, too. The observed distinct asymmetry of peak A is a consequence of its intersection with E_F and it is therefore not surprising that the agreement to the fits is good at temperatures above room temperature, because of the consequent broadening of the Fermi-Dirac distribution. Please note, that this issue is intensified by the better spectral resolution of the TiTe_2 data and thus most likely suppressed by the low resolution in case of TiSe_2 . Using a triple Gaussian fit the agreement at room temperature is significantly enhanced. However, the main contribution to the observed asymmetry is the intersection with the Fermi edge and introducing a third Gaussian in this case just compensates for this effect—such fits tend to yield inconsistent data considering the whole temperature range.

For the TiTe_2 data we apply a hybrid fitting method to compensate for this issue. Qualitatively the double Gaussian fit seems to estimate amplitude, area, and even FWHM quite well. The analysis in section 5.1.4 shows, that the extracted data are consistent with the good fits performed for the higher temperatures. This issue needs, however, to be considered for the interpretation of the temperature dependence. The energy of the peaks on the other hand is not comparable for room and higher temperatures as the quality of the fits deviates too much. To generate a consistent set of energies a fit of two single Gaussians is performed, one for each peak (red, figure A.3). Only the very energy range of the outer flank of the spectrum is chosen for fitting—the red curves actually show the whole energetic range selected. Obviously such fits do not approximate area and FWHM well and even the amplitude deviates, but they fit the energy of the peaks rather well. Although this method is not perfect and slight deviations persist, it yields consistent energies over the whole temperature range. For the TiSe_2 data an alternative fit of the energy of this peak is not possible, thus, the influence of the temperature dependence of the Fermi edge on peak A needs to be considered in this case.

A.1.2 Homogeneity of the TiSe_2 Surface

Photoemission experiments—especially in time resolved mode—are often very time-consuming, thus, small relative movements of the laser and ultrahigh vacuum (UHV) system are to be expected. Although actual sources of such movement like, for example, the small shifts induced by the different weight of liquid nitrogen during cooling (see section 3.1.1) are carefully compensated, we cannot correct for vibrations, laser pointing changes, or the thermal expansion (which we will discuss shortly) of the sample. Regular checking of the laser reflection from the entry window of the UHV chamber revealed only very subtle changes over the course of the experiment.

The TMDC samples used in this work do not provide perfectly homogeneous surfaces and may be considered quite inhomogeneous in comparison to, e. g., metallic single crystals like the $\text{Ag}(111)$ sample used as a reference. This is mainly explained by the

more complicated preparation by cleaving (see section 3.3) which leaves the surfaces prone to corrugations and distortions. Therefore, the homogeneity of the investigated surface area is checked prior to the actual experiments using a series of spectra taken at slightly different sample positions by lateral movement of the crystal itself.

A typical example for the homogeneity to be expected is the 1T-TiSe₂ crystal discussed in section 5.1. We find a sufficiently homogeneous area (vertical: ± 0.15 mm, horizontal: ± 0.05 mm, approximately), i. e. the magnitude of the diameter of the area yielding reasonable stable spectra is typically a few 100 μm . By characterizing the spectral signatures as *reasonable* stable we already imply that perfectly homogeneous areas cannot be found. The example discussed here may be considered a sample of ordinary quality.

We observe the following deviations for movement in two perpendicular directions parallel to the sample surface and defined by the experimental geometry

- vertical (height, perpendicular to plane of incidence)
 - amplitude: decrease by about 4%
 - energy: decrease by $\Delta(E - E_F) < 10$ meV
 - plateau level: increases up to about 13%
 - work function: $\Delta\Phi \lesssim 10$ meV (increase and decrease)
- horizontal (parallel to plane of incidence)
 - amplitude: decrease by about 3%
 - energy: decrease by $\Delta(E - E_F) \lesssim 10$ meV
 - plateau level: increases up to 8%, however, up to about 50% (amplitude decrease by 15%) is easily achieved just outside the given range
 - work function: $\Delta\Phi \approx 15$ meV (increase and decrease)

With the amplitude and energy of the Se 4*p* bands. The homogeneous horizontal range is significantly smaller. The laser spot is broadened in this direction because of the chosen angle of incidence by a factor of $\sqrt{2}$ (see section 3.2.1–b). Considering the beam diameter of the laser of only about 26.2 μm a reduction of only 11 μm of the observed homogeneous area can be explained by the beam broadening itself.¹

The significant energetic shift of the Se 4*p* bands to higher binding energy hints at a curved surface in horizontal direction which basically leads to off-normal photoemission and consequent probing of different areas of *k*-space. The increase of the work function and a slight decrease of the bands' amplitude in one of the horizontal directions supports our interpretation.

¹The homogeneous area is reduced by 200 μm which implies a vertical beam diameter of roughly 480 μm , which is already about 7 times the size of the horizontal homogeneous area and therefore impossible.

The changes of the plateau level are attributed to variations of the Se 4*p* bands. The variation of the probed \mathbf{k}_{\parallel} value of the system because of the sample curvature yields contributions from the Se 4*p* bands at higher binding energies, especially for the Se 4*p_z* band (see section 4.1).

Furthermore, corrugation of the surface also explain the fluctuations of the work function in vertical direction. For a flat surface the low energy cutoff of the spectrum defining the work function shifts closer to the Fermi energy for off-normal photoemission (see section 2.4). However, different crystallographic faces are well known to feature different values of the work function in the 100 meV range for metals [218]. Cleaving might lead to surface corrugations very similar to such a change of the crystal face.

A.1.2–a Spatial Stability of the Laser Beam on the Sample Surface

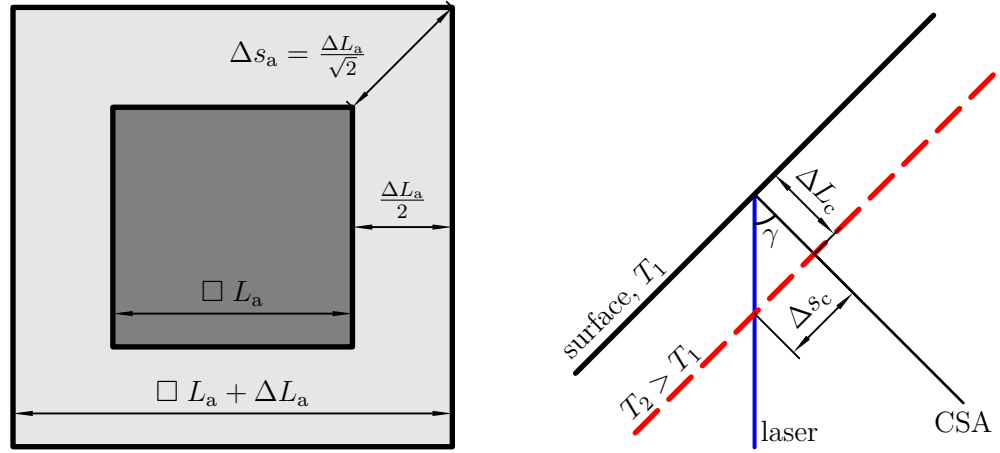
Considering the inhomogeneity of the TMDCs surfaces we need to evaluate the magnitude of the shift of the surface area probed by the incident laser induced by the thermal expansion of the crystals. The experiments at elevated temperatures (see section 5.1) span a range of $\Delta T_{\max} = 175$ K. The linear expansion coefficients of TiSe₂ are parallel to the layers² $\alpha_a = 18.4 \times 10^{-6} \text{ K}^{-1}$ and perpendicular to the layers $\alpha_c = 19.2 \times 10^{-6} \text{ K}^{-1}$ for temperatures above the critical temperature of the charge density wave (CDW) phase transition [236].

Using the definition of the linear expansion coefficient, $\alpha = \frac{1}{L} \frac{\Delta L}{\Delta T}$ (see, e. g., reference [172]), the change in crystal length is $\Delta L = \alpha L \Delta T$. For a worst case estimation of the expansion induced shift of the probed surface area, we assume the laser spot to be positioned at the edge of a large, square crystal [$6 \times 6 \text{ mm}^2$, see section 3.3]. Using α_a the lateral expansion parallel to the crystal surface is calculated as $\Delta L_a = 19 \mu\text{m}$ corresponding to a lateral shift of the laser spot of $\Delta s_a = 14 \mu\text{m}$ —please refer to the scheme in figure A.4(a).

The usual thickness of the samples is about 1 mm (see section 3.3). We will assume a thickness of $L_c = 2 \text{ mm}$ for our worst-case estimate. Figure A.4(b) sketches the experimental situation for perpendicular expansion. We derive $\Delta L_c = 7 \mu\text{m}$ using α_c which yields a lateral displacement of the laser spot of about $\Delta s_c = 7 \mu\text{m}$, because $\Delta s_c = \Delta L_c \tan 45^\circ = \Delta L_c$. This displacement acts parallel to the plane of incidence only, i. e. in the direction we call “horizontal”. Therefore, in a worst-case scenario—depending on the actual sample shape—the maximum lateral horizontal shift induced by the sample itself is $\Delta s_h \leq 21 \mu\text{m}$ and the maximum lateral vertical shift is $s_v = \Delta s_a \leq 14 \mu\text{m}$.

As the TMDC crystals are glued to a copper sample holder, we need to consider this holders expansion. The linear thermal expansion coefficient of copper at room temperature is $\alpha_{\text{Cu}} = 16.6 \times 10^{-6} \text{ K}^{-1}$ [274] which is comparable to TiSe₂. The holder is 3.5 mm thick. The effect of lateral expansion of the holder can be neglected, because the

²Caillé et al. [273] provide a smaller value for α_a which is not used here as we are interested in a worst-case estimate.



(a) Lateral thermal expansion of the sample increases the side length L_a by ΔL_a . The diagonal exhibits the biggest elongation, defining the worst case shift Δs_a .

(b) Perpendicular thermal expansion by ΔL_c . The surface is oriented perpendicular with respect to the CSA. The laser features an angle of incidence of $\gamma = 45^\circ$, leading to a shift of the laser spot on the hot surface of Δs_c .

Figure A.4: Shift of the investigated surface area of the sample at elevated temperatures.

sample is generally glued near the center of the holder. Following the shown schematically in figure A.4(b) we derive a horizontal lateral shift of the copper holder $\Delta s_{Cu} = 10 \mu\text{m}$.

Hitherto, we did not consider the manipulator used for positioning of the sample within the UHV chamber which also contains the resistive heater. However, the manipulator construction is optimized for careful thermal isolation of its sample holding head and the bulk construction, i. e. we expect only the head of the manipulator to heat up considerably. This part is made of molybdenum which features a linear thermal expansion coefficient of only $\alpha_{Mo} = 5.1 \times 10^{-6} \text{K}^{-1}$ [275]. The head plate is about 1 mm thick and a shift of $\Delta s_{Mo} \approx 1 \mu\text{m}$ is expected. Even if the manipulator warms-up during the experiment no significant movement of the sample with respect to the magnitude of the expansion of the crystal itself is expected.

Overall, we therefore estimate a maximum lateral displacement of the laser illuminated sample surface area induced by thermal expansion of the sample, the sample holder and the manipulator of $\Delta s_{h, \text{max}} \leq 32 \mu\text{m}$ in horizontal direction³ and $s_{v, \text{mac}} \leq 14 \mu\text{m}$ vertically. Note, that the manipulator and sample holder only significantly influence

³Wilson and Bastow [276] showed, that the linear expansion coefficient is enhanced at the surface leading to an approximately two times higher value of α at the surface of a metal. Even if we assume Δs_h to be less than $42 \mu\text{m}$ the maximum shift induced by thermal expansion would be $\Delta s_{h, \text{max}} \leq 53 \mu\text{m}$. The investigated area is thus only just exceeded and still partially overlapping with the laser (see following paragraph).

the horizontal direction, as only the expansion perpendicular to the sample surface is relevant. Lateral expansion of the manipulator may only indirectly contribute and for the sample holder this effect is compensated by the centered position of the sample.

The laser spot on the sample surface is elliptical featuring a diameter for second harmonic (SH) emission of $d_h = 37.1 \mu\text{m}$ horizontally and $d_v = 26.2 \mu\text{m}$ vertically (see section 3.2.1–b). Even in our worst-case scenario the investigated surface area still overlaps with the laser spot after the maximum shift. Please note, that our worst-case assumptions do not apply to actual experiments, as we assume measurement at the very edge of a rather big crystal. For probing at the center of the sample the lateral expansion becomes irrelevant, rendering the vertical shift virtually zero and reducing the horizontal shift to about $18 \mu\text{m}$.

The homogeneous area of the sample is smallest in horizontal direction and estimated to be $\pm 50 \mu\text{m}$ in appendix A.1.2. Considering the beam radius in this direction, the sample may shift up to $31.5 \mu\text{m}$, i. e. even for the estimated maximum shift the homogeneous area is not exceeded. In vertical direction thermal expansion is irrelevant as it is smaller and the laser beam diameter is also smaller while the homogeneous area is three times bigger, supporting a maximum shift of $137 \mu\text{m}$.

A closer look at the thermal modifications of the spectral characteristics observed for 1T-TiSe₂ as discussed in section 5.1 enables us to decide, whether surface inhomogeneities (noticeable because of thermal expansion) provide any significant contribution to the observed temperature effects. We begin with the work function data as discussed in section 5.1.3. The work function increases by $\Delta\Phi \approx 40 \text{ meV}$ in the temperature range investigated (175 K). Within the surface area identified as homogeneous, $\Delta\Phi_{\text{hom}} \lesssim 15 \text{ meV}$ is observed. Interestingly, moving the sample in the horizontal direction corresponding to the effect of thermal expansion, the work function actually decreases slightly. Even assuming an increase of work function, the value observed for the homogeneous area is much too small to explain the observed thermal effect. Actually, an extreme vertical shift by about $680 \mu\text{m}$, about 4.5 times the defined area in this direction, is needed to achieve an increase of comparable magnitude.

The most prominent thermal modification of the spectra is the strong reduction of amplitude of the Se $4p$ bands as shown in section 5.1.4–a which leads to a drop of peak intensity by approximately 50 % (absolute intensity, non-normalized). Neither the direction of a possible shift on the surface, nor the magnitude of below 25 % support this behavior, even if we assume shift significantly outside the homogeneous area; within this area the changes are much too small.

We cannot exclude an influence of inhomogeneities on the binding energy of the Se $4p$ bands (see section 5.1.4–b) of their FWHM as changes of comparable, similarly small magnitude, can be observed within the homogeneous area. However, the other, more pronounced effects are not explained by such inhomogeneities, i. e. so far we do not

observe any indications for the relevance of these deviations, and the well defined linear behavior of these modifications substantiate the interpretation in section 5.1.4–b.

Finally, the plateau intensity is easily increased by, e. g., defects or deviations of the crystal. Our discussion in section 5.1.2 therefore incorporates influences of the surface inhomogeneity. The plateau intensity usually increases only very little. If strong deviations are observed, the slope of the low energy cutoff allows us to decide, whether a shift of probed surface area or a change of absorbed laser fluence is the cause. Just outside the homogeneous area increases of the plateau level by up to 50 % are observed. The slope of the low energy cutoff does not change in this case. The TiTe_2 data discussed in section 5.1 on the other hand exhibits a strong increase of slope simultaneously to the plateau intensity increase. Normalization leads to a compensation of both effects, thus confirming a change of laser fluence in this case. We also see in this section that a slight increase of the plateau can be thermally induced. Considering its application for fluence fluctuation compensation, the slope of the low energy cutoff needs to be checked to rule out a dominant influence of inhomogeneities.

We conclude, that thermal expansion does not significantly contribute to the effects discussed throughout section 5 if a sufficiently homogeneous surface area is chosen. Our discussion in this addendum emphasizes the importance of a careful evaluation of the quality of the sample surface in the vicinity of the investigated area; we performed preliminary checks of this quality as described here previous to each series of experiments. To apply normalization to the plateau level it is always necessary to check, whether inhomogeneities led to a change. The low energy cutoff is valuable in this case.

A.2 Definition of Quantities Used for Data Evaluation

A.2.1 The Temperature Coefficient

The data presented in section 5.1 showed that the thermal modification of the spectral characteristics (work function, peak amplitudes, ...) is generally well described by a linear dependence. It is therefore instructive, to perform line fits of such data and compare different data sets using the corresponding temperature coefficients, i. e. the slope of these fits. In this addendum we define the temperature coefficient $\Delta\tilde{x}$ used throughout this work.

The absolute spectral intensities are not exactly comparable, because of differences in the alignment of the laser system and optical setup, as well as deviations between different sample crystals. To circumvent these imponderabilities, we focus on relative changes of the sample parameters, i. e. the temperature dependent data is normalized to a reference value. However, different references also lead to different slopes of the corresponding line fits.

Referencing the temperature dependent data to the spectrum at absolute zero (“0”) temperature seems to be a good choice at first. However, TiSe_2 exhibits a phase transition at low temperatures which also reflects in the behavior of the spectral features (see section 5.3), i. e. a linear extrapolation to absolute zero temperature is strictly not correct. Also, our data at low temperatures is not sufficient for a meaningful extrapolation to $T = 0$ K. We will use such a normalization only for comparison to literature values which are normalized as such—considering the rough nature of the actual comparison in section 5.1 this estimation is practical.

Generally we decided for referencing to the room temperature (“RT”) spectrum for practical reasons. First, we avoid the systematic deviations induced for low temperatures by the CDW phase transition of TiSe_2 . Second, the temperature dependent data is especially useful in comparison to the data on the absorbed laser fluence variation in section 5.2. The natural starting point of an experimental series is in both cases an undisturbed, room temperature spectrum. Considering the linearity of the spectral characteristics in the vicinity of the room temperature, the data becomes easily comparable by inter-/extrapolation to a defined room temperature value (296 K in the mentioned sections). Realistic data as presented in table 5.1, page 141, shows that even for a rather high room temperature fluctuation of ± 5 K we derive a worst case deviation of less than $\pm 2\%$.

The linear behavior of the absolute values of the spectral characteristics shall be defined as:

$$x(T) = x_0 + \frac{dx}{dT} T = x_0 + \Delta x T ,$$

with $x(T)$ being the thermally modified feature (e. g. amplitude, FWHM, work function, ...), $x_0 = x(0 \text{ K})$ and the slope Δx . These data can be normalized to a reference value x_{ref} using:

$$\begin{aligned} \tilde{x}_{\text{ref}} &:= \frac{x(T)}{x_{\text{ref}}} \\ \Rightarrow \tilde{x}_{\text{ref}} &= \frac{x_0}{x_{\text{ref}}} + \Delta \tilde{x}_{\text{ref}} T . \end{aligned} \tag{A.10}$$

We use referencing to absolute zero, x_0 , and room temperature, $x_{\text{RT}} := x(296 \text{ K})$, which simplifies equation (A.10) to:

$$\begin{aligned} \tilde{x}_0 &= 1 + \Delta \tilde{x}_0 T \\ \tilde{x}_{\text{RT}} &= \text{const.} + \Delta \tilde{x}_{\text{RT}} T . \end{aligned} \tag{A.11}$$

Please note, that in case of normalization to room temperature we are only interested in the temperature coefficient $\Delta \tilde{x}_{\text{RT}}$ and consequently include the ordinate intercept $\frac{x_0}{x_{\text{RT}}}$ as an arbitrary constant only.

A.2.2 Evaluation of Spectral Peaks—Characteristics of a Gaussian Shape

We have discussed in section A.1.1–b that in general the spectral peaks are well described by Gaussian curves. We follow the nomenclature of section A.1.1–a. Such a Gaussian-shaped intensity peak, $I(E)$, is described, analogously to equation (3.1) in section 3.2.1–b, by:

$$I(E) = I_{\max} \times \exp \left[-2 \frac{(E - E_c)^2}{w^2} \right],$$

with the maximum I_{\max} , the center energy E_c , and the FWHM w . The area, A , of such a Gaussian curve is defined by:

$$\int_{-\infty}^{\infty} I(E) \, dE = \sqrt{\frac{\pi}{2}} w I_{\max} =: A, \quad (\text{A.12})$$

using reference [143]. The most obvious consequence of equation (A.12) is the resulting proportionality of area and amplitude, if the FWHM is constant. We usually present relative data referenced to the room temperature value. In this case, the temperature dependent amplitude and area actually become equal, $\tilde{I}_{\max}(T) = \tilde{A}(T)$. However, the temperature dependence of both generally deviate (see, for instance, figure 5.16 in section 5.1.4–a) with the amplitude decreasing stronger than the area. This is actually expected, because the FWHM of the spectral structures increases with temperature (about 40 meV for this temperature range, see section 5.1.4–b).

If a simple Gaussian peak shape is assumed, a temperature dependent FWHM, $w(T)$, the room temperature value of the area is defined by equation (A.12) as $A(T_{\text{RT}}) := \sqrt{\frac{\pi}{2}} w(T_{\text{RT}}) I_{\max}(T_{\text{RT}})$, with the room temperature value T_{RT} . This enables us to calculate the relative area, $\tilde{A}(T) = \frac{A(T)}{A(T_{\text{RT}})}$, referenced to the room temperature, as well as to analogously define the relative FWHM, $\tilde{w}(T)$, and amplitude, $\tilde{I}_{\max}(T)$. For a temperature dependent FWHM equation (A.12) yields:

$$\begin{aligned} \tilde{A}(T) &= \frac{A(T)}{A(T_{\text{RT}})} = \sqrt{\frac{\pi}{2}} \frac{w(T) I_{\max}(T)}{A(T_{\text{RT}})} \\ &= \tilde{w}(T) \times \tilde{I}_{\max}(T). \end{aligned} \quad (\text{A.13})$$

For a simple Gaussian peak shape it is therefore sufficient to analyze only two of the three properties (area, amplitude, and FWHM) simultaneously, because the third can be calculated and for relative data the proportionality factor is unity. Our analysis in section 5.1.4–a indeed shows, that even the rather asymmetric peak originating from three superimposed Se $4p$ bands can be evaluated using only FWHM and amplitude—and thus implicitly assuming a single-Gaussian shape (for details refer to that section).

Within this work we generally focus on the amplitude and FWHM when discussing the modifications of the spectral peaks. Both values are directly accessible using different numerical methods (intensity averaging and energy fitting, see section A.1.1) and they are very straightforward with respect to their definition. If both flanks of a peak show the half-value of its maximum intensity the FWHM is easily evaluated and the amplitude is always easily acquirable. The area of a peak cannot be evaluated unambiguously if different peaks overlap.

A.3 Count Rate Drifts of the Experimental Setup—Stable Photoemission Using the CSA

To gain a detailed and quantitative understanding of laser induced modifications of the spectral shape, we performed 2PPE spectroscopy experiments at different absorbed laser fluences, F_{pp} . However, this approach proved to be very challenging especially at small fluences, because we endeavored very slow, long-term changes in the photoemission signal, i. e. after setting a specific value of F_{pp} the spectral intensity is unstable.

Of course, the acquisition of meaningful spectroscopic data requires sufficiently stable conditions—comparability of spectra taken at different fluences is not only crucial for the analysis of laser induced modifications (see section 5.2), but it is also a necessity for time resolved experiments during which the total absorbed laser fluence varies (see section 6, especially 6.1).

In this addendum we discuss a careful investigation of these instabilities, focusing on two problems:

- (i) Which is the source of the observed instability of the photoemission signal? Generally, there are several possible explanations for this effect:
 - a sample intrinsic effect, like a degradation of the crystals, charging or warm-up,
 - charging of some part of the UHV system, like, e. g., the manipulator, a window or the CSA, and
 - drifts of the electronics of the CSA.
- (ii) How can the instability be circumvented or compensated? We discuss,
 - which fluence range is affected,
 - how the best stability may be established within the critical F_{pp} range, and
 - whether such instabilities can be compensated by normalization.

The data presented here is acquired after stabilization of the very slow instabilities of the spectral intensity. Beginning at the lowest fluence value, F_{pp} is slowly increased.

Before acquiring a spectrum, stabilization of the photoelectron count rate is waited for. In the following we present 2PPE spectra of TiSe₂, acquired using the p-polarized SH ($h\nu = 3.18$ eV) emission of laser 3_{TR}. In this appendix we use two normalization procedures. Whenever the spectral intensity is normalized with respect to the absorbed laser fluence, i. e. to a common fluence value, we indicate this by a “normalized” intensity scale. If the spectra are re-normalized to the plateau intensity (see section 5.1.2–c) we denote this by “scaled”.

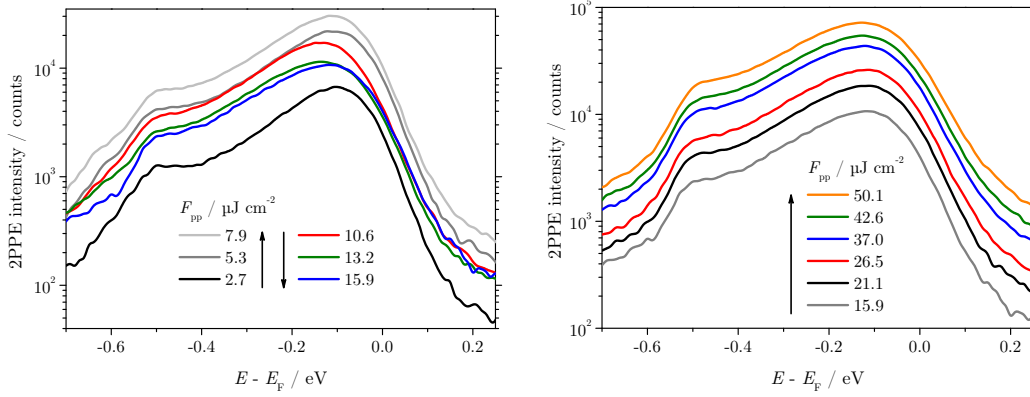
A.3.1 Overview of the Unstable Photoemission Signal

In general, the spectral intensity is expected to increase with the absorbed laser fluence. Nevertheless, taking a close look at the experimental data presented in figure A.5 this is not the case. Figure A.5(a) compares spectra taken for different values of F_{pp} on an absolute, logarithmic photoelectron count rate scale. For fluences $F_{pp} \lesssim 7.9 \mu\text{J cm}^{-2}$ (gray shades) the spectral intensity increases, however, for $F_{pp} \gtrsim 10.6 \mu\text{J cm}^{-2}$ (color) the absolute count rates decrease although the fluence rises. Furthermore, the spectral intensity becomes very unstable. The initial intensity is indeed increased with respect to the preceding value, yet, it rapidly decreases which continues over a long period of time. Finally a stable, lower value is reached.⁴ We identify a threshold fluence at which this slowly evolving count rate instability vanishes of $F_{pp} \approx 20 \mu\text{J cm}^{-2}$. Figure A.5(b) shows spectra in the fluence range of $F_{pp} = 15.9 \mu\text{J cm}^{-2}$ to $50.1 \mu\text{J cm}^{-2}$ which all exhibit the expected increase of intensity with fluence. Such spectra are long-term stable, i. e. no further reduction of the count rate is observed. Because of the loss of spectral intensity at intermediate fluences the plateau intensity ($E - E_F \approx -0.5$ eV to -0.45 eV, see section 5.1.2) increases by a factor of only 16 within the investigated fluence range of $2.7 \mu\text{J cm}^{-2}$ to $50.1 \mu\text{J cm}^{-2}$, although the quadratic dependence of spectral intensity on the fluence in case of 2PPE supports a factor of approximately 344.

The deviation of the photoemission signal becomes even more obvious after normalization of the spectral intensity to the same fluence value—2PPE is a quadratic process in laser fluence, i. e. the increase of spectral intensity induced by a higher fluence can be compensated by using the squared ratio of the fluences. Figure A.5(c) shows the spectra of figures A.5(a) and (b) normalized to a reference fluence of $5.3 \mu\text{J cm}^{-2}$. In the absence of any laser induced in- or extrinsic effects uniform spectra are expected after normalization; this is clearly not the case. This representation reveals stable photoelectron count rates for fluences up to about $5.3 \mu\text{J cm}^{-2}$, followed by a significant reduction over roughly a decade and a second stable regime for $F_{pp} \gtrsim 25 \mu\text{J cm}^{-2}$. For the highest fluences we are able to identify typical modifications of the spectral shape, especially a reduction of the intensity of the Se $4p$ bands.

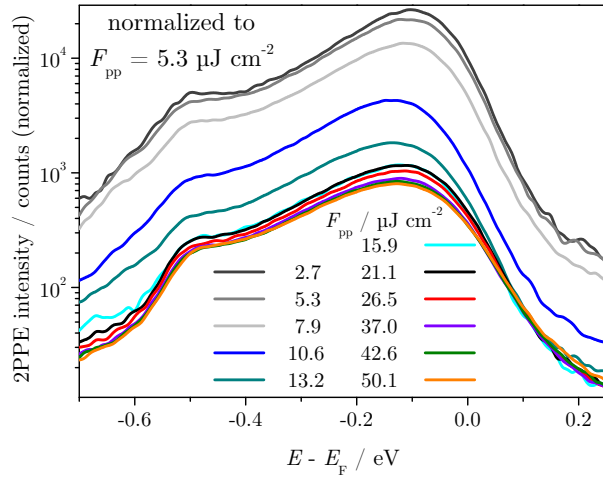
⁴The spectra presented here are virtually stabilized, i. e. the evolution of the count rate almost completely ceased.

A.3 Count Rate Drifts of the Experimental Setup—Stable Photoemission Using the CSA



(a) Anomalous spectral intensity; increase and decrease with absorbed fluence.

(b) Expected increase of spectral intensity with fluence.



(c) Reduction of the count rate.

Figure A.5: The behavior of the spectral intensity with varying absorbed fluence F_{pp} is anomalous. Absolute values of the count rate as acquired with the CSA spanning about 2 decades are presented (a) and (b). (a) For fluences below a certain value, the count rate is unstable, i. e. it decreases over a long period of time (for details see text and figure A.8). Therefore, spectra acquired after stabilization are used here. A fluence of $F_{pp} = 10.6 \mu\text{J cm}^{-2}$ marks the onset of the anomalous decrease of spectral intensity with increasing fluence. (b) At a certain, higher fluence the count rate is stabilized again and the expected increase is observed again. (c) Normalization to a reference fluence ($F_{pp} = 5.3 \mu\text{J cm}^{-2}$, see text) emphasizes the actual decrease of spectral intensity upon increase of fluence; stabilization is reached at $F_{pp} \gtrsim 20 \mu\text{J cm}^{-2}$.

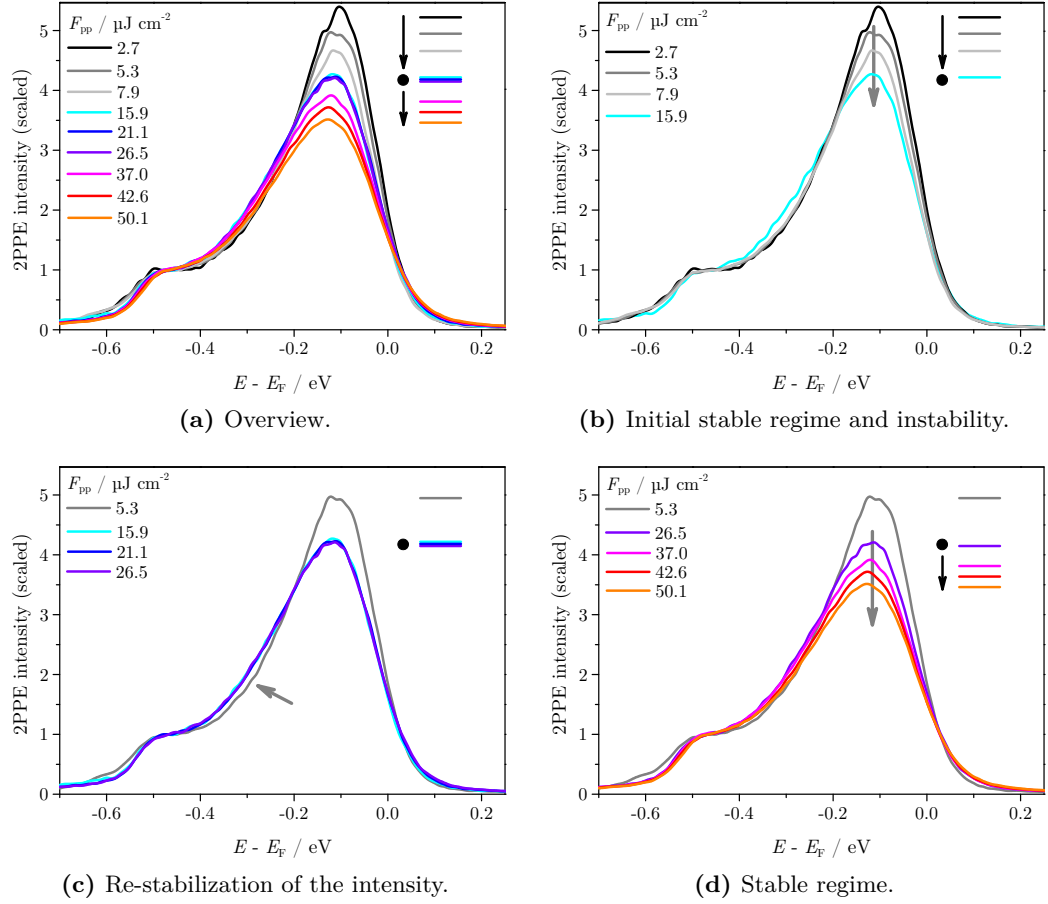


Figure A.6: The data presented in figure A.5 are normalized to the plateau level ($E - E_F \approx -0.5 \text{ eV}$ to -0.45 eV). This compensates the intensity instability of the CSA and enables the observation of spectral modifications. (a) Overview of the full fluence range. (b)–(d) A detailed look into the observed spectral modifications. Arrows emphasize the main effects. The insets (arrows, dot and color bars) allow for easy orientation.

We focus on these laser induced changes in section 5.2, however, we briefly discuss the modification of the spectral weight of the Se4*p* bands here, too, to identify the influence of the CSA instability and to understand, how quantitative data are derived. Figure A.6 presents the spectra from figure A.5 using a linear intensity scale and all spectra are normalized to the plateau intensity (see section 5.1.2-c) which compensates for the intensity drifts.

Please note, that we do not include spectra acquired for the fluences $10.6 \mu\text{J cm}^{-2}$ and $13.2 \mu\text{J cm}^{-2}$ as they deviate significantly in the binding energy of the Se 4*p* bands. A closer look at figure A.6(b) reveals that we seem to observe a change in the surface area of the sample probed by the laser. This shift is rather significant for the omitted data [see figure A.5(c)] and still remains for $F_{\text{pp}} \gtrsim 15.9 \mu\text{J cm}^{-2}$ which is emphasized by the gray arrow in figure A.6(c). A reduction of the amplitude of the Se4*p* bands in combination with an increase of binding energy can be explained by off-normal photoemission (see chapter 4) which may be attributed to changes of the laser pointing in interplay with surface corrugations (refer to appendix A.1.2).⁵ The apparent broadening of the Se 4*p* bands is a consequence of off-normal emission, as the Se 4*p_z* bands is energetically more separated. Please note, that for $F_{\text{pp}} \geq 15.9 \mu\text{J cm}^{-2}$ the spectral shape is modified because the probed surface area is slightly changed, however, the spectra thereafter remain comparable. Also, this is not a laser induced, sample intrinsic effect, because the loss of spectral weight of the Se 4*p* never leads to a crossing of the preceding spectra (see section 5.2)—the spectra before and after this pointing change are indeed compatible with this expectation.

So far, we identified three, distinctive regimes of spectral modifications, presented in figures A.6(b)–(d). The spectroscopic experiment is not influenced by the instability of the CSA at the lowest fluence—probably because modifications are still slow enough to be irrelevant under practical considerations—and for $F_{\text{pp}} \gtrsim 25 \mu\text{J cm}^{-2}$ where the photoelectron count rate does not change anymore with time.

A.3.2 Analysis of the Unstable Photoemission

In this appendix we focus on spectral artifacts induced by the CSA; the data acquired under stable conditions is presented and discussed in section 5.2. The normalized spectra as presented in figure A.6 are also included in this discussion, however, we find, that even using normalization to the plateau a consistent set of data is not derived.

Within the fluence range of the CSA instability we observe a long-term reduction of the spectral intensity. Figure A.7 shows the temporal evolution of the 2PPE intensity measured after increasing the absorbed fluence to $10.6 \mu\text{J cm}^{-2}$. These data demonstrate,

⁵The homogeneity of the investigated surface area is routinely checked. The observed spectral modifications at $F_{\text{pp}} = 10.6 \mu\text{J cm}^{-2}$ to $13.2 \mu\text{J cm}^{-2}$ are compatible with a horizontal shift of about $200 \mu\text{m}$ and a vertical shift of $250 \mu\text{m}$ which could result from momentary pointing problems of the laser system induced by, e. g., temperature drifts.

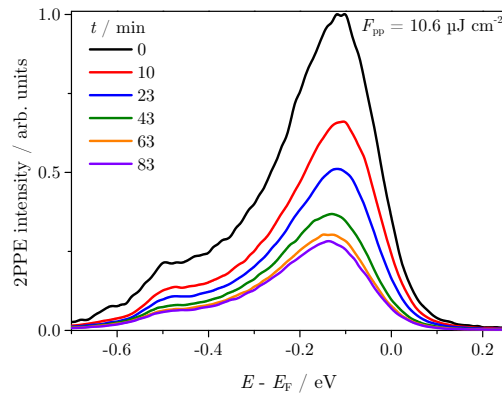


Figure A.7: The photoelectron count rate becomes unstable at certain fluences and does not fully stabilize even within about 1.5 h.

that the observed loss of photoelectron count rate is extremely slow—even after waiting for 83 minutes the decrease does not vanish completely. The stabilized spectra discussed here are therefore actually acquired under “quasi-stable” conditions. We see in section 5.2 that this is quite relevant for the interpretation of the observed spectral modifications—we also discuss a stabilization approach better suited for our experimental needs.

Figure A.8 investigates the spectral modifications and the intensity instability in more detail. Normalization of the spectra in figure A.7 (not shown) to the plateau intensity already indicates, that the spectral shape does not change during the decrease of photoelectron count rate and the question arises, whether this is an instantaneous modification. We do not observe any change of spectral shape or instability of the intensity for at least $F_{pp} = 1.6 \mu\text{J cm}^{-2}$ to $5.8 \mu\text{J cm}^{-2}$. Figure A.8(a) shows the onset of the change of spectral shape. We identify significant modifications and an instability of the photoemission signal at about $7.9 \mu\text{J cm}^{-2}$. Figure A.8(b) investigates this onset in more detail. The unmodified spectrum acquired at a fluence of $5.3 \mu\text{J cm}^{-2}$ is shown for reference. By taking only a single run of the CSA for acquisition of the spectrum instead of several averaged runs we derive a quasi-“instantaneous” spectrum. Please note, that the reference (black) and the quasi-instantaneous (red) spectra are normalized with respect to the absorbed fluence. There is initially neither a change of spectral shape, nor a general loss of intensity observed. After about 10 min the intensity is significantly reduced (green, normalized to the plateau intensity) and the spectral shape is modified, too.

So far, considering the spectral modifications at low absorbed fluences, we find a threshold for changes of the spectral shape and for the instability of the photoelectron count rates. Our data show, that for $F_{pp} \lesssim 6 \mu\text{J cm}^{-2}$ the spectra seem to be uninfluenced by the absorbed laser pulses and stable acquisition is possible. Within

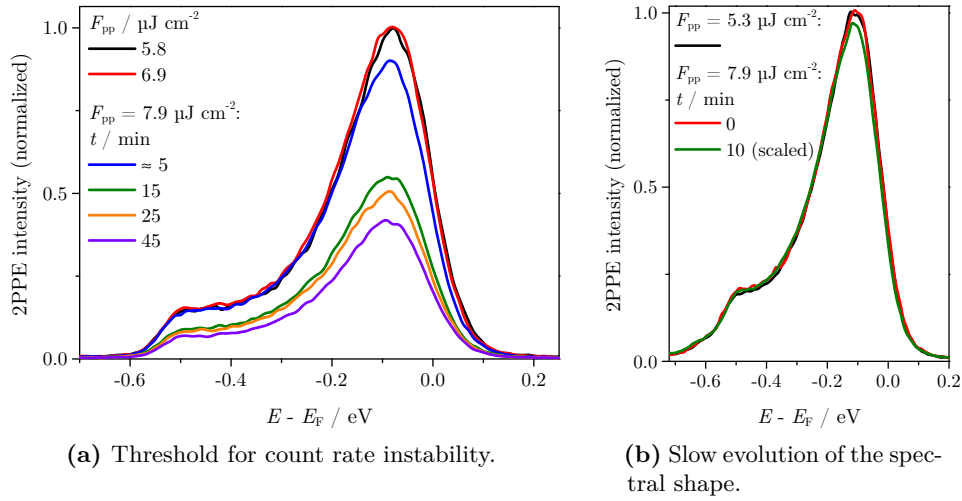


Figure A.8: (a) The onset of the spectral modification and the count rate suppression is identified at $F_{pp} \approx 7.9 \mu\text{J cm}^{-2}$. (b) Normalization to the plateau energy emphasizes the spectral modifications. Initially, the spectral shape remains unchanged. A similar normalization of the spectra in (a) reveal, that the shape stabilizes within about 15 min, i. e. much faster than the general decrease of the intensities.

the fluence regime governed by a strong, slow decrease of photoemission signal the spectral modifications, especially the loss of spectral weight of the Se $4p$ bands, are not instantaneous, however, the spectral shape stabilizes within minutes, whereas the count rate instability persists over hours. Both effects, the shape modification and the energy independent instability seem to be established after a short, initial stability phase.

Now, we investigate the recovery of the modification of spectral shape, as well as the increase of the photoelectron count rate after a reduction of the laser fluence or a prolonged blocking of the laser beam. Such data is presented in figure A.9. Figure A.9(a) shows the effect of a reduction of the absorbed laser fluence from $7.9 \mu\text{J cm}^{-2}$ to $5.3 \mu\text{J cm}^{-2}$. All spectra except the reference spectrum (orange) are acquired using the quasi-instantaneous method discussed for figure A.8(b). The reference spectrum and the last taken spectrum after the fluence reduction (orange and green) are re-normalized to the plateau intensity. The gray curve represents the normalization with respect to the laser fluence. In this representation the recovery of the photoemission signal after 10 min becomes obvious. Please note, that the reference spectrum (orange) features significantly higher intensities. Our observations are summarized as follows: (i) The spectral shape almost recovers within about 1 min, but not instantaneously, which is shown by the good agreement of the blue and (scaled) green to the (scaled) orange reference curve. The

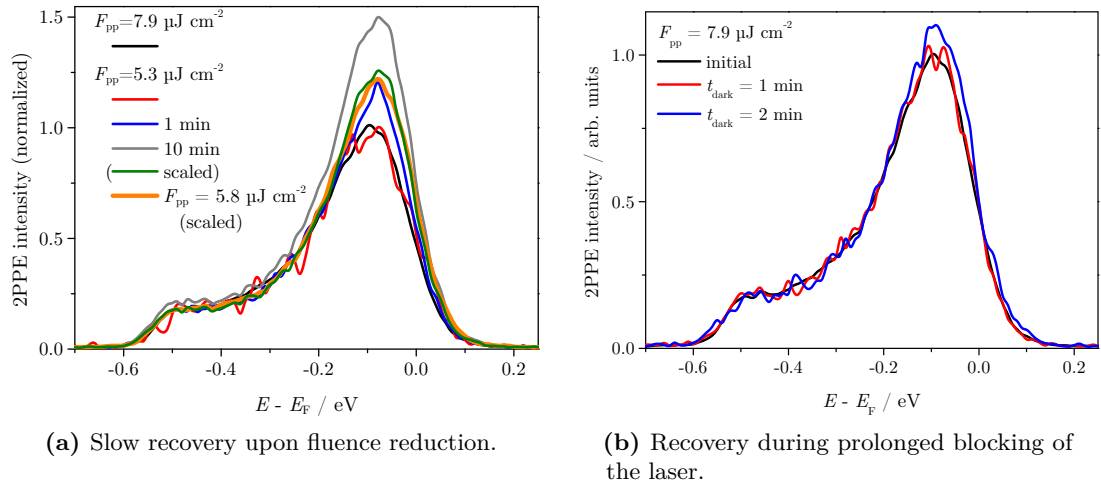


Figure A.9: Recovery of the spectral shape after lowering of the fluence is slow, too. (a) Upon reduction of the fluence, the amplitude of the Se 4*p* bands recovers slowly (within about 10 min). A reference spectrum taken before the fluence increase (orange) is included. Some spectra are re-normalized to the plateau intensity (scaled). (b) A similar recovery is induced by blocking the laser for $t_{\text{dark}} > 1$ min.

instantaneous spectrum⁶ (red), however, does not deviate considerably from the spectrum acquired at the higher fluence (black). After 10 min full recovery is established—the small overcompensation of the amplitude of the Se 4*p* bands is attributed to the slight difference in fluence. (ii) After 10 min an additional increase of the whole spectral intensity is observed, i. e. while the spectral shape does not change anymore, the reduction of the intensity is recovering.

We do not need to decrease the fluence to observe the slow modification of the spectral shape, blocking the incident laser beam for at least 2 min, see figure A.9(b), also leads to a visible recovery of the spectra (quasi-instantaneous acquisition). This shows, that establishment and recovery of the modification proceed rather slow.

A.3.2–a Remarks on Choosing a Suitable Fluence for Time Resolved Experiments

For some of the experiments presented in this work we aim for as little as possible laser induced modifications. For instance, the time-resolved IR-pump SH-probe photoemission experiments (see section 6.2) require probe pulse which do not considerably modify the

⁶In this case the laser was blocked for about one minute before acquisition of the spectrum in one run, i. e. the absence of any recovery in this case is an indication for an even slower recovery than modification.

spectral shape themselves. For the investigation of the temperature dependence in section 5.1 it is also crucial to ensure negligible influence of the probing laser pulses. This is obviously achieved by using a laser fluence as low as possible, however, the photoemission intensity directly relates to the absorbed fluence—in case of 2PPE even quadratically. We need to trade-off sufficient photoelectron count rates and the absence of modifications. We find a fluence of about $5.3 \mu\text{J cm}^{-2}$ (corresponding to mean laser power in front of the UHV chamber of 5 mW) a good choice, because figure A.8(a) shows, that modifications of the spectral shape are virtually non-existent. We cannot exclude a very slow instability of the photoemission count rate at this fluence, as this effect seems to slow down for smaller fluences, but an energetically non-specific change of intensity is easily compensated (see section 5.1.2–c). In section 5.2.2 we find that the analyzer stabilizes at high fluences, however, we prefer a compensable instability of the CSA during the experiment over considerable laser induced effects present at high fluences.

A.3.2–b The Unstable Photoemission—an Instability of the CSA System

In general, we observed two different effects: a slow general reduction of the photoelectron count rate within hours and modifications of the spectral shape which are established within minutes. The latter is attributed to a temperature increase of the sample induced by heat accumulation due to the absorbed laser pulses. The change of spectral shape cannot be completely understood in terms of heat-up of the sample for the low fluences. Figure A.6 shows, that the reduction of spectral weight of the Se $4p$ bands is discontinuous in contrast to data on the temperature dependence of the spectra in section 5.1. We discuss these differences in section 5.2.

The count rate reduction, however, is a sample extrinsic effect which may be explained by, e. g., drifts of the electronics of the CSA and/or charging of the UHV system, for instance, at the manipulator or the electrostatic lenses of the CSA. The striking difference in the observed time scales, as well as the energetically non-specific reduction of the count rate support this assumption.

To understand the origin of the observed instabilities it is very instructive to perform an analogous experiment on the fluence dependence on a simpler sample system, i. e. a metallic single crystal without the layered structure of the TMDCs investigated here. This circumvents a potential charging of the layered crystals. We therefore perform experiments in a similar fluence range on Ag(111); the spectra are presented in figure A.10. Again, the reduction of photoemission signal with increasing fluence is observed [see figure A.10(a)] and the intensity recovers after decreasing the fluence [see figure A.10(b)]. The observed energetically non-specific photoelectron count rate instability is therefore clearly not sample specific. The effect is, however, smaller for silver than for TiSe_2 which may result from the significant difference in photoelectron count rate which is 1–2 orders of magnitude higher for silver. There is no reason why a sample extrinsic effect should be directly related to the absorbed laser fluence and thus the photoemission

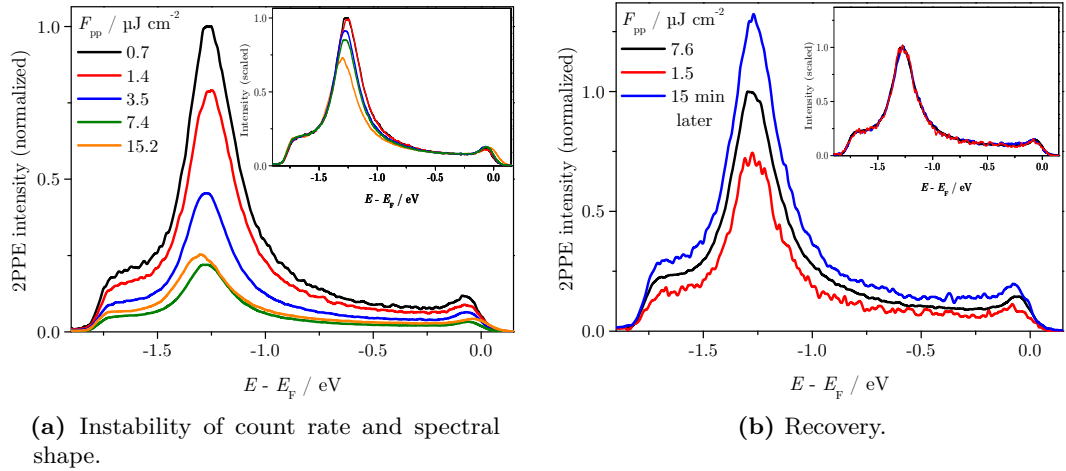


Figure A.10: Angle-integrated SH-2PPE spectroscopy of the low fluence dependence of Ag(111). P-polarized light of $h\nu = 3.18 \text{ eV}$ is used (CSA is set to high resolution, see section 3.1). (a) A decrease of the count rate with increasing fluence is observed. All spectra are normalized to a reference fluence. The inset shows these data manually scaled to the spectral range of $E - E_F \approx -1.75 \text{ eV}$ to -1.50 eV to emphasize changes of the spectral shape. (b) A reduction of the absorbed fluence leads to a recovery of the count rate. The inset shows a scaled version of these data.

intensity is most likely the relevant parameter. The TiSe_2 data in figure A.5(c) show, that the strongest reduction is observed for the smaller fluences/count rates.

Processes within the CSA or its electronics for data acquisition are a possible source of spectral modifications. The different electrostatic lenses of the CSA influence how the photoelectrons are imaged on the detecting channeltron which signal is processed by amplifying and counting electronics. For instance, changes to the settings of the CSA controller adjusting these lenses may modify the spectral shape; especially selective reductions of the count rate are observed. The very slow establishment of the effect on TiSe_2 (time scale of hours) is in agreement to drifts of the electronics, e. g., controlling the electrostatic lenses or, more likely, charging within the CSA, for instance, at named electrostatic lens system or virtually anywhere within the UHV system (manipulator head, CSA entry, ...).

We conclude, that the energetically non-specific reduction of spectral intensity observed at small absorbed laser fluences is clearly not a sample specific effect and thus an extrinsic effect. We find the CSA and its electronics a likely source for such drifts. Nevertheless, because our observations in this addendum indicate that the reduction of intensity is independent on the energy of the photoelectrons, the drift is easily compen-

sated by normalization (see section 5.1.2-c) and thus we do not need to discuss such charging effects in more detail.

A.3.2-c A Closer Look on the Modification of Spectral Shape of Ag(111)

The inset of figure A.10(a) reveals distinct changes of the spectral shape of silver with increasing fluence—seemingly similar to the observations on TiSe₂. These spectra are normalized to the plateau at $E - E_F \approx -1.75$ eV to -1.50 eV. Up to a fluence of about $7.4 \mu\text{J cm}^{-2}$ we observe a reduction of the spectral weight of the dominant peak at $E - E_F \approx -1.25$ eV which is similar, even quantitatively, to the behavior of the Se $4p$ bands of TiSe₂. Interestingly, the spectrum acquired at the highest fluence of $15.2 \mu\text{J cm}^{-2}$ reveals a significant distortion leading to a shift of this peak to higher and shift of the peak close to E_F to lower binding energy. This is an indication of the relevance of a sample extrinsic modification of the spectral shape, i. e. additionally to the thermal effect discussed in section 5.2.

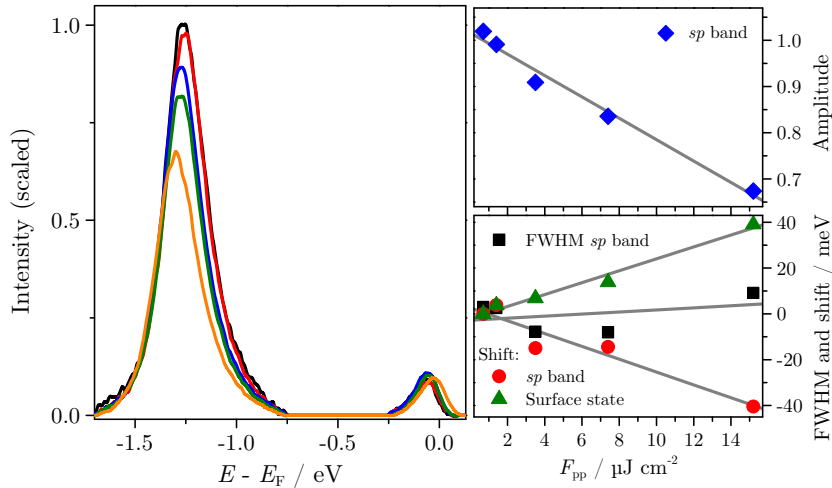


Figure A.11: Background corrected spectra from figure A.10(a). We use a linear background in the energetic range of the two peaks, in between the spectral background signal is subtracted. The range of the linear background for both peaks is fixed to reduce artifacts introduced by the correction. The right hand insets show the relative amplitude, center energy and FWHM of the sp band derived peak, as well as the energy of the Surface state. These data are derived from a fit.

Applying background correction to the data in figure A.10(a)—the outcome is presented in figure A.11—the spectral modifications can be fitted and compared to temperature dependent data by Matzdorf et al. [244] and Paniago et al. [37]. First of all the linear behavior of the investigated spectral features is in good agreement with the expectation for a temperature increase. The corresponding sp band of Cu(100) [244] shows a clear

decrease of the amplitude of the peak and a very small simultaneous increase of its FWHM in good qualitative agreement to the Ag(111) data.

Temperature dependent 2PPE spectroscopy of Ag(111) by Pontius et al. [189] reveals a shift to higher binding energies for the *sp* band and an energy reduction of the surface state. Furthermore, a reduction of the amplitude of the *sp* band with temperature is evident. These temperature dependent spectra show a very good qualitative agreement to our fluence dependent experiment which suggests an explanation of our data by heat-up of the silver crystal. A quantitative analysis shows, however, that the magnitude of the effects is too big. Please note, that we rule out space charging as the source of these spectral modifications (after all, the photoelectron count rate is 1–2 orders of magnitude higher than for TiSe₂), because space charging leads to a broadening of the spectral feature of the order of magnitude of the energetic shifts [277], which is obviously not observed in figure A.11.

We analyzed the data presented by Pontius et al. [189] and extracted temperature coefficients for the energetic shift and the amplitude of the *sp* band. We extract $\Delta E_{c,sp} = (-7.0 \pm 0.9) \times 10^{-5} \text{ eV K}^{-1}$, a value comparable to the TMDCs investigated in this work (see section 5.1.4–d). Our fluence dependent experiment reveals an energetic shift of approximately -40 meV which corresponds, using $\Delta E_{c,sp}$, to a temperature increase of $\Delta T = (576 \pm 70) \text{ K}$ which emphasizes that the fluence induced energetic shift of this band is actually unexpectedly big.

Paniago et al. [37] reported a temperature coefficient of about $17 \times 10^{-5} \text{ eV K}^{-1}$ for the energy of the Shockley surface state and approximately $26 \times 10^{-5} \text{ eV K}^{-1}$ for the low binding energy edge of the *sp* band. The absolute value of the energetic shift of both spectral features is about 40 meV . For the surface state a temperature increase of approximately 234 K at a fluence of $F_{pp} = 15.2 \mu\text{J cm}^{-2}$ is derived. If we assume the energy of the *sp* band center for its edge, a heat-up of $\Delta T \approx 224 \text{ K}$ is derived.⁷

We have also extracted the temperature coefficient of the amplitude of the *sp* band of Ag(111) from reference [189]. For comparability to our data we normalized the amplitude at different temperatures to the corresponding spectral plateau [refer to figure A.10(a)] and we referred the amplitude ratio to the room temperature amplitude ($\tilde{I}_{\text{max,RT}}$ in appendix A.1.1–a). The amplitude at $T_{\text{RT}} = 296 \text{ K}$ is calculated by linear interpolation. We derive a temperature coefficient of $\Delta \tilde{I}_{\text{max,RT}} = (-2.0 \pm 0.1) \times 10^{-3} \text{ K}^{-1}$, again, this value agrees nicely to our TMDC data in section 5.1.4–d. This yields a temperature

⁷Please note, that the energetic shift of the *sp* band observed in one-photon photoemission (1PPE) spectra by Paniago et al. [37] is of the wrong sign with respect to our 2PPE data. Instead of a decrease of binding energy an increase is reported. The peak observed in our spectra originates from a resonant excitation from within the lower into the upper *sp* band at $k_{\perp} \neq 0$ [278]. The peculiar surface perpendicular dispersion of both bands is known to lead to unexpected behavior in photon energy dependent 2PPE experiments [188]. As the change in energy of the corresponding spectral feature results from a direct transition between the lower and upper *sp* band which form the band gap of Ag(111) which is reduced upon heating [37] {this is also the case for Cu(111) [33]}. Indeed, the 2PPE experiment in reference [189] agrees to our observation.

increase corresponding to the laser induced reduction of amplitude of about 30% at $F_{pp} = 15.2 \mu\text{J cm}^{-2}$ of approximately $\Delta T = (150 \pm 6) \text{ K}$. Please note, that a reduction of spectral weight to about 70% at this fluence is observed both for the *sp* band of Ag(111) and the Se 4*p* bands of TiSe₂ (see section 5.2.2), although these features are energetically rather separated (roughly about 1 eV). Additionally, the surface state of Ag(111) does not show the loss of amplitude expected for such a severe temperature increase, which is a hint at a much less pronounced thermal effect.

In conclusion we find for both TiSe₂ and Ag(111) a good agreement for the spectral modifications upon the increase of the absorbed fluence with data on the temperature dependence. However, we make two puzzling observations:

- (i) The spectral shape changes rather slowly within several minutes (see figures A.8 and A.9) which seems to be unlikely for a laser induced heat-up of the sample by heat accumulation.
- (ii) The observed spectral modifications are surprisingly strong. A comparison of the observed changes to temperature dependent data suggests a very high temperature increase.

The TiSe₂ data presented in figure 5.32 in section 5.2.2 show, that the amplitude at fluences below about $15 \mu\text{J cm}^{-2}$ decreases much faster than expected from the temperature scale established by the increase of the work function—this is only observed upon slowly increasing the fluence beginning at the lowest values, i. e. as long the system is not stabilized. This observation is further supported by a similar experiment on Ag(111). The spectral shape stabilizes rather fast within only minutes. We attribute this to the establishment of thermal equilibrium upon changing the fluence (see section A.3.4) which takes some time, because it depends on equilibration of the heat dissipation and absorption. The magnitude of the modifications, however, suggest an additional contribution. The temperature dependence of spectroscopic data of this system reported in several references is compatible with a sample temperature increase of approximately 150 K to 230 K—even up to 570 K—at a fluence of only $15 \mu\text{J cm}^{-2}$. Our approximation of the sample heat-up in section 5.2.2 shows that such a big temperature increase is not expected at these fluences, even for the layered TiSe₂ crystals which are worse heat conductors. Therefore, although the spectral modifications correspond to thermal effects, their magnitude is significantly exaggerated for fluences below about $15 \mu\text{J cm}^{-2}$. We will now discuss, why we believe this to be a consequence of the instability of the CSA.

A.3.3 Influence of the CSA on the Spectral Shape at Low Fluence

At low fluences ($F_{pp} \lesssim 15 \mu\text{J cm}^{-2}$) the spectral shape is modified on a timescale of minutes, i. e. these changes are not instantaneous, in contrast to the high fluences for

which the analyzer allows for stable acquisition of data (see section 5.2.2). Using data of Ag(111) and TiSe₂ we have shown, that the observed modifications are also too pronounced to be explained by an increase of sample temperature alone. Considering that we actually expect a smaller temperature increase from the other spectral features and that the deviating, exaggerated effect is observed on the most prominent spectral feature of both samples, we find the instability of the CSA a likely explanation for this effect. This is supported by experimental observation: by detuning the settings of the electrostatic lens system of the CSA the shape of the photoemission spectra can be severely changed. Drifts of the CSA electronics controlling those lenses is thus sufficient to explain such spectral distortions. The very slow establishment of the modifications also hints at a sample extrinsic effect. We interpret this in terms of a rather small temperature increase, superimposed by an extrinsic effect—it is the latter we like to discuss here in more detail.

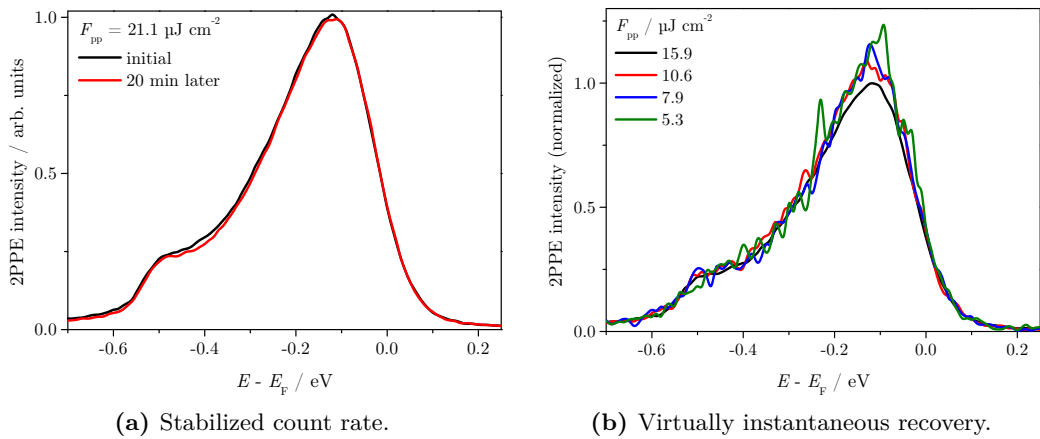


Figure A.12: (a) For $F_{pp} \gtrsim 21.1 \mu\text{J cm}^{-2}$ the 2PPE intensity finally stabilizes, i. e. the slow count rate decrease ceases. (b) In this fluence range an immediate recovery of spectral modifications is observed upon lowering of the fluence. The integration time used is similar to the case presented in figure A.9.

A closer look at the intermediate fluence range of about $15 \mu\text{J cm}^{-2}$ to $25 \mu\text{J cm}^{-2}$ shown in figure A.6(c) reveals a saturation of the reduction of the amplitude of the Se $4p$ bands. Furthermore, this fluence range marks the stabilization of the count rate reduction [see figure A.5(c)] which undergoes only minor changes in this fluence regime and finally stabilizes for the higher fluences. Figure A.12(a) demonstrates this stabilization for spectra acquired at a fluence of $21.1 \mu\text{J cm}^{-2}$. The long-term instability observed in figure A.7 for a lower fluence is definitely absent. Also, in both cases absolute intensities are shown, i. e. the both traces are virtually identical without normalization. However, there is a subtle change in the spectral shape to which we return shortly.

Furthermore, upon lowering of the absorbed laser fluence from $F_{pp} = 15.9 \mu\text{J cm}^{-2}$ to $10.6 \mu\text{J cm}^{-2}$, $7.9 \mu\text{J cm}^{-2}$ and $5.3 \mu\text{J cm}^{-2}$ (the initial fluence is always set in between the successive measurements) we find a virtually instantaneous recovery of the intensity reduction of the amplitude of the Se $4p$ bands; the data is presented in figure A.12(b). To speed up data acquisition only one experimental run is performed and the time needed to change the incident laser power is reduced to 30 s which is only half of what has been needed in case of the low fluence data in figure A.9, i. e. this experiment clearly shows, that the recovery is much faster than in case of low fluences and no delay of establishment and recovery of the shape modification is present.

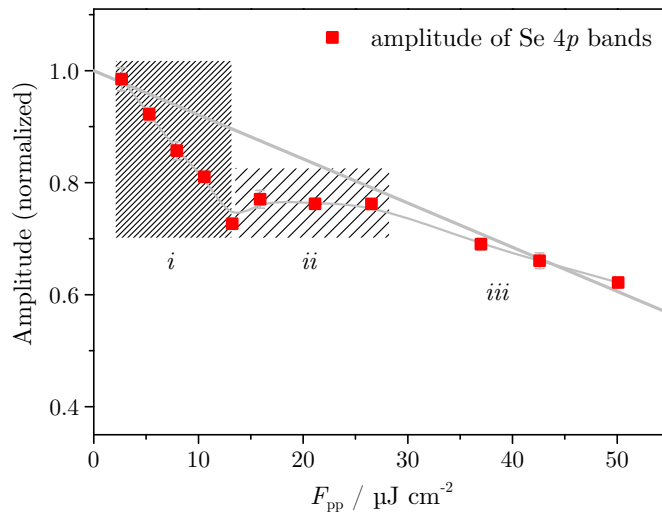


Figure A.13: The amplitude of the Se $4p$ bands for increasing absorbed fluence. A linear fit (see text) is included. We identify deviations (*i*, *ii*; dashed) from and good agreement (*iii*) to the expected linear behavior.

Figure A.13 presents the fluence dependent amplitude of the Se $4p$ bands in as acquired by slowly increasing the fluence at room temperature. This data is discussed and compared to fully stabilized data in section 5.2.2. Our findings in named section support a linear fluence dependence. By fitting the amplitude at the lowest and the three highest fluence values—the most stable data—we derive significant deviations for the fluences in between. We identify the low fluence regime (*i*, densely dashed) and the intermediate saturation of the spectral shape (*ii*, lightly dashed). For high fluences the spectra are stable (*iii*, see section 5.2.2).

This representation emphasizes the exaggeration of the intensity decrease of the amplitude for low fluences. The slope of the curve is much steeper than at high fluences. The intermediate fluence range (*ii*) compensates the too intense initial decrease by connecting the unstable low fluence to the stable high fluence regime. This observation further supports our interpretation in terms of an extrinsic CSA drift. We interpret

the behavior observed in figure A.13 as a stabilization of these extrinsic effects. The actual thermal modification of the spectra is masked by a stronger change of spectral shape induced by instabilities of the CSA. The observed plateau in this figure may be interpreted in terms of a diminishing of these extrinsic effects, transferring the spectral shape to the expected thermal behavior. This becomes all the more obvious if starting the experiment from already stable conditions, i. e. by starting at high fluences and quickly reducing the fluence successively (see section 5.2.2).

A.3.4 Acquisition of Stable Spectra

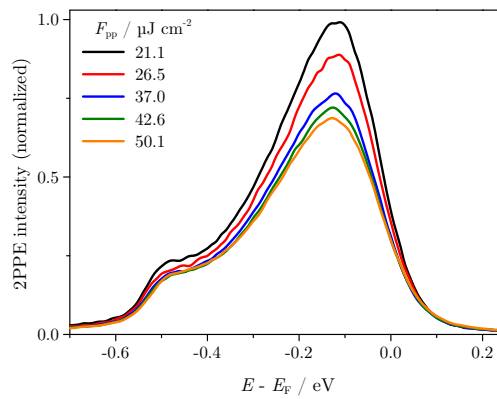


Figure A.14: After reaching a threshold fluence of about $25 \mu\text{J cm}^{-2}$, the overall spectral intensity stabilizes. The spectra are normalized to a reference fluence. Normalization to the plateau intensity is not necessary—these stable spectra are directly comparable.

Figure A.13 showed that for fluences above approximately $25 \mu\text{J cm}^{-2}$ the instabilities complicating our fluence dependent experiment finally vanish. In contrast to our observations at low fluences, the spectral modifications are not established slowly, but seem to be instantaneous. Figure A.14 reproduces spectra from figure A.5(c) for the high fluences, normalized with respect to the absorbed fluence, on a linear intensity scale. These spectra are acquired without the need of stabilization over hours and they are finally comparable (for $F_{\text{pp}} \gtrsim 25 \mu\text{J cm}^{-2}$) using only normalization to a reference fluence. This is nicely demonstrated by the agreement of the plateau intensities—normalization to this intensity is not necessary.

By switching between high and low fluences within the stable range discussed here, we observe virtually instantaneous spectral modifications and recovery thereof in figure A.15(a). Reduction of the fluence (*i*) leads to a recovery of the spectral shape (orange, note the decrease of the work function) which does not change within minutes (red). Increase to the initial fluence (black, refer to gray) reestablishes the modified spectrum.⁸

⁸The small increase of the plateau observed in this case shows, that the instability still persists at

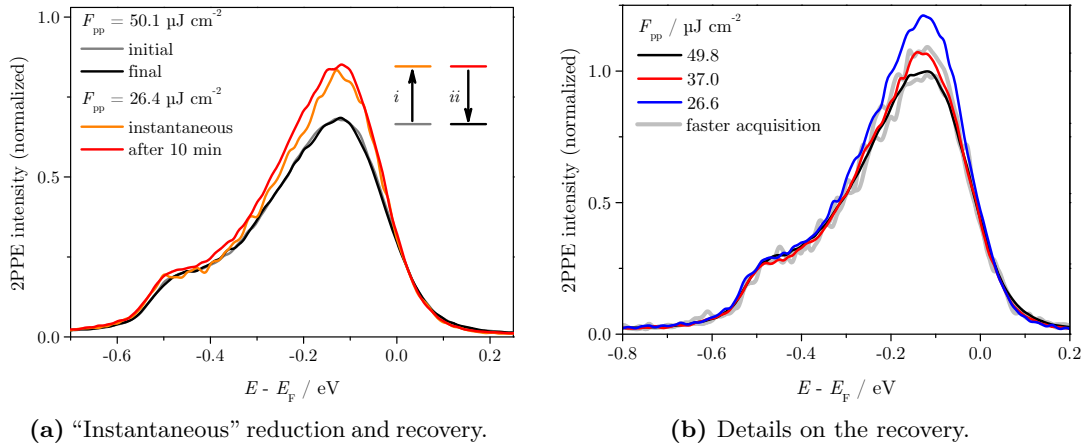


Figure A.15: (a) At stabilized count rates the reduction and recovery of the amplitude is virtually instantaneous (fluence de-/increase: i and ii). (b) Reduction of the laser fluence instantly recovers the amplitude of the Se $4p$ bands in contrast to very low fluences (see figure A.8a). The initial fluence $F_{pp} = 49.8 \mu\text{J cm}^{-2}$ is applied in between the lower fluences; the dark time during changing the incident fluence is kept as short as possible (below 18 s). The gray curves show spectra at an integration time reduced by a factor of ten. Please note, that both gray curves are slightly scaled with respect to the colored curves. This is necessary to compensate for the lower count rates detected at the reduced integration time employed in this case.

The speed of these modifications is investigated in more detail in figure A.15(b). Here, the fluence is initially set to $F_{pp} = 49.8 \mu\text{J cm}^{-2}$ in between the subsequent fluence reductions to ensure stability. If the recovery upon fluence reduction was as slow as observed for the low fluence regime, we should initially see an almost unchanged spectral shape, followed by a slow recovery. This is clearly not the case. In contrast to the slow spectral changes within minutes and hours as observed for low fluences, the observed modifications for high fluences can be considered instantaneous.

An additional experiment (not shown here), similar to the data presented in figure A.9b for low fluences, investigated the reestablishment of spectral instability after blocking of the incident laser. We observe a very similar behavior at a high fluence ($F_{pp} = 49.7 \mu\text{J cm}^{-2}$). A increase of intensity is observed after blocking the laser for about 3 min and, while the intensity recovers rather fast after illumination of the sample by the laser, the spectral shape stays modified a little longer on a second to minutes timescale. By simultaneously reducing the fluence we observe a virtually instantaneous change of spectral shape; only the general increase of intensity is delayed. Therefore, blocking the laser even for short periods of time leads to instabilities of the CSA and a short

$F_{pp} \approx 26 \mu\text{J cm}^{-2}$, leading to an increases of the intensity at this fluence.

stabilization at the high fluence of a few minutes is necessary. The very short time necessary to reestablish the spectral shape after blocking of the laser may be attributed to the heat-up of the sample by the absorbed laser which is governed by the thermal equilibrium of sample, the heat dissipation to the surroundings of the sample and the energy introduced by the laser pulses (see section 5.2 for details).

Why is the heat-up of the sample so slow? The laser beam is absorbed very locally at a small area of the sample surface and with a limited depth of penetration, i. e. only within this small crystal volume the energy of the laser is deposited and a non-equilibrium electron distribution is generated. By thermalization of the electrons and transfer of this energy to the lattice, the latter is finally heated (see e. g. reference [130, 132, 137]). If the heat is fully dissipated between the laser pulses (repetition rate about 80 MHz, corresponding to 12.5 ns) we would not expect any increase of the sample temperature within these static photoemission experiments, as we only observe the initial, non-equilibrium state (see section 5.2). However, heat dissipation is hindered in two ways: (i) the manipulator holding the sample is thermally isolation by a sapphire disc—necessary to separate the liquid nitrogen cooling (see section 3.1.1) from the resistive heating—, and (ii) the layered structure of these TMDCs leads to a strong anisotropy, for example, in the electrical conductivity {typical conductivity ratio with respect to the layer planes is $\sigma_{\parallel}/\sigma_{\perp} \approx 10^2$ to 10^3 for group IV–VI compounds [279]}, i. e. a similar anisotropy for the thermal conductivity is expected (at least) for the electronic contribution, because of the proportionality of thermal and electrical conductivity in metals as described by the Wiedemann-Franz law [172]. The incomplete dissipation of heat therefore leads to the formation of a thermal equilibrium at an increased temperature of the sample. At very high fluences, as achieved with the amplifier system used in chapter 7, even a significant warm-up of the whole sample becomes directly measurable at an external temperature sensor (see also reference [246]).

A.3.5 Some Final Remarks on the Acquisition of Stable Photoemission Spectra

We find two possible methods of acquiring stable photoemission spectra, i. e. spectra not influenced by long-term drifts of the measured photoemission count rate and which yield comparable spectral shapes. The first approach is using a very low fluence in the range of $5 \mu\text{J cm}^{-2}$. We have seen in this section, that the spectral shape and the photoemission count rate seem to stay stable at least for several tens of minutes. The temperature dependent experiment in section 5.1 further shows stability over several hours. However, stability needs to be checked in this case, as we also observe instabilities forming during the experiment. Nevertheless, such a low fluence is usually a good choice for experiments, where we aim at reducing the laser induced modifications of a sample. This method is employed for the two-color pump–probe experiments presented in section 6.2 where we

A.3 Count Rate Drifts of the Experimental Setup—Stable Photoemission Using the CSA

use a small fluence for the probe pulse and a high fluence of the pump pulse. The pump pulse does not generate photoelectrons, i. e. it does not induce the instability of the CSA.

The second approach is stabilization of the CSA at a high fluence— $F_{pp} \approx 50 \mu\text{J cm}^{-2}$ is found to be well suited. If the sample is continuously illumination by the laser we derive stable conditions. This is especially useful for studying laser induced modifications of the photoemission spectrum. By beginning at the highest fluence and then decreasing the fluence well comparable data is acquired. However, for low fluences the instability of the CSA is reestablished—the intensity increases very slowly within hours, i. e. by sufficiently fast acquisition of the data within minutes satisfactory stable spectra are derived. This method is of interest in section 5.2 which focuses on the fluence dependence of the spectroscopic data and for time resolved experiments in the autocorrelated mode (see section 6.1) where the system is stabilized using both pump and probe pulse incident on the sample.

B List of Abbreviations

1D	one-dimensional
1PPE	one-photon photoemission
2D	two-dimensional
2PPE	two-photon photoemission
3D	three-dimensional
3PPE	three-photon photoemission
4PPE	four-photon photoemission
ARPES	angle-resolved photoemission spectroscopy
AR-2PPE	angle-resolved two-photon photoemission
BBO	β -barium borate
CDW	charge density wave
CSA	cylindrical sector analyzer
cw	continuous wave
EDC	energy distribution curve
FFT	fast Fourier transform
FHG	fourth harmonic generation
FS	fused silica
FWHM	full width at half maximum
GVD	group velocity dispersion
HSA	hemispherical energy analyzer
HH	high harmonic

HHG	high harmonic generation
IPE	inverse photoemission
IR	infrared, below about 1.6 eV [280]
LBO	lithium triborate
LEED	low energy electron diffraction
MCP	micro-channel plate
ML	monolayer
PLD	periodic lattice distortion
QWS	quantum well state
sech	hyperbolic secant
SH	second harmonic
SHG	second harmonic generation
TAR-2PPE	time- and angle-resolved two-photon photoemission
TH	third harmonic
THG	third harmonic generation
TMDC	transition metal dichalcogenide
TOD	third order dispersion
TR-2PPE	time-resolved two-photon photoemission
UHV	ultrahigh vacuum
UPS	ultraviolet photoelectron spectroscopy
UV	ultraviolet, about 3.1 eV to 12.4 eV [280]
VUV	vacuum ultraviolet, approximately 6.2 eV to 124 eV [280]
WAM	wide angle mode
XPS	X-ray photoelectron spectroscopy
EUV	extreme ultraviolet, roughly 10.2 eV to 124 eV [280]

Bibliography

- [1] E. Doni and R. Girlanda. *Electronic Energy Bands*, 1–171. D. Reidel Publishing, Dordrecht, Holland, 1986
- [2] M. Grioni and J. Voit. *High-Resolution Photoemission Studies of Low-Dimensional Systems*, chapter 5, 209–281. In [281] (2000)
- [3] O. Anderson, G. Karschnick, R. Manzke, and M. Skibowski. ‘The phase transition in the electronic structure of $1T$ -TiSe₂.’ *Solid State Commun.* **53**(4) 339 (1985)
- [4] L. Perfetti, P. A. Loukakos, M. Lisowski, U. Bovensiepen, H. Berger, S. Biermann, P. S. Cornaglia, A. Georges, and M. Wolf. ‘Time Evolution of the Electronic Structure of $1T$ -TaS₂ through the Insulator-Metal Transition.’ *Phys. Rev. Lett.* **97**(6) 067402 (2006)
- [5] G. Li, W. Z. Hu, D. Qian, D. Hsieh, M. Z. Hasan, E. Morosan, R. J. Cava, and N. L. Wang. ‘Semimetal-to-Semimetal Charge Density Wave Transition in $1T$ -TiSe₂.’ *Phys. Rev. Lett.* **99**(2) 027404 (2007)
- [6] D. Qian, D. Hsieh, L. Wray, E. Morosan, N. L. Wang, Y. Xia, R. J. Cava, and M. Z. Hasan. ‘Emergence of Fermi Pockets in a New Excitonic Charge-Density-Wave Melted Superconductor.’ *Phys. Rev. Lett.* **98**(11) 117007 (2007)
- [7] K. Rossnagel, L. Kipp, and M. Skibowski. ‘Charge-density-wave phase transition in $1T$ -TiSe₂: Excitonic insulator versus band-type Jahn-Teller mechanism.’ *Phys. Rev. B* **65**(23) 235101 (2002)
- [8] F. J. Di Salvo, D. E. Moncton, and J. V. Waszczak. ‘Electronic properties and superlattice formation in the semimetal TiSe₂.’ *Phys. Rev. B* **14**(10) 4321 (1976)
- [9] A. Zunger and A. J. Freeman. ‘Band structure and lattice instability of TiSe₂.’ *Phys. Rev. B* **17**(4) 1839 (1978)
- [10] T. E. Kidd, T. Miller, M. Y. Chou, and T.-C. Chiang. ‘Electron-Hole Coupling and the Charge Density Wave Transition in $TiSe_2$.’ *Phys. Rev. Lett.* **88**(22) 226402 (2002)

- [11] H. Cercellier, C. Monney, F. Clerc, C. Battaglia, L. Despont, M. G. Garnier, H. Beck, P. Aebi, L. Patthey, H. Berger, and L. Forró. ‘Evidence for an Excitonic Insulator Phase in $1T$ -TiSe₂.’ *Phys. Rev. Lett.* **99**(14) 146403 (2007)
- [12] M. M. Traum, G. Margaritondo, N. V. Smith, J. E. Rowe, and F. J. Di Salvo. ‘TiSe₂: Semiconductor, semimetal, or excitonic insulator.’ *Phys. Rev. B* **17** 1836 (1978)
- [13] S. Danzenbächer, S. L. Molodtsova, K. Koepernik, Y. Tamm, and C. Laubschat. ‘Electronic Structure of TiSe₂ and TiSe₂ Intercalated with Eu.’ *Mol. Cryst. Liq. Cryst.* **341** 45 (2000)
- [14] T. Pillo, J. Hayoz, H. Berger, F. Lévy, L. Schlapbach, and P. Aebi. ‘Photoemission of bands above the Fermi level: The excitonic insulator phase transition in $1T$ -TiSe₂.’ *Phys. Rev. B* **61**(23) 16213 (2000)
- [15] J. C. E. Rasch, T. Stemmler, L. Müller, B. and Dudy, and R. Manzke. ‘ $1T$ -TiSe₂: Semimetal or Semiconductor?’ *Phys. Rev. Lett.* **101**(23) 237602 (2008)
- [16] M. H. Whangbo and E. Canadell. ‘Analogies between the concepts of molecular chemistry and solid-state physics concerning structural instabilities. Electronic origin of the structural modulations in layered transition metal dichalcogenides.’ *J. Am. Chem. Soc.* **114**(24) 9587 (1992)
- [17] W. Drube, I. Schäfer, G. Karschnick, and M. Skibowski. ‘Inverse photoemission study of the conduction bands in TiSe₂.’ *Phys. Rev. B* **30**(10) 6248 (1984)
- [18] D. Straub, M. Skibowski, F. J. Himpsel, and W. Drube. ‘Interlayer interaction in the conduction bands of layered transition-metal dichalcogenides studied by inverse photoemission.’ *Phys. Rev. B* **31**(12) 8254 (1985)
- [19] W. Drube, I. Schäfer, and M. Skibowski. ‘The experimental band structure of occupied and unoccupied states of titanium dichalcogenides.’ *J. Phys. C* **20**(26) 4201 (1987)
- [20] T. Fauster and W. Steinmann. *Electromagnetic Waves: Recent Developments in Research, Volume 2: Photonic Probes of Surfaces, Two-photon photoemission spectroscopy of image states*, volume 2, chapter 8, 347–411. Elsevier, Amsterdam, 1995. Preprint
- [21] R. W. Schoenlein, J. G. Fujimoto, G. L. Eesley, and T. W. Capehart. ‘Femtosecond Studies of Image-Potential Dynamics in Metals.’ *Phys. Rev. Lett.* **61**(22) 2596 (1988)

-
- [22] U. Höfer, I. L. Shumay, C. Reuß, U. Thomann, W. Wallauer, and T. Fauster. ‘Time-Resolved Coherent Photoelectron Spectroscopy of Quantized Electronic States on Metal Surfaces.’ *Science* **277**(5331) 1480 (1997)
- [23] J. D. McNeill, R. L. Lingle, N.-H. Ge, C. M. Wong, R. E. Jordan, and C. B. Harris. ‘Dynamics and Spatial Distribution of Electrons in Quantum Wells at Interfaces Determined by Femtosecond Photoemission Spectroscopy.’ *Phys. Rev. Lett.* **79**(23) 4645 (1997)
- [24] M. Weinelt, C. Reuss, M. Kutschera, U. Thomann, I. L. Shumay, T. Fauster, U. Höfer, F. Theilmann, and A. Goldmann. ‘Decay and dephasing of image-potential states due to surface defects and disorder.’ *Appl. Phys. B* **68**(3) 377 (1999)
- [25] K. Ertel, U. Kohl, J. Lehmann, M. Merschdorf, W. Pfeiffer, A. Thon, S. Voll, and G. Gerber. ‘Time-resolved two-photon photoemission spectroscopy of HOPG and Ag nanoparticles on HOPG.’ *Appl. Phys. B* **68**(3) 439 (1999)
- [26] M. Bauer, S. Pawlik, and M. Aeschlimann. ‘Resonance lifetime and energy of an excited Cs state on Cu(111).’ *Phys. Rev. B* **55**(15) 10040 (1997)
- [27] S. Ogawa, H. Nagano, and H. Petek. ‘Phase and Energy Relaxation in an Antibonding Surface State: Cs/Cu(111).’ *Phys. Rev. Lett.* **82**(9) 1931 (1999)
- [28] E. Knoesel, A. Hotzel, T. Hertel, M. Wolf, and G. Ertl. ‘Dynamics of photoexcited electrons in metals studied with time-resolved two-photon photoemission.’ *Surf. Sci.* **368** 76 (1996). 8th International Conference on Vibrations at Surfaces, Birmingham, England, Jun. 23–27, 1996
- [29] C. Frischkorn and M. Wolf. ‘Femtochemistry at Metal Surfaces: Nonadiabatic Reaction Dynamics.’ *Chem. Rev.* **106**(10) 4207 (2006)
- [30] J. P. Gauyacq, A. G. Borisov, and M. Bauer. ‘Excited states in the alkali/noble metal surface systems: A model system for the study of charge transfer dynamics at surfaces.’ *Prog. Surf. Sci.* **82**(4–6) 244 (2007)
- [31] F. Schmitt, P. S. Kirchmann, U. Bovensiepen, R. G. Moore, L. Rettig, M. Krenz, J.-H. Chu, N. Ru, L. Perfetti, D. H. Lu, M. Wolf, I. R. Fisher, and Z.-X. Shen. ‘Transient Electronic Structure and Melting of a Charge Density Wave in TbTe₃.’ *Science* **321**(5896) 1649 (2008)
- [32] P. Heimann and H. Neddermeyer. ‘Temperature effects on ultraviolet photoemission from gold.’ *Solid State Commun.* **26**(5) 279 (1978)

- [33] J. A. Knapp, F. J. Himpsel, A. R. Williams, and D. E. Eastman. ‘Temperature dependence of bulk and surface energy bands in copper using angle-resolved photoemission.’ *Phys. Rev. B* **19**(6) 2844 (1979)
- [34] N. E. Christensen. ‘Photoemission from Au(111) and (110). Temperature effects.’ *Phys. Rev. B* **20**(8) 3205 (1979)
- [35] R. Courths and S. Hüfner. ‘Photoemission experiments on copper.’ *Phys. Rep.* **112**(2) 53 (1984)
- [36] A. Goldmann and R. Matzdorf. ‘Temperature effects in angle-resolved photoemission spectra from metals.’ *Prog. Surf. Sci.* **42**(1–4) 331 (1993)
- [37] R. Paniago, R. Matzdorf, G. Meister, and A. Goldmann. ‘Temperature dependence of Shockley-type surface energy bands on Cu(111), Ag(111) and Au(111).’ *Surf. Sci.* **336**(1–2) 113 (1995)
- [38] K. Rossnagel. ‘Suppression and emergence of charge-density waves at the surfaces of layered $1T$ -TiSe₂ and $1T$ -TaS₂ by in situ Rb deposition.’ *New J. Phys.* **12**(12) 125018 (2010)
- [39] E. Möhr-Vorobeva, S. L. Johnson, P. Beaud, U. Staub, R. De Souza, C. Milne, G. Ingold, J. Demsar, H. Schaefer, and A. Titov. ‘Nonthermal Melting of a Charge Density Wave in TiSe₂.’ *Phys. Rev. Lett.* **107** 036403 (2011)
- [40] J. Demsar, L. Forró, H. Berger, and D. Mihailovic. ‘Femtosecond snapshots of gap-forming charge-density-wave correlations in quasi-two-dimensional dichalcogenides $1T - \text{tas}_2$ and $2H - \text{tase}_2$.’ *Phys. Rev. B* **66** 041101 (2002)
- [41] H. Schäfer, V. V. Kabanov, M. Beyer, K. Biljakovic, and J. Demsar. ‘Disentanglement of the Electronic and Lattice Parts of the Order Parameter in a 1D Charge Density Wave System Probed by Femtosecond Spectroscopy.’ *Phys. Rev. Lett.* **105**(6) 066402 (2010)
- [42] M. Eichberger, H. Schaefer, M. Krumova, M. Beyer, J. Demsar, H. Berger, G. Moriena, G. Sciaini, and R. J. D. Miller. ‘Snapshots of cooperative atomic motions in the optical suppression of charge density waves.’ *Nature* **468**(7325) 799 (2010)
- [43] A. Rundquist, C. G. Durfee, Z. Chang, C. Herne, S. Backus, M. M. Murnane, and H. C. Kapteyn. ‘Phase-Matched Generation of Coherent Soft X-rays.’ *Science* **280**(5368) 1412 (1998)
- [44] M. Bauer. ‘Femtosecond ultraviolet photoelectron spectroscopy of ultra-fast surface processes.’ *J. Phys. D: Appl. Phys.* **38**(16) R253 (2005)

-
- [45] R. A. Bartels, A. Paul, H. Green, H. C. Kapteyn, M. M. Murnane, S. Backus, I. P. Christov, Y. Liu, D. Attwood, and C. Jacobsen. ‘Generation of Spatially Coherent Light at Extreme Ultraviolet Wavelengths.’ *Science* **297**(5580) 376 (2002)
- [46] L. Miaja-Avila, C. Lei, M. Aeschlimann, J. L. Gland, M. M. Murnane, H. C. Kapteyn, and G. Saathoff. ‘Laser-Assisted Photoelectric Effect from Surfaces.’ *Phys. Rev. Lett.* **97**(11) 113604 (2006)
- [47] L. Miaja-Avila, J. Yin, S. Backus, G. Saathoff, M. Aeschlimann, M. M. Murnane, and H. C. Kapteyn. ‘Ultrafast studies of electronic processes at surfaces using the laser-assisted photoelectric effect with long-wavelength dressing light.’ *Phys. Rev. A* **79**(3) 030901 (2009)
- [48] N. A. Papadogiannis, B. Witzel, C. Kalpouzos, and D. Charalambidis. ‘Observation of Attosecond Light Localization in Higher Order Harmonic Generation.’ *Phys. Rev. Lett.* **83** 4289 (1999)
- [49] M. Drescher, M. Hentschel, R. Kienberger, G. Tempea, C. Spielmann, G. A. Reider, P. B. Corkum, and F. Krausz. ‘X-ray Pulses Approaching the Attosecond Frontier.’ *Science* **291**(5510) 1923 (2001)
- [50] P. M. Paul, E. S. Toma, P. Breger, G. Mullot, F. Augé, P. Balcou, H. G. Muller, and P. Agostini. ‘Observation of a Train of Attosecond Pulses from High Harmonic Generation.’ *Science* **292**(5522) 1689 (2001)
- [51] S. Mathias, C. La-O-Vorakiat, P. Grychtol, P. Granitzka, E. Turgut, J. M. Shaw, R. Adam, H. T. Nembach, M. E. Siemens, S. Eich, C. M. Schneider, T. J. Silva, M. Aeschlimann, M. M. Murnane, and H. C. Kapteyn. ‘Probing the timescale of the exchange interaction in a ferromagnetic alloy.’ *P. Natl. Acad. Sci.* (2012). DOI: 10.1073/pnas.1201371109
- [52] C. La-O-Vorakiat, E. Turgut, C. A. Teale, H. C. Kapteyn, M. M. Murnane, S. Mathias, M. Aeschlimann, C. M. Schneider, J. M. Shaw, H. T. Nembach, and T. J. Silva. ‘Ultrafast Demagnetization Measurements Using Extreme Ultraviolet Light: Comparison of Electronic and Magnetic Contributions.’ *Phys. Rev. X* **2** 011005 (2012)
- [53] S. Mathias, M. Wiesenmayer, F. Deicke, A. Ruffing, L. Miaja-Avila, M. M. Murnane, H. C. Kapteyn, M. Bauer, and M. Aeschlimann. ‘Time and angle resolved photoemission spectroscopy using femtosecond visible and high-harmonic light.’ In ‘Yamada Conference LXIII: PIPT 2008,’ volume 148, 012042. IOP Publishing, 2009
- [54] T. Rohwer, S. Hellmann, M. Wiesenmayer, C. Sohrt, A. Stange, B. Slomski, A. Carr, Y. Liu, L. Miaja Avila, M. Källäne, S. Mathias, L. Kipp, K. Rossnagel, and M. Bauer.

- ‘Collapse of long-range charge order tracked by time-resolved photoemission at high momenta.’ *Nature* **471**(7339) 490 (2011)
- [55] C. Monney, H. Cercellier, F. Clerc, C. Battaglia, E. F. Schwier, C. Didiot, M. G. Garnier, H. Beck, P. Aebi, H. Berger, L. Forró, and L. Patthey. ‘Spontaneous exciton condensation in 1T-TiSe₂: BCS-like approach.’ *Phys. Rev. B* **79**(4) 045116 (2009)
- [56] J. A. Wilson and A. D. Yoffe. ‘The Transition Metal Dichalcogenides: Discussion and Interpretation of the Observed Optical, Electrical and Structural Properties.’ *Adv. Phys.* **18**(73) 193 (1969)
- [57] K. Rossnagel. ‘On the Electronic Structure of Layered Transition-Metal Compounds.’ habilitation treatise (2009). Christian-Albrechts-Universität zu Kiel
- [58] H. Isomäki, J. von Boehm, and P. Krusius. ‘Band structure of group IVA transition-metal dichalcogenides.’ *J. Phys. C* **12**(16) 3239 (1979)
- [59] N. Suzuki, A. Yamamoto, and K. Motizuki. ‘Electron-lattice interaction and the CDW state of 1T-TiSe₂.’ *Solid State Commun.* **49**(11) 1039 (1984)
- [60] C. M. Fang, R. A. de Groot, and C. Haas. ‘Bulk and surface electronic structure of 1T-TiS₂ and 1T-TiSe₂.’ *Phys. Rev. B* **56**(8) 4455 (1997)
- [61] C. del Pilar Ramírez García. *Ab initio Study of Alkali Diffusion and Intercalation on Transition Metal Dichalcogenides*. Ph.D. thesis, Christian-Albrechts-Universität zu Kiel (2003)
- [62] F. Clerc, C. Battaglia, H. Cercellier, C. Monney, H. Berger, L. Despont, M. G. Garnier, and P. Aebi. ‘Fermi surface of layered compounds and bulk charge density wave systems.’ *J. Phys.: Condens. Matter* **19**(35) 355002 (2007)
- [63] R. H. Friend and A. D. Yoffe. ‘Electronic properties of intercalation complexes of the transition metal dichalcogenides.’ *Adv. Phys.* **36**(1) 1 (1987)
- [64] R. B. Murray and A. D. Yoffe. ‘The band structures of some transition metal dichalcogenides: band structures of the titanium dichalcogenides.’ *J. Phys. C: Solid State Phys.* **5**(21) 3038 (1972)
- [65] C. Riekel. ‘Structure refinement of TiSe₂ by neutron diffraction.’ *J. Solid State Chem.* **17**(4) 389 (1976)
- [66] E. Pehlke, W. Schattke, O. Anderson, R. Manzke, and M. Skibowski. ‘Photoemission from the (001) surface of 1T-TiSe₂: Comparison of calculation with experiment.’ *Phys. Rev. B* **41**(5) 2982 (1990)

-
- [67] E. A. Marseglia. ‘Transition Metal Dichalcogenides and Their Intercalates.’ *Int. Rev. Phys. Chem.* **3**(2) 177 (1983)
- [68] A. H. Reshak and S. Auluck. ‘Electronic and optical properties of the $1T$ phases of TiS_2 , TiSe_2 , and TiTe_2 .’ *Phys. Rev. B* **68**(24) 245113 (2003)
- [69] E. Pehlke and W. Schattke. ‘The Effect of Frenkel Defects on the Electronic Structure of $1T$ - TiSe_2 .’ *Z. Phys. B* **66**(1) 31 (1987)
- [70] H. I. Starnberg, H. E. Brauer, L. J. Holleboom, and H. P. Hughes. ‘3D-to-2D transition by Cs intercalation of VSe_2 .’ *Phys. Rev. Lett.* **70**(20) 3111 (1993)
- [71] S. E. Stoltz, H. I. Starnberg, and L. J. Holleboom. ‘Evidence for Rb intercalation in TiTe_2 .’ *Europhys. Lett.* **64**(6) 816 (2003)
- [72] S. E. Stoltz, H. I. Starnberg, and L. J. Holleboom. ‘Rb intercalation of $1T$ - TaSe_2 studied by photoelectron spectroscopy.’ *Phys. Rev. B* **67**(12) 125107 (2003)
- [73] S. E. Stoltz, H. I. Starnberg, and L. J. Holleboom. ‘Rb deposition on TiSe_2 and TiTe_2 at 100 K and at room temperature studied by photoelectron spectroscopy.’ *Phys. Rev. B* **71**(12) 125403 (2005)
- [74] L. Perfetti, C. Rojas, A. Reggiani, L. Gavioli, H. Berger, G. Margaritondo, M. Gri-
oni, R. Gaál, L. Forró, and F. Rullier-Albenque. ‘High-resolution angle-resolved
photoemission investigation of the quasiparticle scattering processes in a model
Fermi liquid: $1T$ - TiTe_2 .’ *Phys. Rev. B* **64**(11) 115102 (2001)
- [75] Y. Koike, M. Okamura, T. Nakanomyo, and T. Fukase. ‘Log T Dependence of
Resistivity and Negative Magnetoresistance in the Layered Compound TiTe_2 .’ *J.*
Phys. Soc. Jpn. **52**(2) 597 (1983)
- [76] K. Rossnagel. ‘On the origin of charge-density waves in select layered transition-
metal dichalcogenides.’ *J. Phys.: Condens. Matter* **23**(21) 213001 (2011)
- [77] S. C. Bayliss and W. Y. Liang. ‘Symmetry dependence of optical transitions in
group 4B transition metal dichalcogenides.’ *J. Phys. C* **15**(6) 1283 (1982)
- [78] A. M. Ghorayeb and R. H. Friend. ‘Transport and optical properties of the
hydrazine intercalation complexes of TiS_2 , TiSe_2 and ZrS_2 .’ *J. Phys. C* **20**(26) 4181
(1987)
- [79] D. K. G. de Boer, C. F. van Bruggen, G. W. Bus, R. Coehoorn, C. Haas, G. A.
Sawatzky, H. W. Myron, D. Norman, and H. Padmore. ‘Titanium ditelluride: Band
structure, photoemission, and electrical and magnetic properties.’ *Phys. Rev. B*
29(12) 6797 (1984)

- [80] A. N. Titov and S. G. Titova. ‘Phase diagram and electronic properties of Ag_xTiTe_2 .’ *J. Alloys Compd.* **256**(1–2) 13 (1997)
- [81] G. Lucovsky, W. Y. Liang, R. M. White, and K. R. Pisharody. ‘Reflectivity studies of Ti- and Ta-dichalcogenides: Phonons.’ *Solid State Commun.* **19**(4) 303 (1976)
- [82] P. B. Allen and N. Chetty. ‘ TiTe_2 : Inconsistency between transport properties and photoemission results.’ *Phys. Rev. B* **50**(20) 14855 (1994)
- [83] A. N. Titov, A. N. Skomorokhov, A. A. Titov, S. G. Titova, and V. A. Semenov. ‘The influence of intercalation on the phonon spectrum of titanium dichalcogenides.’ *Phys. Solid State* **49**(8) 1532 (2007)
- [84] A. W. Overhauser. ‘Structure of Nuclear Matter.’ *Phys. Rev. Lett.* **4** 415 (1960)
- [85] W. Tremel and E. W. Finckh. ‘Ladungsdichtewellen: Elektrische Leitfähigkeit.’ *Chem. unserer Zeit* **38**(5) 326 (2004)
- [86] J. Kröger. ‘Electron–phonon coupling at metal surfaces.’ *Rep. Prog. Phys.* **69**(4) 899 (2006)
- [87] L. Fang, P. Zou, Y. Wang, L. Tang, Z. Xu, H. Chen, C. Dong, L. Shan, and H. Wen. ‘Competition of superconductivity and charge density wave order in Na_xTaS_2 single crystals.’ *Sci. Technol. Adv. Mater.* **6**(7) 736 (2005)
- [88] A. Titov, V. Konstantinov, V. Neverov, E. Neifeld, and L. Krasavin. ‘Possible Superconductivity in TiSe_2 Intercalated by Transition Metals.’ *J. Supercond. Nov. Magn.* **19**(1) 73 (2006)
- [89] T. Jeong and T. Jarlborg. ‘Varying Cu-Ti hybridization near the Fermi energy in Cu_xTiSe_2 : Results from supercell calculations.’ *Phys. Rev. B* **76**(15) 153103 (2007)
- [90] A. Pashkin, M. Porer, M. Beyer, K. W. Kim, A. Dubroka, C. Bernhard, X. Yao, Y. Dagan, R. Hackl, A. Erb, J. Demsar, R. Huber, and A. Leitenstorfer. ‘Femtosecond Response of Quasiparticles and Phonons in Superconducting $\text{YBa}_2\text{Cu}_3\text{O}_7 - \delta$ Studied by Wideband Terahertz Spectroscopy.’ *Phys. Rev. Lett.* **105**(6) 067001 (2010)
- [91] R. Claessen, R. O. Anderson, G.-H. Gweon, J. W. Allen, W. P. Ellis, C. Janowitz, C. G. Olson, Z. X. Shen, V. Eyert, M. Skibowski, K. Friemelt, E. Bucher, and S. Hüfner. ‘Complete band-structure determination of the quasi-two-dimensional Fermi-liquid reference compound TiTe_2 .’ *Phys. Rev. B* **54**(4) 2453 (1996)
- [92] B. I. Halperin and T. M. Rice. ‘Possible Anomalies at a Semimetal-Semiconductor Transition.’ *Rev. Mod. Phys.* **40** 755 (1968)

-
- [93] H. Mutka, L. Zuppiroli, P. Molinié, and J. C. Bourgoin. ‘Charge-density waves and localization in electron-irradiated $1T$ -TaS₂.’ *Phys. Rev. B* **23**(10) 5030 (1981)
- [94] N. G. Stoffel, S. D. Kevan, and N. V. Smith. ‘Experimental band structure of $1T$ -TiSe₂ in the normal and charge-density-wave phases.’ *Phys. Rev. B* **31**(12) 8049 (1985)
- [95] F. J. Di Salvo and J. V. Waszczak. ‘Transport properties and the phase transition in Ti_{1-x}M_xSe₂ (M =Ta or V).’ *Phys. Rev. B* **17**(10) 3801 (1978)
- [96] H. Petek and S. Ogawa. ‘Femtosecond time-resolved two-photon photoemission studies of electron dynamics in metals.’ *Prog. Surf. Sci.* **56**(4) 239 (1997)
- [97] P. Aebi, T. Pillo, H. Berger, and F. Lévy. ‘On the search for Fermi surface nesting in quasi-2D materials.’ *J. Electron Spectrosc. Relat. Phenom.* **117–118**(0) 433 (2001)
- [98] W. Kohn. ‘Excitonic Phases.’ *Phys. Rev. Lett.* **19** 439 (1967)
- [99] A. Bussmann-Holder and H. Büttner. ‘Charge-density-wave formation in TiSe₂ driven by an incipient antiferroelectric instability.’ *J. Phys.: Condens. Matter* **14**(34) 7973 (2002)
- [100] K. C. Kao. ‘4 - Ferroelectrics, Piezoelectrics, and Pyroelectrics.’ In ‘Dielectric Phenomena in Solids,’ 213–282. Academic Press, San Diego, 2004
- [101] W. Cochran. ‘Crystal Stability and the Theory of Ferroelectricity.’ *Adv. Phys.* **9**(36) 387 (1960)
- [102] W. Cochran. ‘Crystal stability and the theory of ferroelectricity part II. Piezoelectric crystals.’ *Adv. Phys.* **10**(40) 401 (1961)
- [103] C. Monney, H. Cercellier, C. Battaglia, E. Schvier, C. Didiot, M. Garnier, H. Beck, and P. Aebi. ‘Temperature dependence of the excitonic insulator phase model in $1T$ -TiSe₂.’ *Physica B* **404**(19) 3172 (2009). Proceedings of the International Conference on Strongly Correlated Electron Systems
- [104] J. van Wezel, P. Nahai-Williamson, and S. S. Saxena. ‘An alternative interpretation of recent ARPES measurements on TiSe₂.’ *Europhys. Lett.* **89**(4) 47004 (2010)
- [105] J. van Wezel, P. Nahai-Williamson, and S. S. Saxena. ‘Exciton-phonon-driven charge density wave in TiSe₂.’ *Phys. Rev. B* **81** 165109 (2010)
- [106] F. Träger (editor). *Handbook of Lasers and Optics*. Springer, 2007

- [107] J.-C. Diels and W. Rudolph. *Ultrashort Laser Pulse Phenomena*. Academic Press, 2006, 2nd edition
- [108] H. Lüth. *Solid Surfaces, Interfaces and Thin Films*. Springer, 2001, 4th edition
- [109] D.-I. Lee, Y. Sun, Z. Liu, S. Sun, and P. Pianetta. ‘Angular dependence of the photoelectron energy distribution of InP(100) and GaAs(100) negative electron affinity photocathodes.’ *Appl. Phys. Lett.* **91**(19) 192101 (2007)
- [110] K. Kopitzki and P. Herzog. *Einführung in die Festkörperphysik*. B. G. Teubner, Wiesbaden, 2004, 5th edition
- [111] F. Himpsel. ‘Inverse photoemission from semiconductors.’ *Surf. Sci. Rep.* **12**(1) 3 (1990)
- [112] Z. Hao, J. I. Dadap, K. R. Knox, M. B. Yilmaz, N. Zaki, P. D. Johnson, and R. M. Osgood. ‘Nonequilibrium Band Mapping of Unoccupied Bulk States below the Vacuum Level by Two-Photon Photoemission.’ *Phys. Rev. Lett.* **105** 017602 (2010)
- [113] N. Fischer, S. Schuppler, R. Fischer, T. Fauster, and W. Steinmann. ‘Electronic structure of a single layer of Na on Cu(111).’ *Phys. Rev. B* **43**(18) 14722 (1991)
- [114] J. P. Gauyacq and A. K. Kazansky. ‘Effect of the adsorbate motion on the femtosecond time dependence of the two-photon photoemission signal in the Cs/Cu(111) system.’ *Phys. Rev. B* **72**(4) 045418 (2005)
- [115] M. Bauer, S. Pawlik, and M. Aeschlimann. ‘Decay dynamics of photoexcited alkali chemisorbates: Real-time investigations in the femtosecond regime.’ *Phys. Rev. B* **60**(7) 5016 (1999)
- [116] R. Trebino. *Frequency-Resolved Optical Gating: the Measurement of Ultrashort Laser Pulses*. Kluwer Academic Publishers, Dordrecht, Netherlands, 2000
- [117] M. Aeschlimann, M. Bauer, and S. Pawlik. ‘Competing nonradiative channels for hot electron induced surface photochemistry.’ *Chem. Phys.* **205**(1–2) 127 (1996). Surface Reaction Dynamics
- [118] E. Knoesel, A. Hotzel, and M. Wolf. ‘Ultrafast dynamics of hot electrons and holes in copper: Excitation, energy relaxation, and transport effects.’ *Phys. Rev. B* **57**(20) 12812 (1998)
- [119] M. Bauer, M. Wessendorf, D. Hoffmann, C. Wiemann, A. Monnich, and M. Aeschlimann. ‘Time-resolved 2PPE: Probing adsorbate motion on femtosecond time-scales - what is the role of the laser bandwidth?’ *Appl. Phys. A* **80**(5) 987 (2005)

-
- [120] T. Hertel, E. Knoesel, M. Wolf, and G. Ertl. ‘Ultrafast electron dynamics at Cu(111): Response of an electron gas to optical excitation.’ *Phys. Rev. Lett.* **76**(3) 535 (1996)
- [121] M. Bauer. *Real-time Investigations of the Lifetime of Electronic Excitations at Clean and Adsorbate-covered Metal Surfaces*. Ph.D. thesis, Swiss federal institute of technology Zurich (1997)
- [122] M. Wessendorf. *Manipulation der Zerfallsdynamik elektronischer Adsorbatanregungen mittels niederdimensionaler metallischer Schichtsysteme*. Ph.D. thesis, Technische Universität Kaiserslautern (2005)
- [123] A. Mönnich, J. Lange, M. Bauer, M. Aeschlimann, I. A. Nechaev, V. P. Zhukov, P. M. Echenique, and E. V. Chulkov. ‘Experimental time-resolved photoemission and *ab initio* study of lifetimes of excited electrons in Mo and Rh.’ *Phys. Rev. B* **74**(3) 035102 (2006)
- [124] M. Wiesenmayer, M. Bauer, S. Mathias, M. Wessendorf, E. V. Chulkov, V. M. Silkin, A. G. Borisov, J.-P. Gauyacq, P. M. Echenique, and M. Aeschlimann. ‘Lifetime of an adsorbate excitation modified by a tunable two-dimensional substrate.’ *Phys. Rev. B* **78**(24) 245410 (2008)
- [125] M. Weida, S. Ogawa, H. Nagano, and H. Petek. ‘Ultrafast interferometric pump–probe correlation measurements in systems with broadened bands or continua.’ *J. Opt. Soc. Am. B* **17**(8) 1443 (2000)
- [126] M. Merschdorf, C. Kennerknecht, and W. Pfeiffer. ‘Collective and single-particle dynamics in time-resolved two-photon photoemission.’ *Phys. Rev. B* **70**(19) 193401 (2004)
- [127] T. Fauster and M. Weinelt. ‘Time-resolved photoemission from image-potential states.’ *J. Electron Spectrosc. Relat. Phenom.* **114–116** 269 (2001). Proceeding of the Eight International Conference on Electronic Spectroscopy and Structure
- [128] E. M. Logothetis and P. L. Hartman. ‘Laser-Induced Electron Emission from Solids: Many-Photon Photoelectric Effects and Thermionic Emission.’ *Phys. Rev.* **187** 460 (1969)
- [129] U. Bovensiepen. ‘Coherent and incoherent excitations of the Gd(0001) surface on ultrafast timescales.’ *J. Phys.: Condens. Matter* **19**(8) 083201 (2007)
- [130] J. Hohlfeld, S.-S. Wellershoff, J. Güdde, U. Conrad, V. Jähnke, and E. Matthias. ‘Electron and lattice dynamics following optical excitation of metals.’ *Chem. Phys.* **251**(1–3) 237 (2000)

- [131] W. S. Fann, R. Storz, H. W. K. Tom, and J. Bokor. ‘Electron thermalization in gold.’ *Phys. Rev. B* **46** 13592 (1992)
- [132] R. W. Schoenlein, W. Z. Lin, J. G. Fujimoto, and G. L. Eesley. ‘Femtosecond studies of nonequilibrium electronic processes in metals.’ *Phys. Rev. Lett.* **58**(16) 1680 (1987)
- [133] C.-K. Sun, F. Vallée, L. H. Acioli, E. P. Ippen, and J. G. Fujimoto. ‘Femtosecond-tunable measurement of electron thermalization in gold.’ *Phys. Rev. B* **50**(20) 15337 (1994)
- [134] R. H. M. Groeneveld, R. Sprik, and A. Lagendijk. ‘Femtosecond spectroscopy of electron-electron and electron-phonon energy relaxation in Ag and Au.’ *Phys. Rev. B* **51**(17) 11433 (1995)
- [135] H. E. Elsayed-Ali, T. B. Norris, M. A. Pessot, and G. A. Mourou. ‘Time-resolved observation of electron-phonon relaxation in copper.’ *Phys. Rev. Lett.* **58**(12) 1212 (1987)
- [136] J.-Y. Bigot, M. Vomir, L. Andrade, and E. Beaurepaire. ‘Ultrafast magnetization dynamics in ferromagnetic cobalt: The role of the anisotropy.’ *Chem. Phys.* **318**(1–2) 137 (2005). Molecular Nanoscience - In honour of Daniel S. Chemla on his 65th birthday
- [137] M. Lisowski, P. A. Loukakos, U. Bovensiepen, J. Stähler, C. Gahl, and M. Wolf. ‘Ultra-fast dynamics of electron thermalization, cooling and transport effects in Ru(001).’ *Appl. Phys. A* **78** 165 (2004)
- [138] Donatien Alphonse François, Marquis de Sade. *La Philosophie dans le boudoir ou Les Instituteurs immoraux*. 1795. URL http://www.ebooksgratuits.com/html/sade_philosophie_dans_le_boudoir.html
- [139] *PHOIBOS Hemispherical Energy Analyzer Series*. SPECS GmbH, Berlin, Germany, 2nd edition (2006)
- [140] V. P. Zhukov, O. Andreyev, D. Hoffmann, M. Bauer, M. Aeschlimann, E. V. Chulkov, and P. M. Echenique. ‘Lifetimes of excited electrons in Ta: Experimental time-resolved photoemission data and first-principles $GW + T$ theory.’ *Phys. Rev. B* **70**(23) 233106 (2004)
- [141] R. L. Fork, O. E. Martinez, and J. P. Gordon. ‘Negative dispersion using pairs of prisms.’ *Opt. Lett.* **9**(5) 150 (1984)
- [142] C. E. Shannon. ‘Communication In The Presence Of Noise.’ *Proceedings of the IEEE* **86**(2) 447 (1998)

-
- [143] I. N. Bronstein, K. A. Semendjajew, G. Musiol, and H. Mühlig. *Taschenbuch der Mathematik*. Verlag Harri Deutsch GmbH, Frankfurt am Main, 2005, 6th edition
- [144] Caburn-MDC Europe Ltd. ‘5.1.4 Viewports & Glass Components – Fused Silica Viewports.’ online catalog (2010). URL <http://www.caburn.co.uk/en/catalogue/>
- [145] M. Born and E. Wolf. *Principles of optics*. Cambridge university press, 1999, 7th edition
- [146] T. Hertel. *Zur Dynamik photostimulierter Prozesse an Oberflächen*. Ph.D. thesis, Freie Universität Berlin (1995)
- [147] C. A. Bennett. *Principles of Physical Optics*. John Wiley & Sons, Inc., 2008
- [148] E. Hecht. *Optik*. Oldenbourg Wissenschaftsverlag GmbH, 2005, 4th edition
- [149] K. Stahrenberg, T. Herrmann, K. Wilmers, N. Esser, W. Richter, and M. J. G. Lee. ‘Optical properties of copper and silver in the energy range 2.5–9.0 eV.’ *Phys. Rev. B* **64**(11) 115111 (2001)
- [150] B. Schmidt, M. Hacker, G. Stobrawa, and T. Feurer. ‘LAB2-A virtual femtosecond laser lab.’ (2010). URL <http://www.lab2.de>. V4.0
- [151] C. Ramírez, R. Adelung, R. Kunz, L. Kipp, and W. Schattke. ‘Lithium adsorption by TiSe₂ of varying concentration via density functional theory.’ *Phys. Rev. B* **71**(3) 035426 (2005)
- [152] A. Goldmann. *Group III: Condensed Matter. Volume 23, Electronic Structure of Solids: Photoemission Spectra and Related Data. Subvolume C1, Noble Metals, Noble Metal Halides and Nonmagnetic Transition Metals, Landolt-Börnstein: Numerical Data and Functional Relationships in Science and Technology - New Series, volume III/23 C1*. Springer, Berlin, 2003
- [153] J. Schneider, C. Franke, and D. M. Kolb. ‘Image-potential-induced surface states at the Ag(111)-electrolyte interface.’ *Surf. Sci.* **198**(1–2) 277 (1988)
- [154] F. Steeb, S. Mathias, A. Fischer, M. Wiesenmayer, M. Aeschlimann, and M. Bauer. ‘The nature of a nonlinear excitation pathway from the Shockley surface state as probed by chirped pulse two photon photoemission.’ *New J. Phys.* **11**(1) 013016 (2009)
- [155] ‘NIST/SEMATECH e-Handbook of Statistical Methods.’ online (2010). URL <http://www.itl.nist.gov/div898/handbook/eda/section3/eda35f.htm>

- [156] S. Mathias, A. Ruffing, F. Deicke, M. Wiesenmayer, M. Aeschlimann, and M. Bauer. ‘Band structure dependence of hot-electron lifetimes in a Pb/Cu(111) quantum-well system.’ *Phys. Rev. B* **81**(15) 155429 (2010)
- [157] R. Nitsche, H. U. Bülsterli, and M. Lichtensteiger. ‘Crystal growth by chemical transport reactions–I : Binary, ternary, and mixed-crystal chalcogenides.’ *J. Phys. Chem. Solids* **21**(3-4) 199 (1961)
- [158] R. Dürig. *Profilanalyse winkelaufgelöster Photoelektronenspektren von TiTe₂ und Optimierung der Herstellung von Schichtkristallen*. Master’s thesis, Christian-Albrechts-Universität zu Kiel (1993)
- [159] J. A. Wilson. ‘Modeling contrasting semimetallic characters of TiS₂ and TiSe₂.’ *Phys. Status Solidi B* **86**(1) 11 (1978)
- [160] G. Karschnick, O. Anderson, W. Drube, and M. Skibowski. ‘Adsorbate enhanced Ti-3d photoemission from layered TiSe₂ surfaces.’ *Surf. Sci.* **155**(1) 46 (1985)
- [161] J. Rasch, T. Stemmler, and R. Manzke. ‘Electronic properties of the semiconductor TiSe₂.’ *J. Alloy. Compd.* **442**(1–2) 262 (2007). Proceedings of the 15th International Conference on Solid Compounds of Transition Elements, SCTE2006
- [162] W. Jaegermann, C. Pettenkofer, A. Schellenberger, C. A. Papageorgopoulos, M. Kamaratos, D. Vlachos, and Y. Tomm. ‘Photoelectron spectroscopy of UHV in situ intercalated Li/TiSe₂. Experimental proof of the rigid band model.’ *Chem. Phys. Lett.* **221**(5–6) 441 (1994)
- [163] H. I. Starnberg, H. E. Brauer, and H. P. Hughes. *Photoemission from Intercalated Transition Metal Dichalogenides*, chapter 2, 41–98. In [281] (2000)
- [164] K. C. Woo, F. C. Brown, W. L. McMillan, R. J. Miller, M. J. Schaffman, and M. P. Sears. ‘Superlattice formation in titanium diselenide.’ *Phys. Rev. B* **14**(8) 3242 (1976)
- [165] R. Z. Bachrach, M. Skibowski, and F. C. Brown. ‘Angle-Resolved Photoemission from TiSe₂ Using Synchrotron Radiation.’ *Phys. Rev. Lett.* **37**(1) 40 (1976)
- [166] J. A. Wilson. ‘Concerning the semimetallic characters of TiS₂ and TiSe₂.’ *Solid State Commun.* **22**(9) 551 (1977)
- [167] C. Pettenkofer, W. Jaegermann, A. Schellenberger, E. Holub-Krappe, C. A. Papageorgopoulos, M. Kamaratos, and A. Papageorgopoulos. ‘Cs deposition on layered 2H TaSe₂ (0 0 0 1) surfaces: Adsorption or intercalation?’ *Solid State Commun.* **84**(9) 921 (1992)

-
- [168] H. I. Starnberg, H. E. Brauer, and V. N. Strocov. ‘Low temperature adsorption of Cs on layered TiS_2 studied by photoelectron spectroscopy.’ *Surf. Sci.* **384**(1–3) L785 (1997)
- [169] C. H. Chen, W. Fabian, F. C. Brown, K. C. Woo, B. Davies, B. DeLong, and A. H. Thompson. ‘Angle-resolved photoemission studies of the band structure of TiSe_2 and TiS_2 .’ *Phys. Rev. B* **21**(2) 615 (1980)
- [170] S. Negishi, H. Negishi, K. Shimada, X. Cui, M. Higashiguchi, M. Nakatake, M. Arita, H. Namatame, M. Taniguchi, A. Ohnishi, and M. Sasaki. ‘Photoemission study on electronic structure of TiSe_2 .’ *Physica B* **383**(1) 155 (2006). Proceedings of the Third Hiroshima Workshop on Novel Functional Materials with Multinary Freedoms
- [171] M. Wiesenmayer, S. Hilgenfeldt, S. Mathias, F. Steeb, T. Rohwer, and M. Bauer. ‘Spectroscopy and population decay of a van der Waals gap state in layered TiSe_2 .’ *Phys. Rev. B* **82**(3) 035422 (2010). Copyright 2010 by the American Physical Society
- [172] D. Meschede (editor). *Gerthsen Physik*. Springer, Berlin, 2004, 22nd edition
- [173] N. Fischer, S. Schuppler, T. Fauster, and W. Steinmann. ‘Coverage-dependent electronic structure of Na on $\text{Cu}(111)$.’ *Surf. Sci.* **314**(1) 89 (1994)
- [174] M. Boehme. *Electronic structure of the layered materials TaS_2 and Rb-covered WSe_2* . Ph.D. thesis, Christian-Albrechts-Universität zu Kiel (1998)
- [175] S. Kennou, S. Ladas, and C. Papageorgopoulos. ‘The behavior of Cs on MoS_2 .’ *Surf. Sci.* **152–153**(Part 2) 1213 (1985)
- [176] C. A. Papageorgopoulos. ‘Adsorption of Cs and O_2 on MoS_2 .’ *Surf. Sci.* **75**(1) 17 (1978)
- [177] P. E. Gregory, P. Chye, H. Sunami, and W. E. Spicer. ‘The oxidation of Cs—uv photoemission studies.’ *J. Appl. Phys.* **46**(8) 3525 (1975)
- [178] C. Ramírez and W. Schattke. ‘Diffusion and intercalation of alkali atoms in transition metal dichalcogenides.’ *Surf. Sci.* **482–485**(Part 1) 424 (2001)
- [179] D. Tang and D. Heskett. ‘Unoccupied electronic structure of $\text{Na}/\text{Ni}(111)$.’ *Phys. Rev. B* **47**(16) 10695 (1993)
- [180] D. A. Arena, F. G. Curti, and R. A. Bartynski. ‘Unoccupied electronic states of the Cs/ $\text{Cu}(100)$ and Cs/ $\text{Cu}(111)$ adsorption systems.’ *Phys. Rev. B* **56**(23) 15404 (1997)

- [181] W. Jacob, E. Bertel, and V. Dose. ‘Potassium-induced empty electronic states on Ag(110).’ *Phys. Rev. B* **35**(11) 5910 (1987)
- [182] H. B. Nielsen and W. Thowladda. ‘Position and linewidth of the K-induced $4s$ resonance on Ag(100): a two-photon photoemission study.’ *Surf. Sci.* **284**(1–2) L426 (1993)
- [183] K.-H. Frank, H.-J. Sagner, and D. Heskett. ‘Coverage-dependent shifts of s and p resonances of alkali metals chemisorbed on Al(111).’ *Phys. Rev. B* **40**(5) 2767 (1989)
- [184] S. A. Lindgren and L. Walldén. ‘Energy shifts of a Cu(111) surface band upon adsorption of cesium and oxygen.’ *Surf. Sci.* **89**(1–3) 319 (1979)
- [185] J. P. Muscat and I. P. Batra. ‘Coverage dependence of the work function of metals upon alkali-metal adsorption.’ *Phys. Rev. B* **34**(4) 2889 (1986)
- [186] H. Ishida and K. Terakura. ‘Coverage dependence of the work function and charge transfer on the alkali-metal-jellium surface.’ *Phys. Rev. B* **36**(8) 4510 (1987)
- [187] A. K. Kazansky, A. G. Borisov, and J. P. Gauyacq. ‘Image and adsorbate state dependence on the adsorbate coverage in the Na/Cu(111) system.’ *Surf. Sci.* **544**(2–3) 309 (2003)
- [188] S. Pawlik, R. Burgermeister, M. Bauer, and M. Aeschlimann. ‘Direct transition in the system Ag(111) studied by one- and two-photon photoemission.’ *Surf. Sci.* **402–404** 556 (1998)
- [189] N. Pontius, V. Sametoglu, and H. Petek. ‘Simulation of two-photon photoemission from the bulk sp -bands of Ag(111).’ *Phys. Rev. B* **72**(11) 115105 (2005)
- [190] S. Pawlik, M. Bauer, and M. Aeschlimann. ‘Lifetime difference of photoexcited electrons between intraband and interband transitions.’ *Surf. Sci.* **377–379** 206 (1997). European Conference on Surface Science
- [191] H. Petek, H. Nagano, and S. Ogawa. ‘Hole Decoherence of d Bands in Copper.’ *Phys. Rev. Lett.* **83**(4) 832 (1999)
- [192] S. Ogawa, H. Nagano, and H. Petek. ‘Optical Intersubband Transitions and Femtosecond Dynamics in Ag/Fe(100) Quantum Wells.’ *Phys. Rev. Lett.* **88**(11) 116801 (2002)
- [193] P. S. Kirchmann and U. Bovensiepen. ‘Ultrafast electron dynamics in Pb/Si(111) investigated by two-photon photoemission.’ *Phys. Rev. B* **78**(3) 035437 (2008)

-
- [194] M. K. Brinkley, Y. Liu, N. J. Speer, T. Miller, and T.-C. Chiang. ‘Using Electronic Coherence to Probe a Deeply Embedded Quantum Well in Bimetallic Pb/Ag Films on Si(111).’ *Phys. Rev. Lett.* **103**(24) 246801 (2009)
- [195] S. Mathias, A. Ruffing, F. Deicke, M. Wiesenmayer, I. Sakar, G. Bihlmayer, E. V. Chulkov, Y. M. Koroteev, P. M. Echenique, M. Bauer, and M. Aeschlimann. ‘Quantum-Well-Induced Giant Spin-Orbit Splitting.’ *Phys. Rev. Lett.* **104**(6) 066802 (2010)
- [196] M. Kamaratos, D. Vlachos, C. A. Papageorgopoulos, A. Schellenberger, W. Jaegermann, and C. Pettenkofer. ‘Interaction of Li with the group IV selenide layer compounds at low temperature.’ *J. Phys.-Condens. Mat.* **14**(39) 8979 (2002)
- [197] D. F. Padowitz, W. R. Merry, R. E. Jordan, and C. B. Harris. ‘Two-photon photoemission as a probe of electron interactions with atomically thin dielectric films on metal surfaces.’ *Phys. Rev. Lett.* **69**(24) 3583 (1992)
- [198] M. Wolf, E. Knoesel, and T. Hertel. ‘Ultrafast dynamics of electrons in image-potential states on clean and Xe-covered Cu(111).’ *Phys. Rev. B* **54**(8) R5295 (1996)
- [199] W. Berthold, P. Feulner, and U. Höfer. ‘Decoupling of image-potential states by Ar mono- and multilayers.’ *Chem. Phys. Lett.* **358**(5–6) 502 (2002)
- [200] D. P. Woodruff, S. L. Hulbert, P. D. Johnson, and N. V. Smith. ‘Unoccupied surface resonance on Cu(100) and the effect of vacuum-level pinning.’ *Phys. Rev. B* **31**(6) 4046 (1985)
- [201] D. Velic, A. Hotzel, M. Wolf, and G. Ertl. ‘Electronic states of the C₆H₆/Cu{111} system: Energetics, femtosecond dynamics, and adsorption morphology.’ *J. Chem. Phys.* **109** 9155 (1998)
- [202] G. Dutton, D. P. Quinn, C. D. Lindstrom, and X.-Y. Zhu. ‘Exciton dynamics at molecule-metal interfaces: C₆₀/Au(111).’ *Phys. Rev. B* **72**(4) 045441 (2005)
- [203] S. Hagen, P. Kate, M. V. Peters, S. Hecht, M. Wolf, and P. Tegeder. ‘Kinetic analysis of the photochemically and thermally induced isomerization of an azobenzene derivative on Au(111) probed by two-photon photoemission.’ *Appl. Phys. A* **93**(2) 253 (2008)
- [204] N. V. Baranov, V. I. Maksimov, J. Mesot, V. G. Pleschov, A. Podlesnyak, V. Pomjakushin, and N. V. Selezneva. ‘Possible reappearance of the charge density wave transition in M_xTiSe₂ compounds intercalated with 3d metals.’ *J. Phys. Condens. Matter* **19**(1) 016005 (2007)

- [205] K. Yamazaki, K. Shimada, H. Negishi, F. Xu, A. Ino, M. Higashiguchi, H. Namatame, M. Taniguchi, M. Sasaki, S. Titova, A. Titov, and Y. M. Yarmoshenko. ‘High-resolution angle-resolved resonant-photoemission spectroscopy of Fe_xTiTe_2 .’ *Physica B* **351**(3–4) 262 (2004). Proceedings of The International Symposium on Synchrotron Radiation Research for Spin and Electronic States in *d* and *f* Electron Systems
- [206] H. Isomäki and J. von Boehm. ‘The gaps of the ideal TiS_2 and TiSe_2 .’ *J. Phys. C* **14**(4) L75 (1981)
- [207] I. S. Tilinin, A. Jablonski, and W. S. M. Werner. ‘Quantitative surface analysis by Auger and x-ray photoelectron spectroscopy.’ *Prog. Surf. Sci.* **52**(4) 193 (1996)
- [208] A. Bendounan, H. Cercellier, Y. Fagot-Revurat, B. Kierren, V. Y. Yurov, and D. Malterre. ‘Modification of Shockley states induced by surface reconstruction in epitaxial Ag films on $\text{Cu}(111)$.’ *Phys. Rev. B* **67**(16) 165412 (2003)
- [209] A. Santoni, J. Lancok, V. Dhanak, S. Loreti, G. Miller, and C. Minarini. ‘A valence-band and core-level photoemission study of $a\text{-Si}_x\text{C}_{1-x}$ thin films grown by low-temperature low-pressure chemical vapour deposition.’ *Appl. Phys. A* **81**(5) 991 (2005)
- [210] S. Ogawa, H. Nagano, H. Petek, and A. P. Heberle. ‘Optical Dephasing in $\text{Cu}(111)$ Measured by Interferometric Two-Photon Time-Resolved Photoemission.’ *Phys. Rev. Lett.* **78**(7) 1339 (1997)
- [211] H. Petek, H. Nagano, M. J. Weida, and S. Ogawa. ‘Surface Femtochemistry: Frustrated Desorption of Alkali Atoms from Noble Metals.’ *J. Phys. Chem. B* **105**(29) 6767 (2001)
- [212] M. Wessendorf, C. Wiemann, M. Bauer, M. Aeschlimann, M. Schneider, H. Brune, and K. Kern. ‘Electronic surface structure of n-ML $\text{Ag}/\text{Cu}(111)$ and $\text{Cs}/\text{n-ML Ag}/\text{Cu}(111)$ as investigated by 2PPE and STS.’ *Appl. Phys. A* **78**(2) 183 (2004)
- [213] K. Rossnagel, L. Kipp, M. Skibowski, C. Solterbeck, T. Strasser, W. Schattke, D. Voß, P. Krüger, A. Mazur, and J. Pollmann. ‘Three-dimensional Fermi surface determination by angle-resolved photoelectron spectroscopy.’ *Phys. Rev. B* **63**(12) 125104 (2001)
- [214] V. N. Strocov, E. E. Krasovskii, W. Schattke, N. Barrett, H. Berger, D. Schrupp, and R. Claessen. ‘Three-dimensional band structure of layered TiTe_2 : Photoemission final-state effects.’ *Phys. Rev. B* **74**(19) 195125 (2006)

-
- [215] S. Hilgenfeldt. *Zeitaufgelöste Photoelektronenspektroskopie zum Studium ultraschneller Prozesse an den Schichtkristallen $TiSe_2$ und $TiTe_2$* . Master's thesis, Christian-Albrechts-Universität zu Kiel (2009)
- [216] F. J. Himpsel. 'Angle-resolved measurements of the photoemission of electrons in the study of solids.' *Adv. Phys.* **32**(1) 1 (1983)
- [217] R. Matzdorf, G. Meister, and A. Goldmann. 'Influence of electron-phonon interactions on angle-resolved photoelectron spectra from metals.' *Surf. Sci.* **296**(2) 241 (1993)
- [218] R. Smoluchowski. 'Anisotropy of the Electronic Work Function of Metals.' *Phys. Rev.* **60**(9) 661 (1941)
- [219] C. Herring and M. H. Nichols. 'Thermionic Emission.' *Rev. Mod. Phys.* **21**(2) 185 (1949)
- [220] A. Kiejna. 'On the temperature dependence of the work function.' *Surf. Sci.* **178**(1-3) 349 (1986)
- [221] C. Herring. 'On the Thermodynamic Interpretation of Certain Thermionic and Thermoelectric Phenomena.' *Phys. Rev.* **59**(11) 889 (1941)
- [222] P. J. Mohr, B. N. Taylor, and D. B. Newell. 'CODATA recommended values of the fundamental physical constants: 2006.' *Rev. Mod. Phys.* **80**(2) 633 (2008)
- [223] C. R. Crowell and R. A. Armstrong. 'Temperature Dependence of the Work Function of Silver, Sodium, and Potassium.' *Phys. Rev.* **114**(6) 1500 (1959)
- [224] A. R. Shul'man and T. S. Kirsanova. 'Temperature dependence of the effective work function for the BaO - W system.' *Russ. Phys. J.* **14**(9) 1214 (1971)
- [225] G. A. Haas and R. E. Thomas. 'Work function and secondary emission studies of various Cu crystal faces.' *J. Appl. Phys.* **48**(1) 86 (1977)
- [226] M. Chelvayohan and R. Gomer. 'Temperature dependence of the work function of Cu layers on a W(110) plane.' *Surf. Sci.* **172**(2) 337 (1986)
- [227] R. Bachmann. 'Temperaturabhängigkeit der Austrittsarbeit von Silizium.' *Z. Phys. B Con. Mat.* **8**(1) 31 (1968)
- [228] K. I. Ibragimov and V. A. Korol'kov. 'Temperature Dependence of the Work Function of Metals and Binary Alloys.' *Inorg. Mater.* **37** 567 (2001)
- [229] A. R. Hutson. 'Velocity Analysis of Thermionic Emission from Single-Crystal Tungsten.' *Phys. Rev.* **98**(4) 889 (1955)

- [230] A. Kiejna, K. F. Wojciechowski, and J. Zebrowski. ‘The temperature dependence of metal work functions.’ *J. Phys. F Met. Phys.* **9**(7) 1361 (1979)
- [231] L. W. Swanson and L. C. Crouser. ‘Total-Energy Distribution of Field-Emitted Electrons and Single-Plane Work Functions for Tungsten.’ *Phys. Rev.* **163**(3) 622 (1967)
- [232] M. M. Beerbom, B. Lagel, A. J. Cascio, B. V. Doran, and R. Schlaf. ‘Direct comparison of photoemission spectroscopy and in situ Kelvin probe work function measurements on indium tin oxide films.’ *J. Electron Spectrosc. Relat. Phenom.* **152**(1–2) 12 (2006)
- [233] S. Nien-T’ai and W. Band. ‘An explanation of anomalous thermionic emission current constants.’ *Math. Proc. Cambridge* **42**(01) 72 (1946)
- [234] W. Demtroder. *Experimentalphysik 1 - Mechanik und Warme*. Springer-Verlag, Berlin, 1998, 2nd edition
- [235] S. Seely. ‘Work Function and Temperature.’ *Phys. Rev.* **59**(1) 75 (1941)
- [236] G. A. Wiegers. ‘Physical properties of first-row transition metal dichalcogenides and their intercalates.’ *Physica B+C* **99**(1–4) 151 (1980)
- [237] N. V. Baranov, V. G. Pleshchev, N. V. Selezneva, E. M. Sherokalova, A. V. Korolev, V. A. Kazantsev, and A. V. Proshkin. ‘Ferromagnetism and structural transformations caused by Cr intercalation into TiTe_2 .’ *J. Phys.: Condens. Matter* **21**(50) 506002 (2009)
- [238] K.-S. Lee and M. A. El-Sayed. ‘Gold and Silver Nanoparticles in Sensing and Imaging: Sensitivity of Plasmon Response to Size, Shape, and Metal Composition.’ *J. Phys. Chem. B* **110**(39) 19220 (2006)
- [239] J. F. Zhao, H. W. Ou, G. Wu, B. P. Xie, Y. Zhang, D. W. Shen, J. Wei, L. X. Yang, J. K. Dong, M. Arita, H. Namatame, M. Taniguchi, X. H. Chen, and D. L. Feng. ‘Evolution of the Electronic Structure of $1T\text{-Cu}_x\text{TiSe}_2$.’ *Phys. Rev. Lett.* **99**(14) 146401 (2007)
- [240] O. Anderson, R. Manzke, and M. Skibowski. ‘Three-Dimensional and Relativistic Effects in Layered $1T\text{-TiSe}_2$.’ *Phys. Rev. Lett.* **55**(20) 2188 (1985)
- [241] B. A. McDougall, T. Balasubramanian, and E. Jensen. ‘Phonon contribution to quasiparticle lifetimes in Cu measured by angle-resolved photoemission.’ *Phys. Rev. B* **51**(19) 13891 (1995)

-
- [242] F. Reinert, B. Eltner, G. Nicolay, F. Forster, S. Schmidt, and S. Hüfner. ‘The electron-phonon self-energy of metallic systems determined by angular resolved high-resolution photoemission.’ *Physica B* **351**(3–4) 229 (2004). Proceedings of The International Symposium on Synchrotron Radiation Research for Spin and Electronic States in d and f Electron Systems
- [243] S. Mathias, S. V. Eremeev, E. V. Chulkov, M. Aeschlimann, and M. Bauer. ‘Quantum Oscillations in Coupled Two-Dimensional Electron Systems.’ *Phys. Rev. Lett.* **103**(2) 026802 (2009)
- [244] R. Matzdorf, G. Meister, and A. Goldmann. ‘Temperature-dependent photoemission spectra from Cu(100) and Cu(111) surfaces.’ *Surf. Sci.* **286**(1–2) 56 (1993)
- [245] D. N. Denzler, C. Frischkorn, C. Hess, M. Wolf, and G. Ertl. ‘Electronic Excitation and Dynamic Promotion of a Surface Reaction.’ *Phys. Rev. Lett.* **91**(22) 226102 (2003)
- [246] T. Roth, D. Steil, D. Hoffmann, M. Bauer, M. Cinchetti, and M. Aeschlimann. ‘Dynamics of the coercivity in ultrafast pump–probe experiments.’ *J. Phys. D: Appl. Phys.* **41**(16) 164001 (2008)
- [247] C. Kittel. *Einführung in die Festkörperphysik*. Oldenbourg Wissenschaftsverlag GmbH, München, 2006, 14th edition
- [248] R. A. Craven, F. J. Di Salvo, and F. S. L. Hsu. ‘Mechanisms for the 200 K transition in TiSe₂: A measurement of the specific heat.’ *Solid State Commun.* **25**(1) 39 (1978)
- [249] N. V. Baranov, K. Inoue, V. I. Maksimov, A. S. Ovchinnikov, V. G. Pleschov, A. Podlesnyak, A. N. Titov, and N. V. Toporova. ‘Ni intercalation of titanium diselenide: effect on the lattice, specific heat and magnetic properties.’ *Journal of Physics: Condensed Matter* **16**(50) 9243 (2004)
- [250] W. Demtröder. *Experimentalphysik 2 - Elektrizität und Optik*. Springer-Verlag, Berlin, 1999, 2nd edition
- [251] V. Vanovschi. ‘calculate molecular weight - molar mass calculator.’ online (2011). URL <http://www.webqc.org/mocalc.php>. Retrieved 06/09/2011
- [252] J. M. Lopez-Castillo, A. Amara, S. Jandl, J.-P. Jay-Gerin, C. Ayache, and M. J. Aubin. ‘Phonon-drag effect in TiSe_{2-x}S_x mixed compounds.’ *Phys. Rev. B* **36**(8) 4249 (1987)
- [253] J. M. Hicks, L. E. Urbach, E. W. Plummer, and H.-L. Dai. ‘Can Pulsed Laser Excitation of Surfaces Be Described by a Thermal Model?’ *Phys. Rev. Lett.* **61**(22) 2588 (1988)

- [254] L. Papula. *Mathematische Formelsammlung für Ingenieure und Naturwissenschaftler*. Vieweg & Sohn Verlagsgesellschaft mbH, Braunschweig / Wiesbaden, 2001, 7th edition
- [255] S. Mukherjee and M. Mukherjee. ‘Controlled surface neutralization: A quantitative approach to study surface charging in photoemission.’ *J. Electron Spectrosc. Relat. Phenom.* **154**(3) 90 (2007)
- [256] J. A. Holy, K. C. Woo, M. V. Klein, and F. C. Brown. ‘Raman and infrared studies of superlattice formation in TiSe_2 .’ *Phys. Rev. B* **16** 3628 (1977)
- [257] R. Merlin. ‘Generating coherent THz phonons with light pulses.’ *Solid State Commun.* **102**(2–3) 207 (1997). Highlights in Condensed Matter Physics and Materials Science
- [258] S. Hellmann. ‘design of a suitable fitting routine in IGOR scripting language.’ (2011). Private communication
- [259] D. Steil. ‘discussion and simulation of data using the two temperature model.’ (2012). Private communication
- [260] K. El Sayed, S. Schuster, H. Haug, F. Herzel, and K. Henneberger. ‘Subpicosecond plasmon response: Buildup of screening.’ *Phys. Rev. B* **49** 7337 (1994)
- [261] L. Bányai, Q. T. Vu, B. Mieck, and H. Haug. ‘Ultrafast Quantum Kinetics of Time-Dependent RPA-Screened Coulomb Scattering.’ *Phys. Rev. Lett.* **81** 882 (1998)
- [262] L. Perfetti, P. A. Loukakos, M. Lisowski, U. Bovensiepen, M. Wolf, H. Berger, S. Biermann, and A. Georges. ‘Femtosecond dynamics of electronic states in the Mott insulator $1T\text{-TaS}_2$ by time resolved photoelectron spectroscopy.’ *New J. Phys.* **10**(5) 053019 (2008)
- [263] J. Demsar, K. Biljaković, and D. Mihailovic. ‘Single Particle and Collective Excitations in the One-Dimensional Charge Density Wave Solid $\text{K}_{0.3}\text{MoO}_3$ Probed in Real Time by Femtosecond Spectroscopy.’ *Phys. Rev. Lett.* **83**(4) 800 (1999)
- [264] E. W. Plummer and W. Eberhardt. ‘Magnetic surface states on $\text{Ni}(100)$.’ *Phys. Rev. B* **20**(4) 1444 (1979)
- [265] D. Westphal and A. Goldmann. ‘Polarization dependent photoemission from d-like surface states on Cu.’ *Surf. Sci.* **95**(2–3) L249 (1980)
- [266] K. Giesen, F. Hage, H. J. Riess, W. Steinmann, R. Haight, R. Beigang, R. Dreyfus, P. Avouris, and F. J. Himpsel. ‘Image Potential States Seen via Two-Photon Photoemission and Second Harmonic Generation.’ *Phys. Scr.* **35**(4) 578 (1987)

-
- [267] J. Hermanson. ‘Final-state symmetry and polarization effects in angle-resolved photoemission spectroscopy.’ *Solid State Commun.* **88**(11–12) 1097 (1993). Special Issue A Celebratory Issue to Commemorate 30 Years of Solid State Communications
- [268] O. Andreyev, Y. M. Koroteev, M. Sánchez Albaneda, M. Cinchetti, G. Bihlmayer, E. V. Chulkov, J. Lange, F. Steeb, M. Bauer, P. M. Echenique, S. Blügel, and M. Aeschlimann. ‘Spin-resolved two-photon photoemission study of the surface resonance state on Co/Cu(001).’ *Phys. Rev. B* **74**(19) 195416 (2006)
- [269] P. Marchand and L. Marmet. ‘Binomial smoothing filter: A way to avoid some pitfalls of least-squares polynomial smoothing.’ *Rev. Sci. Instrum.* **54**(8) 1034 (1983)
- [270] D. A. Shirley. ‘High-Resolution X-Ray Photoemission Spectrum of the Valence Bands of Gold.’ *Phys. Rev. B* **5**(12) 4709 (1972)
- [271] G. K. Wertheim and S. B. Diczynski. ‘Least-squares analysis of photoemission data.’ *J. Electron Spectrosc. Relat. Phenom.* **37**(1) 57 (1985)
- [272] E. Raymond (editor). ‘The Jargon File.’ online (2011). URL <http://catb.org/jargon/html/K/KISS-Principle.html>. Version 4.4.7, retrieved 03/29/2011
- [273] A. Caillé, Y. Lepage, M. H. Jericho, and A. M. Simpson. ‘Thermal expansion, ultrasonic velocity, and attenuation measurements in TiS₂, TiSe₂, and TiS_{0.5}Se_{1.5}.’ *Phys. Rev. B* **28**(10) 5454 (1983)
- [274] G. K. White. ‘Thermal expansion of reference materials: copper, silica and silicon.’ *J. Phys. D: Appl. Phys.* **6**(17) 2070 (1973)
- [275] G. K. White. ‘Reference materials for thermal expansion: certified or not?’ *Thermochim. Acta* **218** 83 (1993)
- [276] J. M. Wilson and T. J. Bastow. ‘Surface thermal expansion for Cr(100) and Mo(100) single crystals.’ *Surf. Sci.* **26**(2) 461 (1971)
- [277] S. Hellmann, K. Rossnagel, M. Marczyński-Bühlow, and L. Kipp. ‘Vacuum space-charge effects in solid-state photoemission.’ *Phys. Rev. B* **79**(3) 035402 (2009)
- [278] T. Miller, W. E. McMahon, and T.-C. Chiang. ‘Interference between Bulk and Surface Photoemission Transitions in Ag(111).’ *Phys. Rev. Lett.* **77**(6) 1167 (1996)
- [279] A. D. Yoffe. ‘Layer Compounds.’ *Annu. Rev. Mater. Sci.* **3**(1) 147 (1973)
- [280] ‘Space environment (natural and artificial)—Process for determining solar irradiances.’ (2007)

Bibliography

- [281] H. P. Hughes and H. I. Starnberg (editors). *Electron Spectroscopies Applied to Low-Dimensional Materials*. Kluwer Academic Publishers, Dordrecht, The Netherlands, 2000

List of Publications

Invited talks

- [1] M. Wiesenmayer. ‘Two-photon Photoemission and Time-resolved Photoemission of the Transition Metal Dichalcogenide TiSe_2 .’ Seminar des Graduiertenkolleg 792 “Ultrakurzzeitphysik und nichtlineare Optik” der TU Kaiserslautern (2008)

Journal papers

- [1] S. Mathias, M. Wiesenmayer, M. Aeschlimann, and M. Bauer. ‘Quantum-Well Wave-Function Localization and the Electron-Phonon Interaction in Thin Ag Nanofilms.’ *Phys. Rev. Lett.* **97**(23) 236809 (2006)
- [2] M. Wiesenmayer, M. Bauer, S. Mathias, M. Wessendorf, E. V. Chulkov, V. M. Silkin, A. G. Borisov, J.-P. Gauyacq, P. M. Echenique, and M. Aeschlimann. ‘Lifetime of an adsorbate excitation modified by a tunable two-dimensional substrate.’ *Phys. Rev. B* **78**(24) 245410 (2008)
- [3] S. Mathias, M. Wiesenmayer, F. Deicke, A. Ruffing, L. Miaja-Avila, M. M. Murnane, H. C. Kapteyn, M. Bauer, and M. Aeschlimann. ‘Time and angle resolved photoemission spectroscopy using femtosecond visible and high-harmonic light.’ *J. Phys. Conf. Ser.* **148** 012042 (2009)
- [4] F. Steeb, S. Mathias, A. Fischer, M. Wiesenmayer, M. Aeschlimann, and M. Bauer. ‘The nature of a nonlinear excitation pathway from the Shockley surface state as probed by chirped pulse two photon photoemission.’ *New J. Phys.* **11**(1) 013016 (2009)
- [5] S. Mathias, A. Ruffing, F. Deicke, M. Wiesenmayer, M. Aeschlimann, and M. Bauer. ‘Band structure dependence of hot-electron lifetimes in a Pb/Cu(111) quantum-well system.’ *Phys. Rev. B* **81**(15) 155429 (2010)
- [6] S. Mathias, A. Ruffing, F. Deicke, M. Wiesenmayer, I. Sakar, G. Bihlmayer, E. V. Chulkov, Y. M. Koroteev, P. M. Echenique, M. Bauer, and M. Aeschlimann. ‘Quantum-Well-Induced Giant Spin-Orbit Splitting.’ *Phys. Rev. Lett.* **104**(6) 066802 (2010)

- [7] M. Wiesenmayer, S. Hilgenfeldt, S. Mathias, F. Steeb, T. Rohwer, and M. Bauer. ‘Spectroscopy and population decay of a van der Waals gap state in layered TiSe_2 .’ *Phys. Rev. B* **82**(3) 035422 (2010)
- [8] F. Steeb, S. Mathias, M. Wiesenmayer, A. Fischer, M. Aeschlimann, M. Bauer, and J. P. Gauyacq. ‘Probing adsorbate dynamics with chirped laser pulses in a single-pulse scheme.’ *Phys. Rev. B* **82**(16) 165430 (2010)
- [9] T. Rohwer, S. Hellmann, M. Wiesenmayer, C. Sohrt, A. Stange, B. Slomski, A. Carr, Y. Liu, L. Miaja Avila, M. Källäne, S. Mathias, L. Kipp, K. Rossnagel, and M. Bauer. ‘Collapse of long-range charge order tracked by time-resolved photoemission at high momenta.’ *Nature* **471**(7339) 490 (2011)

Conference papers

- [1] M. Wiesenmayer, M. Wessendorf, S. Mathias, V. M. Silkin, A. G. Borisov, P. M. Echenique, J. P. Gauyacq, E. V. Chulkov, M. Aeschlimann, and M. Bauer. ‘Ultrafast Decay Dynamics of a Photoexcited Adsorbate in Interaction With a Two-dimensional Metallic Substrate.’ In ‘European Conference on Surface Science (ECOSS) 24,’ Paris, 2006
- [2] M. Wiesenmayer, J. Buck, T. Rohwer, K. Rossnagel, L. Kipp, and M. Bauer. ‘Two-photon Photoemission Spectroscopy of the Clean and Alkali-doped $1T$ - TiSe_2 Transition-metal Dichalcogenide.’ In ‘Verhandlungen der Deutschen Physikalischen Gesellschaft,’ 2008
- [3] M. Wiesenmayer, S. Mathias, T. Rohwer, O. Andreyev, and M. Bauer. ‘A Time-resolved Photoemission Study of the TiSe_2 Transition Metal Dichalcogenide Compound.’ In ‘Ultrafast Surface Dynamics 6,’ Kloster Banz, 2008
- [4] M. Wiesenmayer, S. Hilgenfeldt, S. Mathias, T. Rohwer, and M. Bauer. ‘Ultrafast Dynamics in the $1T$ - TiSe_2 Transition-metal Dichalcogenide in the Vicinity of the CDW Phase Transition.’ In ‘Verhandlungen der Deutschen Physikalischen Gesellschaft,’ 2009
- [5] M. Wiesenmayer, T. Rohwer, S. Hellmann, C. Sohrt, A. Stange, M. Källäne, S. Mathias, L. Kipp, K. Rossnagel, and M. Bauer. ‘The Kiel-setup for time- and angle-resolved photoemission using high-harmonic light pulses.’ In ‘Ultrafast Surface Dynamics 7,’ Brijuni islands, Croatia, 2010
- [6] M. Wiesenmayer, A. Fischer, P. Melchior, C. Schneider, D. Bayer, and M. Aeschlimann. ‘Time-Resolved PEEM Investigation of the Interaction of Surface Plasmons with Hot Spots.’ In ‘Verhandlungen der Deutschen Physikalischen Gesellschaft,’ Berlin, 2012

Acknowledgements

Dem geneigten Leser wird die Verwendung des „we“ anstelle eines „I“ in dieser Arbeit nicht entgangen sein. Viele Freunde und Kollegen waren am Gelingen dieses Unterfangens mehr oder minder direkt beteiligt. Ihnen möchte ich an dieser Stelle meinen Dank ausdrücken.

Zunächst danke ich herzlich meinem Betreuer Prof. Dr. Michael Bauer für die Möglichkeit an einem spannenden Material in einer fordernden Laborumgebung forschen zu können sowie für seine fortwährende Unterstützung und Betreuung nunmehr seit meiner Diplomarbeit an der TU Kaiserslautern.

Ich möchte mich bei allen Mitarbeitern der Arbeitsgruppen Bauer und Kipp in Kiel und der Arbeitsgruppe Aeschlimann in Kaiserslautern herzlich bedanken! Ich fand bei Euch ein sehr gutes Arbeitsklima, Hilfsbereitschaft und auch die manches Mal nötige unwissenschaftliche Zerstreung. Es hat immer Spaß gemacht in so guten Teams mitarbeiten zu können. Einigen von Euch muss ich allerdings in besonderem Maße danken:

Mein ganz besondere Dank gilt Dr. Oleksiy Andreyev, der mit mir den Umzug von Kaiserslautern in den hohen Norden vollzogen hat. Ohne ihn wäre die UHV Kammer sicher nicht wieder so schnell in Betrieb gegangen. Außerdem waren seine unermüdlichen Erklärungen zu den Besonderheiten des CSA - kurz sein reichhaltiger Erfahrungsschatz bezüglich dieses Systems - unersetzlich. Ich werde mich wohl immer wehmütig an die nette Zusammenarbeit und spirituelle Weiterentwicklung mit dir zurückerinnern wenn ich "das Radio mit den besten dunklen Liedern" höre. ☺

Stephan „Stigi“ Hilgenfeld - welcher sein Stahlherz im Rahmen seiner Diplomarbeit einzusetzen wusste - steuerte oft die fehlenden 1.21 GW zum Experiment bei. Selten traf ich einen so distinktierten Filmkenner der nicht nur weiß wie man den „Rös'chenhof“ korrekt schreibt, sondern auch stets die feine Linie zwischen Schad-, Nutz- und Problembären zu ziehen vermag. Auch teilten wir - was in langen Messnächten unabdingbar ist - einen kompatiblen Musikgeschmack (hier sei ChroniX Aggression danksam erwähnt) der auch vor der tiefen Verbundenheit mit den autobiographischen Hymnen des Peter M. und Doros hymnischen Hymnen nicht zurückschreckt. Ohne Dich werden Messungen begleitet von den Sub Dubs und John C. nicht mehr so sein. Danke für die gute Zusammenarbeit bei der Erforschung unseres Lieblings-TMDCs TiSe_2 ! Ich werde für den Fall, dass sich unsere Wege in Zukunft erneut kreuzen mögen, immer eine Flasche Blumenkohl bereithalten.

Ankatrin Stange muss im Grunde Stephan und mir danken für die geduldige - und sehr ausgiebige - Einführung in die Welt des Kinos (und des Rös'chenhofs) ☺. Wir hatten

nicht nur eine sehr erfolgreiche, sondern auch sehr angenehme und spaßige Messzeit zusammen. Hoffentlich haben die langen Nächte mit den Verrückten keine allzu großen Wunden gerissen.

Ich möchte Stefan Mathias und dem gesamten „Kammer 4“-Team in Kaiserslautern für die Möglichkeit der Messung der in dieser Arbeit präsentierten ARPES Daten danken. Es macht immer wieder Spaß mit Euch zu messen! Man lernt doch so viel mehr mit dem 2D System.

Meinem lieben Kollegen Nils Heinemann danke ich für die gute Zusammenarbeit im „kleinen Labor“ insbesondere auch bei den viel zu seltenen gemeinsamen Messungen. Ganz besonders werde ich ihn als Büromitbewohner vermissen! Immer wenn Du mal wieder nichts an Deinem Rechner gemacht hast, kannst Du mich gerne anrufen.

Besonderer Dank gilt Stefan Hellmann und Christian Sohr, mit welchen ich nicht nur sehr angenehme Messnächte an der HHG Quelle verbringen durfte, sondern auch reichhaltige Diskussionen um die Welt der TMDCs führen konnte. Stefan hat mich überdies von der Benutzung der Software „IGOR“ überzeugt, welche mir sehr gute Dienste im Rahmen der Auswertung leistete - ihm sei somit sein Mac verziehen. Christian half mir nicht nur das Nebenfachpraktikum zu überstehen, sondern war auch ein ausgesprochen angenehmer Reisepartner auf der abenteuerlichen USD 7.

Herrn Prof. Dr. Eckhard Pehlke möchte ich ganz besonders dafür danken, dass er sich die Zeit nahm eine schon einige Jahre zurückliegende Veröffentlichung seiner Arbeitsgruppe mit mir zu besprechen. Er konnte mir wertvolle Informationen geben und mein Verständnis der Problematik entscheidend verbessern. Vielen Dank!

Joost Jakobs stand mir als Techniker immer hilfreich zur Seite und hat viel zur guten und sicheren Laborausstattung beigetragen. Auch teilt er meine Begeisterung für die Filmkunst, was uns die seltene aber oft nötige Zerstreuung in Filmabenden und „Kinoschnack“ erlaubte.

Erwin Brix hat mir nicht nur als Vermittler zu diversen Paketdiensten sehr geholfen, sondern hat auch immer ein Brötchen oder Huhn griffbereit 😊. Vielen Dank für die vielen schönen Mittagspausen mit Dir und Joost! Wenn es mich mal wieder nach Kiel verschlägt, komme ich mit einem Brathuhn vorbei.

Manfred Stiller hat mehr als nur einmal den Messbetrieb durch schnelle und unkomplizierte Hilfe gerettet wenn einer der zahlreichen Controller plötzlich und unergründlich beschloss, dass das bekannte Funktionalität irgendwie langweilig ist. Vielen Dank dafür, dass Du uns oft vor wochenlangen Reparaturzeiten bewahrt hast!

Ich möchte Wilfried Krüger aus der Arbeitsgruppe von Herrn Prof. Dr. Lutz Kipp herzlich danken für die Zucht der im Rahmen dieser Arbeit verwendeten Kristalle.

Richard Walther hat mir schon oft zu Zeiten meiner Diplomarbeit bei Problemen mit der Elektronik geholfen. Insbesondere hat er einige der TAR-2PPE Experimente dieser Arbeit durch schnelle Reparatur des HSA Netzteils gerettet und dadurch einen vorzeitigen Abbruch der gesamten Messzeit verhindert.

Felix Steeb war die „gute Seele“ von Laser 2 in Kaiserslautern. Er hat mir sehr geholfen,

dieses recht eigenwillige System in den Griff zu bekommen. Auch war er Retter in der Not als er via Mobiltelefon auf der Hochalm sitzend den Laser quasi fernmündlich justierte. Außerdem habe ich immer sehr gerne mit Dir zusammen gemessen. Tja-ja ...

Daniel Steil danke ich für seine kritische Hilfe. Er scheint tiefe Eindrücke, gar Wunden erhalten zu haben, da er mir zur Errettung meiner geistigen Gesundheit ein Katharsis-Bunny zur Seite stellte. Überhaupt hat sich Daniel in großem Maße um den Erhalt eines Restes geistiger Gesundheit hoch verdient gemacht - Bwaaaaaaaaaaaaah!

Ich danke meiner Familie, meinen Eltern Rita und Friedrich für die fortwährende Unterstützung danken. Besonders danke ich meiner Schwester Kathrin für die selbstlose Überlassung ihres Notebooks.

Ich danke Timm Rohwer.

Die besondere Ehre des Letzgenannten kann nur Paul Metternich, seines Zeichens einer der größten Schafszüchter Deutschlands, zufallen, da nur eine Person von seinem Format diese auszufüllen weiß. Du konntest mich immer wieder auf's neue mit Deinen unkonventionellen Ideen motivieren - ich verdanke Dir außerdem tiefe Einblicke in das deutsche Patent- und Markenrecht. Das versprochene Fest zum Abschluß dieses Promotionsverfahrens war mir gerade in den dunkelsten Stunden ein Hoffnungsschimmer der mich weitermachen ließ.

Vielen Dank!

Curriculum Vitæ

Persönliche Daten

Name: Martin Wiesenmayer
Anschrift: Papiermühlstraße 14
67655 Kaiserslautern
Geburtsdatum/-ort: 08.09.1980 in Dernbach (Westerwald)
Staatsangehörigkeit: deutsch
Familienstand: ledig

Schulbildung

08/1987–07/1991 Grundschule, Joseph-Kehrein-Schule Montabaur
08/1991–07/1997 Anne-Frank Realschule Montabaur, Mittlere Reife
08/1997–07/2000 gymnasiale Oberstufe, Mons-Tabor-Gymnasium Montabaur,
Leistungsfächer: Mathematik, Physik
06/2000 Allgemeine Hochschulreife

Studium

10/2000–09/2007 Studium der Physik an der TU Kaiserslautern, Vertiefungsrichtung
Experimentalphysik, Nebenfach Informatik
06/2005–06/2006 Diplomarbeit mit dem Titel: „Adsorption von Cäsium auf Quanten-
trogssystemen - Spektroskopie und Zerfallsdynamik“, Auszeichnung:
Preis der Kreissparkassen-Stiftung (08/2007), Zuerkennung des
akademischen Grades Diplom-Physiker

Promotion

seit 06/2006 Promotion, Betreuung durch Prof. Dr. Michael Bauer
07/2006–06/2007 Stipendium der TU Kaiserslautern zum Zwecke der Förderung zur
Erlangung einer Promotion
12/2006 Fortführung der an der TU Kaiserslautern begonnenen Promotion
an der Christian-Albrechts-Universität zu Kiel
07/2007–06/2011 wissenschaftlicher Mitarbeiter der Christian-Albrechts-Universität
zu Kiel

07/2011–heute

wissenschaftlicher Mitarbeiter der Technischen Universität Kaiserslautern

Kaiserslautern, 2012

Eidesstattliche Erklärung

Hiermit erkläre ich an Eides statt, dass ich diese Arbeit selbständig unter der Beratung meiner wissenschaftlichen Lehrer und nur mit den angegebenen Hilfsmitteln erstellt sowie die Regeln guter wissenschaftlicher Praxis der Deutschen Forschungsgemeinschaft eingehalten habe. Diese Arbeit wurde weder ganz noch in Teilen an anderer Stelle im Rahmen eines Prüfungsverfahrens vorgelegt. Frühere Promotionsversuche wurden von mir nicht unternommen.

Kapitel 4 basiert auf einer Veröffentlichung in *Physical Review B* **82**, 035422, in 2010 durch Wiesenmayer et al. Der Ausblick in Kapitel 7 nimmt Bezug auf unsere Veröffentlichung in *Nature* **471**, 490–493 in 2011 durch Rohwer et al.

Kiel, den

Martin Wiesenmayer